Springer Proceedings in Mathematics & Statistics

Jan Awrejcewicz *Editor*

Dynamical Systems: Modelling

Łódź, Poland, December 7–10, 2015

Springer

Springer Proceedings in Mathematics & Statistics

Volume 181

Springer Proceedings in Mathematics & Statistics

This book series features volumes composed of selected contributions from workshops and conferences in all areas of current research in mathematics and statistics, including operation research and optimization. In addition to an overall evaluation of the interest, scientific quality, and timeliness of each proposal at the hands of the publisher, individual contributions are all refereed to the high quality standards of leading journals in the field. Thus, this series provides the research community with well-edited, authoritative reports on developments in the most exciting areas of mathematical and statistical research today.

More information about this series at http://www.springer.com/series/10533

Jan Awrejcewicz
Editor

Dynamical Systems: Modelling

Łódź, Poland, December 7–10, 2015

Springer

Editor
Jan Awrejcewicz
Department of Automation, Biomechanics
and Mechatronics
Łódź University of Technology
Łódź
Poland

ISSN 2194-1009 ISSN 2194-1017 (electronic)
Springer Proceedings in Mathematics & Statistics
ISBN 978-3-319-42401-9 ISBN 978-3-319-42402-6 (eBook)
DOI 10.1007/978-3-319-42402-6

Library of Congress Control Number: 2016939062

Mathematics Subject Classification (2010): 82-xx, 37-xx, 70-xx, 74-xx

Printed on acid-free paper

This Springer imprint is published by Springer Nature
The registered company is Springer International Publishing AG Switzerland

Preface

It is well known that dynamic phenomena dominate in nature and real-world applications, and that static behaviour can be treated as a particular case of dynamics. Analysis of dynamics can be performed in theoretical, numerical and analytical ways or through experimental observations. This universality of the term of dynamical systems becomes the driving force to make it possible for scientists and researchers from different fields to meet in one place and share results of their investigations. In this book, we provide a part of the results presented during the 13th edition of the conference series devoted to dynamical systems that took place in Lodz (Poland) in December 2015. The comprised research allows to exchange ideas from different branches of theoretical and applied sciences, including not only applied mathematics, physics and mechanics, but also mechatronics, electrical engineering, biomechanics and others.

In Chap. "On Dynamic Behavior of a Nonideal Torsional Machine Suspension Structure", a mathematical model of a nonideal torsional machine suspension structure has been proposed. Natural frequencies of vibrations and the associated modes have been computed. In addition, regions of stability, instability and chaos have been reported.

Babich et al. (Chap. "Structural Probabilistic Modeling of Fatigue Fracture for Piezoceramic Materials Under Cyclic Loading") have developed a structural approach aimed at construction of a statistical criterion of static and fatigue failure for transversely isotropic piezoelectric materials. Daniel's structural model of micro-cracks accumulation as well as the statical criterion has been employed to study fatigue failure under cyclic loading. The research includes derivation of constitutive equations for a damaged material, the fracture criterion and the distribution of micro-damage load. The applied approach has allowed to estimate the residual ultimate strength of the material and the conditional fatigue limit.

In Chap. "Numerical Analysis of Child Restraint System Equipped with Built-in Belts Pretensioner During Frontal Impact", a practical modelling methodology has been proposed regarding the child restraint system equipped with built-in belts

pretensioner during a frontal impact. The effectiveness of the proposed solution has been validated through numerical and experimental tests.

Barros et al. have studied dynamic behaviour of a metallic steel tower supporting a radar antenna, taking into account wind and seismic action (Chap. "Analysis of the Dynamic Behavior of a Radar Tower"). The control of tower vibrations by design and installation of tuned liquid dampers near the top of the radar tower has been also proposed.

Chapter "Determination of the Fatigue Life on the Basis of Fatigue Test and FEM for EN-MCMgY4RE3Zr with Rare Earth Elements" deals with both experimental and numerical investigations of the fatigue wear of an alloy with rare earth elements. Effects of appearance of fatigue cracks based on the alloy composition, morphology and structure have been studied both numerically and experimentally.

Biesiacki et al. have studied dynamic forces in a human upper limb in a forward fall (Chap. "Modelling of Forward Fall on Outstretched Hands as a System with Ground Contact"), putting emphasis on the usually neglected inertia forces. A simplified mechanical model of the human body biokinematic chain has been constructed and then numerically validated.

Chapter "Micelle Confined in Aqueous Environment: Lubrication at the Nanoscale and Its Nonlinear Characteristics" presents simulation results of the constant pressure molecular dynamics of a micelle confined between the surfaces in an aqueous environment. The carried-out analysis yielded an insight into lubrication at the nanoscale of an articulating system.

Chapter "The Sensitivity Analysis of the Method for Identification of Bearing Dynamic Coefficients" is aimed at the sensitivity analysis of the method for identification of bearing dynamic coefficients. The excitation signals and the corresponding system responses have been employed to determine the mass, damping and stiffness coefficients using the impulse excitation technique.

In Chap. "Investigations of Composite Panels Mounted in the Cargo Space of a Freight Wagon", investigations on composite panels mounted in the cargo space of a freight wagon have been carried out. The stress/displacement has been measured in the characteristic points of the side wall of a wagon using the displacement tensors and templates for gap measuring.

Principles of construction of a laboratory stand for vibration testing of a freight wagon have been given in Chap. "Project of Laboratory Stand, and Preliminary Studies of Vibration Shell Freight Wagon". The employed measuring system consists of a drive unit with a freight wagon, a control unit with an inverter and the programmable PLC. In particular, the control panel has been applied to perform long-term studies by means of termination of the number of crossing between gates.

Chapter "Analysis of Dynamical Response of the Freight Wagon" presents the CAD model of a freight wagon as well as its model analysis before and after implementation of new composite materials. Measurements of vibrations have been conducted using piezoelectric foils. The carried-out research is aimed at modernisation of freight wagons during their periodic repairs.

A numerical procedure for the generalisation of sets of synthetic acceleration time histories compatible with an assigned target spectrum has been implemented by Carli and Corina (Chap. "Evolutionary Model for Synthetic Spectrum Compatible Accelerograms"). Both energy distribution in time and contemporary variability of the frequency content have been taken into account.

Christov et al. have performed a parametric study of mixing in a granular flow a bi-axial spherical tumbler in Chap. "A Parametric Study of Mixing in a Granular Flow a Biaxial Spherical Tumbler". The symmetric case has been considered in which the flowing layer depth is the same for each rotation. It has been shown that most choices of angles and most shells (concentric spheroids) throughout the tumbler volume mix well, although there also exist examples of pathological mixing.

Numerical simulation of abrasive wear using the FEM-SPH hybrid approach has been carried out in Chap. "Numerical Simulation of Abrasive Wear Using FEM—SPH Hybrid Approach". The analysis is aimed at the dynamic interaction of counter surface with lining samples rotating with an angular speed. The global model is studied using the finite elements method (FEM), whereas abrasive wear is modelled via the smooth particle hydrodynamics (SPH). In addition, thermal–mechanical coupling and heat generation by friction forces are also included in the modelling process and analysis.

Chapter "A Mathematical Model for Robot-Indenter" presents a study of a dual-arm robot manipulator for executing medical procedures. The investigations take into account torques produced by manipulator motors as well as friction and contact interactions. The applied control aims at obtaining the required indentation of the sensor head into a soft tissue under a few introduced restrictions.

Chapter "A Docking Maneuver Scenario of a Servicing Satellite—Quaternion-Based Dynamics and Control Design" presents a quaternion-based dynamics and control design for a servicing satellite approaching a client satellite. The presented model consists of reaction wheels, thrusters, a drift caused by solar radiation and atmosphere. The novelty of the research is illustrated by a simulation example regarding orbit navigation, attitude control and direct satellite approaching.

The experimental study of the nonlinear dynamics of a vibration harvest-absorber system is presented in Chap. "Nonlinear Dynamics of a Vibration Harvest-Absorber System. Experimental Study". In particular, an induced (with added harvester device) main resonance region has been detected. The influence of the excitation frequency and resistance load on the system dynamics is investigated as well as the mathematical model of the magnetic levitating force has been proposed.

In Chap. "Three-Chamber Model of Human Vascular System for Explanation the Quasi-Regular and Chaotic Dynamics of the Blood Pressure and Flow Oscillations", the arterial blood pressure and flow curves exhibiting quasi-regular and chaotic dynamics have been analysed. It has been found that the quasi-regular dynamics, consisting of different patient-specific patterns of the attractor, correspond to variations of the material parameters within the physiological limits. On

the other hand, it has been detected that the chaotic dynamics appears when wall compliance and/or resistivity of the chamber is too high.

The control study for a vibratory robot modelled by a rigid box with a pendulum enclosed inside has been proposed in Chap. "Maximization of Average Velocity of Vibratory Robot (with One Restriction on Acceleration)". It is assumed that the robot moves forward and backward, and the Coulomb friction is taken into account. It has been demonstrated how the proposed control not only provides motion within the constraints and limitations, but also maximises average robot velocity.

Asymptotic solution to the problems of convective diffusion around the cylinder streamline cross-flow of fluid at low Reynolds numbers has been proposed in Chap. "Asymptotic Solution of the Problem to a Convective Diffusion Equation with a Chemical Reaction Around a Cylinder". The leading terms of the asymptotic solution around the cylinder are constructed employing the method of matched asymptotic expansions.

In Chap. "Assessment of Eigenfrequencies of the Middle Ear Oscillating System: Effect of the Cartilage Transplant", the finite element models of the intact middle ear and a diseased one with eardrums subjected to retractions in the posterosuperior quadrant have been presented. The geometric model of the middle ear consisting of the eardrums, malleus, incus and stapes has been yielded by the tomographic data. The optimal thickness of the cartilage transplant is chosen in a way that the natural frequencies of the reconstructed middle ear are close to the natural middle ear frequencies.

Chapter "The Method of Modeling Human Skeletons Multi-Body System" is devoted to the modification of multi-body system aimed at force and moment modelling for a lower limb exoskeleton design. The introduced modelling of a human skeleton consists of stiff branches (bones) accompanied by flexible and rotatable modes (joints).

It is shown in Chap. "Fragility Estimation and Comparison Using IDA and Simplified Macro-Modeling of In-Plane Shear in Old Masonry Walls" how the fragility function estimation combined with dynamic structural analysis yields an estimation of the magnitude of historical seismic events relying on the behaviour and damage in real historical structures. The employed type of identification strategy resulted in incremental dynamic analysis and efficient fragility function.

An analytical model of the dynamic characteristics of the test system has been proposed in Chap. "Analytical Model of Dynamic Behaviour of Fatigue Test Stand—Description and Experimental Validation". The test system modelled by one and two degrees-of-freedom systems has been applied for fatigue life determination of structural materials by using bending moment resulting from inertia forces.

The methods aimed at safety estimation of buildings subjected to dynamic loads have been presented in Chap. "Assessment of Modal Parameters of a Building Structure Model". Results of the finite element modelling of the column-beam-plate systems has been compared with laboratory tests.

A model of bus dynamics as a tool of energy consumption estimation has been proposed in Chap. "Simplified Model of City Bus Dynamics as a Tool of an Energy Consumption Estimation". Measured average fuel consumption, maximum vehicle

speed and time acceleration have been used as the reference parameters and then been employed to tune the simulation model.

Chapter "Modeling of Buildings Behavior Under Blast Load" concerns the modelling of the behaviour of buildings of reinforced concrete structures under a blast load. The material model has been verified using the beam and deep beam under dynamic loadings. Two types of buildings have been investigated: (i) slabs-column type of structure; (ii) walls type of structure. Displacements as well as the stress–strain states have been computed.

Measurement of the force strike of an athlete who perform competitively combat sports has been reported in Chap. "Force Effect of Strike and the Possibility of Causing a Skull Fracture of a Human Head". Then, the results regarding injuries of a human head caused by impacts of various kinds have been given.

In Chap. "Hydraulically Driven Unit Converting Rotational Motion into Linear One" a unit converting linear motion into linear one, consisting of a stepper motor causing fluid flow through a driving and executive actuators, has been designed and tested. The simulation results conclude very high stiffness and precision of the system, regardless of the applied load.

In Chap. "The Recognition of Human by the Dynamic Determinants of the Gait with Use of ANN", a human recognition method based on dynamic parameters of the human gait is presented. In the method development, artificial neural network algorithm has been employed. All gait parameters have been calculated on a basis of examination of fifteen people with different gait characteristics. Three configurations of the input data have been investigated.

Chapter "Optimization of Micro-Jet Selective Cooling After Low Alloy Steel Welding" is aimed at optimisation of micro-jet dynamical systems cooling after steel welding. The employed method yields very good mechanical properties of low-alloy steel with various micro-jet gases. The developed dynamical systems of micro-jest cooling can find numerous applications in the automotive industry.

Modelling of thermoplastic processes in FEM environment based on experimental results has been employed in Chap. "Modelling of Thermoelectric Processes in FEM Environment Based on Experimental Studies". The modelling process consists of geometry design, sensitivity analysis focused on solver settings discretisation level and their impact on the results. The research output yields the Peltier modulus FE models database to be directly applied in the energy production industry.

Chapter "The Modeling of Nonlinear Rotational Vibration in Periodic Medium with Infinite Number of Degrees of Freedom" is focused on modelling of nonlinear rotational vibration in periodic medium with infinite number of degrees of freedom. In the case of the physical atmospheric phenomena, the hypothetical plates are implemented by electrically charged plates of ice crystals. The author has developed a continuous nonlinear vibration model of the considered medium.

In Chap. "Numerical Model of Femur Part", the authors have developed a numerical model of a femur part using the finite element method. The femur part has been treated as a complex structure composed of a tubercular bone (internal part) and a cordial bone (external part). Similar load boundary conditions including

muscles forces and external moments have been applied. The carried-out research resulted in numerous conclusions regarding the influence of a material/geometric properties and units on a direct application of the employed method in clinical biomechanics.

Chapter "FEA-Based Design of Experiment for the Damping Determination of Thermoplastic-Rubber Compounds" aims at a FEA-based design of an experiment for the damping deformation of thermoplastic-rubber compounds. In the case of different testing conditions, the average strain energy has been estimated numerically since it cannot be directly measured. As an example, cyclic tension and free decay of cantilever beams have been experimentally analysed and numerically validated.

The so far presented and briefly described research results included in this book illustrate the importance of the development of dynamical systems in both theoretical and experimental aspects.

Finally, it has to be mentioned that I do greatly appreciate the help of the Scientific Committee members of the *Dynamical Systems-Theory and Applications* conference, who took part in the review procedure of this book. I would like to also thank the Springer Editor, Dr. Elizabeth Leow, for her support and fruitful collaboration in finalising this book as well as to thank all the referees for their time and help with ensuring that this manuscript is as good as possible.

Łódź, Poland Jan Awrejcewicz

Contents

On Dynamic Behavior of a Nonideal Torsional Machine Suspension Structure

G. Füsun Alışverişçi, Hüseyin Bayıroğlu, José Manoel Balthazar, Jorge Luis Palacios Felix and Reyolando Manoel Lopes Rebello da Fonseca Brasil

Abstract We propose a mathematical model of a suspension, which is comprised of a bar, supposedly rigid, torsion spring, and an electric motor that turns the system due to the touch of a rotating mass, this mechanism has three DOF. The problem was modeled using Lagrange's equations. Subsequently, we calculated the natural frequencies of the system and find the linear normal modes of vibration. Due to the rotating mass of the engine's torque that was addressed in being constant, optimum engine, and also, is not constant, which is not ideal engine. Thus, we checked the stability of the system and hence, it was determined as a region of stability, where parameters were determined for numerical simulation using MATLAB® and MATHEMATİCA software. The concept of nonlinear normal modes (NNMs) was introduced with the aim of providing a rigorous generalization of normal modes to nonlinear systems. Initially, NNMs were defined as periodic solutions of the underlying conservative system, and continuation algorithms were recently exploited to compute them. We use nonlinear normal modes but before a nonideal analysis to obtain chaos, instability, and so on.

G. Füsun Alışverişçi (✉) · H. Bayıroğlu
Yıldız Technical University, Istanbul, Turkey
e-mail: gfusun@yahoo.com.tr

H. Bayıroğlu
e-mail: hbayir@yildiz.edu.tr

J.M. Balthazar
ITA, Rio Claro, Brazil
e-mail: jmbaltha@gmail.com

J.L.P. Felix
UNIPAMPA, RS, SP, Alegrette, Brazil
e-mail: Jorge.felix@unipanpa.edu.br

R.M.L.R. da Fonseca Brasil
Universidade Federal do ABC UFABC, Santo André, Brazil
e-mail: reyolado.brasil@gmail.com

J. Awrejcewicz (ed.), *Dynamical Systems: Modelling*, Springer Proceedings in Mathematics & Statistics 181, DOI 10.1007/978-3-319-42402-6_1

Table 1 Numerical analysis of the system is performed using the following data

k_1 N/m	k_2 N/m	l_1 m	l_2 m	l_3 m	$m_{0\ \mathrm{kg}}$	$m_{1\ \mathrm{kg}}$	J kg m^2	g m/s	ω_1 rad/s	ω_2 rad/s
2000	1500	0.5	0.4	0.3	0.1	10	2	9.81	16.37	21.14

1 Introduction

Nonlinear normal vibration modes (NNMs) are a generalization of the normal vibrations in linear systems. In the normal vibration mode, a finite degree-of-freedom system vibrates like a single-degree-of-freedom conservative one. The damping is large or represented by nonlinear functions then the response of the system may depend not only on the displacement but also on velocities Rosenberg and Vakakis [2, 4, 5]. Shaw and Pierre reformulated the concept of nonlinear normal modes for a general class of nonlinear dissipative systems [3]. In this paper, we characterized the dynamic behavior of a nonideal torsional machine suspension structure. We use nonlinear normal modes but before a nonideal analysis to obtain chaos, instability, and so on. We use the invariant manifold approach for NNMs technic. Such a manifold is invariant under the flow (i.e., orbits that start out in the manifold remain in it for all time), which extends the invariance property of LNMs to nonlinear systems. In order to parameterize the manifold, a single pair of states variables (i.e., both the displacement and the velocity) is chosen as master coordinates, the remaining variables being functionally related to the chosen pair. Therefore, the system behaves likes a nonlinear single-degree-of-freedom system on the manifold [1] (Table 1).

2 Governing Equations

The equation of motion may be obtained using Lagrange's equations

$$\frac{d}{dt}\left(\frac{\partial T}{\partial \dot{q}_i}\right) - \frac{\partial T}{\partial q_i} + \frac{\partial U}{\partial q_i} = Q_i \tag{1}$$

Here, T is the kinetic energy, U is the potential energy, Q is the generalized force. They are given by

$$\begin{aligned} T = {} & \frac{1}{2}(m_0 + m_1)\dot{x}_C^2 + \frac{1}{2}m_0 l_3^2 \dot{\theta}^2 + \frac{1}{2}m_0 r^2 \dot{\varphi}^2 + m_0 r l_3 \dot{\theta}\dot{\varphi}\sin\varphi \\ & + m_0(-l_3\dot{\theta}\sin\theta + r\,\dot{\varphi}\cos\varphi)\dot{x}_C + \frac{1}{2}J\dot{\theta}^2 + \frac{1}{2}J_O\dot{\varphi}^2 \end{aligned} \tag{2}$$

$$U = \frac{1}{2}(k_1 + k_2)x_C^2 + \frac{1}{2}(k_1 l_1^2 + k_2 l_2^2)\sin^2\theta - (k_1 l_1 - k_2 l_2)x_C \sin\theta + m_0 g\, r\sin(\varphi + \theta) \tag{3}$$

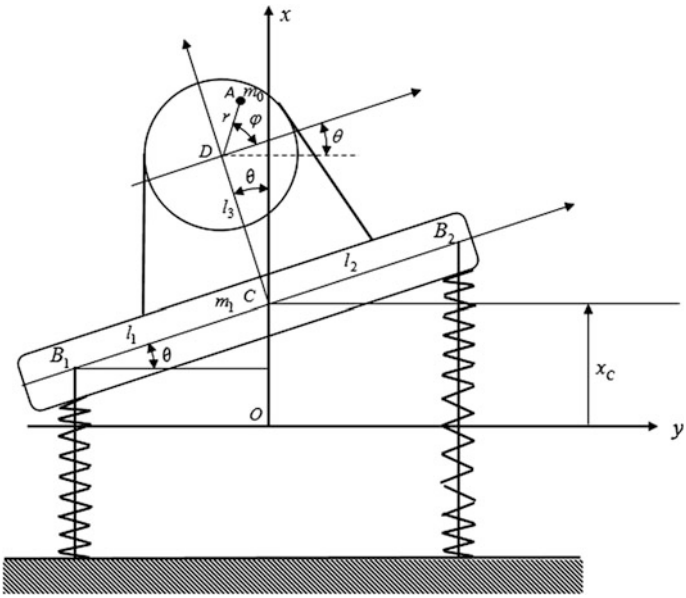

Fig. 1 Model of the nonideal torsional machine

$$Q_1 = 0, \quad Q_2 = 0, \quad Q_3 = M(\dot{\varphi}) = a - b\,\dot{\varphi}, \tag{4}$$

where $x = 0$ is the equilibrium level, the constants k_1 and k_2 are the elastic coefficients of the springs, g is acceleration due to gravity, m_0 is the unbalanced mass, m_1 is the mass of the system (see Fig. 1), r is the eccentricity of the unbalanced mass, φ is the angle of the rotation of the shaft carrying unbalanced mass, θ is the angle of the rotation of the system, J is the inertial moment of the system about mass center, J_0 is the inertial moment of the rotating part in the motor, x_C is the position of mass center of the system, and q_i is the generalized coordinates. Lagrange's equation of motion for the coordinates $q_1 = x_C$, $q_2 = \theta$, and $q_3 = \varphi$ can be written as

$$(m_0 + m_1)\ddot{x}_C + (k_1 + k_2)x_C + m_0(-l_3\dot{\theta}\sin\theta - l_3\theta^2\cos\theta + r\,\ddot{\varphi}\cos\varphi - r\,\dot{\varphi}^2\sin\varphi) - (k_1 l_1 - k_2 l_2)\sin\theta = 0 \tag{5}$$

$$(J + m_0 l_3^2)\ddot{\theta} + m_0 r l_3 \ddot{\varphi}\sin\varphi + m_0 r l_3 \dot{\varphi}^2\cos\varphi - m_0 l_3 \ddot{x}_C \sin\theta + (k_1 l_1^2 + k_2 l_2^2)\sin\theta\cos\theta - (k_1 l_1 - k_2 l_2)x_C\cos\theta = 0 \tag{6}$$

$$(J_O + m_0 r^2)\ddot{\varphi} + m_0 r L_3 \dot{\theta}\sin\varphi + m_0 r\,\cos\varphi\ddot{x}_C + m_0 g\,r\cos\varphi = M(\dot{\varphi}) \tag{7}$$

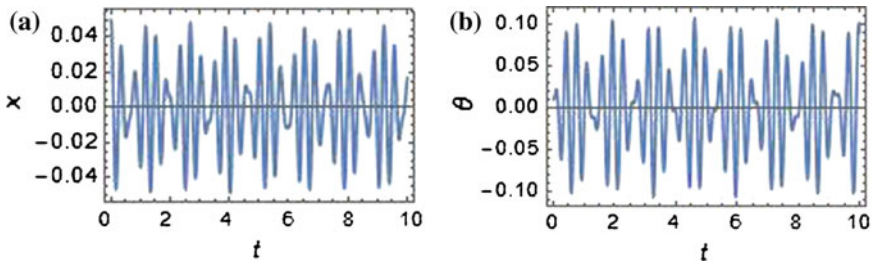

Fig. 2 Time histories in physical coordinates for nonideal system, (**a**) vertical displacement (**b**) angular displacement

Note that in Eqs. (5), (6), and (7), θ is smaller than φ, in this case, takes the forms of $\sin(\varphi+\theta)=\sin\varphi$, $\cos(\varphi+\theta)=\cos\varphi$.

Figure 2 is obtained using Eqs. (5), (6), and (7). This figure shows time histories in physical coordinates (x,t) and (θ,t) for nonideal system. Time histories of x and θ generated for initial conditions $x(0)=0.05$ m, $\dot{x}(0)=0$, $\theta(0)=0.01$ rad., $\dot{\theta}(0)=0$, $\varphi(0)=0$, $\dot{\varphi}(0)=0$ are presented in Fig. 2a, b.

Figure 3 shows a representative bifurcation diagram and the variation of the corresponding Lyapunov exponent. Both curves are obtained by solving numerically from Eqs. (5), (6), and (7).

If $\sin\theta$ and $\cos\theta$ are expanding Taylor series and getting three terms in Eqs. (5) and (6) we get,

$$\ddot{x}(m_0+m_1)+x(k_1+k_2)+\theta(-k_1l_1+k_2l_2)+\frac{1}{6}\theta^3(k_1l_1-k_2l_2)+\frac{1}{6}rt\omega^3\left(-6+t^2\omega^2\right)m_0 + \frac{1}{6}\theta\left(-6+\theta^2\right)\ddot{\theta}l_3m_0-l_3m_0\dot{\theta}^2+\frac{1}{2}\theta^2l_3m_0\dot{\theta}^2=0 \tag{8}$$

$$\left(J+l_3^2m_0\right)\ddot{\theta}+\left(k_1l_1^2+k_2l_2^2\right)\theta+(-k_1l_1+k_2l_2)x+\frac{1}{2}x\theta^2(k_1l_1-k_2l_2)-\frac{2}{3}\theta^3\left(k_1l_1^2+k_2l_2^2\right) - \frac{1}{2}r\omega^2\left(-2+t^2\omega^2\right)l_3m_0+\frac{1}{6}\theta\left(-6+\theta^2\right)l_3m_0\ddot{x}=0 \tag{9}$$

$$kx+m\ddot{x}-q_1\theta+\frac{1}{6}\theta\left(-6+\theta^2\right)\ddot{\theta}l_3+\frac{\theta^3q_1}{6}-l_3\theta^2+\frac{1}{2}l_3\theta^2=0 \tag{10}$$

$$J_1\ddot{\theta}+q_2\theta-q_1x+r\omega^2l_3+\frac{1}{6}\theta\left(-6+\theta^2\right)l_3\ddot{x}+\frac{1}{2}x\theta^2q_1-\frac{2\theta^3q_2}{3}=0, \tag{11}$$

where

$$m=m_0+m_1,\ k=k_1+k_2,\ J_1=J+l_3^2m_0,\ q_1=k_1l_1-k_2l_2,\ q_2=k_1l_1^2+k_2l_2^2,\ q_3=l_3m_0 \tag{12}$$

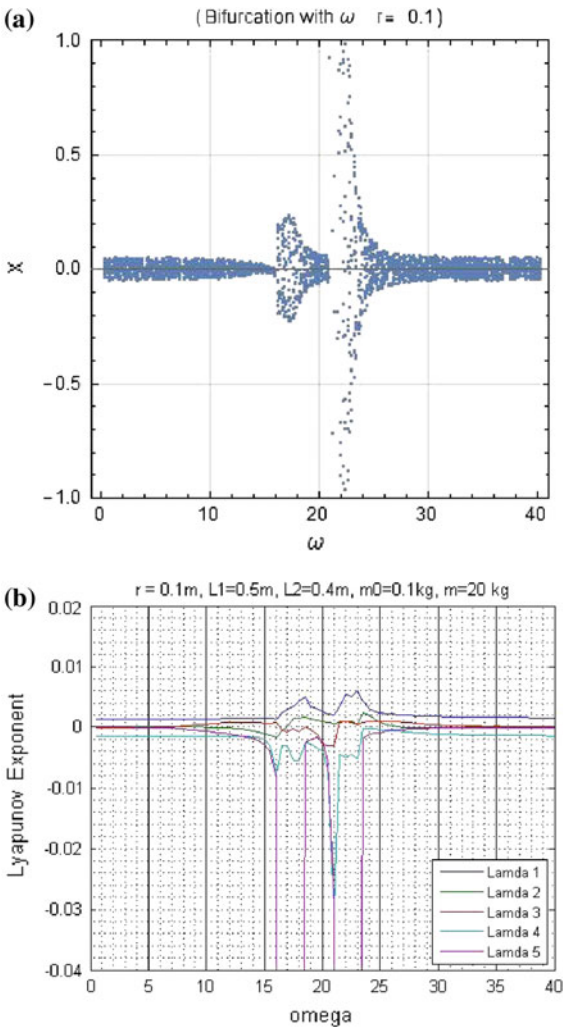

Fig. 3 (**a**) Bifurcation diagram and (**b**) Lyapunov exponent

Assuming that nonlinear terms are zero, we get a linear conservative system and natural frequencies as follows:

$$(m_0 + m_1)\,\ddot{x} + (k_1 + k_2)x + (-k_1 l_1 + k_2 l_2)\theta = 0 \tag{13}$$

$$\left(J + l_3^2 m_0\right)\ddot{\theta} + (-k_1 l_1 + k_2 l_2)x + \left(k_1 l_1^2 + k_2 l_2^2\right)\theta = 0 \tag{14}$$

$$m_m = \begin{bmatrix} m_1 + m_0 & 0 \\ 0 & J + l_3^2 m_0 \end{bmatrix}, \quad k_m = \begin{bmatrix} k_1 + k_2 & -k_1 l_1 + k_2 l_2 \\ -k_1 l_1 + k_2 l_2 & (k_1 l_1^2 + k_2 l_2^2) \end{bmatrix}, \tag{15}$$

where m_m is the mass matrix and k_m is the stiffness matrix. Frequency equation is

$$\text{frequency}Eq = \det[k_m - \lambda\, m_m] = det\begin{bmatrix} k_1 + k_2 - \lambda(m_1 + m_0) & -k_1 l_1 + k_2 l_2 \\ -k_1 l_1 + k_2 l_2 & (k_1 l_1^2 + k_2 l_2^2) - \lambda(J + l_3^2 m_0) \end{bmatrix}, \tag{16}$$

where $\lambda = \omega^2$

$$\begin{aligned}\text{frequency}Eq = &-J\lambda k_1 - J\lambda k_2 + k_1 k_2 l_1^2 + 2k_1 k_2 l_1 l_2 + k_1 k_2 l_2^2 + J\lambda^2 m_0 - \lambda k_1 l_1^2 m_0 \\ &- \lambda k_2 l_2^2 m_0 - \lambda k_1 l_3^2 m_0 - \lambda k_2 l_3^2 m_0 + \lambda^2 l_3^2 m_0^2 + J\lambda^2 m_1 - \lambda k_1 l_1^2 m_1 - \lambda k_2 l_2^2 m_1 + \lambda^2 l_3^2 m_0 m_1\end{aligned} \tag{17}$$

$$\begin{aligned}\lambda_{1,2} = &\frac{k_1 L_1^2 + k_2 L_2^2}{J + L_3^2 m_0} + \frac{k_1 + k_2}{m_0 + m_1} \mp \\ &\frac{1}{\left(J + L_3^2 m_0\right)(m_0 + m_1)} \Big[-4k_1 k_2 (L_1 + L_2)^2 \left(J + L_3^2 m_0\right)(m_0 + m_1) + \\ &\left(k_1 \left(J + L_3^2 m_0 + L_1^2 (m_0 + m_1)\right) + k_2 \left(J + L_3^2 m_0 + L_2^2 (m_0 + m_1)\right)\right)^2 \Big]^{1/2}\end{aligned} \tag{18}$$

3 Nonlinear Normal Modes

For the nonlinear normal modes formulations, the set of equations Eqs. (10) and (11) are rewritten in the form [6, 7],

$$\dot{x}_1 = y_1 \qquad \dot{y}_1 = f_1(x_1, y_1, x_2, y_2) \tag{19}$$

$$\dot{x}_2 = y_2 \qquad \dot{y}_2 = f_2(x_1, y_1, x_2, y_2) \tag{20}$$

It can be chosen master coordinates as

$$x_1 = u \qquad y_1 = v \tag{21}$$

It can be expressed slaved coordinates as

$$x_2 = X_2(u, v) \qquad y_2 = Y_2(u, v) \tag{22}$$

The functions $X_2(u, v)$, $Y_2(u, v)$ are constraint equations and they represent, the so-called, model surfaces. It can be used in the invariant manifold technique to eliminate time dependence.

$$Y_2(u, v) = \frac{\partial X_2(u, v)}{\partial u} v + \frac{\partial X_2(u, v)}{\partial v} f_1(u, v, X_2(u, v), Y_2(u, v)) \tag{23}$$

$$f_2(u, v, X_2(u, v), Y_2(u, v)) = \frac{\partial Y_2(u, v)}{\partial u} v + \frac{\partial Y_2(u, v)}{\partial v} f_1(u, v, X_2(u, v), Y_2(u, v)) \tag{24}$$

It can be approximated a local solution using polynomial expansion of X_1 and X_2 in terms of u and v.

$$X_2 = a_1u + a_2v + a_3u^2 + a_4uv + a_5v^2 + a_6u^3 + a_7u^2v + a_8uv^2 + a_9v^3 \tag{25}$$

$$Y_2 = b_1u + b_2v + b_3u^2 + b_4uv + b_5v^2 + b_6u^3 + b_7u^2v + b_8uv^2 + b_9v^3 \tag{26}$$

$$\dot{X}_2 = a_1u' + a_2v' + 2a_3uu' + a_4uv' + a_4u'v + 2a_5vv' + 3a_6u^2u' + 2a_7uu'v + a_7u^2v' + a_8u'v^2 + 2a_8uvv' + 3a_9v^2v' \tag{27}$$

$$\dot{Y}_2 = b_1u' + b_2v' + 2b_3uu' + b_4uv' + b_4u'v + 2b_5vv' + 3b_6u^2u' + 2b_7uu'v + b_7u^2v' + b_8u'v^2 + 2b_8uvv' + 3b_9v^2v' \tag{28}$$

Considering the above expressions, the last two Eqs. (19) and (20), and going back to the original notation, it can be obtained as

$$y_2 = a_1y_1 + a_2f_1 + 2a_3x_1y_1 + a_4x_1f_1 + a_4y_1^2 + 2a_5y_1f_1 + 3a_6x_1^2y_1 + 2a_7x_1y_1^2 + a_7x_1^2f_1 + a_8y_1^3 + 2a_8x_1y_1f_1 + 3a_9y_1^2f_1 + \cdots \tag{29}$$

$$f_2 = b_1y_1 + b_2f_1 + 2b_3x_1y_1 + b_4x_1f_1 + b_4y_1^2 + 2b_5y_1f_1 + 3b_6x_1^2y_1 + 2b_7x_1y_1^2 + b_7x_1^2f_1 + b_8y_1^3 + 2b_8x_1y_1f_1 + 3b_9y_1^2f_1 + \cdots \tag{30}$$

Next, Eqs. (25), (26), (27), and (28) can be substituted into functions $f_1(x_1, y_1, x_2, y_2) = f_1(u, v, X_2(u, v), Y_2(u, v))$, $f_2(x_1, y_1, x_2, y_2) = f_2(u, v, X_2(u, v), Y_2(u, v))$ in Eqs. (31) and (32). From (Eq. 22), we obtain

$$y_2 - \dot{x}_2 = 0 \qquad f_2(x_1, y_1, x_2, y_2) - \dot{y}_2 = 0 \tag{31}$$

Thus, grouping the terms of (Eq. 31) in a proper order with respect to the master coordinates, we receive a set of two equations composed of the terms: u, v, u^2, uv, v^2, u^3, u^2v, uv^2, v^3. Terms of higher order are truncated from the expansions. We get a set of 18 algebraic nonlinear equations with 18 unknown parameters $a_1, \ldots, a_9, b_1, \ldots, b_9$.

mod 1

$$\ddot{u}_1 + 267.972u_1 = -232.0451u_1^3 + 2.4236u_1\dot{u}_1^2 - 4.7685u_1^3\dot{u}_1^2 \tag{32}$$

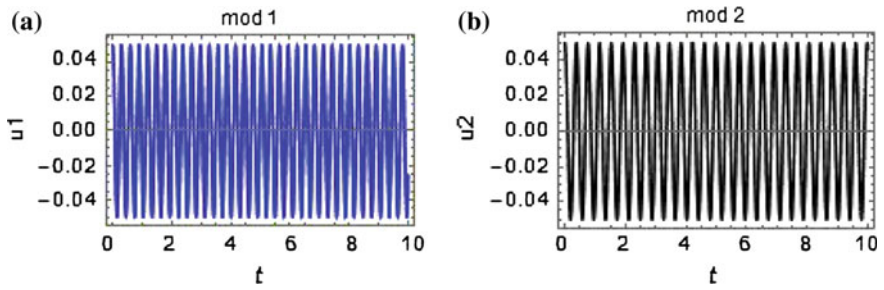

Fig. 4 Time histories in normal coordinates, (**a**) mod1 (**b**) mod2

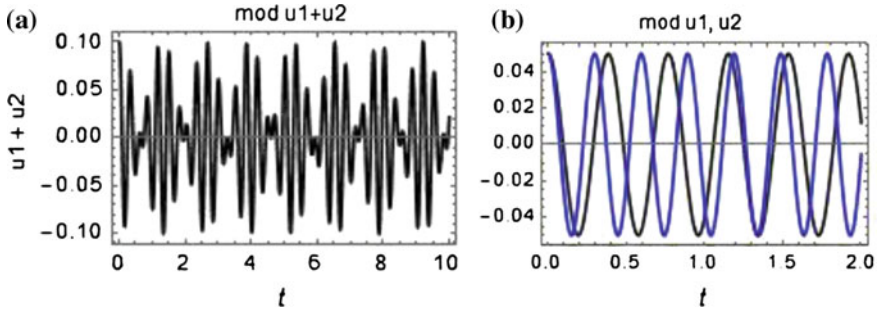

Fig. 5 Time histories in normal coordinates (**a**) mod 1 + mod 2 (**b**) comparison u1 and u2

mod 2

$$\ddot{u}_2 + 446.905u_2 = 268.5671u_2^3 - 3.6076u_2\dot{u}_2^2 + 11.5857u_2^3\dot{u}_2^2 \tag{33}$$

Two extracted normal modes u_1 and u_2 are presented in Figs. 4 and 5. The motion is very well separated.

The slave coordinates x_2, y_2 are related with the master ones u, v by the model functions $X_2(u, v)$, $Y_2(u, v)$. These model surfaces for the first and second modes, respectively, are presented in (Fig. 6).

As a result from the above Fig. 6a, c, the nonlinear model surfaces for angular displacement of the system strongly depend on the displacement but Fig. 6b, d, the nonlinear model surfaces for angular velocity of the system strongly depend both on the displacement and velocity.

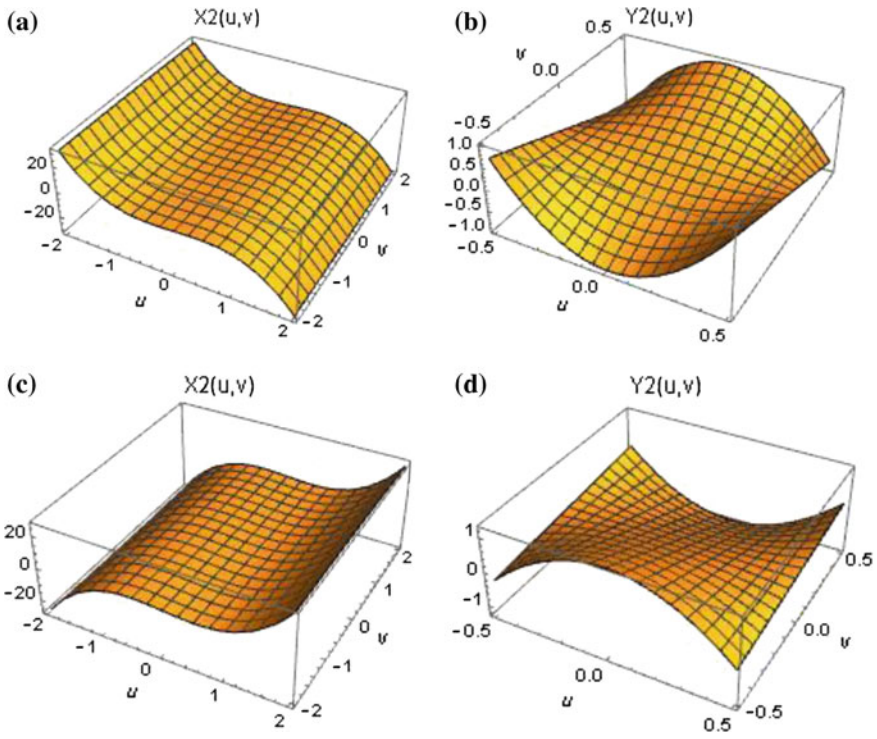

Fig. 6 Nonlinear modal surfaces **a**, **b** mod 1, **c**, **d** mod 2

4 Conclusions

The analysis presented in the paper concerns dynamic behavior of a nonideal torsional machine suspension structure. Initially, NNMs were defined as periodic solutions of the underlying conservative system, and continuation algorithms were recently exploited to compute them. We use nonlinear normal modes but before a nonideal analysis to obtain chaos, instability, and so on. The NNMs are applied to decouple motion of the system.

A width of synchronization regions, near the principal parametric resonance fits very well to the regions found by numerical simulations, presented in the bifurcation and Lyapunov diagrams. The nonlinear model surfaces for angular velocity of the system strongly depend both on the displacement and velocity.

References

1. Kerschen, G., Peeters, M., Golinval, J.C., Vakakis, A.F.: Nonlinear normal modes, part I: useful framework for the structural dynamicst. Mech. Syst. Sig. Process. **23**, 170–194 (2009)
2. Rosenberg, R.M.: Normal modes of non-linear dual-mode systems. J. Appl. Mech. Ser. E **27**(2), 263–268 (1960)
3. Shaw, S.W., Pierre, C.: Normal modes for non-linear vibratory system. J. Sound Vibr. **164**(1), 85–124 (1993)
4. Vakakis, A.F.: Non-linear normal modes (NNMs) and their applications in vibrations theory: an overview. Mech. Syst. Sig. Process. **11**(1), 3–22 (1997)
5. Vakakis, A.F., et al.: Nonlinear Targeted Energy Transfer in Mechanical System and Structures Systems. Springer, New York (2008)
6. Warminsky, J.: Nonlinear normal modes of a self-excited system driven by parametric and external excitations. Nonlinear Dyn. **61**, 677 (2010). doi:10.1007/s11071-010-9679-5
7. Warminsky, J.: Nonlinear normal modes of coupled self-excited oscillators in regular and chaotic vibration regimes. J. Theor. Appl. Mech. Warsaw **46**(3), 693–714 (2008)

Structural Probabilistic Modeling of Fatigue Fracture for Piezoceramic Materials Under Cyclic Loading

D. Babich, O. Bezverkhyi and T. Dorodnykh

Abstract The aim of this paper is to develop a structural approach for the construction of statistical criterion of static and fatigue failure for the transversely isotropic piezoelectric materials. We use a probabilistic model of the mechanism of brittle microfracture. The microdamageability is considered as a process of appearance of flat elliptic or circular microcracks randomly dispersed over volume, the concentration of which increases with a load. Daniel's structural model of accumulation of microcracks is used for progressive microdamageability. Statistical criterion is convenient to use in the study of fatigue failure under cyclic loading. The reason for its applicability in such problems is experimentally established connection of fatigue failure mechanism with the phenomenon of accumulation of microdamages in the material. Statistical criterion relates macrodestruction beginning with a certain critical value of microcracks density. The model consists of derivation of constitutive equations for a damaged material, choosing the fracture criterion and the law of microdamage distribution; and determining effective electroelastic properties of the damaged medium and the model of accumulation of microdamages by the modified Eshelby method. The approach proposed makes it possible to find the residual ultimate strength of the material after n-fold loading and the conditional fatigue limit for the prescribed testing base N.

1 Introduction

The necessity of studying the processes of static and dynamic deformation of piezoceramic bodies is determined by continuously expanding range of application of piezoceramic materials. In frame of the mathematical theory of deforming of the piezoceramic such materials are treated as brittle and their fracture occurs at low strain level. A large body of studies reviewed in [1–5] shows that fatigue failure of

D. Babich · O. Bezverkhyi · T. Dorodnykh (✉)
S.P. Timoshenko Institute of Mechanics, NAS of Ukraine,
Nesterova, 3 str., Kiev 03057, Ukraine
e-mail: domval@ukr.net

J. Awrejcewicz (ed.), *Dynamical Systems: Modelling*, Springer Proceedings
in Mathematics & Statistics 181, DOI 10.1007/978-3-319-42402-6_2

materials is a complex multiple-stage process which includes dispersed microfailure of structural elements. This is attributed to the fact that engineering materials contain randomly scattered over a volume microdefects, which under cyclic loading initiate microcracks. Later these microdefects coalescence lead to formation of macrocracks and loss of the body integrity. Moreover, in accordance with the ideas of the mechanics of deformable solids, the main reason of fatigue failure of structural members under cyclic loading is accumulation of microdefects to the point where their concentration becomes critical due to increase in values of true stresses as a result of decrease in the effective area of a cross section with the cycles of loading. Because of this the inherent random nature of fatigue failure requires a probabilistic treatment to evaluate the life of structural components using the models describing process of simultaneous elastic deformation and dispersed fracture of materials [6, 7]. For example, some life assessment approaches based on the continuum mechanics and fracture mechanics models are outlined in [8, 9].

In the present paper, the new probabilistic structural approach for determining the service life of piezoelectric materials under multiple static or cyclic loading based on the microdamageability model [10] is proposed. In implementing this approach, the statistical fatigue failure criterion expressed in terms of damage measures (microcrack density) is employed in combination with the approximate model of microcrack accumulation under repeated loading. The criterion is identified with the statistical fracture criterion [2, 11]. The statistical nature of such criterion is attributed to the probabilistic character of microfailures in a microinhomogeneous material. The main point of the statistical criterion lies in the fact that the value of microdefect concentration, which origin under the loading kind being considered, is identified with the critical value of microdefect concentration that initiates the start of macrofailure (formation of a macrocrack) independently of the stress-state mode. It is assumed that the microdefect concentration under reversed cyclical loading increases only during the tensile half cycle when the internal stresses increase to amplitude value. At separation-like mode of microfailure, as distinct from shear-like one, the effective area of the load-bearing cross section in compression does not change due to the fact that the planes of the arising cracks are collinear with the direction in which compression acts.

We consider a mechanical failure of material and at this stage of investigation of the problem it is not essential whether such failures are caused by the mechanical, electrical, or electromechanical loading. The general procedure of the approach includes following stages. In the first phase, we derive constitutive equations for a damaged material, choose the fracture criterion and low of microdamage distribution. Such material is simulated by a solid with reduced electroelastic characteristics. In this case the type of elastic symmetry of medium being simulated depends on the pattern of microdamage distribution over the body volume as well as on the stress–strain state volume of a material. At the second phase, the method for determining effective electroelastic properties of the damaged medium and the model of accumulation of microdamages are employed. We assume that during deformation, cracks do not grow, do not interact. The volume density (concentration) of microdefects varies with increase in the level of average stresses due to

features of orientation of anisotropic materials. Destruction of the structural elements occurs at different levels of stress due to random nature of the orientation and differences of the values of ultimate strength of the structural elements in different directions.

2 Structural Model of Accumulation of Flat Microcracks in the Elastic–Brittle Material

To describe the phenomenon of fatigue failure of materials, we use the structural model of material microdamageability. The microdamageability is considered as the process of occurence of the flat scattered microcracks. According to this model, the size and distribution of microcracks in real bodies are associated with discontinuities of structural elements. The shape and dimensions of the cracks are identified with them for ruptures in the cross sections of the structural elements of the material. To describe progressive accumulation of microdamages, the Daniels structural model is used. The main point of this model is outlined in detail in references [11, 12].

With respect to transversally isotropic material, which is simulating prepolarized piezoceramic, the Mises–Hill strength criterion can be used. Let the average stresses σ_{ij} $(i,j=1,2,3)$ be given in the laboratory (fixed) coordinate system $0x_1x_2x_3$, associated with a representative volume of the material, then this criterion can be written as

$$\frac{\sigma_{11}^2}{\sigma_{(bi)11}^2}+\frac{\sigma_{22}^2}{\sigma_{(bi)11}^2}+\frac{\sigma_{33}^2}{\sigma_{(bi)33}^2}+\frac{\sigma_{12}^2}{\sigma_{(bi)12}^2}+\frac{1}{\sigma_{(bi)13}^2}\left(\sigma_{13}^2+\sigma_{23}^2\right)-\left(\frac{2}{\sigma_{(bi)11}^2}-\frac{1}{\sigma_{(bi)33}^2}\right)\sigma_{11}\sigma_{22}$$
$$-\frac{1}{\sigma_{(bi)33}^2}\left(\sigma_{22}\sigma_{33}+\sigma_{11}\sigma_{33}\right)=1. \tag{1}$$

The main axes of symmetry of mechanical properties are directed along coordinate axes ($0x_3$—polarization axis, axes $0x_1, 0x_2$ lie in isotropic plane). According to this criterion, to determine fracture start, it is necessary to know the four constants. These constants characterize fracture under pure tension $(i=1)$ or pure compression $(i=2)$ in main direction of anisotropy $\left(\sigma_{(bi)11}=\sigma_{(bi)22},\ \sigma_{(bi)33}\right)$ and pure shear in main planes $\left(\sigma_{(bi)12},\ \sigma_{(bi)13}\right)$.

For the considered material the tensile strength (compression) and pure shear dependents on the direction determined by angle ϑ—angle of rotation of coordinate system $0x_1x_2x_3$ relative to the axis $0x_2$ or axis $0x_1$. The formulas for the tensile strength (compression) $\sigma_{(bi)\vartheta}$ in a direction determined by the angle ϑ, measured from the $0x_3$ axis, can be written as

$$\sigma'_{(bi)\vartheta} = \sigma'_{(bi)33} = \frac{\sigma_{(bi)33}}{\sqrt{\cos^2\vartheta + \sin^2\vartheta \frac{\sigma^2_{(bi)33}}{\sigma^2_{(bi)11}} + \left(\frac{\sigma^2_{(bi)33}}{\sigma^2_{(bi)13}} - 1\right)\sin^2\vartheta\cos^2\vartheta}}$$
$$= \frac{\sigma_{(bi)33}}{\sqrt{\cos^4\vartheta + \sin^2\vartheta \frac{\sigma^2_{(bi)33}}{\sigma^2_{(bi)11}} + \frac{\sigma^2_{(bi)33}}{\sigma^2_{(bi)13}}\sin^2\vartheta\cos^2\vartheta}}. \quad (2)$$

Let $0'x'_1x'_2x'_3$ be the local coordinate systems chosen in such a way that the $0'x'_3$ axes would be directed along the normal to the sphere (unit radius) surface. The elemental area $d\Omega = \sin\vartheta\, d\vartheta\, d\psi$ is singled out around the $0'x'_3$ axis on the surface of the random sphere. This area cuts N structural elements (ϑ is the longitude; ψ is the latitude). In this case, the same local true stress $\bar{\sigma}_{33}$ acts in the section of the N intersected structural elements. The true stresses $\bar{\sigma}_{33}$ differ from the conditional σ'_{33} in that the first ones refer to the areas of the damaged medium whereas the second ones refer to the areas of the continuous medium. The local conditional stresses σ'_{33} and average stresses σ_{kl} given in the body are connected by equation

$$\sigma'_{33} = \sigma_{kl}\alpha_{3k}\alpha_{3l},$$

where α_{3k}, α_{3l} are the direction cosines of the local coordinate system with respect to the laboratory coordinate system. The relation of the first strength theory

$$\bar{\sigma}_{33} \geq \sigma(\vartheta) \quad (3)$$

Here $\sigma(\vartheta)$ is the random value, which stands for the ultimate magnitude of the true tensile or compressive normal stresses $\bar{\sigma}_{33}$ for differently oriented structural elements. When the true tensile stress $\bar{\sigma}_{33}$ reaches up the level of $\sigma(\vartheta)$ in the appropriate elemental area, the microcracks of rupture are formed with side surfaces being normal to the direction axis $0'x'_3$. When the conditional stress is compressive, the microcracks are oriented predominantly in parallel to the direction of $\bar{\sigma}_{33}$ due to the difference of Poisson's ratio of the structural elements. To approximate distributions of the microstrength properties of structural elements, the power law is used

$$F_i(\sigma_i) = \left(\frac{\sigma_i - \sigma_{0i}}{\sigma_{mi} - \sigma_{0i}}\right)^{\alpha_i} \quad (4)$$

and

$$f_i(\sigma_i) = \frac{dF_i(\sigma_i)}{d\sigma_i} = \alpha_i\left(\frac{1}{\sigma_{mi} - \sigma_{0i}}\right)\left(\frac{\sigma_i - \sigma_{0i}}{\sigma_{mi} - \sigma_{0i}}\right)^{\alpha_i - 1} \quad (5)$$

is the distribution density of the random value σ_i.

$\sigma_{0\,i,}, \sigma_{m\,i}$, α_i are the distribution parameters; $\sigma_{0\,i,}, \sigma_{m\,i}$ are minimal and maximal values of these variables, respectively; α_i is the microstrength scattering parameter. The distribution parameters are determined in sample quantities by the method of moments in particular. For example, it is necessary to determine, using experimental data, two selective moments: average magnitude $\bar{\sigma}_{b1}$ and dispersion of the random value $\bar{D}_{b1}^2$.

$$\begin{aligned}\bar{\sigma}_{b1} &= \int_{\sigma_{01}}^{\sigma_{m11}} \sigma f_1 \mathrm{d}\sigma = \frac{\alpha_1}{1+\alpha_1}\bar{\sigma}_{m1} + \sigma_{01};\\ \bar{D}_{b1}^2 &= \int_{\sigma_{01}}^{\sigma_{m1}} (\sigma - \bar{\sigma}_{b1})^2 f_1 \mathrm{d}\sigma = \frac{\alpha_1}{(\alpha_1+1)^2(\alpha_1+2)}\bar{\sigma}_{m1}^2,\end{aligned} \tag{6}$$

here $\bar{\sigma}_{m1} = \sigma_{m1} - \sigma_{01}$. From (6) follows

$$\begin{aligned}k_1^2 &= \frac{\bar{D}_{b1}^2}{(\bar{\sigma}_{b1} - \sigma_{01})^2} = \frac{(\bar{D}_{b1}/\bar{\sigma}_{b1})^2}{(1 - \sigma_{01}/\bar{\sigma}_{b1})^2} = \frac{1}{\alpha_1(\alpha_1+2)};\\ \alpha_1 &= -1 + \frac{1}{k_1}\sqrt{1+k_1^2}, \bar{\sigma}_{m1} = \frac{1+\alpha_1}{\alpha_1}(\bar{\sigma}_{b1} - \sigma_{01}).\end{aligned} \tag{7}$$

Due to the small size of the structural elements it is impossible to determine $\sigma_{0i,}, \sigma_{mi}$, α_i directly. To find these values indirect methods are used. Experimental data of corresponding conditional parameters of macrostress of rupture is taken from set of macrosamples. The procedure of determining of these parameters is described in more detail in [11].

It should be noted that the element fails when the stress $\bar{\sigma}_{33}$ reaches up to the ultimate magnitude. Failure of single elements forms the population of independent random events. After some quantity of structural elements fail, redistribution of stresses between the nonfailed elements occurs.

If the conditional local tensile stress $\sigma_{33}^{'}$ presents an independent loading parameter, then the true local stress in the sections with nonfailed structural elements can be regarded within the framework of the model being considered as the random value $\bar{\sigma}_{33} = \sigma_{33}^{'}/\left(1 - \frac{n_1}{N}\right)$. The distribution of the true local stress $\bar{\sigma}_{33}$ depends on the number n_1 of the failed elements. N is the total number of the elements. The expected value of the number n_1 has the form $\langle n_1 \rangle = NF_1(\bar{\sigma}_{33})$, and the coefficient of variation becomes $k_{w1} = \left[\frac{1 - F_1(\bar{\sigma}_{33})}{NF_1(\bar{\sigma}_{33})}\right]^{1/2}$. From the last formula, it follows that for real materials it is possible to neglect the scatter of the values n_1 and $\bar{\sigma}_{33}$. As a result, we have

$$\bar{\sigma}_{33} \approx \frac{\sigma'_{33}}{1 - F_1(\bar{\sigma}_{33})} \tag{8}$$

Taking into account (3) and (5), the densities of microcracks of normal rupture under tension or compression are determined by expressions

$$\varepsilon_i = F_i(\bar{\sigma}_{33}) = \left(\frac{\bar{\sigma}_{33} - \sigma_{0i}}{\sigma_{mi} - \sigma_{0i}}\right)^{\alpha_i} (i = 1, 2). \tag{9}$$

In the case of local true tensile stresses $\bar{\sigma}_{33}$, we have formula (8). In the case of compression ($i = 2$), the cracks origin surfaces are parallel to the direction in which local normal stresses act. In this connection the effective area remains unchanged and, as a result, $\bar{\sigma}_{33} = \sigma'_{33}$.

Thereby, the average densities microcracks of structural elements, which are cut by the unit surface of the representative volume, are defined by the relations

$$\varepsilon_1 = \frac{1}{\bar{N}} \int_0^{2\pi} \int_0^{\pi} F_1(\bar{\sigma}_{33}) \mathrm{d}\Omega = \frac{1}{\bar{N}} \int_0^{2\pi} \int_0^{\pi} F_1(\bar{\sigma}_{33}) \sin\vartheta \, \mathrm{d}\vartheta \, \mathrm{d}\psi \tag{10}$$

in case of the stresses σ_{ij} are tensile, and

$$\varepsilon_2 = \frac{1}{\bar{N}} \int_0^{2\pi} \int_0^{\pi} F_2\left(\sigma'_{33}\right) \mathrm{d}\Omega = \frac{1}{\bar{N}} \int_0^{2\pi} \int_0^{\pi} F_2\left(\sigma'_{33}\right) \sin\vartheta \, \mathrm{d}\vartheta \, \mathrm{d}\psi \tag{11}$$

in case of the stresses σ_{ij} are compressive.

$\bar{N} = 4\pi$ is the normalizing factor, which follows from the condition

$$\frac{1}{\bar{N}} \int_0^{2\pi} \int_0^{\pi} F_i(\bar{\sigma}_{33}) \sin\vartheta \, \mathrm{d}\vartheta \, \mathrm{d}\psi \quad = 1.$$

The physical meaning of the values ε_i ($i = 1, 2$) is that it represents the relative fraction of the unit area of the sphere surface where the normal stresses (tensile or compressive) exceed the ultimate strength σ_i of the material of the microparticles that are cut by the surface of this sphere. The volume concentration of flat microdefects which are destroyed under tension or compression is determined by the ratio of the number of destructed microparticles N_{0i} to their total number N ($p_i = N_{0i}/N$) in the representative volume. Such a result can be obtained using the technique that is common in petrography in analyzing the thin sections of sediments, so $p_i = \varepsilon_i$.

3 Statistical Fracture Criterion in Terms of Damage Measures of a Material

Relations (1)–(5) and (8) make it possible to determine the microcrack density allowing for loading rate and their orientation, which depends on the direction of the local conditional stresses $\sigma'_{33}(\vartheta, \psi)$ that cause microcracking. Of especial importance is allowed for the orientation in the case of complex stress state since macrocracks arise mostly in the planes normal (parallel) to the direction in which the maximum tensile (compressive) local stresses $\sigma'_{33_{\max}}(\vartheta_m, \psi_m)$ act.

For two-parametric approximation of the ultimate microstrength distribution, the microcrack concentration in the random volume of transversally isotropic piezoelectric material is defined by the formula

$$\varepsilon_i = F_i(\bar{\sigma}_{33}) = \left(\frac{\bar{\sigma}_{33}}{\sigma_{mi}}\right)^{\alpha_i} \quad (i = 1, 2), \tag{12}$$

where under tensile stress ($\sigma'_{33} > 0$) and under compression ($\sigma'_{33} < 0$) for local stress $\bar{\sigma}_{33}$ there are formulas

$$\bar{\sigma}_{33} \approx \frac{\sigma'_{33}}{1 - F_1(\bar{\sigma}_{33})}, \quad \bar{\sigma}_{33} = \sigma'_{33} \tag{13}$$

The statistical fracture criterion expressed in terms of damage measures of a material is defined by the relation

$$F_i(\bar{\sigma}_{33_{\max}}) \le \varepsilon_{icr} \quad (i = 1, 2), \tag{14}$$

where $F_i(\bar{\sigma}_{33_{\max}}) = \varepsilon_{im}$ is the concentration of cracks in the cross section in which the normal local conditional stress reaches up to the maximum value, and ε_{icr} is the critical value of the concentration of cracks.

It should be noted that the accumulation of microcracks in the material depends on the specific loading of the body (the multiplicity, the loading rate, and others.). We suppose that before the deformation in material was the initial microdamage with density ε_{i0}. The distribution function of the ultimate strength of the structural elements (12) in this case determines the relative proportion of structural elements not destroyed in remaining cross-sectional area of the body. The relative area of undefeated structural elements is $(1 - \varepsilon_{i0})$, and the tensile strength in this area is equal to or less than a certain value σ. Then, under monotonic (static) loading, when stresses increase up to the value σ'_{33} the microcrack concentration is defined as follows:

$$\varepsilon_i = \varepsilon_{i0} + (1-\varepsilon_i)F_i(\bar{\sigma}_{33}) = \varepsilon_{i0} + (1-\varepsilon_i)\left(\frac{\bar{\sigma}_{33}}{\sigma_i}\right)^{\alpha_i} \qquad (i=1,2) \tag{15}$$

Critical concentrations of microcracks when $\varepsilon_{i0}=0$ are determined by the relation

$$\varepsilon_{1cr}(1-\varepsilon_{1cr})^{\alpha_1-1} = \left(\frac{\sigma'_{(b1)33}}{\sigma_{m1}}\right)^{\alpha_1},\ \varepsilon_{2cr} = (1-\varepsilon_{2cr})\left(\frac{\sigma'_{(b2)33}}{\sigma_{m2}}\right)^{\alpha_2}. \tag{16}$$

Here, $\sigma_{(bi)33} = \sigma_{(bi)\,\vartheta}\ (i=1,2)$ are the average values of the ultimate strength, which are calculated by the formula (2) under tension and compression, respectively. Samples of material are cut at an angle ϑ to the direction of the principal axis of anisotropy, which coincides with the axis of the prepolarization.

In the case of complex stress state determined by main stresses $\sigma_{ii}\ (i=1,2,3)$ in the laboratory coordinate system, the strength of statistical criterion for transversely isotropic body can be constructed on the basis of Mises–Hill strength criterion. For this purpose, the expression of Mises–Hill strength criterion (1) is represented in the main stresses

$$\frac{\sigma_{11}^2}{\sigma_{(bi)11}^2} + \frac{\sigma_{22}^2}{\sigma_{(bi)11}^2} + \frac{\sigma_{33}^2}{\sigma_{(bi)33}^2} + \left(\frac{2}{\sigma_{(bi)11}^2} - \frac{1}{\sigma_{(bi)33}^2}\right)\sigma_{11}\sigma_{22} - \frac{1}{\sigma_{(bi)33}^2}(\sigma_{22}\sigma_{33}+\sigma_{11}\sigma_{33}) = 1. \tag{17}$$

Stresses σ_{kk}, $\sigma_{(bi)kk}\ (k=1,2,3)$ in (17) can be expressed by the corresponding densities of microcracks $\varepsilon_{(i)k}$. Using (12), we get following formulas:

$$\begin{aligned}
&\varepsilon_{(i)k} = F_i(\bar{\sigma}_{kk}) = \left(\frac{\bar{\sigma}_{kk}}{\sigma_{(mi)k}}\right)^{\alpha_{(i)k}} (k=1,2,3),\ \varepsilon_{(bi)k} = F_i(\bar{\sigma}_{(bi)kk}) = \left(\frac{\bar{\sigma}_{(bi)kk}}{\sigma_{(mi)k}}\right)^{\alpha_{(i)k}};\\
&H_k = (\varepsilon_{(i)k} - \varepsilon_{(i)k0})^{\frac{1}{\alpha_{(i)k}}}(1-\varepsilon_{(i)k})^{1-\frac{1}{\alpha_{(i)k}}};\\
&G_k = (\varepsilon_{(bi)k})^{\frac{1}{\alpha_{(i)k}}}(1-\varepsilon_{(bi)k})^{1-\frac{1}{\alpha_{(i)k}}};\\
&\sigma_{kk} = H_k\sigma_{(mi)k};\quad \sigma_{(bi)kk} = G_k\sigma_{(mi)k};\quad \left(\frac{\sigma_{kk}}{\sigma_{(bi)kk}}\right)^2 = \left(\frac{H_k}{G_k}\right)^2,
\end{aligned} \tag{18}$$

Thereby, formula (17) can be written in concentrations of microcracks

$$\begin{aligned}
&\sum_{k=1}^{3}\left[\frac{H_k}{G_k}\right]^2 + \left[\frac{2}{G_1^2\left(\sigma_{(mi)1}\right)^2} - \frac{1}{G_3^2\left(\sigma_{(mi)3}\right)^2}\right] \times H_1H_2(\sigma_{(mi)1})^2\\
&\qquad - \frac{H_3}{G_3^2\left(\sigma_{(mi)3}\right)}\sum_{k=1}^{2}\sigma_{(mi)k}H_k = 1.
\end{aligned} \tag{19}$$

In (18) and (19) it is indicated by the index i tension ($i=1$) or compression ($i=2$), the index k is associated with the symbols of the principal axis of the anisotropy of the material.

4 Constitutive Equations of State for the Piezoelectric Ceramics with Cracks

Polarized piezoceramic is modeled as a transversely isotropic medium with the axis of isotropy coincident with the axis of polarization. In the laboratory coordinate system $0x_1x_2x_3$, ($0x_3$ is axis of polarization) state equations have the form

$$\begin{aligned}
&\varepsilon_{11} = a_{1111}\sigma_{11} + a_{1122}\sigma_{22} + a_{1133}\sigma_{33} + d_{113}E_3,\\
&\varepsilon_{22} = a_{1122}\sigma_{11} + a_{1111}\sigma_{22} + a_{1133}\sigma_{33} + d_{113}E_3,\\
&\varepsilon_{33} = a_{1133}\sigma_{11} + a_{1133}\sigma_{22} + a_{3333}\sigma_{33} + d_{333}E_3,\\
&\varepsilon_{23} = a_{2323}\sigma_{23} + d_{233}E_2,\ \varepsilon_{13} = a_{2323}\sigma_{13} + d_{233}E_1,\\
&\varepsilon_{23} = a_{1212}\sigma_{12} = 2\left(a_{1111} - a_{1122}\right)\sigma_{12},\\
&D_1 = \ \ni_{11}\ E_1 + d_{232}\sigma_{13},\ \ D_2 = \ \ni_{11}\ E_2 + d_{232}\sigma_{23},\\
&D_3 = \ \ni_{33}\ E_3 + d_{113}(\sigma_{11} + \sigma_{22}) + d_{333}E_3.
\end{aligned} \tag{20}$$

Suppose that underloading in piezoelectric materials causes microdamages in the form of flat circular cracks. This type of microfracture, most unfavorable to the material because of the degree of influence of microcracks on the stiffness of the material is mainly related to the area and volume of cracks opening.

To determine the effective electroelastic constants in (20), the principle of the energy equivalence is used:

$$W = W^{(0)} + \bar{W} \tag{21}$$

Here,

$$W = \frac{1}{2}\sigma_{ij}\varepsilon_{ij} + E_jD_j = \frac{1}{2}a^{E}_{ijkl}\,\sigma_{ij}\sigma_{kl} + \frac{1}{2}\,E_i\left(d_{ikl}\sigma_{kl} + \ \ni^{\sigma}_{ik}\ E_k\right) \tag{22}$$

is the energy density of deformation of the continuous electroelastic medium [7] that simulates the damaged material;

$$W^{(0)} = \frac{1}{2}a^{E(0)}_{ijkl}\ \sigma_{ij}\sigma_{kl}\ + \frac{1}{2}E_i\left(d^{(0)}_{ikl}\sigma_{kl} + \ \ni^{\sigma(0)}_{ik}\ E_k\right) \tag{23}$$

is the density of the deformation energy of a solid medium; subscripts with E, σ in (23) indicates the dependence of these parameters on the electric (E) field and mechanical stress (σ); $\bar{W}$ is the density of the released internal energy of the

damaged medium, which can be represented as the change in mechanical and electrical energy. These changes in mechanical and electrical energy are associated with the damage of the material in the form of closed or opened flat cracks.

The effective electroelastic constants in (10) are determined from expression (11). For this purpose the terms entering in (11) should be written in terms of the components of the stress tensor σ_{ij} and components of the electric field vector. It is assumed that E_i and $\sigma_{ij}E_i$ are given in a representative volume. The coefficients of the terms σ_{ij}^2, $\sigma_{ij}E_i$, E_iE_j should be equated. It makes it possible to determine the effective compliances a_{ijkl}, piezoelectric coefficients d_{ikl}, and dielectric constants $э_{ik}$ of fractured materials by

$$\begin{aligned} a_{ijkl} &= a_{ijkl}^{(0)} + \bar{a}_{ijkl}, \quad d_{ijk} = d_{ijk}^{(0)} + \bar{d}_{ijk}, \\ э_{ij} &= э_{ij}^{(0)} + \bar{э}_{ij} \ (i, j, k, l = 1, 2, 3), \end{aligned} \tag{24}$$

where the values $\bar{a}_{ijkl}$, $\bar{d}_{ijk}$, $\bar{э}_{ij}$ are the changes in the electroelastic parameters of a continuous medium, due to the disruption of the continuity of the material.

For purely elastic materials, the density of the released elastic energy is determined on the basis of the Eshelby principle [13]. With regard to inhomogeneous electroelastic materials, the Eshelby principle is modified due to the need to take into account the electric component in the overall energy balance of the body. For this purpose, a local criterion of microfracture for electroelastic materials is used [14]. Due to the disruption of connections of the nth crack under rupture and opening (shear) of crack faces, the internal elastic energy is released and electric energy is loosed. The density of the released energy can be represented as the work of relative sliding and opening of crack faces induced by the action of stresses, which may arise under the given loading in the microvolumes of a continuous free of crack medium, and is determined as

$$\bar{W}^n = \frac{1}{2} \int\limits_{s_n} \sum_{i=1}^{3} \left(\sigma_{i3}^{(0)n} \bar{u}_i^n + D_i^{(0)n} \Phi_i^n \right) \mathrm{d}s_n, \tag{25}$$

where $\bar{u}_i^n$ $(i = 1, 2, 3)$ are the discontinuities of displacements at points of the surface of the nth crack in the direction of the local coordinate system; s_n is the half of surface area of the nth crack; $\sigma_{i3}^{(0)n}$ $(i = 1, 2, 3)$ are the components of the tensor of the given average stress in nth cracks coordinate system—$0^n x_1^n x_2^n x_3^n$. In the case of elliptic cracks, the $0x_1^n$, $0x_2^n$ axes are directed along major (a^n) and minor (b^n) semi-axes, respectively, while the $0^n x_3^n$-axis directed along the normal to their planes; $D_i^{(0)n}$, are the components of the electric induction in a solid medium in nth cracks coordinate system, Φ_i^n $(i = 1, 2, 3)$ are the discontinuities of the electric potential at the points of microcracks surfaces, which are directed along the axes in nth cracks coordinate system. With the use of (24) the expression for the change of the density energy of deformation due to the formation of elliptical or circular

microcracks in the inhomogeneous transversely isotropic material is determined in accordance with the procedure for isotropic materials [14]. In particular, the density of the released energy under tensile could be expressed in the form

$$\bar{W} = \frac{1}{12\pi} \sum_{k=1}^{3} \int_0^{2\pi} \int_0^{\pi} F_1(\bar{\sigma}_{33})\, B_k^{'} \sin\vartheta \, \mathrm{d}\vartheta \, \mathrm{d}\psi. \tag{26}$$

In case of the compression, we have

$$\bar{W} = \frac{1}{12\pi} \sum_{k=1}^{2} \int_0^{2\pi} \int_0^{\pi} F_2\left(\sigma_{33}^{'}\right) B_k^{'} \sin\vartheta \, \mathrm{d}\vartheta \, \mathrm{d}\psi. \tag{27}$$

$B_k^{'}$ is determined by expression

$$B_k^{'}(\theta, \psi) = \frac{1}{2\pi} \int_0^{2\pi} \left[\frac{1}{2} S_k^{'} \left(\sigma_{k3}^{'}\right)^2 - \frac{1}{2} E_k^{'} \left(d_{kil} \sigma_{il}^{'} + \vartheta_{ki}\right) E_i^{'} \right] \mathrm{d}\phi \quad k = 1,\ 2,\ 3. \tag{28}$$

$S_k^{'}\left(a_{klmn}^{(0)}, \theta^n, \psi^n, \phi^n\right)$ in (28) denotes compliances of the material in the nth cracks plane. Definition of which is an independent task for individual crack.

Engineering elastic constants are expressed in terms of the effective compliances by relations

$$\frac{1}{E_{ii}} = a_{iiii}, \ -\frac{\nu_{ij}}{E_{ii}} = a_{jjii}, \ G_{ij} = \frac{1}{a_{ijij}} \quad i,j = 1,2,3. \tag{29}$$

E_{ii}, G_{ij}, ν_{ij} are elastic, shift moduli, Poisson's ratios accordingly.

A two-parameter distribution function of the ultimate strength of the structural elements of the material is used to determine the effective electroelastic parameters. Additionally, we rely on the continuum model of piezoelectric ceramics with progressive accumulation of damageability in the form of circular microcracks in the isotropic plane [15]. Material is subjected to uniaxial tension stresses σ_{33} in the direction of polarization. And the component of electrical field E_3^0 is given. Under these assumptions, electroelastic effective parameters are determined by the expression of type (24)

$$\begin{aligned} a_{3333} &= \frac{1}{E_{33}^0} + p\left[\frac{4}{\pi} \ \frac{1 - \left(\nu^{'}\right)^2}{E_{11}^0}\right], \\ \vartheta_{33} &= (1-p) \ \vartheta_{33}^{(0)}, \ d_{333} = (1-p) \ d_{333}^{(0)}. \end{aligned} \tag{30}$$

5 Application of Statistical Fracture Criterion in Problems of Durability Piezoceramic Structures Submission of Electronic Version of Papers

When considering the cyclic alternating load it should be noted the difference in the mechanism of microfracture of material under the same multiple compression and multiple tensile stresses. In the first case, the concentration of microdefects in subsequent compressions (excluding first) is not changed, in the second, it increases due to the decrease in the effective cross-sectional area.

To illustrate the approach for the determination of the durability of structures such as piezoelectric transducers electromechanical power using statistical fracture criterion, we consider the problem of the durability of piezoceramic rods during longitudinal vibrations excited by the time-variable (t) difference of potential exerted on the end faces of the rod in the form

$$\psi_{x_3=0} = \psi_{x_3=l} = \pm V_0 e^{i\omega t}. \tag{31}$$

For solving the problem of the durability of the rods it is necessary and sufficient to have the dates of the maximum values of the axial normal stress under given parameters of external loading, as well as the critical values of concentration of microcracks under pure tensile samples of the concrete material. Procedure for determining the durability of material under more general types of electromechanical loading remains the same for the resource problems with more complex structures. The definition of parameters in (5) is independent task in each case.

Thus, the first step in solving the question of the durability of structures is the solution of the problem of stress–strain state of the structure under specific operational impacts. The problem of the longitudinal vibrations piezoceramic prismatic rod with length l and the axial polarization was considered in [6]. Vibrations excited by the variable potential difference were applied to the electrodes of the end of rod. External stresses on the entire surfaces of the rod are absent. Equation (20) for this case in coordinate system $0x_1x_2x_3$ have the form

$$\begin{gathered}\varepsilon_{ij} = a_{ijkl}\,\sigma_{kl} + d_{ijk}E_k \quad (i, j, k, l = 1, 2, 3);\\ D_i = d_{ijk}\sigma_{jk} + \mathfrak{e}_{ij}\,E_j \quad (i, j, k, l = 1, 2, 3),\\ \varepsilon_{33} = a^E_{3333}\sigma_{33} + d_{333}E_3; \quad D_3 = \mathfrak{e}^\sigma_{33}\,E_3 + d_{333}\sigma_{33}.\end{gathered} \tag{32}$$

The problem on longitudinal vibrations of the rod is reduced to solving of the equation for axial displacements $u(x, t)$

$$\begin{gathered}u_{3,33} + d_{333}\psi_{,33} = \rho a^E_{3333}u_{3,tt};\\ \frac{d_{333}}{a^E_{3333}}u_{3,33} - \mathfrak{e}^\sigma_{33}\left(1 - k^2_{333}\right)\psi_{,33} = 0,\end{gathered} \tag{33}$$

where $k_{333}^2 = d_{333}^2 / a_{3333}^E \, э_{33}^\sigma$ is longitudinal static electromechanical coupling factor, ρ is the density of material.

Solving this task the amplitude value of axial stress in the rod is received in the form

$$\bar{\sigma}_{33} = \frac{A\lambda}{a_{3333}^E\left(1-k_{333}^2\right)}\cos\lambda\left(\frac{l}{2}-x_3\right)+\frac{d_{333}}{a_{3333}^E}B, \tag{34}$$

where

$$\begin{gathered} A=-\frac{d_{333}\left(1-k_{333}^2\right)}{\frac{\lambda l}{2}\cos\frac{\lambda l}{2}-k_{333}^2\sin\frac{\lambda l}{2}}V_0;\ B=\frac{\frac{\lambda l}{2}\cos\frac{\lambda l}{2}}{\frac{\lambda l}{2}\cos\frac{\lambda l}{2}-k_{333}^2\sin\frac{\lambda l}{2}}\left(\frac{2V_0}{l}\right); \\ \lambda=\omega/c,\ c=1/\sqrt{\rho a_{3333}^E\left(1-k_{333}^2\right)}. \end{gathered} \tag{35}$$

ω—is frequency.

According to (34) and (35) the maximum amplitude value of stress is in the middle of the rod

$$\bar{\sigma}_{33} = \frac{A\lambda}{a_{3333}^E\left(1-k_{333}^2\right)}+\frac{d_{333}}{a_{3333}^E}B=\frac{d_{333}\omega\left(\cos\frac{\omega l}{2c}-1\right)}{ca_{3333}^E\left(\frac{\omega l}{2c}\cos\frac{\omega l}{2c}-k_{333}^2\sin\frac{\omega l}{2c}\right)}V_0. \tag{36}$$

Let $\varepsilon_{1(0)}=0$ and material is subjected to uniaxial cyclic tensile stress with amplitude value $\bar{\sigma}_{33}$. The first ($n = 1$) tensile half cycle of the undamaged rod leads to origin of the damage with the density

$$\varepsilon_{1(1)} = \left(1-\varepsilon_{1(1)}\right)^{1-\alpha_1}\left(\frac{\bar{\sigma}_{33(0)}}{\sigma_{m1}}\right)^{\alpha_1} \tag{37}$$

The following n cycles of tensile cause breaking of structural elements in the cross section of the sample whose density is determined by

$$\varepsilon_{1(n)} = \varepsilon_{1(n-1)}+\left(1-\varepsilon_{1(n)}\right)^{1-\alpha_1}\left(\frac{\bar{\sigma}_{33(n-1)}}{\sigma_{m1}}\right)^{\alpha_1}, \tag{38}$$

where $\varepsilon_{1(n-1)}$ and $\bar{\sigma}_{33(n-1)}$ are the concentration of microdefects and amplitude value of the stress, respectively, that have appeared after the previous $(n-1)$th cycle of tensile. The fatigue failure of the specimen begins at the Nth cycle when the microcrack concentration becomes critical, i.e., with $\varepsilon_{1(N)}=\varepsilon_{1cr}$, where

$$\varepsilon_{1cr} = \varepsilon_{1(N-1)}+\left(1-\varepsilon_{1cr}\right)^{1-\alpha_1}\left(\frac{\bar{\sigma}_{33(N-1)}}{\sigma_{m1}}\right)^{\alpha_1} \tag{39}$$

Thus, a number of cycles N determine the cyclical service life of the specimen, which is found either by solving the sequence of Eq. (38) or using an inverse calculation step based on (39).

Two-sided approximate estimation of the durability of the sample can be obtained by identifying the increment of the concentration of microdefects after any act of loading with minimum and maximum increments, respectively.

$$\begin{aligned} \Delta_{\min} &= \varepsilon_{1(2)} - \varepsilon_{1(1)}, \\ \Delta_{\max} &= \varepsilon_{1cr} - \varepsilon_{1(N-1)} = (1-\varepsilon_{1cr})^{1-\alpha_1} \left(\frac{\bar{\sigma}_{33(N-1)}}{\sigma_{m1}} \right)^{\alpha_1}. \end{aligned} \tag{40}$$

According this approach, we get durability N

$$\varepsilon_{1cr}/\Delta_{\max} < N < \varepsilon_{1cr}/\Delta_{\min} \tag{41}$$

Another approximate determination of the service life N is attributed to calculation by (38) the sequence of the n values of increments of the microcrack density $\Delta_n \varepsilon_1$ for sampling acts of tension along the loading path, which is accompanied by the following averaging. Such approach yields

$$N = \varepsilon_{1cr} \left[\frac{1}{n} \sum_{i=1}^{n} \left(\frac{\bar{\sigma}_{33(i)}}{\sigma_{m1}} \right)^{\alpha_1} (1-\varepsilon_{1(i)})^{1-\alpha_1} \right]^{-1}, \tag{42}$$

where $\varepsilon_{1(i)} = i\frac{\varepsilon_{1cr}}{n}$ is the microdefect concentration within the range $\left[\varepsilon_{1(1)}, \varepsilon_{1cr}\right]$.

The approach proposed makes it possible to find the residual ultimate strength of the material $\sigma_{(b1)oc}$ after n-fold loading and the conditional fatigue limit σ_{1yc} for the prescribed testing base N. The unknown values are determined by

$$\begin{aligned} \sigma_{(b1)oc} &= \sigma_{m1} \left(\varepsilon_{1cr} - \varepsilon_{1(n)} \right)^{1/\alpha_1} (1-\varepsilon_{1cr})^{1-1/\alpha_1}; \\ \sigma_{1y} &= \sigma_{m1} \varepsilon_{1cr}{}^{1/\alpha_1} (1-\varepsilon_{1cr})^{1-1/\alpha_1} / N_0^{1/\alpha_1}, \end{aligned} \tag{43}$$

where $\varepsilon_{1(n)}$ is the microdefect concentration caused by the n-fold loadings. In relations (38)–(41) index in brackets show the dependence of the amplitude value of stress $\bar{\sigma}_{33(n-1)}$ on the number of half cycles of tension. Such dependence, according to (36), is associated with the change compliance a^E_{3333}, piezoelectric d_{333} and dielectric $\mathfrak{э}^{\sigma}_{33}$ constants with increasing concentration of microdefects, which increases with the half cycles of tension.

Half cycles of compression in this model does not affect on the constructions resource at the same compressive loading. However, fatigue failure is possible under compression due to increasing the stress amplitude with increasing the compression cycles without changing the effective area.

6 Numerical Example

To illustrate the approach for determining the durability of structures such as piezoceramic transducer of the electromechanical energy using a statistical fracture criterion, the problem of the durability of piezoceramic rods at the longitudinal vibrations is considered. For the piezoelectric ceramic CTBS-3 rod value of cyclical durability N is calculated. Rod has length equal to $l = 0.2$ m and parameters

$$E_{11}^{(0)} = E_{22}^{(0)} = 1.12 \times 10^{11}\ \text{Pa}, \quad E_{33}^{(0)} = 1.19 \times 10^{11}\ \text{Pa}$$

$$\nu_{12}^{(0)} = \nu_{21}^{(0)} = 0.30,\ \rho = 7.10 \times 10^{3}\ \frac{\text{kg}}{\text{m}^3},\ \sigma_{(b3)0} = 0.36 \times 10^{8}\ \text{Pa},\ D_{(b3)0} = 0.14 \times 10^{7}\ \text{Pa},$$

$$k_2 = 0.04,\ \ \ni_{33}^{(0)} = 0.21 \times 10^{-7}\ \frac{\Phi}{\text{m}},\ e_{333}^{(0)} = 0.43 \times 10^{2}\ \frac{\text{Kl}}{\text{m}^2},\ d_{333}^{(0)} = 0.36 \times 10^{-9}\ \frac{\text{Kl}}{\text{N}}.$$

Longitudinal vibrations excited by the time-variable difference of potential is exerted on the end faces

$$V_0 = 2 \times 10^{4} e^{i\omega t},\ \omega = 2 \times 10^{4}\ \text{Hz}.$$

The parameters of (38) and (39), determining the concentration of microdefects under cyclic loading, in accordance with (7), have values

$$\alpha_1 = 24.660,\ \sigma_{m1} = 0.427 \times 10^{8}\ \text{Pa}.$$

Critical concentrations of microcracks in accordance with (16) is

$$\varepsilon_{1cr} = 0.305 \times 10^{-1}$$

Assessment of the durability of piezoceramic rod under cyclic tension which is caused by potential difference accordance of (40) and (41) gives the result

$$0.859 \times 10^{39} > N > 0.305 \times 10^{37}.$$

Using (42), we obtain more specific result: $N = 0.240 \times 10^{38}$.

As it follows from the fatigue theory, such results are well admissible. It should be noted that the service life of the rod is minimal when the exciting frequency coincides with the main frequency of the natural vibrations of the rod, i.e., under conditions of resonance.

7 Conclusions

In the paper, the statistical fracture criterion under static and cyclic loadings has been proposed based on modern ideas about the macrodestruction mechanism of brittle materials. This criterion can be used in the assessment of durability, residual strength for piezoceramic products at electroelasticity loading.

References

1. Suresh, S.: Fatigue of Materials. Cambridge University Press, Cambridge (1998)
2. Bolotin, V.V.: Prediction of Service Life of Machines and Structures. Mashinostroenie, Moscow (in Russian) (1984)
3. Suo, Z., Kuo, C.-M., Barnett, D.M., Willis, J.R.: Fracture mechanics for piezoelectric ceramics. J. Mech. Phys. Solids **40**(4), 739–765 (1992)
4. Fuchs, H.O., Stephens, R.J.: Metal Fatigue in Engineering. Wiley, New York (1980)
5. Pook, L.: Metal Fatigue. Springer, New York (2009)
6. Luo, J., Bowen, P.: A probabilistic methodology for fatigue life prediction. Acta Materiala **51** (12), 3537–3550 (2003)
7. Righiniotis, T.D., Chryssanthopoulos, M.K.: Probabilistic fatigue analysis under constant amplitude loading. J. Construct. Steel Res. **59**(7), 867–886 (2003)
8. Xiao, Y.C., Li, S., Gao, Z.: A continuum damage mechanics model for high cycle fatigue. Int. J. Fatigue **20**(7), 503–608 (1998)
9. Upadhyaya, Y.S., Sridhara, B.K.: Fatigue life prediction. A continuum damage mechanics and fracture mechanics approach. Mater. Des. **35**, 220–224 (2012)
10. Babich, D.V., Bastun, V.N.: On dispersed microdamageability of elastic-brittle materials under deformation. J. Strain Anal. **45**(1), 57–66 (2010)
11. Babich, D.V.: A statistical strength criterion for brittle materials. Strength Mater. **43**(5), 573–582 (2011)
12. Babich, D.V.: Simulation of coupled processes of deformation and cracking in elastic brittle materials. Strength Mater. **36**(2), 178–184 (2004)
13. Eshelby, J.D.: The determination of the elastic field of an ellipsoidal inclusion and related problems. Proc. R. Soc. Lond. A **241**, 376–393 (1957)
14. Parton, V.Z., Kudryavtsev, B.A.: Electromagnetoelasticity of Piezoelectric and Conductive Bodies, Moscow: Nauka, p. 470 (1988). (In Russian)
15. Babich, D.V., Bezverkhyi, O.I., Dorodnykh, T.I.: Continuum model of deformation of piezoelectric materials with cracks. Appl. Mech. Mater. **784**, 161–172 (2015)

Numerical Analysis of Child Restraint System Equipped with Built-in Belts Pretensioner During Frontal Impact

Paweł Baranowski, Jakub Bukała, Krzysztof Damaziak, Jerzy Małachowski, Łukasz Mazurkiewicz and Muszyński Artur

Abstract In this paper a practical modeling methodology and obtained results are presented for a series of finite element method numerical analyses of Child Restraint System (CRS) operation during frontal impact car accident, with particular emphasis on Built-in Belts Pretensioner (BBP) modeling in terms of child's body response. Built-in belts pretensioner is acting similar to the pyrotechnic pretensioners used for adult passengers, reducing seat belts misuse. As a result, the new design gives high level of protection for the child in many different crash scenarios (the maximum values of deceleration are smaller, what in turn translates to smaller forces acting on internal organs). The effectiveness of the new solution was confirmed by numerical tests, however, a sensitivity study on BBP key characteristics has been needed to optimize the system behavior in different conditions. The ATD's head acceleration and relative displacement histories with Head Injury Criterion (HIC) value were measured as functions of key design parameters of BBP. It is shown that the obtained results demonstrate a valuable guideline for future BBP's design process.

1 Introduction

In 2005, in the United States of America only, costs associated with motor vehicle-related fatal and nonfatal injuries among 0–14 year-old children amounted to over 3.6 billion USD [1]. Moreover, European Commission (EC) has reported around 30 000 road fatalities and 250 000 seriously injured in 2012 with similar numbers reported in previous years [2]. Such statistics must draw the attention, which show that motor vehicle crashes are the leading cause of children deaths both in the US and Canada [3]. The same fact applies to European region [4]. What is

P. Baranowski · J. Bukała (✉) · K. Damaziak · J. Małachowski · Ł. Mazurkiewicz · M. Artur
Department of Mechanics and Applied Computer Science, Military University of Technology, 2 Gen. S. Kaliskiego Str., 00-908 Warsaw, Poland
e-mail: jakub.bukala@wat.edu.pl

J. Awrejcewicz (ed.), *Dynamical Systems: Modelling*, Springer Proceedings in Mathematics & Statistics 181, DOI 10.1007/978-3-319-42402-6_3

even more alarming, despite of a mandatory use of various child-resistant systems (CRS) and existence of such regulations as UN/ECE Regulation 44, this situation has not changed over the last few years [5].

Since years, EC has in place special program aimed toward increase of road safety. One of its objectives, recognized as a key to reach this goal, is increase passive safety of vehicles. The most important (from EC point of view) tools to improve road safety are speed limit enforcements and still new obligations put on vehicle makers. Example of such strategy is child seats or more broadly child-resistant systems (CRS). Old provisions for child seats are not very accurately defined. In short, requirements are as follows [6]:

- chest acceleration less than 55 g (for a certain duration of time),
- abnormal penetration of the body in the lower lumbar spine,
- child position after rotation of the chair,
- allowable displacement of a child.

In the reality a lot of side crashes take place when a struck car moves forward. From an analysis of iGLAD accident databases [7], 54 % of crashes involving children and CRS, have almost longitudinal accelerations, the remaining 46 % have transverse acceleration components and only 9 % have pure transversal accelerations (Fig. 1).

The authors of this paper present a concept of Built-in Belts Pretensioner (BBP), similar to the pyrotechnic pretensioners used for adult passengers reducing seatbelts misuse, which is applied in the selected Child Restraint System (CRS).

A series of frontal impact car accident simulations were carried, with particular emphasis on modeling in terms of child's body response. The conditions of simulations correspond to Regulation No 44 of the Economic Commission for Europe of the United Nations (UN/ECE) [6]. Sensitivity study on BBP key characteristics such as the moment of its activation is also shown. The ATD's head acceleration and relative displacement histories with Head Injury Criterion (HIC) value were measured as functions of key design parameters of BBP.

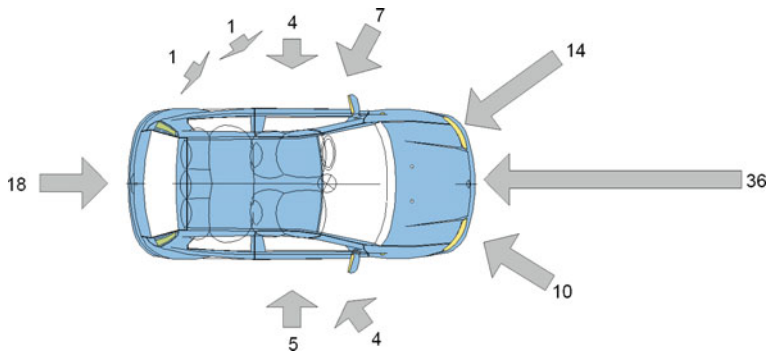

Fig. 1 Percentage of principal direction of force during the impact in accident involving CRS [7]

2 Numerical Modeling of CRS with BBP

Explicit numerical software was chosen to carry out analyses. The Finite Element Method (FEM) based code uses an explicit time integration scheme to analyze short duration events. It is a well-recognized tool used worldwide to analyze motor vehicle crash events.

During the investigations, the central difference method for integration over time was adopted, which is one of the variant of the finite difference method [8]. Assuming very small time steps, the equilibrium equation can be described as follows:

$$\boldsymbol{M}\,\ddot{\boldsymbol{x}}_{\boldsymbol{n}} + \boldsymbol{C}_d\,\dot{\boldsymbol{x}}_{\mathbf{n}} + \boldsymbol{F}_n^{\text{int}} = \boldsymbol{F}_n^{ext} \tag{1}$$

where: $\ddot{\boldsymbol{x}}_{\mathbf{n}}$, $\dot{\boldsymbol{x}}_{\mathbf{n}}$—acceleration and velocity vectors at t_n, $\boldsymbol{F}_n^{\text{int}} = \boldsymbol{K}_n \mathbf{x}_{\boldsymbol{n}}$—vector internal forces at t_n, $\boldsymbol{F}_{\mathbf{n}}^{\mathbf{ext}}$—vector of external forces at t_n.

A solution of the above equation is obtained with numerical integration of acceleration $\ddot{\mathbf{x}}_{\mathbf{n}}$ under the assumption that $\dot{\mathbf{x}}_{\mathbf{n}} \approx \dot{\mathbf{x}}_{\mathbf{n}-\frac{1}{2}}$:

$$\ddot{\mathbf{x}}_{\mathbf{n}} = \mathbf{M}^{-1}\left(\mathbf{p}_{\mathbf{n}} - \mathbf{C}\,\dot{\mathbf{x}}_{\mathbf{n}-\frac{1}{2}} - \mathbf{F}_n^{\text{int}}\right), \tag{2}$$

the implementation of the central difference equations for the velocity and displacement results in:

$$\ddot{\mathbf{x}}_{\mathbf{n}} = \frac{1}{\Delta t_n}\left(\dot{\mathbf{x}}_{\mathbf{n}+\frac{1}{2}} - \dot{\mathbf{x}}_{\mathbf{n}-\frac{1}{2}}\right) \Rightarrow \dot{\mathbf{x}}_{\mathbf{n}+\frac{1}{2}} = \dot{\mathbf{x}}_{\mathbf{n}-\frac{1}{2}} + \Delta t_n\,\ddot{\mathbf{x}}_{\mathbf{n}}\,, \tag{3}$$

$$\dot{\mathbf{x}}_{\mathbf{n}+\frac{1}{2}} = \frac{1}{\Delta t_{n+\frac{1}{2}}}\left(\mathbf{x}_{\mathbf{n}+\mathbf{1}} - \mathbf{x}_{\mathbf{n}}\right) \Rightarrow \mathbf{x}_{\boldsymbol{n}+\boldsymbol{1}} = \mathbf{x}_{\mathbf{n}} + \Delta t_{n+\frac{1}{2}}\,\dot{\mathbf{x}}_{\mathbf{n}+\frac{1}{2}}\,, \tag{4}$$

The major advantage of this method is lack of time-consuming operations involving the stiffness matrix inversion. Instead, only a diagonal matrix of mass is inverted. However, the main disadvantage is that the method is conditionally stable requiring a time step to be limited according to the Courant–Friedrichs–Lewy (CFL) stability condition [8]:

$$\Delta t^{n+1} = C \cdot \min(\Delta t_1, \Delta t_2, \Delta t_2, \ldots., \Delta t_N), \tag{5}$$

where: N—number of elements, C—scale factor related to (CFL) condition.

2.1 Numerical Model of CRS with Dummy

In the investigations, the verified numerical model of the representative ISOFIX mounted CRS prototype was used. Most of the structure was modeled using 4 node shell elements utilizing Belytschko-Tsay formulation [8], however, *t*-shell and brick elements were also used. Different elements of CRS had different material properties listed in Table 1. Stress–strain relationships for narrow and wide CRS were acquired experimentally using Instron 8802 test device. Foams material properties for the described parts were adopted with characteristics obtained during parallel studies concerning CRS testing. Quasi-static axial compression tests (using the same machine) were carried out with cubical specimens of 100 mm width and 50 mm height with the strain rate influence taken into consideration.

The child was represented by the FE model of Q3 Anthropomorphic Test Device (ATD) by Humanetics Innovative Solutions company. It represents about 3YO child, weighted 14.5 kg. It consists of 165 different parts.

The final, complete numerical model consisted of:

- CRS (51296 elements and 62951 nodes),
- seat (1488 elements and 2080 nodes),
- backseat (1176 elements and 1744 nodes),
- Q3 dummy (92176 elements and 51062 nodes).

The major and the most important aspect of CRS and a dummy interaction simulation is the proper modeling of seatbelts. First, mechanical properties of the belt material were described based on the results obtained from uniaxial tension tests carried out for two different seatbelts of CRS [9, 10]. The data was implemented into the selected constitutive model that provides a correct description of the belt material behavior during analyses. The seatbelt system consisted of 2D elements combined with 1D elements and null elements to properly simulate

Table 1 Material properties adopted in CRS model

	Density ρ (kg/m^3)	Young modulus E (GPa)	Poisson ratio ν (–)	Yield stress Re (MPa)	Tangent modulus E_{tan} (MPa)
Steel	7850	210	0.3	400	1000
Polyamide	1130	3	0.3	85	100
Aluminum	2700	70	0.3	120	500
Polypropylene (Tiplen)	900	1.3	0.45	7	Curve
Headrest foam	60	0.00025	–	–	Curve
Polystyrene foam	27	0.019	0.3	–	–
Fabric	970	E_a = 6.2 / E_a = 6.2	0.3	–	Curve

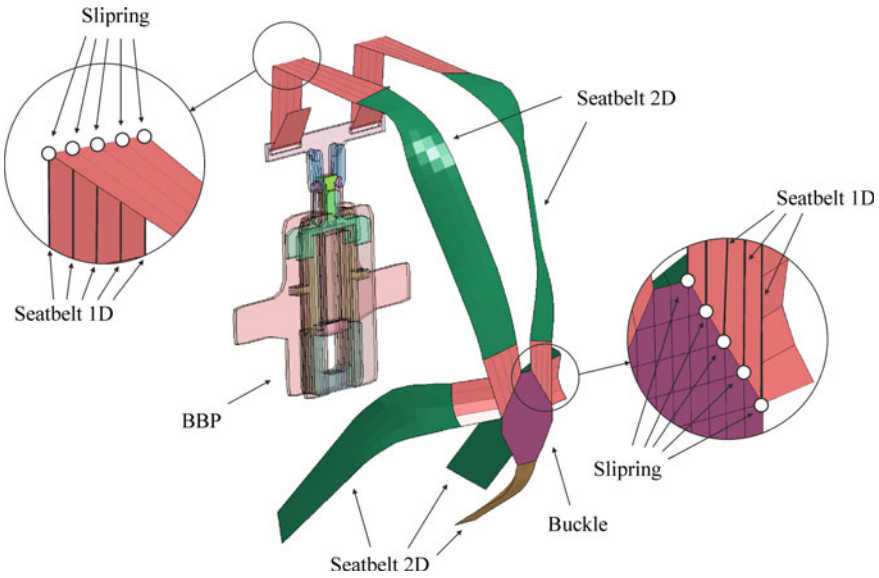

Fig. 2 Seat belt modeling in carried out analyses

interaction with the dummy. 2D seatbelts parts were finely meshed to accurately distribute contact forces between dummy parts and the belt itself. To simulate slipping of the belt in the buckle, an additional feature was added to numerically simulate such an effect (slip ring). The described seatbelt system is presented in Fig. 2, whereas the whole numerical model ready for simulations with applied initial boundary conditions is presented in Fig. 3.

General concept of the analyses was to perform crash test similar to the one described in Regulation 44 as mentioned earlier. Prescribed velocity in global X direction was applied to the seat, backseat, and ISOFIX mounts. The velocity profile was defined according to the procedure described in the Regulation 44 (Fig. 4).

In the paper, six different scenarios with different moments of activation of BBP were simulated and compared in terms of accelerations acting on the dummy and its behavior during the impact:

- analysis no. 1 with $t_1 = 5$ ms taken as activation time,
- analysis no. 2 with $t_2 = 10$ ms taken as activation time,
- analysis no. 3 with $t_3 = 20$ ms taken as activation time,
- analysis no. 4 with $t_4 = 30$ ms taken as activation time,
- analysis no. 5 with $t_5 = 40$ ms taken as activation time,
- analysis no. 6 with $t_6 = 50$ ms taken as activation time.

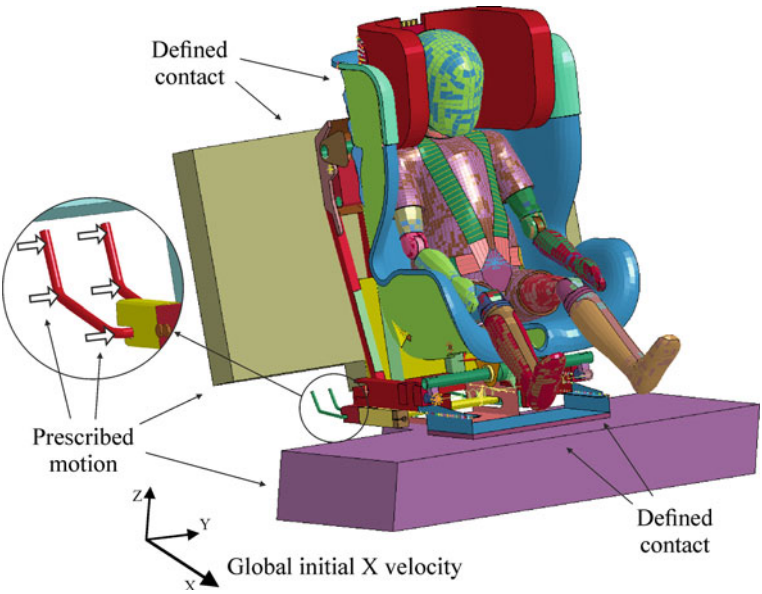

Fig. 3 Numerical model with applied initial boundary conditions

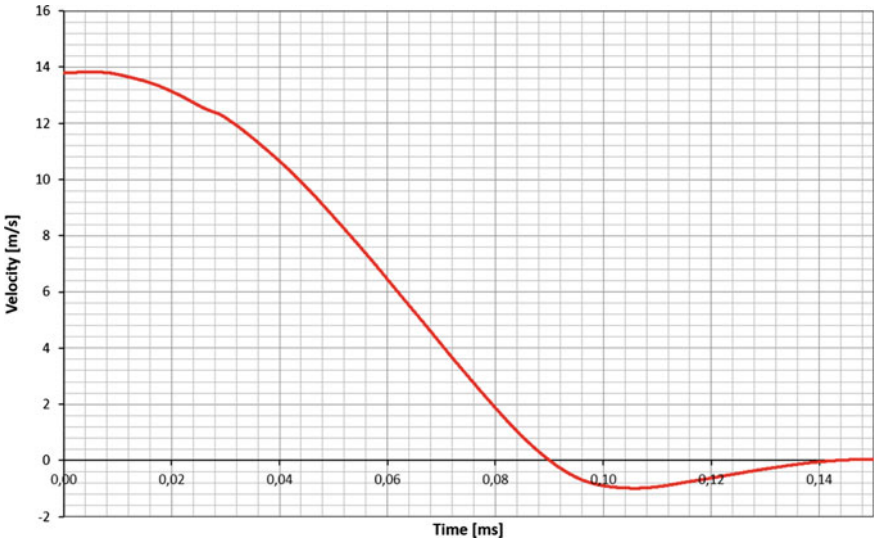

Fig. 4 Velocity curve applied in model

Penalty Contact Implementation in a FE Code

In all carried out analyses, the interaction between all parts of the model was simulated using the penalty-based method the principal of which feature can be described as placing normal interface springs between all nodes that penetrate the contact surface [8, 11, 12].

Currently, three different penalty algorithms are available:

1. Standard penalty formulation—typically used in most cases.
2. Segment-based penalty formulation, which is different from a traditional slave node-master segment approach and uses a slave segment–master segment algorithm.
3. Soft constraint penalty formulation, which is implemented in contact between bodies with dissimilar material stiffness. In fact, this approach was used by the authors in presented investigations.

By using the soft constraint approach the excessive penetration is to be eliminated due to different calculation of the contact stiffness. Therefore, an additional stiffness, apart from the slave and master contact stiffness, is calculated. It is based on the Courant–Friedrichs–Lewy (CFL) stability condition [8] of the local system comprised of two masses of segments connected by the fictional spring. Thus, for the parts with different stiffness a stability contact stiffness $k_{cs}(t)$ is determined by [8]:

$$k_{cs}(t) = \frac{1}{2} S_{soft}\, m * \left(\frac{1}{\Delta t_c(t)}\right), \tag{6}$$

where: S_{soft}—scaling factor, $m*$—function dependent on masses of master and slave nodes, Δt_{cs}—initial solution time step (if the solution time step grows, Δt_c is reset to the current time step to prevent unstable behavior of the simulation).

Subsequently, the maximum value of the traditionally calculated contact stiffness and the CFL contact stiffness k_{cs} is taken [8]:

$$k_{soft=1} = \max\left\{k_{cs},\, k_{soft=0}\right\}, \tag{7}$$

In the formula (6) one can see that the contact stiffness depends inter alia on Δt_c—which in turn is estimated based on the following formula:

$$\Delta t = \min(\Delta t_{con},\, \Delta t_{FE}), \tag{8}$$

where Δt_{con}—time step size depended on the contact procedure, Δt_{FE}—time step size determined by taking a minimum value over the elements

It should be pointed out that in the contact procedure the Coulomb friction model was used which includes the static and kinetic coefficients of friction [8]:

$$\mu = \mu_D + (\mu_S - \mu_D)e^{-D_C|V_W|}, \tag{9}$$

where: μ_D—dynamic coefficient of friction, μ_S—static coefficient of friction, D_C—exponential coefficient, V_W—relative velocity between two bodies in contact.

2.2 BBP Description

The BBP device is intended to reduce the possibility of uncontrolled movement of the child's body in relation to the seat shell in the initial phase of a frontal or side collision of a vehicle and to actuate within as short a time as possible. The application of a safety belt pretensioning system makes it possible to reduce the maximum decelerations that act on the body of a child transported in a motor vehicle in a safety seat during a road accident. Thanks to this, the risk of serious injuries to the child's body may be thus reduced.

The principal of BBP operation is as follows (Fig. 5):

1. Initial position of locking elements (red) prevents movement of actuating mechanism (blue).
2. Activation element (yellow) expands locking elements (red).
3. Actuating mechanism (blue) pulls seatbelts (red).

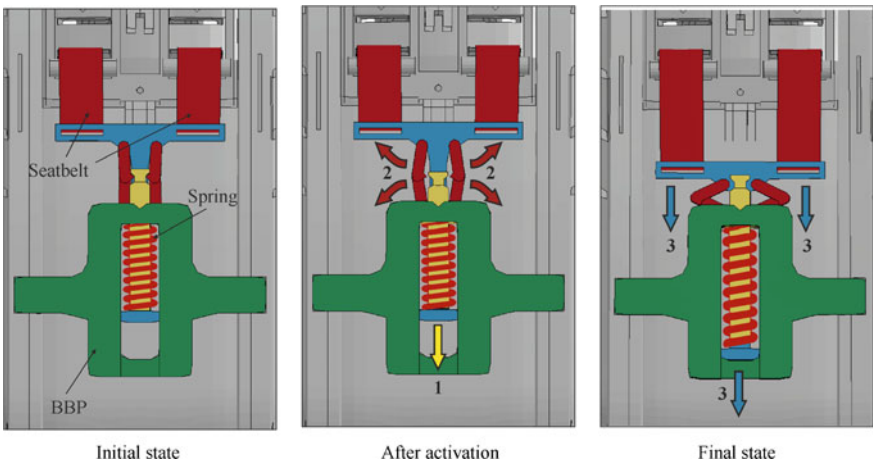

Fig. 5 Three selected BBP operating states

3 Results and Discussion

One of the most important injury criteria used to evaluate severity of the crash is head injury criteria (HIC). It is based on an acceleration history measured in the ATD's head. It is given by the following formula:

$$HIC = \max\left[\frac{1}{(t_2 - t_1)}\int_{t_1}^{t_2} a(t)dt\right]^{2.5}(t_2 - t_1) \tag{10}$$

where $a(t)$—acceleration measured in head, t_1—beginning of time interval, t_2—end of time interval.

The time interval for HIC calculation presented below was 36 ms. According to NHCTSA, limiting HIC limit value for this time interval is 1000 [13].

From the simulations carried out a general behavior of the CRS–BBP–Dummy system was obtained (Fig. 6). In Fig. 7 the ATD's head acceleration histories are shown for all six simulations and for the case without the pretensioner. At first glance the curves seem to be similar, however, more thorough analysis of the results show that the worst scenario is the one where the pretensioner was not used: the calculated HIC value was the largest one. For better presentation of differences between the obtained results the HIC versus activation time graph is shown in Fig. 8. One can notice that for analysis with $t_1 = 5$ ms HIC value was the lowest one, whereas increasing time of activation resulted in the increase of HIC value. However, between the first four analyses (from $t_1 = 5$ ms to $t_4 = 30$ ms) the maximum difference is 20. On the other hand a difference between analysis no. 1 and no. 5 is by one order of magnitude. Additionally, discussed results are listed in Table 2.

In Fig. 9 maximum value of ATD's relative (between ISOFIX and center of head) head displacement versus activation time graph is presented. Here, similar

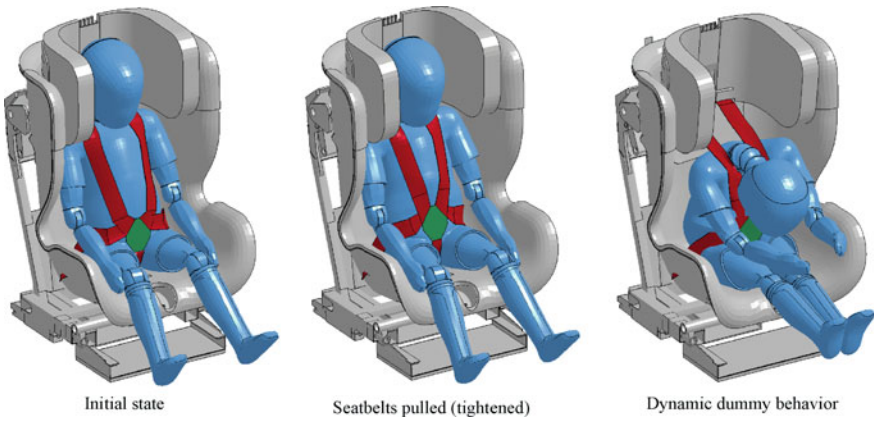

Fig. 6 Dummy behavior during simulation (activation time $t_1 = 5$ ms)

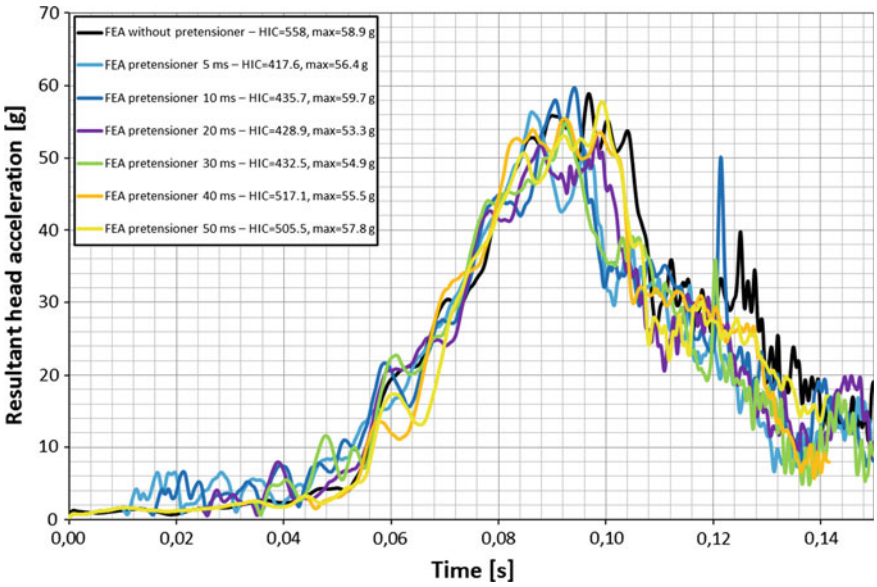

Fig. 7 Time histories of resultant acceleration in ATD head for all simulated scenarios

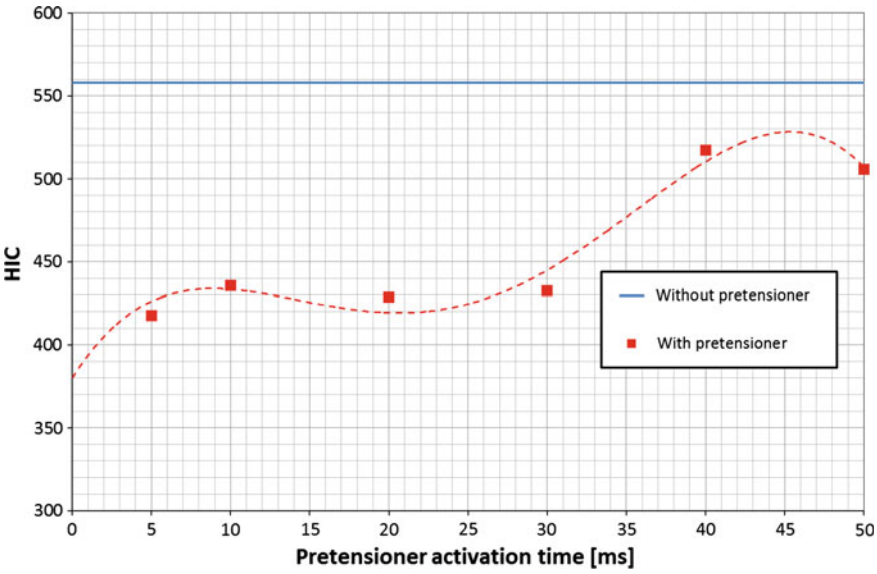

Fig. 8 HIC versus pretensioner activation time

Table 2 HIC values in all simulated scenarios

Activation time	5 ms	10 ms	20 ms	30 ms	40 ms	50 ms	No pretensioner
HIC	417.6	435.7	428.9	432.5	517.1	505.5	558

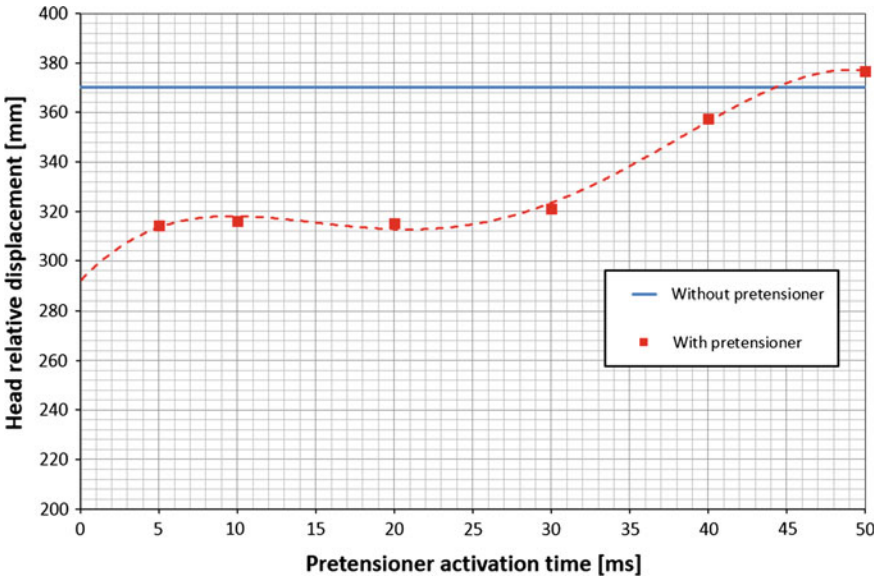

Fig. 9 Maximum head relative displacement versus pretensioner activation time

conclusions can be withdrawn. BPP activation time from $t_1 = 5$ ms to $t_4 = 30$ ms resulted in smaller discrepancies between the obtained maximum displacement. Increasing the activation time to $t_5 = 40$ ms and $t_6 = 50$ ms caused a major increase of maximum ATD's head displacement. However, lower maximum displacement was obtained for the analysis no. 6 ($t_6 = 50$ ms) than in case of CRS without the pretensioner.

4 Summary

The authors present the idea of a BBP–CRS system allowing for better protection of children transported in CRS during vehicle frontal impact. In the paper the basic concept with its principle of operation is presented. Moreover, its numerical implementation with numerical simulations reflecting frontal impact procedure described in UN/ECE Regulation 44 are also described. The results show BPP influence on ATD's head acceleration and displacement; by introducing the device

their values became smaller. The results also show that the earlier action of the child's body on safety seat components means earlier start of the process of slowing down the child's body during a frontal vehicle collision. Therefore, the risk of serious injuries to the child's body may be reduced.

References

1. Naumann, R.B., Dellinger, A.M., Zaloshnja, E., Lawrence, B.A., Miller, T.R.: Incidence and total lifetime costs of motor vehicle-related fatal and nonfatal injury by road user type, United States. Traffic Inj. Prev. **11**(4), 353–360 (2010)
2. http://ec.europa.eu/transport/road_safety/pdf/vademecum_2013.pdf
3. NHTSA. Traffic safety facts: Children. 2010 data. NHTSA. DOT HS 811 641 (2012). http://www-nrd.nhtsa.dot.gov/Pubs/811641.pdf)
4. World Health Organization. European status report on read safety, Copenhagen (2009)
5. Arbogast, K: A public health priority for only ten percent of the car occupant population: why focus on children and how are they different biomechanically. In: Proceedings of the International Conference on the Biokinetics of Impact. Berlin, Germany (2014)
6. UNECE Regulation No. 44
7. http://www.iglad.net
8. Hallquist, J.O.: LS-DYNA Theory Manual. Livermore Software Technology Corp, Livermore (2006)
9. Muszyński, A., Trzaska, P., Wicher, J., Mazurkiewicz, Ł.: Analiza sił działających w taśmach pasów podtrzymujących dziecko w foteliku bezpieczeństwa (in polish). Archiwum Motoryzacji **67**(1), 239–252 (2015)
10. Baranowski, P., Damaziak, K., Malachowski, J., Mazurkiewicz, L., Muszynski, A.: A child seat numerical model validation in the static and dynamic work conditions. Arch. Civ. Mech. Eng. **15**(2), 361–375 (2015)
11. Vulovic, S., Zivkovic, M., Grujovic, N., Slavkovic, R.A.: Comparative study of contact problems solution based on the penalty and Lagrange multiplier approaches. J. Serb. Soc. Comput. Mech. **1**(1), 174–183 (2007)
12. Belytschko, T., Liu, W.K., Moran, B.: Nonlinear Finite Elements for Continua and Structures. Wiley, UK (2000)
13. Eppinger, R., Sun, E., Bandak, F., Haffner, M., Khaewpong, N., Maltese, M., Kuppa, S., Nguyen, T., Takhounts, E., Tannous, R., Zhang, A., Saul, R.: Development of Improved Injury Criteria for the Assessment of Advanced Automotive Restraint Systems—II. National Highway and Traffic Safety Administration (1999)

Analysis of the Dynamic Behavior of a Radar Tower

Rui Barros, Hugo Guimarães and Manuel Braz César

Abstract The present work addresses the study of the dynamic behavior of a metallic steel tower 45 m high, supporting a radar antenna. Some methodologies are followed for the characterization of the major external excitation on the radar tower, namely the environmental actions due to wind and the seismic action as well. A complementary study associated with the dynamic effects due to the antenna rotation is also emphasized, since it is related with crucial malfunctioning of the mounted equipment. Finally, it is proposed a solution for the control of vibrations, through the design and installation of tuned liquid dampers at the instrumental platform near the top of the radar tower; a few advantages associated with such improved implementation are discussed.

1 Introduction

Nowadays, with the possibility of free movement of people among member states of the Schengen Agreement, Europe needs to take special care with the maritime borders since many illegal operations and black market play an increasingly

R. Barros (✉)
Faculty of Engineering, Department of Civil Engineering, University of Porto,
Rua Dr. Roberto Frias s/n, 4200-465 Porto, Portugal
e-mail: rcb@fe.up.pt

H. Guimarães
Institute for Sustainability and Innovation in Structural Engineering,
University of Minho, Campus de Azurém, 4800-058 Guimarães, Portugal
e-mail: hugo.guimaraes@fe.up.pt

M.B. César
Department of Applied Mechanics, Polytechnic Institute of Bragança,
Quinta de S. Apolónia, 5300-253 Bragança, Portugal
e-mail: brazcesar@ipb.pt

J. Awrejcewicz (ed.), *Dynamical Systems: Modelling*, Springer Proceedings
in Mathematics & Statistics 181, DOI 10.1007/978-3-319-42402-6_4

prominent role. Illegal immigration, drugs trafficking, smuggling, illegal fishing, and piracy are examples of threats that coastal areas have to deal with. Hence, the implementation of coastal surveillance systems such as radar towers has been growing in the past few years bringing new challenges for structural engineers regarding to design of high height supporting structures.

Radar towers are normally self-supporting lattice towers, since their prime requirement is the antenna elevation. These towers are lightweight and slender structures, which make them quite sensitive to dynamic actions, especially of environmental origin, such as wind gusts and earthquakes. The vibrations induced by these causes cover an ample spectrum of frequencies which affects the towers in different ways, ranging from serviceability problems, to fatigue or collapse [1].

This work seeks to evaluate the dynamic behavior of a 45 m high radar tower, with multiple implementations sites at Portuguese coast. The symmetric four-legged self-supporting tower presents excessive oscillations when the antenna is operating at high rotational speeds (above 50 rpm). The interaction between structure's natural vibration and unbalanced forces caused by antenna rotation can be observed even without instrumentation. In order to avoid these performance drawbacks, antenna rotating speed is limited, being consequently, its range affected.

According to the literature review, there are no bibliographical references whose research faced this type of interaction. However, several authors have dealt with similar situations, e.g., bells swinging at bell towers [2].

Our strategic approach to identify the observed vibration problem was first characterizing the tower's dynamics properties and the excitation frequency spectrum. Therefore, a structural finite element model (FEM) was developed using SAP2000 and modal analysis results were validated with theoretical simplified expressions [3].

Concerning to antenna rotation, rigid body dynamics theory was clearly found insufficient to determine the associated dynamic action. Assuming the antenna as a massless flexible beam with two end lumped masses, in which its midpoint and rotation shaft are coincident, allowed to overcome this obstacle. Then, to describe the dynamic action a parametric study concerning the presence of two scenarios of eccentricities was performed. Transversal and longitudinal eccentricities along antenna's cross-section and length, respectively, were considered. Herein both formulation and reasoning regarding these limit situations, which led to an unbalanced harmonic excitation, are discussed.

In order to mitigate simulated dynamic effects, the installation of a suitable vibration control system is investigated. Hence, a solution based on the application of a tuned liquid damper (TLD) at the top of the structure is presented. Regarding the liquid hydrodynamic behavior, a simplified mechanical model is assumed based on state of the art. Finally, both installation recommendations and solution's detailing are highlighted and conclusions are drawn.

2 Dynamic Action Due to Antenna Rotation

Aiming to understand the dynamic interaction between structure's natural vibration and antenna rotation, it is crucial to reliably obtain the dynamic properties of tower. Therefore, both stiffness and mass quantities have to be carefully treated in order to properly characterize modal shapes and its frequencies. Besides, describing excitation frequency spectrum also helps to identify beforehand possible resonance phenomena. In this chapter, modal analysis results are presented, later the parametric study is formulated.

2.1 Modal Analysis

A structural finite element model was developed using SAP2000, regarding the symmetric four-legged self-supporting steel tower, which is schematically represented in Fig. 1. The connections between structural members and between structure and the foundation are assumed to be rigid; these insure absence of semi-rigid joint behavior and of soil-structure interaction effects. Due to the slenderness of the

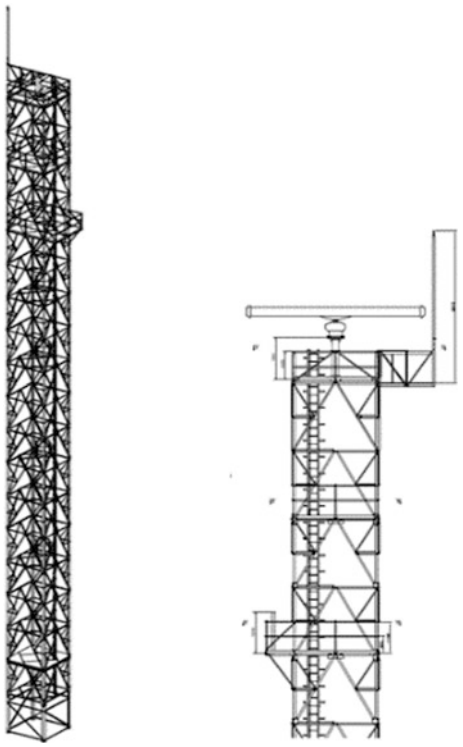

Fig. 1 Representation of the radar tower

Table 1 Natural modes and frequencies of the tower

Mode	Frequency (Hz)	Description
1	0.91	1st flexural mode (X)
2	0.91	1st flexural mode (Y)
3	3.22	Torsional mode
4	4.87	2nd flexural mode (X)
5	4.90	2nd flexural mode (T)

angle profiles used in the tower structural design, shear deformability is disregarded.

According to a modal analysis through eigenvalues and eigenvectors determination, the structure presents five significant vibration modes. Natural frequencies and description of the undamped free-vibration mode shapes are presented in Table 1.

2.2 Scenarios Formulation for Dynamic Interaction

In relation to antenna rotation two different regimes can be distinguish, namely transient regime and steady-state regime. The first refers to antenna' status when it is changing from one steady-state regime to another. The second concerns a constant angular velocity state.

According to rigid body dynamics only in transient regimes, involving nonzero acceleration, a torsional moment or torque is applied to the structure. However, in this case study, excessive oscillations are experienced even in steady-state regimes. Since this theory is clearly insufficient to determine a dynamic action associated to antenna rotation, it was assumed that the antenna can be idealized as a massless flexible beam with two end lumped masses, in which its midpoint and rotation shaft are coincident.

By doing so, an external dynamic excitation can be developed when considering the presence of geometric asymmetries. In fact, two different scenarios of eccentricities were formulated. The first scheme was devised considering a permanent deformation of the beam, changing the two lumped masses' position, i.e., both particles move from the original location to a new deflected point. This distortion can be caused by several reasons, such as wind drag force, temperature changes within the body or even manufacturing imperfections. These transverse displacements e_t only create a resultant force F_R when they occur in same direction of the antenna cross-section. A scheme representing these geometric transversal eccentricities is shown in Fig. 2a.

The second scenario assumes uneven distribution of mass around the rotation axis, so that the center of gravity is out of alignment with the center of rotation, i.e., there is a longitudinal eccentricity. This phenomenon is the so-called rotating unbalance that has been object of research and developments in the field of mechanical vibrations [4].

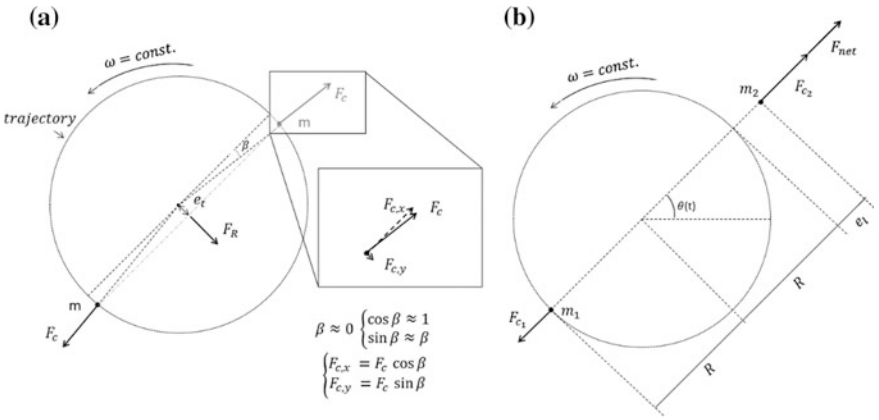

Fig. 2 Geometric eccentricities representation

Unbalance force F_{net} causes a harmonic excitation in both orthogonal axes (i.e., in the x-axis and y-axis), since the centrifugal force is attached to the antenna circular motion, as well as the aforementioned resultant force. A representation of the geometric longitudinal eccentricity is presented in Fig. 2b.

With these considerations, both eccentricities allow to induce dynamic nature to the antenna rotation. Indeed, in each scenario there is a noncompensated centrifugal force attached to antenna's circular periodic motion. In terms of magnitude, F_R and F_{net} are equal when the longitudinal eccentricity is the double of the transversal eccentricity. Regarding their direction, these forces are perpendicular.

2.3 Linear Time-History Analysis

Multiple time-history analysis was performed to assess the dynamical response of the structure subjected to the aforementioned external excitation. In fact, both displacements and acceleration at the top of the structure were analyzed for different longitudinal and transversal eccentricities. Maximum values allowed were assumed as equal to 5 % of antenna's dimensions. Both steady-state and transient regime were evaluated as it is resumed in Table 2. Note that a suitable time step must be chosen to properly estimate the dynamic response.

Table 2 Dynamic action characterization at evaluated scenarios

Eccentricity \regime	Steady state	Transient
Longitudinal	$F_R = 2m \cdot \omega^2 \cdot e_t$	$F_R(t) = 2m \cdot \omega^2(t) \cdot e_t$
Transversal	$F_{net} = m \cdot \omega^2 \cdot e_l$	$F_{net}(t) = m \cdot \omega^2(t) \cdot e_l$

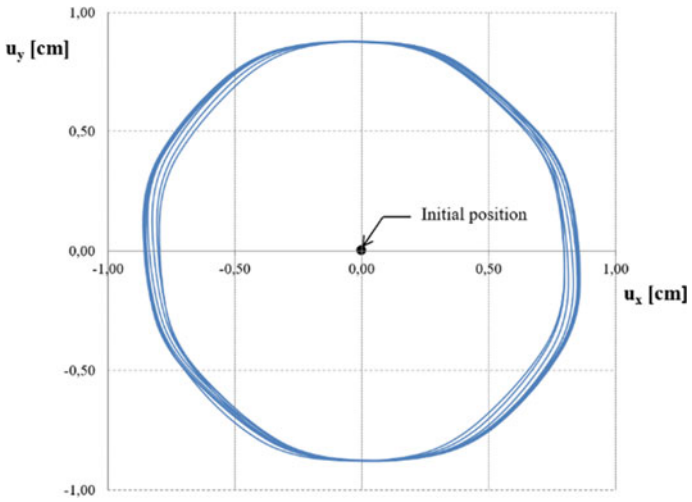

Fig. 3 Time-varying movement of the radar platform center during the steady-state regime (60 rpm; 1 Hz)

The results obtained regarding the modal time-history analysis showed that both formulations lead to quite excessive vibrations, which correspond to a resonance phenomenon between excitation and the first two bending modes (in the x and y directions). For excitation frequencies close to the first harmonic, the displacements and accelerations at the top of the tower are extreme, and hence, the structure steady response is ruled by the dynamic amplification factor. Since the structure is nearly symmetric, when the antenna is operating at its maximum angular velocity (60 rpm), a noncompensated centrifugal force excites the structure with a frequency of 1 Hz leading the structure to experience a circular movement around its center of rotation. Figure 3 shows representatively the variation over time of the center position of the radar equipment platform, where the antenna is installed, regarding its steady-state regime associated with the mentioned pair (60 rpm; 1 Hz).

3 Vibration Control System

Aiming at reducing the dynamic effects on structures, several types of vibration control systems can be installed. These devices are able to generate compensatory forces that reduce the system dynamic response. In this work the installation of a vibration control system capable of damping vibration effects, namely through the use of tuned liquid dampers (TLD), is discussed. A TLD consist of a tank partially filled with a free surface liquid that is (usually, but not exclusively) in contact with atmospheric pressure. This device is connected to the top of the structure so that, when it is dynamically excited, the liquid movements alter the dynamic properties

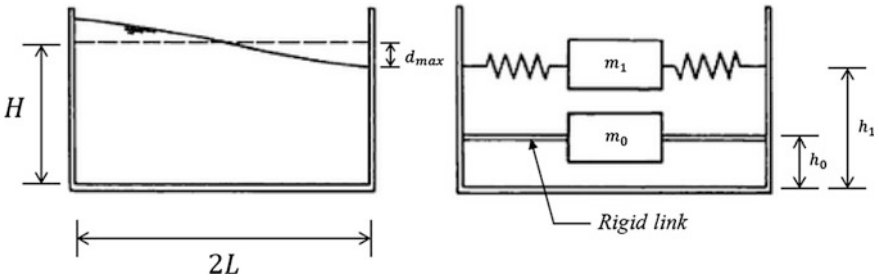

Fig. 4 Simplified mechanical model of sloshing (adapted from [8])

of the system. The main energy dissipation mechanism is associated with the waves generated by the oscillation of the liquid in the container. This phenomena so-called sloshing, occurs when the fluid is excited into resonance, which depends on the container's dimensions [5]. Although the liquid complete hydrodynamic behavior is quite complex, certain assumptions can be taken in order to achieve a simplified mechanical model, as the model proposed by Abramson [6].

Mechanical models can be helpful to investigate the dynamic behavior of the complete system. Supported by the linear wave theory described by Lamb [7], Abramson proposed an equivalent mechanical model representative of the liquid sloshing motion, based on an equivalent system with point masses, springs, and shock absorbers whose parameters are dependent on the vibration mode. Since in most current cases the fluid dynamic behavior can be represented by its fundamental mode, Housner [8] suggested a simplified equivalent model for rectangular tanks as shown in Fig. 4.

Assuming that the fluid is incompressible and that excitation amplitudes are small, components of the impulsive (m_0) and convective (m_1) masses are given by

$$m_0 = M_t \tanh \beta_0 / \beta_0 \tag{1}$$

$$m_1 = 5/6 M_t \tanh \beta_1 / \beta_1 \tag{2}$$

where M_t is the total water mass in the tank, $\beta_0 = \pi/2\ (L/H)$, $\beta_1 = 3^{1/2}\ (L/H)$, H is the water level, and L is half the tank's length in the direction of oscillation.

After characterizing Housner's model, the sizing and modeling of the TLD was conducted through an analogy to an equivalent tuned mass damper [3]. Thus, the impulsive mass is added as a dead weight to the structure, while the convective mass is the damper's mass. Although the tuning procedure corresponds to guarantee the resonance between the vibration mode to control and the fluid's fundamental mode of oscillation, it was found to be beneficial in this case to tune the frequency of maximum excitation (according to Table 1, they are in fact similar). Regarding the use of rectangular tanks, natural frequency of liquid sloshing motion is given by

$$f_{\mathrm{TLD}} = (1/2\pi)\sqrt{(\pi g/2L)\tanh(\pi H/2L)} \quad (3)$$

In addition to the tuning procedure, the damping due to the fluid motion within the tank can be also considered. According to aforementioned assumptions, the damping coefficient of liquid sloshing without additional devices was estimated by

$$\xi_{\mathrm{TLD}} = (1/2H)\sqrt{(\upsilon/\pi f_{\mathrm{TLD}})}\ (1 + H/B) \quad (4)$$

in which ν is the kinematic viscosity of the fluid and B is the width of the tank [9].

The numerical modeling of the damper behavior was performed in SAP2000 and was achieved using a link element type which is responsible for connecting two nodes. At this connection can be assigned different rheological behavior, having been introduced TLD axial stiffness in the direction of oscillation of the liquid.

The corrective intervention of this team of researchers recommended the installation of four TLDs situated at each corner on the tower platform where the antenna is located. This approach brings several potential advantages, such as less area occupied, better control of the sloshing frequency, and decreased effect of drag forces due to wind action. The properties of each damper are presented in Table 3.

Considering preventing some constraint regarding the application of the control system at the top of structure, this study also included the possibility of installation of the proposed control system at an alternative platform level immediately below the platform of the antenna. The reduction of the dynamic effects associated with antenna rotation in steady state (1 Hz) is presented in Table 4. Additionally, Fig. 5 schematically shows the reduction in the amplitude of displacements.

By analyzing the response it is noted that, as expected, the application of the TLDs at the top of the structure is more effective. However, the mitigation measure is also effective, with reductions in the order of 40 %, when the TLDs are located on the alternative platform immediately below the radar location platform level. Notice that the obtained results did not consider any damping of the liquid, since for the suggested dimensions (deep water tank) its value is almost irrelevant. However, it is

Table 3 Properties of each sloshing tank regarding the proposed solution

f_{TLD} (Hz)	L (cm)	H (cm)	m_{TLD} (ton)	m_0 (ton)	M_t (ton)	Ω_{TLD} (rad/s)	k_{TLD} (kN/m)
1.00	65	25	0.0609	0.0690	0.1056	6.283	2.405

Table 4 Solution performance at reducing oscillations and accelerations

	Without dampers	Control elevation (m)	
		45	40
Maximum displacement amplitude (cm)	1.8	0.8	1.0
Percentage reduction		56 %	45 %
Maximum acceleration (cm s^{-2})	56	35	40
Percentage reduction		38 %	29 %

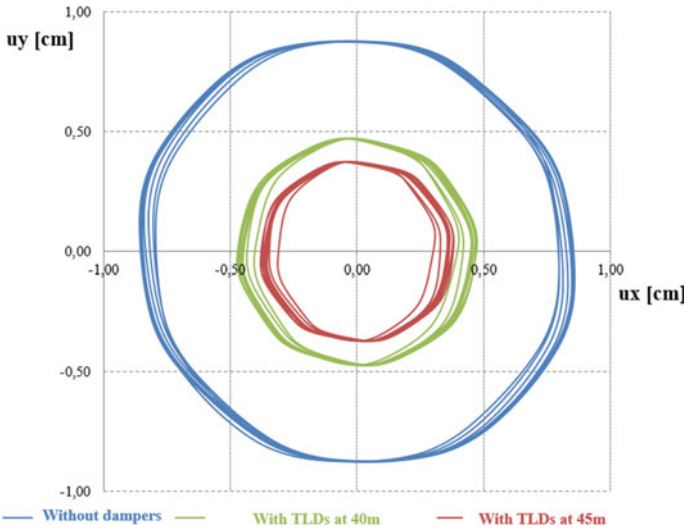

Fig. 5 Amplitude reduction of displacements at tower's top due to TLDs installation

possible to improve the dissipative behavior of the sloshing phenomenon, using either the so-called baffles or screens or additives introduced into the liquid in order to make it more viscous.

4 Conclusions

In this paper, a case study regarding the dynamic behavior of a forty-five meters high radar tower was presented. Possible causes of excessive oscillations when the antenna is operating at high rotational speeds (above 50 rpm) were investigated. Since rigid body dynamics theory was clearly found insufficient to determine the dynamic phenomena, a parametric study considering two types of eccentricities was performed. Assuming an uneven distribution of antenna's mass around its rotation shaft allowed to identify a probable cause for detected resonance phenomenon.

The presence of an unbalanced force attached to the antenna circular motion causes a harmonic excitation in both orthogonal axes, similar to a widely known phenomenon in mechanical vibrations field, namely, rotating unbalance. To mitigate observed dynamic effects, a vibration control system based on the application of a tuned liquid damper (TLD) coupled to the top of the structure is recommended. This solution encompasses the installation of four small tanks at each corner. The main dissipation mechanism is given by the sloshing phenomenon, which is tuned to control the first two natural frequencies. By doing so, results obtained using state-of-the-art simulation indicate that significant reductions of the dynamic response can be achieved, estimated in the order of 50 %.

References

1. Penalba, C.U.: Vibration control in lattice communication towers. In: Structures Congress—Proceedings, pp. 983–986 (1999)
2. Ivorra, S., Pallarés, F.J., Adam, J.M.: Dynamic behaviour of a modern bell tower: a case study. Eng. Struct. **31**, 1085–1092 (2009)
3. Guimarães, H.: Análise do comportamento dinâmico de um Torre Radar de 45 metros de altura. MSc Dissertation in Civil Engineering—Structural Engineering, Faculty of Engineering of University of Porto (2013)
4. Kelly, S.G.: Fundamentals of Mechanical Vibrations. McGraw-Hill Education (1992)
5. Swaroop, S.K.: Liquid dampers for mitigation of structural response: theoretical development and experimental validation. PhD Thesis, University of Notre Dame (2001)
6. Abramson, H.N.: The Dynamic Behavior of Liquids in Moving Containers. NASA SP-106 (1966)
7. Lamb, H.: Hydrodynamics. University Press (1916)
8. Housner, G.W.: Selected Earthquake Engineering Papers of George W. American Society of Civil Engineers, Housner (1990)
9. Sun, L.M., Fujino, Y., Chaiseri, P., Pacheco, B.M.: Properties of tuned liquid dampers using a TMD analogy. Earthquake Eng. Struct. Dyn. (1995)
10. Chopra, A.: Dynamics of Structures: Theory and applications to Earthquake Engineering. Pearson Education Inc. (2007)
11. Kareem, A., Sun, W.J.: Stochastic response of structures with fluid-containing appendages. J. Sound Vib. (1987)
12. Smith, B.W.: Communication Structures. Thomas Telford (2007)
13. Holmes, J.D.: Wind loading of Structures. Taylor & Francis (2007)

Determination of the Fatigue Life on the Basis of Fatigue Test and FEM for EN-MCMgY4RE3Zr with Rare Earth Elements

Henryk Bąkowski and Janusz Adamiec

Abstract Fatigue wear is the type of wear, wherein the local loss of cohesion and the associated material losses are caused by fatigue due to the cyclic interaction of the contact stresses at the surface layer. During fatigue wear changes are multiple macroscopic elastic deformations, surface fatigue cracks arise in friction, typically under the influence of multiple elasto-plastic or plastic deformation. Defects occurring in the process influence on the ultimate service life under real conditions. The appeared cracks or microcracks in the material may cause the nucleation of defects and their propagation leading to the through cracks—particularly dangerous for the structure. For the study, we used EN-MCMgY4RE3Zr (WE43) casting magnesium alloys to determine the fatigue strength on the stand bench for testing of unilateral bending. Casting of magnesium alloys with rare earths, for example, yttrium, zirconium, silver have high strength properties that are comparable with the properties of titanium alloys, or steel. The study compared the effects of the appearance of fatigue cracks on the alloy, both in experimental (laboratory) and the simulation using the FEM (Finite Elements Method).

1 Introduction

Fatigue wear is the type of wearing in which local loss of cohesion and the associated material losses are caused by fatigue as a result of cyclic impact of the contact stresses in the surface layer and friction-associated components. Most often we the elements added to magnesium alloys are aluminum, zinc, and manganese. These alloys are characterized by good machinability and mechanical properties at ambient temperature, good corrosion resistance, and low price. They are used for

H. Bąkowski (✉)
Faculty of Transport, Silesian University of Technology, Katowice, Poland
e-mail: henryk.bakowski@polsl.pl

J. Adamiec
Department of Materials Science, Silesian University of Technology, Katowice, Poland

J. Awrejcewicz (ed.), *Dynamical Systems: Modelling*, Springer Proceedings in Mathematics & Statistics 181, DOI 10.1007/978-3-319-42402-6_5

components which require good impact strength and fracture toughness combined with sufficient strength (Fig. 1) [1].

To increase the strength properties of the used heat treatment consisting of precipitation hardening (Fig. 2). The disadvantage of magnesium alloys containing aluminum, zinc, and manganese is their low resistance to creep, which limits the operating temperature to 125 °C. The addition of rare earth elements allows to improve the creep resistance of magnesium alloys [2]. This enables the use of alloys in automotive and aerospace, where the operating temperature of the gearbox housing is 175, 200 °C engine block and pistons more than 300 °C [1]. Welding technology in magnesium alloys are used for joining metal components wrought and cast in the connecting structures. Joints made of magnesium alloy should have

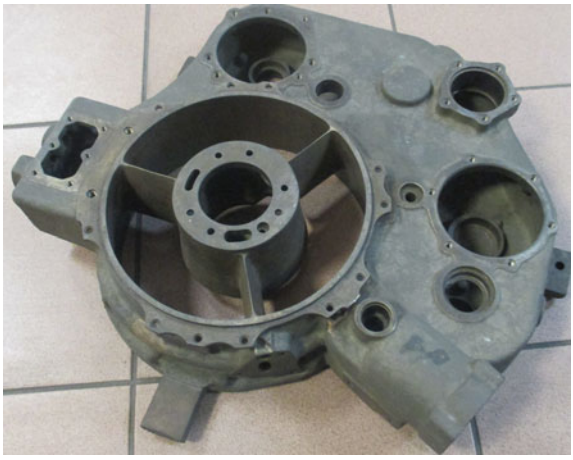

Fig. 1 Application of magnesium alloy cast: fuselage engine intake aircraft

Fig. 2 The application of magnesium alloy cast: the back of engine cover

suitable properties to meet the requirements of the structure which they made of it. In the literature there is no information on the properties of welded joints of cast magnesium alloys. There is therefore a need to define those properties in simulated conditions. To increase the strength properties at elevated temperatures are introduced rare earths and zirconium [3]. An example would be the alloy WE43 used to a temperature of 300 °C, which, after extrusion and heat treatment the obtained tensile strength $Rm = 270$ MPa, $Re =$ yield strength of 195 MPa and an elongation $A = 15$ % [4, 5]. For the study casting magnesium alloys with rare earth elements were used. The high strength properties are comparable to those of alloys of titanium or steel. Continuous development of magnesium alloys has meant that current yields are used in many fields of technology, and the maximum operating temperature is about 250 °C.

The structure of the cast magnesium alloy parts is common to casting defects and welding. These defects are repaired surfacing or welding methods. Welding technologies may also be used for connecting the elements Mg alloy and the repair of cast after use operating (Fig. 3).

Appearing cracks or microcracks in the alloy material also misruns casting and shrinkage porosity may cause the nucleation of defects and their propagation leading to a crack through—particularly dangerous for the structure. In the study a casting magnesium alloy WE43 was used to determine the fatigue strength of the position to investigate unilateral bending. In this paper, the impact of the emergence of fatigue cracks (determination of fatigue strength) using fatigue tests and simulation using Finite-Element Method was compared, depending on the morphology of the structure which determines the propensity for cracking.

The factors influencing correct methodological disclosure material microstructure, i.e.,: etching methods, methods of image acquisition structure may be common to the casting of magnesium alloys, but are often different. This is mainly due to the different chemical composition and the same structure. The method of sampling and the number depends on the reproducibility of the chemical composition and structures within the same method of production for each batch of products (castings, gravity die castings, forgings,) in all their volume.

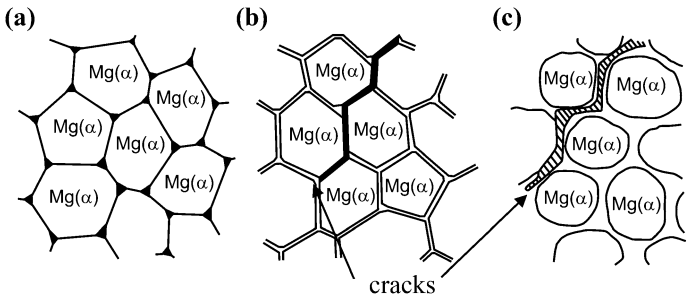

Fig. 3 The structure of the Mg alloy in the process of crystallization: **a** without a eutectic point, **b** a small amount of the eutectic, **c** with the amount of eutectic sufficient for the "healing" of cracks resulting hot [6]

Table 1 The results of the quantitative evaluation of the structure

Parameter	α-Mg	
	Average	Variability index (%)
Average grain lateral area $\bar{A}$ (μm^2)	4208	79
Area fraction A_A (%)	98	87
Average diameter $\bar{d}$ (μm)	74.84	41
Elongation index $\bar{f}$	1.42	18
Shape index $\bar{\xi}$	0.79	12

The variability of the material influences the way of sampling and the number of micro-areas analyzed for each sample (Table 1). If the objective of research is representative of the manufacturing process and it has a homogeneous microstructure, it can be evaluated qualitatively on a random sample taken. The number of necessary measurements, to ensure the determination of established accuracy parameters of integral and local used in quantitative metallography can be calculated from the relationship [7]:

$$N = \left(\frac{u_\alpha \cdot s(x)}{\gamma \cdot \bar{x}} \right)^2 \tag{1}$$

where u_a—the value of a variable standardized normal distribution, which is determined from tables for the assumed confidence level, x—the measurement result, $S(x)$—standard deviation, γ—the accuracy of the data.

Engineering materials have a heterogeneous structure. An excellent example is the casting of magnesium alloys. In these alloys due to the various chemical composition and manufacturing technologies a heterogeneous structure is observed.

1.1 Test Equipment and Parameters

For the quantitative evaluation of the structure, the investigated magnesium alloys after heat treatment (Fig. 4) used the software developed at the Department of Materials Science, Silesian University of Technology.

Therefore, an important factor determining the sampling strategy will be the resultant of: homogeneity of the chemical composition, size and shape of the casting and the technology of welding or surfacing by welding. For correct image acquisition, macrostructure connector should use the technique of observation in the dark on a stereoscopic microscope, and the observation of the microstructure should be performed in the field on a bright light microscope at magnifications from 50× to 500× (Figs. 5 and 6).

Fig. 4 Sample

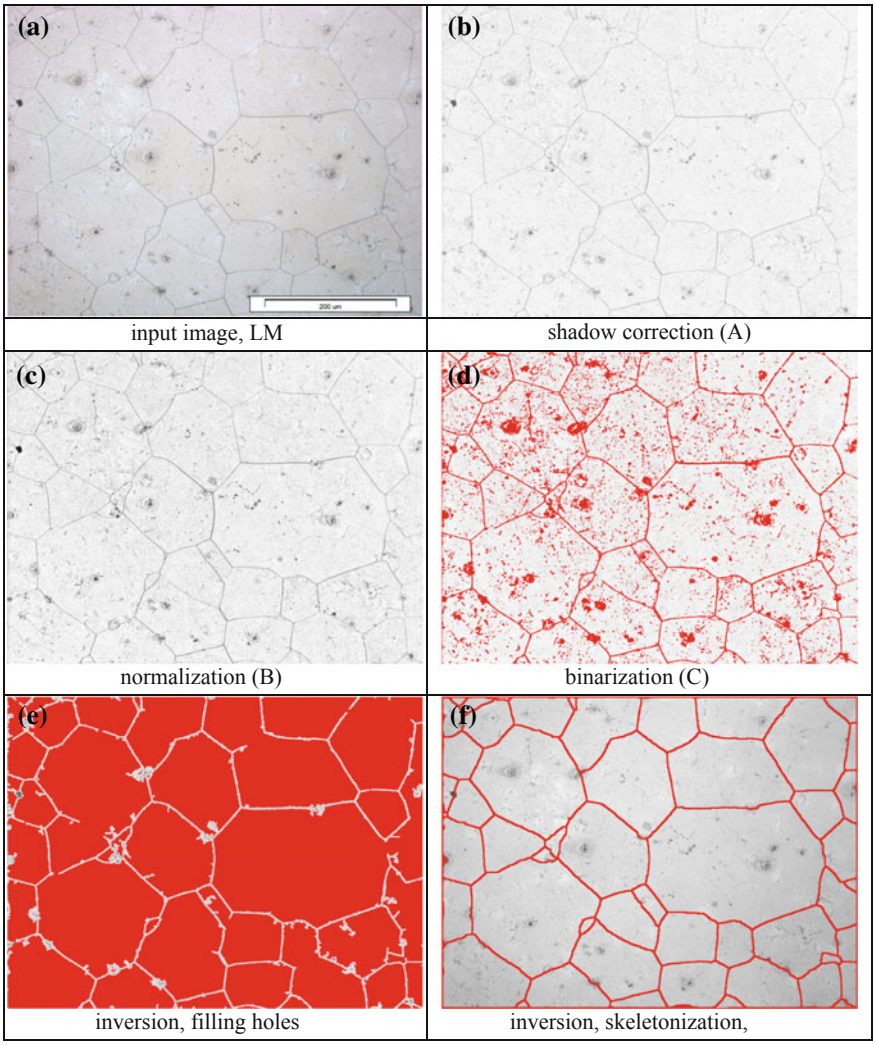

Fig. 5 Detection of the grain boundaries of the home terminal material alloy WE43 after heat treatment (T6)

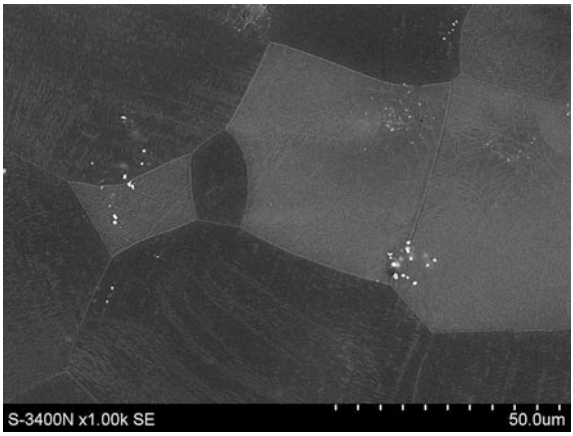

Fig. 6 The structure of the alloy WE43 after heat treatment T6

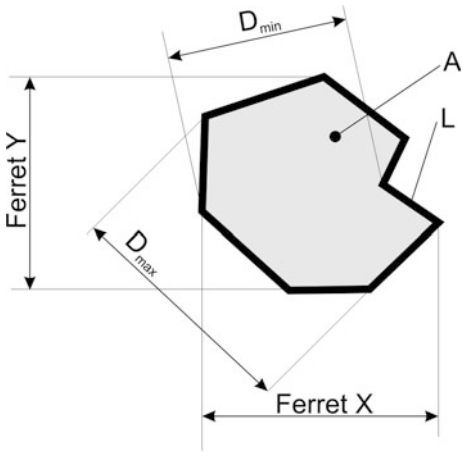

Fig. 7 Basic parameters for the quantitative assessment of the shape and size of the phases in the structure

The test machine is used for fatigue testing of samples of the tested metals (Fig. 7). Test samples are subjected to one-sided-pulsating loads during pure bending. Elements that come into direct contact with the test sample rotate around its axis, so it can be said that the friction between them and the sample is very small and the study followed practically at the one-sided bending (Fig. 8).

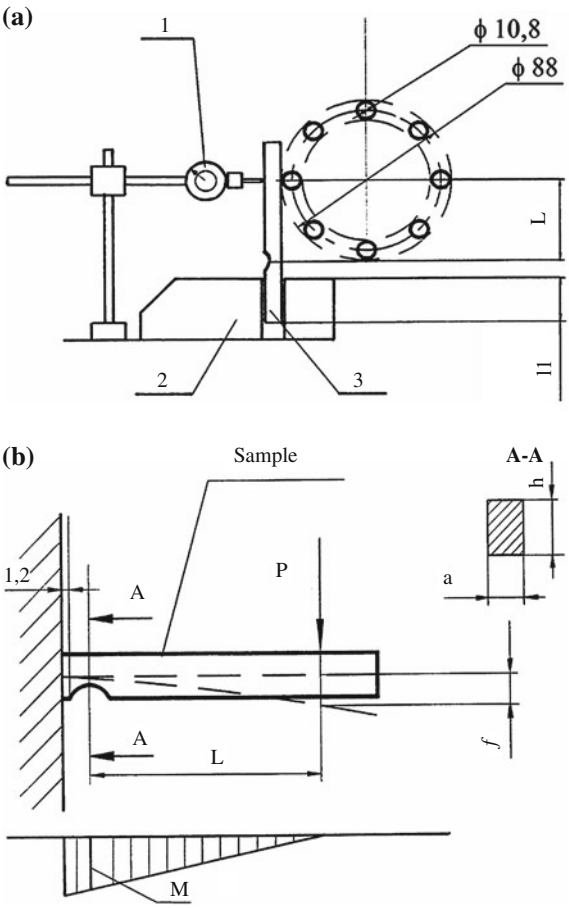

Fig. 8 View of the scheme machine: **a** stand scheme; **b** system testing and bending moment diagram; *1* dial indicator, *2* vice, *3* sample, *l* arm's length while bending, *l1* length of restraint, *P* load, *a* width of sample, *h* sample height, *f* deflection, *M* bending moment, *1,2* safe distance from restraint

2 Results and Discussion

Fatigue tests were carried out with a repetition of multiple in order to obtain fatigue strength diagram Wohler. The position of the fatigue curves in Logsigma-LogN presented on Fig. 9 is illustrated.

Metallographic at the macro level on the fracture surfaces of the fatigue revealed the presence of lines of fatigue characteristic for high cycle fatigue strength (Fig. 10).

As a result of quantitative analysis of metallographic structure stereological WE43 defined features that are needed to create a geometric model which is similar to the real structure. Simulation calculations were carried out which showed that the places most likely to break are on the grain boundaries (Fig. 11).

FEM software is a comprehensive durability analysis and fatigue prediction. It provides a variety of "crack-initiation" life criteria for the calculation of material fatigue and the prediction of structural life (Figs. 12, 13, 14 and 15).

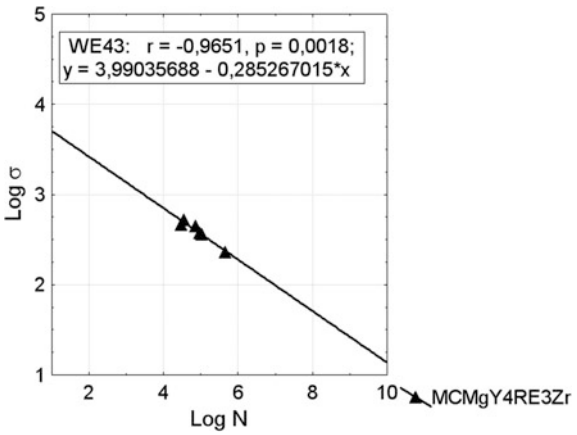

Fig. 9 Curves of fatigue strength

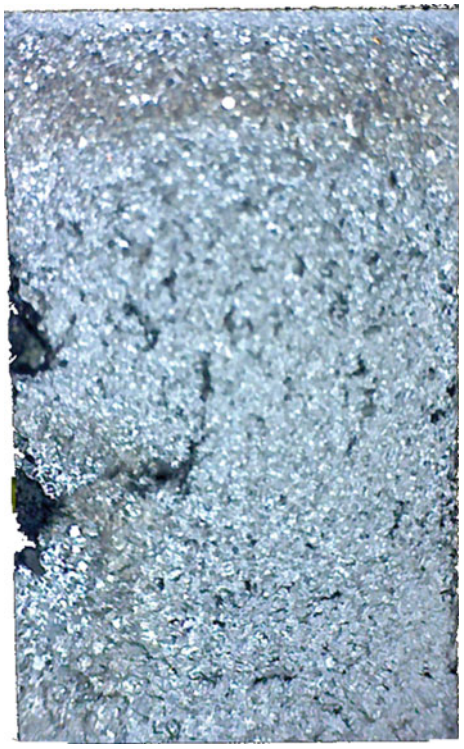

Fig. 10 Fatigue fracture of MCMgY4RE3Zr after fatigue test

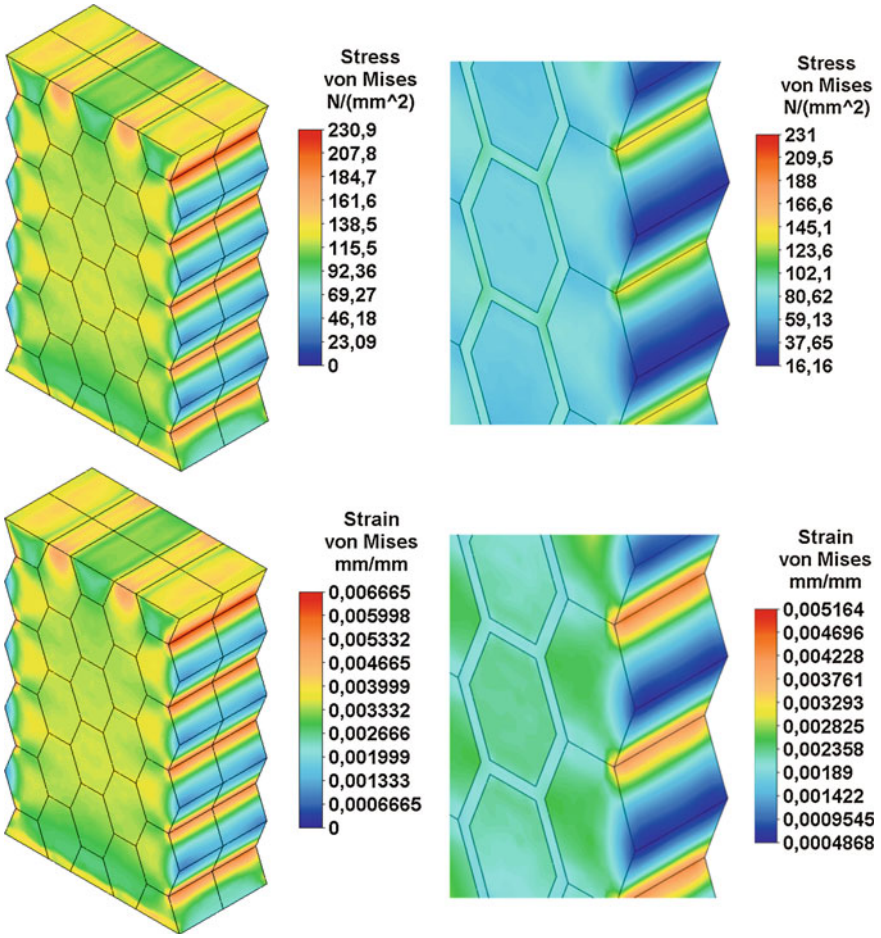

Fig. 11 Distribution of stresses and strains in geometrical model of the structure WE43

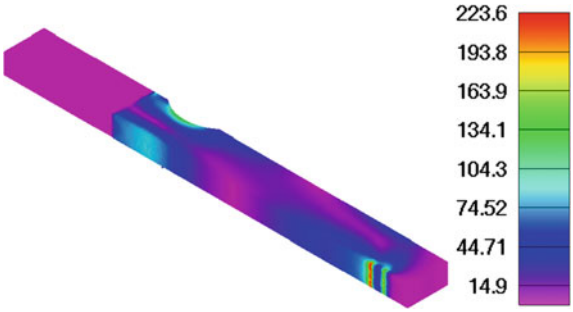

Fig. 12 Distribution of stress of the sample under one-sided bending

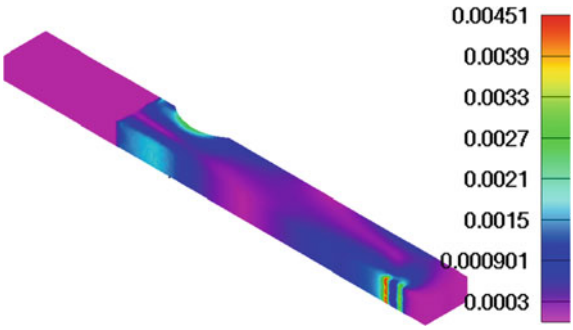

Fig. 13 Distribution of strain of the sample under one-sided bending

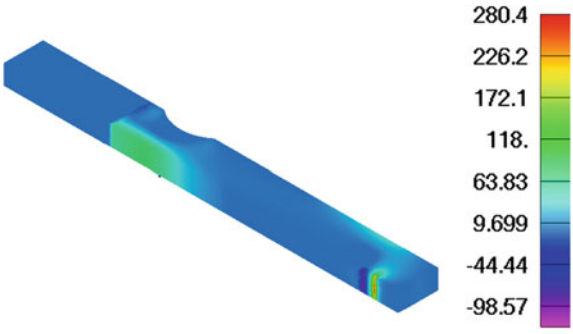

Fig. 14 Distribution of the maximum principal stress of the sample under one-sided bending

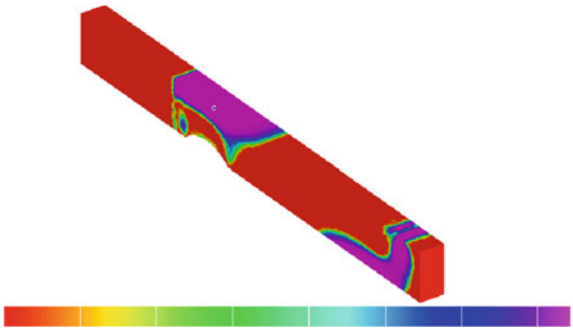

Fig. 15 Areas with higher risk for fatigue wear

3 Conclusion

Based on the tests results analysis of welded joints of the alloy WE43 after heat treatment T6 indicates that the structure of the connector is composed of a base material characterized by a polygonal grain of the solid solution α-Mg, which is strain precipitation small dispersion intermetallic phases narrow heat-affected zone

(HAZ), in which the grains feature a small dimensions relative to the base material, causing obtaining higher values of fatigue strength. In calculated simulation by means of FEM observed the place most vulnerable to wear.

References

1. Yang, Z., Li, J.P., Zhang, J.X., Larimer, G.W., Robson, J.: Review and research and development of magnesium alloys. Acta Metall. Sin. **5**, 313–328 (2008)
2. Pekguleryuz, M.O., Kaya, A.A.: Creep resistant magnesium alloys for Powertrain applications. In: Keiner, K.U. (ed.) Proceedings of the 6th International Conference Magnesium Alloys and Their Applications, Weinheim (2004)
3. Kun, Y., Wen-xian, L., Ri-chu, W.: Mechanical properties and microstructure of as-cast and extruded Mg-(Ce, Nd)-Zn-Zr alloys. J. Central South Univ. Technol. **12**(5), 499 (2005)
4. Avedesian, M., Baker, H.: Magnesium and magnesium alloys. ASM Speciality Handbook (1999)
5. Elektron WE43 wrought alloy, Data sheet 478, Magnesium Elektron, United Kingdom (2006)
6. Mordike, B.L., Wiesner, P.: Fugen von Magnesium Werkstoffen. DVS Verlag (2005)
7. Rzychoń, T., Kiełbus, A., Szala, J.: Microstructure and quantitative analysis of cast ZRE1 magnesium alloy. Arch. Foundry Eng. **7**(2007), 175 (2007)

Modelling of Forward Fall on Outstretched Hands as a System with Ground Contact

Paweł Biesiacki, Jerzy Mrozowski, Dariusz Grzelczyk and Jan Awrejcewicz

Abstract Forward falls on outstretched hands are caused by unexpected lost of stability and they are always related with different kinds of injuries. This paper takes attempt to explain and figure out the multifaceted problems of forward fall. In order to estimate the critical value of the force acting on the hands at the moment of impact on the ground, the relative simple mechanical model is proposed. Mathematical model is described by the second order differential equations obtained by the Newton–Euler method, and its parameters are identified and validated using experimental data from one of the recent paper. Some interesting results are obtained, presented and discussed. The presented numerical simulations show that the proposed model demonstrate good accordance with real tested objects presented in the literature. The model predicts the highest impact force and finally allows to simulate various scenarios of human falls.

1 Introduction

Slips, Trips and Falls (STF) are the highest single cause of upper limb injuries. Falls occur in all age groups and the falls on the outstretched hand are a significant cause of upper limb injury including 90 % of fracture at the distal radius region [1]. A forward fall is the most common type of fall and more than half of the falls among

P. Biesiacki (✉) · J. Mrozowski · D. Grzelczyk · J. Awrejcewicz
Department of Automation, Biomechanics and Mechatronics,
Lodz University of Technology, 1/15 Stefanowski Street,
90-924 Lodz, Poland
e-mail: 800045@p.lodz.pl

J. Mrozowski
e-mail: jerzy.mrozowski@p.lodz.pl

D. Grzelczyk
e-mail: dariusz.grzelczyk@p.lodz.pl

J. Awrejcewicz
e-mail: jan.awrejcewicz@p.lodz.pl

J. Awrejcewicz (ed.), *Dynamical Systems: Modelling*, Springer Proceedings in Mathematics & Statistics 181, DOI 10.1007/978-3-319-42402-6_6

the elderly occur in the forward direction. An attempt to determine the biomechanical factors which have the greatest influence on the risk of injury has been made in [2]. On the basis of impact forces measured during low-height forwards falls onto the outstretched hand, a two degrees of freedom, lumped-parameter mathematical model reflecting the real impact forces has been created. Computer simulations in ADAMS (multibody dynamics simulation software created originally by Mechanical Dynamics Incorporated and then developed by MSC Software Corporation) was used to predict the extent to which age-related muscle atrophy may adversely affect the safe arrest of a forward fall onto the arms. The biomechanical factors affecting the separate risks for wrist fracture or head impact is examined using a two-dimensional, 5-link, forward dynamic model [3]. In reference [4] other two degree of freedom discrete impact model is constructed through system identification and validated using experimental data, in order to understand the dynamic interactions of various biomechanical parameters in bimanual forward fall arrests. To evaluate a worst case scenario well-known falling situations of snowboarders are modelled in paper [5] in different falling scenarios of snowboarders and simulated in order to calculate the resulting loads in the upper extremity. In the mentioned paper numerical simulations are carried out using the multi body dynamics software package SIMPACK 9.0 (SIMPACK AG, Wessling, Germany). The backward fall on outstretched joints of the upper extremity is evaluated as worst case scenario. In reference [6] numerical model of upper limb constructed from computed tomography (CT) data under load of real contact force using Finite Element Method (FEM) is calculated in order to obtain stress distribution and evaluate the most risk areas of fracture bones. In turn, a three degree of freedom mathematical model of human body during forward fall on outstretched hands is presented in [7], where dynamical forces acting on the human parts are obtained by solving the appropriate second order differential equations of motion. Also many other papers have shown utilizing spring-damper to contact modelling of human parts with the ground in various types of motion (for instance, see references [8–11]). Motivated by the references mentioned in this paper, we present a dynamic model with "soft" spring-damper contact which allows to predict ground reaction force in different scenario of human fall.

2 Model of the Biomechanical System

The human forward fall on outstretched hands is schematically presented in Fig. 1. The main assumption for working out the appropriate mathematical model is to take into account flat two degrees of freedom mechanical model.

In Fig. 1, the angle $\varphi_1(t)$ denotes the angle between horizontal x axis and the longitudinal axis of the body 1. The angle $\varphi_2(t)$ is the angle measured from the axis of the body 1 to the axis of the body 2 (its value is defined in the range from 0 to 90 degrees and increases during falling). Parameters a_1 and a_2 denote distances between the centres of mass and rotation axes for bodies 1 and 2, respectively, l_1 is a distance form support point to shoulder joint and l_2 is whole length of the upper

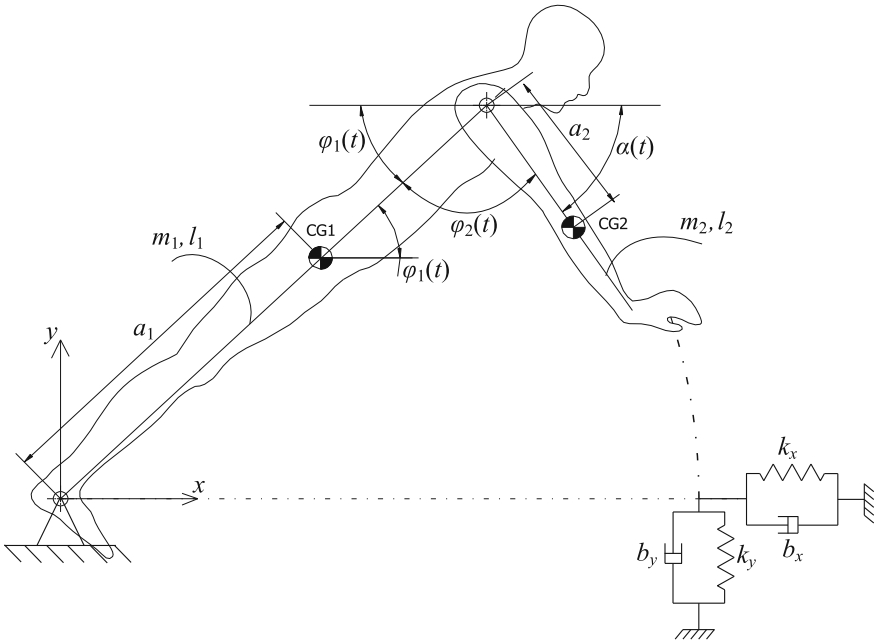

Fig. 1 Model of the investigated biomechanical system

limb. The bodies 1 and 2 have masses m_1, m_2 and moments of inertia about centres of the masses I_1 and I_2, respectively. The appropriate values of the viscous damping coefficients in the joints 1 and 2 equal to c_1 and c_2, respectively, are also included. The equations of motion describing the dynamics of the considered mechanical system have been obtained by the Newton–Euler method. Free Body Diagrams (FBD's) of the considered system are shown in Fig. 2.

In our model, we take the following vectors:

$$\mathbf{r}_{C1}(t) = [x_1(t), y_1(t), 0]^T = [a_1 \cos\varphi_1(t), a_1 \sin\varphi_1(t), 0]^T, \tag{1}$$

$$\mathbf{r}_{C2}(t) = [x_2(t), y_2(t), 0]^T = [l_1 \cos\varphi_1(t) + a_2 \cos\alpha(t), l_1 \sin\varphi_1(t) - a_2 \sin\alpha(t), 0]^T, \tag{2}$$

$$\mathbf{l}_1(t) = [l_1 \cos\varphi_1(t), l_1 \sin\varphi_1(t), 0]^T, \tag{3}$$

$$\mathbf{l}_2(t) = [l_1 \cos\varphi_1(t) + l_2 \cos\alpha(t), l_1 \sin\varphi_1(t) - l_2 \sin\alpha(t), 0]^T, \tag{4}$$

where $\alpha(t) = \pi - \varphi_1(t) - \varphi_2(t)$.

The forces $\mathbf{Q}_1 = [0, -m_1 g, 0]^T$ and $\mathbf{Q}_2 = [0, -m_2 g, 0]^T$ are the gravity forces acting on the centre of gravity of bodies 1 and 2, respectively, where g denotes gravity coefficient ($g = 9.81\ \mathrm{m \cdot s^{-2}}$). The force $\mathbf{R}(t) = [R_x(t), R_y(t), 0]^T$ is the join 1 reaction

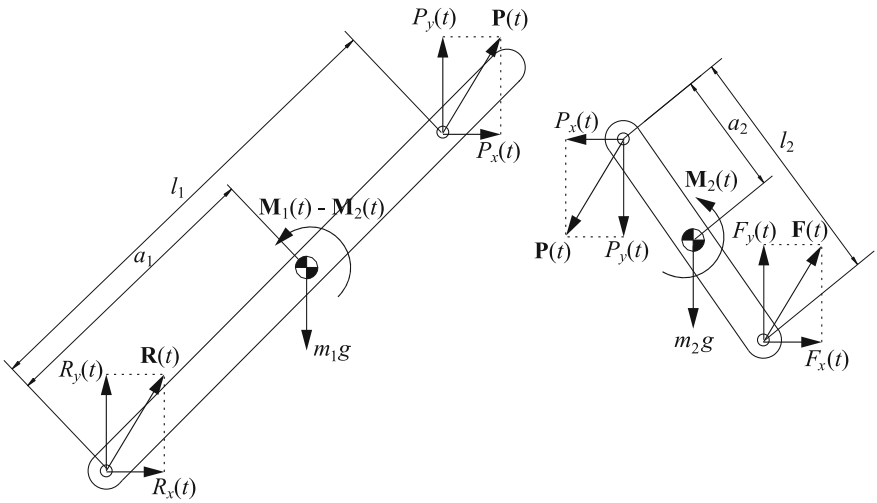

Fig. 2 Free body diagrams of the considered biomechanical system

force. The unknown joint force presented in the free-body diagrams (Fig. 2) is denoted as $\mathbf{P}(t) = [P_x(t), P_y(t), 0]^T$. In turn, the force $\mathbf{F}(t) = [F_x(t), F_y(t), 0]^T$ is the ground reaction force. Next, let $\mathbf{M}_1(t) = [0, 0, 0]^T$ and $\mathbf{M}_2(t) = [0, 0, M_{2z}(t)]^T$ denote the torques generated in joints 1 and 2, respectively. Then, for two considered in Fig. 2 free bodies, we can write down the following equations of motion in vector form.

For body 1, we have

$$m_1 \ddot{\mathbf{r}}_{C1}(t) = \mathbf{R}(t) + \mathbf{Q}_1 + \mathbf{P}(t), \tag{5}$$

$$I_1 \ddot{\varphi}_1(t) + c_1 \dot{\varphi}_1(t) = \mathbf{M}_1(t) - \mathbf{M}_2(t) + \boldsymbol{\tau}_{\mathbf{R}}(t) + \boldsymbol{\tau}_{\mathbf{P}1}(t), \tag{6}$$

and for body 2 we have

$$m_2 \ddot{\mathbf{r}}_{C2}(t) = -\mathbf{P}(t) + \mathbf{Q}_2 + \mathbf{F}(t), \tag{7}$$

$$I_2 \ddot{\varphi}_2(t) + c_2 \dot{\varphi}_2(t) = \mathbf{M}_2(t) + \boldsymbol{\tau}_{\mathbf{P}2}(t) + \boldsymbol{\tau}_{\mathbf{F}}(t), \tag{8}$$

where

$$\begin{aligned} \boldsymbol{\tau}_{\mathbf{R}}(t) &= -\mathbf{r}_{C1}(t) \times \mathbf{R}(t) = \\ &= [0, 0, a_1 R_x(t) \sin\varphi_1(t) - a_1 R_y(t) \cos\varphi_1(t)]^T, \end{aligned} \tag{9}$$

$$\begin{aligned} \boldsymbol{\tau}_{\mathbf{P}1}(t) &= [\mathbf{l}_1(t) - \mathbf{r}_{C1}(t)] \times \mathbf{P}(t) = \\ &= [0, 0, (l_1 - a_1) P_y(t) \cos\varphi_1(t) - (l_1 - a_1) P_x(t) \sin\varphi_1(t)]^T, \end{aligned} \tag{10}$$

$$\begin{aligned}\boldsymbol{\tau}_{\mathbf{P}2}(t) &= -\left[\mathbf{l}_1(t) - \mathbf{r}_{C2}(t)\right] \times \mathbf{P}(t) = \\ &= \left[0, 0, a_2 P_y(t)\cos\alpha(t) + a_2 P_x(t)\sin\alpha(t)\right]^T,\end{aligned} \tag{11}$$

$$\begin{aligned}\boldsymbol{\tau}_{\mathbf{F}}(t) &= \left[\mathbf{l}_2(t) - \mathbf{r}_{C2}(t)\right] \times \mathbf{F}(t) = \\ &= \left[0, 0, (l_2 - a_2)F_y(t)\cos\alpha(t) + (l_2 - a_2)F_x(t)\sin\alpha(t)\right]^T,\end{aligned} \tag{12}$$

are the moments generated by the forces $\mathbf{R}(t)$, $\mathbf{P}(t)$ and $\mathbf{F}(t)$, respectively. Writing down this vector form equation in the scalar form we obtain the following system of differential equations:

$$\begin{cases} m_1\ddot{x}_1(t) = R_x(t) + P_x(t) \\ m_1\ddot{y}_1(t) = R_y(t) - m_1 g + P_y(t) \\ I_1\ddot{\varphi}_1(t) + c_1\dot{\varphi}_1(t) = -M_{2z}(t) + a_1 R_x(t)\sin\varphi_1(t) - a_1 R_y(t)\cos\varphi_1(t) + \\ \quad + (l_1 - a_1)P_y(t)\cos\varphi_1(t) - (l_1 - a_1)P_x(t)\sin\varphi_1(t) \\ m_2\ddot{x}_2(t) = -P_x(t) + F_x(t) \\ m_2\ddot{y}_2(t) = -P_y(t) - m_2 g + F_y(t) \\ I_2\ddot{\varphi}_2(t) + c_2\dot{\varphi}_2(t) = M_{2z}(t) + a_2 P_y(t)\cos\alpha(t) + a_2 P_x(t)\sin\alpha(t) + \\ \quad + (l_2 - a_2)F_y(t)\cos\alpha(t) + (l_2 - a_2)F_x(t)\sin\alpha(t). \end{cases} \tag{13}$$

Equation (13) can be written in the form

$$\begin{aligned} I_1\ddot{\varphi}_1(t) + c_1\dot{\varphi}_1(t) = &-M_{2z}(t) + a_1 R_x(t)\sin\varphi_1(t) - a_1 R_y(t)\cos\varphi_1(t) + \\ &+ (l_1 - a_1)P_y(t)\cos\varphi_1(t) - (l_1 - a_1)P_x(t)\sin\varphi_1(t), \end{aligned} \tag{14}$$

$$\begin{aligned} I_2\ddot{\varphi}_2(t) + c_2\dot{\varphi}_2(t) = &M_{2z}(t) + a_2 P_y(t)\cos\alpha(t) + a_2 P_x(t)\sin\alpha(t) + \\ &+ (l_2 - a_2)F_y(t)\cos\alpha(t) + (l_2 - a_2)F_x(t)\sin\alpha(t), \end{aligned} \tag{15}$$

where

$$P_x(t) = F_x(t) - m_2\ddot{x}_2(t), \tag{16}$$

$$P_y(t) = F_y(t) - m_2\ddot{y}_2(t) - m_2 g, \tag{17}$$

$$R_x(t) = m_1\ddot{x}_1(t) - P_x(t) = m_1\ddot{x}_1(t) + m_2\ddot{x}_2(t) - F_x(t), \tag{18}$$

$$R_y(t) = m_1\ddot{y}_1(t) + m_1 g - P_y(t) = m_1\ddot{y}_1(t) + m_2\ddot{y}_2(t) + m_1 g + m_2 g - F_y(t). \tag{19}$$

At the time of stumble over an obstacle, human instinctively hold out his hands quickly to the front to fall on them and in this way to absorb the fall. With a rough approximation, it can be assumed that a human hold his hands quickly to such a position φ_0 that at the moment of the fall, they are adjusted approximately perpendicular to the axis of the body ($\varphi_0 \approx 90°$). Due to the hands moment of inertia

the time needed for hold out both hands it is non-zero, so we assumed angle graph $\varphi_2(t)$ as

$$\varphi_2(t) = \varphi_0(1 - e^{-\lambda t}), \tag{20}$$

where φ_0 denotes the angle between torso with legs and hands, while constant parameter λ corresponds to "speed" hold out the hands by human. Knowing the function graph $\varphi_2(t)$ on the basis of Eq. (15) the torque generated by human hands at their extraction in the process of falling can be calculated as follows:

$$\begin{aligned} M_{2z}(t) &= I_2\ddot{\varphi}_2(t) + c_2\dot{\varphi}_2(t) - a_2P_y(t)\cos\alpha(t) + \\ &- a_2P_x(t)\sin\alpha(t) - (l_2 - a_2)F_y(t)\cos\alpha(t) - (l_2 - a_2)F_x(t)\sin\alpha(t). \end{aligned} \tag{21}$$

Finally, substituting Eqs. (21) to (14) gives one differential equation for the rotation of the body 1, whose the solution is function $\varphi_1(t)$.

Ground reaction forces modelling

At the end of the second body the force $\mathbf{F}(t)$ is applied, which corresponds to the force resulting from impact. This force occurs only in the contact point of the ground (with no contact this force is zero). The force $\mathbf{F}(t)$ is applied at the tip of body 2 meaning the end of the second link (point hand contact with the ground). In a real system the connection between the parts of the human body are stiffness and damped. Damping forces in assumed model are not included, but this behaviour of real joints is modelled as ground stiffness and damping, which followed the fall of the human body. The stiffness and damping parameters of the ground are chosen such that the obtained numerical results coincide with the experimental results presented in the literature.

The impact force, including stiffness and damping of the ground, is taken into account in the following form

$$F_x(t) = -[k_x(x(t) - x_0) + b_x\dot{x}(t)] \cdot \mathbf{1}(-y(t)), \tag{22}$$

$$F_y(t) = -[k_y y(t) + b_y\dot{y}(t)] \cdot \mathbf{1}(-y(t)), \tag{23}$$

where k_x, k_y are ground stiffness coefficients, b_x, b_y are ground viscous damping coefficients, $x_0 = \sqrt{l_1^2 + l_2^2 - 2l_1l_2\cos\varphi_0}$, $x(t) = l_1\cos\varphi_1(t) + l_2\cos\alpha(t)$, $y(t) = l_1\sin\varphi_1(t) - l_2\sin\alpha(t)$, and the function $\mathbf{1}(-y(t))$ is the step function defined as follows:

$$\mathbf{1}(-y(t)) = \begin{cases} 1 & \text{if} \quad y(t) < 0, \\ 0 & \text{if} \quad y(t) \geq 0. \end{cases} \tag{24}$$

The initial conditions

To carry out numerical simulation of the proposed mathematical model initial conditions $\varphi_1(0)$ and $\dot{\varphi}_1(0)$ are required. Assuming that before stumbling human

has hands stacked along the torso, we take $\varphi_1(0) = \pi/2$ (see Fig. 1). In turn, the initial velocity $\dot{\varphi}_1(0)$ is estimated based on the linear velocity v_0 of human motion at the moment of stumbling, and assuming that the rotation of his body takes about a fulcrum feet (see Fig. 1). The principle of conservation of momentum yields

$$(m_1 + m_2)(0 - v_0) = F\Delta t, \tag{25}$$

where $F\Delta t$ is an impulse force that causes rotation of the human at the moment of stumbling an obstacle. In turn, rotational motion of a human body around the axis of rotation (around the legs) is governed by the equation

$$I\frac{\Delta\varphi_1(t)}{\Delta t} = rF \Rightarrow \Delta\varphi_1(t) = -\frac{(m_1 + m_2)v_0 r}{I} = \dot{\varphi}_1(0), \tag{26}$$

where I is the moment of inertia of the human around the legs axis with his hands adjusted along the body, and r is the distance of the centre of human gravity in a standing position with hands adjusted along the body from the ground.

3 Simulation Results

The results of numerical simulations were obtained using Mathematica 10 software. In order to determine the centre of gravity of a component of the human parts and the moments of inertia, one can employ the proper command of the programs AutoDesk Inventor. The full 3D scanned human body model is presented in Fig. 3 due to courtesy of Rory Craig (GrabCAD) [12]. Even though human body does not consist of a homogenous structure, the value of the mass is calculated assuming the average density $\rho = 1050\ \mathrm{kg \cdot m^{-3}}$. Parameters used in numerical simulations are presented in Table 1. The simulations presented in Figs. 4, 5, 6, 7 and 8 are carried out for the fixed ground parameters: $k_x = k_y = k = 16\ 000\ \mathrm{N \cdot m^{-1}}$ and $b_x = b_y = b = 1\ 000\ \mathrm{N \cdot s \cdot m^{-1}}$.

Figure 4 shows a times histories of force $F_y(t)$ acting on the single hand for $v_0 = 0$, $\lambda = 4\ \mathrm{s^{-1}}$ and for the different angle ϕ_{Arm} between the arm and normal axis of the ground. In the case of free fall of the human body the influence of the angle ϕ_{Arm} at the moment of the fall on the F_{ymax} can be neglected. Small differences in larger values of force F_{ymax} and shorter time falling are caused by the higher amount of torque generated by human hands $M_{2z}(t)$, which is transformed to the human body and causes its rotation about a support point.

The results presented in Figs. 5 and 6 show the influence of different values of the velocity v_0 and parameter λ on time histories of force $F_y(t)$.

Figure 5 shows that for larger values the parameter λ, the time of falling process on the ground is lower, but this has no significant impact on the force F_{ymax}.

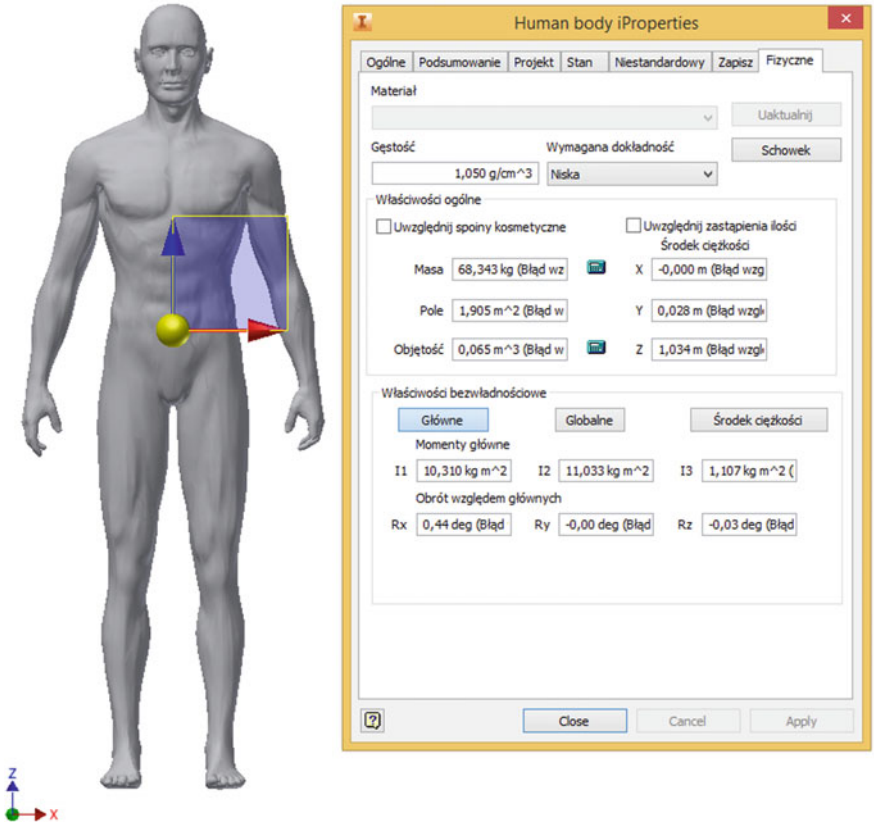

Fig. 3 Calculation of parameters for the human body [12]

Table 1 Body segment lengths, masses, moments of inertia and damping coefficients

		Value	Unit
Parameters	a_1; a_2	1.01; 0.22	m
	l_1; l_2; r	1.4; 0.53; 1.03	m
	m_1; m_2	61.0; 7.4	kg
	I_1; I_2; I	9.9; 0.232; 10.3	kg · m^2
	c_1; c_2	0.1; 0.1	N · m · s

Figure 6 shows that the initial value of the speed of the falling of human is much higher. Furthermore, in this case, ($v_0 = 2\ \mathrm{m \cdot s^{-1}}$) the influence of the parameter λ is higher than for the case of velocity $v_0 = 0$.

Figures 7 and 8 show the influence of parameters v_0 and λ on times histories of force for different angle values ϕ_{Arm} angles with a simultaneous increase of the velocity v_0 and λ (at higher initial velocity value of human hold out hands). As might be expected, higher initial velocities v_0 imply a rapid human fall on the

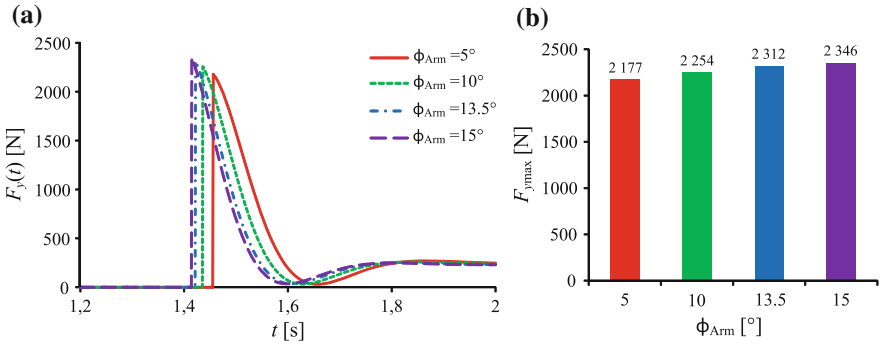

Fig. 4 Time histories of contact force $F_y(t)$ **a** and its maximum values F_{ymax} **b** for different angle ϕ_{Arm} ($v_0 = 0$, $\lambda = 4\ s^{-1}$)

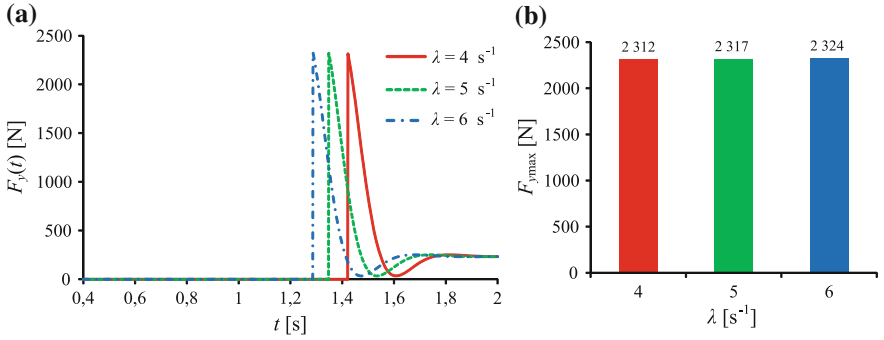

Fig. 5 Time histories of contact force $F_y(t)$ **a** and its maximum values F_{ymax} **b** for different parameters λ ($\phi_{Arm} = 13.5°$, $v_0 = 0$)

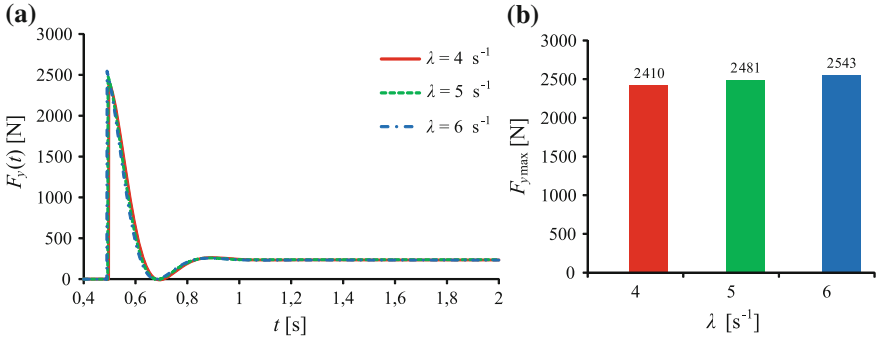

Fig. 6 Time histories of contact force $F_y(t)$ **a** and its maximum values F_{ymax} **b** for different parameters λ ($\phi_{Arm} = 13.5°$, $v_0 = 0$)

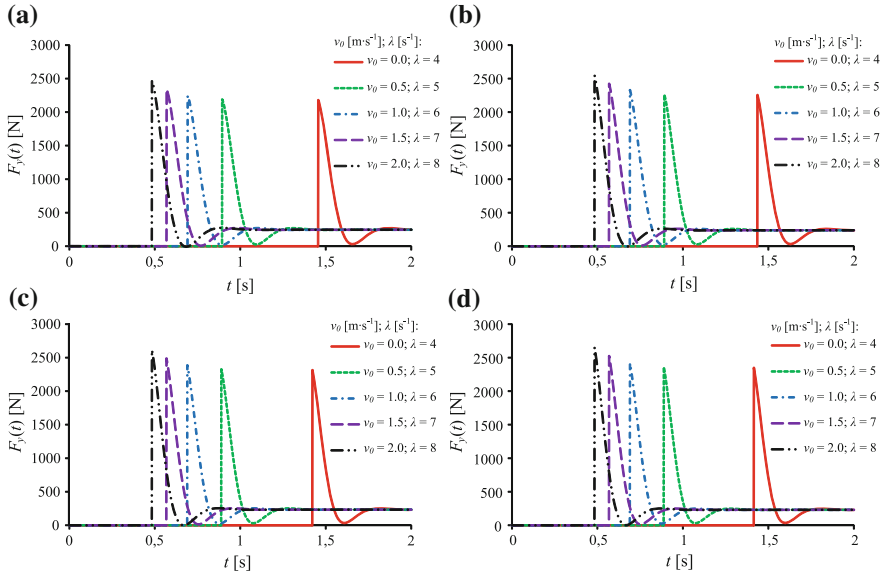

Fig. 7 Time histories of contact force $F_y(t)$ for different values of parameters v_0 and λ. **a** $\phi_{\text{Arm}} = 5°$, **b** $\phi_{\text{Arm}} = 10°$, **c** $\phi_{\text{Arm}} = 13.5°$, **d** $\phi_{\text{Arm}} = 15°$

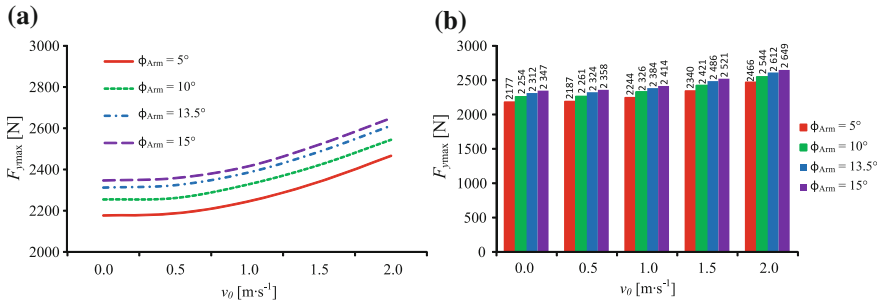

Fig. 8 Maximum values F_{ymax} of contact force as a function of velocity v_0 for different angles ϕ_{Arm}

ground and influence of the angle ϕ_{Arm} has also an impact on the force F_{ymax} (Fig. 9).

In what fallows we study the impact of ground parameters (stiffness and damping) on the obtained results. The following parameters are fixed: $\phi_{\text{Arm}} = 13.5°$, $v_0 = 2\ \text{m} \cdot \text{s}^{-1}$ and $\lambda = 8\ \text{s}^{-1}$. As can be seen, the highest effect on the maximum force value $F_y(t)$ has damping of the ground. It follows from the fact that when human hand is in a contact with the ground, the force of the damping is activated by the ground, which is proportional to the impact velocity with the coefficient of proportionality b. Component of the force $F_y(t)$ associated with the ground stiffness

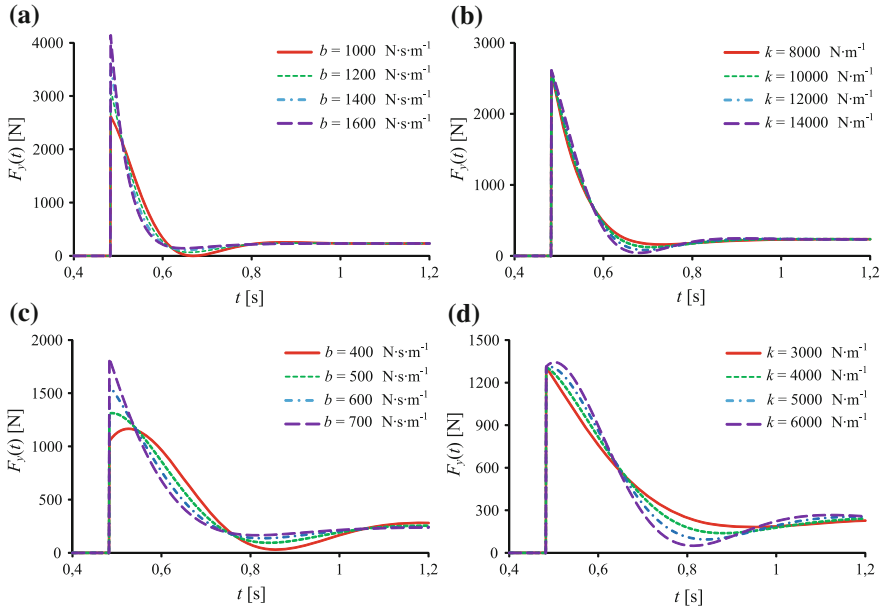

Fig. 9 Time histories of contact force $F_y(t)$ for different values of parameters b and k ($\phi_{\text{Arm}} = 13.5°$, $v_0 = 2\ \text{m} \cdot \text{s}^{-1}$, $\lambda = 4\ \text{s}^{-1}$). **a** $k = 16000\ \text{N} \cdot \text{m}^{-1}$. **b** $b = 1000\ \text{N} \cdot \text{s} \cdot \text{m}^{-1}$. **c** $k = 5000\ \text{N} \cdot \text{m}^{-1}$. **d** $b = 500\ \text{N} \cdot \text{s} \cdot \text{m}^{-1}$

k does not essentially affect the value of the maximum $F_{y\max}$ (it increases from zero at the time of hand contact with the ground, proportionally to the penetration depth into the ground.

4 Conclusions

This paper presents a relatively simple mechanical model governing the forward fall on outstretched hands. The considered model is constructed based on a mechanical system with two degrees of freedom and classical impact notion. Numerical simulations are performed for the parameters obtained based on the scanning computer model of the human body. In turn, biochemical properties of the human cartilage joint are modelled by the properties of the ground stiffness and damping. As it is shown, the obtained results fit well with experimental results presented in the literature, both from a qualitative and quantitative point of view. In particular, the model allows to estimate magnitude of contact force in various scenarios of falling process. The numerical simulations show that the essential influences on the obtained results have not only parameters describing the human body, but also the parameters modelling the ground. Although the proposed model is relatively simple, it has been validated by numerical computations. Further modifications and

improvements of the proposed model relies on taking into account the stiffness and damping in each of the joints as well as through increase of the number of degrees of freedom of the human body. These issues will be the subject of our further investigations related to the problem of the forward fall on the outstretched hands.

Acknowledgments The work has been supported by the National Science Centre of Poland under the grant OPUS 9 no. 2015/17/B/ST8/01700 for years 2016–2018.

References

1. Nevitt, M.C., Cummings, S.R.: Type of fall and risk of hip and wrist fractures: the study of osteoporotic fractures. J. Am. Geriatr. Soc. **41**, 1226–1234 (1993)
2. Chiu, J., Robinovitch, S.N.: Prediction of upper extremity impact forces during fall on the outstretched hand. J. Biomech. **31**, 1169–1176 (1998)
3. DeGoede, K.M., Ashton-Miller, J.: Biomechanical simulations of forward fall arrest: effects of upper extremity arrest strategy, gender and aging-related declines in muscle strength. J. Biomech. **36**, 413–420 (2003)
4. Kim, K.J., Ashton-Miller, J.: Segmental dynamics of forward fall arrest: a system identification approach. Clin. Biomech. **24**, 348–354 (2009)
5. Lehner, S., Geyer, T., Michel, F.I., Schmitt, K.U., Senner, V.: Wrist injuries in snowboarding—simulations of a worst case scenario of snowboard falls. Procedia Engineering **72**, 255–260 (2014)
6. Biesiacki, P., Awrejcewicz, J., Mrozowski, J., Woźniak, K.: Nonlinear biomechanical analysis of the human upper limb in a outstretched forward fall. In: Awrejcewicz, J., Kaźmierczak, M., Olejnik, P., Mrozowski, J. (eds.) Dynamical Systems–Applications. Publishing House of Lodz University of Technology, pp. 229–240 (2013)
7. Biesiacki, P., Mrozowski, J., Awrejcewicz, J.: Study of dynamic forces in human upper limb in forward fall. In: Awrejcewicz, J., Kaźmierczak, M., Mrozowski, J., Olejnik, P. (eds.) Dynamical Systems—Applications. Publishing House of Lodz University of Technology, pp. 65–76 (2015)
8. Silva, M., Barbosa, R., Castro, T.: Multi-legged walking robot modelling in MATLAB/Simmechanics™ and its simulation. In: Proceedings of the 2013 8th EUROSIM Congress on Modelling and Simulation, EUROSIM, Cardiff, Wales, pp. 226–231, 10–13 Sept 2013
9. Yamaguchi, G.T.: Dynamic Modelling of Musculoskeletal Motion: Springer-Science + Business Media, B.V. (2001)
10. Anderson, F.C., Pandy, M.G.: Dynamic optimization of human walking. J. Biomech. Eng. **123**, 381–390 (2001)
11. Neptune, R.R., Wright, I.C., van den Bogert, A.J.: A method for numerical simulation of single limb ground contact events: application to heel–toe running. Comput. Methods Biomech. Biomed. Eng. **3**, 321–334 (2000)
12. GrabCAD: Open CAD library (2016). https://grabcad.com/library

Micelle Confined in Aqueous Environment: Lubrication at the Nanoscale and Its Nonlinear Characteristics

P. Bełdowski, R.G. Winkler, W.K. Augé II, J. Hładyszowski and A. Gadomski

Abstract We present constant pressure molecular dynamics simulation results of a micelle in an aqueous environment confined between two surfaces. The lipid-water interactions are described in terms of the MARTINI force field, and the constant pressure simulation approach as described in Winkler and Hentschke (J Chem Phys 99:5405–5417 (1993), [1]) is applied. The fluid–surface interactions are taken into account by a static external potential field. Our results provide a molecular picture of the surface-induced structure of the fluid, the fluid dynamics, and the corresponding non-linear properties of the micelle as a mechanical system. Hence, the performed analyses provide insight into lubrication at the nanoscale of the articulating system; the lubrication effect becomes nonlinear in terms of the basic defect creation-annihilation mechanism. According to the model of facilitated lubrication Gadomski et al. (Tribol Lett 30:83–90 (2008), [2]), micellar interactions contribute to a lowering the friction coefficient of articular cartilage (AC).

P. Bełdowski (✉) · A. Gadomski
University of Science and Technology, Bydgoszcz, Poland
e-mail: piotr.beldowski@utp.edu.pl

A. Gadomski
e-mail: agad@utp.edu.pl

R.G. Winkler
Theoretical Soft Matter and Biophysics, Institute for Advanced Simulation, Forschungszentrum Jülich, Jülich, Germany
e-mail: r.winkler@fz-juelich.de

W.K. Augé II
NuOrtho Surgical Inc., Fall River, MA, USA
e-mail: nnmoc@aol.com

J. Hładyszowski
Department of Physical Chemistry, Wroclaw Medical University, Wrocław, Poland
e-mail: Jerzy.Hladyszowski@umed.wroc.pl

J. Awrejcewicz (ed.), *Dynamical Systems: Modelling*, Springer Proceedings in Mathematics & Statistics 181, DOI 10.1007/978-3-319-42402-6_7

1 Introduction

Lubrication at the nanoscale is supposed to contribute to the mechanism of ultralow friction in articular cartilage (AC) viewed as a complex viscoelastic system [1, 2]. According to [2–9] surface active phospholipids may play a crucial role in biolubrication at different levels of dynamic matter organisation. The synovial fluid

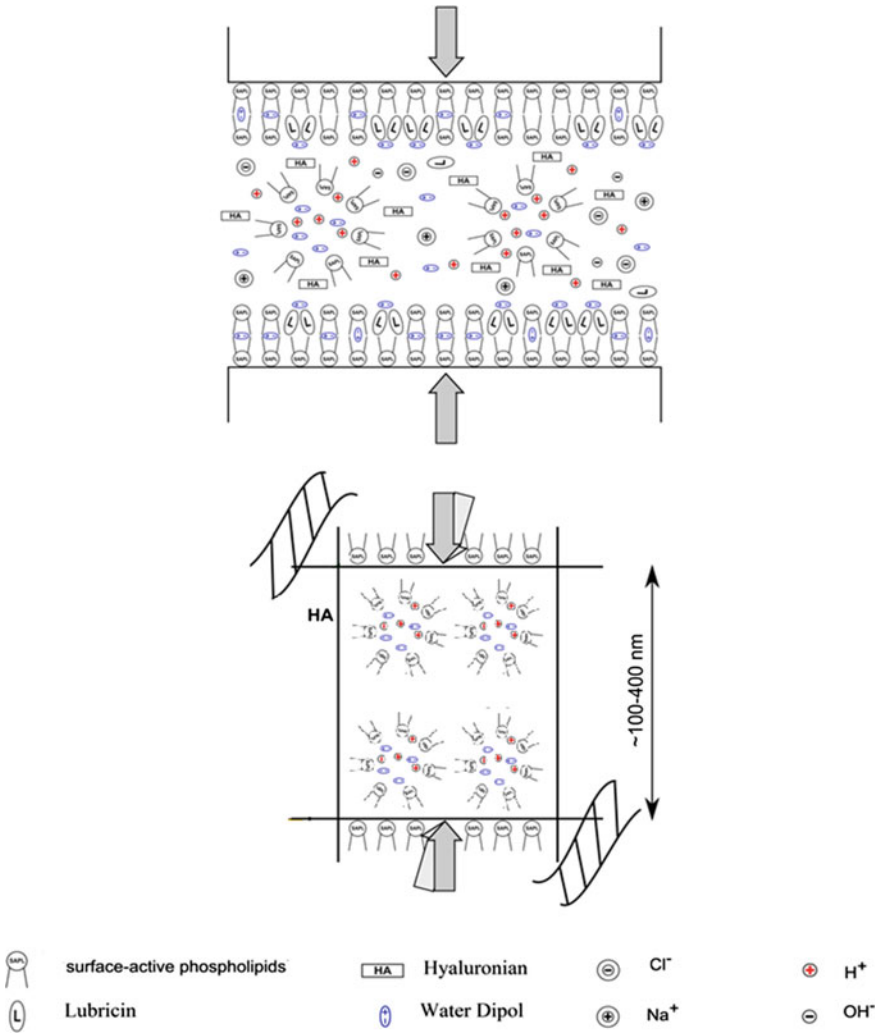

Fig. 1 Artistic presentation of the system of interest. On the *left hand side*, the AC system composed of two rubbing surfaces filled with the SF is displayed. The components of SF are depicted in the legend. On the *right hand side*, a view of the hyaluronic acid (HA) [17] net with phospholipids in form of reversed micelles as well as attached HA polymers is drawn. The ribon-like objects in the corners are meant to represent collagen fibers

(SF) is a complex fluid Fig. 1, also equipped with magnetosensitive living-matter elements (specialised cells [10]), providing extraordinary conditions for sustaining periodic load as well as lowering friction forces of an articular joint at nanoscopic levels [11–15]. Nanolubrication is an effect induced by amphiphilic molecules self-assembled into spherical micelles that becomes relevant when sliding friction is replaced by its rolling bearing counterpart. Here, we examine the mechanical properties of amphiphilic soft colloids when applying an external force. We conjecture that such a process may influence the overall lubricating properties of the SF. We use DPC (Dodecylphosphocholine) surfactants, as they have the natural tendency of creating normal spherical micelles and their similarity to the most common lipids in synovial fluid, namely DPPC (Dipalmitoylphosphatidylcholine) [16], is striking. In addition, we note that DPPC molecules are suitable candidates for improving the AC lubrication conditions because of their sphere-shaped aggregates, which constitute a solid ordered phase right at normal physiological conditions (at 310 K) [3]. The proposed micelles involving dynamical system [2], responsible for the biolubrication, bears a generic nonlinearity that substantiates the principal mechanism of creating defects (linear in concentration of lipids) at the rubbing surfaces, while recovering them after load's action right at the surface(s)—their magnitude is assumed quadratic in the lipid concentration argument.

2 Methods

We apply the molecular dynamics simulation package LAMMPS [18] and perform the simulations using a 8 core processor. The MARTINI coarse-grained (CG) force field [19] has been adopted to mimic interactions among water, lipids, and graphite molecules. MARTINI uses a four to one mapping of atoms, thus, each CG atom represents four real atoms (except of graphite molecules, for which we use a two to one mapping to obtain a hexagonal graphite structure [20]). Molecules are divided into four main groups: charged (Q), polar (P), nonpolar (N), and apolar (C), where each group has its subgroups. In total, the whole system contains 18 basic atoms from which one can build lipids, proteins, etc. A shifted Lennard-Jones (LJ) 12-6 potential energy function is used to describe the nonbonded interactions with σ representing the closest distance of approach between two particles and the strength of their interaction is denoted by ε

$$U = 4\varepsilon \left(\left(\frac{\sigma}{r} \right)^{12} - \left(\frac{\sigma}{r} \right)^{6} \right). \tag{1}$$

Interactions between two particles have been divided into 9 types, differing by their ε and σ values. In addition, charged groups (type Q) bear a full charge q interacting with each other via a shifted Coulomb potential, wherein the term 'shifted' means a properly renormalized interaction distance [20], with a relative dielectric constant

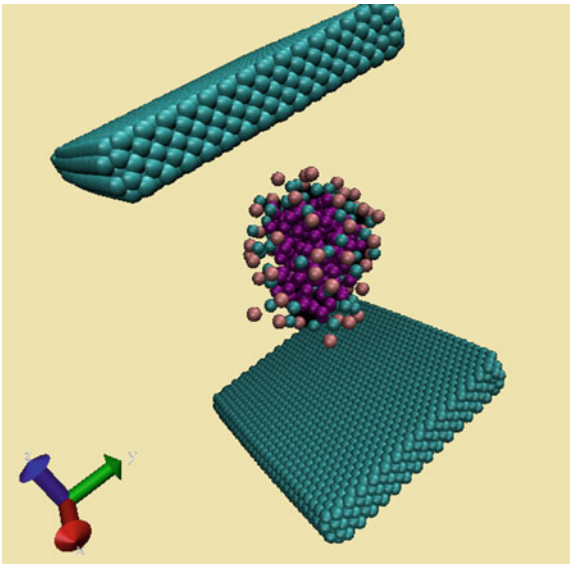

Fig. 2 Snapshot of the simulation box with a compressed micelle. The water molecules are not depicted. The upper and lower graphite surface are colored in *blue*, polymer tails in *violet*, their heads in *blue* and *pink*. The system is confined along the z-direction of the Cartesian reference frame

of $\varepsilon = 15$, so modified toward a lower value to account for the explicit screening conditions. Intramolecular interactions are taken onto account by bond and bond-angle potentials.

The modeled system is composed of 18,000 molecules (water (polar), lipids and graphite (apolar)). NPT simulations have been performed by moving two graphite surfaces toward each other (see Fig. 2), while water and lipids are dynamically captured between them. Each surface is composed of five graphite layers for better stabilizations of its structure. The time step is chosen to be 10 fs. A micelle is composed of 60 DPC lipids. A DPC molecule comprises five CG sites: two oppositely charged atoms, representing the hydrophilic head, and three nonpolar sites representing the hydrophobic tail. Graphite is composed of the same kind of atoms as the tail, however, it has been slightly modified to obtain right properties [20]. Due to the high affinity of lipid tails to a graphite surface, we increased the interaction strength between the hydrophobic tails to avoid undesired effects of tail clustering at the surface.

3 Results and Discussion

We perform simulations of two graphite walls moving toward each other, which causes micelle deformations in response to changes of the slit width. Thereby, the walls are periodically moved according to

$$z = z_0 + A \sin(\omega t). \tag{2}$$

At the beginning, the walls are separated by 4 nm, whereas the micelle diameter is 3.5 nm. We perform simulations for the amplitudes $A = 0.6$, 0.8, and 1.0 nm, and time periods 40, 80, and 160 ps.

The morphology of micelles changes in response to the external load conditions. The latter are represented by a periodic load factor in which both the amplitude and period are subject to change. In the presentation of the results, we follow the idea of morphological phase diagrams. As a consequence, the basic parameter of the periodic load is the ratio of the amplitude A and period T. It is thought to reflect the confining speed resulting from load by the surfaces exerted on the micelle. On the other hand, the center of mass of the confined micelle is allowed to perform a translational random motion a (sub-)diffusive random motion in a type of cage built up of the two rubbing surfaces. In what follows, we present the main results of the micelle's confined random motion under such dynamic arrest. Most of the plots presented below are given dimensionless quantities such as: $R_{\alpha\beta}/R_{\alpha\beta_0}$, wherein α and β capture adequately the notion of all three space directions: x, y, and z.

Figure 3 presents snapshot of micelles before and after a load has been applied. Evidently, a micelle under load is deformed and the lipid tails are preferentially at the wall. This is caused by the tails higher affinity to the hydrophobic (graphite) surfaces. Figure 4 displays morphological shape changes of a micelle characterized by the radius of gyration

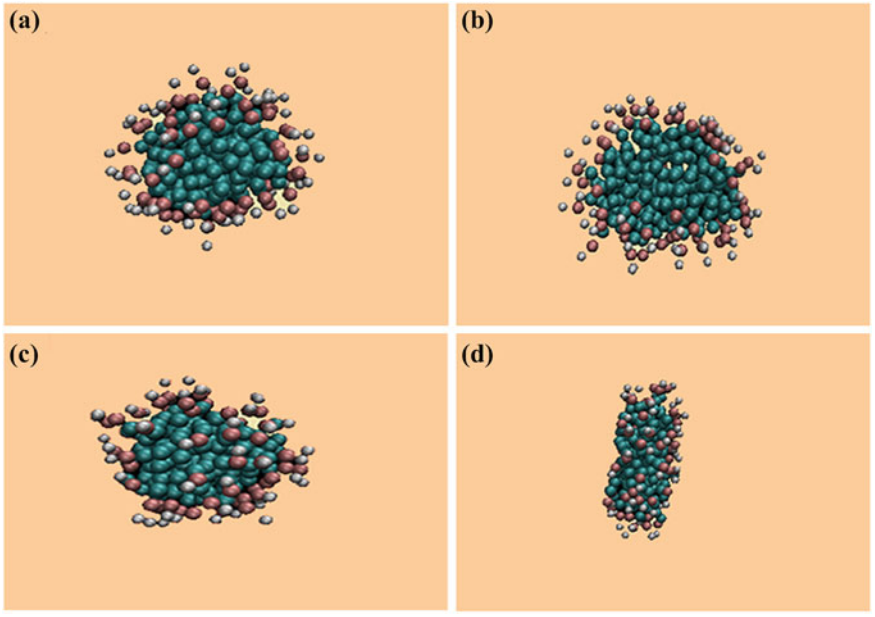

Fig. 3 Snapshot of simulated micelle in two stages of confinement. On the *left hand side* one can see micelle morphology from x-y (*top*) (**a**) and (**b**); y-z (*bottom*) (**c**) and (**d**) axes, respectively, before applying an external pressure. On the *right hand side* one can see morphology of micelle at the moment of the biggest confinement (**b**) and (**d**)

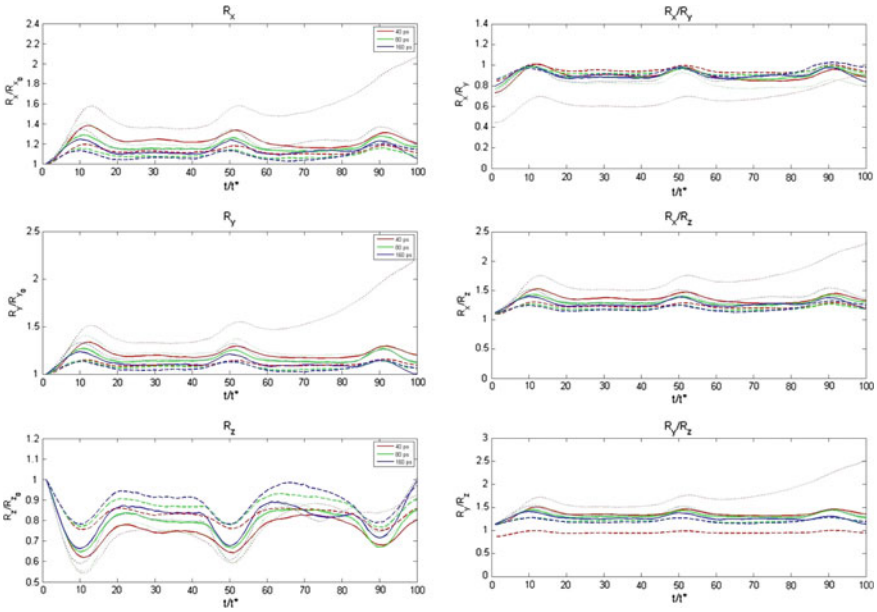

Fig. 4 Morphological changes of micelle as function of time. t* is chosen to obtain multiple periods for each case. On the left hand side, we present radii of gyration divided by their initial values along all three axes. On the right hand side, ratios of (deformed) radii of gyration are displayed along the x- and y-axis. Each color represents a different case of period changes as depicted in the legend, whereas the different line styles depict the corresponding amplitude changes. Dotted lines correspond to A = 1.0 nm, dashed lines to A = 0.6 nm, and solid lines to A = 0.8 nm

$$R^2_{\alpha\beta} = G_{\alpha\beta} = \frac{1}{N}\sum_{i=1}^{N}\langle \Delta r_{i,\alpha}\Delta r_{i,\beta}\rangle, \tag{3}$$

where the sum runs over all monomers of a micelle and $\Delta r_{i,\alpha}$ denotes the distance of the monomer i to the micelle center-of-mass.

Along the x- and y-direction, a micelle undergoes similar shape changes. For most of the cases, micelles are deformed from their (quasi)spherical initial to disc-like structures. However, for the most extreme condition (highest amplitude and shortest period) there is an apparent collapse of micelles under the external load. It seems that the micelle relaxation time is to long to allow it to response to the external load. However, this is rather the exception than the rule and the effect is random and appears occasionally. For longer periods, micelles have enough time to relax and, thus, exhibit the smallest shape changes for all amplitudes under study. The radius of gyration along the z-direction is most stable, but this is caused by boundary condition for this axis. Figure 4 presents shape changes as ratios of two radii of gyration components. Apparently, a sphere-to disc-like shape (morphological) transition appears for all the cases. Figure 5 displays mean square displacements (MSD) of a micelles, which is defined as $\langle (x(t) - x_0)^2 \rangle$. The χ parameter is defined as

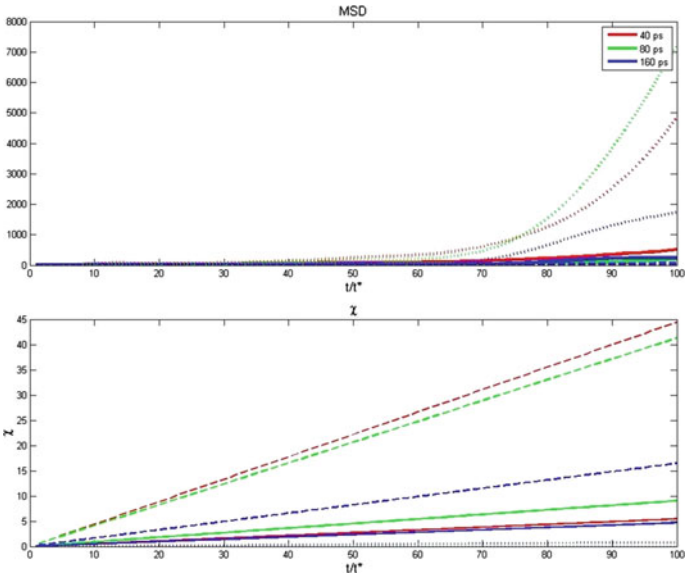

Fig. 5 MSD and χ as a function of time. t* is chosen to obtain multiple periods for each case. Each color represents different case of period change as depicted in legend, whereas relief of the lines depicts the corresponding amplitude changes. Dotted line depicts A = 1.0 nm, dashed line A = 0.6 nm and solid line A = 0.8 nm

$$\chi = \frac{v_{SM}}{v_{RW}}, \tag{4}$$

where $v_{SM} = A/T$ and $v_{RW} = \lambda_{MSD}/t$. T is the period of the displacement, A the displacement amplitude, λ_{MSD} is the mean free path length, and t denotes the time span of a mean-free-path realization, defined by sum of subsequent distances traveled by micelle's mass center, as revealed by the computer simulations. These parameters characterize the micelle translational motion. The amplitude of the wall motion is the more important factor as there are three distinct regimes: for high, medium, and low amplitude. After an initial load applied to a micelle, it moves in a similar way for all the cases studied. After the load is repeated, there appears a difference between cases as micelles cannot relax properly any more. For the last load repetition, micelles bear the overall tendency of a non-relaxing micellar surface preserved even more when compared to both preceding cases. This tendency also reveals a dynamic morphological phase transition in a micelle-surface system. In our simulation as yet, while based on the micellar shape-changes crude analysis, one may opt for having a mechanical-shape nonlinearity, because of applying the same load either on a sphere or on a cylinder. But, when anticipating the simplest Hooke-type (linear law) applied here upon squeeezing, there appears a distinct difference in shape: the cylinder can buckle, which introduces another, topologically nonlinear, quality.

The buckled cylinder becomes an intermediate form, between ellipsoid and squeezed cylinder, cf. Fig. 3c. This type of shape effect may either be deleterious or beneficial when inspecting the actual lubricating conditions, e.g., shape changes may influence the conductivity of active ions (e.g., H^+) contributing to overall lubrication effect [2].

Acknowledgments This work has been sponsored by BS39/2014.

References

1. Winkler, R.G., Hentschke, R.: J. Chem. Phys. **99**, 5405–5417 (1993)
2. Gadomski, A., Pawlak, Z., Oloyede, A.: Tribol. Lett. **30**, 83–90 (2008)
3. Sivan, S., et al.: Langmuir **26**(2), 1107–1116 (2010)
4. Hills, B.A.: Proc. Inst. Mech. Eng. Part H - J. Eng. Med. **214**, 83–94 (2000)
5. Gadomski, A., Bełdowski, P., Rubi, J.M., Urbaniak, W., Augé II, W.K., Santamaría-Holek, I., Pawlak, Z.: Math. Biosc. **244**, 188–200 (2013)
6. Pawlak, Z., Oloyede, A.: Biosystems **94**, 193–201 (2008)
7. Pawlak, Z., Figaszewski, Z., Gadomski, A., Urbaniak, W., Oloyede, A.: Tribol. Int. **43**, 1719–1725 (2010)
8. Pawlak, Z., Petelska, A.D., Urbaniak, W., Yusuf, K.Q., Oloyede, A.: Cell Biochem. Biophys. **65**, 335–345 (2013)
9. Wierzcholski, K.: Int. J. Appl. Mech. Eng. **11**, 515–527 (2006)
10. Kharchenko, V.O., Goychuk, I.: Phys. Rev. E **87**, 052119–052128 (2013)
11. Seror, J., Merkher, Y., Kampf, N., Collinson, L., Day, A.J., Maroudas, A., Klein, J.: Biomacromolecules **12**, 3432–3443 (2011)
12. Seror, J., Merkher, Y., Kampf, N., Collinson, L., Day, A.J., Maroudas, A., Klein, J.: Biomacromolecules **13**, 3823–3832 (2012)
13. Trunfio-Sfarghiu, A.-M., Berthier, Y., Meurisse, M.-H., Rieu, J.-P.: Langmuir **24**, 8765–8771 (2008)
14. Harvey, N.M., Yakubov, G.E., Stokes, J.R., Klein, J.: Biomacromolecules **12**, 1041–1050 (2011)
15. Daniel, M.: Role of surface-active lipids in cartilage lubrication. In: Iglic, A. (ed.) Advances in Planar Lipid Bilayers and Liposomes, pp. 225–243. Elsevier - Academic Press, Amsterdam (2012)
16. Hills, B.A., Butler, B.D.: Ann. Rheum. Dis. **43**, 641–648 (1984)
17. Dedinatè, A.: Soft Matter **8**, 273–284 (2012)
18. http://lammps.sandia.gov/
19. Marrink, S.J., et al.: J. Phys. Chem. B **111**, 7812–7824 (2007)
20. Gobbo, C., et al.: J. Phys. Chem. C **117**, 15623–15631 (2013)

The Sensitivity Analysis of the Method for Identification of Bearing Dynamic Coefficients

Łukasz Breńkacz and Grzegorz Żywica

Abstract This article presents the sensitivity analysis of the method for determination of mass, damping and stiffness coefficients using the impulse excitation technique for a rotor-bearing system. Such an experimental approach is an adequate tool for the estimation of 24 dynamic coefficients, that is 4 damping coefficients, 4 mass coefficients and 4 stiffness coefficients for each bearing. As yet, the literature is exclusive of any researches into the sensitivity of this experimental method itself. However, the influence of several parameters (e.g. supply pressure, bearing geometry, etc.) on the calculation results concerning bearing dynamic coefficients had already been examined in detail. The preparation of the numerical model of the rotor made it possible to assess how influential are the input parameters—such as position and angle of an excitation force or movements of the sensor heads used to measure the displacements of bearing journals—to the results. The potential impact of changing parameters, such as stiffness of rotor material, its unbalance or its geometry, on the values of calculated stiffness, damping and mass coefficients in tested rotor-bearing system was also verified. The paper presents the calculation results of dynamic coefficients for the bearings along with their relative errors. It was shown how the calculated values change according to the different input parameters. The excitation signals and the corresponding system responses were also provided. Moreover, the article contains information on how to enhance the accuracy of calculations.

Ł. Breńkacz (✉) · G. Żywica
Department of Turbine Dynamics and Diagnostics, The Szewalski Institute of Fluid-Flow Machinery PAS, Fiszera 14, 80-231 Gdańsk, Poland
e-mail: lukasz.brenkacz@imp.gda.pl

G. Żywica
e-mail: grzegorz.zywica@imp.gda.pl

J. Awrejcewicz (ed.), *Dynamical Systems: Modelling*, Springer Proceedings in Mathematics & Statistics 181, DOI 10.1007/978-3-319-42402-6_8

1 Introduction

A number of methods for determining the stiffness and damping coefficients of bearings on the basis of experimental tests have been described in scientific literature. The impulse response method for identification of mass, damping and stiffness coefficients of rotor-bearing system was described in the article [1]. It presents the calculation algorithm and its results for different identification ranges and the corresponding measurement error. The Impulse Excitation Technique (IET)—based on calculations in the frequency domain, is considered to be the most economically efficient and giving one of the most reliable results [2]. It is a linear method.

There are a number of experimental methods for identifying bearing dynamic coefficients [3, 4]. The stiffness and damping coefficients vary with the rotational speed [5]. When it comes to slide bearings, they are inherently non-linear in nature, which means that their dynamic behavior may change at constant rotational speed, as well as they depend on the excitation force [6]. Dynamic coefficients also change with the ambient temperature, bearing supply pressure and load [7]. The computations of bearing force coefficients are often used for the bearings with unknown design parameters and the ones of complex structure [8].

Tiwari and Chakravarthy [9] proposed to improve the algorithm for the estimation of stiffness and damping coefficients of bearings in such a way that it additionally enables estimation of the residual unbalance of a rotor. Nowadays, various works are under way aimed at the modification of experimental methods in order to achieve an increased accuracy. Miller and Howard [10] described the method for the identification of bearing rotor-dynamic coefficients using the extended Kalman filter. The calculations were carried out using the linearized stiffness and damping coefficients in rotor-bearing systems, considering the noise and unbalance. The method was successfully used to assess the main stiffness coefficients, whereas the cross-coupling damping coefficients were calculated with the lower accuracy. Application of the Monte Carlo method for investigation of dynamical parameters of rotor supported by magnetorheological squeeze film damping devices was shown in [11]. The new way of identification of the stiffness and damping characteristics of bearings using phase-plane diagrams was presented in the publication [12]. The authors highlight that a reliable assessment of bearing dynamic coefficients is a major challenge, particularly in non-linear systems. They claim that there is no single universal model for calculation of system characteristics because their identification depends on measurement data and reference model.

Numerical determination of dynamic coefficients in the case of foil bearings can be a very difficult task because of their complex structure [13]. The results of the experimental identification of these coefficients for the large-diameter hybrid foil bearing were presented in paper [14]. This article contains dynamic characteristics of hybrid (hydrodynamic + hydrostatic) foil bearing with a diameter of 101.6 mm and a length of 82.6 mm. The stiffness coefficients were determined using two different methods: first, with a quasi-static method based on the load-deflection curves in the time domain; second, with the frequency domain impulse response

method. The damping coefficients were obtained using only the impulse response method. The stiffness coefficients values from both methods were close to each other. The article [15] presents the experimental studies on hybrid gas bearing, characterized by a complex design of foil, which is quite tolerant to high supply pressure. The bearing utilized two lubricating films: hydrostatic and hydrodynamic. The paper [16] presents the calculation results of aerostatic radial bearings on the example of Bently Nevada test rig. The tests with various types of bearings were carried out in order to analyze their static and dynamic characteristics. Only the main stiffness and damping coefficients were calculated. The influence of cross-coupling stiffness and damping parameters on the results was assessed on the basis of numerical simulations. During the calculations, the mass matrix elements were considered as known. The stiffness and damping matrixes had to be calculated. The authors recommend that the main coefficients should be estimated at the beginning of the experiment, and then the cross-coupling coefficients, in the next step, since they are more vulnerable to errors. Another example of experimental identification of aerostatic bearing was shown in [17]. The numerical models for calculating stiffness and damping parameters of bearings are not only used for radial bearings, they also continue to make a successful contribution to axial bearing investigations. Experimental identification of stiffness and damping coefficients of an axial foil bearing was shown in the article [18].

2 The Calculations of Bearing Dynamic Coefficients

The numerical model of the rotor, which have been used for the sensitivity analysis of the method, was created on the basis of the test rig called SpectraQuest Machinery Fault and Rotor Dynamics Simulator. This test rig is located at the Szewalski Institute of Fluid-Flow Machinery PAS, in Gdańsk. The numerical model was created in the Samcef Rotors software (Fig. 1). The model consists of a shaft rotating at 2800 rpm and bearings modeled using the stiffness and damping coefficients in the orthogonal and cross-coupling directions. The rotor during the

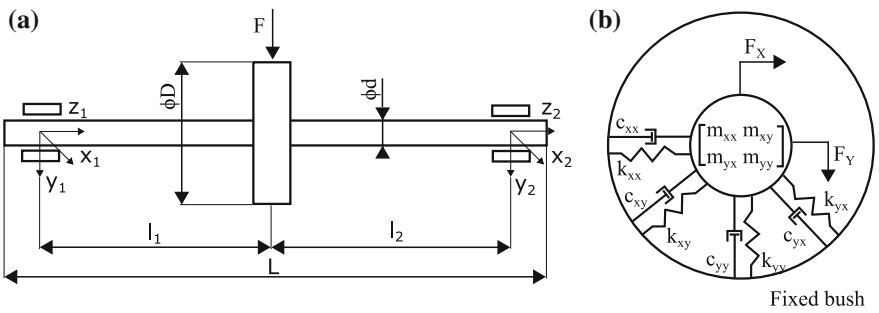

Fig. 1 **a** Rotor model prepared in the Samcef Rotors software, **b** Bearing model

simulation had been excited by a known value of excitation force, in the central part, in the X direction. Then the vibration amplitude of the rotor was measured in each bearing in X and Y directions. Then, the simulation was repeated, this time using the same excitation force, but model has been excited in the Y direction. In this case, the vibration amplitudes of the rotor in the bearings in the direction of X and Y were measured. When the vibration in the X direction in the first bearing after excitation in the Y direction was measured, signal has been described as ${D^1}_{XY}$. Based on the excitation signals and the response signal generated by the Samcef Rotors program the stiffness, damping and mass coefficients of the bearings were calculated. Because the stiffness and damping coefficients were defined in the Samcef Rotors program, calculated coefficients can be compared with their actual values. Taking into consideration different parameters, it was possible to compare results with expected values and calculate the relative error.

The calculations are carried out for two bearings simultaneously. Indexes '1' and '2' stand for the first and the second bearing. The index 'i' designates frequency range. The first of double index indicates the direction of the system response, the second index indicates the direction of the excitation force. For example, ${D^1}_{YX}$ element defines the vibrations of the rotor at the first bearing in the X direction after excitation in the Y direction. The least squares method is used to solve the equations and it requires the signal to be represented in the frequency domain. This is achieved by Fourier transform of the force signal and the system response from the time domain. In order to obtain the dynamic compliance the signal representing the displacement in the bearing is multiplied by the signal representing the excitation force. Flexibility is defined as the inverse of mechanical impedance. The least squares method can be applied to the Eq. (1). In this equation, A_i is a matrix in which the signals are elements of flexibility matrix and frequency vector. It was formed by decomposition of real and imaginary part (2). Matrix I is defined by Eq. (3), while the matrix Z consists of stiffness, damping and mass coefficients of the rotor-bearing system (4). If we assume that the parameters are obtained for 100 frequency samples (it is determined by the index (i) the matrix A will have dimension 800 × 12, matrix I will have dimension 800 × 2, while the matrix Z will have dimension 2 × 12.

$$Z = (A_i^T A_i)^{-1} A_i^T I_i, \tag{1}$$

$$A_i = \begin{bmatrix} \mathrm{Re}\left[F_i^1 \cdot \begin{bmatrix} 1 & 0 & 0 & 0 & -(\omega_i)^2 & 0 & 0 & 0 & \omega_i & 0 & 0 & 0 \\ 0 & 1 & 0 & 0 & 0 & -(\omega_i)^2 & 0 & 0 & 0 & \omega_i & 0 & 0 \end{bmatrix}\right] \\ \mathrm{Re}\left[F_i^2 \cdot \begin{bmatrix} 0 & 0 & 1 & 0 & 0 & 0 & -(\omega_i)^2 & 0 & 0 & 0 & \omega_i & 0 \\ 0 & 0 & 0 & 1 & 0 & 0 & 0 & -(\omega_i)^2 & 0 & 0 & 0 & \omega_i \end{bmatrix}\right] \\ \mathrm{Im}\left[F_i^1 \cdot \begin{bmatrix} 1 & 0 & 0 & 0 & -(\omega_i)^2 & 0 & 0 & 0 & \omega_i & 0 & 0 & 0 \\ 0 & 1 & 0 & 0 & 0 & -(\omega_i)^2 & 0 & 0 & 0 & \omega_i & 0 & 0 \end{bmatrix}\right] \\ \mathrm{Im}\left[F_i^2 \cdot \begin{bmatrix} 0 & 0 & 1 & 0 & 0 & 0 & -(\omega_i)^2 & 0 & 0 & 0 & \omega_i & 0 \\ 0 & 0 & 0 & 1 & 0 & 0 & 0 & -(\omega_i)^2 & 0 & 0 & 0 & \omega_i \end{bmatrix}\right] \end{bmatrix}, \tag{2}$$

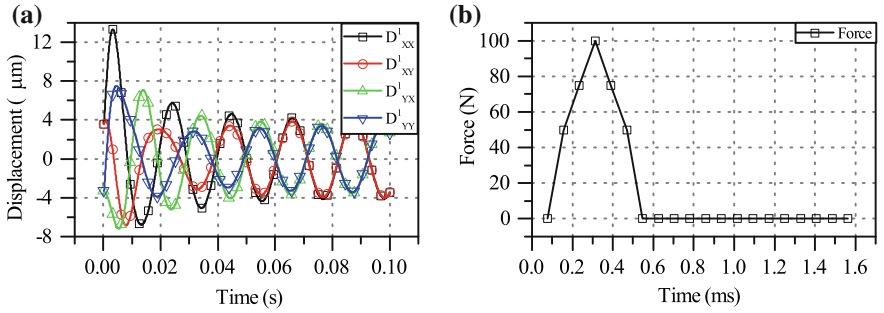

Fig. 2 **a** Graph of the bearing bush displacement versus time after excitation of the rotor in its central part, **b** Force in the X direction versus time

$$I_i \begin{bmatrix} 1 & 0 & 1 & 0 & 0 & 0 & 0 & 0 \\ 0 & 1 & 0 & 1 & 0 & 0 & 0 & 0 \end{bmatrix}. \tag{3}$$

Figure 2 a contains the graph of bearing displacement versus time, drawn up after the rotor was excited in its central part. It is composed of the component resulting from the excitation and the constant component linked to the existence of rotor unbalance. In the next step of the algorithm, the constant component mentioned in the previous sentence should then be deducted from the obtained signal. Figure 2b presents the signal which represents the excitation force. It was defined in the Samcef Rotors software as a vector containing force values at successive time steps. The numerical simulation was carried out for the time steps having the same resolution of 1/12800 [s].

3 Sensitivity Analysis of the Numerical Model

The carried out sensitivity analysis was not aimed at looking into all the possible parameters but to indicate the parameters which substantially affect the results of the calculation. Figure 3 contains the flowchart according to which the sensitivity assessment of the experimental identification method used to be performed. On its left side one can see the parameters which were altered during the determination of bearing dynamic coefficients. The calculation algorithm, used in the method described here, can be seen in the central part of the flowchart. The right-hand side of Fig. 3 shows that a summary of the bearing coefficients results for various input parameters together with the calculation error estimation have been created, at the last stage of the sensitivity analysis. As the stiffness and damping coefficients are known for the rotor concerned, the calculated values and real values of the bearing coefficients can be directly compared (Table 1).

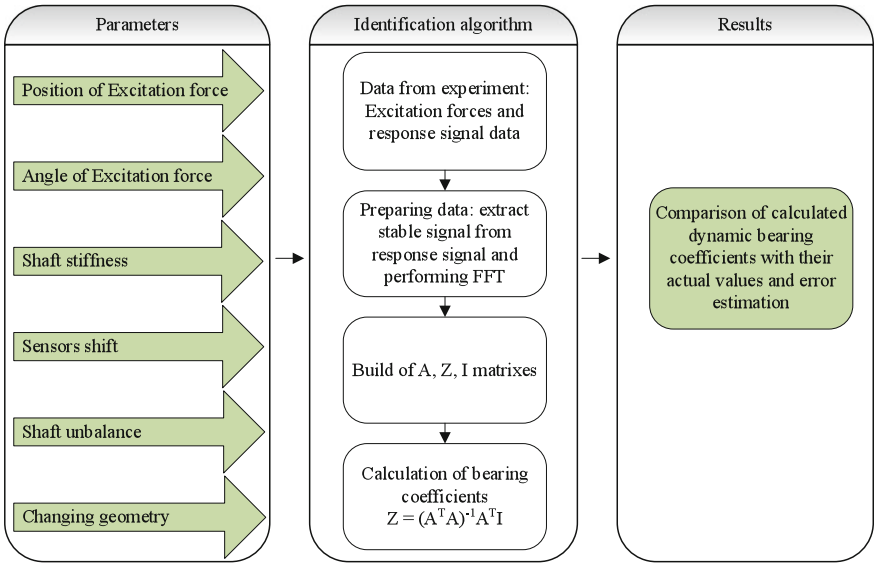

Fig. 3 Sensitivity analysis flowchart

Table 1 Parameters of the numerical model

Parameter	Value
Length	L = 0.92 m
Distance between bearings	$2 \times l_1 = 0.58$ m
Rotor shaft diameter	d = 19.05 mm
Disk diameter	D = 152.4 mm
Young's modulus	$E = 205 \times 10^9$ Pa
Poisson's ratio	0.3
Material density	$\rho = 7800$ kg/m^3

4 Calculations Concerning the Reference Model

The signals generated using Samcef Rotor program were used to calculate the stiffness, damping and mass coefficients of the rotor-bearing system. The model of symmetric rotor was considered, but the stiffness and damping coefficients (including cross-coupling ones) have different values. In the hydrodynamic bearings, the cross-coupling part of damping coefficients C_{xy} and C_{yx} has got the same values [4], in this case they have different values in order to show how the method works. Since the values of stiffness and damping coefficients were taken from the numerical model of an existing rotor, it was possible to compare them directly and, on that basis, the calculation error of force coefficients was estimated.

The calculation results together with the corresponding relative errors are shown in Table 2. It has to be mentioned that the operations were carried out upon the

Table 2 List of actual and calculated stiffness, damping and mass coefficients for both bearings, reference case. The relative errors were also listed

	Stiffness coefficients N/m							
	k^1_{xx}	k^1_{yy}	k^1_{xy}	k^1_{yx}	k^2_{xx}	k^2_{yy}	k^2_{xy}	k^2_{yx}
Values	500000	450000	250000	240000	550000	470000	270000	260000
Calculated	498232	450488	248338	240544	548107	470504	268288	260583
Error %	0.35	0.11	0.66	0.23	0.34	0.11	0.63	0.22
	Damping coefficients N · s/m							
	c^1_{xx}	c^1_{yy}	c^1_{xy}	c^1_{yx}	c^2_{xx}	c^2_{yy}	c^2_{xy}	c^2_{yx}
Values	500	550	250	260	550	560	260	270
Calculated	507.5	547.7	259.4	258.8	558.1	558.3	269.2	270.7
Error %	1.50	0.42	3.76	0.46	1.47	0.30	3.54	0.26
	Mass coefficients kg							
	m^1_{xx}	m^1_{yy}	m^1_{xy}	m^1_{yx}	m^2_{xx}	m^2_{yy}	m^2_{xy}	m^2_{yx}
Actual	2.423	2.423	0.000	0.000	2.423	2.423	0.000	0.000
Calculated	2.338	2.404	–0.071	–0.029	2.497	2.451	–0.035	–0.053
Error %	3.49	0.77	–	–	3.07	1.18	–	–

signal only after eliminating the constant component. The rotor rotational speed was 2800 rpm. The signal related to the rotational speed, which was represented in the frequency domain falls into the resonance range of the rotor. The relative error estimated for the bearing stiffness coefficients does not exceed 0.7 %. This is a quite accurate estimation, especially given the fact that the error of calculating the stiffness coefficients in the main coordinates (which are more significant in further modeling of the dynamics of the system) does not exceed 0.4 %. The error resulting from the calculation of damping coefficients is small and does not exceed 3.8 %. This error appears only in the calculation of the cross-coupling part of damping coefficients. The error concerning the damping coefficients in main coordinates is up to about 1.5 %. The weight of the shaft modeled in Samcef Rotors program is 4.845 kg. The calculated weight of the shaft based on described algorithm and numerical model of the shaft is 4.845 kg. This mass was calculated by adding the mass coefficients on the main diagonal (*XX* and *YY*), and dividing this value by two. Interpretation of mass coefficient values is as follows: the mass coefficient m^1_{xx} is the mass of part of the shaft involved with the vibration in the *X* direction allocated to the first bearing after excitation in the *X* direction. In contrast, the mass coefficient in m^1_{yy} is the mass of part of the shaft involved with the vibration in the *Y* direction allocated to first bearing after excitation in the *Y* direction. Dividing the sum of the weight coefficients by two to calculate the mass of the shaft is applied because the system was excited twice. Cross-coupling mass coefficients (*XY YX*) should be close to zero. The error of calculating weight coefficient is 0.003 %. These results mean that the rotor weight 4.845 kg can be estimated with an accuracy of ±0.0001 kg.

The subsequent sensitivity analysis consisted in changing the stiffness of rotor material. The value of Young's modulus has been significantly increased, namely by 100 times. This test was intended to check whether material stiffness affects the calculation results. After this test, it turned out that the equivalent results were obtained in two cases. This means that the value of modulus of elasticity for steel, corresponding to the most frequently encountered shaft materials, does not affect calculation results of stiffness, damping and mass coefficients of rotor-bearing system.

5 Impact of Unequal Excitation Distribution on Two Bearings

The algorithm described here assumes a symmetrical distribution of excitation force between two bearings. This assumption requires rotor excitation to be performed in its central part, however it is not possible to implement for each type. In the course of model testing it turned out that the small shift of excitation force position (as small as by five per cent of the distance between bearings) may lead to identification of bearing dynamic coefficients with an error rate around a dozen percent. Appropriate unsymmetrical distribution of the excitation force between two bearings results in a satisfactory outcome of such calculations. Note that in the example described above, the shift of force from the center of the shaft was 30 mm (denoted as "s"). This represents 5 % of the shaft length between bearings. The results were compared with those obtained earlier for the force F_{ref} aligned on the center of the rotor's shaft.

In the algorithm applied for computing the bearing dynamic coefficients one can introduce modifications in order to enhance calculation accuracy. Force values related to the bearings should be calculated on the basis of geometrical proportions. Adjustment of the excitation force shall be to multiply every element of the force vector by the expressions (4, 5). The force values divided proportionally and not proportionally between the first and the second bearing were taken into account in the Eq. (2). F_1 denotes the value of force applied to first bearing, while $F_{1\text{shifted}}$ represents the same force after its proper transformation. The l_1 and l_2 dimensions define the distances of the bearing supports from the center of the shaft. The values denoted as l_{1f} and l_{2f} specify the distances of the force to the bearings.

$$F_{1\text{shifted}} = F_1 \cdot \frac{l_{2f}}{2 \cdot l_1}, \tag{4}$$

$$F_{2\text{shifted}} = F_2 \cdot \frac{l_{1f}}{2 \cdot l_2}. \tag{5}$$

In the case when in the algorithm the force was not shifted properly the relative errors were up to 12, 15.5, and 1.73 % for stiffness, damping and mass coefficients, respectively. After shifting the excitation force the relative errors concerning dynamic coefficients has changed radically. They were as follows: below 0.73 % for stiffness, below 3.73 % for damping and around 0.2 % for mass. In this place it should be mentioned that the calculation accuracy for main stiffness and damping coefficients is higher than it is the case with the cross-coupling coefficients.

It is worth noting that a shaft mass is often known parameter before starting the calculation process, contrary to stiffness and damping coefficients. If this is the case, once all bearing dynamic coefficients have been calculated, the calculation error corresponding to mass coefficients can be assessed. This enables to reject incorrect estimates at an early stage of the identification. The expected values of main mass coefficients (in *xx* and *yy* directions) are equal to half of shaft mass in the tested model. After the calculations were carried out with not shifted excitation force, one can say that these expected values of mass coefficients and calculated ones varied considerably (approximately 12.4–18.4 %). Then, considering the uneven division of the excitation force in the calculations, the relative errors were ranging from 2.8 to 6.1 %.

6 Change of Excitation Force Direction and Its Consequences

The experimental studies are carried out by double exciting the rotating shaft using an impact hammer in a direction transverse to the axis of rotation of the rotor. On the basis of the example provided in the previous chapter, it may be said that in order to obtain correct results of dynamic coefficients identification, it is necessary to adopt good definition of excitation force. This chapter describes the case in which a hammer hits the rotating rotor at a certain angle in relation to the intended orientation. In order to achieve this effect, the impact marked $F_{x\alpha}$ was introduced into the numerical model. It designates an impact hammer hit at an angle of 15° to the intended direction. The impact marked F_y means that the impact acted along the *Y* axis. Figure 4a presents the diagram of an excitation force acting at a certain angle in relation to the intended orientation while Fig. 4b shows the system response for the bearing number 1. Only the system responses in *X* and *Y* directions after the excitation in *X* direction were presented. They are characterized by the highest difference in the results. The notation $D^1{}_{XX}$ ref and $D^1{}_{YX}$ ref indicates system response for the force F_x acting in *X* direction. The signals $D^1{}_{XX}$ and $D^1{}_{YX}$ are generated after excitation of the system by means of the force $F_{x\alpha}$ applied in an angle 15°. It should also be emphasized that the angle of application of the excitation force is quite high and should be minimized, to the greatest possible extent, when conducting experimental tests.

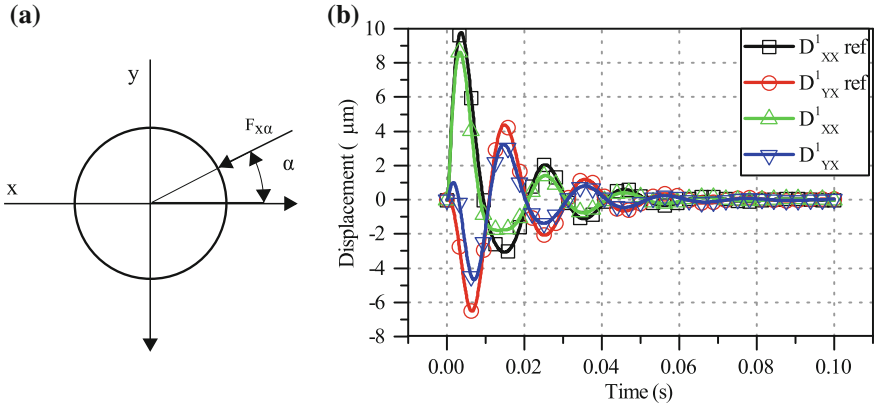

Fig. 4 **a** Diagram presenting the force applied at a certain angle **b** System response signals in *X* and *Y* directions after its excitation by using force at an angle of 0° and 15°

Table 3 List of actual and calculated stiffness, damping and mass coefficients for both bearings, case with the excitation force applied at an angle of 15°

	Stiffness coefficients N/m							
	k^1_{xx}	k^1_{yy}	k^1_{xy}	k^1_{yx}	k^2_{xx}	k^2_{yy}	k^2_{xy}	k^2_{yx}
Values	500000	450000	250000	240000	550000	470000	270000	260000
Calculated	516049	383855	257221	106858	567699	398520	277880	113519
Error %	3.21	14.70	2.89	55.48	3.22	15.21	2.92	56.34
	Damping coefficients N · s/m							
	c^1_{xx}	c^1_{yy}	c^1_{xy}	c^1_{yx}	c^2_{xx}	c^2_{yy}	c^2_{xy}	c^2_{yx}
Values	500	550	250	260	550	560	260	270
Calculated	523.9	478.5	267.8	123.4	576.2	486.5	277.9	121.7
Error %	4.78	13.00	7.12	52.54	4.76	13.13	6.88	54.93
	Mass coefficients kg							
	m^1_{xx}	m^1_{yy}	m^1_{xy}	m^1_{yx}	m^2_{xx}	m^2_{yy}	m^2_{xy}	m^2_{yx}
Values	2.423	2.423	0.000	0.000	2.423	2.423	0.000	0.000
Calculated	2.426	2.424	–0.071	–0.065	2.591	2.462	–0.034	–0.072
Error %	0.16	0.07	–	–	6.95	1.62	–	–

Table 3 lists the results of stiffness, damping and mass coefficients calculated on the basis of system response signals generated after excitation of the system in X direction by the force applied at an angle of 15° (which is identified by "α" in Fig. 4 a. In the calculation algorithm the whole of the value of the force is treated as if the excitation was introduced at an angle of 0°. It turns out that the relative errors corresponding to stiffness coefficients, damping coefficients and shaft mass were around 56, 55 and 2.2 %, respectively. It should be noted in this respect that the relative errors for some coefficients do not exceed 3 %, so not all of the results are

burdened with a considerable error. The highest levels of relative errors resulted from the identification of cross-coupling coefficients *YX*. The calculation of *YY* coefficients also produced significant errors. The relatively small errors were observed in the calculation of *XX* and *YY* coefficients.

7 The Impact of Sensors Shifting

The identification of bearing dynamic coefficients is carried out on the basis of excitation force signal and system response coming from actual location of bearings. Since sensor placement inside bearing support is usually impossible, one has to check how the placement of sensors right next to the bearing supports affects the results of the calculations. The ideological diagram of arrangement of bearing supports and measurement sensors was presented in Fig. 5. The s_1 and s_2 dimensions define the distances of the bearing supports from the center of the shaft. The values denoted as l_{1p} and l_{2p} specify the distances of the sensors to the center-point of the system. The rotor length was marked with the letter L.

The calculations that were carried out after the measuring points had been moved toward the center of the shaft by 30 mm (it corresponds to 5 % of the distance between the bearing supports) show that the relative errors relating to stiffness, damping, and mass coefficients amounted to about 2 %. In order to enhance the accuracy of calculations, Eqs. 6 and 7 shall be applied. When system response signal measured at the placement of the sensors was multiplied by the expressions listed below, the calculation results concerning bearing dynamic coefficients were consistent with those generated on the basis of the signals measured in the center of bearing supports.

$$\begin{bmatrix} XX_1 & YY_1 \\ XX_2 & YY_2 \end{bmatrix} = \frac{1}{s_1+s_2} \cdot \begin{bmatrix} s_2+l_1 & s_1-l_1 \\ s_2-l_2 & s_1+l_2 \end{bmatrix} \begin{bmatrix} XX_{1p} & YY_{1p} \\ XX_{2p} & YY_{2p} \end{bmatrix}, \tag{6}$$

$$\begin{bmatrix} XY_1 & YX_1 \\ XY_2 & YX_2 \end{bmatrix} = \frac{1}{s_1+s_2} \cdot \begin{bmatrix} s_2+l_1 & s_1-l_1 \\ s_2-l_2 & s_1+l_2 \end{bmatrix} \begin{bmatrix} XY_{1p} & YX_{1p} \\ XY_{2p} & YX_{2p} \end{bmatrix}. \tag{7}$$

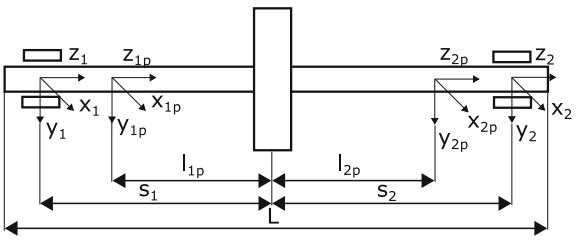

Fig. 5 Ideological diagram on which are marked points of measurement relating to the bearings and the distances taken into account during calculation of bearing dynamic coefficients

8 Case of Asymmetrical Rotor

It often happens that it is necessary to identify bearing dynamic coefficients for a system in which the bearings are at different distances from the ends of the shaft. The objective of this chapter is to put into analysis the calculation results obtained for an exemplary asymmetrical rotor. For this purpose, one shaft end has been shortened by 60 mm. Schematic view of the rotor is presented in Fig. 6. The rotor dimensions were as follows: $l_1 = l_2 = 290$ mm, $L_1 = 460$ mm, and $L_2 = 400$ mm. The system response at the bearing no. 1 after applying the excitation force between the bearings was shown in Fig. 7. The change in the rotor's geometry described above caused that the rotor mass has decreased slightly to 4.71 kg.

Table 4 lists the stiffness, damping and mass coefficients in the case of asymmetrical rotor. The relative errors concerning the stiffness coefficients and damping coefficients do not exceed 0.6 and 4 %, respectively. The shaft mass which was 4.71 kg was determined as 4.709 with accuracy of 0.012 %. Also in this case, all the main coefficients were identified with higher accuracy than the cross-coupling ones.

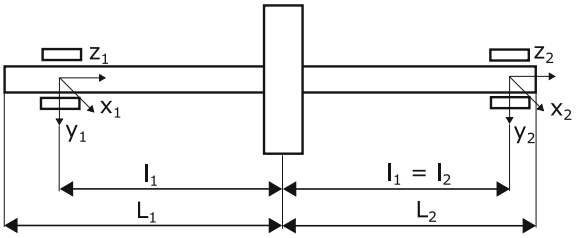

Fig. 6 Schematic view of the asymmetrical rotor

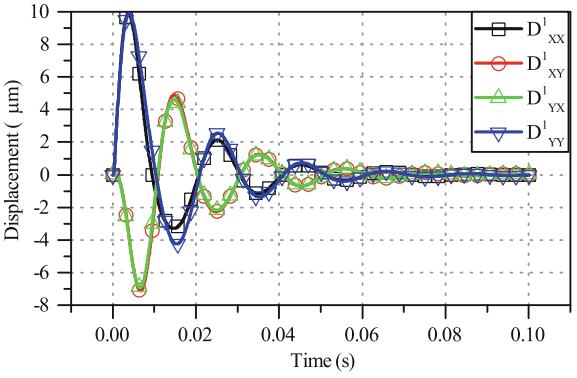

Fig. 7 Response signal of the asymmetrical system

Table 4 List of actual and calculated stiffness, damping, and mass coefficients for both bearings, asymmetrical rotor case

	Stiffness coefficients N/m							
	k^1_{xx}	k^1_{yy}	k^1_{xy}	k^1_{yx}	k^2_{xx}	k^2_{yy}	k^2_{xy}	k^2_{yx}
Values	500000	450000	250000	240000	550000	470000	270000	260000
Calculated	498198	450495	248331	240585	548158	470442	268370	260557
Error %	0.36	0.11	0.67	0.24	0.33	0.09	0.60	0.21
	Damping coefficients N · s/m							
	c^1_{xx}	c^1_{yy}	c^1_{xy}	c^1_{yx}	c^2_{xx}	c^2_{yy}	c^2_{xy}	c^2_{yx}
Values	500	550	250	260	550	560	260	270
Calculated	506.9	547.2	259.7	259.5	557	558.6	268.7	271.9
Error %	1.38	0.51	3.88	0.19	1.27	0.25	3.35	0.70
	Mass coefficients							
	m^1_{xx}	m^1_{yy}	m^1_{xy}	m^1_{yx}	m^2_{xx}	m^2_{yy}	m^2_{xy}	m^2_{yx}
Value kg	–	–	–	–	–	–	–	–
Calculated	2.364	2.430	–0.069	–0.028	2.341	2.284	–0.027	–0.055
Error %	–	–	–	–	–	–	–	–

9 Summary and Conclusions

The article presents the sensitivity analysis of the method for the determination of 24 bearing dynamic coefficients. These coefficients are determined experimentally for a rotor system supported by two bearings, in a single operation by making use of the method of least squares. The 16 dynamic coefficients (including 4 stiffness, 4 damping, and 4 mass ones) are identified for each bearing at one time. For the purpose of verifying the sensitiveness of the key input parameters, a numerical model in Samcef Rotors program was created. The model containing a rotor supported by two bearings allowed to change the parameters which are difficult or even impossible to verify during experimental tests.

As part of this work, the calculations were carried out for a reference model of the rotor—symmetrical rotor with the disk located in the middle of the shaft, and the shaft was equipped with two bearings equidistant from its center. As the values of stiffness and damping coefficients as well as the shaft mass were known in advance, there was a possibility to make a direct comparison between the calculated values and actual values. After performing the calculations for the reference model, the maximum relative error concerning the stiffness coefficients amounted to 0.63 %. The same error in comparison to the damping coefficients did not exceed 3.76 %. In addition, it was noted that the main stiffness and damping coefficients were calculated with an accuracy two times higher relating to the cross-coupling stiffness and damping coefficients. The shaft mass can be identified with an accuracy of 0.003 %. Such good calculation accuracy allows to calculate the shaft mass, which in reality weighs 4.845 kg, with an accuracy of 0.0001 kg.

One of the parameters examined concerned shifting of the excitation force from the initial position located in the middle of the shaft by 30 mm from the disk. It turns out that even this small shift (5 % of the distance between the bearings) leads to the relative errors amounting to around 12, 15.5, and 0.2 % for the stiffness, damping and mass coefficients, respectively. A modification of the calculation algorithm was described, which involves an uneven distribution of the excitation force on each bearing. This modification improved the accuracy of the results obtained and the relative errors were at a level similar to errors calculated for the reference model. It was quite interesting to compare the calculated mass coefficients with their actual values (half of the shaft mass). In the case of initial version of the algorithm (without correction) the relative errors concerning these coefficients were around 15 %, while introducing the appropriate correction into the algorithm reduced these errors to approximately 3.8 %. By checking the values of mass coefficients, we are able to assess the correctness of the whole set of bearing dynamic coefficients in a preliminary stage. This example illustrates how convenient it is to carry out the calculation of all coefficients (not only stiffness and damping coefficients) in a single operation.

A well-defined excitation force in the calculation algorithm produces correct results of bearing dynamic coefficients. The force generated by an impact hammer is not always applied in the intended direction. In the course of the experimental research there is a possibility to make an "imprecise" impact, which leads to applying the force in an unintended direction. This was the reason why it was decided to analyze the case in which the angle of the excitation force F_x was changed by 15°. It is quite a large angle; however, it is worth checking what the discrepancy between the results this change entails. The calculations of bearing dynamic coefficients were carried out as if the excitation angle α was 0°. It turns out that such an "imprecise" impact, i.e., deviation of ±15° from the intended direction of impact, results in the relative error amounting to 56 %. Such a high level of error appears only for certain coefficients. The highest levels of relative errors resulted from the identification of cross-coupling coefficients *YX*. The calculation of *YY* coefficients also produced significant errors. Other coefficients were determined with accuracy of 3 %.

Most often it is not possible to make direct measurements of the bearings in the course of experimental research. Therefore, the calculations of bearing dynamic coefficients were performed on the basis of the signal measured at a distance of 30 mm from the middle of the bearing. It turns out that the appropriate transformation of the signals ensures the possibility to get correct values of dynamic coefficients. Ignoring this shift entails an error of measurement amounting to around 2 %.

In the course of experimental research activities consisting of excitation the rotating shaft twice with an impact hammer, the impact of changes in shaft material stiffness on calculation results was also investigated. All previous calculations were carried out assuming that the shaft is an object made of steel. The analysis was then conducted in which the value of Young's modulus was 100 times higher than that of conventional steel. After this test, the calculation results of bearing dynamic

coefficients have not changed. This means that the longitudinal modulus of elasticity of the shaft material does not affect the calculated stiffness and damping coefficients.

In order to verify the calculation results concerning asymmetrical rotor the base numerical model of the rotor has been modified. One free end of the shaft was shorter than the other one by 60 mm. This situation occurs when, for example, the installation of a coupling on one side of the shaft is necessary. The determination of the bearing dynamic coefficients obtained by simulation studies for such asymmetrical rotor can be considered satisfactory. The relative error values were very close to those from the reference model.

The examination of the results has led to the conclusion that some parameters do not affect the calculation results whereas the subsequent correction of the parameters which may have impact on the results is difficult. The article shows that certain parameters such as shifting of excitation force or different placement of measurement sensors result in measuring errors. However, it was demonstrated that their negative impact on the calculation results can be reduced by some minor corrections/improvements. The hints given in this article can be useful in experimental determination of bearing dynamic coefficients, and their detailed description gives some indication of the possibilities and limitations of the method itself.

Acknowledgments The paper is financed by Polish National Science Centre as a research project number 2015/17/N/ST8/01825. I would like to thank the employees of the Department of Turbine Dynamics and Diagnostics for their valuable comments and suggestions. I would like also to thank Mr Bart Peeters for the valuable support and the possibility of using Samcef Rotors program.

References

1. Breńkacz, Ł.: Identification of stiffness, damping and mass coefficients of rotor-bearing system using impulse response method. J. VibroEng. **17**(5), 1392–8716 (2015)
2. Qiu, Z.L., Tieu, A.K.: Identification of sixteen force coefficients of two journal bearings from impulse responses. Wear **212**, 206–212 (1997)
3. Tiwari, R., Lees, A.W., Friswell, M.I.: Identification of dynamic bearing parameters: a review. Shock Vibr. Digest. **36**, 99–124 (2004)
4. Dimond, T.W., Sheth, P.N., Allaire, P.E., He, M.: Identification methods and test results for tilting pad and fixed geometry journal bearing dynamic coefficients—a review. Shock Vibr. **16**, 13–43 (2009)
5. Kiciński J, Żywica G: Steam Microturbines in Distributed Cogeneration. Springer monograph (2014)
6. Kiciński, J.: Dynamika wirników i łożysk ślizgowych (English translation: the dynamics of rotors and slide bearings. IMP PAN, Maszyny Przepływowe, Gdańsk (2005)
7. Hamrock, B.J., Schmid, S.R., Jacobson, B.O.: Fundamentals of Fluid Film Lubrication Second Edition. (2004)
8. Fertis, D.G.: Nonlinear Structural Engineering: With Unique Theories and Methods to Solve Effectively Complex Nonlinear Problems. Springer, Berlin (2010)
9. Tiwari, R., Chakravarthy, V.: Simultaneous estimation of the residual unbalance and bearing dynamic parameters from the experimental data in a rotor-bearing system. Mech. Mach. Theory **44**, 792–812 (2009)

10. Miller, B.A., Howard, S.A.: Identifying bearing rotor-dynamic coefficients using an extended kalman filter. Tribol. Trans. **52**, 671–679 (2009)
11. Zapomel, J., Ferfecki, P., Kozánek, J.: Application of the Monte Carlo method for investigation of dynamical parameters of rotors supported by magnetorheological squeeze film damping devices. Appl. Comput. Mech. **8**, 129–138 (2014)
12. Jáuregui, J.C., Andrés, L.S., Santiago De, O.: Identification of bearing stiffness and damping coefficients using phase-plane diagrams. In: ASME Turbo Expo 2012: Turbine Technical Conference and Exposition, vol 7, pp. 731–737 (2012)
13. Kozanecki, Z., Kiciński, J., Żywica, G.: Numerical Model of the High Speed Rotors Supported on Variable Geometry Bearings. In: IUTAM Bookseries, pp. 217–227 (2011)
14. Wang, Y.P., Kim, D.: Experimental identification of force coefficients of large hybrid air foil bearings. In: ASME Turbo Expo 2013: Turbine Technical Conference and Exposition, volume 7B (2013)
15. Delgado, A.: Experimental identification of dynamic force coefficients for a 110 MM compliantly damped hybrid gas bearing. J. Eng. Gas Turbines Power. **137** (2015)
16. Kozánek, J., Simek, J., Steinbauer, P., Bílkovskỳ, A.: Identification of stiffness and damping coefficients of aerostatic journal bearing. Eng. Mech. **16**, 209–220 (2009)
17. Kozánek, J., Půst, L.: Spectral properties and identification of aerostatic bearings. Acta. Mech. Sin. **27**, 63–67 (2011)
18. Arora, V., Van Der Hoogt, P.J.M., Aarts, R.G.K.M., De Boer, A.: Identification of stiffness and damping characteristics of axial air-foil bearings. Int. J. Mech. Mater. Des. **7**, 231–243 (2011)

Investigations of Composite Panels Mounted in the Cargo Space of a Freight Wagon

Andrzej Buchacz, Andrzej Baier, Krzysztof Herbuś, Michał Majzner and Piotr Ociepka

Abstract The paper presents a series of experimental and numerical studies, carried out under the project number PBS2/A6/17/2013 realized as a part of the Applied Research Program, funded by the National Research and Development Centre. The aim of this project is to develop technology, manufacture, and assembly of composite panels on the side of a freight wagon in order to prolong the this operation. The article describes research which aimed to strength analysis of the side of the freight wagon and analysis of the behavior of structural connections of composite panels mounted on the side of the wagon. These studies were carried out on the test bench developed by the authors. During the research stresses and displacements has been analyzed at selected structural elements of the wagon before and after the modifications. The research also included an analysis of the behavior of the connections composite panels with steel components by static extortion on the side of the wagon. In parallel with the ongoing laboratory research steps have been taken to set up a FEM model by means of which was carried out similar numerical studies. Comparison of the results made it possible to adjust (tune) FEM model.

1 Introduction

The aim of the study was to determine the state of stress which occurs in components of the side of a freight wagon before modification and after applying composite panels [1–5]. Composite panels are mounted during the repair process of the wagon in order to strengthen corroded steel elements, which should significantly prolong its further exploitation. Research was carried out with respect to the freight car 418 V, of which CAD model is shown in Fig. 1.

A. Buchacz (✉) · A. Baier · K. Herbuś · M. Majzner · P. Ociepka
Faculty of Mechanical Engineering, Institute of Engineering Processes Automation and Integrated Manufacturing Systems Silesian University of Technology, Gliwice, Poland
e-mail: andrzej.buchacz@polsl.pl

J. Awrejcewicz (ed.), *Dynamical Systems: Modelling*, Springer Proceedings in Mathematics & Statistics 181, DOI 10.1007/978-3-319-42402-6_9

Fig. 1 CAD model of a freight wagon

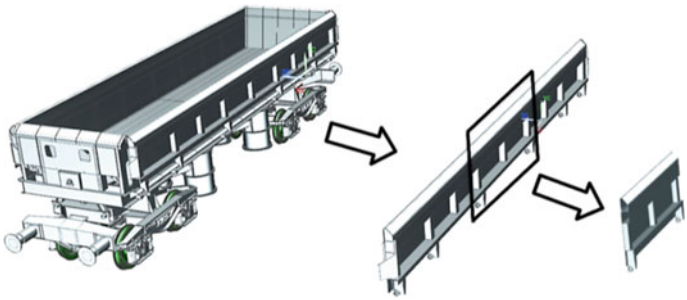

Fig. 2 Selected portion of the side of the analyzed wagon

Due to the large dimensions of the analyzed object, to perform the studies the central part of the side was selected (Fig. 2). In this part of the side appears the largest displacement values during operation of the wagon, why on this fragment of the side was expected to be the most unfavorable phenomena in places composite panels are joined.

In addition, a selected portion of the side was made on a scale of 1:2 which allowed to significantly reduce the size of constructed test bench (1400/800 mm).

2 Test Bench Description

For the purpose of the study was designed and manufactured a research position in which the essential elements are shown in Fig. 3. The position consists of a support frame (1), to which is affixed a portion of the side (2). In the lower part of the frame was fixed a hydraulic cylinder (3) which acts by force on the analyzed fragment of the side. To the piston rod is screwed a removable a press element (5), which presses against the sheathing of the side. The modular pressing element makes it possible to obtain different types of loads (point, surface). The control system

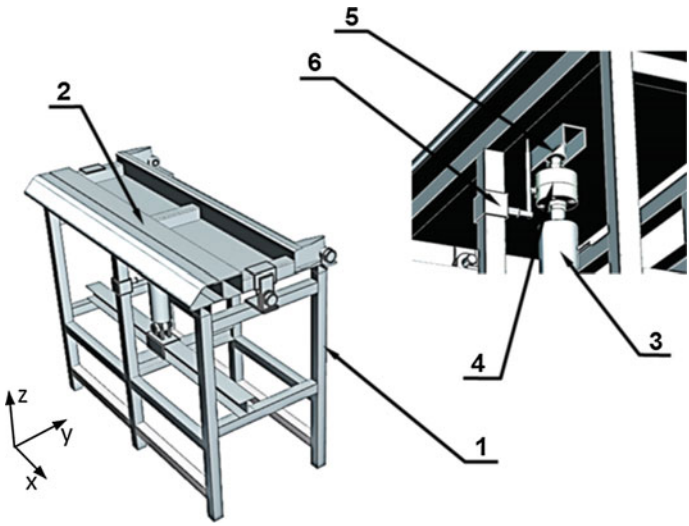

Fig. 3 CAD model of the test bench

allows to smooth force adjustment force in the range 0–30 kN. In addition, the actuator can smoothly move in X-Y plane allowing generation of the load in different areas of sideboard. It is possible to expanding the position and using more actuators (up to four cylinders), which allows to generate multipoint load.

3 Measurement Path and Data Acquisition

The developed test stand is equipped with a sensor system that is necessary to carry out the planned course of study. It was assumed that the state of stresses and displacements will be analyzed on board before and after installation of composite panels. Strain resistance (120 Ω) has been used for strain measurement, mounted with an adhesive at selected measurement points (see Fig. 4a). Applied force sensor (HBM U2B) for measuring the strength force (4), which is mounted on the piston rod of the hydraulic cylinder. Displacement measuring side displacement transducer (6) was used (WA-T HBM) with which the displacement of side portion was measured, under a given force (see Fig. 4b).

For data acquisition and visualization, a measuring system as shown in Fig. 5 was established. The signals from resistance strain gauges were sent through a multi-channel amplifier CANHED to a computer, where the application Catman is installed. This application is used for visualization and data acquisition. The obtained data packets were stored in a format compatible with the software MS Excel. Data processing and visualization of graphs were performed in relation to the analyzed values. Similarly measurements and analysis were performed for force and displacement.

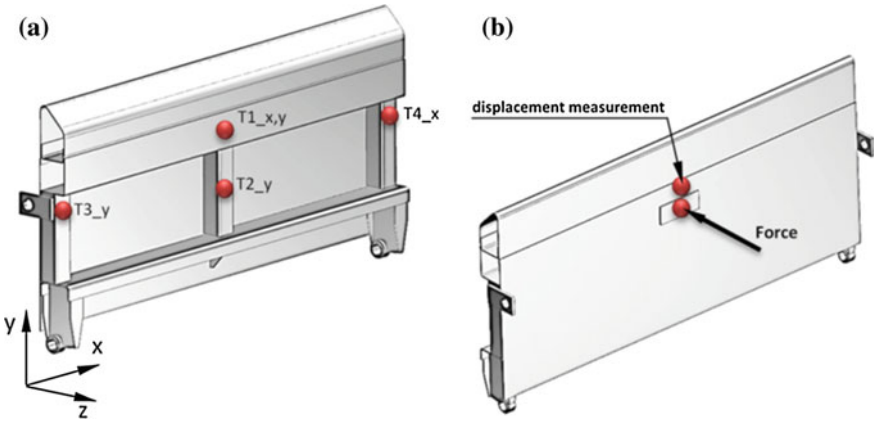

Fig. 4 Measuring points on the analyzed portion of the side

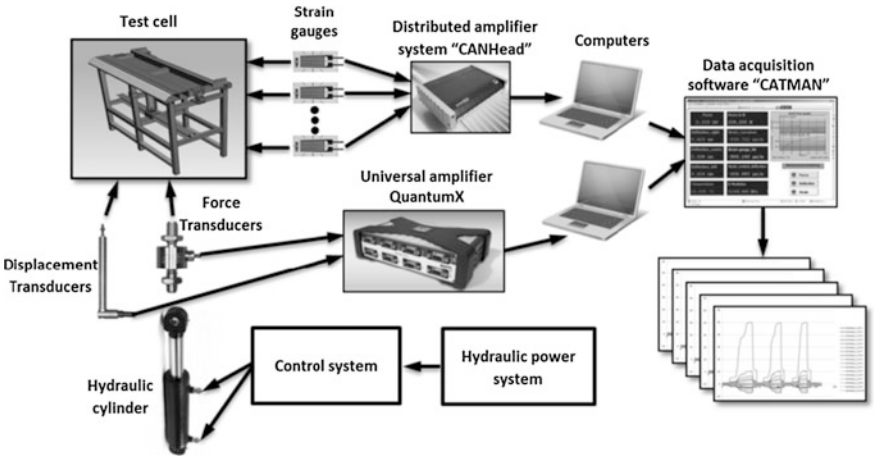

Fig. 5 Methodology of measurements

Signals from the transducer displacement and force transducer were sent through a multi-channel amplifier QuantumX to a computer and using the application Catman the received data packets were stored.

4 The Experimental Results

Analysis of data obtained allowed to determine and compare the value of strain (stress indirectly) that occur when attempting static load on a part of the side of freight wagon to load a static portion of the test side. A plan for research that

involves the following course. The research included analysis of 3 types of connections of the composite panels; front-attached, front-attached with the dilatation and a lap joint. Each test was repeated 3 times. The study was carried out for three different values of pressing force. In addition, also was made measurements of the extortion as a force values and the maximum displacement. For the tests with composite panels measurement was performed of the value of the gap that is formed between sheets under a given load. The phenomenon of enlarging the gap causes the penetration of small parts or water between panels and trim steel wagon, which can have undesirable effects on the operation of the wagon. Figures 6 and 7 shows an example of the results obtained when attempting to load a force of 15 kN.

Table 1 shows the average stress values which were recorded during the tests performed on the bench in relation to the fragment of the side. Comparison of the value of the stresses in T1_x reference point for all variants were performed:

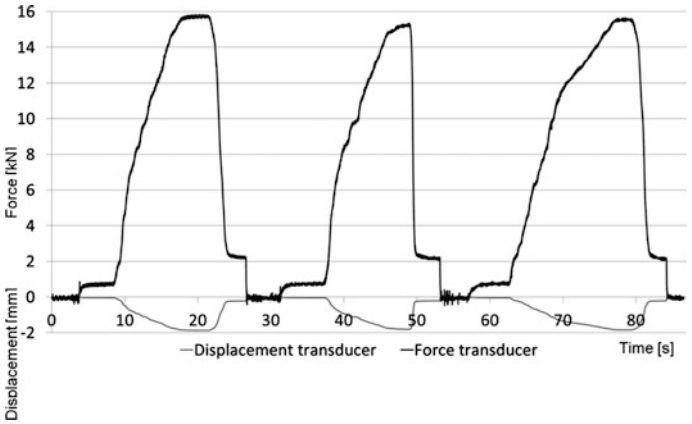

Fig. 6 Graph showing the value of the measured force and displacement during attempts at a load force 15kN

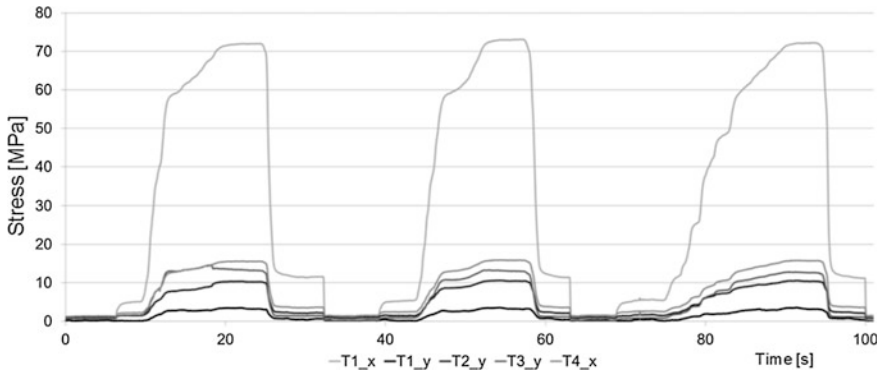

Fig. 7 Graph showing the stress at the load 15 kN

Table 1 Summary of average stress values recorded at the T1_x measurement point

F (kN)	σ (MPa)			
	Without panels	With panels		
		J_1	J_2	J_3
5	24.7	21.3	22.6	21.1
10	50.1	39.8	40.6	41.1
15	71.8	58.2	60.6	60.7

J_-1–lap joint, J_2–front-attached, J_3–front-attached with dilatation

without composite panels, with composite panels (three variants of contact). Tests with mounted panels were carried out for: lap joint (J_1), front-attached (J_2), and front-attached with dilatation (J_3) 3 mm wide.

The installation of composite panels reduced the stress of steel sheathing of the wagon by approx. 15–20 %. However, using different types of connections panel does not cause a significant change in the value of stresses in steel sheathing of the side. In the case of use of a combination front-attached without dilatation increases stress present in the composite plates. This is due to the interaction of the combined panels. The use of dilatation reduces stress.

5 Numerical Research

Simultaneously with laboratory tests similar numerical studies were carried out [6]. Strength analysis and the behavior of the composite panel connections analyses were made using PLM Siemens NX 10 software. 3D model of position was created for this purpose. The 3D model allows you to perform similar to research on the bench using FEM numerical analyses. The process of creating the FEM model was as follows:

- Create a 3D model of the selected portion of side.
- Discretization of the model. Creating a finite element mesh type of CTETRA (10) for steel parts and CHEXA (8) for composite components.
- Assignment of material properties in relation to steel elements.
- Assignment of material properties in relation to composite panels [7]. Determination of the composite material of the panel (glass woven fabric, plain weave, with the epoxy resin) as the composition of four layers (no angular offset between the individual layers).
- Defining the boundary conditions similar to those of occurring on the bench.
- Perform numerical analysis using NX Nastran solver.
- Analysis and visualization of results.

There have been several iterations of analyses to fine tune (adjust) the FEM model. Every time the process of comparing was carried out and the results were

obtained and made modifications to the model. Converging results were achieved by changing the size of the applied finite elements. Also size of the gap was recorded that is generated by the confluence composite panels lap jointed. In the case of stand tests, the gap was measured with a feeler gauge. In actual combination of composite panels gap formed at the stage of installation and thus were analyzed the relative increase in the gap. In the case of numerical analysis, relative movement between the engaging plates were analyzed. Figure 8 shows the position in which the gap is formed, and Fig. 9 shows a graph from which to read the size of formed gap. The results of numerical analysis are consistent for measuring on a bench and the maximum difference does not exceed 10 %.

Table 2 shows a comparison of results of measurements on the bench compared with the results obtained by FEM. The presented results refer to the test without

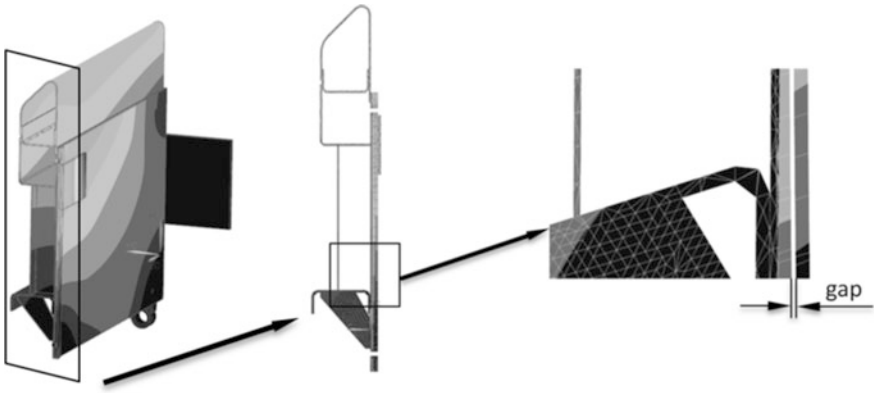

Fig. 8 Visualization of the gap observed in numerical analysis

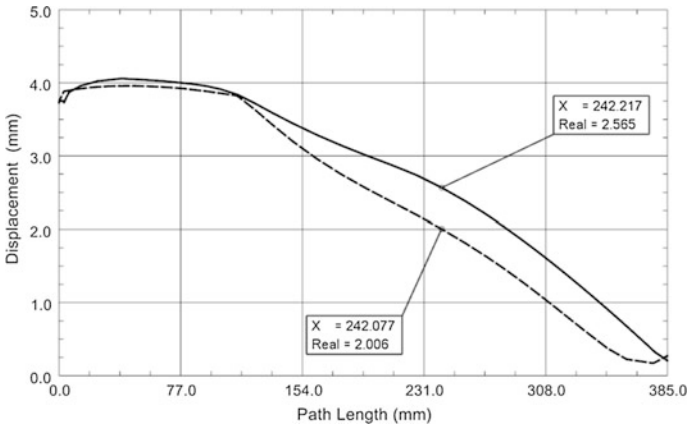

Fig. 9 The relative displacement between the composite

Table 2 Comparison of the results of measurements on the bench with the results obtained by FEM (for the test with a force of 15 kN extortion at the measurement point T1_x)

Measured parameter	Test bench measurements		Numerical analyze FEM	
	Without panels	With panels	Without panels	With panels
Stress (MPa)	71.8	58.2	81.6	64.1
Displacement (mm)	2.05	1.55	2.18	1.71
Gap (mm)	–	0.65	–	0.55

panels installed and attempts with panels connected by the use of lap joint. The results of numerical analysis were obtained by fine tuning the model FEM. In the first iteration of computing the deviation of the compared result was 40 %. After tuning the model difference decreased to 10 %.

6 Summary

The conducted strength analysis has identified changes in stress caused by the use of composite panels. Mounting the panels reduces stress values by 15–20 %. Linkage analysis of composite panels confirmed the phenomenon of (increasing) gap between the connected composite panels. The obtained results will be the basis for attempts to minimize the negative effects of a gap by applying: higher number of fasteners (rivet nuts) or special sealing materials. The results of numerical analysis are consistent to the results obtained during the experimental measurements, which confirms the validity of numerical analysis. Matching FEM model can be used to perform stress analysis for the entire full-size model of the wagon.

Acknowledgments The work was carried out under the project number PBS2/A6/17/2013 realized as a part of the Applied Research Program, funded by the National Research and Development Centre.

References

1. Baier, A., Majzner, M.: Analysis of composite structural elements. J. Achiev. Mater. Manuf. Eng. 43/2, 577–584 (2010)
2. Buchacz, A., Baier, A., Świder, J., Jamroziak, K., Majzner, M., Żółkiewski, S., Wróbel, A.: Experimental Tests of Chosen Fibre-metal Laminates, Monograph 374. Silesian University of Technology Press, Gliwice (2012). ISBN 978-83-7335-936-9
3. Buchacz, A., Baier, A., Herbuś, K., Majzner, M., Ociepka, P.: Application of programs of the CAD/CAE class for creating the virtual laboratory stand. Appl. Mech. Mater. **809–810**, 841–846 (2015)
4. Płaczek, M., Buchacz, A., Wróbel, A.: Use of piezoelectric foils as tools for structural health monitoring of freight cars during exploitation. Eksploatacja i Niezawodność—Maintenance Reliab **17**(3), 443–449 (2015)

5. Wróbel, A., Płaczek, M., Buchacz, A., Majzner, M.: Study of mechanical properties and computer simulation of composite materials reinforced by metal. Int. J. Mater. Product Technol. **50**(3/4), 259–275 (2015)
6. Banaś, W., Herbuś, K., Kost, G., Nierychlok, A., Ociepka, P., Reclik, D.: Simulation of the Stewart platform carried out using the Siemens NX and NI LabVIEW programs. Adv. Mater. Res. **837**, 537–542 (2014)
7. Buchacz, A., Baier, A., Herbuś, K., Majzner, M., Ociepka, P.: Examination of a cargo space of a freight wagon modified with composite panels. Appl. Mech. Mater. **809–810**, 944–949 (2015)

Project of Laboratory Stand, and Preliminary Studies of Vibration Shell Freight Wagon

Andrzej Buchacz, Andrzej Wróbel and Marek Płaczek

Abstract The article presents the basic principles of construction of laboratory stand for vibration testing of a freight wagon. The measuring system consists of a drive unit with a freight wagon made in scale, the control unit with inverter and programmable PLC. Identification of vibration using the piezoelectric sensor was presented. By means of the PLC program it was allowed to set any ramp-up time, driving time of fixed speed, the braking time and achieved high repeatability crossings. The control panel is designed in such a way to be able to perform long-term studies by determining the number of crossings between gates or test time.

1 Introduction

Modern rail transport has a particularly important meaning in the transport of bulk cargoes for long distances. However, it loses its importance in the carriage of cargo on short routes, it is because of long time unloading and loading. Current researches associated to railway transport [17, 19] are related to: improve security, extend the time between renovation of wagons, the use of new materials as assemblies of the wagon [5, 9–13, 15, 16, 20]. The main aim of the presented work was to design laboratory stand to verify if it will be possible to infer about state of the structure based on the measured dynamic response. The project is carried out by the consortium composed of: Institute of Engineering Processes Automation and Integrated

A. Buchacz (✉) · A. Wróbel · M. Płaczek
Mechanical Engineering Faculty, Department of Engineering Processes Automation and Integrated Manufacturing Systems, Silesian University of Technology, Konarskiego 18A, 44-100 Gliwice, Poland
e-mail: andrzej.buchacz@polsl.pl

A. Wróbel
e-mail: andrzej.wrobel@polsl.pl

M. Płaczek
e-mail: marek.placzek@polsl.pl

J. Awrejcewicz (ed.), *Dynamical Systems: Modelling*, Springer Proceedings in Mathematics & Statistics 181, DOI 10.1007/978-3-319-42402-6_10

Fig. 1 Real view of object under consideration

Manufacturing Systems from the Silesian University of Technology, and DB Schenker and Germaz companies [8]. The aim of this research project is to modernize the analysed wagon during its renovation using new materials [1, 2, 18] (Fig. 1).

The main idea of the paper was to present possibilities of test stand and conduct the first tests confirming correctness of the lab stand and model. Complete cycle of researches is presented in the next article of authors titled "Analysis of dynamical response of the freight wagon". The main objective of the work is to modernize the wagon during its renovation using new innovative composites in order to protect sheathing of the wagon against corrosion. This work is a continuation of the previous research works concerned with analysis of new, composite materials application if freight wagons [1, 3, 4].

2 Laboratory Stand

In this chapter, the laboratory stand for study the possibility of changing the shell of a freight wagon was presented. Modern cars are manufactured from standard materials such as steel plates and profiles. During meetings with representatives of the leading transport companies the following issues concerning the application of the existing structure were reported. The material being carried in the winter term freezes to the surface plates, and makes it impossible to rapid unloading. In order to unload the wagon it is necessary to warm up the walls or use mechanical tools for separation of the material. However, the biggest problem is the corrosion of metal parts. This concerns mainly plating the walls and floor of the wagon. As part of its work use of innovative composite materials as components or assemblies freight wagon in order to eliminate the presented problems is described. In order to confirm or deny the possibility of using these materials a model car and a drive unit were created. The wagon was designed to allow easily changing the shell. To change travel parameters as acceleration, delay, variable speed travel, the electrical control

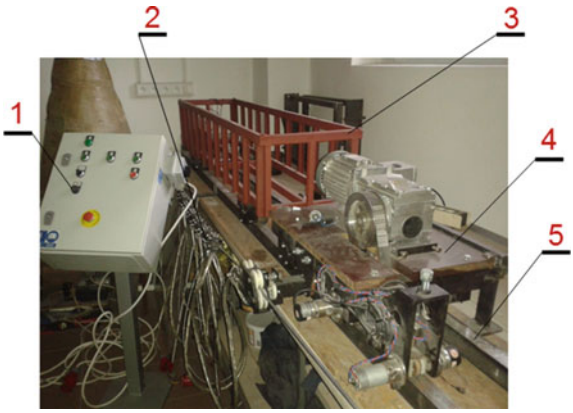

Fig. 2 View of laboratory stand

box with inverter were established. In Fig. 2 model for the analysis of observed driving was shown.

where: 1—control box; 2—slides for power supply, 3—skeleton of a freight wagon, 4—drive unit, 5—tracks.

The control unit contains residual current devices and overcurrent protection necessary for safe operation of the station. In order to determine the running speed, acceleration and deceleration times and the number of cycle travel LG inverter was used. The view of control box is shown in Fig. 3.

The applied inverter has the possibility of programming using the Drive View programmer.

In Fig. 4a the mapping of areas recording parameters from the controller "PLC" was presented, in Fig. 4b, c addresses and records of the frequency inverter are shown. One of the assumptions of our work was to allow the setting of cyclic runs, including the use of two limit switches at both ends of the tracks [14]. Program written to PLC controller was presented on Fig. 5.

LG inverter has both properties as gives a standard inverter which enables you to adjust the speed by varying the frequency, but also has an integrated module PLC.

Fig. 3 View of control box

(a)

Code	Parameter Name	Value	Default	Unit
60	PLC Wr Data 1	0x380	0x0000	Hex
61	PLC Wr Data 2	0x0000	0x0000	Hex
62	PLC Wr Data 3	0x0000	0x0000	Hex
63	PLC Wr Data 4	0x0000	0x0000	Hex
64	PLC Wr Data 5	0x0000	0x0000	Hex

(b)

Address	Parameter	Scale	Unit	R/W	Detailed Description	
0x0380	frequency command	0.01	Hz	R/W	Command Frequency Setting	
0x0381	RPM command	1	RPM	R/W	Command RPM Setting	
0x0382	operating command	-	-	R/W	BIT3	Changed from 0 to 1: Free-run to stop
					BIT2	Changed from 0 to 1: Trip Reset
					BIT1	0: Reverse Command 1: Forward Command
					BIT0	0: STOP Command 1: RUN Command
					Ex) Forward run command:0003h, Reverse run command:0001h	

(c)

▶ Special D registers of PLC for inverter control corresponding to APO60 ~ 67

Register	Use of the Register	Remark
D4454	Data to inputted in the common area parameter address set up by AP060 (PLC Wr Data 1).	PLC option →Inverter (Control)
D4455	Data to inputted in the common area parameter address set up by AP061 (PLC Wr Data 2).	PLC option →Inverter (Control)
D4456	Data to inputted in the common area parameter address set up by AP062 (PLC Wr Data 3).	PLC option → Inverter (Control)
D4457	Data to inputted in the common area parameter address set up by AP063 (PLC Wr Data 4).	PLC option → Inverter (Control)
D4458	Data to inputted in the common area parameter address set up by AP064 (PLC Wr Data 5).	PLC option → Inverter (Control)
D4459	Data to inputted in the common area parameter address set up by AP065 (PLC Wr Data 6).	PLC option → Inverter (Control)
D4460	Data to inputted in the common area parameter address set up by AP066 (PLC Wr Data 7).	PLC option → Inverter (Control)
D4461	Data to inputted in the common area parameter address set up by AP067 (PLC Wr Data 8).	PLC option → Inverter (Control)

Fig. 4 Windows of DriveView programmer

This module has inputs and digital outputs for easy control of the object. In Fig. 6 the program for implementing the following algorithm is presented: the start button runs driving the car in the right direction until it reaches to the end position (signal from the limit switch is located at the end of the track), car starts braking and change the direction to the opposite. Braking and acceleration are performed with set times in the manner as shown in Fig. 6. At any time you can stop the drive by pressing the stop button or unplug the power by pressing the emergency stop.

Because of the great possibilities of the LG inverter, electrical connections in the control box can be kept to a minimum. In Fig. 7 wiring diagram to connect the inverter LG was presented.

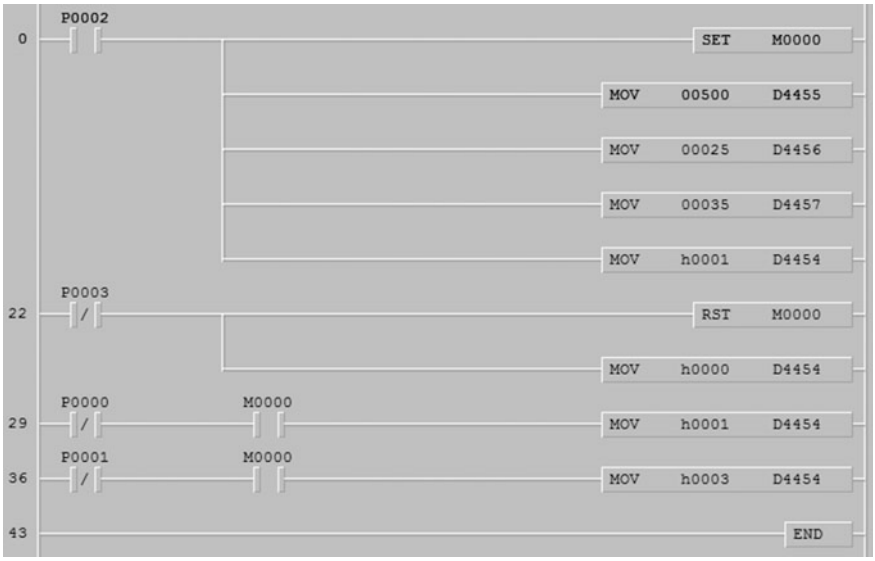

Fig. 5 Program for control drive unit

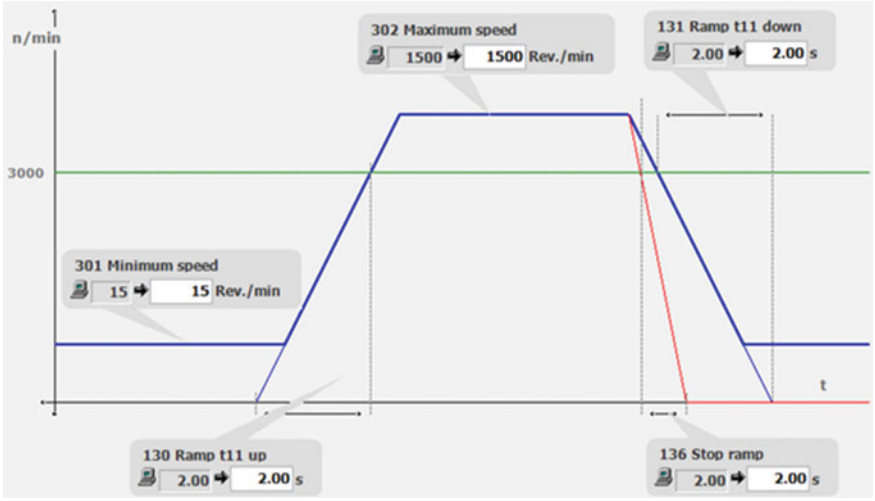

Fig. 6 Simulation of acceleration and deceleration in the SEW MotionStudio

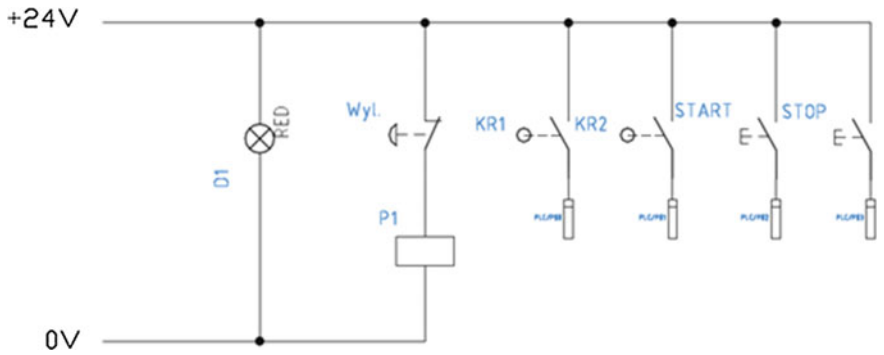

Fig. 7 View of control box

3 Measuring Tests

Laboratory stand will allow for a series of studies related to the change of assemblies and subassemblies of modernized wagons. In the first step it was assumed that drive with piezoelectric sensors in order to explore the possibility of identifying changes in the structure of the wagon [6, 7] will be tested. So comparing the test signals from piezoelectric sensors which are glued according to the points indicated in Fig. 9. In the next step the authors will change construction, e.g., by adding the extra weight to the upper frame. If registration and identification of changes in signals from the sensors (Fig. 8) are possible, as part of future work composite panels with varying numbers of layers produces with different materials in order to compare the standard wagon and the modernized wagon vibration will be installed.

For the measurement of vibration of the constructed piezoelectric sensor, amplifier HBM MGC plus connected with a data acquisition board and software CatmanEasy were used. The sensor was fixed to the model by wax [21–25].

Fig. 8 Piezoelectric sensor and HBM measurement amplifier

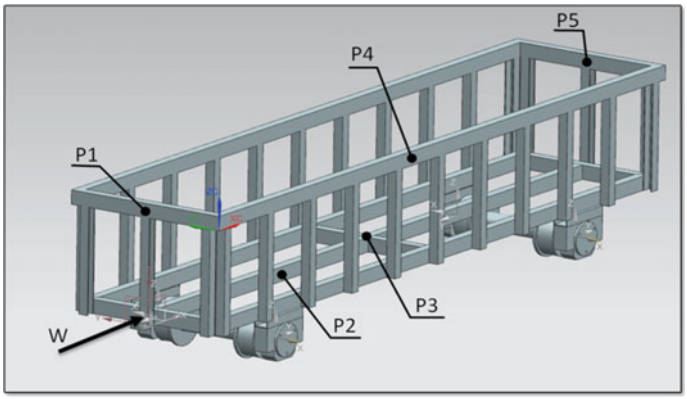

Fig. 9 CAD model of the laboratory stand with measuring points

Table 1 Results of the measurements using accelerometers

Measuring point	Without load		With load	
	A_{max} (m/s^2)	t_{damp} (s)	A_{max} (m/s^2)	t_{damp} (s)
P3	22	0.35	7	0.15

4 Results of Tests

As part of the first tests of the selected measuring point marked in Fig. 9 as number 3 was choose. At the trackway metal components as vibration excitation car were welded.

In the Table 1 a comparison of the obtained during trips results were shown.

Noteworthy that the differences between the results obtained for journeys with load and without load are the clearly visible. It can be observed that values of the maximum acceleration of the excited system for the measuring point P3 are about 22 m/s^2 without load and 7 m/s^2 with load. Time of vibrations damping is 0.35 s for the point P3 without load and 0.15 s with load.

The presented results are archived and processed in the program HBM Catman. The results are a confirmation of the thesis adopted by the authors, it is possible to observe structural changes in the cars at the designed position.

5 Conclusions

The main aim of the presented article is to show the laboratory stand for vibration structure monitoring of the wagon. In the paper only preliminary results which confirm the possibility of further researches are presented. Measurements of

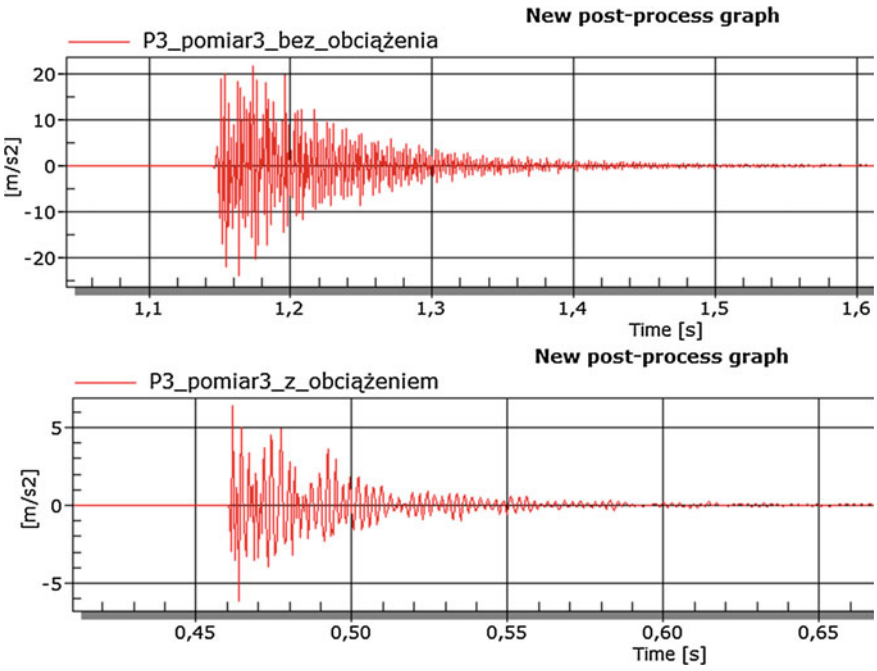

Fig. 10 Results of the measurements conducted using accelerometer for the point number 3 without load—the upper figure, and with the load—lower figure

vibration construction of a freight wagon done by both accelerometer and piezo films will be done in the next articles of authors. Difference in the amplitude of the vibrations recorded for empty and loaded wagon were noticed on Fig. 10. Also, the time of suppress the vibration clearly indicates differences.

This work is a part of the research project which aims to modernize freight wagons using new composite materials during their renovation. It was proved that it is easy to observe changes in the dynamic response of the system using the proposed measuring apparatus when parameters of the system are changed.

Acknowledgments The work was carried out under the project number PBS2/A6/17/2013 agreement implemented under the Applied Research Program, funded by the National Centre for Research and Development.

References

1. Baier, A., Zolkiewski, S.: Initial research of epoxy and polyester warp laminates testing on abrasive wear used in car sheathing. Eksploatacja i Niezawodnosc—Maint. Reliab. **15/1**, 37–43 (2013)

2. Baier, A. et al.: Experimental Synthesis and Analysis of Geometric and Structural Properties of Chosen Elements of Railway Wagons. Silesian University of Technology Publishing House, Gliwice (2012)
3. Białas, K.: Mechanical and electrical elements in reduction of vibrations. J. VibroEng. **14**(1), 123–128 (2012)
4. Białas, K: Passive and active elements in reduction of vibrations of torsional systems, mechatronic systems and materials: mechatronic systems and robotics. Solid State Phenom. **164**, 260–264 (2010)
5. Bruni, S., Vinolas, J., Berg, M., Polach, O., Stichel, S.: Modelling of suspension components in a rail vehicle dynamics context. Veh. Syst. Dyn. **49**(7), 1021–1072 (2011)
6. Buchacz, A., Płaczek, M., Wróbel, A.: Modelling and analysis of systems with cylindrical piezoelectric transducers. Mechanika **20**(1), 87–91 (2014). ISSN 1392-1207
7. Buchacz, A., Płaczek, M., Wróbel, A.: Modelling of passive vibration damping using piezoelectric transducers—the mathematical model. Eksploatacja i Niezawodnosc—Maint. Reliab. **16/2**, 301–306 (2014)
8. Dymarek, A., Dzitkowski, T.: Method of active synthesis of discrete fixed mechanical systems. J. VibroEng. **14**(2), 458–463 (2012)
9. Iacob-Mare, C., Manescu, T.S.: Experimental analysis of strains occurring during the gondola freight wagons' exploitation. Metalurgia **65/7**, 19 (2013)
10. Iacob-Mare, C., Manescu, T.S.: Study of the freight wagon body through the method of finite elements. Metalurgia **65/7**, 13 (2013)
11. Jönsson, P.A., Andersson, E., Stichel, S.: Experimental and theoretical analysis of freight wagon link suspension. Proc. Inst. Mech. Eng. Part F: J. Rail Rapid Transit. **220**(4), 361–372 (2006)
12. Jönsson, P.A., Stichel, S., Persson, I.: New simulation model for freight wagons with UIC link suspension. Veh. Syst. Dyn. **46**, 695–704 (2008)
13. Kovalev, R., Lysikov, N., Mikheev, G., Pogorelov, D., Simonov, V., Yazykov, V., Zakharov, S., Zharov, I., Goryacheva, I., Soshenkov, S., Torskaya, E.: Freight car models and their computer-aided dynamic analysis. Multibody Sys.Dyn. **22**(4), 399–423 (2009)
14. Kuś, W.: Sterowanie wektorowe silników AC. Rozwiązanie alternatywne do stosowania silników DC. „Elektronika Praktyczna" **9**, 51–56 (2000)
15. Okabe, Y., Nakayama, F.: Damage Detection in CFRP Laminates by Ultrasonic Wave Propagation Using MFC Actuator and FBG Sensor. Trans. Space Technol. Japan **7**(26), 7–12 (2009)
16. Rusiński, E., Koziołek, S., Jamroziak, K.: Quality assurance method for design and manufacturing process of armoured vehicles. Eksploatacja i Niezawodność—Maint. Reliab. **3**, 70–77 (2009)
17. Song, Z., Fang, S., Zhang, Y., Xie, J.: Cracking analysis of bolster cover plate in C70 freight wagons. Eng. Fail. Anal. **30**, 43–60 (2013)
18. Wróbel, A., Płaczek, M., Buchacz, A., Majzner, M.: Study of mechanical properties and computer simulation of composite materials reinforced by metal. Int. J. Mater. Product Technol. **50**(3/4), 259–275 (2015)
19. Zakharov, S., Goryacheva, I.: Rolling contact fatigue defects in freight car wheels. Int. J. Sci. Technol. Frict. Lubr. Wear **258**(7–8), 1142–1147 (2005)
20. Zhai, W.M.: Modelling and experiment of railway ballast vibrations. J. Sound Vib. **270**(4–5), 673–683 (2004)
21. http://machinedesign.com/sensors/sensorless-vector-control
22. http://www.hbm.com. Accessed 10 Aug 2015
23. http://www.aniro.pl/do-pobrania/do-pobrania/viewcategory/58-instrukcja-pl.html. Accessed 14 May 2015
24. http://www.aniro.pl/do-pobrania/do-pobrania/viewcategory/67-instrukcja-karta-plc.html. Accessed 14 May 2015
25. http://automatykaonline.pl/Artykuly/Sterowanie/falowniki-sterowanie-skalarne-wektorowe. Accessed 14 May 2015

Analysis of Dynamical Response of the Freight Wagon

Andrzej Buchacz, Marek Płaczek and Andrzej Wróbel

Abstract Paper presents results of works concerned with modernization of freight wagons during their periodic repairs. In this paper, the freight car type 1415 A3 designed for coal and aggregate transport is analyzed. The aim of the research project is to minimize problems occurring during its exploitation. The main idea is to use innovative materials and technologies to repair this type of wagons. The CAD model of analyzed freight wagon is presented. Also results of tests realized on the created laboratory model of the wagon are presented. Measurements of vibrations of the model were carried out using piezoelectric foils in order to verify if it is possible to infer about the state of the system taking into account its dynamical response that occurs as a result of excitation generated during its exploitation.

1 Introduction

Railway transport is very important for the development of the modern economy this is why many research works concerning with problems occurring in this way of transport and its development are being carried out all the time. The goal of those works is usually to develop the infrastructure that is used for transport of goods and people, make it more cost-effective, safe, and less burdensome for the environment [1, 17]. Very important are the problems of freight car dynamics during exploitation different driving conditions [5, 8, 18]. In all of those works, the problem of modeling of real object has a strong influence on obtained results and has to be solved using

A. Buchacz (✉) · M. Płaczek · A. Wróbel
Mechanical Engineering Faculty, Department of Engineering Processes Automation and Integrated Manufacturing Systems, Silesian University of Technology, Konarskiego 18A, 44-100 Gliwice, Poland
e-mail: andrzej.buchacz@polsl.pl

M. Płaczek
e-mail: andrzej.wrobel@polsl.pl

A. Wróbel
e-mail: marek.placzek@polsl.pl

J. Awrejcewicz (ed.), *Dynamical Systems: Modelling*, Springer Proceedings in Mathematics & Statistics 181, DOI 10.1007/978-3-319-42402-6_11

precise methods [5, 12, 16, 19]. This is why computer-aided methods including finite element method, are used very often [11, 14]. On the other hand, experimental analysis and tests are also very important in order to verify results of calculations and simulations and to carry out the process of used models validation [10, 12].

Presented paper is a part of research works concerning possibilities of freight wagon modernization using new composite materials [2, 3]. The aim is to modernize freight wagons during their renovation. The project is carried out by the consortium that consists of the scientific entity—the Institute of Engineering Processes Automation and Integrated Manufacturing Systems from the Silesian University of Technology and enterprises—DB Schenker and Germaz. The aim of this research project is to modernize the analyzed wagon during its renovation using new materials. Effects that are to be achieved by the modernization are

- better corrosion protection of the wagon elements,
- easier unloading of the wagon in winter conditions (no freezing of the cargo to the sides and floor of the wagon),
- reduction of the weight of the wagon while its load increases,
- easier management of freight cars during exploitation.

This work is a continuation of the previous research works concerned with analysis of new, composite materials application if freight wagons [2, 3]. The research team includes authors and also deals with the tasks of synthesis and analysis of vibrating systems, including piezoelectric transducers [4, 6, 7, 9].

In this paper, results of the dynamic response measurements of the freight wagon model supporting structure are being presented. Those works were mainly carried out in order to verify the possibility to create a mechatronic system that can be integrated with the modernized freight car and used for its management during exploitation. The system that is intended to be created should allow monitoring of the freight car dynamic parameters during its normal exploitation and inferred on its basis about the status of the wagon.

As the first step of the whole research project, CAD models of a few selected freight wagons were created using Siemens NX 8.5 software. Precision of the created models was verified by checking its mass after defining material properties of wagon components and juxtaposing it with the mass of the real wagon. After verification, the models were used in strength analysis using the finite element method in NX software.

In the next step, a physical laboratory model of the supporting structure of one of the analyzed freight wagons (signed 1415 A3) was built. It was also modeled using CAD system. In order to carry out the validation process of the CAD models, the dynamical parameters of the laboratory model were measured using accelerometers and PVDT piezoelectric films.

The measurements were carried out twice—for the wagon without and with load. Obtained results were juxtaposed and analyzed. The possibility of measuring the dynamic response of the supporting structure of the wagon using PVDF films was verified as well—obtained results were juxtaposed with results obtained using classical piezoelectric accelerometers.

The 4-axle open wagon series EAOS type 1415 A3 produced by BREC Belgium was being taken into consideration because it is one of the most popular type of wagons designed to unload with the use of tipplers. Main problems during exploitation of this type of wagons are

- corrosion of plating of the wagon's plating,
- mechanical damage of the wagon's plating—usually as a result of the improper unloading (using buckets and excavators instead of tipplers).

At the same time the type 1415 A3 wagon has a high strength of the supporting box (top girder, lateral reinforcing strip, etc.).

The main aim of the presented works was to verify if it will be possible to infer about state of the structure based on the measured dynamic response. This information will be used in the designed system for management of freight cars during exploitation.

2 Virtual and Laboratory Modes

In this work, the process of modeling of the analyzed freight wagon using Siemens NX 8.5 software is only mentioned. Details of this process and analysis of the created virtual model will be presented in other publications. The 3D model was created on the basis of very incomplete documentation and measurements of the real object. It is presented in Fig. 1.

Precision of the created model was verified by checking its mass after defining material properties of wagon components and juxtaposing it with the mass of the real wagon (data from the wagon's documentation).

The created 3D model is very detailed and obtained discrepancy is 5.34 % of the real wagon mass. The difference is the result that the model does not include the braking system (pipes and pneumatic cylinders, brake pads, etc.) After its

Fig. 1 The CAD model of the considered 4-axle open wagon series EAOS type 1415 A3

verification, the model was used in strength analysis using the finite element method in NX software. Obtained results—stress and displacements of elements were calculated. Results of the analysis will be presented in other publication.

In the next step, a physical laboratory model of the supporting structure of the considered 1415 A3 freight wagon was built in scale. The laboratory model is presented in Fig. 2. There are a lot of simplifications in the created model juxtaposed with the real object. The purpose is that the laboratory model was created only for initial verification of the possibility to measure the dynamical response of the wagon using piezoelectric films. In the future works, more detailed laboratory models of the wagon elements will be created and analyzed, also measurements on the real object will be carried out.

The laboratory stand was also modeled using NX 8.5 CAD system (see Fig. 4) in order to carry out the validation process of the CAD model. It is very important to check the accuracy of the created CAD models of such complicated structures in order to be sure that using those CAD models we can obtain results similar as on the real object. It is difficult to make some measurements and analysis on the real freight wagon, this is why as the first step the laboratory stand was created and its CAD model will be used. To be sure that obtained results of computer-aided analysis and simulations using CAx systems are as exact as possible, the CAD model should be subjected to the validation process.

In the first test, vibration of the laboratory model was excited by the pendulum of mass rotated through specified value of an angle. The pendulum arm length is 0.5 m. In order to separate the system from external influences it was created as the half determined system (see Fig. 2).

Fig. 2 The laboratory model of the freight wagon

3 Measuring Devices and Software

In the presented work three different tests were carried out. In the first test, measurements of the dynamical response were realized using piezoelectric accelerometer and pendulum was used to excite vibration. In the second test, the piezoelectric PVDF film was used as a sensor and pendulum was used for excitation. In the last one, the Macro Fiber Composite (MFC) piezoelectric transducer was used for vibration excitation and PVDF piezoelectric foil was used as sensor.

In the first step, the 352C68 model of the piezoelectric accelerometer produced by the PCB Piezotronics company was used. It is the high sensitivity, miniature, ceramic shear accelerometer. As a measuring amplifier the MGCplus with the AP18i measuring card produced by HBM Company was used together with Catman Easty software. MGCPlus is a modern, fully scalable, and customizable measuring amplifier with a modular architecture for use as a data acquisition system. Catman Easy software is a universal tool for measurement, analysis, and processing the results.

The sensor was attached to the structure of a freight wagon model using the adapter and wax. Then a special, low-loss shielded cable sensor is connected to the card of measuring amplifier. Measurements were repeated five times for all measuring points to verify repeatability of results.

Next, measurements were carried out using PVDF film. The PVDF film was glued on the frame of the laboratory model in the position of the second measuring point (P2 in Fig. 4).

Polyvinylidene fluoride is a thermoplastic polymer with a high degree of crystallization. PVDF has good mechanical, electrical, and thermal properties. PVDF piezoelectric film, and more particularly the sensor LDT, which was used in this study consists of three layers: polyester laminate, a piezoelectric film, and a protective coating. The PVDF piezoelectric film elements produce more than 10 mill volts per micro strain and about 60 dB higher than the voltage output of a foil strain gage. Their capacitance is proportional to the area and inversely proportional to the thickness of the element. Such kinds of sensors are the simplest form of piezoelectric film sensors that can be used for example as dynamic strain gages and contact microphones for vibration or impact detection. They can be readily adhered to a surface with double-sided tape or epoxy. In carried out tests a model LDT1-028 K was used. It is multifunctional piezoelectric film designed to detect vibration or impact. The film is laminated by a layer of polyester. The minimum impedance of the sensor is 1 MΩ. The output voltage is between 10 mV and 100 V, depending on the strain and circuit impedance.

In the presented study, a PVDF film was used as a vibration sensor glued to the superstructure of the freight wagon model. The sensor was glued to the beam frame of the wagon model, as shown in Fig. 3a. Sensor cables were connected to the analog input of a real-time computer Compact RIO. In presented works, Compact RIO was connected to a PC via Ethernet for communication that takes place

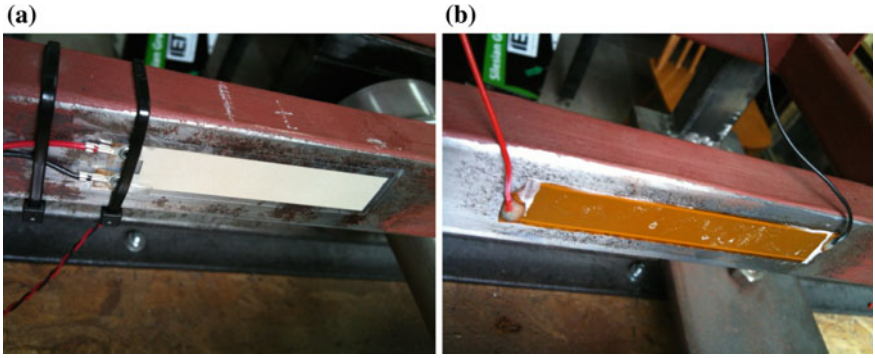

Fig. 3 PVDF (**a**) and MFC (**b**) piezoelectric films glued on the surface of the laboratory model

during measurement. Measurement card NI9234 with 4 analog inputs ±5 V (AC/DC) and 24-bit measurement resolution was used. Software for data acquisition LabVIEW was used. It is very large measurement environment and has a great potential for signal analysis.

In the last test the MFC piezoelectric transducer was used as vibration actuator. The MFC transducer bonded to the surface of the model is presented in Fig. 3b. In this test the PVDF piezoelectric foil was also used as the sensor connected to the real-time computer.

Applications growth of piezoelectric transducers is parallel to the process of piezoelectric materials development. New, more efficient transducers are searched all the time. Very important step in this process was done in 1996 by NASA when a Macro Fiber Composite (MFC) was invented [21]. MFC transducer consists of rectangular piezo ceramic rods sandwiched between layers of adhesive, electrodes, and polyimide film. Main benefits of the MFC given by the manufacturer are: increased strain actuator efficiency, damage tolerance, environmentally sealed packages, available as elongators and contractors.

In order to excite vibration of the model, the MFC transducer was supplied by a signal generated by a laboratory waveform generator Tabor WW5064. This signal was amplified using an amplifier Smart Material HVA1500/50. Tabor WW5064 is a fully digital generator of sine waves, square waves, and many others. It was connected to the special high-voltage power supply, used to supply a piezoelectric MFC foils used as actuators in various applications. The power supply can generate a voltage of +1500 to −500 V, depending on the level of the signal that is sent to its input from the laboratory generator.

All measurements were carried out twice: for the laboratory model of the wagon with and without load in order to verify whether it is possible to observe changes in the dynamic response of the system using the proposed measuring apparatus when parameters of the system are changed. The load of the wagon weights made of steel was used. Results of both tests were presented on charts and analyzed.

4 Results

As the first step of the measurements, the piezoelectric accelerometers were used to measure the dynamic response of the laboratory model. Measuring points were selected and are presented in Fig. 4. The system was excided using the pendulum rotated through an angle 12°. Different measuring points were tested in order to examine the intensity of the dynamical response of the model. The measuring points and the point of the excitation of the system by the pendulum are marked in the figure. After the five measurements for each measuring point carried out for the loaded and unloaded model, it was found that the results of the measurements are repeatable.

Selected results of the first test realized using the 352C68 PCB accelerometer are presented in Figs. 5 and 6 for two selected (P1 and P2) measuring points separately for the system with and without load.

It is easy to see that changes in the dynamic response of the system with and without load can be easily observed. It can be observed that values of the maximum acceleration of the excited system for the measuring point P1 are about 42 m/s^2 without load as well as with it. For the second measuring point P2 values are 15 and 8 m/s^2, respectively. Time of vibrations damping is 0.45 s for the first point P1 without load and 0.23 s with load. For the second measuring point P2 it is 0.65 and 0.35 s, respectively. Very similar results were obtained also for the rest of measuring points. They are juxtaposed in Table 1.

In the second test, the system was excited in the same way but measurements were carried out using PVDF piezoelectric foil. In Fig. 7, results of the measurements conducted using PVDF piezoelectric foil glued in the position of the P2 measuring point are presented. It can be observed that this time, maximum values of the voltage

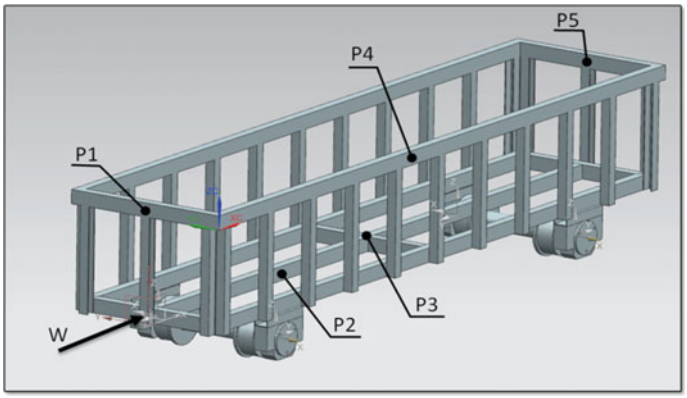

Fig. 4 CAD model of the laboratory stand with measuring points

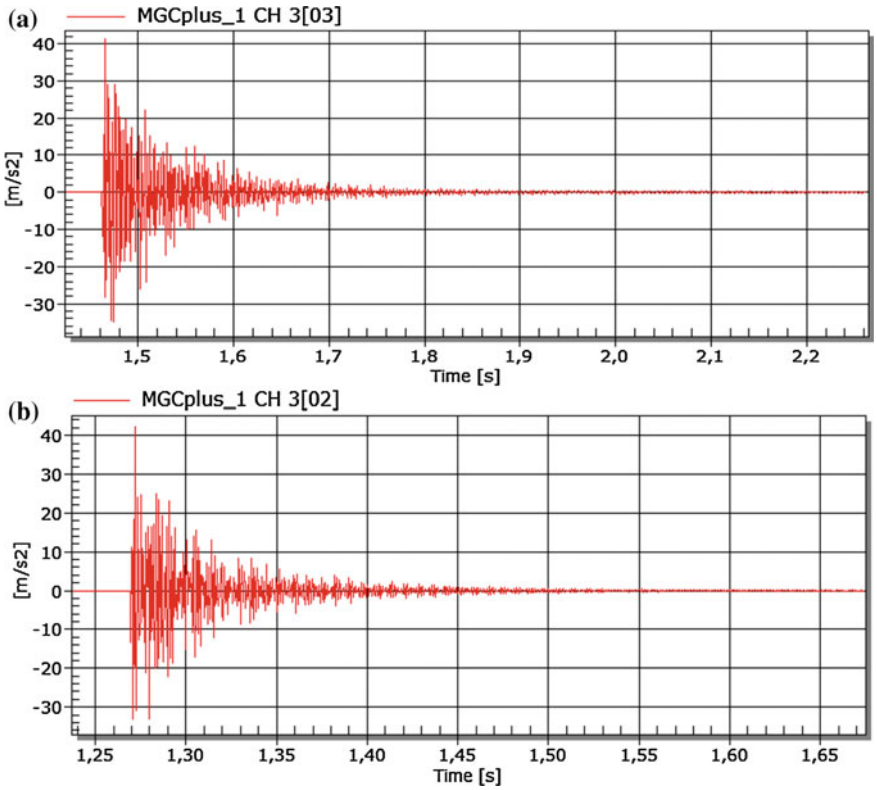

Fig. 5 Results of the measurements conducted using 352C68 PCB accelerometer for the P1 measuring point without load (**a**) and with load (**b**)

signal generated by the PVDF foil are very similar for both measurements—with and without load. The time to damp vibrations is shorter for the system with load.

In the last test, measurements were made at excitation frequencies: 10, 25, 75, 100, and 200 Hz. At each frequency were performed two measurements—for model loaded and for the wagon model with no load. Measurements were repeated to verify the repeatability of the results. The time of each measurement was 10 s. Measurement data were saved in a CSV file. The fast Fourier transform was performed to determine the spectrum of the measured signal. It should be noted that in each measurement there is a frequency of 50 Hz included. It is caused by interference from the power grid. Results of all measurements are juxtaposed in Table 2. All values have been reduced to one level in order to make possible their easy comparison.

Comparing the value it was found that the load significantly affects the transmission of vibration of the wagon body. The resulting values of the amplitude at the loaded wagon are smaller than without load. It can also be noted that the amplitude

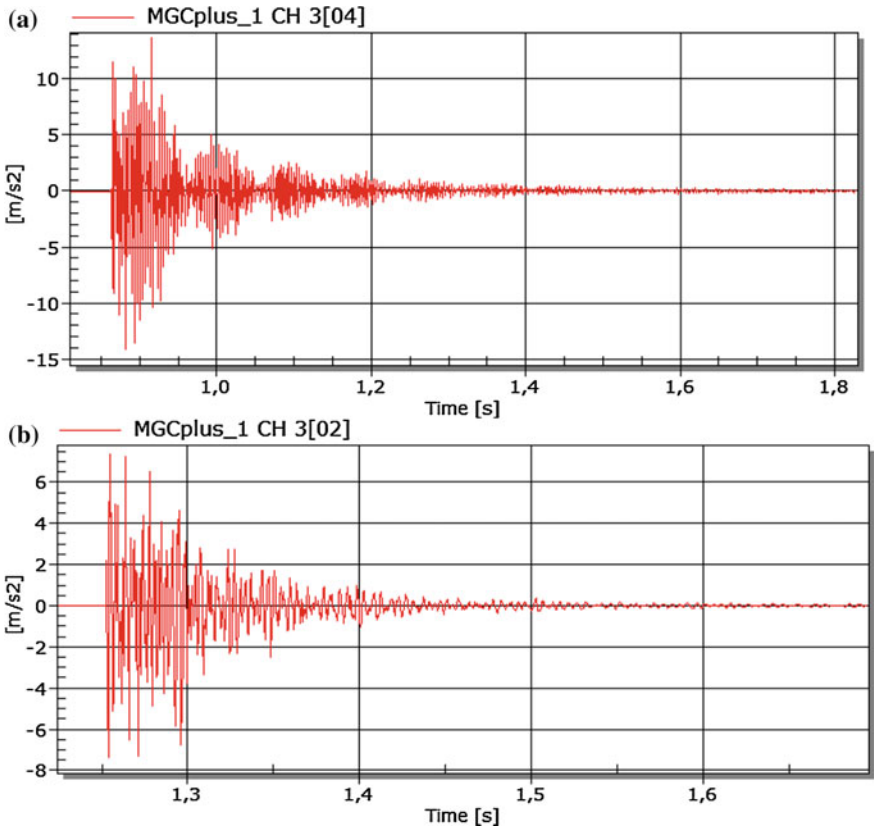

Fig. 6 Results of the measurements conducted using 352C68 PCB accelerometer for the P2 measuring point without load (**a**) and with load (**b**)

Table 1 Results of the measurements using accelerometers

Measuring point	Without load		With load	
	A_{max} (m/s^2)	t_{damp} (s)	A_{max} (m/s^2)	t_{damp} (s)
P1	42	0.45	42	0.23
P2	15	0.65	8	0.35
P3	20	0.5	7	0.25
P4	25	0.8	15	0.4
P5	50	0.5	50	0.35

increases while the excitation frequency is increasing. The voltage values obtained from the PVDF film used as a vibration sensor are small, because the model is quite stiff and there are no large displacements.

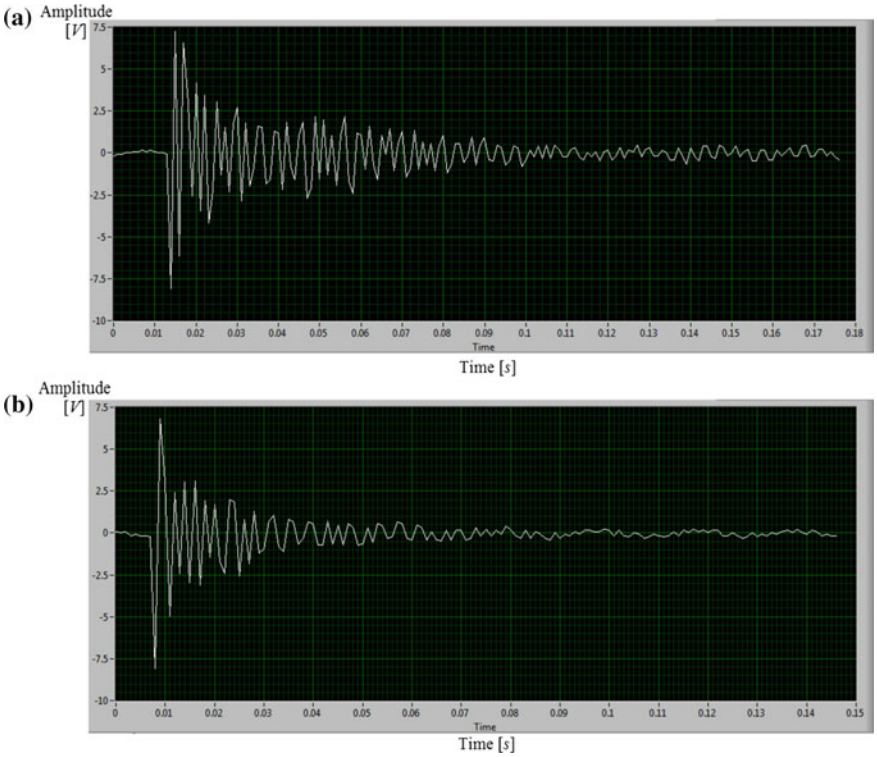

Fig. 7 Results of the measurements conducted using PVDF piezoelectric foil for the P2 measuring point without (**a**) and with load (**b**)

Table 2 A comparison of measurements at different frequencies

Frequency (Hz)	Without load	With load	Without load	With load
	The spectrum amplitude (dB)		Amplitude (V)	
10	0.12e-7	0.095e-7	0.001	0.0007
25	0.75e-7	0.58e-7	0.001	0.0005
75	4.9e-7	5e-7	0.0015	0.0015
100	11e-7	6.9e-7	0.002	0.0015
200	190e-7	16e-7	0.0065	0.0025

5 Discussion and Conclusions

Presented results of dynamic response measurement of the freight car laboratory model are the first step of the work that aims to design mechatronic system for monitoring status of the modernized freight cars. It is predicted to use piezoelectric foils as sensors in this system. Signals generated by the piezoelectric transducers

(PVDF or MFC) glued on the surface of the freight car elements and protected from the weather conditions and vandalism are used to infer about the status of the wagon. This information can be used in the process of freight car management. The work that was done so far proved that there is such possibility, however, there are some disadvantages of this solution. Piezoelectric film, used as a sensor in presented application generates a small voltage, which affects the measurement accuracy. Superstructure of a freight wagon, on which the study was conducted, is quite stiff, so the deformations of the system are of limited value. There is necessary to carry out the research works to find the optimal place for sensors in order to obtain maximum efficiency of their work. This will be done during the next work. It is predicted to carry out computer-aided analysis using CAD models and also tests on laboratory stands and on the real object.

Interference, occurring during measurement using MFC actuator was the widespread presence of an electric field of 50 Hz grid, which introduces a distortion of the measurement path. There will not be this problem on the real object because the system will be self-excited. It will not be necessary to excite vibrations of the system. On the other hand, it will be necessary to create some mathematical algorithm that allows inferring about the status of the system on the basis of measured vibrations caused by a random force generated during the movement of a wagon. In order to do that it is necessary to carry out a lot of tests on the real object and measurements during its normal exploitation.

An important thing is also that the laboratory conditions, in which the measurements were made, differ significantly from the real working conditions of a freight wagon. The real working conditions of the wagon will enter additional factors, noise and unwanted vibration. The atmospheric conditions causing corrosion and icing can also adversely affect on the designed system.

During the test with excitation of vibration by piezoelectric MFC transducer resulting values of the amplitude at the loaded wagon were smaller, except of the values at the excitation frequency of 75 Hz. It can be interpreted as a frequency located near the resonant frequency and should be verify in the future tests.

For measurements using accelerometers it was shown, moreover, that at the measuring points P1 and P5 acceleration amplitude is the greatest, and after the model was loaded its changes were small. Large amplitude of the acceleration at these points is caused by the fact that the sensor was placed in the direction of exciting force. In the case of the remaining points acceleration amplitude significantly decreases when the model of the freight wagon was loaded. After the freight car model was loaded a faster damping of vibrations in the system can be observed. Acceleration amplitude is the smallest at the points P2 and P3, what is due to location of the measurement points in the rigid part of the supporting structure and transverse sensor location with respect to the exciting force. This gives a basis for inference about the effectiveness of this method of measurement and optimal places of the sensors.

Process and results of the dynamical response measurements of the freight wagon laboratory model were presented. This work is a part of the research project which aims to modernize freight wagons using new composite materials during

their renovation including the possibility to use nondestructive testing method of the technical condition of construction [15]. It was proved that it is easy to observe changes in the dynamic response of the system using the proposed measuring apparatus when parameters of the system are changed.

Using piezoelectric accelerometers placed on the selected measuring points of the analyzed construction it can be observed that changes of the system's parameters (load) cause no reduction of the maximum acceleration value for the P1 point while for the P2 measuring point it is about 53.3 %. At the same time, the time of the vibration damping is reduced by about 51.1 % for the P1 and 53.8 % for the P2 measuring points. Observed differences between values of the acceleration and time reduction for analyzed measuring points are the result of the different directions of the measurements axis. For the first point (P1) it was the same as the axis of the excitation, while for the second one (P2) it was perpendicular to it. In the second test, similar results were obtained for the measurement process conducted using PVDF piezoelectric foil glued to the surface of the wagon model only taking into account reduction of the time of vibrations damping, while values of the maximum acceleration of vibrations are very similar for system with and without load. Although it is still possible to detect changes of the system's parameters using this kind of sensor. Those conclusions were also proved by the last test with use of the MFC and PVDF piezoelectric foils.

The carried out work proved that there is a possibility to create a mechatronic system that can be integrated with the modernized freight car and used for its management during exploitation. Such system can be based on piezoelectric foils application. The system that is intended to be created will allow monitoring of the freight car dynamic parameters during its normal exploitation and inferred on its basis about the status of the wagon. In future works tests on the real objects will be carried out.

Acknowledgments The work was carried out under the project number PBS2/A6/17/2013 agreement implemented under the Applied Research Program, funded by the National Centre for Research and Development.

References

1. Andersson, E., Häggström, J., Sima, M., Stichel, S.: Assessment of train-overturning risk due to strong cross-winds. Proc. Inst. Mech. Eng. Part F: J. Rail Rapid Transit. **218**(3), 213–223 (2004)
2. Baier, A., Zolkiewski, S.: Initial research of epoxy and polyester warp laminates testing on abrasive wear used in car sheathing. Eksploatacja i Niezawodnosc—Maint. Reliab. **15/1**, 37–43 (2013)
3. Baier, A. et al.: Experimental Synthesis and Analysis of Geometric and Structural Properties of Chosen Elements of Railway Wagons. Silesian University of Technology Publishing House, Gliwice (2012)
4. Białas, K.: Mechanical and electrical elements in reduction of vibrations. J. VibroEng. **14**(1), 123–128 (2012)

5. Bruni, S., Vinolas, J., Berg, M., Polach, O., Stichel, S.: Modelling of suspension components in a rail vehicle dynamics context. Veh. Syst. Dyn. **49**(7), 1021–1072 (2011)
6. Buchacz, A., Gałęziowski, D.: Synthesis as a designing of mechatronic vibrating mixed systems. J. VibroEng. **14**(2), 553–559 (2012)
7. Buchacz, A., Płaczek, M., Wróbel, A.: Modelling of passive vibration damping using piezoelectric transducers—the mathematical model. Eksploatacja i Niezawodnosc—Maint. Reliab. **16/2**, 301–306 (2014)
8. Connolly, D.P., et al.: Assessment of railway vibrations using an efficient scoping model. Soil Dyn. Earthquake Eng. **58**, 37–47 (2014)
9. Dymarek, A., Dzitkowski, T.: Method of active synthesis of discrete fixed mechanical systems. J. VibroEng. **14**(2), 458–463 (2012)
10. Iacob-Mare, C., Manescu, T.S.: Experimental analysis of strains occurring during the gondola freight wagons' exploitation. Metalurgia **65/7**, 19 (2013)
11. Iacob-Mare, C., Manescu, T.S.: Study of the freight wagon body through the method of finite elements. Metalurgia **65/7**, 13 (2013)
12. Jönsson, P.A., Stichel, S., Persson, I.: New simulation model for freight wagons with UIC link suspension. Veh. Syst. Dyn. **46**, 695–704 (2008)
13. Jönsson, P.A., Andersson, E., Stichel, S.: Experimental and theoretical analysis of freight wagon link suspension. Proc. Inst. Mech. Eng. Part F: J. Rail Rapid Transit. **220**(4), 361–372 (2006)
14. Kovalev, R., Lysikov, N., Mikheev, G., Pogorelov, D., Simonov, V., Yazykov, V., Zakharov, S., Zharov, I., Goryacheva, I., Soshenkov, S., Torskaya, E.: Freight car models and their computer-aided dynamic analysis. Multibody Sys.Dyn. **22**(4), 399–423 (2009)
15. Okabe, Y., Nakayama, F.: Damage detection in CFRP laminates by ultrasonic wave propagation using MFC actuator and FBG sensor. Trans. Space Technol. Jpn **7**(26), 7–12 (2009)
16. Rusiński, E., Koziołek, S., Jamroziak, K.: Quality assurance method for design and manufacturing process of armoured vehicles. Eksploatacja i Niezawodność—Maint. Reliab. **3**, 70–77 (2009)
17. Song, Z., Fang, S., Zhang, Y., Xie, J.: Cracking analysis of bolster cover plate in C70 freight wagons. Eng. Fail. Anal. **30**, 43–60 (2013)
18. Zakharov, S., Goryacheva, I.: Rolling contact fatigue defects in freight car wheels. Int. J. Sci. Technol. Frict. Lubr. Wear **258**(7–8), 1142–1147 (2005)
19. Zhai, W.M.: Modelling and experiment of railway ballast vibrations. J. Sound Vib. **270**(4–5), 673–683 (2004)
20. http://www.pcb.com/Products.aspx?m=352C68
21. http://www.smart-material.com/

Evolutionary Model for Synthetic Spectrum Compatible Accelerograms

Fabio Carli and Claudio Carino

Abstract This paper proposes a numerical procedure for the generation of sets of synthetic acceleration time histories that result compatible with an assigned target design spectrum. The proposed formulation is able to take into account both the energy distribution in time and the contemporary variability of the frequency content. The approach allows the recognition of strict relations between recorded signals at a site and the underlying evolutionary model recently introduced for the generation of spectrum compatible time histories. A high seismicity Italian area is selected for the numerical example: results are given in terms of synthetic signals whose corresponding spectra versus the design spectrum at the site are compared.

1 Introduction

Today's structural design codes are defined to be "performance based" in contrast with the previously "prescriptive" standards. That change of point of view comes from the idea that safety goals and design solutions must comply with given requirements for any specific application. For earthquake design, the design forces are usually obtained via parametric design spectra consistent at the specific site with the performance requirements obtained by seismic microzonation studies. An equivalent linear static/dynamic modelling by modal combination rules stay behind that approach but, in many important cases it cannot be considered enough, e.g.: the seismic performance evaluation of large/nonlinear systems can be hardly evaluated in correct way. Therefore when modal combination is lacking the seismic load must be represented by a suitable set of earthquake time histories [1]. Unfortunately records of natural seismic events rarely comply with the code requirements given in

F. Carli (✉) · C. Carino
Department of Civil Engineering and Architecture (DICAr), University of Pavia,
Via Ferrata 3, 27100 Pavia, Italy
e-mail: fabio.carli@unipv.it

C. Carino
e-mail: claudio.carino@unipv.it

J. Awrejcewicz (ed.), *Dynamical Systems: Modelling*, Springer Proceedings
in Mathematics & Statistics 181, DOI 10.1007/978-3-319-42402-6_12

terms of design response spectra at the specific site. This lack of coherence produces the need of suitable methods for the digital generation of synthetic accelerograms from the knowledge of a target response spectrum given by the design code. The procedure used for the generation of load histories at prescribed effect can be considered as an inverse problem without unique solution and approach. As a natural consequence many different methods are present in literature at this purpose: models based on filtering and windowing Gaussian noise or filtering white noise with given analytical spectral shape, auto regressive models with/without moving average and more recently also wavelet-based outlines. Most of them rely on quasi-stationary processes with time amplitude modulation but more recently efforts were spent to include both amplitude and frequency content variation in time.

Another common classification is based on the underlying logical approach: database models (founded on the selection, scaling and averaging of natural records), seismological models (in which the source and site characterization rely on geophysical basis), pure signal analysis models and response spectrum compatible approaches. In particular the present work belongs to this last type: a generation procedure for sets of simulated accelerograms is proposed on the basis of an assigned target design spectrum usually provided by country specific design rules. The described approach is able to take into account both the energy release in time and the contemporary variability of the frequency content. It is based on the assumption of decoupling the energy emission from the variability of the predominant frequency content. This evolutionary approach makes use of two time functions: one responsible for the energy distribution and the other for the frequency content variation in time. The model suggests strict relations between recorded accelerograms at a site and the underlying evolutionary description proposed for the generation of spectrum compatible time histories. A usual window function in signal analysis [2] is here tested as initial approximation for the spectral content in time; besides an improvement of the correcting weight function is also introduced. The numerical example used for testing these refinements is based on a seismic signal recorded at a reference Italian site. The corresponding site dependent design spectrum prescribed by the Italian design code [3] gives the remaining information used for the complete definition of the simulation procedure.

2 Basics

A useful description of a generic natural seismic acceleration record $r(t)$ can be obtained by means of a suitable one-to-one mapping of $r(t)$ in time t and frequency f by means of its complex spectral representation $R(f, t)$ [4]. If $r(t)$ can be described as a quasi-stationary stochastic process of finite duration, an estimate of its power spectral density function $G_r(f, t)$ is obtained by the following approximation: $G_r(f, t) = A_r(f, t)^2/d_0$ where $A_r(f, t)$ is settled to be a smooth version of the amplitude spectrum $R(f, t)$, while d_0 represents the equivalent stationary duration of the signal. Early work [5] shows the effectiveness of the separation of the amplitude variability

in time from the changing of the frequency content by the following basic relations and considerations: $r(t) = i(t)\ s(t)$ with $i(t)$ the intensity function of the process $r(t)$ and $s(t)$ the derived amplitude stationary and frequency non-stationary process having $R_s(f,\ t)$ as spectral counterpart.

Hence $R_s(f,\ t)$ represents a bivariate function that supplies a constant release in time of the power while permitting the variation of the frequency content. In terms of its power spectrum $G_s(f,\ t)$ it can be stated that

$$\int G_s(f,t)\mathrm{d}f = \text{constant}, \forall t_i \tag{1}$$

with $G_s(f,\ t) = R_s^2(f,\ t)/d$ and d the total duration of the amplitude stationary process $s(t)$. With this approach the intensity function $i(t)$ is therefore the only responsible of the power release of the process along the time axis.

The given relations can be considered to be a reasonable approximate description of the signal behaviour in case of regular fluctuation in time of its energy. Many different analytical formulations for a smooth approximation $A_s(f,\ t)$ of $R_s(f,\ t)$ are given in literature ranging from physical (seismological) models to pure numerical approximation procedures without any link to the observable event.

The main target of this work is the formulation of a model suitable for the generation of time histories with spectral compatibility towards a target design response spectrum at the site as given by many modern structural design codes. The construction of such model involves the ability to describe the behaviour in both frequency and time of a real signal.

3 Parametric Frequency Model

In previous work by the author [5], the formulation of an analytical model both simple and handy passed through the use of the well-known similarity between the amplitude spectrum of a record and its zero damping pseudo-velocity response spectrum. Conversely in this work, the interest is moved to testing the capability of the iterative numerical procedure to converge to reasonable results starting from a more generic shape for the time stationary modelling spectrum $A_s(f,\ t)$.

In particular is here tested a formulation based on a composite function commonly used in signal analysis. It is given by a modification of the side decaying branches of the classic Tukey window here used in the frequency domain. The window is completely defined by the four frequency parameters f_1, f_2, f_3 and f_4.

More precisely the following description of the $A_s(f,\ t)$ spectrum is adopted

$$A_s(f,t) = A_s(f, f_0(t)) \tag{2}$$

whose analytical shape at time t changes on the basis of the single frequency parameter $f_0(t)$ that moves in time, consequently altering the shape of the modified

Tukey window. In particular the frequency parameters are defined by the following set of conditions: (a) the low frequency cut-off is set to zero $f_1 = 0$ Hz; (b) the high-frequency cut-off is fixed at $f_4 = 16$ Hz observing that higher frequencies do not play a significant role in the nonlinear response of structures to an earthquake load; c) the roll-on frequency is set to be dependent on the function $f_0(t)$: $f_2(t) = f_2((f_0(t))$; d) the high-frequency roll-off f_3 is set at constant distance from the preceding f_2: $f_3 = f_2 + \Delta f$ with Δf assigned to be equal to the flat portion of the design spectrum prescribed at the site. More specifically: $f_2(t) = f_0(t) - \Delta f/2$ with a suitable function $f_0(t)$ able to drive in concise way the changing of the central frequency value in $A_s(f, t)$. An exponential decaying function is here adopted for $f_0(t)$:

$$f_0(t) = f_0(t_d) + (f_0(t_r) - f_0(t_d)) \exp\left(-\pi t^2 / f_b\right) \quad , \quad t = [0, d] \tag{3}$$

where the time parameter d is the total duration of the accelerogram, the rise time t_r is the starting of the strong ground motion part, the decay time t_d is the starting of the decay part of the time history while the difference $t_d - t_r = d_0$ defines the equivalent stationary duration of the accelerogram. The frequency parameter $f_0(t_d)$ is set equal to the mean value of the central frequency observed in interval $[t_d, d]$ while to $f_0(t_r)$ is assigned the mean value of the central frequency in the interval $[0, t_r]$ and f_b rules the width of the function.

The given exponential shape of $f_0(t)$ consistently follows the natural behaviour of a seismic record: high-frequency content in the initial part decaying in time till the low-frequency content that predominates along the whole tail of the record.

This approach gives great importance to a rational characterization of the frequency content variation in time expected at the site. The given scheme leads to the almost complete decoupling of the two main sources responsible for the non-stationary behaviour of strong ground motions, besides the central frequency function $f_0(t)$ is strictly dependent too on the time characterization procedure. The frequency modulating function $f_0(t)$ remains the single link between the t-domain and the f-domain in driving the variation of the frequency content in time.

4 Time Functions

The identification of the time parameters to be used in the model for the simulation of the accelerograms is strictly controlled by the intensity function $i(t)$. In fact it is used for the estimate of the equivalent stationary duration d_0 and its location in time from t_r to t_d, while ruling the distribution in time of the energy. Therefore it is also of fundamental importance for the estimate of the previously defined frequency modulating function $f_0(t)$.

In literature different methods were proposed for the definition of the equivalent stationary duration d_0 but all the proposals show pro and cons [6]. Among the methods introduced by the first author [5] is here used the one based on the classic

definition of effective bandwidth B_e [4] that holds for signals delivering smooth transitions from the rise to the peak an then to the fall off

$$B_e = \left(\int_0^d i(t)\mathrm{d}t \right)^2 / \left(\int_0^d i^2(t)\mathrm{d}t \right) = d_0 \tag{4}$$

In particular the classic definition of envelope $e(t)$ of a signal is here used for the evaluation of the intensity function $i(t)$

$$e(t) = \sqrt{r(t)^2 + r_H(t)^2} \quad \Rightarrow \quad i(t) = e(t) / \max[e(t)] \tag{5}$$

where $r_H(t)$ is the Hilbert transform of the record $r(t)$ and $e(t)$ the envelope function. The intensity function is then obtained by unit peak scaling of the envelope. The time location of the equivalent stationary duration is estimated maximizing the energy release of the record during d_0. At that purpose the cumulate energy function $C_r(t)$ of the record can be usefully employed

$$C_r(t) = \int_0^t r^2(\tau)d\tau, \quad t = [0, d] \tag{6}$$

The position of d_0 is obtained by the following condition solved for t

$$t_r = t(\max[C_r(t + d_0) - C_r(t)]), \qquad t = [0, d - d_0] \tag{7}$$

The time decay parameter t_d is simply obtained: $t_d = t_r + d_0$.

The presented procedure for the evaluation of the intensity function and the estimation of the time parameters needed for the definition of the strong motion part of the seismic record, shows to be independent from the amplitude of the record itself: any scale factor applied to $r(t)$ will give the same intensity function $i(t)$ and equivalent stationary duration d_0.

5 Identification Procedure for Target Spectrum Simulation

The operative flow practiced in the present work for the complete definition of all the variables and functions used for the time–frequency characterization of the presented model is now summarized.

5.1 Time Domain Identification Procedure

1. selection from a public database of seismic records, of one or more suitable accelerograms $r(t)$ to be used as reference descriptors of the local seismicity
2. evaluation of the intensity function $i(t)$, equivalent stationary duration d_0, rise time t_r, decay time t_d and signal duration d employing the approach described in Eqs. (4–7)
3. segmentation of the selected record by short-time Δt windowing using one of the many different functions used in signal analysis [2, 4]; here a classic Tukey window with bandwidth $\Delta t = 1\ s.$ is used
4. evaluation of the evolutionary amplitude spectrum $R(f,\ t)$ of the seismic record with estimation the central frequency $f_0(t_i|\Delta t)$ of each time section t_i
5. construction of the continuous function $f_0(t)$ in Eq. (3), by approximation of the previously obtained time-varying central frequency values $f_0(t_i|\Delta t)$, $\vee t_i$.

5.2 Frequency Domain Identification Procedure

1. given $f_0(t)$ and using the conditions stated in paragraph **3**, the four corner frequency f_1, f_2, f_3 and f_4 of the modified Tukey function in frequency can be estimated. The modified window is here used as basis for the analytical description of the raw initial time-varying amplitude spectrum $A_s(f,\ f_0(t))$
2. the one-sided real-valued time–frequency spectrum $A_s(f,\ t) = A_s(f,\ f_0(t))$, underlying the evolutionary process in frequency but stationary in time $s(t)$, can be generated under the condition of constant power release;

$$\iint A_s^2(f,t))\mathrm{d}f\,\mathrm{d}t = \int s^2(t)\mathrm{d}t \qquad \text{with } \int A_s^2(f,t)\mathrm{d}f = \text{const.}, \forall t \tag{8}$$

6 Time Histories Simulation for Target Design Spectrum

The objective of the simulation is to obtain the desired number of different synthetic accelerometric signals that perform similarly in term of response spectra while evidencing the typical characters of a seismic record. Among others the two most important seismic features for the structural behaviour are: (a) the energy release in time always shows a usually short initial rise-up followed by the strong ground motion part and a longer decay time; (b) the predominant frequency content changes in time ranging from higher frequencies at the beginning to lower frequencies at decay

Once the site of interest is given, current seismic design codes provide the structural engineer with the design requirements in terms of elastic response spectra $S_{vd}(f)$. The iterative generation procedure here described is aimed to obtain synthetic signals having both the characters of a seismic record and fulfilling the requirement of the design code at the site.

An initial amplitude stationary (with frequency evolution in time) accelerogram $a_s(t)$ is obtained using the classic approach

$$a_s(t) = \sum_i A_s(f_i, t)\cos(2\pi f_i t + \varphi_i), \quad \varphi_i = [0, 2\pi] \tag{9}$$

where φ_i is random phase angle. Then a first simulated acceleration time history $a(t)$ is obtained by amplitude modulation of $a_s(t)$:

$$a(t) = i(t)\, a_s(t) \tag{10}$$

The zero damping pseudo-velocity elastic response spectrum $S_v(f)$ of $a(t)$ is calculated and the corresponding percentage distance, or error, $\Delta S_v(f)$ from the coded target design response spectrum $S_{vd}(f)$ is evaluated

$$\Delta S_v(f) = (S_{vd}(f) - S_v(f))/S_{vd}(f) \tag{11}$$

A correction to $A_s(f, t)$ is applied by the $\Delta S_v(f)$ factor.

A new simulated accelerogram can then be obtained and the previous steps can be iterated until the following global convergence criterion is fulfilled

$$\int |\Delta S_v(f)|df \leq 0.1 \int S_{vd}(f)df \tag{12}$$

The applied convergence criterion seems to be rather loose, but the random nature of the signal and the code requirements given to the entire set of simulated accelerograms, suggest to leave space to some variability in the structural response.

A side effect of the nature of the stochastic process is the presence of sharp high peaks in $\Delta S_v(f)$ that can produce convergence problems. To improve this aspect of the iterative procedure the sharp error function $\Delta S_v(f)$ is substituted by its smoothed version $\Delta S_w(f)$ by convolution with a suitable window function $w(t)$.

7 Numerical Example

The set-up of the numerical example has the main goal to show the behaviour and effectiveness of the proposed procedure for the generation of evolutionary spectrum compatible time histories. The compatibility with the code prescribed elastic spectrum at the site is verified employing as reference signal one of the most significant seismic records of the Friuli Region (Italy). The record is used to

estimate the input data needed for the set-up of the simulation, but all the required data could also be assigned in independent way from any real record or even by experience. The selected site belongs to one of the most active Italian seismic area (Zone 1, characteristic peak ground acceleration 0.25 g $\leq a_g \leq$ 0.275 g) with availability of public seismic records. In particular the accelerogram was recorded in that region during the last main earthquake in 1976 and shows a significant variation of the frequency content in time. The signal $r(t)$ employed for the time–frequency characterization of the simulation model is the NS component of the acceleration recorded at the station of Forgaria-Cornino in data 15.09.1976, starting time h.09.21.18, sampling period: 0.01 s, record length: 24.59 s with instrumental correction [7].

The first step of the characterization procedure was the evaluation of the intensity function $i(t)$ by means of Eq. (5), followed by the equivalent stationary duration ($d_0 = 4.99$ s) estimated with Eq. (4) and its placement along the time axis by Eq. (6) that gives: rise time $t_r = 1.47$ s and decay time $t_d = 6.46$ s. The original record $r(t)$, its cumulate energy function and the obtained time parameters are summarized in Fig. 1. A window function of Tukey type with time width $\Delta t = 1s$ is used to perform a short-time spectral estimation of the accelerogram. Being $r_i(t)$ the i-th time segment and $R_i(f)$ the corresponding one-sided amplitude spectrum, the central frequency $f_0(t_i|\Delta t)$ of $R_i(f)$ can be promptly calculated allowing the evaluation of the approximating function $f_0(t)$ given in Eq. (3). The calculated values $f_0(t_i|\Delta t)$, the corresponding central frequency function $f_0(t)$ and the equivalent stationary duration portion are plotted in Fig. 2.

Once estimated $f_0(t)$, the analytical form defining the frequency evolutionary, time stationary spectrum $A_s(f, t)$, Eq. (8), is obtained and the numerical simulation procedure given in Eq. (9) is set up. In Fig. 3 $A_s(f, t)$ is plotted with its time section

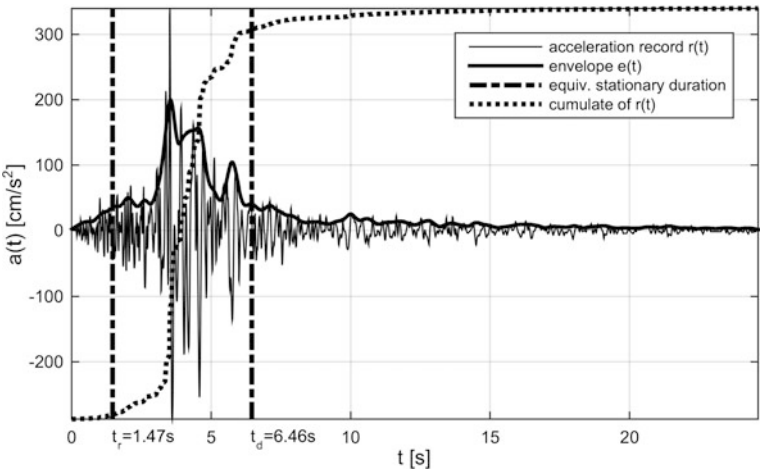

Fig. 1 The Forgaria-Cornino record $r(t)$, its cumulate function $C(t)$ and envelope $e(t)$ with localization of the equivalent stationary duration $d_0 = t_d - t_r$

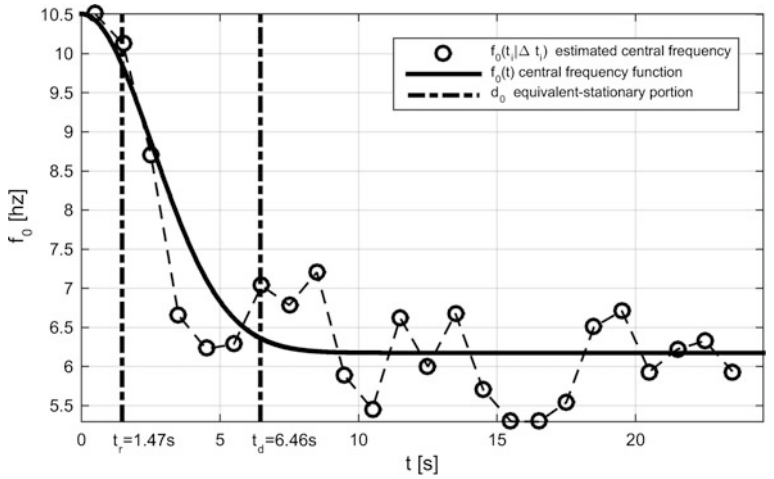

Fig. 2 Central frequency values estimated from the segmented spectral analysis of $r(t)$, the frequency modulation function $f_0(t)$ with the position of the equivalent stationary duration d_0

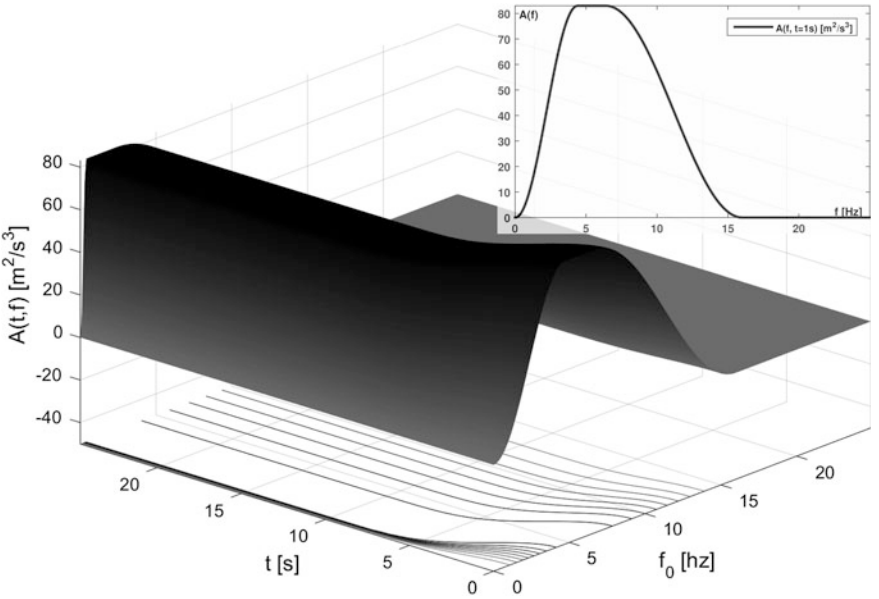

Fig. 3 The analytic spectrum $A(f, t)$ normalized to have constant energy in time, adopted for the initial simulation with its time section at $t = 1$ s

at 1 s, and Fig. 4 gives few samples of simulated signals at convergence. For one of the simulated accelerograms (#7) its initial and final (at convergence) pseudo-velocity zero damping response spectra $S_v(f)$ are calculated and plotted in Fig. 5

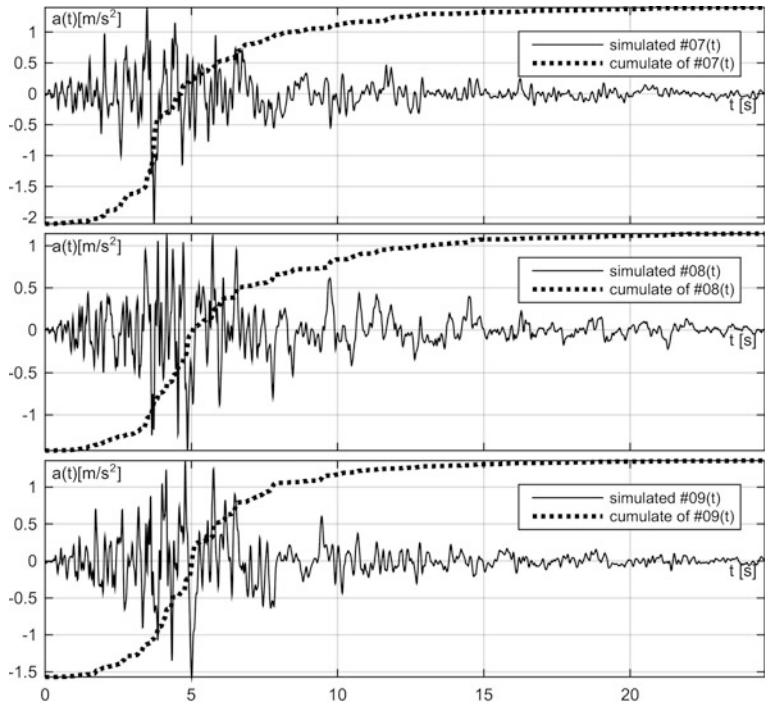

Fig. 4 Few examples of the synthetic accelerograms obtained with the simulation procedure

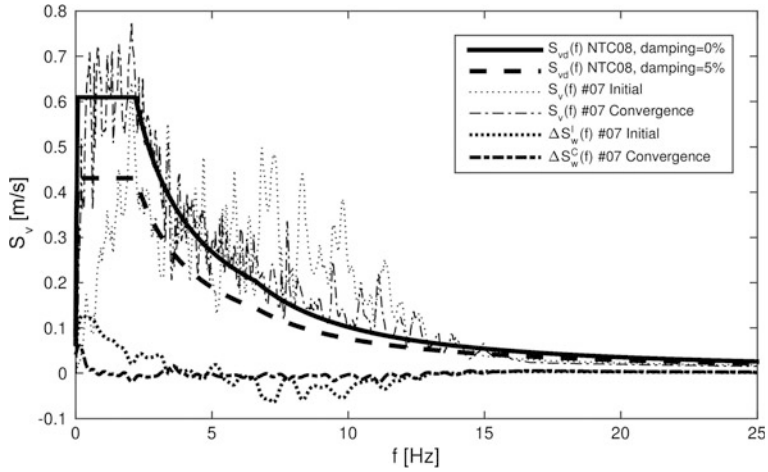

Fig. 5 Damped and undamped pseudo-velocity design response spectra $S_{vd}(f)$ versus the response spectra $S_v(f)$ of one of the simulated accelerogram (#7) at the beginning of the iterative simulation procedure and at convergence with the corresponding smoothed errors $\Delta S_w^I(f)$ and $\Delta S_w^C(f)$

with the code prescribed design spectra at the site $S_{vd}(f)$ given for 0 and 5 % damping. The corresponding smoothed errors $\Delta S_w^I(f)$, initial, and $\Delta S_w^C(f)$, at convergence, complete the graphic representation.

8 Conclusions

A generation procedure for seismic-like accelerograms is formulated and the numerical characterization is detailed. A distinctive feature of the formulation is the use of an evolutionary approach producing signals with both amplitude and frequency content variation in time, resembling the behaviour of natural seismic records. Complete non-stationarity is obtained by a decoupled description in time and frequency. The numerical example points out the small amount of data required for the site localization and nice results at convergence despite the raw shape of the analytic spectrum used. The obtained accelerograms show a natural appearance and their spectra significantly approach the target design spectrum.

References

1. Trifunac, M.D.: Earthquake response spectra for performance based design—A critical review. Soil Dyn. Earthquake Eng. **37**, 73–83 (2012)
2. Geckinli, N.C., Yavuz, D.: Discrete Fourier Transformation and Its Application to Power Spectra Estimation. Elsevier, Amsterdam (1983)
3. Ministero delle Infrastrutture: Norme tecniche per le costruzioni. Sup.Ord. GU 4.2.2008, no. 29
4. Newland, D.E.: An Introduction to Random Vibration, Spectral and Wavelet Analysis. Longman Scientific & Technical, NewYork (1983)
5. Carli, F.: Generation of spectrum-compatible accelerograms. In: Proceedings of the ANIDIS "L'Ingegneria Sismica in Italia", Taormina, Italy (1997) (in Italian)
6. Potnis, S.C., Desai, R.S., Gupta, I.D.: Estimation of strong ground motion stationary duration from stochastic structural response analysis. In: Proceedings of the 14th WCEE, Beijing, China (2008)
7. Ambraseys, N., Smit, P., Sigbjornsson, R., Suhadolc, P., Margaris, B.: Internet-site for european strong-motion data. In: European Commission Research, Environment and Climate Programme. http://www.isesd.hi.is (2002)

A Parametric Study of Mixing in a Granular Flow a Biaxial Spherical Tumbler

Ivan C. Christov, Richard M. Lueptow, Julio M. Ottino and Rob Sturman

Abstract We report on a computational parameter space study of mixing protocols for a half-full biaxial spherical granular tumbler. The quality of mixing is quantified via the intensity of segregation (concentration variance) and computed as a function of three system parameters: angles of rotation about each tumbler axis and the flowing layer depth. Only the symmetric case is considered in which the flowing layer depth is the same for each rotation. We also consider the dependence on $\bar{R}$, which parametrizes the concentric spheroids ("shells") that comprise the volume of the tumbler. The intensity of segregation is computed over 100 periods of the mixing protocol for each choice of parameters. Each curve is classified via a time constant, τ, and an asymptotic mixing value, *bias*. We find that most choices of angles and most shells throughout the tumbler volume mix well, with mixing near the center of the tumbler being consistently faster (small τ) and more complete (small *bias*). We conclude with examples and discussion of the pathological mixing behaviors of the outliers in the so-called τ-*bias* scatterplots.

I.C. Christov (✉)
Theoretical Division and Center for Nonlinear Studies,
Los Alamos National Laboratory, Los Alamos 87545, USA
e-mail: christov@alum.mit.edu

R.M. Lueptow · J.M. Ottino
Department of Chemical and Biological Engineering, Department of Mechanical Engineering and The Northwestern Institute on Complex Systems (NICO),
Northwestern University, Evanston 60208, USA
e-mail: r-lueptow@northwestern.edu

J.M. Ottino
e-mail: jm-ottino@northwestern.edu

R. Sturman
Department of Applied Mathematics, University of Leeds, Leeds LS2 9JT, UK
e-mail: r.sturman@maths.leeds.ac.uk

J. Awrejcewicz (ed.), *Dynamical Systems: Modelling*, Springer Proceedings in Mathematics & Statistics 181, DOI 10.1007/978-3-319-42402-6_13

1 Introduction

Most granular flows encountered in nature and industry are three-dimensional (3D). However, the mathematical modeling and analysis, and the experimental and computational visualization of 3D flows remain a challenge. Yet, 3D granular flows reveal many features of complex systems far from equilibrium. Rotating drums, also known as tumblers, are one of six fundamental systems in which dense granular flows are studied [1] and are a common device in the pharmaceutical and other powder processing industries [2]. Here, we consider a simple, but realistic, analytically tractable 3D granular flow termed the blinking spherical tumbler flow because of its analogy to an early example of 2D chaotic mixing [3]: the blinking vortex flow [4].

A quasi-3D granular flow, specifically weak rocking motions of a rotating cylindrical container, appears to be one of the first experimentally and numerically studied examples [5]. More recently, spherical tumblers were analyzed experimentally and computationally [6–9]. Through a dynamical systems framework, it has become possible to gain a deeper understanding of how mixing and segregation manifest themselves in these 3D systems [8, 10, 11]. Even so, chaotic transport and mixing in 3D flows remains relatively unexplored, especially given the great variety of new (i.e., distinct from those in 2D) behaviors possible [12].

In the present work, we are interested in *quantifying* mixing in a 3D chaotic granular flow. Although many recent studies have focused on understanding the kinematic structures created by 3D chaotic flows and maps, only a few studies quantify mixing in a *global* way for *genuinely* 3D flows: e.g., via numerical simulations in a cavity flow with translating side walls [13, 14] and in an "ABC" flow [15], and via experiments in a container with counter-rotating lids [16] and for granular flows in blade and bin blenders [2, 17, 18]. Given the uniquely distinct dynamics of granular flow in a biaxial spherical tumbler, here we seek to connect the "degree of mixing" to the independent parameters of this system and to also understand how mixing varies across the volume of a half-full tumbler. To this end, we present a parametric study of mixing in the so-called symmetric case of a half-full blinking spherical tumbler using the technique of τ-*bias* scatterplots [19].

2 Continuum Model of Granular Flow in a Spherical Tumbler

In this section, we summarize only the necessary details of the continuum model (see, e.g., [8, 20] for derivations) for the kinematics of granular flow in the continuous-flow (rolling) regime of a half-full spherical tumbler rotated about two orthogonal axes (for the present purposes, the z- and x-axes as shown in Fig. 1).

Without loss of generality, we take the first rotation of the half-full spherical tumbler of radius R to be clockwise about the z-axis at a rate of $\omega_z (> 0)$ for a duration T_z. We employ a Cartesian coordinate system with its origin at the center of the sphere,

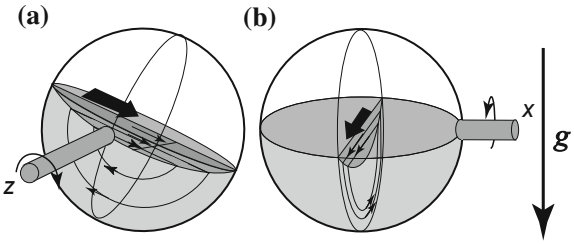

Fig. 1 Schematic of a half-full blinking spherical tumbler. Streamlines are shown in the cross sections for rotation around the **a** z- and **b** x-axis. Flow in each cross section consists of solid body rotation in the bulk, followed by a rapid cascade down a thin flowing layer at the free surface. Reproduced with permission from [7]

the initial streamwise direction is along the x-axis, and the transverse direction is along the z-axis. The streamwise velocity v_x varies linearly with the depth y in the flowing layer so that the shear rate $\dot{\gamma}_z = \partial v_x/\partial y$ is constant.[1]

We make x, y, z, L, δ dimensionless by rescaling by $1/R$ and t is made dimensionless by rescaling by ω_z (for rotation about the z-axis) or ω_x (for rotation about the x-axis). The velocity field in the bulk (bed of solid body rotation) is then

$$\dot{x} = y, \qquad \dot{y} = -x, \qquad \dot{z} = 0; \qquad y \le -\delta_z(x,z). \tag{1}$$

The boundary of the flowing layer [8, 10, 11] is the surface

$$\delta_z(x,z) = \delta_0(z)\sqrt{1 - x^2/L(z)^2} = \varepsilon_z\sqrt{1 - x^2 - z^2}, \tag{2}$$

where $\delta_0(z) = L(z)\sqrt{\omega_z/\dot{\gamma}_z}$ and $L(z) = \sqrt{1 - z^2}$ are the local (dimensionless) depth and half-length of the flowing layer, respectively. Naturally, the definition of $\varepsilon_z := \delta_0(0)/L(0) \equiv \sqrt{\omega_z/\dot{\gamma}_z}$ as the maximal depth at $x = z = 0$ follows since $L(0) = 1$. Meanwhile, the velocity field in the flowing layer [8, 10, 11] can be written as

$$\dot{x} = \left[\delta_z(x,z) + y\right]/\varepsilon_z^2, \qquad \dot{y} = x\,y/\delta_z(x,z), \qquad \dot{z} = 0; \qquad y > -\delta_z(x,z). \tag{3}$$

In dimensionless units, the tumbler is rotated about the z-axis by the angle $\theta_z = \omega_z T_z$.

The blinking spherical tumbler protocol alternates between rotations about two orthogonal axes (Fig. 1). Once the rotation about the z-axis is complete, a rotation about the x-axis at constant rate ω_x for a duration T_x follows,[2] with the streamwise direction now along the z-axis and Eqs. (1)–(3) still holding after formally exchang-

[1] In an experiment, the flowing layer is at an angle with respect to the horizontal, while, in the model, the coordinate system is rotated backwards by this fixed angle. Also, we assume that the effects of side walls and transport in the transverse direction are negligible.

[2] In an experiment, several intermediate steps are performed between the rotations [8], however, as far as the mathematical analysis is concerned, the rotations are completely independent.

ing "x" and "z." Specifically, the interface between the flowing layer and the bulk for rotation about the x-axis is given by $\delta_x(x,z) = \varepsilon_x\sqrt{1-x^2-z^2}$, where $\varepsilon_x = \sqrt{\omega_x/\dot{\gamma}_x}$.

Note that if $\varepsilon_z = \varepsilon_x$, then $\delta_z(x,z) \equiv \delta_x(x,z)$. We refer to this as the *symmetric case*. Naturally, $\varepsilon_z \neq \varepsilon_x$ will be termed the *nonsymmetric case*. It is important to note that different values for ε_z and ε_x arise in physical systems due to different rotation rates ω_z and ω_x [21]. Thus, the symmetric case occurs for identical rotation rates about the two axes, while the nonsymmetric case arises from different rotation rates.

3 Parametric Study of Mixing in the Symmetric Case

While previous studies [8, 10, 11] have focused on the qualitative structure of the template for chaotic transport in the blinking spherical tumbler, here we study the "quality of mixing" quantitatively by measuring the decay of the variance of the concentration of a species. For the remainder of the discussion, we restrict the analysis to the symmetric case (i.e., $\varepsilon_z = \varepsilon_x$) of the half-full blinking spherical tumbler, and we fix the initial condition (IC) such that tracer particles within the quarter-sphere $\mathfrak{Q} = \left\{(x,y,z) \in \mathbb{R}^3 \mid x^2+y^2+z^2 \leq 1,\ -1 \leq y \leq 0,\ 0 \leq x \leq 1\right\}$ are colored gray at $n = 0$, while those in the remainder of the filled volume (i.e., $\{(x,y,z) \in \mathbb{R}^3 \mid x^2+y^2+z^2 \leq 1,\ -1 \leq y \leq 0,\ -1 \leq x < 0\}$) are black. From the assumption of $\varepsilon_z = \varepsilon_x$, as shown in [10, 11], it follows that trajectories of these tracer particles are restricted to 2D invariant surfaces, which are hemispherical in the bulk, determined by their ICs [11]. Therefore, it is convenient to introduce the "artificial" parameter, termed the *shell radius*, $\bar{R} \in (\varepsilon_z, 1)$ that denotes the (constant) radius from the origin of the hemispherical bulk portion of the 2D invariant surfaces upon which tracer particles are restricted. Since the dynamics depends strongly upon which hemispherical shell is considered [11], the shell radius $\bar{R}$ is a useful parameter.

Given the nondimensionalization introduced in Sect. 2, it is clear there are four independent parameter in our model of a half-full blinking spherical tumbler, namely ε_z, ε_x, θ_z and θ_x. Indeed, in a quasi-2D experiment, there are only four quantities that vary independently once the tumbler and granular material are chosen [21]. Specifically, fixing the rotation rate in the laboratory yields unique values for the shear rate and maximal depth of the flowing layer, though the precise functional relationships remains a topic of research (see, e.g., [21] and the references therein). In our model, we set the flowing layer depth, which is thus equivalent to setting the rotation rate in an experiment. Additionally, in the present analysis there may be different angles of rotation about each axis but the flowing layer depths for rotation about each axis are equal ($\varepsilon_x = \varepsilon_x$) because we have limited ourselves to the symmetric case. Therefore, including $\bar{R}$, there are four independent parameters.

With this in mind, we can "bin" (see [20, Appendix B] for details) the part of the invariant surface in the bulk into $N \times N$ surface elements, each of area A_i. For the sake of simplicity we construct bins with equal areas, i.e., $A_i \equiv A\ \forall i$. In each, we uniformly distribute $M_b \times M_b$ tracer particles throughout the area. Then, these

particles are advected for p flow periods, where the flow period is the total time required to complete a rotation about each of the two axes (i.e., an iteration of the blinking protocol). Finally, the concentration c_i of gray (equivalently, black) tracer particles can be computed in each of the original bins as $c_i = \#_{g,i}/(\#_{g,i} + \#_{b,i})$, where $\#_{g,i}$ and $\#_{b,i}$ denote the number of gray and black particles in the ith bin, respectively. Following Danckwerts [22], consider the first moment (mean) of this distribution

$$\langle c \rangle = \frac{\sum_{i=1}^{N^2} c_i A_i}{\sum_{i=1}^{N^2} A_i} = \frac{1}{N^2} \sum_{i=1}^{N^2} c_i, \tag{4}$$

where the last equality follows from the fact that $A_i \equiv A \; \forall i$. Then, the second moment (variance) of the distribution of concentrations is given by

$$\langle\langle c \rangle\rangle \equiv \langle (c - \langle c \rangle)^2 \rangle = \frac{\sum_{i=1}^{N^2} (c_i - \langle c \rangle)^2 A_i}{\sum_{i=1}^{N^2} A_i} = \frac{1}{N^2} \sum_{i=1}^{N^2} (c_i - \langle c \rangle)^2. \tag{5}$$

It is convenient to normalize $\langle\langle c \rangle\rangle$ by introducing the *intensity of segregation* [22]

$$\mathscr{I} = \frac{\langle\langle c \rangle\rangle}{\langle c \rangle (1 - \langle c \rangle)}, \tag{6}$$

where now $0 \leq \mathscr{I} \leq 1$ with $\mathscr{I} = 0$ and 1 corresponding to perfect mixing (i.e., $c = \langle c \rangle$ everywhere) and perfect segregation (i.e., $c = 0$ or 1 for any given surface element in the domain), respectively.

For the simulations presented below, we divide the bulk (hemispherical) portion of the 2D invariant surface on which the dynamics are restricted into $N = 14$ longitudinal and $N = 14$ latitudinal bins with $M_p \times M_p = 10^2$ uniformly distributed tracers in each ($\Rightarrow$ 19,600 tracers total). These are advected for a total for $p = 200$ flow periods using the exact solution for rotations about the z- and x-axis given in [11, 20]. The intensity of segregation $\mathscr{I}(n)$ is tracked as a function of the period $n = 1, \ldots, p$. Following [19], using MATLAB's Curve Fitting Toolbox, we find τ and *bias* such that the fit based on the following ansatz is "best" in a least-squares sense[3]

$$\mathscr{I}(n) \sim (\mathscr{I}(0) - bias)\, \mathrm{e}^{-n/\tau} + bias, \tag{7}$$

where $\mathscr{I}(0) = 1$ for the chosen completely segregated IC. Note that τ is dimensionless and has the meaning of "number of periods," while *bias* allows for cases where $\mathscr{I} \nrightarrow 0$ as $n \to \infty$ (see, e.g., the discussion in [23]).

An example is shown in Fig. 2 for two different values of θ_z and θ_x and at two shell radii $\bar{R}$. The left images show the mixing of gray and black, 100 iterations after

[3] In Figs. 2, 4, 5 and 6 below, the quality of this fit is given as two numbers in brackets in the legend of the rightmost plot. The first number is the coefficient of determination R^2; the second number is the root-mean-squared error in the fit.

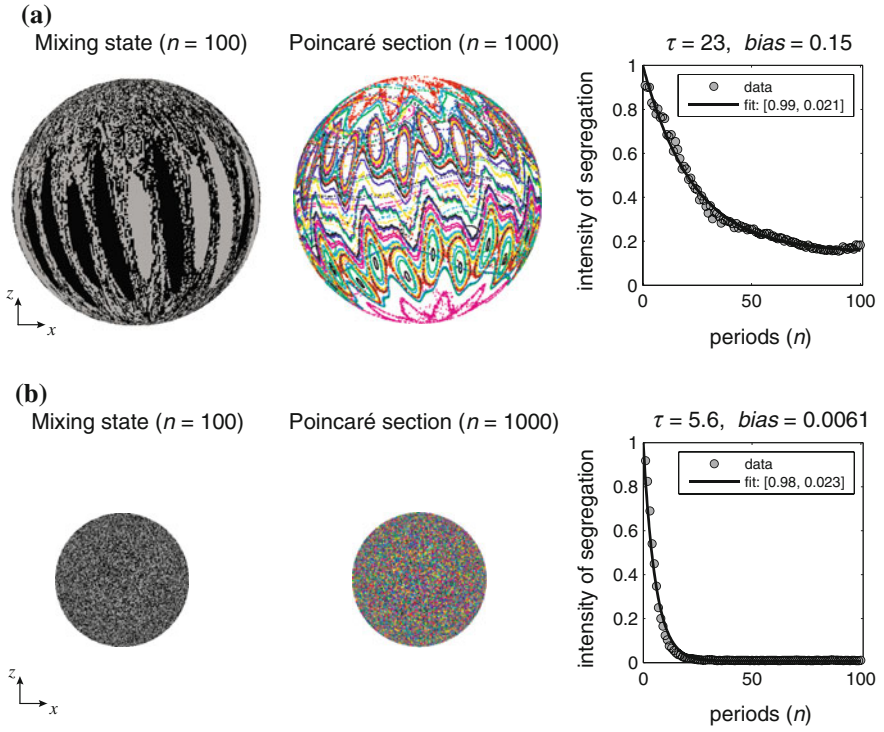

Fig. 2 Examples of mixing behaviors in the half-full blinking spherical tumbler with symmetric typical-thickness flowing layers: $\varepsilon_z = \varepsilon_x = 0.15$. **a** $\theta_z = 30°$, $\theta_x = 5°$ and $\bar{R} = 0.9$. **b** $\theta_z = 45°$, $\theta_x = 65°$ and $\bar{R} = 0.5$

starting completely segregated. The right graphs show the decay of $\mathscr{I}$. In both cases, $\mathscr{I}$ starts at 1 due to the completely segregated IC. The case in Fig. 2a mixes to some extent but not completely after 100 iterations, resulting in a relatively large *bias* of 0.15. The case in Fig. 2b mixes quickly and completely resulting in a smaller τ than the case in Fig. 2a and a *bias* of almost 0.

Therefore, we have two numbers, namely τ and *bias*, that measure the "quality of mixing" for each numerical mixing experiment—τ is a time constant measuring how quickly the mixture is homogenized, while *bias* is a measure of how thoroughly the asymptotic state is mixed. Large *bias* corresponds to incomplete mixing and suggests the presence of large unmixed Kolmogorov–Arnold–Moser (KAM) "islands." Meanwhile, a large τ corresponds to slow mixing, say on a surface with large area with suboptimal choice of rotation angles. Finally, a low τ and a low *bias* correspond to "good" mixing as the homogenization of the segregated IC is fast and thorough. Next, we study how τ and *bias* vary with the parameters of the model.

The most natural parameters to vary are the angles of rotation about each axis, θ_z and θ_x, and the shell radius $\bar{R}$. Additionally, ε_z ($\equiv \varepsilon_x$ in the symmetric case) can be varied, corresponding to different types of granular materials in the tumbler or

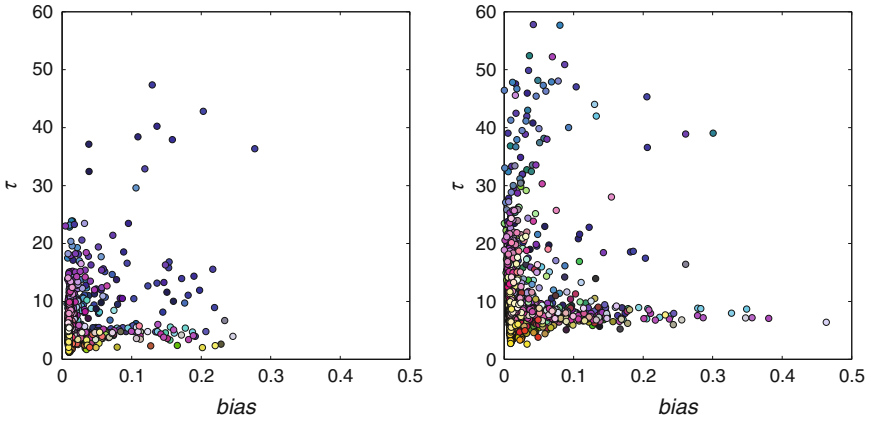

Fig. 3 τ-*bias* scatterplots for $\varepsilon_z = \varepsilon_x = 0.15$ (*left*) and $\varepsilon_z = \varepsilon_x = 0.05$ (*right*). $\mathscr{I}$ is computed on hemispherical shells with $\bar{R}$ as a parameter. Data points are color-coded based on the values of θ_z, θ_x and $\bar{R}$ as described in the text

different rotation rates. To ascertain the effect of the variation of θ_z, θ_x and $\bar{R}$, in Fig. 3 we show a scatterplot of τ versus *bias* for independent choices of θ_z and θ_x between 5° and 355° in increments of 25° and 10 equispaced values of $\bar{R}$ between $\varepsilon_z + 0.1$ and 0.95. Additionally, two values of ε_z are considered: (a) $\varepsilon_z = 0.15$, a value realized for a dry granular system of 3 mm chrome steel beads in a tumbler of 28 cm diameter rotating at 0.168 rad/s, and (b) $\varepsilon_z = 0.05$, a thinner flowing layer observed for 1.16 mm steel beads in this same tumbler rotating at 0.052 rad/s [24].[4]

Each data point in Fig. 3 is color-coded as follows: it has an red-green-blue (RGB) additive color intensity with %R given by $\theta_z/(2\pi)$, %G given by $\theta_x/(2\pi)$ and %B given by $\bar{R}$. Hence, data points in the blue spectrum correspond to angles of rotation close to 5° and shell radii $\bar{R}$ close to 1. Similarly, data points that appear orange correspond to angles of rotation close to 355° but shell radii close to $\varepsilon_z + 0.1$. Likewise, white corresponds to both θ_z and θ_x near 355° with $\bar{R}$ near 1, and so forth.

First, consider the black-blue-purple range of colors of data points, which correspond to θ_z and θ_x both near 5° for a variety of $\bar{R}$. It is immediately clear that these represent the majority of the "outliers" in the scatterplots in Fig. 3. To see why, recall that our IC is symmetric about $z = 0$ and antisymmetric about $x = 0$. In addition, θ_z is the angle of rotation about the z-axis, which is the first axis of rotation in this protocol. It follows that for values of θ_z close to 5°, the IC is barely altered by the rotation about the first axis. Then, since the angle of rotation about the second axis is small (θ_x near 5° for these data points), the almost-z-symmetric state that the mixture is left in leads to very little rearrangement of the material during the second

[4]Though these numbers are for a quasi-2D circular tumbler, they are relevant here too thanks to the geometric similarity assumption used to construct the 3D continuum model. That is to say, if we suppose the quasi-2D tumbler of Jain et al. [24] is the $x = 0$ (or $z = 0$) cut through the 3D spherical tumbler considered here, then ε_z (or ε_x) herein is precisely δ_0/R in [24].

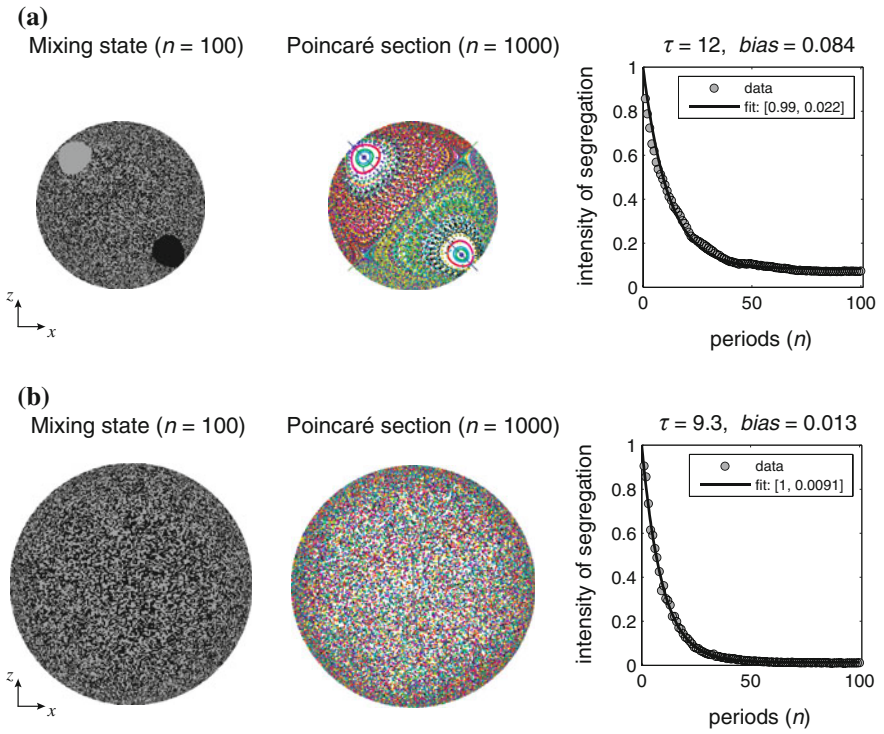

Fig. 4 Further examples of mixing behaviors in the half-full blinking spherical tumbler with symmetric typical-thickness flowing layers: $\varepsilon_z = \varepsilon_x = 0.15$. **a** $\theta_z = \theta_x = 180°$ and $\bar{R} = 0.62$. **b** $\theta_z = 355°$, $\theta_x = 180°$ and $\bar{R} = 0.88$

rotation. Figures 2a and 5a illustrate a typical such scenario for $\varepsilon_z(= \varepsilon_x) = 0.15$ and $\varepsilon_z(= \varepsilon_x) = 0.05$, respectively. We term it "lots of cutting but no shuffling," using the terminology introduced in [7, 10], due to the pattern of thin filaments that are barely reoriented from each other that emerges in the mixture after 100 periods. Not surprisingly, the corresponding Poincaré sections in Figs. 2a and 5a show a great deal of regularity, especially in Fig. 2a, rather than chaos. As θ_z becomes larger, the distribution of material is "less symmetric" about the z when the rotation about the x begins, so the $(\tau, bias)$ pairs, which are now in the pink color spectrum, are no longer on the outer edges of the scatterplot.

Next, we observe the large cluster of data points, situated near $(\tau, bias) = (0, 0)$ in the scatterplots, that have mostly colors in the white-yellow-orange-red spectrum. From the color-coding convention, these correspond to choices of θ_z near 355°, and choices of θ_x that increase proportionately with $\bar{R}$. Notice this avoids the "lots of cutting and no shuffling" scenario previously described. Figures 2b and 5b show such cases for $\varepsilon_z(= \varepsilon_x) = 0.15$ and $\varepsilon_z(= \varepsilon_x) = 0.05$, respectively. It appears the dynamics on the 2D invariant surfaces on which particles are restricted for these sets of para-

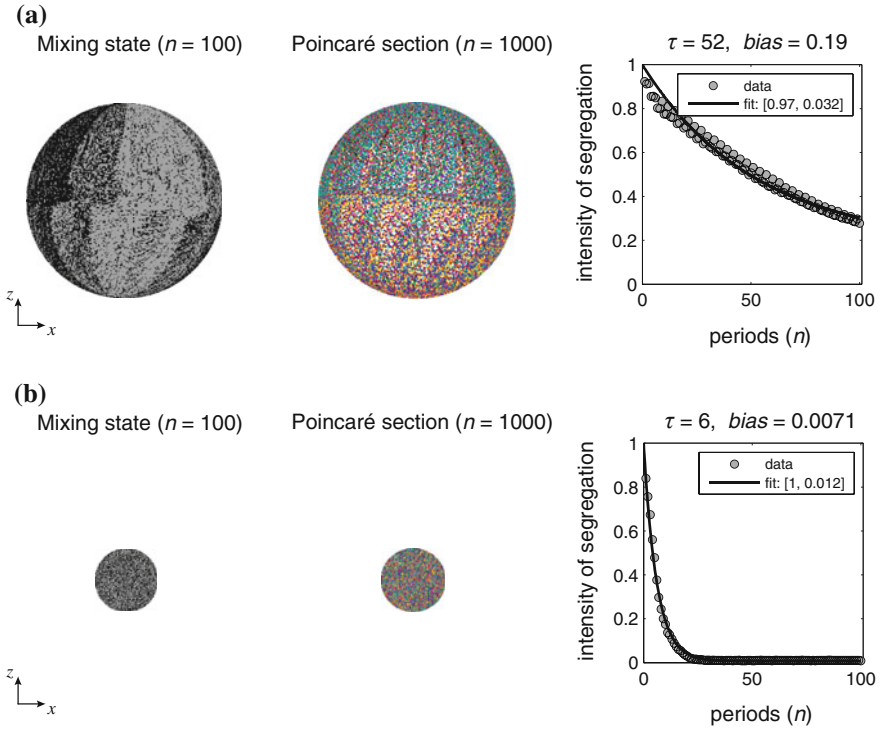

Fig. 5 Examples of mixing behaviors in the half-full blinking spherical tumbler with symmetric thin flowing layers: $\varepsilon_z = \varepsilon_x = 0.05$. **a** $\theta_z = 30°$, $\theta_x = 180°$ and $\bar{R} = 0.71$. **b** $\theta_z = 305°$, $\theta_x = 55°$ and $\bar{R} = 0.23$

meters are fully chaotic, i.e., mixing occurs and no KAM islands or other barriers to transport can be distinguished. This is further supported by considering the Poincaré sections in Figs. 2b and 5b, which exhibit no regularity of any kind.

As mentioned earlier, low-period islands are barriers to transport and they lead to incomplete mixing [3]. An example of period-one KAM islands can be found in Fig. 4a, while an example of period-two islands is presented in Fig. 6a. Though *bias* is significant for both of these cases, τ is not very large, showing that a significant "chaotic sea" exists between the islands and the material therein is quickly homogenized. This is clearly seen in both the mixing patterns and the Poincaré sections in Figs. 4a and 6a, with the islands from the Poincaré sections clearly corresponding to unmixed regions of the same shape.

Independent of low-period structures, some protocols mix very slowly. Examples of such protocols that do eventually homogenize most of the mixture are shown in Figs. 4b and 6b. This is not due to KAM islands because, as the Poincaré sections corresponding to these figures show, there are none on these shells. It is simply that these protocols do not reorient material effectively due to the choice of rotation angles (specifically $\theta_z \approx 360°$). Consequently, mixing is "suboptimal."

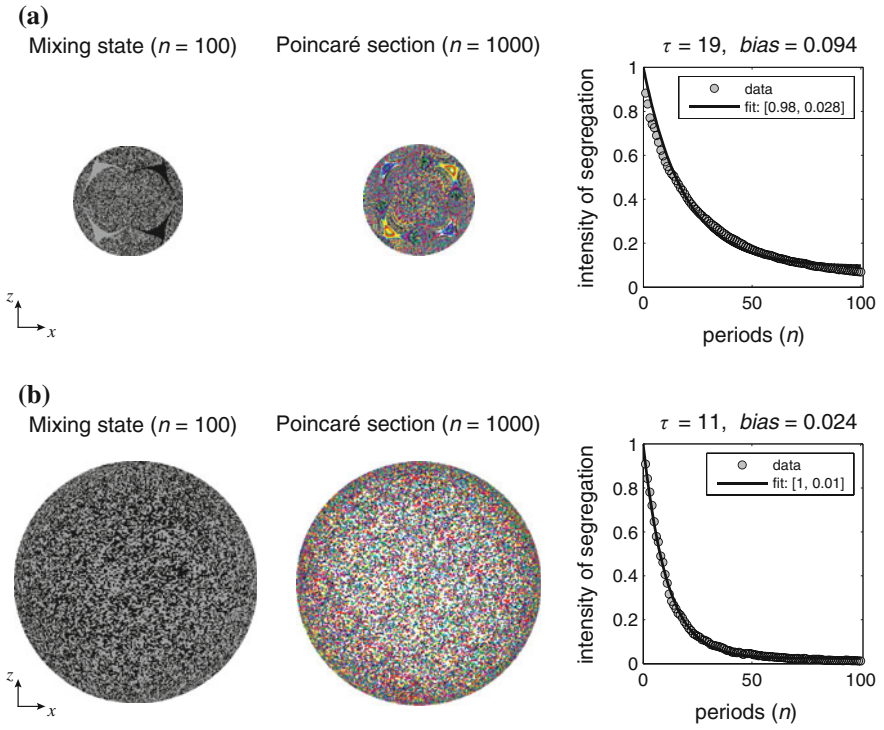

Fig. 6 Further examples of mixing behaviors in the half-full blinking spherical tumbler with symmetric thin flowing layers: $\epsilon_z = \epsilon_x = 0.05$. **a** $\theta_z = \theta_x = 85°$ and $\bar{R} = 0.4$. **b** $\theta_z = 355°$, $\theta_x = 205°$ and $\bar{R} = 0.88$

To better summarize the data from the scatterplots in Fig. 3, in Fig. 7 we show some statistics of the distributions of the values of τ and *bias*. Clearly, the τ distribution's peak for the case with a thinner flowing layer is shifted to a larger value of τ showing that mixing is generally worse for a thinner flowing layer. However, for both Fig. 7a, b we see that, for most choices of angles, most shells mix quickly and thoroughly with the poor mixing examples falling in the tails of the distributions. Additionally, when all τ and *bias* values corresponding to a given $\bar{R}$ are averaged over all choices of (θ_z, θ_x) a clear trend emerges. Larger $\bar{R}$ correspond to slower and less complete mixing, on average. This can be explained by noting that larger shells have more area, thus mixing is (on average) slower. In addition, the shells with large $\bar{R}$ are those that mix the poorest, by far, when θ_z and θ_x are near 5°, therefore large $\bar{R}$ also correlates with incomplete mixing, on average. One way to motivate this is to realize that for some of the lowest angles of rotation material on the shells with largest radius either never enters the flowing layer or becomes "stuck" in the flowing layer due to the small rotations about each of the two axes.

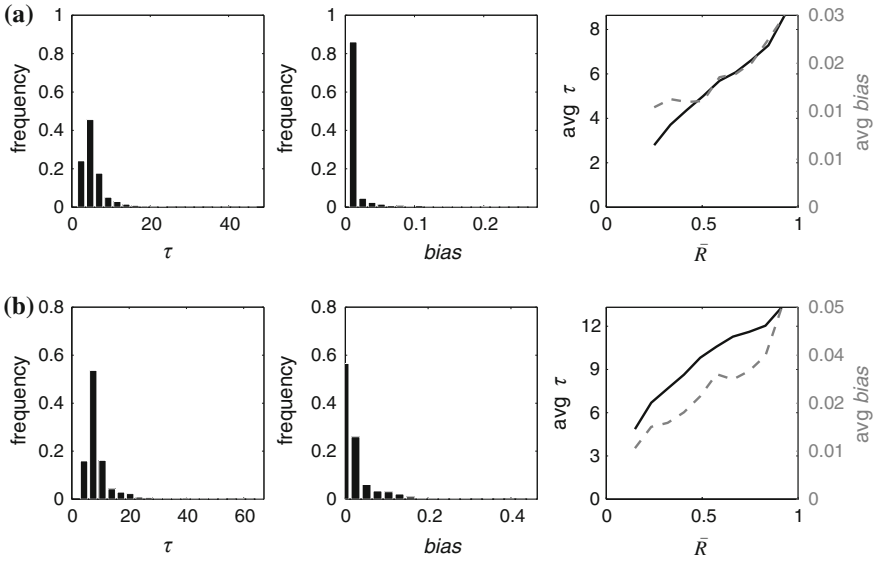

Fig. 7 Statistics of the τ-*bias* scatterplots from Fig. 3. In the rightmost column, the *black solid* and *dashed gray curves* represent the averages of τ and *bias*, respectively, over all (θ_z, θ_x) as functions of $\bar{R}$. For large τ and large *bias* there are very few contributions to the histograms, nevertheless we show the full range for completeness. Note the shift of the peak to the bin centered at $bias = 0$ in (**b**). **a** Flowing layer of typical thickness: $\varepsilon_z = \varepsilon_x = 0.15$. **b** Thin flowing layer: $\varepsilon_z = \varepsilon_x = 0.05$

4 Conclusion

The work described above exemplifies the practical difficulty in determining the "best" parameters for "good mixing" in a physically realistic 3D chaotic flow. Both the time to mix and the degree of mixing are important. The τ-*bias* approach is useful in identifying which parameters result in good mixing according to both of these measures, but does have some drawbacks. First, it requires methodically testing the entire parameter space (here, θ_z, θ_x, $\varepsilon_x = \varepsilon_z$ and $\bar{R}$), which is possible due to the availability of a continuum model with an analytic solution [11, 20]. Still, studying mixing would be much more difficult with a more complicated flow model or, worse, no model at all. Second, the τ-*bias* approach only clarifies "what" protocols mix or do not mix, but not "why" they do or do not. Clarifying the latter still requires interpretation and physical insight. Nevertheless, the results presented above demonstrate a methodology to analyze the quality of mixing in a 3D chaotic system.

Acknowledgments I.C.C. was supported, in part, by a Walter P. Murphy Fellowship from the Robert R. McCormick School of Engineering and Applied Science and by US National Science Foundation grant CMMI-1000469 at Northwestern and by the LANL/LDRD Program through a Feynman Distinguished Fellowship at Los Alamos National Laboratory, which is operated by Los Alamos National Security, L.L.C. for the National Nuclear Security Administration of the U.S. Department of Energy under contract DE-AC52-06NA25396. We thank Stephen Wiggins for suggesting the τ-*bias* scatterplots and useful discussions.

References

1. MiDi, G.D.R.: Eur. Phys. J. E **14**, 341 (2004). doi:10.1140/epje/i2003-10153-0
2. Mehrotra, A., Muzzio, F.J.: Powder Technol. **196**, 1 (2009). doi:10.1016/j.powtec.2009.06.008
3. Ottino, J.M.: The Kinematics of Mixing: Stretching, Chaos, and Transport, Cambridge Texts in Applied Mathematics, vol. 3. Cambridge University Press, Cambridge (1989)
4. Aref, H.: J. Fluid Mech. **143**, 1 (1984). doi:10.1017/S0022112084001233
5. Wightman, C., Moakher, M., Muzzio, F.J., Walton, O.: AIChE J. **44**, 1266 (1998). doi:10.1002/aic.690440605
6. Gilchrist, J.F., Ottino, J.M.: Phys. Rev. E **68**, 061303 (2003). doi:10.1103/PhysRevE.68.061303
7. Juarez, G., Lueptow, R.M., Ottino, J.M., Sturman, R., Wiggins, S.: EPL **91**, 20003 (2010). doi:10.1209/0295-5075/91/20003
8. Meier, S.W., Lueptow, R.M., Ottino, J.M.: Adv. Phys. **56**, 757 (2007). doi:10.1080/00018730701611677
9. Zaman, Z., D'Ortona, U., Umbanhowar, P., Ottino, J.M., Lueptow, R.M.: Phys. Rev. E **88**, 012208 (2013). doi:10.1103/PhysRevE.88.012208
10. Sturman, R., Meier, S.W., Ottino, J.M., Wiggins, S.: J. Fluid Mech. **602**, 129 (2008). doi:10.1017/S002211200800075X
11. Christov, I.C., Lueptow, R.M., Ottino, J.M., Sturman, R.: SIAM J. Appl. Dyn. Syst. **13**, 901 (2015). doi:10.1137/130934076
12. Wiggins, S.: J. Fluid Mech. **654**, 1 (2010). doi:10.1017/S0022112010002569
13. Anderson, P.D., Galaktionov, O.S., Peters, G.W.M., van de Vosse, F.N., Meijer, H.E.H.: J. Non-Newtonian Fluid Mech. **93**, 265 (2000). doi:10.1016/S0377-0257(00)00120-8
14. Galaktionov, O.S., Anderson, P.D., Kruijt, P.G.M., Peters, G.W.M., Meijer, H.E.H.: Comput. Fluids **30**, 271 (2001). doi:10.1016/S0045-7930(00)00020-7
15. Schlick, C.P., Christov, I.C., Umbanhowar, P.B., Ottino, J.M., Lueptow, R.M.: Phys. Fluids **25**, 052102 (2013). doi:10.1063/1.4803897
16. Lackey, T.C., Sotiropoulos, F.: Phys. Fluid **18**, 053601 (2006). doi:10.1063/1.2201967
17. Porion, P., Sommier, N., Faugère, A., Evesque, P.: Powder Technol. **141**, 55 (2004). doi:10.1016/j.powtec.2004.02.015
18. Remy, B., Glasser, B.J., Khinast, J.G.: AIChE J. **56**, 336 (2010). doi:10.1002/aic.11979
19. McIlhany, K.L., Wiggins, S.: Microfluid Nanofluid **10**, 249 (2010). doi:10.1007/s10404-010-0656-6
20. Christov, I.C.: From streamline jumping to strange eigenmodes and three-dimensional chaos: a tour of the mathematical aspects of granular mixing in rotating tumblers. Ph.D. thesis, Northwestern University, Evanston, Illinois (2011)
21. Pignatel, F., Asselin, C., Krieger, L., Christov, I.C., Ottino, J.M., Lueptow, R.M.: Phys. Rev. E **86**, 011304 (2012). doi:10.1103/PhysRevE.86.011304
22. Danckwerts, P.V.: Appl. Sci. Res. A **3**, 279 (1952). doi:10.1007/BF03184936
23. Lacey, P.M.C.: J. Appl. Chem. **4**, 257 (1954). doi:10.1002/jctb.5010040504
24. Jain, N., Ottino, J.M., Lueptow, R.M.: J. Fluid Mech. **508**, 23 (2004). doi:10.1017/S0022112004008869

Numerical Simulation of Abrasive Wear Using FEM—SPH Hybrid Approach

Krzysztof Damaziak and Jerzy Małachowski

Abstract In the article fully dynamic analysis of a special stand for wear measurements is presented. The analysis is focused on the dynamic interaction of lining samples rotating with high angular speed and counter surface, with the special attention to wear process. Typical approach to include abrasive wear in the numerical simulations of structure modeled in a macro scale is to use one of many semi-analytical wear laws. One of the most important phenomena accompanying abrasive wear, i.e., change of geometry of interacting surfaces is usually neglected. The main idea of the proposed approach is to merge meshless smoothed particle hydrodynamic (SPH) method with finite element (FE) model. The global model is described with FE, while surface layer, where abrasive wear takes place, is modeled using SPH. Owing this, it is possible to introduce sudden change of discretization level in the numerical model. Due to properties of mathematical description of SPH, simulation of abrasion with this technique is much closer to the physical phenomena. Proposed modeling technique is presented in the numerical model simulating dynamic interaction between samples of lining and counter sample surface of special testing stand. Due to very dynamic nature of abrasive wear process, explicit time integration scheme is used. Thermal–mechanical coupling and heat generation by friction forces are also included in the model. Rate of change of geometry of surface, as well as obtained temperature gradients proofs rightness of choice of explicit time integration scheme.

K. Damaziak (✉) · J. Małachowski (✉)
Faculty of Mechanical Engineering, Department of Mechanics and Applied Computer Science, Military University of Technology, 2 Gen. S. Kaliskiego Str., 00-908 Warsaw, Poland
e-mail: krzysztof.damaziak@wat.edu.pl

J. Małachowski
e-mail: jerzy.malachowski@wat.edu.pl

J. Awrejcewicz (ed.), *Dynamical Systems: Modelling*, Springer Proceedings in Mathematics & Statistics 181, DOI 10.1007/978-3-319-42402-6_14

1 Introduction

Numerical modeling of brakes engages scientists and engineers since decades. One of the most important causes of demand for braking simulation is squeal—vibrations during braking [1]. These vibration and noise of braking systems are significant criteria that govern machine quality [2] and are main driving force behind ongoing search of analytical tools capable to accurate predicting of a brake behavior.

All of the most important phenomena influencing brake behavior have their source in the micro level and are directly connected to the surface wear. This also includes vibrations excitation, which is connected to the ongoing changes of contact surface geometry [2–4] resulting from wear processes. The classical way to account for wear, which is to employ approach based on Archard's law, does not give an answer to the problem, since geometry "changes" during simulation are introduced by parametric measure of wear and not real change of coordinates. Due to this fact, in numerical analyses of brakes, the focus was shifted from classical dynamics in frequency domain to the problem of inclusion of changes of the shape of contacting surfaces. Two major ways to address the problem evolved. It is done either by enrichment of macro models of full brakes by formulas accounting for wear [5–7], or by development of micro-scale models [8, 9]. The common idea behind these attempts is to find a way to account for changes in contact parameters caused by a change of surface layer geometry. Unfortunately, wear processes are very complex, which lead to a vast number of simplifications used in these models. Therefore, none of the mentioned approaches was able to become commonly accepted method or tool of wear modeling [10, 11].

In the paper the authors introduce yet another idea of the abrasive wear modeling. The method is based solely on governing equations and commonly used material models and therefore does not require extensive tribological tests. The idea is to combine finite element method (FEM) with meshless description of continuum implemented in smoothed particle hydrodynamics (SPH) environment. The reason for combination of these two methods lies in limitation of FEM when dealing with large deformations and elements numerical erosion (not to be confused with erosive wear). Compared to FEM, a removal of the eroded particle does not introduce geometry discontinuities. Moreover, SPH is better suited to handle large distortions [12].

2 Adopted Modeling Method

Abrasive wear takes place in the surface layers belonging to contacting bodies in relative motion. It becomes dominating wear mechanism in case of interaction of surfaces with significantly different hardness, which is typical for lining and brake disk. During the tangential motion the material is removed from softer surface by

combined action of micro-ploughing and micro-cutting [13]. In other words, it is a phenomenon connected with dynamic interaction between contacting bodies that takes place in microscale and involves loss of material cohesion. Additionally, in the case of brake operation, kinetic energy is changed to the heat and thus high temperature strongly influences the process. From the point of view of numerical methods all above translates to presence of material nonlinearities, geometrical nonlinearities, thermal–mechanical coupling, boundary conditions nonlinearities (contact), and loss of cohesion. The problem is nonstationary.

Looking at the capabilities of a numerical subroutines, finite element method—the numerical method most common used today—can handle all of the above-mentioned tasks, with some reservation relating to the decohesion process. The real problems arise when we start to look at the dimensions.

As it was mentioned, abrasive wear takes place in the surface layer and its "natural size" are micrometers at most [14]. On the other hand, typical size of the whole brake is tens of centimeters. So, if we want to include effects of abrasive wear in the FE model of the whole brake, we will have to make sure, that discretization level is sufficient for both scales. This can easily end up with the model that is too big for the available hardware.

The other very unpleasant FE feature connected with the decohesion modeling is that the most of the techniques adopted by FEM generates results that are element size dependent and are introducing discontinuities. Figure 1 shows typical situation during simulation with element erosion included. Empty spaces left after eroded elements are clearly visible. Though the loss of cohesion is included, obviously we are far away from the effects of abrasion.

One of the methods that could overcome these problems is the smoothed particle hydrodynamics. It belongs to the family of so-called meshfree methods and therefore it overcomes number of problems related to domain discretization using elements with predefined geometry and finite dimensions. The basic concept behind SPH is the representation of a body by an ensemble of particles i, each carrying mass m_i,

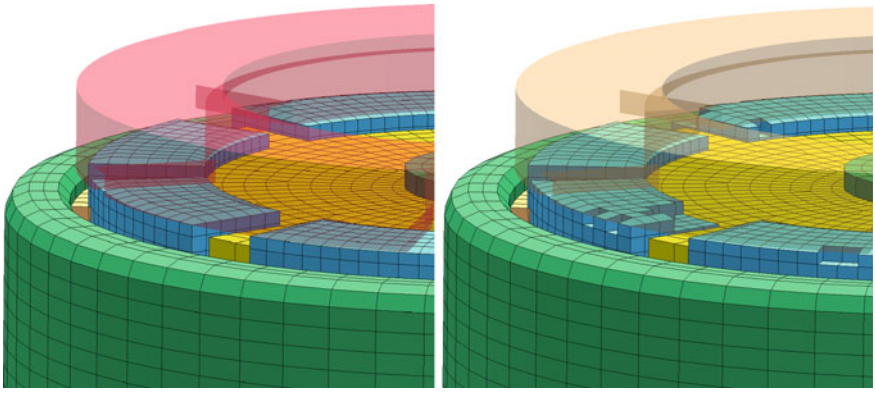

Fig. 1 Erosion of a material in the FE domain

momentum $m_i v_i$, and other functions f_i. The concept was developed independently by Lucy [15] and Gingold and Monaghan [16]. They assumed that the values of a function are obtained by a local averaging process using the expression (1) [17, 18]:

$$f(x) \simeq <f>(x) = \int_{\Omega} f(x^{'}) W(x - x^{'}, h)\, \mathrm{d}x^{'}, \tag{1}$$

where $f(x)$—value of a function at x, $<f>$—local average (approximation) of $f(x)$, $f(x')$—value of a function in the location other than x, $W(x - x', h)$—smoothing kernel, h—independent variable called smoothing length, Ω—domain.

The concept, that domain represented by points is replaced by a body represented by particles allows to transform integration into summation over discrete set of particles

$$\langle f \rangle(x) = \int_{\Omega} f(x^{'}) W(x - x^{'}, h)\, \mathrm{d}x^{'} \simeq \sum_{q=1}^{N} f(x_q) W(x - x_q, h)\, \Delta V_q, \tag{2}$$

where N—number of particles within W support, V—volume covered by W.

Taking density ρ as an example we obtain

$$\langle \rho \rangle(p) = \sum_{q} m_q W(|x_p - x_q|, h), \tag{3}$$

where p—particle for which density value is approximated, q—particle within the W support and x_p, x_q describe particles coordinates.

It can be said, that the mass of each particle is smeared out over its kernel function's W support. The density of the particle p is obtained by summing over the contributions of particles q. The graphic representation of particle p, q, and variable h is presented in Fig. 2.

For the purpose of this article, it is important to notice that removal of one particle from the set representing a body does not introduce any discontinuities to the model.

Functions W are very often spherical or bell-like functions, just like the function (4) used by Monagham and Lattanzio [19]:

$$W(R,h) = \alpha_d \begin{cases} \frac{2}{3} - R^2 + \frac{1}{2}R^3, & 0 \le R < 1 \\ \frac{1}{6}(2-R)^3, & 1 \le R < 2 \\ 0, & R \ge 2 \end{cases}, \tag{4}$$

where $\alpha_d = \frac{1}{h}$; $\frac{15}{7\pi h^2}$; $\frac{3}{2\pi h^3}$ for 1-D, 2-D and 3-D space, respectively. Figuratively speaking, image of a small sphere that is very often connected to the word "particle" is quite close to the actual mathematical description of a continuum adopted in SPH. Coming back to the modeling of brake linings that are very often

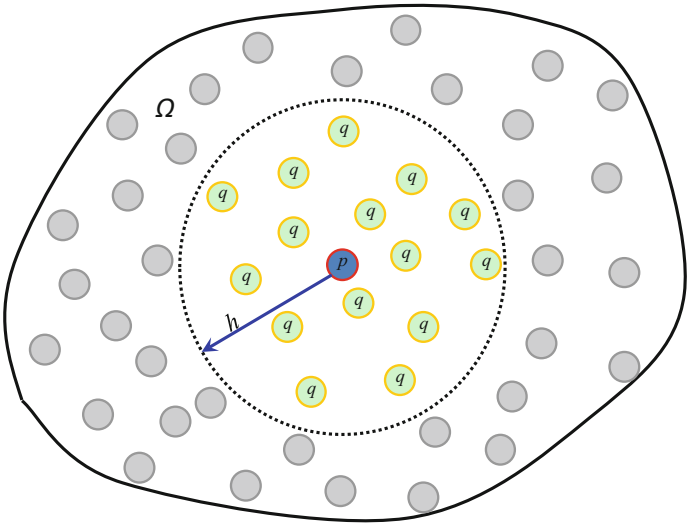

Fig. 2 Graphic representation of the particle approximation concept

made from granular materials, it must be said that such "spherical in nature" numerical representation of lining surface layer is much closer to the reality than hexagons or tetragons used by FEM.

SPH features described above underlying the choice of the method to represent surface layer in the numerical simulation of braking. It was decided, that most of the model will be represented by FEM and a layer where abrasive wear is expected will be represented by SPH. Both domains will be connected via kinematic constrains forcing set of SPH particles to follow movement of set of FE nodes (see Fig. 3).

It was decided that the wear will be connected with the effective plastic strain (see Eq. (5)), i.e., the particle where predefined value of effective plastic strain will be achieved, will "erode," that is its stiffness will be set to 0.

$$\varepsilon_{ef}^{p} = \int_{0}^{t} \left(\frac{2}{3} \dot{\varepsilon}^{p} \right)^{\frac{1}{2}} \mathrm{d}t, \tag{5}$$

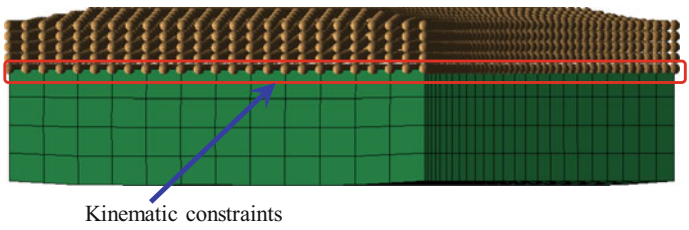

Fig. 3 FEM and SPH domains. Zone where kinematic constraints were introduced is marked

where $\dot{\varepsilon}^p$—plastic strain rate.

The mechanical part of the problem was solved by the integration of full dynamic equation in time domain using explicit central difference method [20].

Thermal part of the problem was shrink to a conduction problem, described by the Fourier's equation (6)

$$\frac{\mathrm{d}E_T}{\mathrm{d}t} = \frac{1}{\rho}\nabla(k\nabla\Theta), \tag{6}$$

where E_T—thermal energy per unit mass ρ—density, Θ—temperature, k—thermal conductivity. This applies for both methods, meaning that the Eq. (6) is the governing equation in FEM and in SPH. In case of FEM, above equation takes form [21]:

$$\mathbf{C}\frac{\mathrm{d}\boldsymbol{\Theta}}{\mathrm{d}t} + \mathbf{K}\boldsymbol{\Theta} = \mathbf{R}, \tag{7}$$

where $\mathbf{C}$—heat capacity matrix, $\mathbf{K}$—conductivity matrix, $\mathbf{R}$—vector of heat sources, $\boldsymbol{\Theta}$—temperature, while in SPH Eq. (6) is approximated by [22]

$$\frac{\mathrm{d}E_T}{\mathrm{d}t} = \sum_j \frac{m_j}{\rho_i\rho_j}\frac{k_i - k_j}{\left|x_{ij}\right|^2}x_{ij}\nabla_i W_{ij}, \tag{8}$$

where m—mass of particle, W—kernel function, x—location of particles.

So-called one-way thermal–mechanical coupling was used in analyses. Equations (7) and (8) were solved for the temperature Θ independently to the mechanical part of the problem. Then displacement field and strain tensor are updated to account for the thermal expansion.

3 Numerical Model

In general, numerical model used in simulations was the simplified version of the FEM model of IL-68 machine [23]. The IL-68 machine was designed and built in the Institute of Aviation located in Warsaw (Poland). It was created to test performance of brake pads used by aero industry. General view of the testing stand is shown in Fig. 4.

Basically, it consists of a rotating part with so-called counter sample mounted in it, which is acting as brake disk and a head pushing against counter sample, where lining samples are mounted. The special stand enabled the measurement of such quantities as angular velocity of the rotating part, moment generated by friction forces, braking time, and wear of lining defined as its thickness reduction. The schematic explaining its principle of work is shown in Fig. 5.

The numerical model mapping work of the IL-68 machine is shown in Fig. 6.

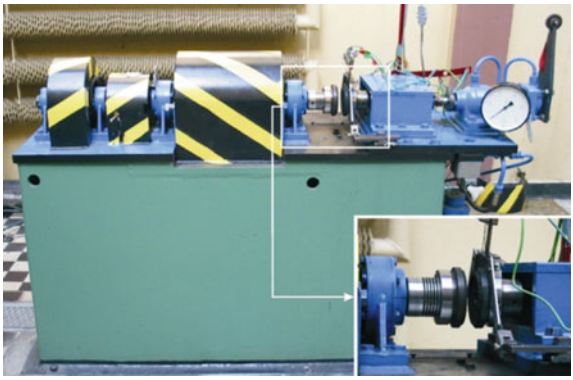

Fig. 4 General view of IL-68 machine

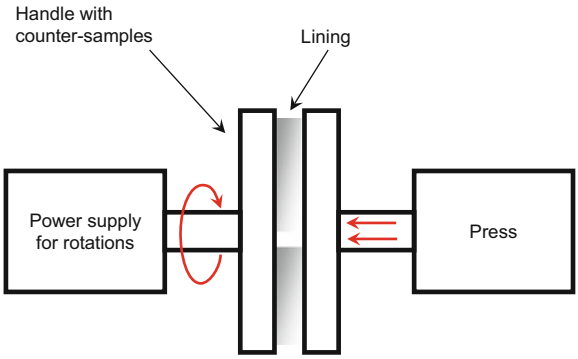

Fig. 5 Schematic describing the special stand IL-68 principle of work

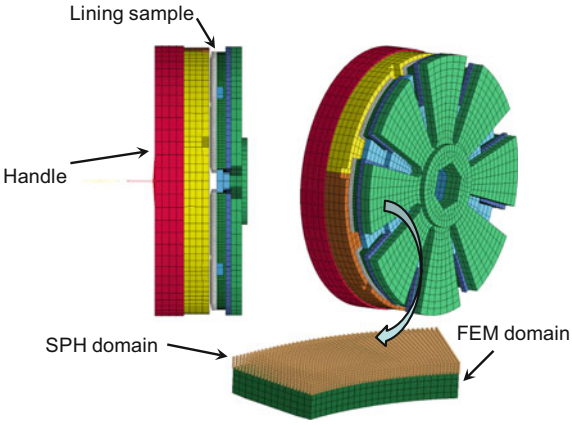

Fig. 6 Numerical model representing IL-68 machine. Lining sample presented in the *bottom* utilized hybrid representation consists of FE and SPH domains

Initial boundary conditions are shown in Fig. 7 and listed in Table 1. Initial angular velocity ω_0 was defined for counter samples. Lining samples had predefined linear velocity $v(t)$ changing over time, so that they move toward the counter samples up to the moment when spring k generates force pressing counter samples

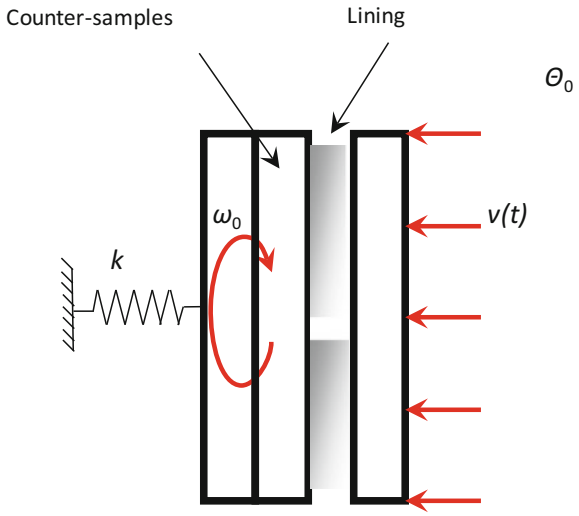

Fig. 7 Schematics of boundary conditions applied to the numerical model of IL-68

Table 1 Initial and boundary conditions

Name	Symbol	Value
Prescribed velocity	$v(t)$ (mm/s)	$v = 200\cos(0.002t/\pi)$
Initial temperature	Θ_0 (°)	20°
Initial angular velocity	ω_0 (rad/s)	628

against lining. All elements had prescribed initial temperature Θ_0. The model consisted of 75612 nodes, 17407 elements, and 49000 particles. As it was mentioned earlier, SPH material had added failure criterion based on effective plastic strain (see Table 2). Explicit algorithm was chosen to integrate equation of motion over time. In thermo-mechanically coupled analysis heat generation by friction forces was included.

Although the numerical model was built based on the IL-68 testing machine, it should be stressed that its purpose was to develop methodology to include abrasive wear in the macroscopic model of brake and not to validate results. Therefore the surface layer modeled using SPH domain was relatively thick, to save computational time.

Table 2 Material properties of SPH domain

Name	Symbol	Value
Elastic modulus	E (MPa)	2.2×10^5
Yield stress	σ_y (MPa)	513.0
Poisson ration	ν	0.3
Plastic strain at failure	ε_f	0.1
Density	ρ (t/mm^3)	7.0×10^{-9}
Specific heat	c_p (mm^2/s^2 deg)	4.8×10^8
Thermal conductivity	k (t mm/s^2 deg)	50.0

4 Results

In the following figures, global view of the lining samples presenting temperature and equivalent Huber–Mises–Hencky (HMH) stresses distribution is shown (Figs. 8 and 9).

It can be noticed that temperature raise is very rapid. After 0.023 s of analysis time maximum local temperature in the most loaded particles raised from initial 20° to 314°. As it was shown in reference [23] such rapid temperature change is in line with measurements using thermovision camera and results obtained using FEM model. This shows that implementation of explicit time integration is the necessity to accurately cover such rapid changes. Unfortunately, this is also one of the biggest drawbacks of the proposed method. Keeping in mind that braking process usually last a few seconds and average integration time step was $\Delta t \approx 4.36 \times 10^{-8}$ s (with taking into consideration stability condition), it is easy to realize that analyses run times were extremely long.

Figure 10 shows one of the samples after $t = 0.09$ s of analysis time. Change in surface geometry due to particles erosion is evident. Figure 11 shows HMH stress

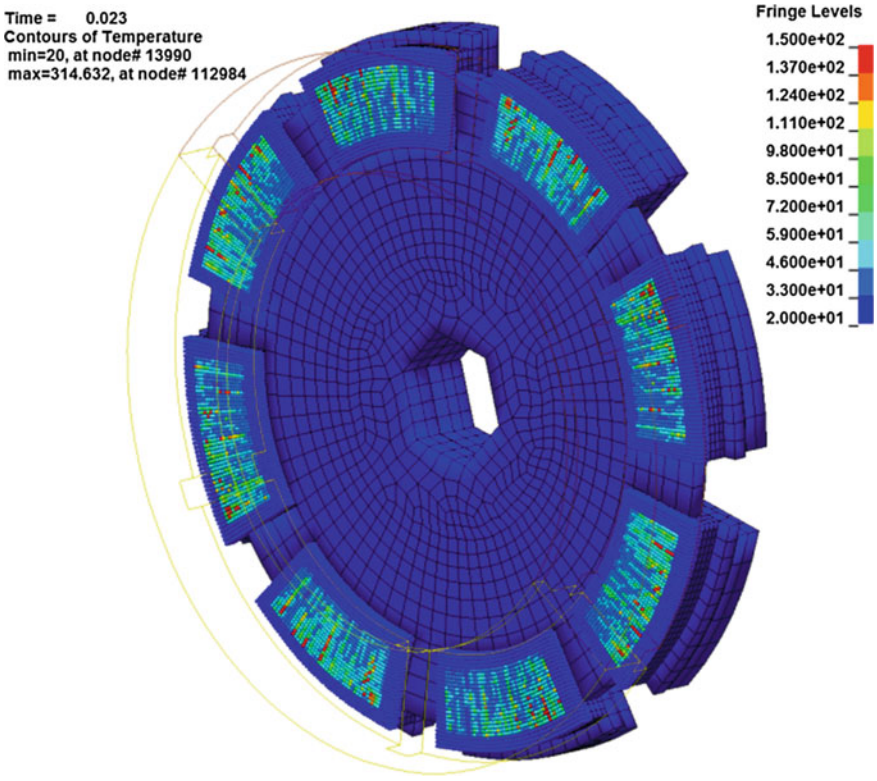

Fig. 8 Temperature (°) distribution for moment $t = 0.4$ s

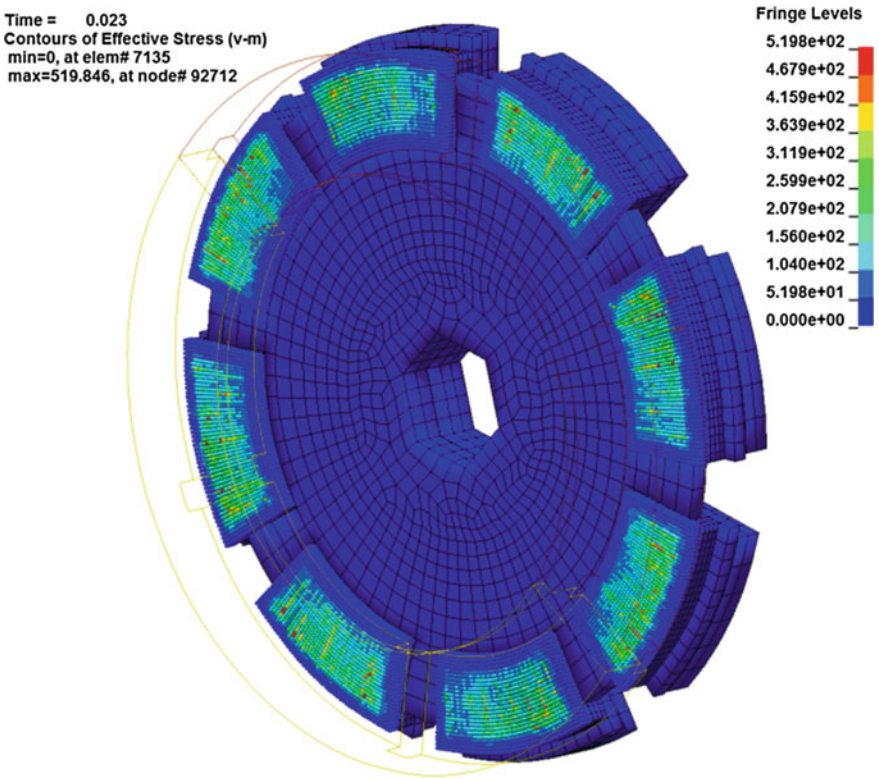

Fig. 9 Equivalent HMH stress (MPa) distribution for moment $t = 0.4$ s

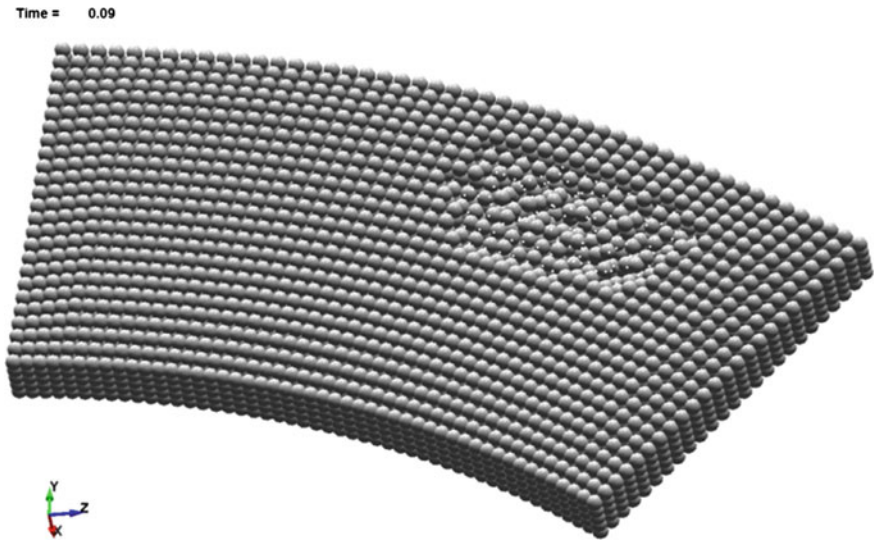

Fig. 10 Sample of lining in the analysis moment $t = 0.09$ s. Effects of numerically simulated abrasion are clearly seen

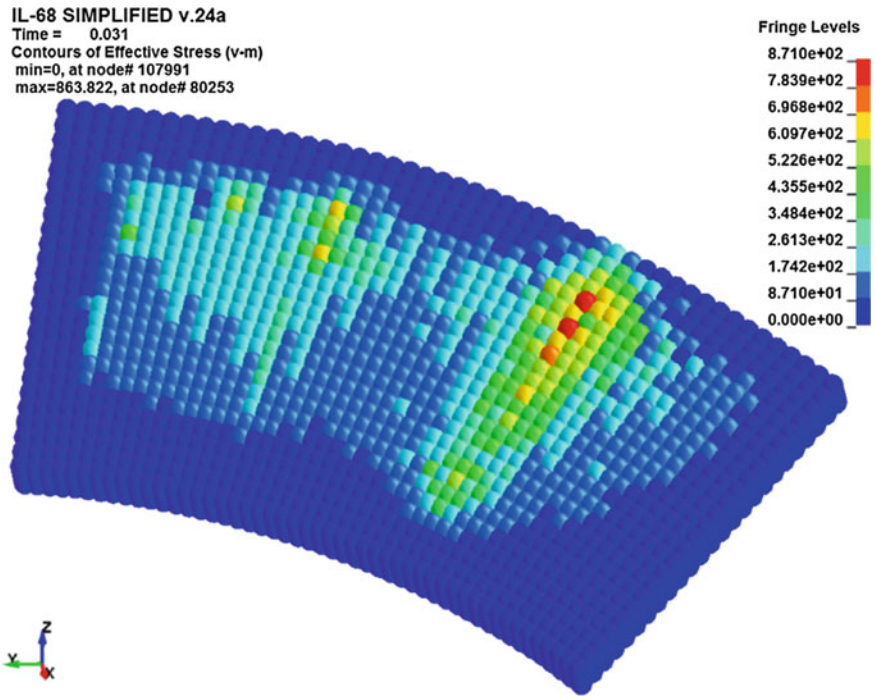

Fig. 11 HMH equivalent stress (MPa) in the sample of lining in the analysis moment $t = 0.031$ s

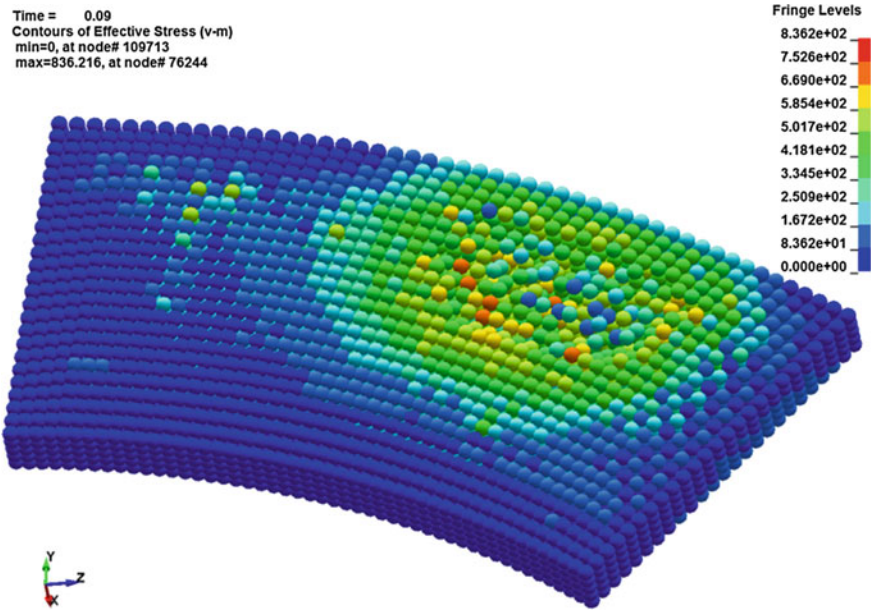

Fig. 12 HMH equivalent stress (MPa) in the sample of lining in the analysis moment $t = 0.09$ s

value in the same sample in the moment $t = 0.031$ s, when there was no wear, while Fig. 12 shows the sample in the moment $t = 0.09$ s, when wear process was already in place. Comparison of the two figures proves that numerical model predicts stress redistribution caused by change of surface layer geometry, what is in parallel with real-live observations [24].

5 Conclusions

The purpose of presented study was to develop methodology allowing to account for effects of abrasive wear in global numerical models of brakes. To reach the goal, the authors choose technique of hybrid modeling coupling the FEM and SPH method. The latter caught the attention due to properties of the mathematical model lying behind the concept of the body made of particles.

Obtained results show that the procedure can be used to describe abrasion. In the presented numerical example, heat due to friction forces, together with normal contact pressure generate strains up to the defined limit, causing particles erosion. This leads to change of geometry of the surface layer and stress redistribution.

Although proposed method does not cover many physical phenomena accompanying braking (like melting of lining particles), but still it is closer to them, than traditional FEM-based modeling methodology.

The only problem connected with the proposed approach is the necessity of implementation of explicit time integration scheme that comes from the fact that during brake process, change of such quantities like temperatures and material erosion are characterized with very dynamic nature.

In future works authors will focus on validation of the developed methodology.

References

1. Mohammed, A.A.Y., Rahim, I.A.: Analyzing the disc brake squeal: review and summary. Int. J. Sci. Technol. Res. **2**(4), 60–72 (2013)
2. Sergienko, V.P., Bukharov, S.N., Kupreev, A.V.: Noise and vibration in brake systems of vehicles. Part 1: experimental procedures. J. Friction Wear **29**(3), 234–241 (2008)
3. Anderson, A.E., Knapp, R.A.: Hot spotting in automotive friction systems. Wear **135**(2), 319–337 (1990)
4. Eriksson, M.: Friction and contact phenomena of disc brakes related to squeal. Ph.D. Thesis, Acta Universitatis Upsaliensis, Uppsala University (2000)
5. Chichinadze, A.V.: Theoretical and practical problems of thermal dynamics and simulation of the friction and wear of tribocouples. J. Friction Wear **30**(3), 199–215 (2009)
6. Müller, M., Ostermeyer, G.P.: A cellular automaton model to describe the three-dimensional friction and wear mechanism of brake systems. Wear **263**(7–12), 1175–1188 (2007)
7. Sorokatyi, R.V., Pisarenko, V.G., Dykha, M.A.: Analysis of wear surface geometry formation in plain bearings with misaligned shaft and bush axes. J. Friction Wear **34**(4), 274–280 (2013)

8. Akarca, S.S.: Modeling of subsurface deformation and damage in an aluminum-silicon alloy subjected to sliding contact. Ph.D. Thesis, University of Windsor, Ontario, Canada (2006)
9. Kucharski, S., Mroz, Z.: Identification of wear process parameters in reciprocating ball-on-disc tests. Tribol. Int. **44**, 154–164 (2011)
10. Sergienko, V.P., Bukharov, S.N., Kupreev, A.V.: Noise and vibration in brake systems of vehicles. Part 2: theoretical investigation techniques. J. Friction Wear **30**(3), 216–226 (2009)
11. Demkin, N.B., Izmailov, V.V.: The relation between the friction contact performance and the microgeometry of contacting surfaces. J. Friction Wear **31**(1), 48–55 (2010)
12. Wang, Y.-F., Yang, Z.-G.: A coupled finite element and meshfree analysis of erosive wear. Tribol. Int. **42**, 373–377 (2009)
13. Stolarski, T.: Tribology in Machine Design. Butterworth-Heinemann, Oxford (2000). ISBN 0 7506 3623 8
14. Bettge, D., Starcevic, J.: Topographic properties of the contact zones. Wear **254**(3–4), 195–202 (2003)
15. Lucy, L.B.: A numerical approach to the testing of the fission hypothesis. Astronom. J. **82**(12), 1013–1024 (1977)
16. Gingold, R.A., Monaghan, J.J.: Smoothed particle hydrodynamics: theory and application to non-spherical stars. Mon. Not. Roy. Astr. Soc. **181**, 375–389 (1977)
17. Liu, G.R., Gu, Y.T.: An Introduction to meshfree methods and their programming. Springer, Dordrecht (2005). ISBN 10: 9048168198
18. Liu, M.B., Liu, G.R.: Smoothed particle hydrodynamics (SPH): an overview and recent developments. Arch. Comput. Methods Eng. **17**, 25–76 (2010)
19. Monaghan, J.J., Lattanzio, J.C.: A refined particle method for astrophysical problems. Astron. Astrophys. **149**(1), 135–143 (1985)
20. Belytschko, T., Liu, W.K., Moran, B.: Nonlinear Finite Elements for Continua Structures. Wiley, Chichester (2006). ISBN -13 978-44719873-4
21. Lewis, R.W., Nithiarasu, P., Seetharamu, K.N.: Fundamentals of the Finite Element Method for Heat and Fluid Flow. Wiley, West Sussex (2004). ISBN 0-470-84788-3
22. Xu, J.: Heat transfer with explicit SPH method in LS-Dyna. In: Proceedings of 12th International LS-Dyna Users Conference (2012)
23. Baranowski, P., Damaziak, K., Małachowski, J., Mazurkiewicz, Ł., Polakowski, H., Piątkowski, T., Kastek, M.: Thermovision in the validation process of numerical simulation of braking. Metrol. Meas. Syst. **21**(2), 329–340 (2014)
24. Baranowski, P., Damaziak, K., Jachimowicz, J., Malachowski, J.: Propostion of numerical friction lining wear process simulation method in disk brakes. Logistyka-Nauka **3**, 75–82 (2011)

A Mathematical Model for Robot-Indenter

Marat Dosaev, Yury Okunev, Ren-Chyuan Luo, Vitaly Samsonov and Olga Vasiukova

Abstract A Dual Robot Arm manipulator for executing medical procedures is studied. An important stage of investigation is constructing a mathematical model that takes into account useful torques produced by manipulator motors, friction of different nature, etc., as well as effects of a contact interaction between manipulator sensitive element and soft biological tissue, and allows to create and to numerically work out algorithms for motor control torques. Video-tactile sensor is used as a sensitive element of the manipulator. This sensor allows estimating mechanical characteristics of soft tissue and providing control on active impact on soft tissue. During contact interaction with soft tissue, it is necessary to provide special contact conditions, such as smoothness of approaching, applied force restrictions, and so on. The control task is to realize required indentation of sensor head into soft tissue under such restrictions on applied force and indentation speed as well as on the presence of available observed data.

M. Dosaev (✉) · Y. Okunev · V. Samsonov · O. Vasiukova
Institute of Mechanics of Lomonosov Moscow State University, Moscow, Russia
e-mail: dosayev@imec.msu.ru

Y. Okunev
e-mail: common@imec.msu.ru

V. Samsonov
e-mail: samson@imec.msu.ru

O. Vasiukova
e-mail: vasyukovaola@yandex.ru

R.-C. Luo
International Center of Excellence on Intelligent Robotics and Automation Research,
National Taiwan University, Taipei, Taiwan
e-mail: renluo@ntu.edu.tw

J. Awrejcewicz (ed.), *Dynamical Systems: Modelling*, Springer Proceedings
in Mathematics & Statistics 181, DOI 10.1007/978-3-319-42402-6_15

1 Introduction

Currently, there is an active robotisation of medicine. This work is dedicated to the robot-manipulator that contacts with a soft biological tissue. Such a device can be used for massage, manual therapy, as well as in medical engineering to determine the type of soft biological tissue. Development of intellectual robotic-manipulators for medical purposes is very relevant. Robots, that equipped by tactile sensor, facilitate and accelerate a process of determining the type of tissue and searching inclusions. Using such robot for intellectual massage will make the medical massage wholesale available, which will improve health and increase efficiency of people.

For the development of a robot-manipulator that contacts with a soft biological tissue it is necessary to choose a type of a tool that generates pressure on the surface of the tissue. In the capacity of such operating element of robot it would be beneficial to use a sensor that can provide some contact interaction characteristics. For the choice of such important part of medical manipulator it is necessary to provide a mathematical modeling of robot operation including description of contact interaction between working element of robot and biological tissue.

Approaches used for the description of the mechanics of the robot-manipulator are widely covered in [1]. Developments in modeling, simulation, and control of robot manipulators are presented, for examples in [2]. Methods of control described in [3] can be used to achieve more precise operation of the manipulator.

Methods of contact mechanics are widely used in the diagnosis of pathological conditions of soft biological tissues. Survey of different models of contact problems arising from the interaction of the working element of the instrument with a tissue is covered in [4]. Manipulating robots can be used in regenerative medicine. A method for position-force control of robot-manipulator designed for massage is proposed in [5] with power training. Series of algorithms are suggested for implementing this method. Classification of the existing types of tactile sensors is listed in paper [6] with respect to technique of feedback control.

Video-tactile sensor proposed in [7, 8] allows determining the nature of tissue by estimating its effective modulus of elasticity. The silicon sensor head can be also used for executing an active pressing with a predetermined force, which will vary depending on the particular type of tissue.

We consider a problem of performing a specified manipulator links motion that will provide the determination of mechanical properties of the tissue at a given point [9]. In this paper, we consider both the video-tactile sensor (VTS) and usual sensor of longitudinal load (which costs much less than VTS) for determining a posture of the last (operating) link of the manipulator.

In this paper, we examine the mode of operation of the manipulator, in which the last link of the robot-manipulator performs a translational motion that is perpendicular to the surface of the soft tissue. We propose an approach for restoring a normal to the surface at the contact point, depending on the information obtained from the VTS or from an axial load sensor. We find relations between the angles of orientation

of the manipulator links needed for providing the motion of the sensor head along the normal to the surface.

We present an algorithm for the estimation of small deviations from the normal direction during the orthogonal indentation of the third link into the tissue using an axial load sensor readings.

2 Formulation of the Problem

The three-link robot-manipulator that contacts with soft tissue is considered. All joints of the manipulator are rotational. Manipulator control is carried out by the torques at the joints that are implemented by applying voltages to motors. Operating element is rigidly attached to the last link of the robot.

We use VTS (for example proposed in [7]) and longitudinal (axial) load sensor (LLS) as the operating element of robot. VTS [7] is intended for determining effective Young modulus of the soft tissue. Consider a such sensor that contains a semi-spherical elastic head contacting with soft tissue, a light source, lens, and a video camera, which allows obtaining a visual representation of the area of contact between the head and the tissue (Fig. 1). The sensor head is manufactured from silicon that is suitable for contacting biological tissue.

For simplicity we assume that the robot is planar. We introduce an inertial fixed coordinate system O_1xyz with an origin point at a fixed hinge (Fig. 2). O_1y -axis is directed vertically upwards, O_1z coincides with the axis of rotation of the first link.

Each link is considered as a rigid body. The links are connected with joints at points O_2, O_3. We introduce coordinate systems $O_1x_1y_1z_1$, $O_2x_2y_2z_2$, $O_3x_3y_3z_3$, rigidly connected with the links 1, 2, and 3 correspondingly. Axes O_1z_1, O_2z_2, O_3z_3 have the same direction with the axis O_1z. Planes $O_ix_iy_i, i = 1, 2, 3$ lie in a vertical plane O_1xy. Lengths of the links are introduced as follows: $O_1O_2 = l_1$, $O_2O_3 = l_2$, $O_3P = l_3$.

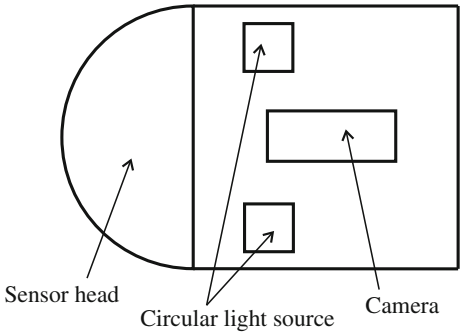

Fig. 1 Longitudinal section of video-tactile sensor

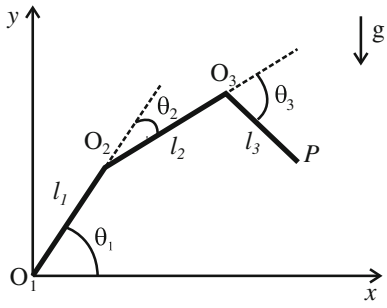

Fig. 2 Scheme of a three-link robot-manipulator

Axes O_1x_1, O_2x_2, O_3x_3 directed along O_1O_2, O_2O_3, O_3P respectively. Axes O_1y_1, O_2y_2, O_3y_3 completed the corresponding coordinates systems as right-handed ones. VTS is attached to the third link so that the axis of the sensor symmetry is directed along O_3P.

We denote masses of manipulator's link with m_1, m_2, m_3. The center of mass of the i-th link in i-th coordinate system is defined by the vector $\mathbf{r_i}$, $i = 1, 2, 3$. Moment of inertia of the i-th link with respect to the axis S_iz_i is accordingly J_i, where S_i is a center of mass of i-th link.

As generalized coordinates describing the position of the system we introduce angles θ_1, θ_2, θ_3, where θ_1 is the angle between axis O_1x and O_1x_1, θ_2 is the angle between axis O_1x_1 and O_2x_2, θ_3 is the angle between axis O_2x_2 and O_3x_3.

The gravity forces $m_i\mathbf{g}$ and control torques U_i in the joints act to each i-th link. Contact force $\mathbf{N} = -q\varepsilon\mathbf{e}_{\mathbf{x_3}}$ is applied to the end of the third link, where ε is the depth of the sensor head indentation into the tissue, q is a constant effective stiffness coefficient.

The Lagrange's equations for the given system are the following:

$$\frac{d}{dt}\frac{\partial(T-P)}{\partial\dot{\theta}_i} - \frac{\partial(T-P)}{\partial\theta_i} = U_i + M_{F_i} + Q_{N_i}, i = 1, 2, 3 \tag{1}$$

Here K is the kinetic energy of the manipulator, V is the potential energy of the manipulator, M_{F_i} are the friction torque, Q_{N_i} is the generalized force, in particular, Q_{N_3} is a force of contact interaction of third link with a tissue.

Part of our task is to determine the motion of the links that would provide the definition of mechanical properties of the tissue at a given point. Denote this contact point by A. To estimate the effective Young modulus of tissue under consideration at point A by video-tactile sensor, robot should perform an orthogonal indentation of sensor head into the tissue at this point. This requires determining a configuration of the manipulator that allows third-link motion along a normal to the tissue surface at the point A of contact.

3 Finding a Normal to the Surface at the Contact Point

For simplicity, let us assume that the surface of the tissue is planar in some neighborhood of the contact point.

To study the mechanical properties of the tissue we want to ensure that the link O_3P of the manipulator contacted with the tissue surface, moving along a normal line to this surface. Our objective is to find the normal to the surface in the point A when the head of the manipulator reaches that point. Line l (see Fig. 3) models the tissue surface. We model the surface of the sensor head with a semisphere of radius R. Then d is a distance between the axis of symmetry of the sensor and point A. We denote $\alpha = \theta_3 + \theta_2 - \theta_1$ as an angle between the axis O_1x and the axis O_3x_3.

Than angle β between the line l and axis Ox is expressed by the following relation:

$$\beta = \arccos \frac{d}{R} - \alpha \tag{2}$$

If robot perform an orthogonal indentation of sensor head into the tissue at point, we have $\alpha + \beta = \pi/2$

Let us write down the equation of the line l in axes O_1xy

$$y = \tan \beta \, x + y_A - \tan \beta \, x_A \tag{3}$$

Here (x_A, y_A)-coordinates of the point A, which have the following form:

$$x_A = l_1 \cos \theta_1 + l_2 \cos (\theta_1 - \theta_2) + l_3 \cos \alpha \tag{4}$$

$$y_A = l_1 \sin \theta_1 + l_2 \sin (\theta_1 - \theta_2) - l_3 \sin \alpha \tag{5}$$

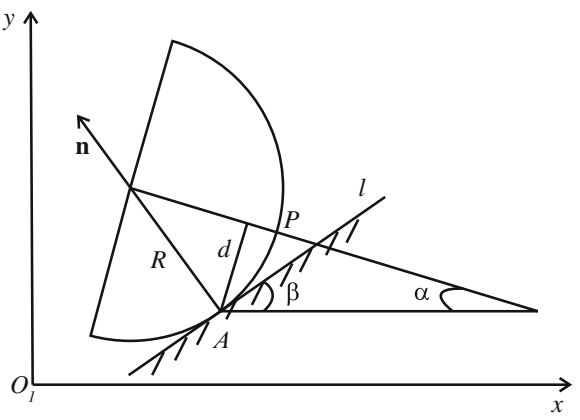

Fig. 3 Contact of the sensor head and the surface

The normal to the tissue surface in point A (orthogonal line to the line l) is given by following expression:

$$\mathbf{n} = (\tan\beta, y_A - \tan\beta\, x_A) \tag{6}$$

4 Sensor Head Translational Motion Along the Normal to the Tissue Surface

When the normal to the tissue surface at the point A is found, we rotate the executive link of the manipulator so that it is directed along this normal. Then we assign translational motion of the third link of the robot-manipulator along the normal at the point of contact to determine the mechanical properties of the tissue. The angle α between the third link and O_1x is fixed during this translational motion. Two relations appear between the angles θ_1, θ_2 and θ_3 that provides constancy of the angle α and the distance O_1E (Fig. 4). Thus, we can assume that the system has one degree of freedom during this motion.

Let us find the relations between the angles θ_1, θ_2 and θ_3 that provides the constancy of α and the distance O_1E.

$$\alpha = \theta_3 + \theta_2 - \theta_1 = const \tag{7}$$

There is a following geometric relationship:

$$O_1E = O_2C + l_1\cos\theta_1 + \frac{l_1\sin\theta_1}{\tan\alpha} = const \tag{8}$$

Consider the triangle O_2O_3C to find O_2C:

$$O_2C = \frac{l_2\sin\theta_3}{\sin\alpha} \tag{9}$$

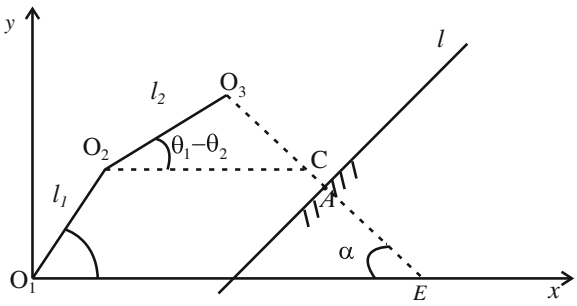

Fig. 4 Case of motion of the third link along the normal to the surface l

Thus, the relationship between angles θ_1 and θ_2, that provides the constancy of the distance O_1E, has a form

$$\frac{l_2 \sin\theta_3}{\sin\alpha} + l_1 \cos\theta_1 + \frac{l_1 \sin\theta_1}{\tan\alpha} = const \tag{10}$$

5 Deviation of the Working Element from the Desired Normal Direction to the Tissue Surface

Consider the case when line O_3P deflected from desired normal in the contact point. We show that it is not necessary using the video-tactile sensor to find the error in the angle of the third-link indentation. It is enough to use a longitudinal load sensor rigidly attached to the last link.

We assume that we have already selected a specific point A on the tissue surface and determined the normal direction for the surface in this point with some error. The manipulator has a configuration in which the last link is oriented at a fixed angle α to axis O_1x (Fig. 5) and has performed small translational indentation into tissue keeping this orientation. An angle δ is a small deviation of the third link from the normal direction to the tissue surface. One can estimate this deviation by LLS readings using the following approach.

Consider an equilibrium of the mechanical system in position when the third link is oriented along the normal direction to the tissue surface ($\delta = 0$). Equilibrium equations can be obtained from the torque balances of the external forces applied to the system about the points O_1, O_2, O_3

$$M_1 - N(\sin\alpha\, x_A + \cos\alpha\, y_A) = U_1, \tag{11}$$

$$M_2 - N(\sin\alpha(x_A - l_1\cos\theta_1) + \cos\alpha(l_1\sin\theta_1 - y_A)) = U_2, \tag{12}$$

$$M_3 = U_3, \tag{13}$$

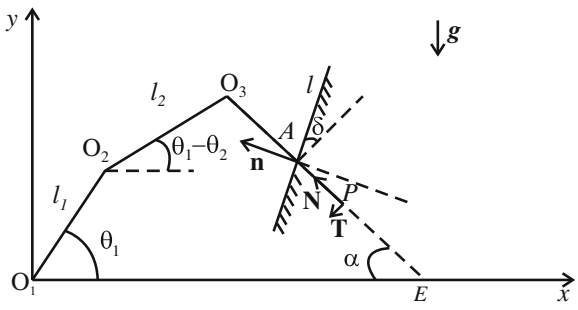

Fig. 5 The case of the orthogonal indentation with a small deviation of the sensor into the tissue

where M_1, M_2, M_3 are moments of gravity of links about the points O_1, O_2, O_3 respectively

$$M_1 = m_1 g r_1 \cos\theta_1 + m_2 g(l_1 \cos\theta_1 + r_2 \cos(\theta_1 - \theta_2)) + \\ + m_3 g(l_1 \cos\theta_1 + l_2 \cos(\theta_1 - \theta_2) + r_3 \cos\alpha) \tag{14}$$

$$M_2 = m_2 g r_2 \cos(\theta_1 - \theta_2) + m_3 g(l_2 \cos(\theta_1 - \theta_2) + r_3 \cos\alpha) \tag{15}$$

$$M_3 = m_3 g r_3 \cos\alpha \tag{16}$$

From expressions (11), (12) we get two values for estimation of the contact force N

$$N_1 = \frac{M_1 - U_1}{\sin\alpha\, x_A + \cos\alpha\, y_A} \tag{17}$$

$$N_2 = \frac{M_2 - U_2}{\sin\alpha(x_A - l_1 \cos\theta_1) + \cos\alpha(l_1 \sin\theta_1 - y_A)} \tag{18}$$

The third value of contact force N_3 we obtain from LLS sensor data. If $|N_1 - N_3| \gg |N_2 - N_1|$ (and consequently $|N_2 - N_3| \gg |N_2 - N_1|$) then angle δ is considerably greater than zero. There exists tangential force $\mathbf{T}$ applied to the end of the third link. In this case Eq. (13) looks like the following:

$$T l_3 = U_3 - M_3 \tag{19}$$

We propose a following algorithm for estimating the angle δ. Consider the average value of the contact force N

$$N_a = \frac{N_1 + N_2 + N_3}{3} \tag{20}$$

Then value of angle between the normal to the working surface and third link axis has the following form:

$$\delta = \arctan\frac{T}{N_a} \tag{21}$$

where the value of force T can be determined from expression (19).

6 Algorithm for Estimating an Effective Stiffness of the Tissue

After the correction of the direction of penetration of the working element to point A by the angle δ we can achieve the accurate orthogonal indentation of the working element into the tissue. According to the LLS readings, we can determine the

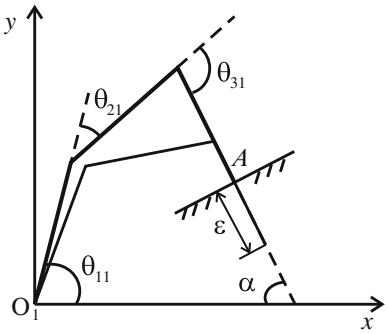

Fig. 6 Two configurations of the manipulator under the orthogonal indentation

stiffness of the tissue under consideration. Consider two different configurations of the robot-manipulator. The first configuration corresponds to the robot position when operating element just touches the tissue in the point A. In this case the contact force is equal zero. The second configuration corresponds to robot position when it performs orthogonal indentation of the sensor head into the tissue with small depth ε (Fig. 6).

The first configuration is set by the angles $\theta_{11}, \theta_{21}, \theta_{31}$ and the second configuration is given with angles values $\theta_{12}, \theta_{22}, \theta_{32}$. Assume that $\theta_{i2} - \theta_{i1} = \delta\theta_i, i = 1, 2, 3$ are small values.

During the translational motion of the third link with the fixed angle α, relations (7)–(10) must be satisfied. Then we have following equations:

$$\theta_{31} + \theta_{21} - \theta_{11} = \theta_{32} + \theta_{22} - \theta_{12} \tag{22}$$

$$\frac{l_2 \sin\theta_{31}}{\sin\alpha} + l_1 \cos\theta_{11} + \frac{l_1 \sin\theta_{11}}{\tan\alpha} = \frac{l_2 \sin\theta_{32}}{\sin\alpha} + l_1 \cos\theta_{12} + \frac{l_1 \sin\theta_{12}}{\tan\alpha} \tag{23}$$

Dependence of the indentation depth ε on angles characterizing the first and second configuration looks as following:

$$\varepsilon \cos\alpha = l_1 \cos\theta_{12} + l_2 \cos(\theta_{12} - \theta_{21}) - l_1 \cos\theta_{11} - l_2 \cos(\theta_{11} - \theta_{21}) \tag{24}$$

We substitute small increments of the angles $\delta\theta_i, i = 1, 2, 3$ to Eqs. (22)–(24). Then Eqs. (22)–(24) at a first approximation take the following form:

$$\delta\theta_3 + \delta\theta_2 - \delta\theta_1 = 0 \tag{25}$$

$$\frac{l_2 \cos\theta_{32}}{\sin\alpha}\delta\theta_3 + l_1 \left(\frac{\cos\theta_{12}}{\tan\alpha} - \sin\theta_{12} \right) \delta\theta_1 = 0 \tag{26}$$

$$\varepsilon \cos\alpha = -l_1 \sin\theta_{12}\delta\theta_1 - l_2 \sin(\theta_{12} - \theta_{22})(\delta\theta_1 - \delta\theta_2) \tag{27}$$

We obtain ϵ from the (27). Knowing e and the force, which the tissue is exerting along the axis of the third link, we find the estimation for effective stiffness coefficient

$$q = \frac{N}{\epsilon} \tag{28}$$

Equations (25)–(26) can be used to acquire errors and to correct the operation regime.

7 Conclusions

The problem of the motion of three-link robot-manipulator designed for medical applications is considered. The mode of operation of the manipulator is studied, in which the last link of the robot-manipulator performs a translational orthogonal indentation into the surface of the soft tissue. Relations between the angles of orientation of the manipulator links needed for providing the motion of the sensor head along the normal to a tissue surface are found. The approach for restoring a normal to the surface at the contact point is proposed, depending on the information obtained from the VTS or from the LLS. The algorithm for the estimation of small deviation of the third link from the normal direction is proposed using LLS readings. The algorithm for determining the effective stiffness coefficient of the tissue at the given point is developed.

Acknowledgments The work is partially supported by Russian Foundation for Basic Research (grant 14-08-92010).

References

1. Craig, J.J.: *Introduction to Robotics: Mechanics and Control*, 2nd edn. p. 450. Addison-Wesley (1989)
2. Tokhi, M.O., Azad, A.K.M. (eds.): *Flexible Robot Manipulators: Modelling, Simulation and Control*, p. 584. IET (2005)
3. Ajwad, S.A., Iqbal, J., Ullah, M.I., Mehmood, A.: A systematic review of current and emergent manipulator control approaches. Front. Mech. Eng. **10**(2), 198–210 (2015)
4. Sadovnichiy, V.A., Goryacheva, I.G., Akayev, A.A., Martynenko, Yu.G., Okunev, Yu.M., Vlakhova, A.V., Bogdanovich, I.Yu.: Application of contact mechanics in diagnosing pathological conditions of soft biological tissues, p. 306. Moscow University, Moscow (2009)
5. Golovin, V., Arkhipov, M., Zhuravlev, V.: *Force training for position/force control of massage robots.* New Trends in Medical and Service Robots, pp. 95–107. Springer International Publishing (2014)
6. Kappassov, Zh., Corrales, J.A., Perdereau, V.: Tactile sensing in dexterous robot hands–review. Robot. Auton. Syst. (2015)
7. Dosaev, M., Goryacheva, I., Martynenko, Yu., Morozov, A., Antonov, F., Su, F.Ch., Yeh, Ch.H., Ju, M.Sh.: Application of video-assisted tactile sensor and finite element simulation for estimating youngs modulus of porcine liver. J. Med. Biol. Eng. (2014). doi:10.5405/jmbe.1909

8. Yeh, Ch.H., Su, F.Ch., Goryacheva, I., Martynenko, Yu., Dosaev, M.Z., Ju, M.Sh.: Image-assisted method for estimating local stiffness of soft tissues and calibration of bias due to aqueous humor effect. Sens. Actuators A: Phys. **212**, 4251 (2014)
9. Vasiukova, O.E., Okunev, Yu.M., Luo, R.C., Chen, Sh.Yu.: Modeling of a three-link robot-manipulator contacting a soft biological tissue. In: XXVIII International Scientific Conference. Mathematical Methods in Technology, vol. 1, pp. 84–87. Saratov (2015)

A Docking Maneuver Scenario of a Servicing Satellite—Quaternion-Based Dynamics and Control Design

Elzbieta Jarzebowska and Michal Szwajewski

Abstract The paper presents a quaternion-based dynamics formulation for a servicing satellite approaching a client satellite. For understanding the dynamics behavior of the satellite, the orbit dynamics is presented in the paper with focus on the integration error for on-orbit dynamics. The mission scenario presented in the paper is applicable for geostationary satellite servicing missions or conceptual missions for a satellite of a modular structure, which allows changing components, for example a broken sensor. Quaternion-based dynamics is used to omit problems with Euler angle functions singularity during approaching maneuvers to a target satellite. Investigation in space flight dynamics and control is an active research area due to their practical and financial significance. Docking to well-known objects with defined and cooperative interfaces is known and proved, for example docking to International Space Stations. New areas of investigation are the non-cooperative objects approaching and interception, like space debris, broken satellites, or prolongation of satellite operational functions. The quaternion-based dynamics model presented in the paper describes functionality of all effectors, which allow orientation of the satellite on its orbit. The orbit dynamics accompanying attitude dynamics form a complete model for a satellite control design.

1 Introduction

From the first days of humans in space, modeling and prediction of behavior of a spacecraft were a challenge for science. Main missions are focused on placing objects on defined orbits. Very few tasks in space were performed to catch, service,

E. Jarzebowska (✉)
Institute of Aeronautics and Applied Mechanics, Warsaw University of Technology, Nowowiejska 24, Warsaw, Poland
e-mail: elajarz@meil.pw.edu.pl

M. Szwajewski
SENER Spz.o.o., AlejeJerozolimskie 202, 02-486 Warsaw, Poland
e-mail: michal.szwajewski@sener.pl

J. Awrejcewicz (ed.), *Dynamical Systems: Modelling*, Springer Proceedings in Mathematics & Statistics 181, DOI 10.1007/978-3-319-42402-6_16

or overtake functions of the spacecraft. Investigation in space flight dynamics and control is an active research area due to their practical and financial importance. Docking to well-known objects with defined and cooperative interfaces is known and proved, for example docking to International Space Stations, were docking interfaces and docking vehicles were specially designed. New areas of investigations are the non-cooperative objects approaching and interception, like space debris, broken satellites, or prolongation of satellite operational functions. Analysis and investigation of rendezvous maneuvers and formation flying is actually focused on three main mission's concepts. The first one is removing existing debris from the LEO and middle attitude orbits. Actually, the space debris causes serious problems for newly launched satellites. Removal space debris is under investigation of DLR with the concept mission DEOS. This concept is now under implementation as E-DeOrbit mission. A spacecraft with a dedicated robotic arm may catch debris and deorbit them. The second area relates to formation flying maneuvers. The example of such mission is PROBA 3. This mission is a formation of flying algorithms technology proof mission. Two satellites on strongly elliptical orbits will create a scientific instrument, a coronagraph. Satellites will be launched, connected, and after release it will separate to create a formation and operate as an optical instrument. In the scenario of the mission, it was taken into account that after the operational time, the satellite will deorbit to not add debris on this orbit. The third area of investigation is servicing missions. Servicing missions require precision maneuvers and a rendezvous maneuver cannot impact on other operating systems of a target satellite. The scenario of the mission has to be well defined and planned at each step of the mission and flight away maneuvers.

Servicing missions are actively investigated by researchers because of their complexity and planning requirements. The need of such missions is also under investigation by the SENER Company, where analysis and analytical investigations were performed. Missions for on-orbit servicing can be multifunction and multitask. One of the mission scenario presented in this paper is servicing a satellite on a geo synchronous orbit. The goal is to dock to a satellite and take over their functions. Other mission concept, which the presented scenario can cover, is servicing a building blocks concept satellite [1]. The servicing satellite would be equipped with a functional iBOSS—intelligent building blocks for on-orbit-satellite servicing. In this concept, the one servicing satellite could service a sort of satellites with intelligent building blocks.

In this paper, a novel approach to the mission analysis is presented. The complete concept with attitude and orbit dynamics equations is presented. The quaternion-based dynamics model presented in the paper describes a complex functionality of all effectors, which allow orientation of the satellite on an orbit. The model includes reaction wheels, thrusters, and an influence of a drift caused by solar radiation and by the atmosphere. The significant investigation is performed in presenting the satellite body motion in the gravitational field. The standard Runge Kutta or Rosenbrock integration procedures do not provide correct solutions to a satellite dynamic equations. The reason is that the standard Runge Kutta or Rosenbrock integration procedures do not conserve the satellite energy and it does

not stay on the defined orbit but drifts away with an increasing integration error. For the orbit dynamics, Gauss–Jackson Integration [2] has to be implemented. The integration is a multistep predictor corrector method, which allows maintaining potential of the satellite stable.

The theoretical development presented in the paper is illustrated by the simulation study of potential servicing satellite approaching a target satellite. The scenario presented in the simulation is limited to rendezvous and does not include docking itself. The simulations also present trajectories of the satellites in the inertial reference frame.

2 "Mission Protocol" Description

The starting point for the analysis is when a satellite is already at the geostationary orbit. The target satellite is non-cooperative, what implies no motion for assisting docking. This assumption is justified, taking into account a servicing telecommunication satellite, which can still operate, but must be transferred to a graveyard orbit in a short time period. For the mission analysis, a coordinate system fixed in a target satellite is used, according to axes defined in [3]. In the literature such coordinate system is also called LVLH—Local-vertical/Local-horizontal (Fig. 1).

For the mission analysis the geostationary orbit with the radius 42 164 km is assumed.

The mission can be divided into three main phases. The first phase is to locate the satellite as close enough on V bar, to allow detection of a target satellite. The second phase is the flight around maneuver to change the location from V bar to R bar to initiate the third phase, which is approaching the target satellite on R bar for final docking. The summarized detailed protocol of the mission is presented in Table 1.

Time defined for each maneuver can vary and depends on instruments used on the satellite. The calculations presented in the Table 1 are based on the visual navigation system defined by the SENER Company. The control points and trajectories are presented in the section discussing simulation results.

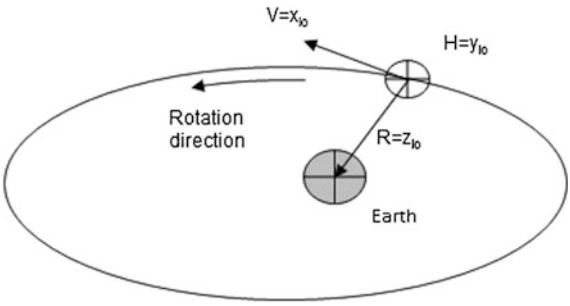

Fig. 1 LV/LH coordinate system

Table 1 Mission protocol description

Control Points	Duration	Description
A1 (+35 km on Vbar)	6 h	The satellite is on Vbar and is searching the target. The GNC system is defining the orbit of target and servicing satellites
A1 to A2	12 h	Transferring to A2 point. Approaching to the target
A2 (+2 km on Vbar)	1 h	Approaching to the target at 2000 m. Searching and defining the satellite motion
A2–A3a (+400 m on Vbar)	2 h	Preparation to a spiral approach
A3a to A3b (−200 on V bar)	1 h	Approaching and orbit determination
A3b to A3 (+100 on V bar)	1 h	Motion form Vbar to R bar
A3–A4 (−500 m on R bar)	6 h	Approaching on R bar
A4 do A5 (−20 m on R bar)	10 min	Satellite is about 20 m from the target
A5 do A6 (7 m from the target)	10 min	At A6 point servicing satellite is at a distance of about 7 m from the target
A6 (−7 m on Rbar)	10 min	Servicing satellite is starting docking
A6 do A7	20 min	Servicing satellite is ready to dock

2.1 Calculations of a Total Velocity Change for a Mission Analysis

The preliminary mission analysis is performed to define the maximal velocity change with respect to the time required for that change. For this simplified analysis, the Clohessy–Wiltshire model is adopted. The relative motion of a chaser with respect to a target satellite can be described by the C-W equations of motion. They require some specific nomenclature and concepts, which are defined in Fig. 2.

In the Table 2, the orbital elements are specified and described.

The first step to obtain the C-W equations is to define the position and velocity vectors in the orbital coordinate system, i.e.,

$$r_a = \frac{h^2}{\mu} * \frac{1}{1 + e^* \cos\theta} * \begin{pmatrix} \cos\theta \\ \sin\theta \\ 0 \end{pmatrix} \tag{1}$$

$$v_x = \frac{\mu}{h} + \begin{pmatrix} -\sin\theta \\ e + \cos\theta \\ 0 \end{pmatrix} \tag{2}$$

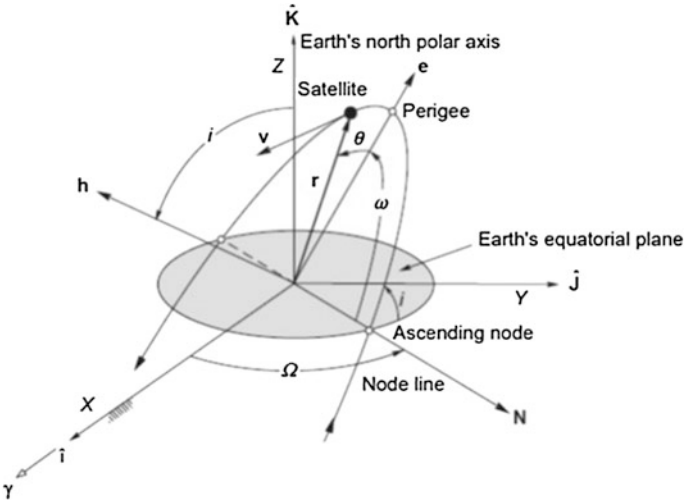

Fig. 2 Orientation of orbit in space (from Ref. 7)

Table 2 Orbital elements description

Symbol	Description
α	Semi major axis
e	Eccentricity
i	Inclination
Ω	Right ascension of ascending node
ω	Argument of perigee
θ	True anomaly

To express the location and velocity vectors in the Earth Centered Coordinate system, a transformation matrix between coordinate systems has to be define as follows:

$$Q_{Aa} = \begin{bmatrix} \cos(\omega) & \sin(\omega) & 0 \\ -\sin(\omega) & \cos(\omega) & 0 \\ 0 & 0 & 1 \end{bmatrix} \begin{bmatrix} 1 & 0 & 0 \\ 0 & \cos(i) & \sin(i) \\ 0 & -\sin(i) & \cos(i) \end{bmatrix} \begin{bmatrix} \cos(\Omega) & \sin(\Omega) & 0 \\ -\sin(\Omega) & \cos(\Omega) & 0 \\ 0 & 0 & 1 \end{bmatrix} \quad (3)$$

Inversing the above matrix and multiplying it by the position vector or the velocity vector, the position and velocity vectors in the Earth Centered Coordinate System can be derived as

$$r_A = Q_{aA} * r_a \quad (4)$$

$$v_A = Q_{aA} * v_a \quad (5)$$

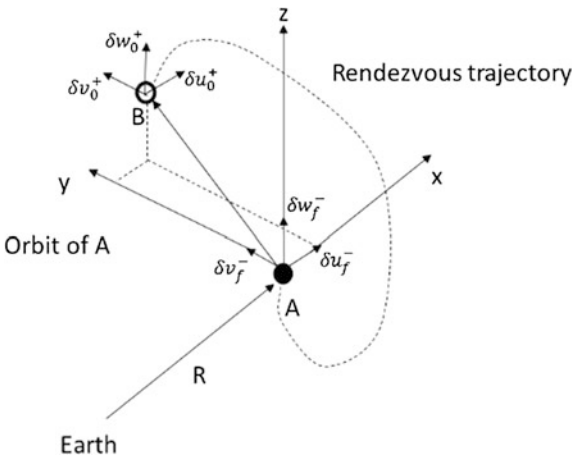

Fig. 3 Randevouz trajectory in two impulse case (from Ref. [7])

When the position and velocity were defined in each of coordinate systems, the velocity vector change can be derived. The change of the satellite position is achieved by two impulses of forces. This assumption allows using a simplified equation. To initiate the motion, a force should act on the satellite. In the equations that follow, it will result with velocities denoted by a sign "+". To stop the motion, the force should act against this motion and velocities will be denoted by a sign "−". Figure 3 presents the rendezvous trajectory of the satellite B to reach a point/satellite A.

According to Fig. 3, knowing velocity and a position of the satellite B and the satellite A at the time t_0 and using the C-W equations, the total velocity change can be specified as

$$\Delta v_{total} = ||\Delta v_0|| + ||\Delta v_f|| \tag{6}$$

where

$$\Delta v_0 = \delta v_0^+ - \delta v_0^- = \begin{pmatrix} \delta u_0^+ \\ \delta v_0^+ \\ \delta \omega_0^+ \end{pmatrix} - \begin{pmatrix} \delta u_0^- \\ \delta v_0^- \\ \delta \omega_0^- \end{pmatrix} \tag{7}$$

and

$$\delta v_0^+ = -\Phi_{rv}(t_f)^{-1}\Phi_{rr}(t_f) * r_0 \tag{8}$$

$$\delta v_f^- = \phi_{vr}(t_f)\delta r_0 + \phi_{vv}(t_f)\delta v_0^+ \tag{9}$$

$$\Delta v_f = \delta v_f^+ - \delta v_f^- \tag{10}$$

The notation in Eqs. (6)–(10) is δv_0^+ is the velocity to initiate the start of motion and δv_f^- is the velocity to stop the rendezvous maneuver. Based on Eqs. (6)–(10) the total change of velocity can be determined. Lacking information are C-W relations, which are presented below

$$\Phi_{rr} = \begin{bmatrix} 4-3\cos(nt) & 0 & 0 \\ 6(\sin(nt)-nt) & 1 & 0 \\ 0 & 0 & \cos(nt) \end{bmatrix} \tag{11}$$

$$\Phi_{rv} = \begin{bmatrix} \frac{1}{n}\sin(nt) & \frac{2}{n}(1-\cos(nt)) & 0 \\ \frac{2}{n}(\cos(nt)-1) & \frac{1}{n}(4\sin(nt)-3nt) & 0 \\ 0 & 0 & \frac{1}{n}\sin(nt) \end{bmatrix} \tag{12}$$

$$\Phi_{vr} = \begin{bmatrix} 3n\sin(nt) & 0 & 0 \\ 6n(\cos(nt)-1) & 0 & 0 \\ 0 & 0 & -n\sin(nt) \end{bmatrix} \tag{13}$$

$$\Phi_{vv} = \begin{bmatrix} \cos(nt) & 2\sin(nt) & 0 \\ -2\sin(nt) & 4\cos(nt)-3 & 0 \\ 0 & 0 & \cos(nt) \end{bmatrix} \tag{14}$$

where n is the angular velocity for a circular orbit and it is expressed as

$$n = \frac{v}{r} = \sqrt{\frac{\mu}{r_0^3}} \tag{15}$$

Based on the scheme of the satellite action sequences presented in this section, the rendezvous mission scenario can be developed. A detailed description of different approaches to mission maneuvers such as continuous burn transfers can be found in [4]. For a mission planning, a simplified calculation can be conducted to assess the amount of fuel required for each maneuver. Each mission is assigned an optimization function, in which selected factors are defined as the most efficient ones. In case of a mission whose main purpose is servicing more than one satellite, the main parameter is fuel. A servicing of building block satellite can be a good example of this.

3 Servicing Satellite Dynamics

The satellite dynamics and orbit perturbation can be expressed in different coordinate systems. For the purpose of this paper, inertial reference frame is used as shown in Fig. 2. Other more sophisticated and accurate reference frames could be used to define, for example the elliptical Earth, as the geodetic reference frame described in [5], but it is not the purpose of this paper. In this section, a model of

satellite dynamics is presented. It is developed in a body and inertial reference frames with the use of quaternion. The attitude dynamics model describes effectors, which can act on the satellite and torques which can change the satellite orientation. Also, the model of an orbit perturbation is presented and simulation problems and a solver selection for integrating the satellite dynamics is discussed.

3.1 Satellite Attitude Dynamics

The satellite dynamics is composed of translational and rotational motion equations. A description of translation is discussed with the orbit perturbations taken into account. Equations of rotation of the satellite are based upon the Euler equations, i.e., that the time rate of change of an angular momentum is equal to the sum of external moments applied to a body. In equations that follow, the upper case at each variable indicates the reference frame, where a letter E stands for the inertial frame and B specifies a body fixed reference frame. The satellite dynamics is based upon the development presented in [5].

$$I^B \frac{d\omega^{BE}}{dt} = \sum \mathrm{M_B} \tag{16}$$

In Eq. (16) the right-hand side moments about the center of mass of the satellite are the moments generated by reaction wheels, thrusters used for fast reorientation, or perturbation moments that may act on the satellite.

Taking the Euler angle description, Eqs. (16) can be transformed to the satellite body reference frame. Also, note that the change of the satellite inertia is negligible, what results in the following rotational motion equations.

$$\frac{d\omega^B}{dt} = \left(I^B\right)^{-1}\left[\left(-\Omega^B\right)\left(I^B\right)\omega^B + m_B\right], \tag{17}$$

where

$$\omega^B = \begin{bmatrix} p \\ q \\ r \end{bmatrix} \tag{18}$$

$$\Omega^B = \begin{bmatrix} 0 & -r & q \\ r & 0 & -p \\ -q & p & 0 \end{bmatrix} \tag{19}$$

Equation (17) consists of three first-order nonlinear differential equations. Due to the well-known singularity problems related to Euler angle functions, the final satellite dynamics is derived in Euler parameters, i.e., quaternion description.

The four-dimensional space is the rotation quaternion, i.e.,

$$q = q_0 + iq_1 + jq_2 + kq_3 \tag{20}$$

The norm of the quaternion is to be

$$q_0^2 + q_1^2 + q_2^2 + q_3^2 = 1 \tag{21}$$

This norm can be treated as a constraint equation for the four parameters. It has to be satisfied then and checked during an integration process, and corrected if needed. Practically, due to the finite length of an integration step, the norm has to be corrected by some factor in the same way as a constraint equation.

$$[q] = \begin{bmatrix} q_0 \\ q_1 \\ q_2 \\ q_3 \end{bmatrix} = \begin{bmatrix} \cos\left(\frac{\varepsilon}{2}\right) \\ \sin\left(\frac{\varepsilon}{2}\right) n_1 \\ \sin\left(\frac{\varepsilon}{2}\right) n_2 \\ \sin\left(\frac{\varepsilon}{2}\right) n_2 \end{bmatrix} \tag{22}$$

Relations between the four Euler parameters and body fixed angular velocities can be written as follows:

$$\begin{bmatrix} \dot{q_0} \\ \dot{q_1} \\ \dot{q_2} \\ \dot{q_3} \end{bmatrix} = \frac{1}{2} \begin{bmatrix} 0 & -p & -q & -r \\ p & 0 & r & -q \\ q & -r & 0 & p \\ r & q & -p & 0 \end{bmatrix} \begin{bmatrix} q_0 \\ q_1 \\ q_2 \\ q_3 \end{bmatrix} \tag{23}$$

These differential equations are linear and are free of singularities. The initialization for the equation could be done by Euler angles and using Eqs. (21) and (22), which allow to define the initial quaternion. As mentioned, during the integration process of Eq. (23), the unit norm of the quaternion could drift along the simulation. To control the quaternion norm, we introduce a correcting factor following [5]. It can be selected based on simulation experiments.

$$\begin{bmatrix} \dot{q_0} \\ \dot{q_1} \\ \dot{q_2} \\ \dot{q_3} \end{bmatrix} = \frac{1}{2} \begin{bmatrix} 0 & -p & -q & -r \\ p & 0 & r & -q \\ q & -r & 0 & p \\ r & q & -p & 0 \end{bmatrix} \begin{bmatrix} q_0 \\ q_1 \\ q_2 \\ q_3 \end{bmatrix} + K\lambda \begin{bmatrix} q_0 \\ q_1 \\ q_2 \\ q_3 \end{bmatrix} \tag{24}$$

where $\lambda = 1 - (q_0^2 + q_1^2 + q_2^2 + q_3^2)$ is the correcting factor.

The satellite dynamics simulation results presented in quaternion description are not easy to interpret, so the Euler angles as functions of quaternion are welcome. The relations are as follows:

$$\tan(\psi) = \frac{2(q_1 q_2 + q_0 q_3)}{q_0^2 + q_1^2 - q_2^2 - q_3^2} \tag{25}$$

$$\sin(\theta) = -2(q_1 q_3 - q_0 q_2) \tag{26}$$

$$\tan(\phi) = \frac{2^*(q_2 q_3 + q_0 q_2)}{q_0^2 - q_1^2 - q_2^2 - q_3^2} \tag{27}$$

The quaternion-based dynamic equations for the satellite attitude consist of three dynamic equations for the rate of change of the satellite angular velocities and four kinematic differential equations in quaternion. Additionally, the transformation matrix for expressing the quaternion in the inertial reference frame is as follows:

$$M^{BE} = \begin{bmatrix} q_0^2 + q_1^2 - q_2^2 - q_3^2 & 2(q_1 q_2 + q_0 q_3) & 2(q_1 q_3 - q_0 q_2) \\ 2(q_1 q_2 - q_0 q_3) & q_0^2 - q_1^2 + q_2^2 - q_3^2 & 2(q_2 q_3 + q_0 q_1) \\ 2(q_1 q_3 + q_0 q_2) & 2(q_2 q_3 - q_0 q_1) & q_0^2 - q_1^2 - q_2^2 + q_3^2 \end{bmatrix} \tag{28}$$

3.2 Equations of the Satellite Perturbed Motion

The equations of motion for the satellite moving around the point mass planet is given in the internal frame by the equation below

$$\frac{d^2 r}{dt^2} = -\frac{\mu}{r^3}\boldsymbol{r} \tag{29}$$

where, r is the position vector of the satellite, μ is the gravitational constant, and t is time. The position vector can be presented in a general function form or orbit elements. To derive an equation of motion with perturbation, a resultant vector of acceleration has to be added to the right-hand side of Eq. (29) as follows:

$$\frac{d^2 r}{dt^2} = -\mu\frac{\boldsymbol{r}}{r^3} + ap \tag{30}$$

The main perturbations in the solar system can be divided in two categories according to [6], as gravitational and no gravitational. The sources of the gravitational acceleration are third bodies as the sun or the moon and the no spherical Earth. The sources for nongravitational acceleration are atmosphere drag, solar radiation pressure, out-gassing, or the tidal friction effect. The other classification of perturbations calls them conservative if they depend on positions only or non-conservative when they depend on positions and velocities [6]. In the non-conservative perturbation case, the energy transfer occurs. In the solar system the perturbation acceleration for all satellite orbits is 10 times smaller than the central force or two body accelerations.

In this paper, we present a step-by-step numerical integration method called "Special perturbation method" [6]. This is the straightforward method for a solution of two body equations of motion with perturbation. Equation (30) is a second-order nonlinear differential equation which can be reduced to two first-order differential equations as presented in Eq. (31) or used directly in Gauss–Jackson method of integration.

$$\begin{cases} \dot{r} = v \\ \dot{v} = -\frac{\mu}{r^3}\boldsymbol{r} + a_p \end{cases} \tag{31}$$

4 Simulation Study—a Satellite Motion and Approaching a Target

In this section simulation studies are presented. They are based on the satellite dynamics models (24) and (30). The simulation case study considers the servicing mission of a telecommunication satellite. The servicing satellite moments of inertia are $Ixx = 2645$, $Iyy = 698$, $Izz = 2355$ kg/m^2. The orbit of the simulation is a circular orbit with inclination 0 and altitude of 35786 km.

The first study is to simulate the servicing satellite approaching the telecommunication satellite. The analysis was performed according to the mission's protocol collected in Table 1. The docking maneuver may start after reaching the location A6. The coordinate system is located in the center of mass of the target satellite. Simulation results are presented in Fig. 4.

The second simulation study is for the attitude dynamics in the quaternion description. The quaternion norm is checked in each simulation time step. In this simulation, torques generated by reaction wheels were introduced. Figure 5 shows changes of the satellite angular velocities when the reaction wheels act during a 10 min long maneuver. Figures 6 and 7 present time changes of quaternion components and the norm preservation along simulation, respectively.

Figure 8 presents changes of Euler angles during the simulation time.

The orbit motion of the satellite was simulated with the use of the Gauss–Jackson method, which allows integrating second-order equations directly without the need of reducing them to two first-order differential equations. The satellite unperturbed motion on its orbit is presented in Fig. 9. The perturbed motion is depicted in Fig. 10.

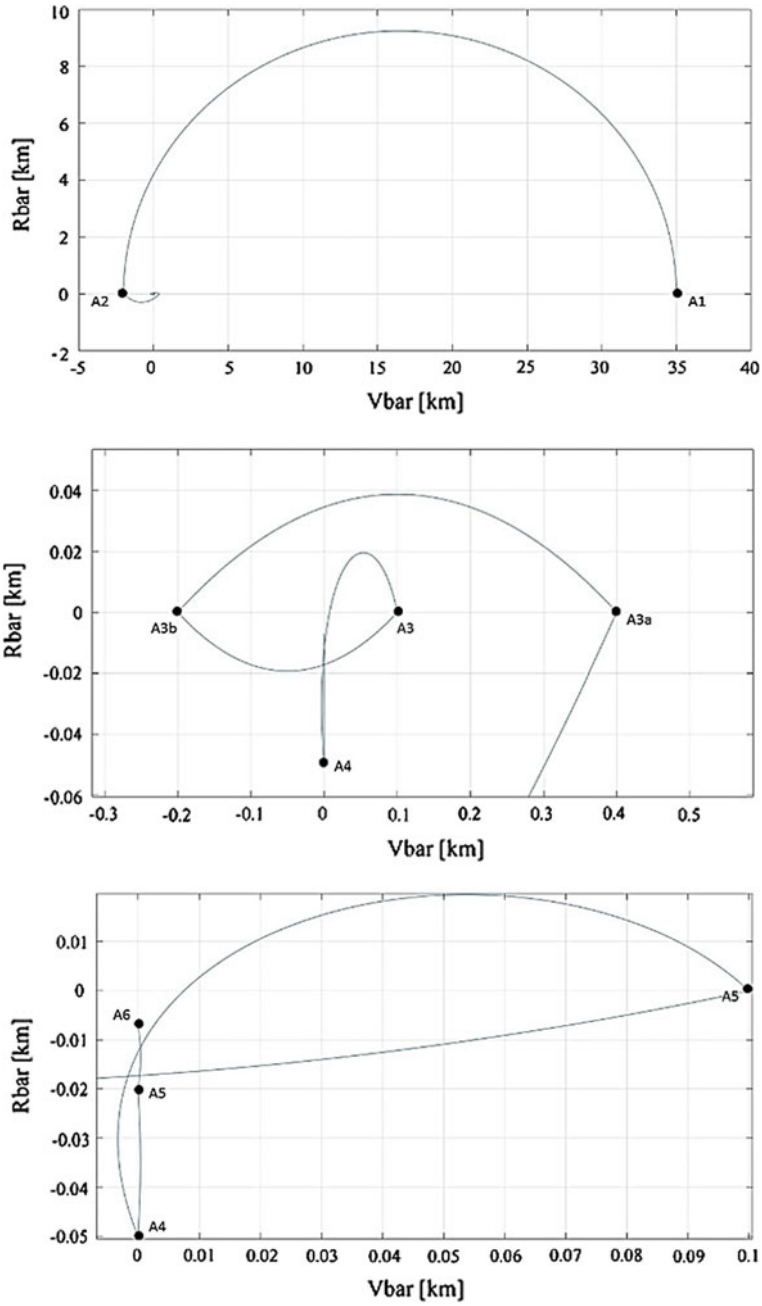

Fig. 4 Approaching sequences to the target satellite

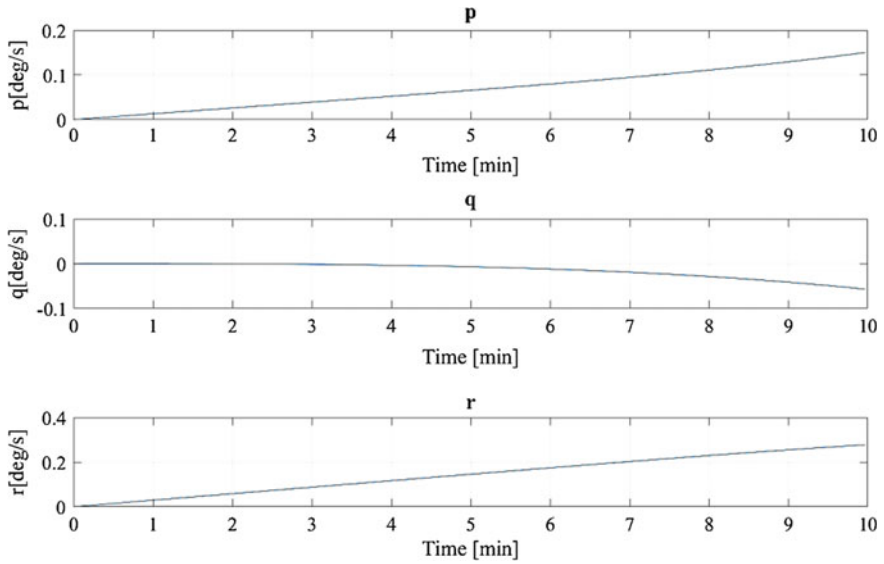

Fig. 5 Changes of the satellite angular velocities under the action of reaction wheels

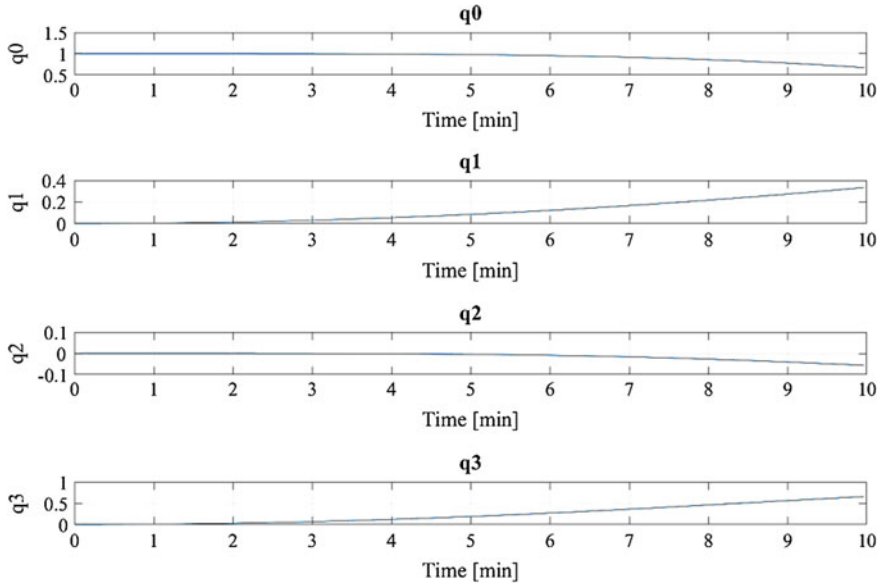

Fig. 6 Euler parameters changes in time

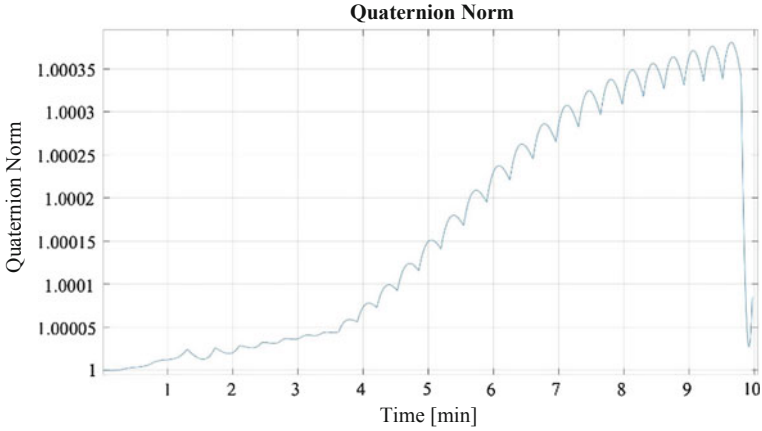

Fig. 7 Quaternion norm along the simulation

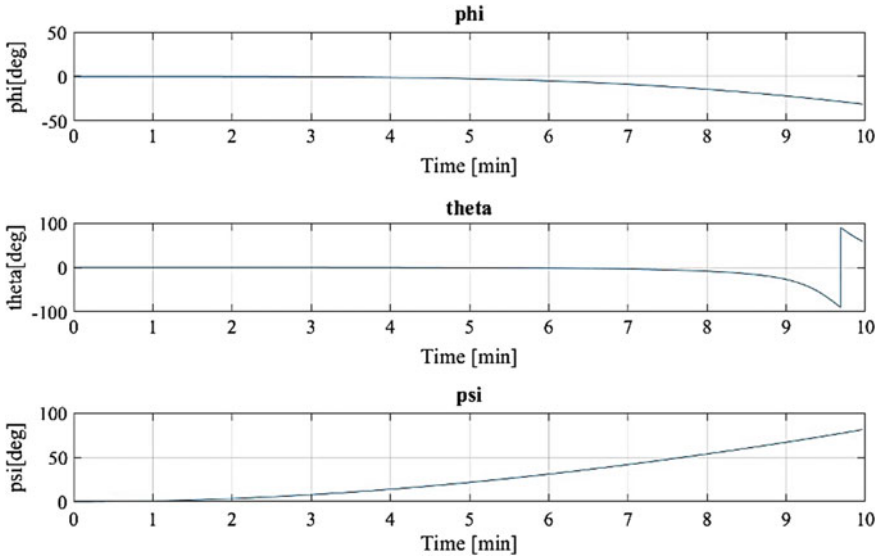

Fig. 8 Euler angles changes in time

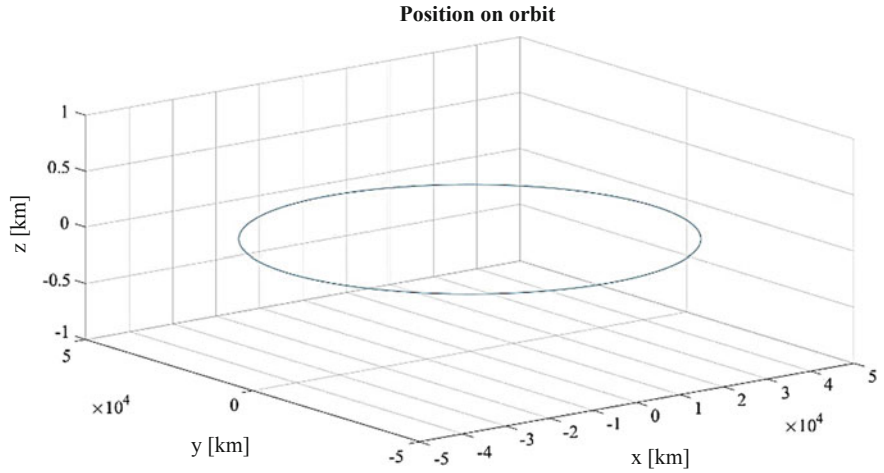

Fig. 9 Unperturbed satellite motion on the orbit

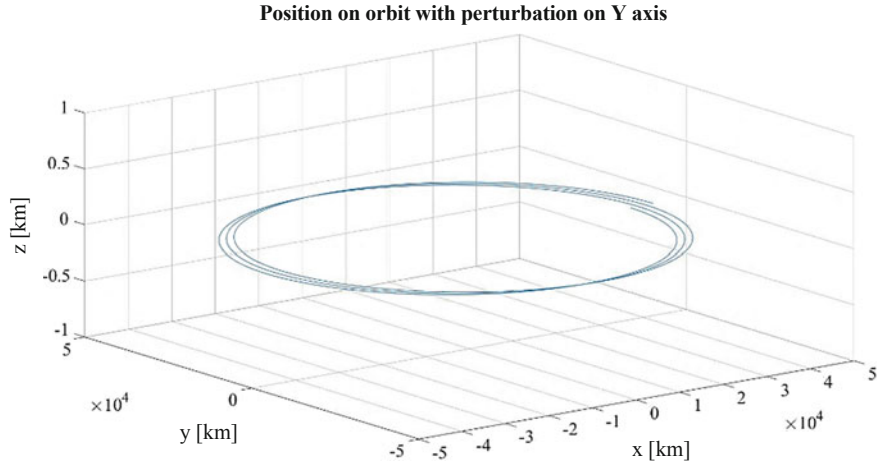

Fig. 10 Perturbed satellite motion on the orbit with the perturbation acting along Y axis

5 Conclusions

The paper presents the development of the satellite dynamics for a servicing mission scenario. The mission is to approach and dock to a client non-cooperating satellite. The attitude satellite dynamics is presented in quaternion description and simulated with the action of the satellite reaction wheels. The satellite unperturbed

and perturbed on-orbit motions are simulated using the Gauss–Jackson method. The developed models of the attitude and on-orbit dynamics enable simulating the docking maneuver. They can be incorporated with control algorithms for other servicing missions, e.g., a satellite module exchanging.

References

1. Weise, J., Brieß, K.: An Intelligent Building Blocks Concept for On-Orbit-Satellite Servicing, Turin, Italy, 4–6 Sept 2012
2. Berry, M.M., Healy, L.M.: Implementation of Gauss-Jackson integration for orbit propagation. J. Astronaut. Sci. **52**(3), 331–357 (2004)
3. Wigbert, F.: Automated Rendezvous and Docking of Spacecraft. Cambridge Aerospace Series, November 2008. ISBN: 9780521089869
4. Carrou, J.P.: Spaceflight Dynamics. Cepadues Editions. ISBN: 2.85428.376.7
5. Zipfel, P.H.: Modeling and Simulation of Aerospace Vehicle Dynamics, 2nd edn. AIAA. ISBN-13: 978-1-56347-875-8 (alk. paper)
6. Chobotov, V.A.: Orbital Mechanics, 3rd edn. AIA. ISBN: 1-56347-537-5
7. Curtis, H.D.: Orbital Mechanics for Engineering Students. Elsevier (2014). ISBN: 978-0-0-80-97747-8

Nonlinear Dynamics of a Vibration Harvest-Absorber System. Experimental Study

Krzysztof Kecik and Andrzej Mitura

Abstract This paper presents experimental analysis prospect of using a vibration absorber for possible energy harvesting results. To achieve this goal, a classical pendulum-oscillator system (dedicated to vibration suppression) is modified by adding an electromagnetic harvester device. The electromagnetic energy harvester consists of a two fixed and one levitating magnets. The induced energy results from relative movement between magnet and coil, which produces a voltage in the coil by electromagnetic induction phenomenon. When an external excitation is applied to the harvest-absorber system, the levitating magnet will start to oscillate due to the magnetic repulsion of the two fixed magnets. The main goal of this work is to show induced energy of a pendulum-oscillator system with added harvester device, near the main resonance region. The influence of frequency of excitation and resistance load is shown. Additionally, a mathematical model of magnetic levitating force is proposed.

1 Overview of Energy Harvesting

Energy harvesting (EH) is commonly referred to as a process where a given amount of ambient energy is transformed into electrical energy. The ambient energy could be the kinetic energy of a moving or vibrating structure (vibrational harvesters), the radiant energy of sunlight (photonic harvesters) or the thermal energy (radial harvesters), of a warm object [6]. The vibrational devices feed off motion produced as a by-product in order to generate power, and so are natural AC power sources.

K. Kecik (✉) · A. Mitura
Department of Applied Mechanics, Lublin University of Technology,
Nadbystrzycka 36, 20-618 Lublin, Poland
e-mail: k.kecik@pollub.pl

A. Mitura
e-mail: a.mitura@pollub.pl

J. Awrejcewicz (ed.), *Dynamical Systems: Modelling*, Springer Proceedings
in Mathematics & Statistics 181, DOI 10.1007/978-3-319-42402-6_17

Nowadays, there are several energy harvesting methods that convert mechanical energy into electrical energy. The most popular are: electromagnetic energy harvesters (called induction energy harvesters), piezoelectric energy harvesters, magnetostrictive energy harvesters, and electrostatic energy harvesters.

The magnetic induction harvesters generate power through relative motion between a coil of wire and a magnet [8, 15]. The motion of magnet causes the magnetic flux, which leads to generation of a voltage [11]. The level of recovered energy depends mainly on the size of the system and velocity of magnet. The magnitude of energy harvested can vary from milliwatts up to kilowatts [13].

The piezoelectric harvesters produce a voltage when deformed under an applied stress. The magnitude of recovered energy from piezoelectric systems equal from microwatts to watts [1, 14]. Similarly, a magnetostrictive harvester which is based on properties of magnetostrictive material will produce a magnetic field when deformed. The electrostatic energy harvesters use the vibration of a host structure to vary the capacitance of an initially charged capacitor. This variable capacitor acts like a current source that can power an electrical circuit [2]. Energy electromagnetic harvesters based on magnetic levitation started to be studied in the last time [10], especially due to their mechanical structure simplicity (lack of springs or other mechanical elastic elements of suspension), which ensures a high reliability in work.

Similar to harvest energy process is the suppression vibration phenomenon by dynamic absorbers. Therefore, the combination of energy harvesting and vibration suppression seems very promising. The conception of simultaneous vibration suppression and energy harvesting can be found in the literature. Kecik and Borowiec [7] proposed an autoparametric pendulum system to energy harvesting. They propose the rotatory harvester mounted in the pendulum pivot. Energy harvesting effectiveness due to different kinds of pendulum motion is analyzed. The obtained results show that, the chaotic motion of the pendulum generates highest voltage. Hassaan [5] proposes a novel concept for using the mass-spring vibration absorber as energy harvester, and defines a new frequency depending on the mass ratio of the absorber. Mitura et al. [12] proposed a numerical model of a pendulum system with an added harvester device. The magnetic levitation force is treated as linear spring force. Different kind of the pendulum behavior was studied from energy harvesting point of view. The higher recovered energy is obtained for the chaotic motion.

In this paper, the prospect of using a vibration absorber for possible energy harvesting from low frequency vibrations is presented. The studies are carried out on a special laboratory rig. The influence of the excitation frequency and the resistance load on recovered energy is presented. Additionally, the model of the magnetic levitated force is proposed.

2 Concept of Harvest-Absorber System

2.1 Pendulum Absorber System

The experimental study has been performed on a special laboratory rig at Lublin University of Technology. General view of the experimental apparatus is shown in Fig. 1. The main elements are: a mechanical system consists of the pendulum and the oscillator (vibration suppression device), the electromagnetic harvester with electrical circuit and the control-measured module. The system has three degrees of freedom for the mechanical parts and one for the electrical circuit. The data acquisition and control of the system is realized by platform module DSP module and with the help of camera Phantom Miro120 (for magnet measuring).

The harvest-absorber system (Fig. 2) consists of: the pendulum (absorber, (1)), the oscillator (2) and the levitating magnet of harvester device (3). Inside the pendulum the magnetic harvester consist of three magnets is mounted. The detailed description of harvester is presented in the next section. The pivot of the pendulum is connected with an encoder MHK 40 (4). The oscillator (called main system) can be fitted for required dynamical conditions by changing of mass (5). The spring which connects mass of the oscillator and base is linear. The different spring stiffness can be applied depending on dynamical conditions. The dynamics of the

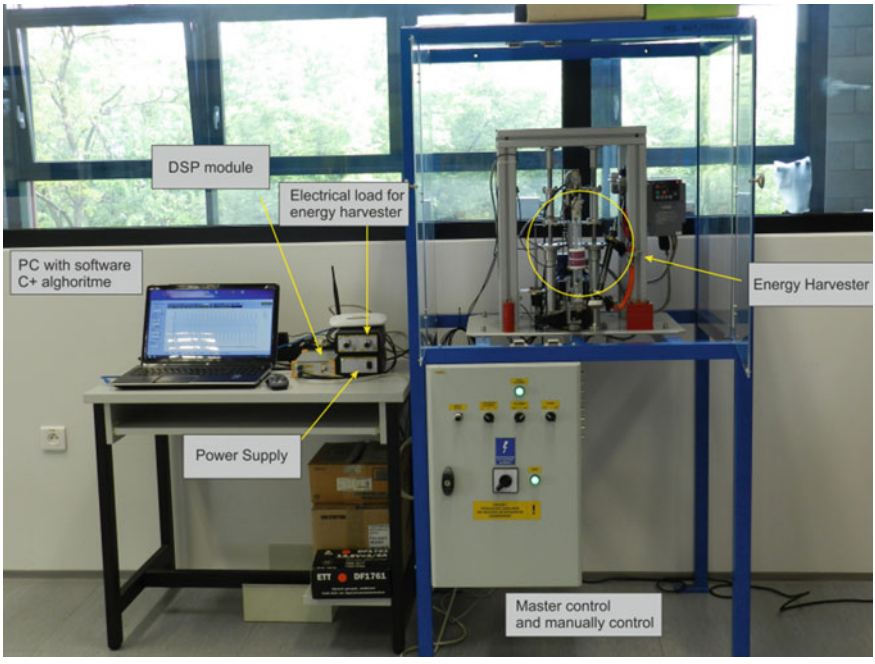

Fig. 1 General view of the experimental apparatus

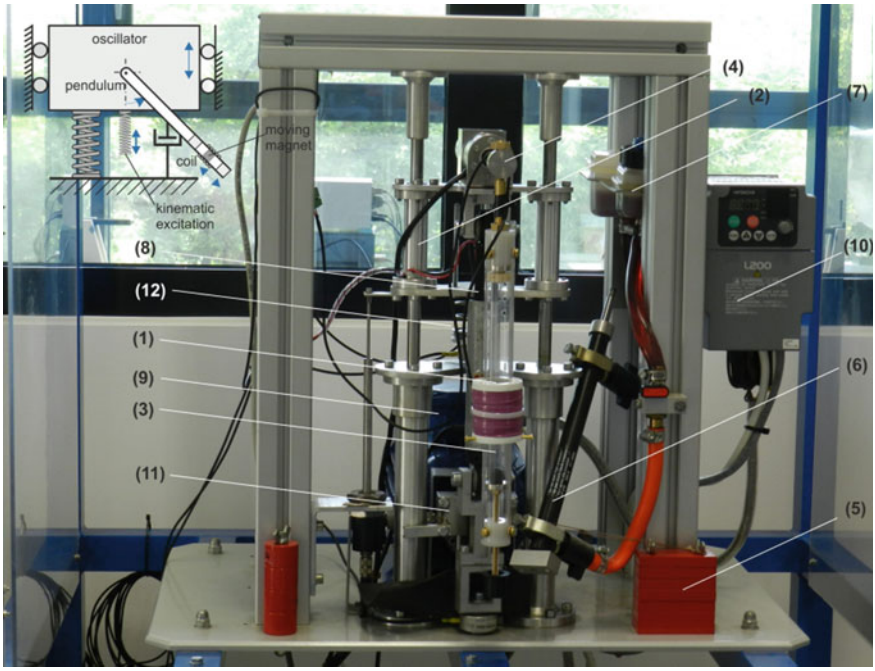

Fig. 2 The oscillator-pendulum system with energy harvester

system is investigated for two dampers variants: a classical linear viscous damper (6) which is controlled by a hydraulic valve connected to an oil tank (7), or a nonlinear magnetorheological damper RD1097-01 (8) with a suitable control system.

The motion of the system is realized by mechanism: a motor 1.5 kW (9), an inverter (10), and a special system which changes rotation of the DC into translational motion of the slider (11). The slider is connected to the main system by the linear spring (12), (kinematic excitation). The mounted spring transmitting motion from motor to oscillator is linear. To verify the harmonic motion of excitation, the slider motion was measured by high-speed camera.

2.2 Electromagnetic Induction Device

A schematic diagram and a photo of the electromagnetic harvester are presented in Fig. 3. From a functional principle point of view, electromagnetic generator is similar to a shaker, but the conversion process is reversed [4]. The electromagnetic harvester device (Fig. 3a) consists of a circular permanent neodymium magnet NdFeB (1), (known as Neo) with axial direction of magnetization and anticorrosion

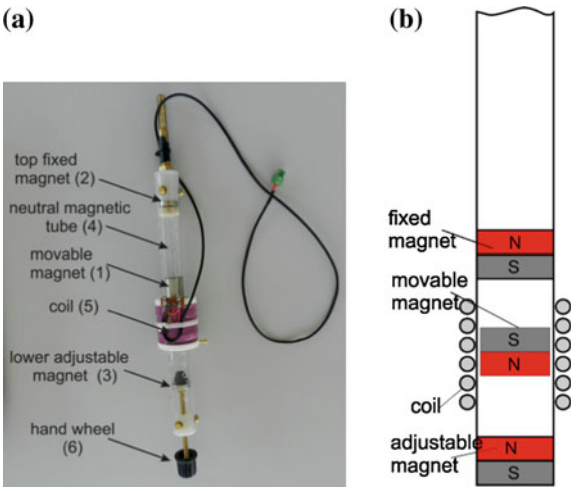

Fig. 3 The view of magnetic pendulum harvester system (**a**) and its scheme (**b**)

coat levitating between two fixed magnets. Two permanent neodymium magnets, top (2) and lower (3) are rigidly fixed to the tube and are oriented such that the middle, unfixed magnet levitates in an equilibrium position. The magnets are placed in such way that all of the magnets facing the surface have the same oriented pole (Fig. 2b). The magnets are a type of strong, and are made of an alloy composed of neodym, iron, and boron to form Nd2Fe14B tetragonal structure. This levitating magnet is free to move vertically within the tube (practically no friction). The position of the lower magnet can be regulated (6), and equilibrium position of the middle magnet is possible to set. The harvester housing is made as a cylindrical piece of tubing (4) from plexiglass material. Transparent material of the tube enables observation motion (displacement and velocity) of the magnet by a camera. In order to ensure free motion, the holes in the tube housing are made (to reduce compressed air).

The both fixed magnets are ring shaped with outer diameter of 20 mm and height of 5 mm. At the outside of the pendulum a wire-wound copper coil (5) is wrapped around outside of the inner tube connected to the resistance load. It can be set by the precision potentiometer from the range of 0–10 kΩ.

The circuit dissipates the produced energy across a load resistor and it is not capable of storing energy. The parameter lists of the magnetic harvester device are presented in Table 1.

When an external excitation is applied to the harvest-absorber system, the middle magnet (levitating) will start to oscillate due to the magnetic repulsion of the two fixed magnets, so a voltage is induced and flows through the circuit.

This relative oscillating motion causes a variation magnetic flux inside the coil. Using Faraday's law the voltage induced in the coil is obtained

Table 1 Measured parameters for the magnetic harvester

Magnet	
Height	35 (mm)
Diameter	20 (mm)
Mass	98 (g)
Coil	
Coil resistance	1150 (Ω)
Coil inductance	1463.6 (mH)
Wire diameter	0.14 (mm)
Turn of winding	12740 (-)
Tube	
Total length	340 (mm)
Mass with two fixed magnets	350 (g)

$$\varepsilon = -\frac{d\phi}{dt}, \tag{1}$$

where ε is the voltage induced and $d\phi$ is the magnetic flux. The residual flux density for a neodymium magnet is around 1.15 T [9]. This value depends on the separation distance between the magnet and the coil.

The induced voltage strongly depends on the position and velocity of the levitating magnet relative to the coil. Therefore, the current through the coil will depend upon the position and velocity of the magnet.

The relationship between the magnet velocity and current for system with an active pendulum in Fig. 4 is presented. The peak harvest current equals 6 mA, for the magnet velocity 0.15 m/s. In Fig. 4a presents the velocity–current phase, for time period 5 s, while in Fig. 5b, only for one cycle (0.5 s). Note, that this figure shows a magnetic hysteresis.

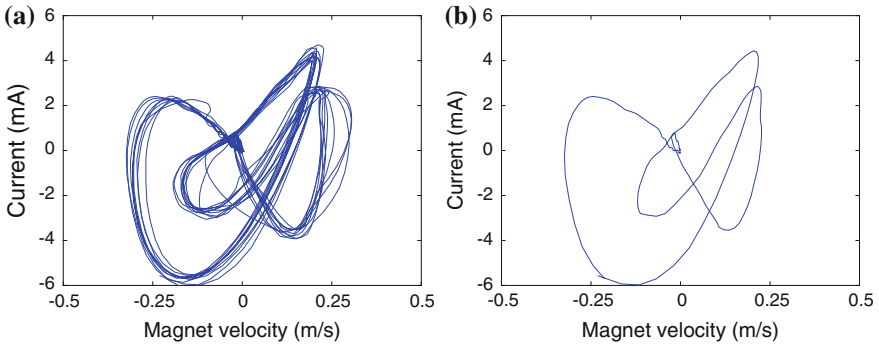

Fig. 4 Experimental results: the levitating magnet velocity versus induced current, for time period 5 s (**a**) and 0.5 s -one cycle (**b**). The frequency of excitation 1.9 Hz, the resistance load 1.15 kΩ, the amplitude of kinematic excitation 20 mm

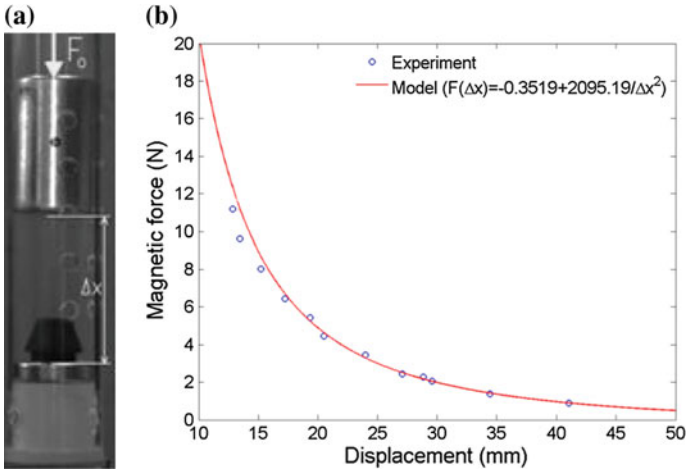

Fig. 5 Photo of the levitating magnet (**a**) and the magnet restoring force $F(\Delta x)$ (**b**) plotted as a function of the separation distance between the movable and bottom magnet (Δx)

The numerical model of the laboratory rig is presented by authors in paper [12], where equations of motion (three for the mechanical parts and one for the electrical circuit) are obtained by the Lagrange's approach. In this model assume that magnetic force is linear function of the magnet's displacement.

3 Results and Discussion

3.1 Static Analysis of Levitating Magnet

Free vibration test was performed to identify the dynamic properties of the harvester device. The natural frequency of the pendulum was identified to 6.47 rad/s. The viscous damping coefficient equals 0.012 Nms.

In the literature, usually levitation of the magnet is treated as magnet suspended on the linear or nonlinear spring [3]. The simply force-displacement test (Fig. 5a) shows that relationship between static force and displacement exhibits strongly nonlinear behavior, especially for large displacements (Fig. 5b). Only, in the small range of displacement it can be assumed as linear characteristics. This test was done with help of high-speed camera Phantom Miro 120 (with resolution 256 × 1024 pixels). In Fig. 5b, blue points mean experimental results, while the continuous line (red) presents a proposed model of the magnetic force.

We proposed the mathematical model of the magnetic force $F(\Delta x)$, based on approximation of the experimental data based on power function

$$F(\Delta x) = a_1 + \frac{a_2}{\Delta x^2}, \tag{2}$$

where a_1 and a_2 are the estimated parameter from experiment.

Optimal value of a_1 and a_2 can be found by minimization of index W

$$W(a_1,\ a_2) = \frac{1}{n}\sum_{i=1}^{n}\left|\sqrt{\frac{a_2}{F_{exp} - a_1}} - \Delta x_{exp}\right|, \tag{3}$$

where n is number of experimental points, F_{exp}, Δx_{exp} are experimental measured restoring force and displacement. In our case the model of magnetic force has a form shown in Fig. 5b.

3.2 Energy Recovery Analysis

The first step of energy harvesting analysis is to find resonance region. The resonance curves are obtained by experimental study of effective power versus the frequency of excitation. In Fig. 6a, b, the resonance responses for the load resistance of 1.15 and 6 kΩ are presented. The amplitude of the excitation was 20 mm. The resonance region where the pendulum executes swings, in both cases, exists in the same range of 1.65–2.05 Hz. The red line corresponds to the nontrivial solution (the oscillator and pendulum oscillates, denoted NT), while the black line indicates semi-trivial solution (only the oscillator vibrates, denoted ST). The black points are experimental results obtained from the laboratory rig.

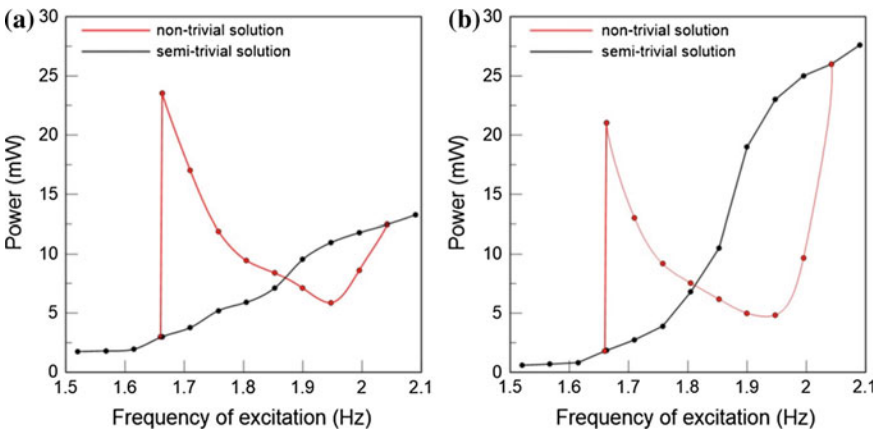

Fig. 6 The power response of the harvest-absorber system for the load resistance 1.15 kΩ (**a**) and 6 kΩ (**b**)

The maximal recovered power is observed for pass to nontrivial solution and equals about 24 mW, for the resistance load 1.15 kΩ (Fig. 6a). Interestingly, that swinging of the pendulum recovered higher energy (compared to semi-trivial solution) for the frequency smaller than 1.85 Hz ("effective pendulum region").

After crossing this value, induced energy is higher, if the pendulum stays in equilibrium. Similar results are observed for 6 kΩ, but the region of "effective pendulum" is smaller. The recovered energy for ST solution increases together with frequency of excitation, especially for the large load resistance (Fig. 6b).

A load resistance circuit is used to experimentally assess the performance of the harvester. The level of damping in the energy harvester can be modified by increasing or decreasing the load resistance. In order to illustrate the energy harvesting consideration, a series of experimental tests have been done. The experimental relationship between the load resistance and response of a nonlinear magnetic harvester is shown in Fig. 7. These results were done in two variants: for ST (Fig. 7a) and NT (Fig. 7b) solutions.

The blue line (with triangle markers) means induced voltage, the red line (circle markers) denotes generated current, while the black line denotes (with cross markers) power. The displacement of the pendulum is described by the green line with square markers. Please note that pendulum in Fig. 7a is inactive (stopped in lower equilibrium position). The increase of the load resistance causes growth of voltage up to 12 V (for 10 kΩ), for ST solution (Fig. 7a). The maximal power corresponds to the resonance peak for the load resistance 6 kΩ and yield 17 mW. Note that higher power differs from the literature suggestion, where usually the power peak is located nearly the coil resistance [6].

The next diagram shows similar results, but in this case of an active absorber (Fig. 7b). In this case, maximal induced power is about 7.5 mW, for the resistance load peak of 3 kΩ.

Interestingly, that displacement of the pendulum practically is independent of the resistance load. The pendulum executes swinging with the same amplitude (the green line has identical level).

Comparing the results of Fig. 7a, b we observe that recovered voltage for the semi-trivial solution is much higher, especially for the resistance load higher than 4 kΩ. However, for lower resistances, the pendulum induces higher power.

Note that for high frequency and/or certain values of load resistance, the magnet jumps out of the coil, what can essential influence on energy harvesting.

The exemplary time histories of the harvest-absorber system in Fig. 8 are presented. The harmonic kinematic excitation with amplitude 20 mm and period 0.525 s is shown in Fig. 8a. The angular pendulum displacement in Fig. 8b is presented. The frequency ratio between the pendulum and the excitation is ½. Note that pendulum executes large swings about 65°.

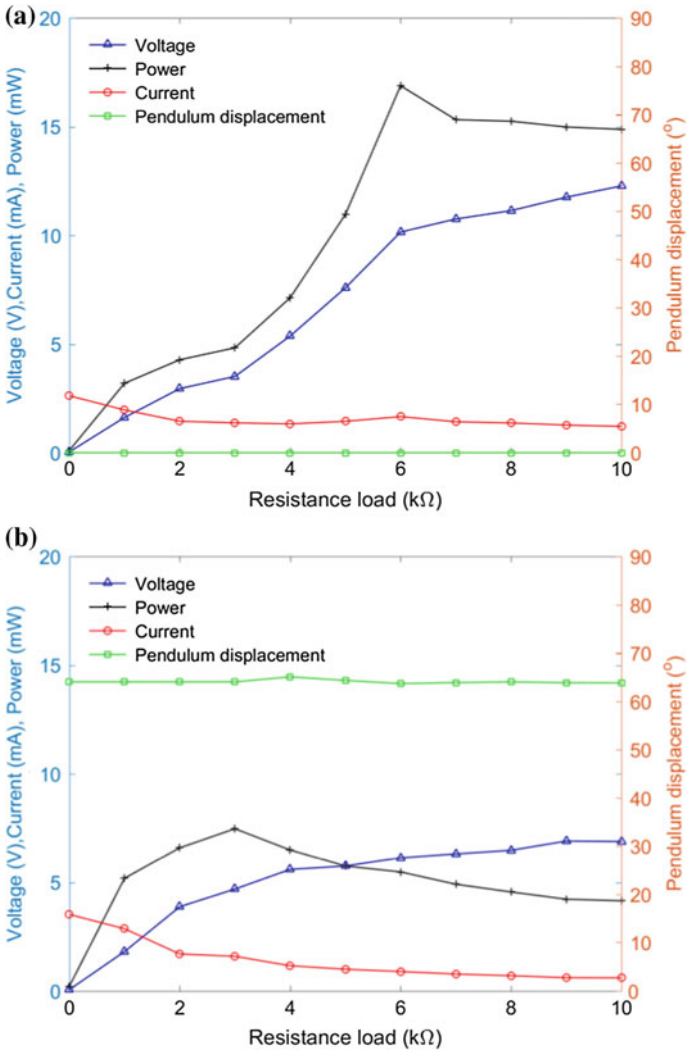

Fig. 7 The induced: power, voltage and current displacement versus the load resistance, for the inactive (**a**) and active (**b**) pendulum, for frequency 1.9 Hz

The velocity of magnet (Fig. 8c) and induced current (Fig. 8d) shows different motion compared to the pendulum. The magnet shows much more complicated behavior compared to the pendulum. This can be the results of impact in the air cushion and small friction of magnet in the tube.

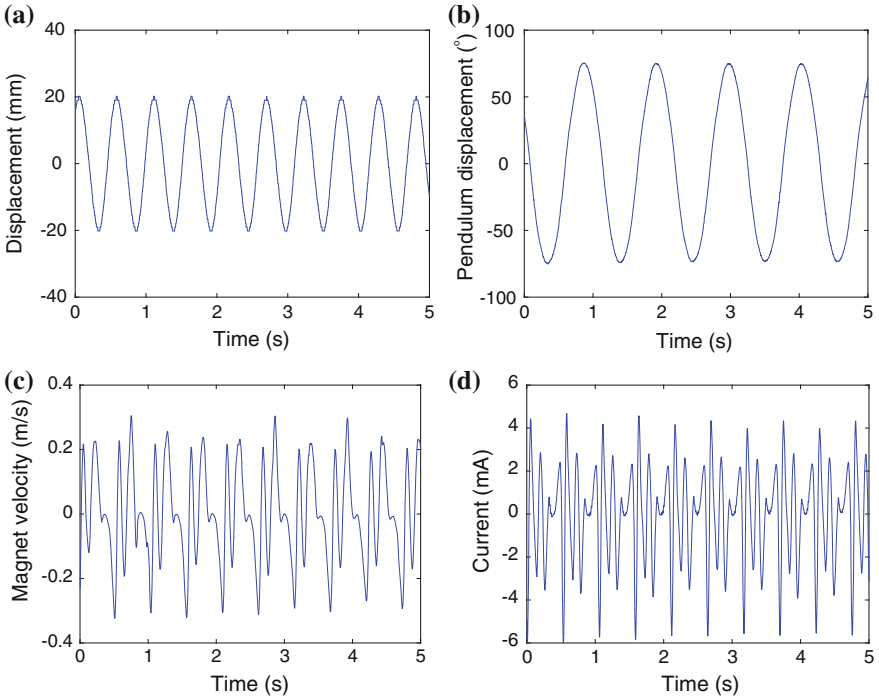

Fig. 8 Experimental results: excitation of the oscillator (**a**), the pendulum (**b**) displacements, velocity of levitation magnet (**c**) and recovered current (**d**), for the frequency 1.9 Hz, the load resistance 1.15 kΩ

4 Conclusions

The paper delivers an energy harvesting analysis focused on experimental results. The harvester device based on the levitating magnet inside the vibration absorber (the pendulum), which is attached to the main system (the oscillator). The concept is dedicated to the pendulum swings. This motion usually is dedicated for dynamic absorbers. The analysis was done near the main parametric resonance, where the pendulum cannot stay in the equilibrium point.

If the pendulum executes a swinging, induced power can be lower or higher and the stay in equilibrium depends on the frequency of excitation and the resistance load. The maximal power obtained for frequency 1.65 Hz and load resistance 1.15 kΩ is about 24 mW. However, the analysis of load resistance influences show that maximal induced power exists for 3 kΩ.

If the pendulum stopped in equilibrium, then the highest recovered power was 25 mW for 2.1 Hz. However, the resistance analysis shows that resonance peak is located for 6 kΩ.

For the vibration suppression, the lower frequencies and the load resistances are recommended. In our case, the frequency and the load resistance should be lower than 1.8 Hz and 4 kΩ. The activation of the pendulum influences on the power peak location. Interestingly, that load resistance not influences on the pendulum's amplitude. The recovered energy strongly depends on the magnet's velocity.

Additionally, we propose the model of the magnetic force based on power function.

The next step will be the numerical simulations of harvest-absorber system. Additionally, to find the compromise between energy harvesting and vibration suppression is one of the aims.

Acknowledgments This work was financially supported under the project of National Science Centre according to decision no. DEC-2013/11/D/ST8/03311.

References

1. Adhikari, S., Friswell, M.I., Inman, D.J.: Piezoelectric energy harvesting. From broadband random vibrations. Smart Material. Structure **18**(11), 115005 (2009)
2. Basset, P., Galayko, D., Cottone1, F., Guillemet, R., Blokhina, E., Marty, F., Bourouinal, T.: Electrostatic vibration energy harvester with combined effect of electrical nonlinearities and mechanical impact. J. Micromech. Microeng. **24**(3) (2014)
3. Foisal, A.R., Hong, C., Chung, G.S.: Multi-frequency electromagnetic energy harvester using a magnetic spring cantilever. Sens. Actuators A: Phys. **182**, 106–113 (2012)
4. Ghreca, R., Olaru, R.: Harvesting vibration energy by electromagnetic induction. Ann. Univ. Craiova Electr. Eng. **35**, 7–12 (2011)
5. Hassaan, G.A.: Optimal design of a vibration absorber-harvester dynamic system. Int. J. Res. Eng. Technol. **3**(6), 325–329 (2014)
6. Joyce, B.S.: Development of an electromagnetic energy harvester for monitoring wind turbine blades. Ph.D. Thesis, Virginia Polytechnic Institute and State University (2011)
7. Kecik, K., Borowiec, M.: An autoparametric energy harvester. Eur. Phys. J. Spec. Top. **222**(7), 1597–1605 (2013)
8. Kulkarni, S., Koukharenko, E., Torah, R., Tudor, J., Beeby, S., O'Donnell, T., Roy, S.: 2008, Design, fabrication and test of integrated micro-scale vibration-based electromagnetic generator. Sens. Actuators A Phys. J. **145**, 336–342 (2008)
9. Magcraft, Permanent Magnet Selection and Design Handbook. Vienna, VA (2007)
10. Mann, B.P., Sims, N.D.: Energy harvesting from the nonlinear oscillations of magnetic levitation. J. Sound Vibr. **319**(1–2), 515–530 (2009)
11. Mitcheson, P.D., Green, T.C., Yeatman, E.M., Holmes, A.S.: Architectures for vibration-driven Micropower Gener. J. Microelectromech. Syst. **13**(3), 429–440 (2004)
12. Mitura, A., Kecik, K., Warminski, J., Jarzyna, W., Lenci, S.: A numerical study of an autoparametric system with electromagnetic energy harvester. In: Proceedings of the ECCOMAS Thematic Conference on Multibody Dynamics 2015, pp. 609–615 (2015)
13. Sivananda, K.R.: Operational behavior of a doubly-fed, permanent magnet generator for wind turbines. MS Thesis, Massachusetts Institute of Technology (2005)
14. Sodano, H., Inman, D., Park, G.: Comparison of piezoelectric energy harvesting devices for recharging batteries. J. Intell. Mater. Syst. Struct. **16**(10), 799–807 (2005)
15. Williams, C., Yates, R.: Analysis of a micro-electric generator for microsystems. Sens. Actuators A Phys. J. **52**, 8–11 (1996)

Three-Chamber Model of Human Vascular System for Explanation the Quasi-Regular and Chaotic Dynamics of the Blood Pressure and Flow Oscillations

Natalya Kizilova

Abstract Arterial blood pressure P(t) and flow V(t) curves measured by ultrasound or other technique exhibit quasi-regular dynamics with clear patterns of the P(V) loops. In this paper, the curves measured in central aorta, upper, and low extremities of young healthy volunteers and patients with cardiovascular disorders are studied. Both quasi-regular and chaotic dynamics of the P(t) and V(t) signals are found. A mathematical model of a series connection of three nonlinear viscoelastic chambers representing central (1) and peripheral arterial (2) and peripheral venous (3) compartments are proposed. The pressure and flow oscillations in each compartment are computed at different model parameters such as resistivity of the microcirculatory bed, elastic and viscous parameters of the arterial and venous walls. It was found the quasi-regular dynamics with different patient-specific patterns of the P(V) attractor are proper to variations of the material parameters within the physiological limits, while the chaotic dynamics appear when wall compliance and/or resistivity of the chambers (2) or (3) are too high. Those variations are proper to deep vein thrombosis, microcirculatory disorders, and age-related degradation of the blood vessel wall.

1 Introduction

Blood flow in the blood vessels is pulsatile that is determined by periodic heart contractions [1]. The heart provide mechanical work to pump an ejected volume of blood against the aortic pressure, gravitation (in the upper arteries and veins) and

N. Kizilova (✉)
Interdisciplinary Centre for Mathematical and Computational Modeling,
Warsaw University, Ul.Prosta, 69, 00-838 Warsaw, Poland
e-mail: n.kizilova@gmail.com

J. Awrejcewicz (ed.), *Dynamical Systems: Modelling*, Springer Proceedings
in Mathematics & Statistics 181, DOI 10.1007/978-3-319-42402-6_18

accelerate the volume up to $v = 60–80$ cm/s in aortic root. Motion of the heart and the valves produces small excitations of both pressure and flow velocity in the aorta and other arteries. In that way, the blood flow is composed of the periodic component pumped at the velocities $v \sim 20–80$ cm/s depending on the diameter of the artery, and the wave component propagating at the wave velocity in the fluid-filled compliant tubes, which is $c \sim 5–8$ m/s in the arteries of a healthy individual and $c \sim 12–15$ m/s in the elderly with more rigid arterial walls affected by atherosclerotic plaques with calcium deposition [2].

The propagating waves are reflected at different nonuniformities in geometric and mechanical properties, such as tapering of the tube, wall thickening and thinning, lesions, stenosis, aneurism, twist, bends, and branching of the arteries. Superposition of the propagated and reflected waves produces complex blood pressure P(t) and flow V(t) waveforms that can be measured invasively via catheters or noninvasively by ultrasound, plethysmography, magnetic resonance imaging, and other techniques. At low wave velocities the reflected waves come back at diastole and produce secondary (dicrotic) peak or peaks on the descending part of the P(t) and V(t) waveforms. At higher wave velocities the reflected waves come at the end- or even mid-systole that gives the waveforms without dicrotic peak but with higher main (anacrotic) peak that gives higher pressure oscillations affecting the vessel wall.

In that way, dynamics of the blood flow in the arteries is complex and may exhibit either regular or chaotic nature [3, 4]. Chaotic spectra of the measured signals have been detected in the renal [5], pulmonary [6, 7], brachial [8], epicardial coronary [9], myocardial [1], central ear [10] arteries of humans and laboratory animals, finger plethysmograms [9], and some other organs. Transitions to the low-dimensional chaos have been observed. Some indexes of the chaotic dynamics have been used in clinical diagnostics of mental disorders [11], lower extremity peripheral arterial disease in diabetic foot [12], and some others [13].

Chaotic dynamics of the blood flow is determined by nonlinear viscoelastic properties of the blood vessel wall [1], flow instability development due to fluid-structure interaction [14, 15], non-Newtonian properties of the blood, nonlinear local and central regulation of the vessel lumen and rigidity with time delay [1], heart rate variability which is chaotic small amplitude variations in the heart rate (beat-to-beat) interval. The last phenomenon is inherent to normal healthy heart, while the others are proper to pathological or age-related changes in the blood and vessel wall properties. A detailed review of existing mathematical models describing the regular and chaotic dynamics of the blood flow is presented in [4].

In this paper the results of experimental study of the blood flow dynamics are presented and importance of the venous compartment of the blood circulation system in development of the chaotic dynamics is shown. A simple mathematical model describing the influence of the viscoelastic properties of the compartments on the blood flow dynamics is developed.

2 Materials and Methods

A series of measurements has been carried out on a control group of young healthy volunteers (11 male, 14 female, age = 23 ± 4 years). Arterial blood pressure curves P(t) in thoracic aorta $P_a(t)$, femoral $P_{fl}(t), P_{fr}(t)$ and brachial $P_{bl}(t), P_{br}(t)$ arteries (both right and left) have been computed from the blood vessel oscillation curves $D(t)$ measured by ultrasound scanner Elegra Advanced (Siemens). The procedure has been described in [3]. The group of patients with age-related cardiovascular diseases (hypertension, atherosclerosis, deep veins thrombosis) consisted of 12 males and 13 females (age = 64 ± 6 years). The measured signals have been treated by Bayesian filter.

Heart rate variability and the phase curves $D'(D)$, where $D' = dD/dt$ have been studied. Some preliminary results of the study have been reported in [4]. Different types of the measured signals have been distinguished (Figs. 1, 2 and 3). The control group demonstrated regular dynamics with high synchronization of the blood pressure oscillations in aorta and peripheral arteries. The example is presented by the curves 1 ($P_a(t)$) and 2 ($P_{fl}(t)$) in Fig. 1. The time shift between the peaks of the anacrotic and dicrotic waves in $P_a(t)$ and $P_{fl}(t)$ is almost constant and

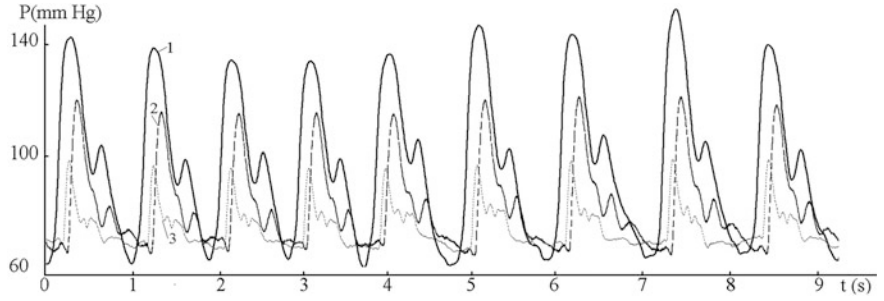

Fig. 1 Pressure oscillations in the abdominal aorta (*1*), *left* (*2*) and *right* (*3*) femoral arteries in a healthy young volunteer

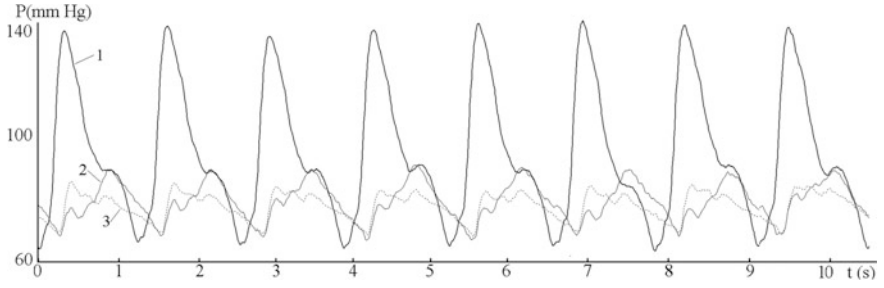

Fig. 2 Pressure oscillations in aorta (*1*), *left* (*2*) and *right* (*3*) femoral arteries in an adult volunteer with deep varicose veins in the *left* leg

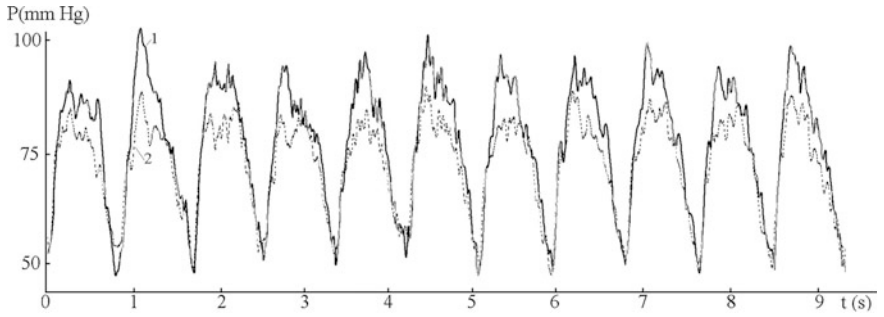

Fig. 3 Pressure oscillations in the *left* (*1*) and *right* (*2*) femoral arteries in an adult volunteer with deep vein thrombosis and atherosclerosis

the end-systolic and end-diastolic blood pressure decay at the same attenuation rate. This correspondence between the $P_a(t)$, $P_{bl}(t), P_{br}(t)$ and $P_{fl}(t), P_{fr}(t)$ has been detected in 21 volunteers from the control group, while four others (two male and two female) exhibited a discordance between one of the $P_{bl}(t), P_{br}(t)$ or $P_{fl}(t), P_{fr}(t)$ curves with others. For instance, the data presented in Fig. 1 show good correspondence between $P_a(t)$ and $P_{fl}(t)$ while the $P_{fr}(t)$ curve possess earlier anacrotic peak provided by the higher pulse wave velocity due to the more rigid arterial walls and faster end-systolic and end-diastolic decay with a series of small amplitude peaks determined by the complex peripheral wave reflection and high compliance of the microcirculatory system. The reported discordance may serve as early index of developing vascular pathology in young individuals.

In the group of elderly patients, good synchronization has not been found. One subgroup demonstrated smooth and regular central aortic pressure with low peak pressure and late dicrotic wave that corresponds to normal compliance of the arterial wall, while the shape of the blood pressure curves measured in the low extremities did not correspond to $P_a(t)$ (Fig. 2). The amplitude of the waves was low and in some cases the dicrotic wave produced by the wave reflection was bigger than the anacropic wave with noticeable and varying time delay between the two waves (curves 2 and 3 in Fig. 2). The delay may be connected with enormously high compliance of the periphery vascular bed and nonlinear properties of the walls. The patients who exhibited this behavior of the measured signals were diagnosed deep varicose vein problems.

The patients with age-related degeneration of the blood vessel walls, atherosclerosis, and thrombosis of deep veins demonstrated very complex discordant high oscillating pressures (Fig. 3). The phase curves $D'(D)$ for that subgroup of patients exhibited chaotic dynamics as it was reported in [4]. In the control group the clear quasi-regular dynamics has been detected even in those individuals who possessed asymmetric signals on their left and right extremities. Involvement of the state of the veins in different blood pressure dynamics means that the mathematical model of the studied system must include not only arterial but also the microcirculatory and venous compartments.

The very good correspondence between the pressures in aorta and left femoral artery (Fig. 4a), and in the left and right brachial arteries (Fig. 4b) in healthy young volunteers also demonstrates quasi-regular dynamics. The systolic parts of the pressure curves correspond to the parallel straight and curved lines in Fig. 4, while the diastolic part may vary from beat-to-beat but with insignificant deviations. Those deviations are practically absent when the arterial junctions are well matched and produce almost zero wave reflection, so the arterial system between aorta and brachial artery serves as optimal waveguide (Fig. 4a). The correlation between the pressure oscillations in the left and right extremities (both upper and low) is not so clear and the straight lines in the $P_{bl}(P_{br})$ and $P_{fl}(P_{fr})$ loops are absent even in the young healthy subjects. In the elderly the arterial junctions are not well matched and produce many reflected waves while the incident wave generated by the heart is propagated along the arterial waveguide. Big area of the loops $P_a(P_l)$ and $P_{bl}(P_{br})$ in Fig. 4 corresponds to high compliancy of arteries in young individuals [16].

The elderly patients with atherosclerosis and varicose veins demonstrated chaotic dynamics in the dependences between different pressure signals. For instance, in the $P_{fl}(P_{fr})$ curve presented in Fig. 5a there is a short linear part at the beginning of systole when the arterial wall is not stretched (below the gray straight line), but the dynamics of the pressure oscillations demonstrate irregular jumps between the subpart of the plane below and over the straight line. This dynamics correspond to uncoordinated variations when the anacrotic or dicrotic peaks of one curves may be lower or higher than the same peaks in the second curve, like in the curves 2 and 3 in Fig. 2. In the studied group those cases corresponded to the deep varicose veins in one or both legs. The beat-to-beat study of separate loops revealed that in some cases a series consequent beats could locate below the grey straight line (in the linear region), but then beat one or a chain of beats jumps into the chaotic region (above the straight line). The jumps between the two regions are irregular and unpredictable. Correlation analysis did not reveal any regularity.

The dependence $P_{bl}(P_{br})$ is almost linear but has random deviations within narrow limits of pressure (Fig. 5b). The small area of the loop corresponds to high

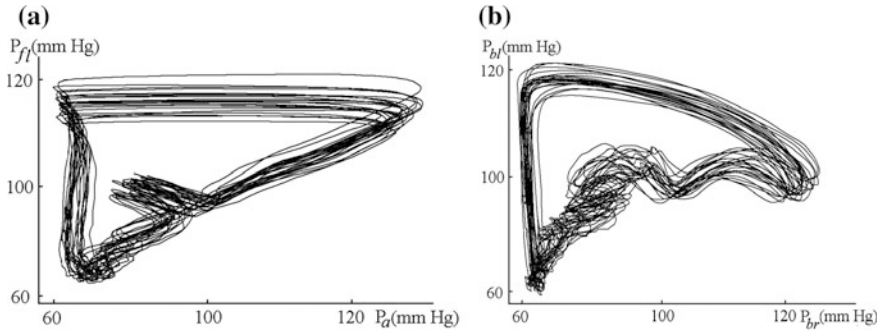

Fig. 4 Dependence between the pressures in aorta and *left* femoral (**a**) and two brachial (**b**) arteries in a healthy young volunteer

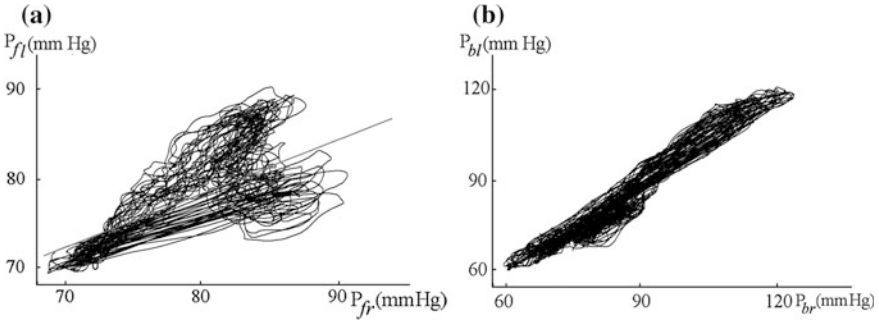

Fig. 5 Dependence between the pressures in *left* and *right* femoral (**a**) and brachial (**b**) arteries in an adult volunteer with deep varicose veins in the *left* leg

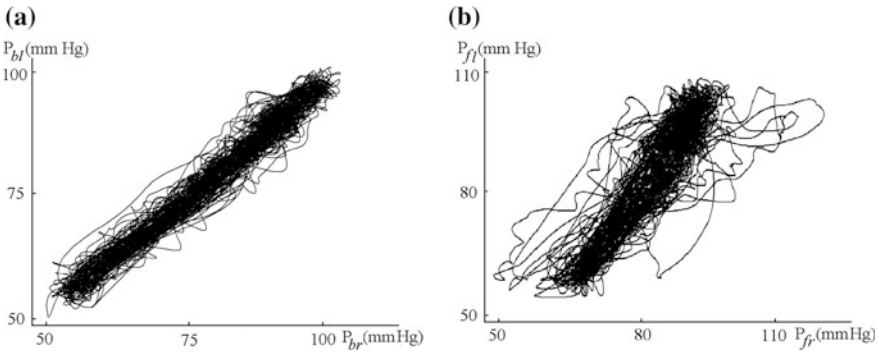

Fig. 6 Dependences between the pressures in *left* and *right* brachial (**a**) and femoral (**b**) arteries in an adult volunteer with deep varicose veins in both legs and atherosclerosis

rigidity of the arterial wall caused by atherosclerosis. The elderly patients with complex cardiovascular diseases demonstrated the chaotic dependencies with large-amplitude high-frequency oscillations (Fig. 6a, b). The small areas of the loops corresponded to high rigidity of the blood vessel wall and noticeable chaotic time delay between the pressures in the symmetric extremities produced by high compliance of the venous compartment.

3 Three-Chamber Mathematical Model

As it was shown by the foregoing measurement data, the compliance of the venous compartment may influence the blood flow dynamics and provide transition from quasi-regular to chaotic behavior. The simplest model describing the pulsatile nature of the blood flow is the Windkessel model [1] that was found useful for

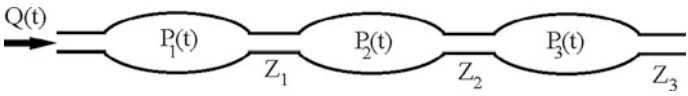

Fig. 7 The model of 3 viscoelastic chamberw in a series connection

explanation of the main features of blood circulation as well as for preliminary modeling and qualitative estimations of regularities in interaction different arterial and venous compartments (Fig. 7). Recently, the novel approach based on superposition of the reservoir (Windkessel) and the wave flows has been proposed [17].

The more complex two-dimensional models of the blood flow in compliant ducts and axisymmetric wave propagation with fluid-wall interaction shows complexity of the flow and appearance of the fluid-based and wall-based unstable modes than could influence the flow stability and lead to transition from the regular to chaotic dynamics [14, 15]. The two-dimensional and one-dimensional models describe the blood flow in separate vessels as compliant tubes and direct computations on the multi-vessel models of arterial vasculatures couples with venous systems is time-consuming and strongly depends on geometry of the organ and vasculature [18, 19]. In that way, the simple Windkessel model (Fig. 7) is considered for quantitative estimations of interactions between the compartments with different compliance of their walls. The model has been tested in [4] for the elastic walls and here the generalization for the viscoelastic wall is proposed.

The Windkessel equations for the viscoelastic walls have the form [1, 4]

$$\begin{aligned} \frac{dV_j(t)}{dt} &= Q_j^{in}(t) - Q_j^{out}(t), \\ Q_{j+1}^{in}(t) &= Q_j^{out}(t), \\ Q_j^{out}(t) &= \frac{P_j(t) - P_{j+1}(t)}{Z_j(t)}, \end{aligned} \tag{1}$$

where V_j, P_j are volume and pressure in the $j = 1, 2, 3$ chambers, $Z_j(t)$ are resistivity of the chambers, $Q_1^{in}(t) \equiv Q(t)$ is known as blood ejection function.

The wall rheology is described by the Kelvin–Voigt viscoelastic body

$$\boldsymbol{\tau}_j \frac{dV_j(t)}{dt} + V_j(t) = F_j(P_j) + \boldsymbol{\lambda}_j \frac{dP_j(t)}{dt}, \tag{2}$$

where $\boldsymbol{\tau}_j$ and $\boldsymbol{\lambda}_j$ are strain and stress relaxation parameters, $F_j(P_j)$ is the elastic law for the passive wall which in a general case is a nonlinear function. The parameters $\boldsymbol{\tau}_j$ and $\boldsymbol{\lambda}_j$ are pressure dependent because the wall thickness, elasticity, and viscosity depends on the pressure in the chamber, but in this model the constant values for $\boldsymbol{\tau}_j$ and $\boldsymbol{\lambda}_j$ are accepted for simplicity.

In the commonly used Windkessel models $Z_j = \text{const}$, $\tau_v = \tau_p = 0$, $F(P) = kP$, k is the wall rigidity.

Substitution of (2) into (1) gives three ODEs for the pressures

$$\begin{aligned}
\frac{d}{dt}\left(F_1(P_1)+\lambda_1\frac{dP_1}{dt}\right) &= \left[I+\tau_1\frac{d}{dt}\right]\left(Q(t)-\frac{P_1-P_2}{Z_1(t)}\right),\\
\frac{d}{dt}\left(F_2(P_2)+\lambda_2\frac{dP_2}{dt}\right) &= \left[I+\tau_2\frac{d}{dt}\right]\left(\frac{P_1-P_2}{Z_1(t)}-\frac{P_2-P_3}{Z_2(t)}\right),\\
\frac{d}{dt}\left(F_3(P_3)+\lambda_3\frac{dP_3}{dt}\right) &= \left[I+\tau_3\frac{d}{dt}\right]\left(\frac{P_2-P_3}{Z_2(t)}-\frac{P_3}{Z_3(t)}\right),
\end{aligned} \tag{3}$$

where I is the unit operator.

The system (3) may be reduced to the six-order nonlinear ODE for any P_j. The final form is not presented here due to complexity. The main sources of nonlinearities are nonlinearity of the vessel walls $F_j(P_j)$, time-dependent resistivity $Z_j(t)$ that may be time delay function $Z_j(t-\varsigma)$ and the time delay ς determined by active respond of the vessel wall or/and central nervous and humoral regulation is different in young healthy and elderly individuals. Introduction the pressure-dependent functions $\tau_j(P_j)$ and $\lambda_j(P_j)$, as well as more complex active resistivity $Z_j(t, P_j, P_{j+1})$ determined by the influence of the pressures in the adjacent chambers will add new sources of nonlinear behavior of the system.

Solution of the nonlinear system (3) as expansion over a small parameter has been proposed in [20] for the case $\lambda_j = 0$. When the walls are pure elastic and the rheological law $F_j(\mathrm{P}_j)$ is the same in the three chambers, (3) can be reduced to the third-order ODE [4].

Since numerical estimations on (3) accounting for time and pressure-dependent parameters are senseless for medical applications because the dependencies $\tau_j(P_j)$, $\lambda_j(P_j)$, $Z_j(t, P_j, P_{j+1})$ are not known for the compartment, the simplified model with $\lambda_j = 0$, $\tau_j, Z_j = \text{const}$ is considered. When $F_j(P_j)$ are linear functions (linear elasticity of the chamber walls) then (3) can be reduced to the third-order linear ODE with constant coefficients

$$\begin{aligned}
&([\mathfrak{T}_2][\mathfrak{T}_4]+[\mathfrak{T}_2][\mathfrak{T}_5]-[\mathfrak{T}_3][\mathfrak{T}_6])[\mathfrak{T}_1]P_2(t) =\\
&=[\mathfrak{T}_2][\mathfrak{T}_5]\left(Q(t)\cdot I+\tau_1\frac{dQ(t)}{dt}\right),
\end{aligned} \tag{4}$$

where $[\mathfrak{T}_1] = \frac{1}{Z_1}I + \frac{\tau_1}{Z_1}\frac{d}{dt}$, $[\mathfrak{T}_2] = \frac{Z_2+Z_3}{Z_2Z_3}I + \frac{(Z_2+Z_3)\tau_3}{Z_2Z_3}\frac{d}{dt}$, $[\mathfrak{T}_3] = \frac{1}{Z_2}I + \frac{\tau_3}{Z_2}\frac{d}{dt}$, $[\mathfrak{T}_4] = -\frac{1}{Z_1}I + \frac{\tau_2}{Z_1}\frac{d}{dt}$, $[\mathfrak{T}_5] = \frac{Z_1+Z_2}{Z_1Z_2}I + \frac{(Z_1+Z_2)\tau_2}{Z_1Z_2}\frac{d}{dt}$, $[\mathfrak{T}_6] = \frac{1}{Z_2}I + \frac{\tau_2}{Z_2}\frac{d}{dt}$.

Equation (4) describes regular dynamics of the blood pressure oscillations in the three chambers. To describe the influence of the nonlinear wall on the blood flow dynamics, let us introduce the rheological law for the chamber wall in the form [21]

$$F_j(P_j) = \frac{4}{3\pi}\left(\frac{3f_j(1-\sigma_j^2)(P_j(t)-g_j)}{4\sqrt{\pi}E_j h_j}\right)^3, \tag{5}$$

where f_j, g_j are constants, h_j, E_j, σ_j are thickness, Young modulus, and Poisson ratio of the walls.

Solution of the nonlinear system (3), (5) can be found using the method of expansions developed in [21]. Then the first-order approximation can be found from the linearized model. Here the consecutive approximation method has been used for numerical computations on the nonlinear model. The characteristic values $f_j, g_j, \tau_j, h_j, E_j, \sigma_j$ proper to the arterial ($j = 1$), microsirculatory ($j = 2$), and venous ($j = 3$) compartments. The physiological limits for the normal and pathological walls [1] have been used to describe the blood dynamics in young healthy individuals and elderly persons. Since the resistivity Z_j reflecting the net effect of the resistive blood vessels of the compartments are not well estimated in the literature, the characteristic value Z^* has been introduced and the difference in the young and elderly systems has been described by relatively low (young) and high (elderly) values. The influence of the dimensionless parameters Z_j/Z^* has been studied in numerical computations. The averaged arterial, capillary, and venous pressures have been used as initial approximation. The periodic function $Q(t) = \alpha \sin(2\pi t/T) + \beta cos(2\pi t/T)$ has been used in order to apply the model to any measured input function $Q(t)$ by its Fourier expansion. Convergence of the iterative process has been controlled by comparison of the difference in the consecutive solutions.

4 Results and Discussions

The computations have been aimed at determination of the model parameters responsible for transition from the regular to chaotic dynamics, especially the wall compliance and viscosity determined by E_j and τ_j, and relative resistivity $Z_1/Z_2, Z_2/Z_3$. The regular input signal $Q(t)$ may produce chaotic dynamics in the $P_j(t), Q_j(t)$ when the system is not linear and described by ODE of order ≥ 3. Validity of the model has been checked by comparative analysis of dynamics of the systems with high and low compliance of the chamber walls. The computed dimensionless pressure-flow rate $P(Q)$ loops in the arterial chamber ($j = 1$) in the case of high $E^* \sim 10^5 Pa$ (Fig. 8a) and low (Fig. 8b) distensibility. When the chamber walls are more rigid, the bigger pressure is needed to provide the even smaller flow rate (Fig. 8b) than in the chamber with more compliant wall (Fig. 8a) The tangent $\tan\alpha = dP/dQ$ that determines the pulse wave velocity in arteries is smaller in the compliant (Fig. 8a) and bigger in the rigid (Fig. 8b) chambers that correspond to theoretical derivations for the fluid-filled compliant tubes. The smoothness of the upper parts of the loops is determined by the wall viscosity. For

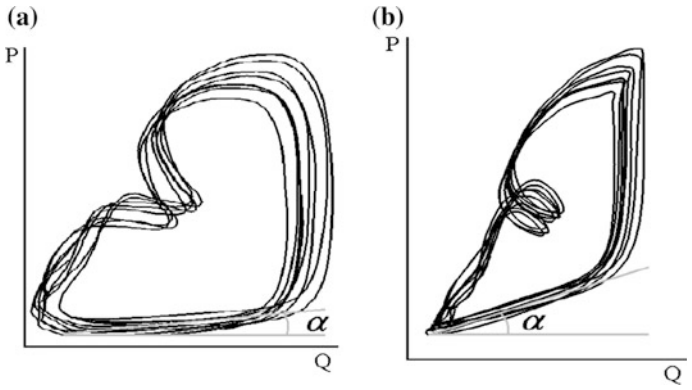

Fig. 8 $P(Q)$ loops in the chamber with compliant (**a**) and more rigid (**b**) wall

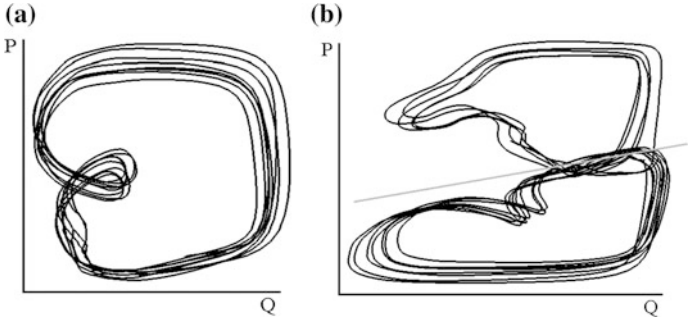

Fig. 9 $P(Q)$ loops for the regular (**a**) and chaotic (**b**) dynamics

the pure elastic wall $\tau_j = 0$ the loops have acute part (Fig. 8b). The presence and size of the secondary small loops in the pressure-decaying part of the loops is determined by differences in τ_1/τ_2, τ_2/τ_3 (Fig. 9a, b).

5 Conclusions

The phenomena of quasi-regular blood flow dynamics in young healthy individuals and chaotic dynamics in the elderly have been studied by experimental measurements of the pressure signals in aorta, brachial, and femoral arteries. The chaotic dynamics connected with varicose and thrombosis of deep veins is studied. The mathematical model describing the circulation system as a series connection of arterial, capillary, and venous chambers with nonlinear walls is formulated. The

model is based on three nonlinear ODEs for the pressures $P_{1-3}(t)$. Numerical computations for the model parameters corresponded to the physiological data revealed the transition from regular to chaotic dynamics when the chamber wall compliance and resistivity differs 2–3 orders of magnitude that corresponds to the physiological measurement data.

References

1. Nichols, W., O'Rourke, M., Vlachopoulos, C.H. (Eds.): McDonald's Blood Flow in Arteries: Theoretical, Experimental and Clinical Principles. Hodder Arnold (2011)
2. Milnor, W.R.: Hemodynamics. Williams & Wilkins, Baltimore (1989)
3. Kizilova N., Philippova H., Zenin O.: A realistic model of human arterial system: blood flow distribution, pulse wave propagation and modeling of pathology. In: Korzynskiego, M., Cwanka, J. (eds.) Mechanika w Medycynie, vol. 10, pp. 103–118. Rzeszow (2010)
4. Kizilova, N.: Blood flow in arteries: regular and chaotic dynamics. In: Awrejcewicz, J., Kazmierczak, M., Olejnik, P., Mrozowski, K. (eds) Dynamical Systems. Applications, pp. 69–80. Lodz Politechnical University Press (2013)
5. Wagner, C.D., Persson, P.B.: Nonlinear chaotic dynamics of arterial blood pressure and renal blood flow. Am. J. Physiol. **268**(2), H621–H627 (1995)
6. Glenny, R.W., Polissar, N.L., Mckinney, S., Robertson, H.T.: Temporal heterogeneity of regional pulmonary perfusion is spatially clustered. J. Appl. Physiol. **79**, 986–1001 (1995)
7. Venegas, J.G., Galletti, G.G.: Low-pass filtering, a new method of fractal analysis: application to PET images of pulmonary blood flow. J. Appl. Physiol. **88**, 1365–1373 (2000)
8. Shirouzu E., Tsuda Y., Sugano H.: Nonlinear analysis of pulse waves measured at brachial artery. In: Proceedings of 1st Joint BMES/EMBS Conference, vol. 2, p. 901 (1999)
9. Trzeciakowski, J., Chilian, W.: Chaotic behavior of the coronary circulation. Med. Biol. Eng. Comput. **46**(5), 433–442 (2008)
10. Shlesinger, M.F.: Fractal time and 1/f noise in complex systems. Ann. N. Y. Acad. Sci. **504**, 214–228 (1987)
11. Oyama-Higa, M., Miao, T.: Representation of a physio-psychological index through constellation graphs. Lect. Notes Comput. Sci. **2610**, 811 (2005)
12. Li, Ch-M, Du, Y-Ch., Wu, J.-X., et al.: Dynamic analysis with a fractional-order chaotic system for estimation of peripheral arterial disease in diabetic foot. Meas. Sci. Technol. **24**(8), 1–11 (2013)
13. Chen, H.-K., Lee, Ch-I: Anti-control of chaos in rigid body motion. Chaos, Solitons Fractals **21**(4), 957–965 (2004)
14. Hamadiche, M., Kizilova, N.N.: Temporal and spatial instabilities of the flow in the blood vessels as multi-layered compliant tubes. Int. J. Dyn. Fluids **1**(1), 1–23 (2005)
15. Kizilova, N., Hamadiche, M., Gad-el-Hak, M.: Mathematical models of biofluid flows in compliant ducts: a review. Arch. Mech. **64**(1), 1–30 (2012)
16. Kizilova, N.N.: Pulse wave reflections in branching arterial networks and pulse diagnosis methods. J. Chin. Inst. Eng. **26**(6), 869–880 (2013)
17. Tyberg, J.V., Davies, J.E., Wang, Z.h., et al.: Wave intensity analysis and the development of the reservoir–wave approach. Med. Biol. Eng. Comput. **47**, 221–232 (2090)
18. Zenin, O.K., Kizilova, N.N., Philippova, E.N.: Studies on the structure of human coronary vasculature. Biophysics. **52**(5), 499–503 (2007)
19. Kizilova, N.: A detailed digital model of the human arterial system. In: Proceedings of the 1st International Conference on Complex Medical Engineering, pp. 287–292. Japan (2005)

20. Kizilova, N.: A novel model for explanation the regular and chaotic dynamics in arterial blood flow. In: Dynamical Systems and their Applications, p. 30. Book of abstracts, Kiev (2015)
21. Alastruey, J., Khir, A.W., Matthys, K.S., et al.: Pulse wave propagation in a model human arterial network: assessment of 1-D visco-elastic simulations against in vitro measurements. J. Biomech. **44**, 2250–2258 (2011)

Maximization of Average Velocity of Vibratory Robot (with One Restriction on Acceleration)

Maria Golitsyna and Vitaly Samsonov

Abstract The subject of the study is control synthesis for a vibratory robot, which is presented by a rigid box with a pendulum inside it. The robot can move forward and backward and there is a Coulomb friction between the box and the surface. There are considered certain constraints of motion of the robot and limitations of control. In this paper, there is shown that the proposed control not only provides motion within the constraints and limitations but also maximizes average velocity of the robot. This control contains two phases on each period: resting phase where the box is standing still and gliding phase where the robot is moving forward. To show the advantages of the proposed solution there is provided numerical comparison between different types of control. Numerical experiments also show that the considered control appears to be energetically efficient.

1 Introduction

Lately, the theme of vibration-driven robots has drawn interest of scientists both from Russia and other countries. Vibratory robots are usually presented by mechanisms that can transform oscillations into linear motion and turning of the robot.

The main advantage of vibratory robots compared to robots with wheels, legs, caterpillar treads, and other outer manipulators is that the considered class of robots can be represented by solid capsule, so that no interaction with outer world is guaranteed. Such robots can be used in aggressive environment as their vehicles are hard to damage.

M. Golitsyna (✉)
Department of Mechanics and Mathematics, Lomonosov Moscow State University, Michurinski Prosp. 1, 119192 Moscow, Russian Federation
e-mail: marykulikovskaya@gmail.com

V. Samsonov
Institute of Mechanics, Lomonosov Moscow State University, Michurinski Prosp. 1, 119192 Moscow, Russian Federation
e-mail: samson@imec.msu.ru

J. Awrejcewicz (ed.), *Dynamical Systems: Modelling*, Springer Proceedings in Mathematics & Statistics 181, DOI 10.1007/978-3-319-42402-6_19

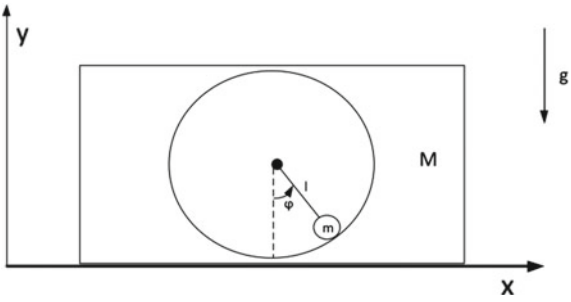

Fig. 1 Considered model of vibratory robot

The dynamics of plane motion of vibratory robots was investigated in papers [7–10, 15–17]. One-dimensional motion with movable inner masses is considered in studies [1–6, 9, 11–14]. Robots can be presented by several bodies connected with each other by a spring [14] or by a single body with internal oscillating elements [1–13, 15–17]. Several authors solve the problem of search of control, assuming that the movement is made in viscous environment and that there is either quadratic or piecewise smooth friction law [3, 4, 16]. In most papers devoted to the theme one-dimensional motion of the main body is provided either by horizontal movement of one mass [2–6, 13] or by two masses, one of which is moving along horizontal axis and the other—along vertical [1, 5, 9].

In this paper, a research of the control synthesis for a vibratory robot is provided. Consider the movement of the system to be in two dimensions, and the robot to be presented by a rigid box with a pendulum inside it. Assume the mass of the rigid box to be denoted as M and of the pendulum—m, respectively (see Fig. 1). The box can move along Ox axis forward and backward, and there is a Coulomb friction between the box and the surface. In study [11] viscous friction in the joint is taken into account, in the current paper we will ignore it.

The unicity of the considered model is that, provided by rotation of the inner mass, the control moment can impact not only on the sign of the tractive force but also on the value of the normal support reaction force and the friction force, respectively.

2 Problem Definition

There are two coordinates, that define the state of the system: x—corresponds to the coordinate of center of mass of the box and φ—the angle of pendulum deviation from the direction of the gravitational acceleration (φ is measured counterclockwise). We will consider the motion class that corresponds to the following conditions:

1. The size of the box guarantees nontoppling of the system.
2. Value of the normal support reaction force is nonnegative (this condition ensures that there will be no hopping of the box).

The task is to find the control law in the considered class of motion such that:

1. The control of the robot is represented by a choice of angular acceleration $\ddot{\varphi}$ of the pendulum.
2. There are two phases on one revolution of the pendulum: gliding phase, where $\dot{x} > 0$ and resting phase, where $\dot{x} = 0$.
3. Angular velocity of the pendulum $\dot{\varphi} > 0$.
4. The motion of the robot is 2π-periodic.
5. There is a restriction on the maximum value of angular acceleration $\ddot{\varphi}_{max}$. This restriction corresponds with technical characteristics of the DC motor that provides rotation of the pendulum. In the current problem definition, we will assume that there is no restriction on the minimum value of angular acceleration, considering that the system can slow down using other mechanical elements (friction in joint, etc.).
6. The chosen control law should provide maximum average velocity of the box.

Let us write down the equation of motion of center of mass along Ox axis for the case when $\dot{x} > 0$:

$$(m + M)\ddot{X}_{cr} = -\mu N, \tag{1}$$

where $X_{cr} = \frac{Mx+m(x+lsin\varphi)}{m+M}$ is the coordinate of center of mass of the whole system, N—the normal support reaction force. The expression of N can be derived from the principle of motion of center of mass projected on the vertical axis:

$$N = (m + M)g - ml(cos\ddot{\varphi}) \tag{2}$$

Let us introduce dimensionless and characteristic quantities:

$$\tilde{x} = \frac{x}{\eta}, \tilde{t} = \frac{t}{\tau}, \tilde{\varphi} = \frac{\varphi}{\phi}, \tag{3}$$

From now on, let (η, τ, ϕ) denote the characteristic quantities, and $(\tilde{\bullet})$ the dimensionless quantities. Let's define the characteristic quantities in the following way: $\eta = \frac{ml}{m+M}$, $\tau = \sqrt{\frac{\eta}{g}}$, $\phi = 1$ rad.

After substituting Eq. 2 into Eq. 1, considering Eq. 3, we will get

$$(\tilde{x} + (sin\tilde{\varphi} - \mu cos\tilde{\varphi}))'' = -\mu, \tag{4}$$

Equation 4 is the motion equation of the gliding phase. It is clear that in the dimensionless quantities, the motion of the robot depends on only one parameter $-\mu$.

Similarly, the equation of motion of center of mass projected on Ox axis for the case $\dot{x} = 0$ can be written down. Bellow, there are presented the equations of motion of the pendulum, that provide its maximum acceleration (when the value of the friction is at its maximum in absolute value, and its vector is directed along the growth

of the x coordinate) and maximum slow-down (when the value of the friction is at its maximum in absolute value, and its vector is directed along the descent of the x coordinate):

$$(sin\tilde{\varphi} + \mu cos\tilde{\varphi})'' = \mu \tag{5}$$

$$(sin\tilde{\varphi} - \mu cos\tilde{\varphi})'' = -\mu \tag{6}$$

3 Gliding Phase

Assume that at $\tilde{t} = 0$, the robot starts its gliding phase. Suppose that Eq. 4 is valid. The second motion equation must be defined, such that it would enforce effective motion of the robot in positive direction.

Lemma 1 *If the second motion equation for the gliding phase would be the following:*

$$\tilde{N} = 0, \tag{7}$$

then the resulting motion would appear to have maximum value of center-of-mass velocity.

The proof of the lemma can be obtained from Eq. 1, because in the right part of the equation there is a non-positive quantity that reaches its maximum when $\tilde{N} = 0$.

Such choice of the second motion equation on the gliding phase provides movement of the robot without friction with constant center-of-mass velocity. Constancy of velocity is provided by zero value of the forces projected on Ox axis.

If we solve Eq. 7 for vertical position of the pendulum ($\tilde{\varphi} = \pi$) then we can derive respective value of angular velocity ($\tilde{\varphi}' = 1$). Therefore to get initial and terminal angular velocity–angle relationship, we should integrate Eq. 2:

$$\tilde{\varphi}'_0 = \sqrt{2(1 + cos\tilde{\varphi}_0)}/csc\varphi_0, \tag{8}$$

where $\tilde{\varphi}_0$ and $\tilde{\varphi}'_0$ denote starting angle and angular velocity, respectively.

Assume that there is a minimum acceleration constraint $\tilde{\varphi}'' > \tilde{\varphi}''_{min}$, where $\tilde{\varphi}''_{min}$ is a parameter.

If there are acceleration constraints of the form $\tilde{\varphi}''_{min} < \tilde{\varphi}'' < \tilde{\varphi}''_{max}$, than initial and terminal values of angle and angular velocities can be uniquely determined from Eq. 7, after substitution of the constraints and expression of angular velocity Eq. 8. Taking as initial (terminal) value of angle something different from the given above will lead to breaking one of the restrictions. For instance, if initial value of angle is below $\tilde{\varphi}_0$ then the restriction on maximum value of angular acceleration would be broken and if the value of initial angle would appear to be above $\tilde{\varphi}_0$ then the normal support reaction force would become negative.

Given the fact that there are the restrictions on maximum and minimum values of angular acceleration, the gliding phase would consist of three parts:

1. movement provided by rotation of the pendulum with its' minimum angular acceleration ($\tilde{\varphi}'' = \tilde{\varphi}''_{min}$) up to the moment when the angle would become equal to $\tilde{\varphi}_0$;
2. motion defined by Eq. 7 that is movement without friction up to the moment when the restriction on the maximum value would be reached;
3. motion is provided by rotation of the pendulum with maximum angular acceleration $\tilde{\varphi}'' = \tilde{\varphi}''_{max}$ up to the moment when the box of the robot will stop ($x' = 0$).

The choice of the part without friction was reasoned above already, so it is necessary now to explain the choice of the first and the third part of the phase. It is not possible to stop the motion of the box of the robot on the second part of the phase as there is the restriction on maximum angular acceleration $\tilde{\varphi}''_{max}$. This means that it is necessary to change the law of movement. After running several numerical tests it was shown that if on the first and the third part of the phase angular acceleration would appear less then restrictions allow, then average velocity of the robot x' would also appear less then in case when moving along restrictions.

Lemma 2 *Absolute freedom in choice of angular acceleration allows achieving infinitely large average velocity of center of mass of the robot.*

Proof Let us derive angular acceleration from Eq. 7:

$$\tilde{\varphi}'' = \frac{-1 - \tilde{\varphi}'^2 cos\tilde{\varphi}}{sin\tilde{\varphi}}$$

This expression implies that achieving angles equal to ϵ or $2\pi - \epsilon$, where ϵ is a small quantity, can be provided by angular accelerations, which are of order $\frac{1}{\epsilon^3}$. If it will be considered that there are no restrictions on angular velocity, then the loop (by loop here we mean one cycle) can be closed and hence movement without friction can be provided. This lemma combined with Eq. 1 implies that angular velocity of center of mass of the robot is always equal to zero and thus any value of average velocity can be maintained (even infinitely large velocity).

Note 1 Maximum value of average velocity of center of mass of the robot is defined by restrictions on angular acceleration of the pendulum.

Note 2 Lemma 2 also implies that restriction on angular acceleration can be derived in order to provide any predefined average velocity of center of mass of the robot.

Hence, if the system can be optimized by choosing restrictions on angular acceleration of the pendulum (both maximum and minimum value), then it would lead to infinite values.

4 Resting Phase

It is necessary to maximize average velocity of the robot throughout the cycle, for resting phase it means to maximize average angular velocity

$$\frac{_{delta}\tilde{\varphi}}{\tilde{t}} \tag{9}$$

There will be used two considerations to find optimal control on the resting phase:

1. Maximization of average angular velocity of the pendulum.
2. The movement has to be 2π-periodic.

Let us denote by $\tilde{\tau}_1$ the time, when the box of the robot is moving forward, while the pendulum is rotating with minimum angular acceleration $\tilde{\varphi}'' = \tilde{\varphi}''_{min}$ (from starting point up to the moment when it is possible to move without friction ($\tilde{\varphi} = \tilde{\varphi}_0$)). $\tilde{\tau}_1$is a parameter of the system, so if $\tilde{\tau}_1$ and $\tilde{\varphi}''_{min}$ are given then both starting and terminal conditions of the resting phase are determined.

Let us prove the following lemma:

Lemma 3 *To provide maximum average angular velocity of the pendulum on the resting phase laws of control should be chosen as follows:*

1. *First part—motion, provided by maximum possible angular velocity along cone of friction* (Eq. 5) *up to the moment when the restriction on maximum acceleration* $\tilde{\varphi}''_{max}$ *is reached.*
2. *Second part—motion with* $\tilde{\varphi}'' = \tilde{\varphi}''_{max}$.
3. *Third part—motion with* $\tilde{\varphi}'' = \tilde{\varphi}''_{min}$.
4. *Forth part—motion, provided by minimum possible angular velocity along cone of friction* (Eq. 6) *up to the moment when starting conditions of the gliding phase are reached.*

Before proving the lemma let us make the following note:

Note 3 The moment of switching from the second part to the third part of the resting phase can be defined uniquely, given the knowledge that the motion has to be 2π-periodic and that starting and terminal conditions of the phase are determined.

Proof of Lemma 3.

In Fig. 2, angular velocity–angle dependency curve is drawn. The crosshatched region corresponds to the resting phase and numbers above correspond to the parts of the phase with respect to the numbers given in the lemma.

$\tilde{\varphi}_e$ and $\tilde{\varphi}_b$, are starting and terminal angles of the resting phase. If any other law of control was chosen, then corresponding line would lie within the crosshatched region, this means that provided control law for every angle between $\tilde{\varphi}_e$ and $\tilde{\varphi}_b$ ensures maximum angular velocity and this, in turn, proves that the chosen control provides maximum average angular velocity on the resting phase.

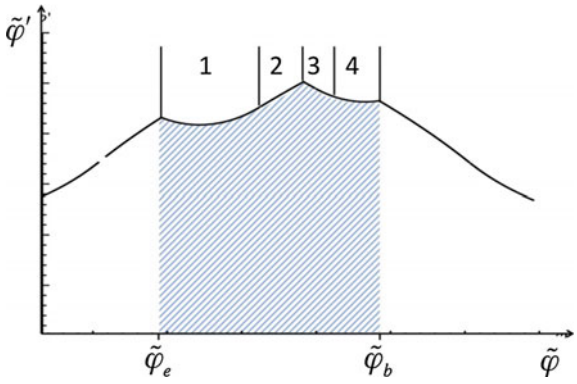

Fig. 2 Angular velocity versus angle curve

Note 4 In previous research, the optimization of the control by choosing right parameter $\tilde{\tau}_1$ was already conducted. It turned out there that $\tilde{\tau}_1$ should be increased up to its maximum value. Maximum value of the parameter is defined by condition of 2π-periodicity. This optimization leads to shortening of the resting phase by two parts, so that optimal control on the phase would consist only from the first and the second part, defined in the Lemma 3, respectively.

In Fig. 3, angular velocity angle curve is shown for the case where the value of $\tilde{\tau}_1$ is optimal in terms of maximization of average velocity of the robot.

Thus, in this part of the paper, a core principle of control synthesis for the resting phase that maximizes average velocity of the box was shown.

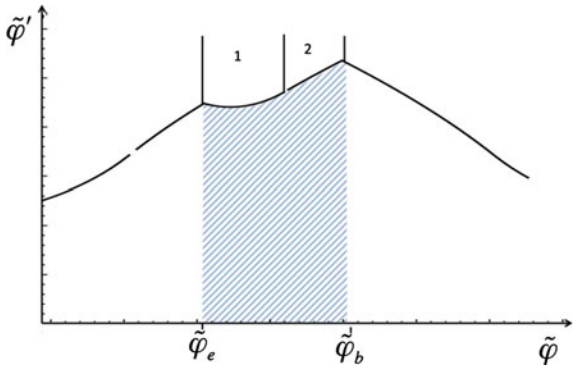

Fig. 3 Angular velocity versus angle curve

5 Numerical Experiments and $\tilde{\varphi}''_{min}$ Optimization

Let us take the following characteristic parameters for the numerical experiments: $\mu = 0.05$, $\eta = 0.04$ (For instance, these parameters can correspond to these values $m = 1$ kg, $M = 4$ kg, $l = 0.25$ m, $g = 9.8$ m/s^2).

Let us consider that the restriction on maximum acceleration is $\tilde{\varphi}''_{max} = \frac{100}{49}$ (respective dimensional value is 500 rad/s^2), and the restriction on the minimum value $\tilde{\varphi}''_{min} = -\frac{100}{49}$, then the optimal value of the parameter $\tilde{\tau}_1 = 0.47$.

Figure 4 demonstrates angular acceleration time dependency, where orange parallel lines correspond to the restrictions on angular acceleration ($\tilde{\varphi}''_{max}$ and $\tilde{\varphi}''_{min}$). The diagram shows that throughout all the time of motion all restrictions are met. Below main diagram there is a detalization of one period, numbers there correspond to different parts of motion. Numbers from 1 to 3 correspond do gliding phase: motion with minimum angular acceleration, motion without friction and motion with maximum angular acceleration. Numbers 4 and 5 correspond to resting phase and these parts conform to 1 and 2 part of the phase, described in Lemma 3.

Figure 5a illustrates dependency between time and angle modulo 2π. The gray line corresponds to 2π value. This diagram shows that angle is time periodic, and this means that considering that the system is 2π-periodic is equivalent to considering that it is time periodic with some period T.

In Fig. 5b the normal support reaction force time dependency is drawn. This diagram illustrates that the normal support reaction force is always non-negative and that there are phases when $\tilde{N}$ is equal to zero.

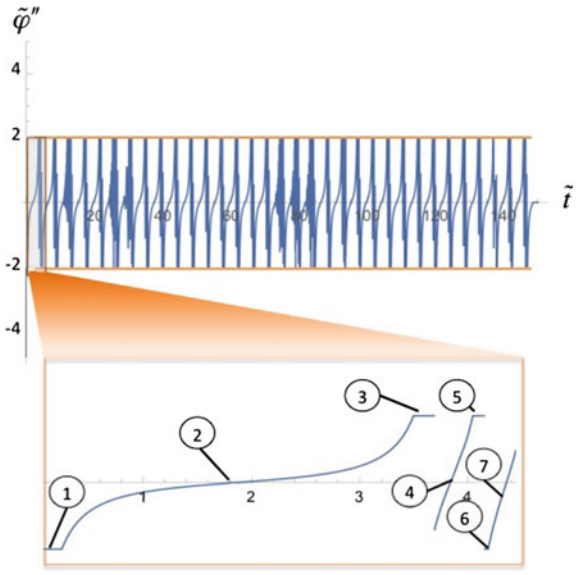

Fig. 4 Angular acceleration–time dependency

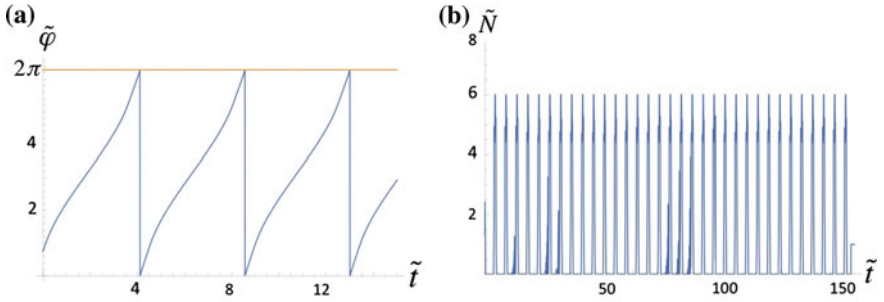

Fig. 5 **a** Angle modulo 2π-time dependency, **b** normal support reaction force–time dependency

Lemma 4 *Average velocity of the box of the robot increases as the restriction on the minimum angular acceleration* $\tilde{\varphi}''_{min}$ *goes down. Maximum average velocity of the box of the robot with the chosen control synthesis can be achieved with the restriction on minimum angular velocity such that*

- *There is* 2π*-periodicity.*
- *Optimal* $\tilde{\tau}_1$ *is equal to zero, so that the gliding phase would consist from 2 parts: movement without friction and movement with maximum angular velocity.*

To show the validity of the statement there was numerically performed several experiments and average velocity of the box versus absolute value of the restriction on minimum angular acceleration dependency was drawn (Fig. 6a). The starting restriction on minimum angular acceleration was chosen equal to the restriction on maximum angular acceleration in absolute values, after that every calculation was made with step $\frac{1}{10}$ up to the moment when the first hypothesis of the lemma stopped to be true. This diagram shows that indeed the average velocity of the box of the robot increases with growth of the restriction on minimum angular acceleration in absolute values.

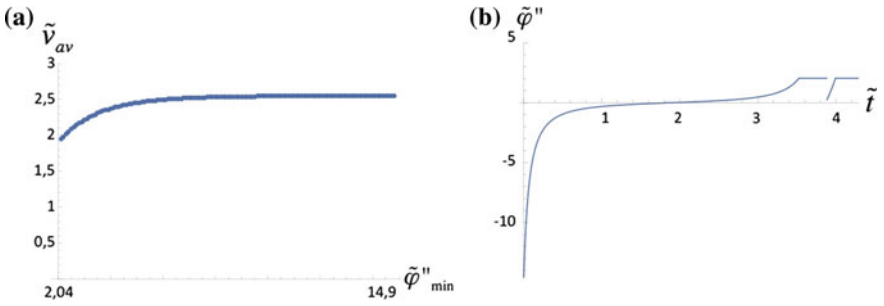

Fig. 6 **a** Average velocity–absolute value of minimum angular acceleration dependency, **b** angular acceleration–time dependency on one period

Figure 6b depicts angular acceleration time dependency calculated for the optimal choice of the restriction on minimum value of angular acceleration. In Fig. 6b, the dependency is drawn for only one period, as it can be seen, the gliding phase now consists form only two parts, so that there is no part of the phase where the robot is moving with minimum angular acceleration, thus optimal $\tilde{\tau}_1$ here is equal to zero. This condition determines the choice of the optimal restriction on the minimum angular acceleration. If the restriction on the angular velocity will be less than its optimal value, than the condition of 2π-periodicity would not be fulfilled, because beginning the gliding phase with minimum value of angular acceleration requires higher angular velocity then it could be provided on the resting phase.

Hence, following equations can represent optimal control synthesis:

$$\begin{cases} \tilde{N} = 0 & \text{if } \tilde{\varphi}_0 < \tilde{\varphi}(mod 2\pi) < \tilde{\varphi}_1 \\ \tilde{\varphi}'' = \tilde{\varphi}''_{max} & \text{if } \tilde{\varphi}_1 \le \tilde{\varphi}(mod 2\pi) \bigcup \tilde{x}' \ge 0 \\ (\sin\tilde{\varphi} + \mu\cos\tilde{\varphi})'' = \mu & \text{if } \tilde{\varphi}'' \le \tilde{\varphi}''_{max} \\ \tilde{\varphi}'' = \tilde{\varphi}''_{max} & \text{if } \tilde{\varphi}(mod 2\pi) \le \tilde{\varphi}_0 \end{cases} \tag{10}$$

In the system Eq. 10 starting and terminal angels of the part, where robot is moving without friction, are denoted by $\tilde{\varphi}_0$ and $\tilde{\varphi}_1$, respectively. The first two equations of the system correspond to the gliding phase and the second two—to the resting phase.

For this set of parameters optimal value of the restriction on minimum value of angular acceleration $\tilde{\varphi}''_{min} = -15.2$.

In Fig. 7, a comparison between different types of control synthesis is shown. There is drawn coordinate of center of mass of the robot versus time dependency for following control laws:

1. Orange curve corresponds to a relay control, which ensures periodic motion.
2. Blue line corresponds to a control law similar to the described above. The main difference of the control method lie in the fact that in place of the condition of 2π-periodicity there is a condition of symmetry of the resting phase. This solution is described in more detail in paper [12].
3. Velvet line corresponds to a control law with equal in absolute values restrictions on maximum and minimum angular acceleration ($|\tilde{\varphi}''| \le \tilde{\varphi}''_{max}$) and with non-optimal choice of the parameter $\tilde{\tau}_1 = 0.25$.
4. Brown line corresponds to a control law same as previous but with optimal choice of parameter $\tilde{\tau}_1$ ($\tilde{\tau}_1 = 0.47$).
5. Black line corresponds to a control law with both optimal value of parameter $\tilde{\tau}_1$ and optimal value of the restriction on minimum value of angular acceleration.

The restrictions on maximum angular velocity and initial conditions for all simulations were the same, thus such comparison is legitimate. In dimensional quantities the time of simulation is equal to 10 s, and black control law allows the robot to cover 15.8 m, brawn—11.8 and velvet—9.5 m, respectively, which is more then twice as much as can be covered by orange control law. This diagram shows that every step of optimization allows significant improvement of solution of the optimization problem.

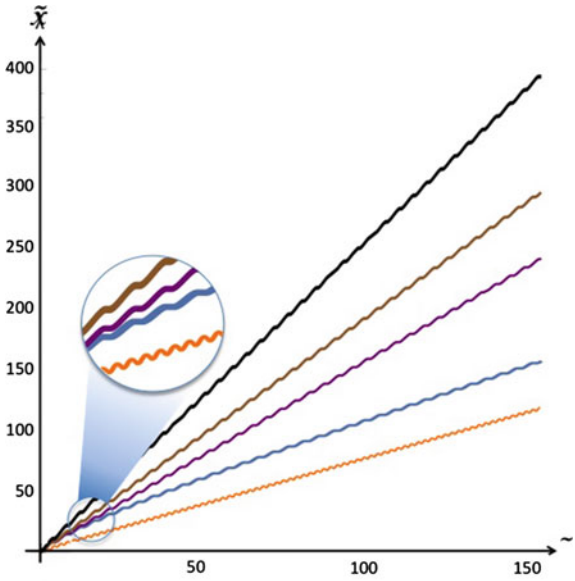

Fig. 7 Comparison of several control law on a diagram of center of masses of the robot–time dependency

Solution described in this paper and similar solutions (2–4) described in papers [12] and the other previous research also show energy efficiency in comparison with relay control law (1). This conclusion could be made from detailed part of Fig. 7, where it could be seen that orange curve has its ups and downs (this corresponds to moving forwards and backwards, respectively), while all other curves do not have intervals, corresponding to moving backwards. This means that for control laws (2–5) all energy is used to move the robot forwards, while in orange control law some energy is wasted on moving backwards.

6 Conclusion

In this article, there has been found optimal control for the vibratory robot, represented by a box and a pendulum within it.

Optimal control here is defined in terms of maximization of average velocity of the robot along Ox axis and the chosen class of motion.

It is also important to point out that according to Eq. 10 to implement this control it is necessary to measure not only the angle of the pendulum, but also angular acceleration and velocity of center of mass of the robot.

There has been made several numerical experiments that illustrated that chosen control law provides movement of the robot within all restrictions. There has been also provided numerical comparison between different control laws and it demonstrated that chosen control ensures fastest motion.

It has been also shown that such control laws (represented by (2–5) in Fig. 7) are more energetically efficient then the relay control law.

References

1. Bolotnik, N.N., Figurina, T.Yu.: Optimal control of the rectilinear motion of a rigid body on a rough plane by means of the motion of two internal masses. J. Appl. Math. Mech. T. **72**(2), 126–135 (2008)
2. Bolotnik, N.N., Zeidis, I.M., Zimmermann, K., Yatsun, S.F.: Dynamics of controlled motion of vibration-driven systems. Izvestiya Akademii Nauk. Teoriya i Sistemy Upravleniya **5**, 157–167 (2006)
3. Chernous'ko, F.L.: Analysis and optimization of the motion of a body controlled by means of a movable internal mass. J. Appl. Math. Mech. **70**(6), 819–842 (2006)
4. Chernous'ko, F.L.: The optimal periodic motions of a two-mass system in a resistant medium. J. Appl. Math. Mech. T. **72**(2), 126–135 (2008)
5. Chernous'ko, F.L., Bolotnik, N.N.: Mobile robots controlled by the motion of internal bodies. Tr. Inst. Mat. i Mekh. UrO RAN **16**(5), 213–222 (2010)
6. Gerasimov, S.A.: Vibration drift with quadratic drag. Mech. Solids **42**(2), 184–189 (2007)
7. Grankin, A.N., Yatsun S.F.: Investigation of vibroimpact regimes of motion of a mobile microrobot with electromagnetic drive. Izvestiya Akademii Nauk. Teoriya i Sistemy Upravleniya **1**, 163–171 (2009)
8. Ivanov, A.P., Sakharov, A.V.: Dynamics of rigid body, carrying moving masses and rotor, on a rough plane. Nelin. Dinam. **8**(4), 763–772 (2012)
9. Jatsun, S.F., Bolotnik, N.N., Zimmerman, K., Zeidis, I.: Modeling of motion of vibrating robots. In: Proceedings of 2th IFToMM World Congress, June 18–21 (2007)
10. Jatsun, S.F., Shevyakin, V.N., Volkova, L.Yu., Serebrovskiy, V.V.: Dynamics of operated movement of three-mass robot on a flat surface. T. Izvestiya of the Samara Scientific Centre of the Russian Academy of Science, vol. 13, no. 4–4, 1134–1138 (2011)
11. Kulikovskaya, M.V.: Control of vibratory robot. In: Proceedings of International Youth Scientific and Practical Conference "Mobile robots and Mechatronics" (Russia), pp. 100–104 (2011)
12. Kulikovskaya, M.V.: Maximization of velocity of vibratory driven robot. In: Proceedings of the XXVIII International Conference "Mathematical Methods in Engineering and Technology" (Russia), 6 pages, (2015)
13. Sorokin, K.S.: Motion of a mechanism along a rough inclined plane using the motion of internal oscillating masses. J. Comput. Syst. Sci. Int. **4**(6), 993–1001 (2009)
14. Vartholomeos, P., Papadopoulos, E.: Dynamics, design and simulation of a novel microrobotic platform employing vibration microactuators. J. Dyn. Syst. Meas. Control **128**(1), 122–133 (2005)
15. Vartholomeos, P., Papadopoulos, E.: Analysis, design and control of a planar micro-robot driven by two centripetal-force actuators. In: International Conference on Robotics and Automation-ICRA, pp. 649–654 (2006)
16. Volkova, L.Yu., Jatsun, S.F.: Control of the three-mass robot moving in the liquid environment. Nelin. Dinam. **7**(4), 845–857 (2011)
17. Zhan, X., Xu, J.: Locomotion analysis of a vibration-driven system with three acceleration-controlled internal masses. Adv. Mech. Eng. **7**(3) (2015). doi:10.1177/1687814015573766

Asymptotic Solution of the Problem to a Convective Diffusion Equation with a Chemical Reaction Around a Cylinder

Rustyam G. Akhmetov and Natalya V. Maksimova

Abstract We consider the convective diffusion around the cylinder streamlined cross-flow of fluid at low Reynolds numbers, in view of the volume of the chemical reaction. The characteristic peculiarity of the task is the presence of the large number dimensionless parameters: Peclet numbers and constants of chemical reaction. The relation of these of parameters is supposed to be constant. The leading terms of the asymptotic solution around the cylinder are constructed. The method of matched asymptotic expansions is used for solving the problem.

1 Introduction

Let the cylinder with radius a streamlined cross flow of ideal fluid with velocity U at infinity. The study will be carried out in a cylindrical coordinate system with the origin on the axis of the cylinder, where the angle is measured from the direction of the flow at infinity. The distribution concentrations in dimensionless variables satisfies to the equation (e.g., see., [1], ch. 5, (6.1)−(6.3))

$$\varepsilon^2 \Delta u - \frac{1}{r}\left(\frac{\partial u}{\partial r}\frac{\partial \psi}{\partial \theta} - \frac{\partial u}{\partial \theta}\frac{\partial \psi}{\partial r}\right) - \mu F(u) = 0, \tag{1}$$

Where $\mu = \frac{k_\nu}{Pe}$ is a constant, $\varepsilon = Pe^{-1/2}$ is a small parameter, $Pe = \frac{aU}{D}$ is Peclet number, D is the diffusion coefficient of the substance in the outer phase, k_ν is a parameter depending on the chemical reaction rate.

R.G. Akhmetov (✉) · N.V. Maksimova
Bashkortostan State Pedagogical University, Faculty of Physics and Mathematics,
ul. Oktyabr'skoy Revolutsii 3a, 450000 Ufa, Russia
e-mail: akrust@mail.ru

N.V. Maksimova
e-mail: Natasha18091986@mail.ru

J. Awrejcewicz (ed.), *Dynamical Systems: Modelling*, Springer Proceedings
in Mathematics & Statistics 181, DOI 10.1007/978-3-319-42402-6_20

The boundary conditions are the form

$$u = 1 \text{ at } r = 1, u \to 0 \text{ at } r \to \infty. \tag{2}$$

The velocity field of fluid out of the cylinder is determined by the expression [2]

$$\upsilon_r = \frac{1}{r}\frac{\partial \psi}{\partial \theta}, \upsilon_\theta = -\frac{\partial \psi}{\partial r}, \tag{3}$$

$$\psi(r, \theta) = \left(r - \frac{1}{r}\right)\sin\theta, \tag{4}$$

where $\psi(r, \theta)$—is a stream function (e.g., see., [3], ch. 6, Sect. 5, (39)).

It is assumed that $F(u)$ is continuous and satisfy the conditions of

$$F: R^1 \to R^1, F(0) = 0, F'(u) > 0, F(u) \in C^\infty(R). \tag{5}$$

In the vicinity of a cylinder, one has to consider several boundary layers. In each region new independent variables are introduced, then Eq. (1) is recorded in these variables, and the solution is constructed by the method of matched asymptotic expansions (Fig. 1). For convenience, we introduce the mutually overlapping region, we assume that α, β, γ satisfies the inequalities $0 < \alpha < \beta < \gamma < 1$.

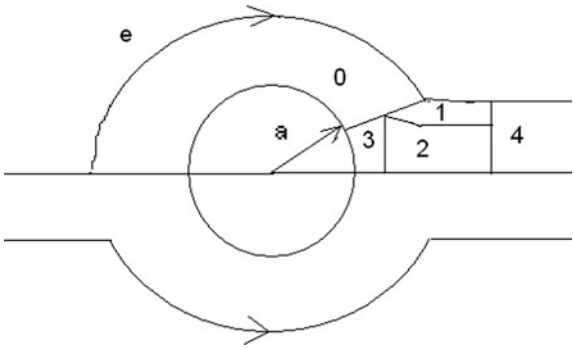

Fig. 1 e—is the exterior domain: $D^{(e)} = \{\varepsilon \le r - 1, \varepsilon \le \psi\}$, 0—is the diffusion boundary layer: $D^{(0)} = \{0 \le r - 1 \le 2\varepsilon^{1-\alpha}, \varepsilon^\beta \le \theta \le \pi\}$, 1—is the convective boundary layer: $D^{(1)} = \{\varepsilon^{1-\alpha} \le r - 1 \le 2\varepsilon^{\alpha-1}, \varepsilon^{\gamma+1} \le \psi \le 2\varepsilon^\gamma\}$, 2—is the internal domain of the diffusion trail: $D^{(2)} = \{\varepsilon^{1-\alpha} \le r - 1 \le 2\varepsilon^{\alpha-1}, 0 \le \psi \le 2\varepsilon^{\gamma+1}\}$, 3—is the rear stagnation point domain: $D^{(3)} = \{0 \le r - 1 \le 2\varepsilon^{1-\alpha}, 0 \le \theta \le 2\varepsilon^\beta\}$, 4—is the mixing domain: $D^{(4)} = \{\varepsilon^{\alpha-1} \le r, \psi \le 2\varepsilon^\gamma\}$

2 The Diffusion Boundary Layer

The asymptotic solution of the diffusion boundary layer is built in variables $t = \varepsilon^{-1}(r-1)$, θ, for the main term of the expansion we obtain the following equation:

$$\frac{\partial^2 u^{(0)}(t,\,\theta)}{\partial t^2} - 2t\cos\theta\frac{\partial u^{(0)}(t,\,\theta)}{\partial t} + 2\sin\theta\frac{\partial u^{(0)}(t,\,\theta)}{\partial\theta} - \mu F(u^{(0)}(t,\,\theta)) = 0, \quad (6)$$

$$u^{(0)}(0,\theta) = 1; u^{(0)}(t,\,\theta) \to 0 \text{ as } t \to \infty, \frac{\partial u^{(0)}}{\partial\theta}(t,\,\pi) = 0. \quad (7)$$

Construction of the solution of the problem (6), (7) are first performed together with the construction of the asymptotic expansion of the solution at $\theta \to \pi$, in particular, in the region $\{(t,\theta): t \geq 0,\ \delta_1 \leq \theta \leq \pi\}$ for some $\alpha_1 > 0,\ \delta_1 > 0$ and satisfies the estimate (see [4, 5])

$$0 < u^{(0)}(t,\theta) \leq \exp(-\alpha_1 t^2).$$

The structure of the asymptotics of $u^{(0)}(t,\theta)$ at $\theta \to 0$ is different for small and large values of ψ. For small ψ asymptotic expansion is constructed in the variables t, θ, and if the values ψ are separated from zero in the variables ψ_0, τ, where $\tau = \frac{1}{2}(1+\cos\theta)$.

The asymptotics of the function $u^{(0)}(t,\,\theta)$ as $\theta \to 0$ is sought in the view

$$u_0(t) + o(\theta),$$

where the function $u_0(t)$ is constructed [6] for small μ as the solution for the problem

$$\frac{\partial^2 u_0(t)}{\partial t^2} - 2\,t\,\frac{\partial u_0(t)}{\partial t} - \mu F(u_0(t)) = 0, \quad (8)$$

The boundary conditions have the following form

$$u_0(0) = 1; u_0(t) \to 0 \text{ at } t \to \infty. \quad (9)$$

The study [6, 7] gives the following.

Theorem *Let $F(u)$ satisfy condition (5), then the solution of the Eq. (8) for $t \to +\infty$ has the following asymptotic expansion*

$$u_0(t) = \sum_{i=1}^{\infty} \sum_{k=0}^{\infty} c_{k,i} t^{-i\delta - 2k}, \tag{10}$$

where $\delta = \frac{\mu}{2}$ *and* $c_{k,i}$ *have the form:* $c_{0,1} = \text{const}, c_{1,1} = -\frac{\delta^2 + \delta}{4} c_{0,1}, c_{0,2} = F_2 c_{0,1}^2, c_{1,2} = \frac{1}{\delta+1}(2\,\delta F_2 c_{0,1} c_{1,2} - \delta\, c_{0,2}(1+2\,\delta)), c_{0,3} = \frac{1}{2}(2\,F_2 c_{0,1} c_{0,2} + F_3 c_{0,1}^3), \ldots$.

The idea of the proof is similar to works [8, 9].

In [6, 7] the coefficients $c_{k,i}$ are found numerically.

In Eq. (6) the function $F(u_0^{(0)})$ can be represented as a Taylor series with remainder term and linear part are left on the left side, the rest move to the right side of the equation. Then we get the following equation:

$$L\,u^{(0)} - \mu_1\, u^{(0)} = f_0(u^{(0)}), \tag{11}$$

where $L\,u \equiv \frac{\partial^2 u}{\partial t^2} - 2t\cos\theta \frac{\partial u}{\partial t} + 2\sin\theta \frac{\partial u}{\partial \theta}$, $f_0 = \mu\big(F(u) - F'(0)u\big) = \frac{\mu}{2} F''(\tilde{u})(u)^2$ and $\mu_1 = \mu F'(0)$. For convenience, we set $F'(0) = 1$.

In Eq. (11) we make the following change of functions and variables [10]

$$\psi_0 = t\sin\theta,\ \tau = \frac{1}{2}(1 + \cos\theta),\ u = g\,V = \left(\frac{1+\tau}{1-\tau}\right)^{-\mu/4} V. \tag{12}$$

Then (11) takes the form

$$\frac{\partial^2 V(\psi_0, \tau)}{\partial \psi_0^2} - \frac{\partial V(\psi_0, \tau)}{\partial \tau} = q(\nu) g^{-1}(\tau) f_0\big(V(\psi_0, \tau)\big), \tag{13}$$

where $q(\tau) = O(\tau^{-1})$ as $\tau \to 0, q(\tau) = O((1-\tau)^{-1})$ as $\tau \to 1$ and $f_1 = g^{-1}(\tau) f_0$.

The boundary conditions have the following:

$$V = \left(\frac{1+\tau}{1-\tau}\right)^{\mu/4},\ \psi_0 \to 0,\ \tau > 0, \tag{14}$$

$$V \to 0 \text{ as } \psi_0 \to \infty. \tag{15}$$

We consider the auxiliary problem

$$\frac{\partial^2 V(\psi_0, \tau)}{\partial \psi_0^2} - \frac{\partial V(\psi_0, \tau)}{\partial \tau} = 0. \tag{16}$$

The solution of (16), (14) and (15) are described by the expression:

$$V(\psi_0,\tau)=\frac{1}{2\sqrt{\pi}}\int\limits_0^{\tau}\left(\frac{1+t}{1-t}\right)^{\mu/4}\frac{\psi_0}{(\tau-t)^{3/2}}\exp\left(-\frac{\psi_0^2}{4(\tau-t)}\right)dt. \tag{17}$$

Then the solution of the problem (11), (14), (15), when $f_0\equiv 0$ will have the form

$$g^{(0)}(\psi_0,\tau)=\frac{1}{2\sqrt{\pi}}\left(\frac{1-\tau}{1+\tau}\right)^{\mu/4}\int\limits_0^{\tau}\left(\frac{1+t}{1-t}\right)^{\mu/4}\frac{\psi_0}{(\tau-t)^{3/2}}\exp\left(-\frac{\psi_0^2}{4(\tau-t)}\right)dt. \tag{18}$$

In the case when the function $F(u)$ is a linear formula analogous of (18) is obtained in [7]

$$u^{(0)}(t,\theta)=g^{(0)}(\psi_0,\tau)+O(\varepsilon^{2\delta-\gamma_0}).\ \text{as}\ y=O(\varepsilon^{-\delta/4})\ \text{for a certain}\ \gamma_0>0. \tag{19}$$

3 The Rear Stagnation Point Domain

The solution is constructed in the area of the rear stagnation point in the variables $\xi=\frac{\theta}{\varepsilon}$, $t=\frac{r-1}{\varepsilon}$, for the main member we have the following equation:

$$\frac{\partial^2 u^{(3)}(\xi,t)}{\partial t^2}+\frac{\partial^2 u^{(3)}(\xi,t)}{\partial \xi^2}-2t\frac{\partial u^{(3)}(\xi,t)}{\partial t}+2\xi\frac{\partial u^{(3)}(\xi,t)}{\partial \xi}-\mu F(u^{(3)}(\xi,t))=0, \tag{20}$$

the boundary conditions

$$u^{(3)}(\xi,0)=1;\ \frac{\partial u^{(3)}(\xi,t)}{\partial \xi}=0\ \text{as}\ \xi=0 \tag{21}$$

and matching condition as $\xi\to\infty$

$$u^{(3)}(t,\xi)-u_0(t)\to 0. \tag{22}$$

The function defined by $u^{(3)}(t,\xi)=u_0(t)$ is the solution of problem (20)–(22) where $u_0(t)$ has the form (10) constructed in Theorem.

4 The Convective Boundary Layer

The solution of the convection-diffusion boundary layer region is sought in the following variables $\gamma = \frac{\psi}{\sqrt{\varepsilon}} = \frac{f(y)\sin\theta}{\sqrt{\varepsilon}}$, $y = r - 1$. Then Eq. (1) is reduced to the form

$$\frac{f(y)}{y+1}\frac{\partial u^{(1)}(y,\gamma)}{\partial y} + \mu F(u^{(1)}(y,\gamma)) = 0. \tag{23}$$

The solution should satisfy the following matching condition

$$u^{(1)}(y,\gamma) - u^{(0)}(t,\theta) \to 0 \text{ at } y \to 0. \tag{24}$$

in the area $D^{(0)} \cap D^{(1)}$.

We consider the equation

$$\frac{f(y)}{y+1}\frac{\partial u^{(1)}(y,\gamma)}{\partial y} + \mu u^{(1)}(y,\gamma) = f_0(u^{(1)}(y,\gamma)), \tag{25}$$

where the right side is the same as in (11).

The solution of the homogeneous equation has the form

$$u^{(1)}(y,\psi_1) = c(\psi_1) y^{-\frac{\mu}{2}} e^{-\mu(y - \ln\sqrt{y+2})}, \tag{26}$$

Function $c(\psi_1)$ is obtained from a function

$$c(\psi_1) = \frac{c_{0,1}\exp(-\mu\ln\sqrt{2})}{2\sqrt{\pi}} \left(\frac{\delta_0}{2-\delta_0}\right)^{\mu/4} \int_0^{1-\delta_0} \left(\frac{1+t}{1-t}\right)^{\mu/4} \frac{\psi_1}{(1-t)^{3/2}} \exp\left(-\frac{\psi_1^2}{4(1-t)}\right) dt, \tag{27}$$

passing to the limit when $\delta_0 \to 0$, where $\psi_1(r,\gamma) = \left(r - \frac{1}{r}\right)\gamma$, and $c_{0,1}$ **is the same constant that in Theorem**. Then the solution of the problems (23)–(24) takes the form

$$u^{(1)}(y,\psi_1,\varepsilon) = \varepsilon^{\frac{\mu}{2}} y^{-\frac{\mu}{2}} e^{-\mu(y - \ln\sqrt{y+2})} c(\psi_1) + O(\varepsilon^{2\delta - \gamma_0}) \text{ for a certain } \gamma_0 > 0. \tag{28}$$

5 The Internal Domain of the Diffusion Trail

The solution of the internal region of the diffusion trace is sought in variables $\rho = \varepsilon^{-1}\psi = \varepsilon^{-1} f(y)\sin\theta$, $y = r - 1$. The equation for the field has the form

$$\frac{f^2(y)}{(y+1)^2}\frac{\partial^2 u^{(2)}}{\partial \rho^2} = \frac{f(y)}{(y+1)}\frac{\partial u^{(2)}}{\partial y} + \mu F(u^{(2)}). \tag{29}$$

We construct a solution of Eq. (29) satisfying the following conditions:

$$\frac{\partial u^{(2)}}{\partial \rho}(y,\ \rho) = 0 \text{ as } \rho = 0 \tag{30}$$

and matching conditions

$$u^{(2)}(\varepsilon, y, \rho) - u^{(3)}(\varepsilon, t, \xi) \to o(\varepsilon^{\delta+\lambda}) \text{ at } y \to 0 \text{ in the area } D^{(2)} \cap D^{(3)}, \tag{31}$$

$$u^{(2)}(\varepsilon, y, \rho) - u^{(1)}(\varepsilon, y, \gamma) \to o(\varepsilon^{\delta+\lambda}) \text{ at } \rho \to \infty \text{ in the area } D^{(2)} \cap D^{(1)} \tag{32}$$

for some $0 < \lambda < \frac{1}{2}$.

In Eq. (30) we make the change of variables $z = y + \frac{1}{y+1}$, ρ. Then Eq. (29) with the conditions (29) takes the form

$$\frac{\partial^2 u^{(2)}(z,\rho)}{\partial \rho^2} - \frac{\partial u^{(2)}(z,\rho)}{\partial z} = \mu\, q(z) F(u^{(2)}(z,\rho)), \tag{33}$$

where $q(z) = \sqrt{z-1} + O(z-1)$ at $z \to 1$, $q(z) = z + O(1)$. at $z \to \infty$.

We construct a solution of Eq. (33) satisfying the condition $\frac{\partial u^{(2)}(z,\rho)}{\partial \rho} = 0$ at $\rho = 0$, and matching conditions

$$u^{(2)}(\varepsilon, z, \rho) - u^{(3)}(\varepsilon, t, \xi) \to o(\varepsilon^{\delta+\lambda}) \text{ at } z \to 1 \text{ in the area } D^{(2)} \cap D^{(3)}, \tag{34}$$

$$u^{(2)}(\varepsilon, z, \rho) - u^{(1)}(\varepsilon, y, \gamma) \to o(\varepsilon^{\delta+\lambda}) \text{ at } \rho \to \infty \text{ in the area } D^{(2)} \cap D^{(1)}. \tag{35}$$

Then the solution of problem (33)–(35) takes the form

$$u^{(2)}(y,\rho) = \varepsilon^{\frac{\mu}{2}} y^{-\frac{\mu}{2}} \frac{c_{0,1}}{2\sqrt{\pi}} \frac{e^{-\mu \ln\sqrt{2}}}{e^{\mu(y - \ln\sqrt{y+2})}} + O(\varepsilon^{2\delta-\gamma_0}). \tag{36}$$

It is necessary to explore the area mixing for sufficiently small values of the rate constant of a chemical reaction. The function $e^{-\mu y} \to 1$ for $\mu \to 0$.

6 The Mixing Domain

The solution is sought in variables $\upsilon = \varepsilon^{-1/2} f(y) \sin\theta$, $\eta = \varepsilon\,(y+1)$. Then we obtain the equation

$$\frac{\partial^2 u^{(4)}(\upsilon,\eta)}{\partial \upsilon^2} - \frac{\partial u^{(4)}(\upsilon,\eta)}{\partial \eta} = 0. \tag{37}$$

The solution is constructed with the conditions

$$u^{(4)}(\upsilon,\eta) \to 0 \text{ at } \eta \to \infty,\ \frac{\partial u^{(4)}(\upsilon,\eta)}{\partial \upsilon} = 0,\ \ at\ \upsilon = 0, \tag{38}$$

$$u^{(4)}(\varepsilon,\upsilon,\eta) - u^{(1)}(\varepsilon,y,\psi_1) \to o(\varepsilon^{\delta+\lambda}) \text{ at } \eta \to 0, \text{ in the area } D^{(4)} \cap D^{(1)}. \tag{39}$$

The solution (37)–(39) has the form

$$u^{(4)}(\varepsilon,\upsilon,\eta) = \frac{1}{2\sqrt{\pi\eta}} \int_0^\infty u^{(1)}(x) \left[e^{-\frac{(\upsilon-x)^2}{4\eta}} + e^{-\frac{(\upsilon+x)^2}{4\eta}} \right] dx + O(\varepsilon^{2\delta-\gamma_0}), \tag{40}$$

where $u^{(1)}(\upsilon)$ is the leading term of asymptotics $u^{(1)}(\varepsilon,y,\psi_1)$ at $y \to \infty$.

7 Conclusion

This paper considers the problem of convective diffusion streamlined cross-flow of an ideal fluid around the cylinder in the presence of volumetric chemical reaction. The neighborhood of the cylinder is divided into several boundary layers, in each region, and the independent variables are introduced. The solution of the problem is constructed by the method of matched asymptotic expansions for the main terms. Similar results were obtained in the flow drops. The linear problem of convective diffusion of about a drop in the presence of the bulk chemical reaction where [10], and in [6]—were considered nonlinear problems in the diffusion boundary layer.

References

1. Gupalo, Y.P., Polyanin A.D., Ryazantsev, Y.S.: Mass and heat transfer between reacting particles and the flow. Nauka. Moscow, Russia (1985)
2. Levich, V.G.: Physicochemical fluid dynamics. Fizmatgiz, Moscow, Russia (1959)
3. Privalov, I.I.: Introduction to the Theory of Functions of a Complex. Nauka, Moscow, Russia (1967)

4. Akhmetov, R.G.: Asymptotics of the solution for a problem of convective diffusion with volume reaction near a spherical drop. Proc. Steklov Inst. Math. **S8-S12**(Suppl. 1) (2003)
5. Maksimova, N.: The asymptotic behavior of solutions for a class of ordinary differential equations. In: Collection of Scientific. articles 13, pp. 30−36. BSPU, Ufa (2012)
6. Akhmetov, R.G.: The asymptotic expansions of the solution for the boundary value problem to a convective diffusion equation with volume chemical reaction near a spherical drop. Commun. Nonlinear Sci. Numer. Simul. CSNS **15**, 2308−2312 (2011)
7. Maksimova, N.V., Akhmetov, R.G.: The asymptotic solutions for boundary value problem to a convective diffusion equation with chemical reaction near a cylinder. Lat. Am. J. Solids Struct. **10**, 123−131 (2013)
8. Fedoruk, M.V.: The WKB-method for a nonlinear equation of the second order. Comput. Math. Math. Phys. **26**(1), 121–128 (1986)
9. Kalyakin, L.A.: Justification of asymptotic expansion for the principal resonance equation. Proc. Steklov Inst. Math. Suppl. 1, S108−S122 (2003)
10. Zhivotyagin, A.F.: Influence of a homogeneous chemical reaction on the distribution of concentration in a diffusion wake of a droplet. Vestn. Mosk. Gos. Univ. Ser. 1. Mat. Mekh. . **6**, 73−78 (1980)

Assessment of Eigenfrequencies of the Middle Ear Oscillating System: Effect of the Cartilage Transplant

Gennady Mikhasev, Sergei Bosiakov, Lyudmila Petrova, Marina Maisyuk and Kirill Yurkevich

Abstract Finite-element models of the intact middle ear and the diseased one with the eardrum subjected to retraction in the *posterosuperior* quadrant are proposed. Because the natural frequencies of the middle ear oscillating system are the principle dynamic characteristics, finite-element calculations of eigenfrequencies for both the normal middle ear and the middle ear with pathological changes of the tympanic membrane in the *posterosuperior* quadrant are carried out. The geometrical model of the middle ear consisting of the eardrum, malleus, incus, and stapes was obtained on basis of the tomographic data. When the eardrum has a retraction pocket, a cartilage transplant superimposed on the *posterosuperior* quadrant is considered as a reinforcing element. The optimal thicknesses of the cartilage transplant are defined in such a manner that the natural frequencies of the reconstructed middle ear were as close to those of the normal middle ear as possible. The obtained results can be used to predict the thickness of the cartilage transplant needed to restore the functions of the human middle ear.

G. Mikhasev · S. Bosiakov (✉) · K. Yurkevich
Belarusian State University, 4 Nezavisimosti Avenue, 220030 Minsk, Belarus
e-mail: bosiakov@bsu.by

G. Mikhasev
e-mail: mikhasev@bsu.by

K. Yurkevich
e-mail: YurkevichKS@bsu.by

L. Petrova
Belarusian Medical Academy of Post-Graduate Education,
3, Brovki str., build 3, 220013 Minsk, Belarus
e-mail: bsm21@mail.ru

M. Maisyuk
State Enterprise "National Centre of Otorhinolaryngology",
8, Suhaya str., 220004 Minsk, Belarus
e-mail: merylmmm@mail.ru

J. Awrejcewicz (ed.), *Dynamical Systems: Modelling*, Springer Proceedings in Mathematics & Statistics 181, DOI 10.1007/978-3-319-42402-6_21

1 Introduction

The retraction pocket of the tympanic membrane (TM) is a clinical manifestation of atelectatic otitis media. For many reasons this pathology of the middle ear deserves special attention. In particular, it is necessary to assess correctly the nature of the pathogenesis and formulate a treatment strategy to repair the retraction pocket formed as a result of the cholesteatoma growth in the middle ear [1, 11]. The retraction of the TM can be formed due to an imbalance of pressure in the middle ear cavity (negative pressure conserved in the middle ear cavity for a long time) and changes in the structure of the tympanic membrane (thinning and changing its physical properties) [5]. The process of retraction is accompanied with irreversible changes in the TM structure and consequently, with a significant reduction of its elastic characteristics. For this reason the weakened segment of the eardrum, more often the *posterosuperior* quadrant of *pars tensa*, comes into contact with underlying auditory ossicles (the long crus of incus, the incudo-stapedial articulation). This inevitably leads to their erosion [3] and epidermal ingrowth into the middle ear cavity with cholesteatoma formation. And the recent clinical study by Lee et al. [8] showed that even a tiny retraction of the *pars flaccida* may results in attic cholesteatoma. Retraction pockets are therefore dangerous because they are asymptomatic for a long time but ultimately lead to permanent irreversible hearing loss.

One of the preventive measures of the middle ear cholesteatoma is "early" surgical approach in treatment of retraction pockets. This approach involves the installation of a cartilage transplant in the *posterosuperior* quadrant of the *pars tensa* to increase the rigidity of this TM part and preserve its auditory function [4, 10]. An average thickness of the cartilage transplant for different techniques of myringoplasty is about 500 μm. The cartilage transplant of such thickness can prevent the TM retraction and results in the good sound conduction. At the same time, objective advices on the prediction of the optimal thickness of a cartilage needed to restore the basic function of the middle ear are absent. The acoustic performance of eardrums reinforced with cartilage grafting and their postoperative functions has not been also well analyzed.

The basic purpose of this study is an assessment of the geometric dimensions of the cartilage transplant at various pathologies of the TM to create sound conditions corresponding to functions of the normal TM. We aim to estimate the optimal thickness of cartilage transplants which would result in the natural frequencies close to those of the intact middle ear. Another goal is to formulate some recommendations for the operations envisaging a removal of the retraction pocket in the TM. The finite-element method (FEM) will be used to reach these aims.

2 Geometric and Finite-Element Models

A solid 3D model of the TM was obtained by gluing different parts of the *pars tensa* and *pars flaccida*. The thickness $h_{pf} = 30$ μm of the *pars flaccida* was taken in our study. The *posterosuperior* quadrant of the *pars tensa* of the thickness

$h_{ps} = 60$ μm involves two layers, and the remaining part of the eardrum of the thickness $h_{rp} = 90$ μm composes three layers. The above geometrical data, h_{pf}, h_{ps}, h_{rp}, are typical of an adult and may vary slightly. All the dimensions of the TM shown in Fig. 1 are given in millimeters (mm).

The solid 3D models of the malleus, incus and stapes were generated in the SolidWorks 2010 using a tomogram of the middle ear. The characteristic dimensions of the middle ear model under consideration are shown in Fig. 2.

The finite-element segmentations of the eardrum and auditory ossicles as well are presented in Fig. 3.

In order to simplify the FEM analysis, the effect of the cochlear liquid, ligaments and muscles (4 malleus ligaments, musculus tensor tympani, stapedial tendon, and stapedial annular ligament) are not taken into account in what follows.

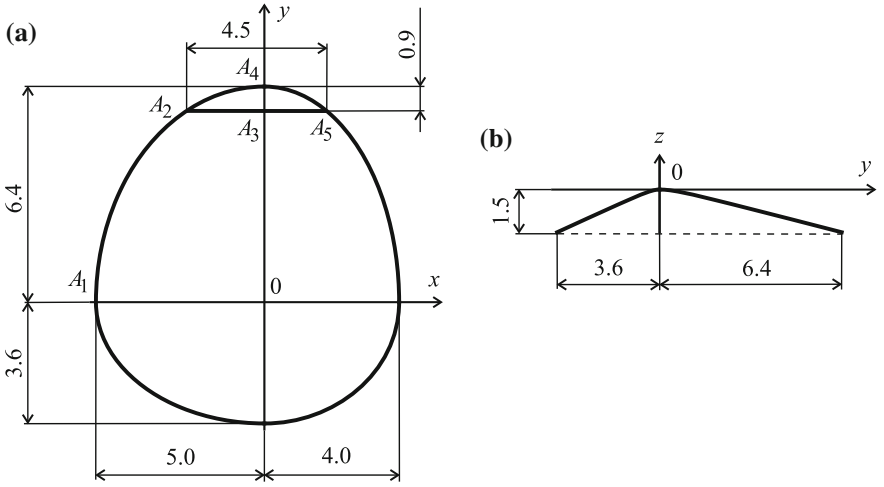

Fig. 1 Geometrical dimensions of the TM: **a** external view, **b** plane section of the TM at $x = 0$ ($0A_1A_2A_3$ is the *posterosuperior* quadrant of the *pars tensa*, $A_2A_4A_5$ is the *pars flaccida*)

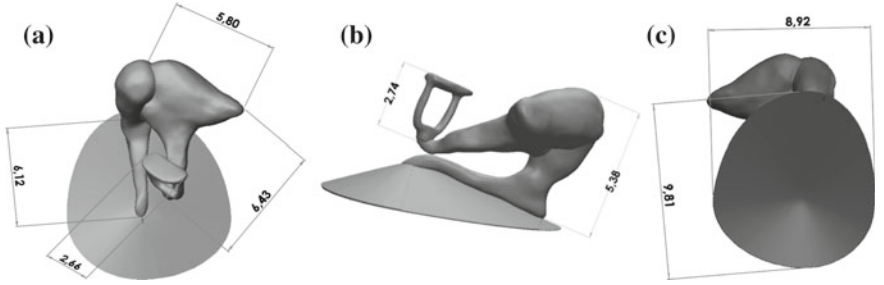

Fig. 2 Geometric model of the middle ear and its characteristic dimensions: **a** internal view; **b** side view; **c** external view

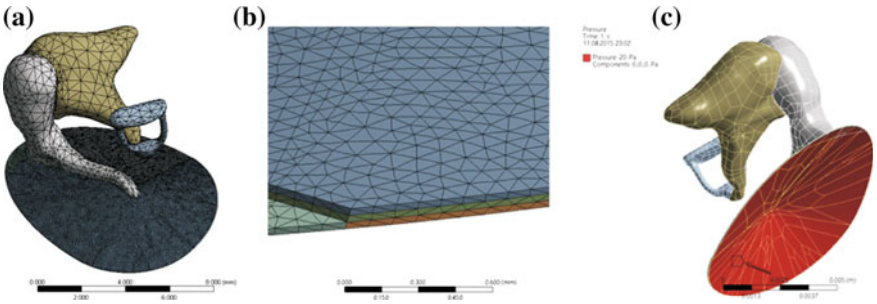

Fig. 3 Discrete models of the middle ear: **a** FEM models of the TM, malleus, incus and stapes; **b** finite-element segmentation of the TM layers in the *pars tensa* segment; **c** the external surface of the TM experiencing static pressure

The rigid clamp conditions at the tympanic ring were considered as the boundary ones for the TM. Contact between the eardrum and the malleus handle as well as contacts between the auditory ossicles were described by using ANSYS 15.0 'Bonded-type' (corresponding to absence of slip and penetration). For this type of contact all gaps between contacting surfaces are closed, i.e., the contacting surfaces are bonded. The finite-element segmentation was carried out in the semi-automatic mode. The maximal dimensions of the finite-element rib for the auditory ossicles and eardrum were 0.3 mm and 0.1 mm, respectively. The total number of nodes and elements used for the FEM simulation amounted to 239379 and 149863, respectively.

We assumed homogeneous isotropic elastic material properties for all the auditory ossicles with the average values of Young's modulus $E_b = 20$ GPa, Poisson's ratio $\nu_b = 0.3$ and density $\rho_b = 2$ mg/mm^3 taken from references [2, 6, 12]. The microstructure of the TM was taken into consideration by also anisotropic elastic material properties with the elastic moduli $E_{pt} = 33$ MPa, $E_{pf} = 11$ MPa for the *pars tensa* (excepting the *posterosuperior* quadrant $0A_1A_2A_3$) and the *pars flaccida*, respectively, and Poisson's ratio $\nu_{pt} = \nu_{pf} = 0.4$ for these two segments [7, 12]. The elastic modulus of the normal *posterosuperior* quadrant $0A_1A_2A_3$ is about $E_{ps} = 33$ MPa. In the case of pathological changes of elastic properties of the *posterosuperior*, its elastic modulus E_{ps} were varied from 11 to 22 MPa. The densities for the *pars tensa* and the *pars flaccida* were assumed to be the same, and were taken to be [12] $\rho_{pt} = \rho_{pf} = 1.2$ g/cm^3.

When the TM has a retraction pocket in the *posterosuperior* quadrant $0A_1A_2A_3$, a cartilage transplant superimposed on the weakened part of the TM was considered as an additional element in our model. We considered cartilage slices having different thicknesses $h_c = 250, 500, 750$ μm, but covering all the region $0A_1A_2A_3$. Different types of cartilage transplants from the cavum, conchae or tragus are usually applied for restoration of an eardrum. Here, slices of transplant made from the tragal cartilage with Young's modulus $E_c = 3.4$ MPa, Poisson's ratio $\nu_c = 0.3$ [9], and density $\rho_c = 1.1$ g/cm^3 were considered. In what follows, we consider a rigid coupling

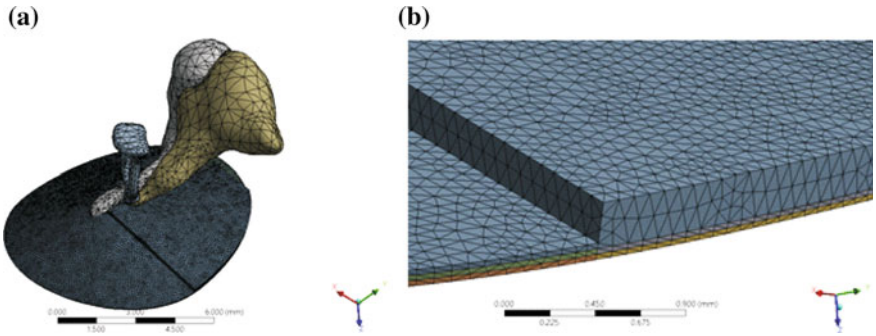

Fig. 4 FEM model of the middle ear with the cartilage transplant on the *posterosuperior* quadrant: **a** side view; **b** fragment of the *posterosuperior* segment with the cartilage transplant

between the cartilage transplant and TM, whereas the contour of the transplant along the tympanic ring was assumed to be rigidly clamped. The FEM models of the middle ear with the cartilage transplant of the thickness $h_c = 500$ μm are shown in Fig. 4.

3 Static Model of Middle Ear with Negative Pressure in Tympanic Cavity

Because the negative pressure in the tympanic cavity may be considered as a reason leading to formation of retraction pockets, the first step in our study was to examine the influence of this pressure on the static deflection of the eardrum for two different cases: (1) elastic properties of the *posterosuperior* quadrant are typical of a healthy middle ear, (2) the elastic modulus E_{ps} is reduced because of pathological changes in the TM microstructure.

The negative pressure in the tympanic cavity, leading to the eardrum retraction, was simulated by the static normal pressure $p_S = 20$ Pa ($p_{SPL} = 120$ dB) applied to the external side of the eardrum. Figure 5 shows the distribution of total deformations (displacements, mm) in the eardrum for the normal middle ear (a) and for that with the reduced elastic modulus $E_{ps} = 11$ MPa for the *posterosuperior* quadrant subjected to pathologic changes (b) as well. It is seen, for both the normal middle ear and the diseased one the greatest displacements of the TM under the standard negative pressure is observed in the *posterosuperior* quadrant. For the normal middle ear with $E_{ps} = 33$ MPa, the maximum deflection is equal to 3.0186 μm, while for the middle ear with the reduced elastic modulus, $E_{ps} = 11$ MPa, the maximum deflection amounts to 8.0395 μm. As seen, the reduction of the elastic modulus E_{ps} of the *posterosuperior* quadrant from 33 to 11 MPa results in the increase of the TM retraction up to about 3 times.

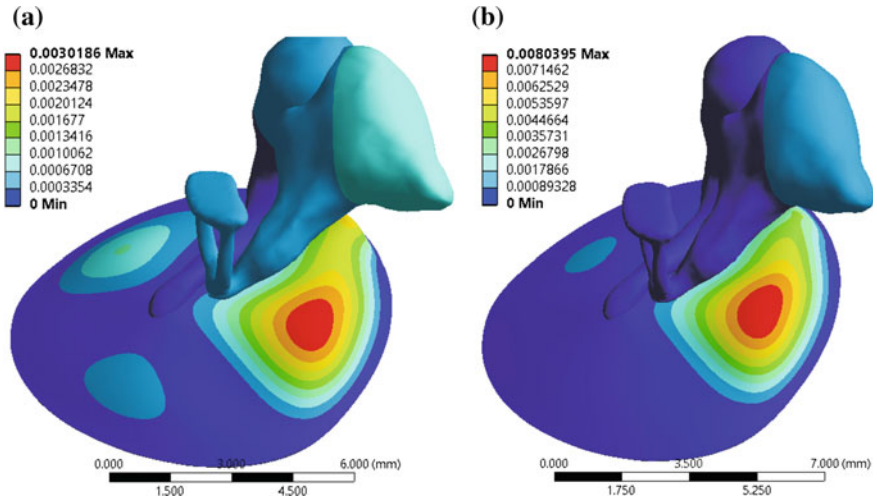

Fig. 5 Distribution of total deformations (displacements, mm) in the eardrum under action of the external pressure $p_S = 20$ Pa: **a** normal middle ear; **b** middle ear with the reduced elastic modulus $E_{ps} = 11$ MPa for the *posterosuperior* quadrant

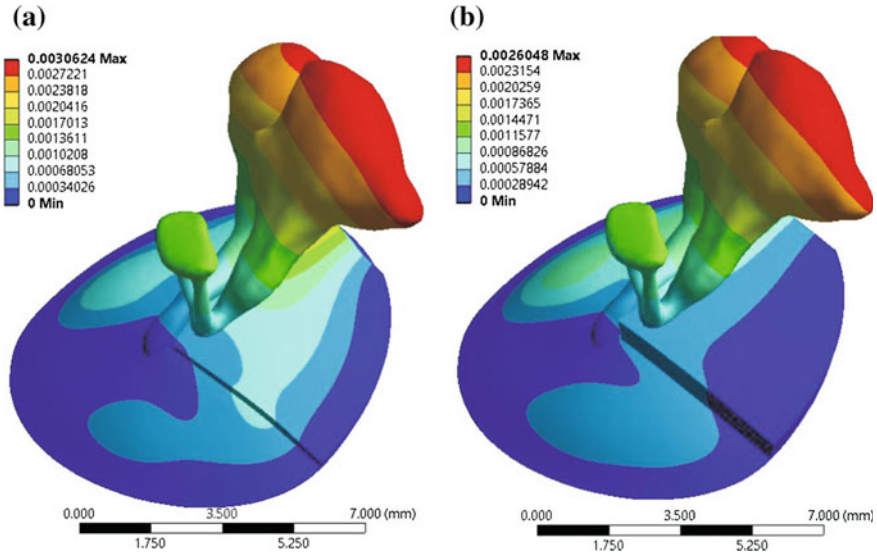

Fig. 6 Distribution of total deformations (displacements, mm) in the reinforced eardrum with the reduced elastic modulus $E_{ps} = 11$ MPa of the *posterosuperior* quadrant under action of the external pressure $p_S = 20$ Pa at different thicknesses h_c of the superimposed cartilage transplant: **a** $h_c = 250$ μm; **b** $h_c = 750$ μm

We examined also the influence of installed cartilage grafts of different thicknesses $h_c = 250, 750$ μm on static deflections of the reinforced eardrum (with the reduced modulus $E_{ps} = 11$ MPa) under the same external pressure $p_S = 20$ Pa (see Fig. 6). It is seen that the attachment of the cartilage slice results in increasing the total rigidity of the reinforced composite eardrum and, as a consequence, gives a reduction of the TM retraction. The comparison of Figs. 5b and 6 shows that the maximum retraction of the reconstructed TM with $h_c = 250$ μm is 12 times less then the retraction of the eardrum without a transplant, and for $h_c = 750$ μm this reduction amounts to 18 times. Apparently, the thinner cartilage transplant is, the larger the total rigidity of the composite TM is, and the smaller probability of forming retraction pocket becomes. However, it is also obvious that too high total rigidity of an reinforced TM might lead to undesirable effects, such as desensitization of the eardrum to the sound signal, decreasing the transfer function of the middle ear, and the significant shift of the natural frequency spectrum. Therefore, it is very important to define such optimal dimensions of the transplant which would result in mechanical characteristics close to characteristics of the normal middle ear.

4 Eigenfrequencies of Diseased Middle Ear with Reinforced Eardrum

In this section we perform the FEM simulation of free vibrations of the oscillating system of the normal and diseased middle ear with pathological changes of elastic properties of the eardrum in the *posterosuperior* segment. In the case of the diseased middle ear, the model of the reconstructed middle ear with cartilage transplants of different thicknesses attached to the eardrum in the region of the *posterosuperior* quadrant is considered. In all calculations, the initial strain–stress state of the TM and its initial deflections as well, caused by the standard negative pressure $p_S = 20$ Pa, are taken into consideration.

The eigenfrequencies ω, kHz, of the normal middle ear as well as of the diseased one with the reduced elastic moduli $E_{ps} = 11, 22$ MPa for the different mode shapes are shown in Fig. 7. As seen, the assumed reduction in the modulus E_{ps} does not influence the natural frequencies corresponding to the first three modes ($n = 1, 2, 3$). However, this effect appears at $n \geq 4$ and becomes noticeable for high eigenfrequencies, including frequencies from the auditory range, 16 Hz $\leq \omega \leq$ 20 kHz. The reduction of Young's modulus E_{ps} in the *posterosuperior* quadrant results in the strong decrease of all eigenfrequencies beginning with the 4^{th} mode.

Note, in spite of the fact that all ligaments and muscles were not taken into account, the eigenfrequencies found here for the normal middle ear turned out to be very close to the data obtained by Mikhasev et al. [9]. This coincidence may be treated as wholly satisfactory verification of our model.

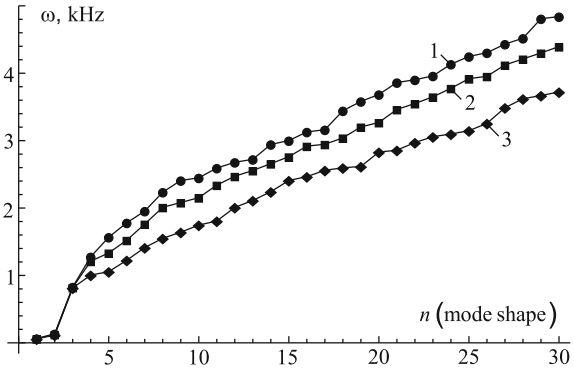

Fig. 7 Eigenfrequencies of the normal middle ear and the diseased one with pathological changes of the TM elastic properties for different mode shapes: *1*—normal middle ear; *2*—middle ear with the elastic modulus $E_{ps} = 22$ MPa for the *posterosuperior* quadrant; *3*—middle ear with the elastic modulus $E_{ps} = 11$ MPa for the *posterosuperior* quadrant

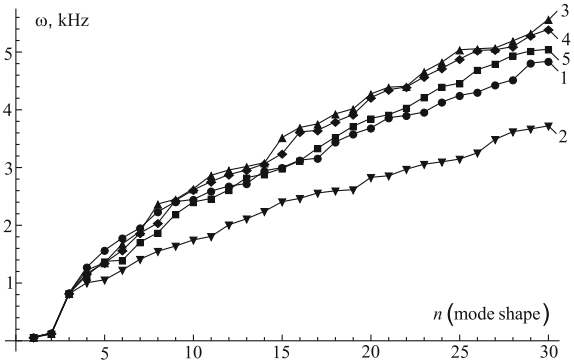

Fig. 8 Eigenfrequencies for different mode shapes: *1*—normal middle ear; *2*—middle ear with elastic modulus of the *posterosuperior* quadrant of 22 MPa; *3*, *4* and *5*—middle ear with elastic modulus of the *posterosuperior* quadrant of 22 MPa and the cartilage transplant thickness of 750 μm, 500 μm and 250 μm, respectively

In Fig. 8, the natural frequencies of the diseased middle ear with the reduced elastic modulus $E_{ps} = 22$ MPa versus the mode number are shown for different thicknesses of the attached cartilage transplant $h_c = 250, 500, 750$ μm. The same plots, but for $E_{ps} = 22$ MPa, are presented in Fig. 9. In both Figures, curves corresponding to the oscillating systems of the normal and diseased middle ear without a cartilage graft are also drawn.

As expected, using cartilage transplants with the purpose of reinforcement of the weakened *posterosuperior* quadrant does not allow to get the oscillated system whose natural frequencies would be as much as possible close to those of the normal middle ear **for all modes**. For thick laminas of a cartilage (at $h_c > 500\mu$m), the mentioned closeness of eigenfrequencies is observed only for the first 15 modes, whereas

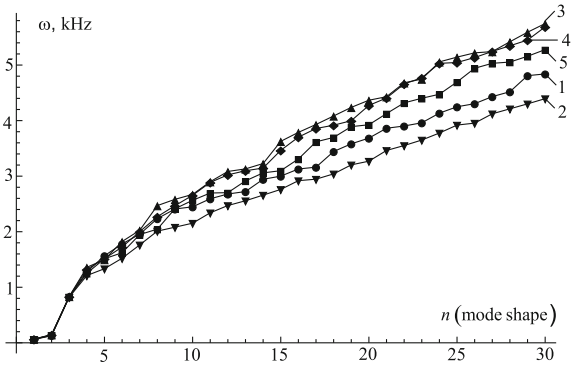

Fig. 9 Eigenfrequencies for different mode shapes: *1*—normal middle ear; *2*—middle ear with elastic modulus of the *posterosuperior* quadrant of 11 MPa; *3*, *4* and *5*—middle ear with elastic modulus of the *posterosuperior* quadrant of 11 MPa and the cartilage transplant thickness of 750 μm, 500 μm and 250 μm, respectively

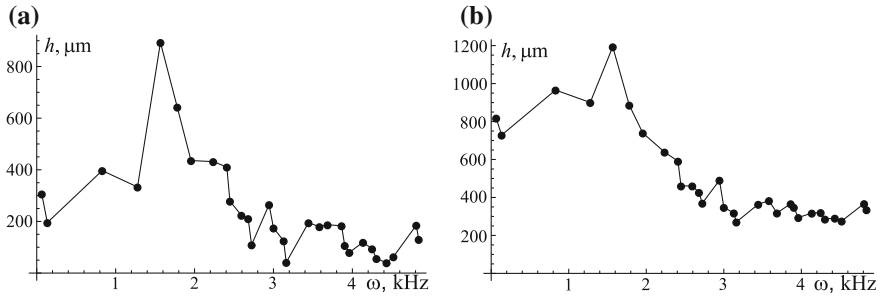

Fig. 10 Diagrams "eigenfrequency of normal middle ear—thickness of cartilage transplant"; the cartilage transplant is superimposed on the *posterosuperior* quadrant of TM with elastic modulus: **a** E_{ps} =22 MPa; **b** E_{ps} =11 MPa

for high modes the divergence between frequencies for the normal and reconstructed systems grows together with the mode number. Furthermore, the smaller the modulus E_{ps} is, the larger this divergence becomes (compare Figs. 8 and 9 for a large n). The comparison of data presented in both the Figures allows to conclude that the optimal thickness of the cartilage transplants under consideration should not exceed 500 μm.

More detailed information on coupling "eigenfrequency of the normal middle ear—optimal thickness of cartilage transplant" is shown by the diagrams in Fig. 10. The diagrams are plotted using the exponential regression functions on basis of the date presented in Figs. 7, 8 and 9. Each of these diagrams gives the cartilage transplant optimal thickness h_c which has to be chosen for the oscillating system of the reinforced middle ear to have the eigenfrequency close to that of the normal middle ear. It is seen that the size of changing of the optimal thickness h_c is too wide and depends on the rate of destruction of the TM in the region of the *posterosuperior*

segment. If $E_{ps} = 22$ MPa, then this diapason is 40 μm $\leq h_c \leq$ 890 μm, and for $E_{ps} = 11$ MPa, it is as follows: 250 μm $\leq h_c \leq$ 1200 μm. When taking into account the basic auditory range (spoken), 500 Hz $\leq \omega \leq$ 2 kHz, then the recommendations are as follows: in the case of a minor destruction of the eardrum, with $E_{ps} \approx 20$ MPa, the average thickness h_c of the cartilage transplant should be about 200 μm, and for the greatly weakened eardrum, with $E_{ps} \approx 10$ MPa, it is encourage to use more thin graft with $h_c \approx 400$ μm.

5 Conclusions

Three-dimensional FEM models of the intact middle ear and the diseased one with the eardrum subjected to retraction in the *posterosuperior* quadrant have been proposed. The middle ear was considered as the oscillating system consisting of the tympanic membrane, malleus, incus and stapes. Solid 3D models of the auditory ossicles were generated in the SolidWorks 2010 on the basis of the tomographic data of all elements of the bio-mechanical system. The functions of ligaments in the tympanic cavity were not taken into account.

The retraction pocket in the *posterosuperior* quadrant of the TM was treated as a result of initial deformations (retractions) of the eardrum with pathological changes of elastic properties under action of the negative pressure in the tympanic cavity. In order to reinforce the weakened eardrum, the diseased segment on the TM was covered by a slice of the cartilage graft made from tragal cartilage. The cartilage transplant attached to the TM was considered as an additional element (a thin shell) coupling rigidly to the surface of the TM. All elements of the middle ear oscillating system as well as the cartilage transplant were assumed to be homogeneous and elastic with mechanical characteristics taken from available references.

On basis of the developed FEM models, the two different problems were studied in the paper. First, the FEM analysis of the initial deformations of the diseased TM with the reduced Young's modulus E_{ps} of the *posterosuperior* segment under static external pressure $p_S = 20$ Pa applied to the TM was performed. The static FEM analysis has revealed that the reduction of the elastic modulus E_{ps} of the *posterosuperior* quadrant from 33 to 11 MPa results in the increasing the TM retraction up to about 3 times. The influence of imposed cartilage transplants of different thicknesses $h_c = 250, 750$ μm on static deflections of the reinforced eardrum (with the reduced modulus $E_{ps} = 11$MPa) under the same external pressure $p_S = 20$ Pa has also been studied. It was shown that the attachment of the cartilage slice may lead to the noticeable decrease of the TM retraction. So, the maximum retraction of the reconstructed TM with the attached cartilage transplant of the thickness $h_c = 250$ μm turned out to be 12 times less then the retraction of the eardrum without a transplant.

The second problem of our study concerned the FEM simulation of free vibrations of the normal and diseased middle ear with the eardrum having the reduced Young's modulus in the *posterosuperior* quadrant. In the dynamic analyses, the initial static strain–stress state of the TM caused by the standard negative pressure $p_S = 20$ Pa

were taken into consideration. Calculations have revealed that decreasing Young's modulus E_{ps} from 33 to 11 MPa does not influence the natural frequencies corresponding to the first three modes ($n = 1, 2, 3$). However, this effect becomes very strong at $n > 4$: the reduction of the modulus E_{ps} may result in very strong dropping all eigenfrequencies from the auditory range.

In order to study the effect of the cartilage transplant superimposed on the weakened *posterosuperior* segment, the FEM simulations of the reconstructed middle ear with the reinforced TM have been performed. Use of the cartilage transplants had not enabled us to get the oscillating system with eigenfrequencies close to those of the normal middle ear for all modes. For instance, superimposing cartilage transplants with thicknesses $h_c > 500\,\mu$m resulted in very good coincidence of the natural frequencies of the intact and reconstructed oscillating systems only for the first 15 modes, whereas closeness of the corresponding frequencies for higher modes turned out to be not wholly satisfactory.

To select the optimal thickness of the cartilage transplant, the detailed analysis on coupling "eigenfrequency of the normal middle ear—optimal thickness of cartilage transplant" has been made. This analysis permits to give the following recommendations:

(i) If an eardrum in the *posterosuperior* segment has minor destructive changes, and is characterized by Young's modulus $E_{ps} \approx 20$ MPa, then the average thickness h_c of the cartilage transplant should be about 200 μm.
(ii) When the pathological changes in elastic properties of the *posterosuperior* quadrant is too great, with Young's modulus E_{ps} dropped up to about 10 MPa, it is required to utilize more thick slices of a cartilage with $h_c \approx 400\,\mu$m.

Acknowledgments The research leading to these results has received funding from the People Programme (Marie Curie Actions) of the European Union's Seventh Framework Programme FP7-PEOPLE-2013-IRSES "Trans-Atlantic Micromechanics Evolving Research: Materials containing inhomogeneities of diverse physical properties, shapes and orientations" (TAMER)

References

1. Ars, B., Decraemer, W.: Tympanic membrane lamina propria and middle ear cholesteatoma. In: Proceedings of the 3rd International Conference on Cholesteatoma and Mastoid Surgery, pp. 429–432. Amsterdam/New York, Kugler Publications (1989)
2. Beer, H.-J., Bornitz, M., Hardke, H.-J., Schmidt, R., Hofman, G., Vogel, U., Zahnert, T., Hüttenbrink, K.-B.: Modeling of components of the human middle ear and simulation of their dynamic behavior. Audiol. Neurotol. **4**, 156–162 (1999)
3. Borqstein, J., Gerritsma, T., Bruce, I.: Erosion of the incus in pediatric posterior tympanic membrane retraction pockets without cholesteatoma. Int. J. Pediatr. Otorhinolaryngol. **72**, 1419–1423 (2008)
4. Cassano, M., Cassano, P.: Retraction pockets of pars tensa in pediatric patients: clinical evolution and treatment. Int. J. Pediatr. Otorhinolaryngol. **74**, 178–182 (2010)
5. Esteve, D., Dubreuil, Ch., Delia Vedova, Cl., Normand, B., Lavieille, J. P., Martin, Ch.: Physiologic et physiopathologie de la fonction d'ouverture de la trompe auditive: apports de la tubomanometrie. J. Fr ORL. **50**, 233–241 (2001)

6. Fung, Y.C.: Biomechanics: Mechanical Properties of Living Tissues, 2nd edn. Springer, New York (1993)
7. Kirikae, J.: The Middle Ear. The University of Tokyo Press, Tokyo (1960)
8. Lee, J.H., Honga, S.M., Kima, ChW, Parkb, Y.H., Baek, S.-H.: Attic cholesteatoma with tiny retraction of pars flaccida. Auris Nasus Larynx. **42**, 107–112 (2015)
9. Mikhasev, G., Ermochenko, S., Bornitz, M.: On the strain-stress state of the reconstructed middle ear after inserting a malleus-incus prosthesis. Math. Med. Biol. **27**, 289–312 (2010)
10. Neumann, A., Jahnke, K.: Wie Trommelfellrekonstruktion mit Knorpel: Indikationen. Techniken und Ergebnisse. HNO. **53**, 573–586 (2005)
11. Ohinishi, T., Shirahata, Y., Fukami, M., Hongo, S.: The atelectatic ear and its classification. Auris Nasus Larynx. **12**, 211–213 (1985)
12. Wada, H., Koike, T., Kobayashi, T.: Three-dimensional finite-element method (FEM) analysis of the human middle ear. In: Huttenbrink, K.-B. (ed.) Middle Ear Mechanics in Research and Otosurgery, pp. 76–81. Department of Otorhinolaringology, University of Technology, Dresden (1997)

The Method of Modeling of Human Skeletons Multi-Body System

Tomasz Miroslaw

Abstract The analyses of human movement are interesting subjects for medicine, sport, or for bionics robots designers as well as people, who have been looking for analytical tools for many years, and one of them is the multi-body system analysis. In this paper, a short overview of different methods of analysis of multi-body systems is presented. These methods are very important and effective for analyses and designing of defined mechanical structures and their control. But during physical movement the skeleton changes its structure from close to open. The mechanical energy accumulated in skeleton's bones and muscles are cyclically converted from kinetic to potential and vice versa. Hence, the direct usage of multi-body analyses does not appear to be effective enough. In this paper, the author presents a new modification of the multi-body system modeling method which enables dynamic analyses of changing structures. The model is a structure of stiff branches (bones) as well as flexible and rotatable nodes (joints) with the branches moving in accordance to forces and torques. The movement causes the relative displacements of two elements generating reaction forces and torques in joints. This force then flows to a particular element where it is added to others. This method was used for force and movement modeling for low lamb exoskeleton designing. In addition, the simplified model of human leg and the result of simulation are also presented in this paper.

1 Introduction

The human body has been the subject of artists, medical practitioners, sportsmen, and technicians for many years showing admiration for this study in ancient sculpture, sketches, or drawings made by Leonardo da Vinci, Mikael Angelo, and other artists.

T. Miroslaw (✉)
Warsaw University of Technology, Faculty of Automotive and Construction Machinery
Institute of Construction Machinery Engineering, 84 Narbutta Str. 02-524, Warsaw, Poland
e-mail: tmiroslaw@simr.pw.edu.pl

J. Awrejcewicz (ed.), *Dynamical Systems: Modelling*, Springer Proceedings
in Mathematics & Statistics 181, DOI 10.1007/978-3-319-42402-6_22

At present, the body structure and its movements for human body analyses play very practical role in sports, healthcare, industry as well as safety and security or defense systems. The ergonomics is autonomous science which helps to design: tools, workplaces, houses, vehicles interiors, etc. Sportsmen analyze human body, its movement mechanism, in order to devise ways to move better and quicker. That is why specialists of ergonomics have been trying hard to find ways to realize work with minimal effort, or how to design vehicles which will protect car passengers during accidents etc. They all would like to know how the human body works or how it would respond to various forms of stimulation. For finding the answers to these questions, some real models have been built which imitate human. Of course the range of imitation is optimized to find answer to the main question. So we have many models depending on the question we would like to answer.

It is worth adding that the search for systems which could make us stronger, quicker, happier has continued unabated. But currently, people are still exposed to diseases, injuries which limit the human mobility skill. The population is becoming older and the problems with walking have continued to limit people's activities. Another substantive problem worth pointing out is the amount of people injured in accidents and recovery. Today's level of technological advancement enables construction of exoskeletons which can help people solve these problems. This idea, since it appeared in the 1960s, has remained very attractive hitherto. In the medical and technical magazines or the Internet there are a lot of exoskeleton examples. The most exciting solutions are dedicated to the military, however, at a demonstrative stage.

There are some exoskeletons on the market which are dedicated to rehabilitation.

They help with the recovery process from illness or accidents to start again, getting people on their feet again [5–8]. They are carriers of human body which carry and force its parts to move, thereby realizing the programmed pattern of movement. Although the exoskeleton does not only propel the legs and arms but also helps keep and maintain balance. It is quite a complicated and expensive device used by qualified medics, rehabilitants, in special environments. This equipment is very useful as it speeds up recovery process, though people might need more, even as some old people have to use sticks or other devices to aid movement—making them more active or self-sufficient when they could be supported by special exoskeleton. On the other hand this exoskeleton has to support the human body, strengthen its muscles (only in needed range), maintain balance, and protect the body against harm. Having such devices people will be able to feel better and save a lot of money, though it is quite a long way toward building such devices. The main problem in exoskeleton designing is the human body. All of us differ from one to other and our way of movement is also different. We tend to move in different ways depending on the weight of our outfit, the ground surface as well as our mood, to name a few. Let me also add that our movements are not repetitive so, if a self-movable man would like to be supported by such devices he should be only assisted and supported by it only in required states. Should exoskeleton do everything for us, it could end up hindering the development of (human) skills and resulting in the loss of mobility. On the other hand exoskeleton

cannot move the human body in a programed way, because it could cause harm while trying to move by taking a step in a different way due to some obstacles or change of mind during movement.

These problems are very strongly visible during designing exoskeletons for the military. Contemporary battle field requires soldiers to carry more and more as well as heavier equipment. Thanks to these exoskeletons, soldiers are able to stand longer, walk long distance, and maintain the ability to take rapid unexpected steps (Fig.1) [9, 10]. The exoskeleton for soldiers or disabled-assistants should be imperceptible carrying its load and moving simultaneously with him and working indefinitely [4].

When we are thinking about exoskeleton for soldiers, it should move in similar way like man dose, and not cause any additional load for him and be similarly efficient like soldier is.

To design such devices, we need to model how man is moving [8–10]. The most interesting thing is efficiency of human moving way, what is still better than others waking machines. Man intuitively set body in way what take advantages on gravity, landform, muscle, sinew, and bones springiness. But the most important is there is no universal pattern or rules of movement that will suit to all of us. Everybody moves in their own way. The only common thing is we need to generate force to overcome movement resistance and carry body load.

2 Remarks on Human Body Movement Analyses

As it was said, there is no universal model of human movement. Everyone is moving in different way even in the same day. We can be recognized by our relatives by our walk or running style. So what can we do to find the way to support people in walking with load, or make this walk longer or faster?

Against above remark, some common features or rules of human movement have been pointed. To find them analyses of sportsmen, soldier, and street people movement were recorded and analyzed [1]. For analyses some typical actions have chosen like standing (with burden), walking, running, and others like kneeling, squat, or stars climbing.

2.1 Standing

Standing is quite tiring “activity” especially if you need to stay in one place and carry some burden. Our body is uptight and we need to change muscles tension from time to time changing our position by waving or move our body load from one leg to other. The mass center is moved through the field between feet. (It is presented in Fig. 2). We keep it above this surface by all body muscle tensions and configuration.

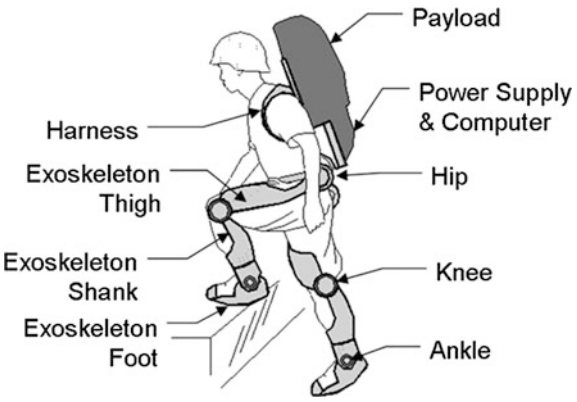

Fig. 1 Conceptual sketch of a lower extremity human exoskeleton [9, 10]

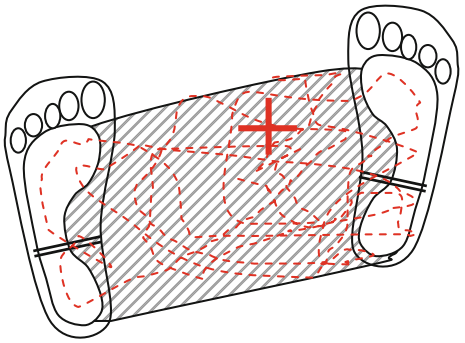

Fig. 2 The "support field" between feet and mass center track

We swing moving in our hips or bending knees. The high of mass center is changing slightly. Our mechanical work is not too big, but the chemical process in our muscles is running and we are getting tired. Some time we release our muscle too much or by other disturbance we can lose balance during standing and we automatically change position of one leg to change the support field. The graph diagram of standing is presented in Fig. 3.

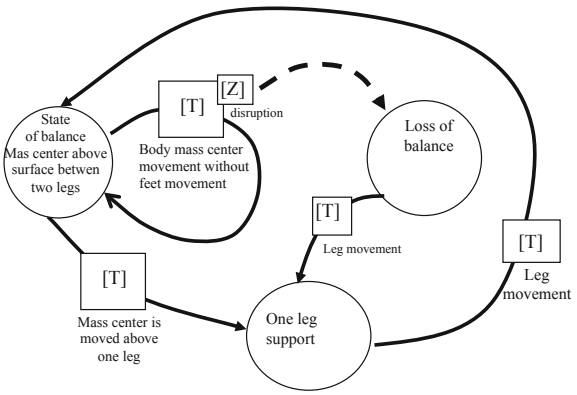

Fig. 3 Graph diagram for standing ([T] means operation of body structure transformation, [Z] external disruption)

2.2 Walking

This the most characteristic action and occurs in a individual way depending on various conditions. During walking at least one leg is supporting us and the mass center is swinging from one leg to other and rise and down.

We can have few types of walking. Below are the three most different styles are presented.

The silent "cat's walk" when man is moving on legs with knees and moves feet low over the ground and step them slowly. The moving leg is always ready to support body (Fig. 3).

Slow stable walk when man is moving stable, without losing the balance and the mass center is always above or between supporting legs. In this style we can see the "rolling triangle" presented in Fig. 4. The mass center is above standing foot. When we move the second leg forward this center is moving but it is still above support surface. When we put the second foot on the ground we move the weight over it. This move is realized by hill erection calf caused by rotation of foot around toes axle.

In this style the toes and feet rolling play important role. The calf muscles are the main propellers.

When we speed up, the movement loses its stability and the mass center is not always above support. The balance is temporarily lost which is used for speed up or keep the speed of movement.

When we lengthen our steps we lose balance and our walk is quicker but we can stop immediately. Our body fall down and its energy is partly absorbed by hill and transform to thigh's "muscle" which is accumulated and release in rising cycle. The movement of mass center needs the energy so the "walker" set his legs in unnatural way to reduce mass center with high changes. But "normal" walking people also take advantage on gravity and use the falling cycle of walking to accelerate body

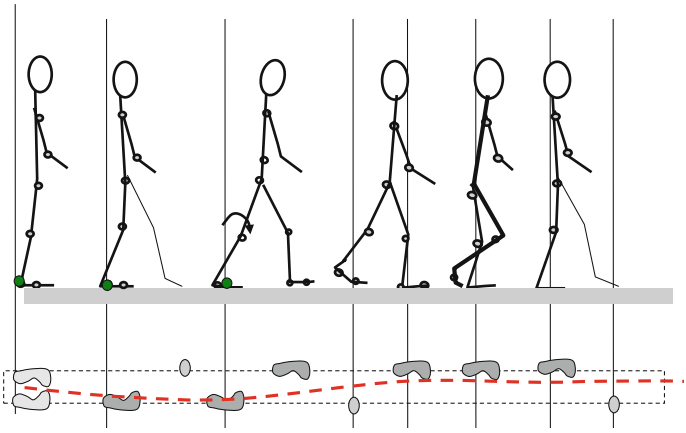

Fig. 4 "Cat's Walking" movement phases with support surfaces and trace of mass center

and the kinetic energy of it is accumulated in “muscles and sinews” and is released during rising. Human during movement take advantage on gravity.

We can see that the waking is realized by combination of rotation of all body and its parts in hill, knee, hip. The propelling torques come from gravity and muscles. Depending on the style, movement is stable with the balance kept all the time or with lose of balance. Normally our walking is a combination of many styles (Figs. 5, 6 and 7).

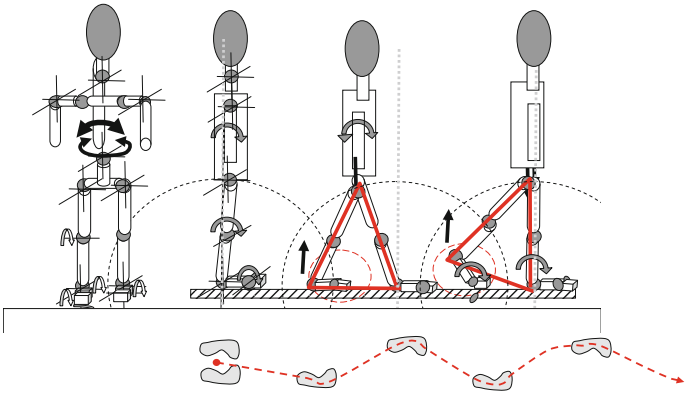

Fig. 5 “Stable Walk” movement phases with rolling triangle; below relevant support surfaces and “trace” of mass center

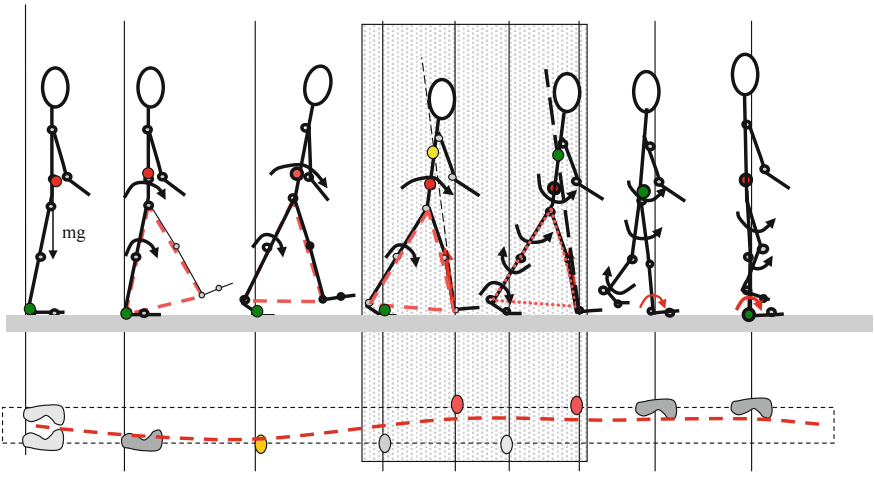

Fig. 6 “Dynamic Walk”—movement phases with support surfaces and trace of mass center

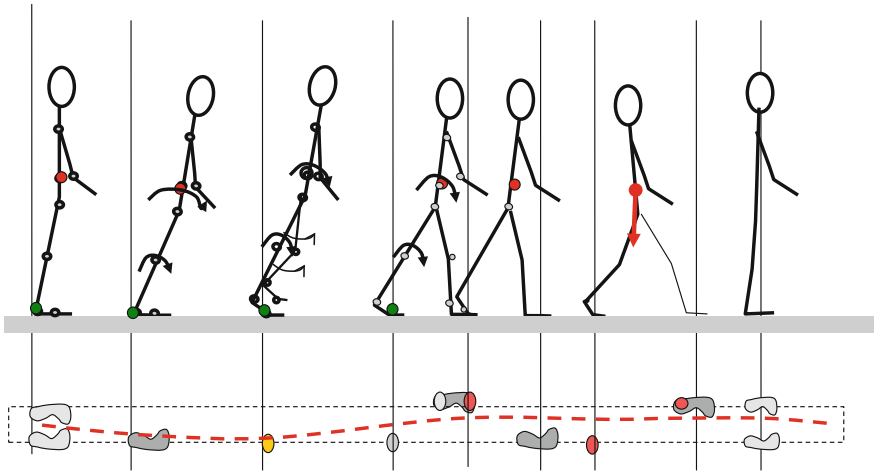

Fig. 7 The acceleration and braking during walking by gravity utilization—movement phase with the body support surface

2.3 Running

Running is the action what is not in interest in medical exoskeletons or exoskeletons dedicated for load carrying. But it is very important for sportsmen soldiers. The run phase study is presented in Fig. 8. To start running we bend our body to lose balance and jump from one leg second. We take the balance back for a while by setting the landing leg below mass center. We rotate around toes moving body forward and push when mass center is forward supporting place. It gives us the propelling force as the combination gravity and muscle force. When we our leg hits on the ground it is slightly bent in knee. During landing some part of energy is accumulated in thigh by extension of straightening muscles.

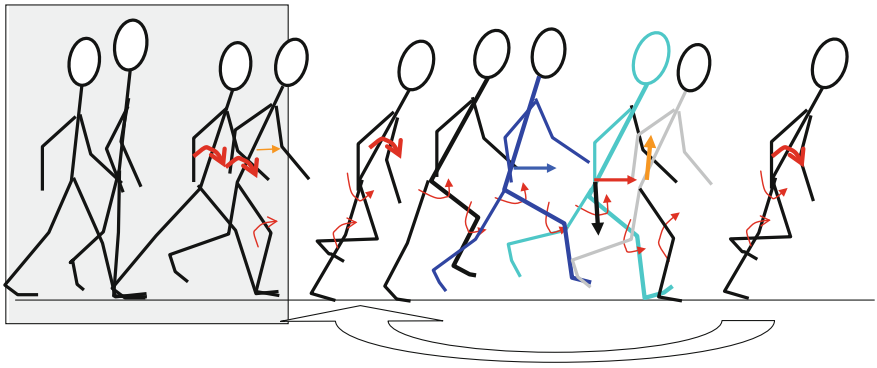

Fig. 8 Run phase study

This energy is used back during taking off. When we do not land on the bent leg we will feel pain in knee.

2.4 Summary of Analyses

Basing on these short analyses, we can assume that our movement is a combination of body part rotation caused by muscles forces or by gravity.

The body structure and force acting points is various and it is very difficult to be predicted.

The flexibility of our muscles helps us to recuperate energy and bounce from the ground. The analyses pointed that lower limb model should consist of 4 elements toes, foot, calf, and thigh as bodies and joints toes, hill, knee, hip. Some models do not care about toes which they play important role in walking.

The main force what effect on human body is gravity, ground reaction or wing. So we can analyze our movement in reference to the natural horizontal-vertical frame of system.

We manage our mechanical energy by controlled conversion from gravity potential energy by kinetic, to spring "muscle" and back to kinetic and potential energy. The energy conversion model is presented in Fig. 9.

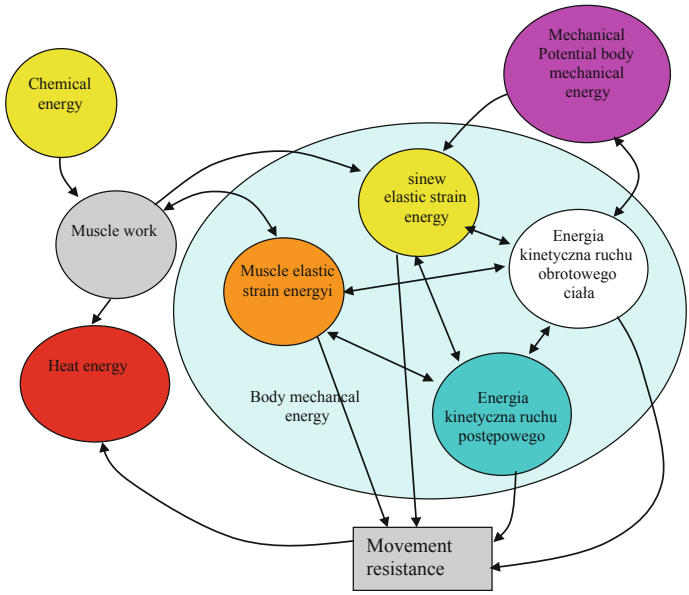

Fig. 9 The energy conversion cycle

This energy transformation is the crucial problem in exoskeleton designing. To do it we build the human body model whicht help us better understanding of its behavior and predict its movement when we will affect on it external forces.

3 Human Body Models

Many computer models of human body are available, especially prepared for computer games, movies etc. Those models are focused at movement visualization based on videos recorded in real tests of body position data or on mathematical model of body kinetics describing body part movement in time.

We can find models which help us to calculate forces or torques in particular body elements and joints, for set structure. But it is very difficult to find the model of body behavior as the response to the torques and forces generated in joints are acting on body.

The theory of muti-body analyses is basing on mathematical matrix operations what in author's opinion does not describe the real phenomena in systems. When we have the so long chain of bodies what could work in open or close structure the matrix calculation especially the revers task (finding position as the force acting result) is very difficult.

The modeling is the sequence of differential equation system solutions for one parameter changing in the time. Some times this system is unsolvable.

Many models assume that the body structure is the mutli-body stiffness elements structure. This assumption helps to use the matrix operation. But our body is not stiff, we are flexible and our muscles could be modeled like it is presented in Fig. 10.

So the human body which consist of stiff elements are propelled with flexible muscles. So we can build model like in Fig. 11 [3].

But this model is not easy to be transformed into computer model. Because it is a parallel system of stiff and flexible elements which effect one on others. So we need other methods.

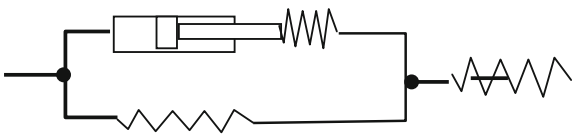

Fig. 10 Model of human muscle. It consists of three passive elements: a series elastic element corresponding to tendon and connective tissue, parallel elastic element and damper [2]

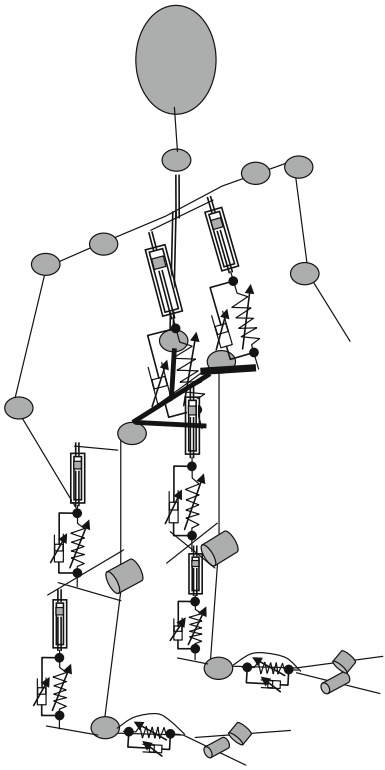

Fig. 11 Model o human body as the stiff skeleton and flexible muscles

4 Methods of Multi-Body Modeling with Flexibility

4.1 Concept of Model

Basing on other models and provided research on human movement the new concept of modeling is proposed. The main assumptions are that the model structure should reflect human body structure as the mutli-body systems with bodies and joints, the modeled body movement should be the effect of combination of rotation in joints. The energy conversion should be reflected in model. It should be as one universal model for open or close structure and reflect body behaviors when it is supported on the ground or it is in the fly state. As the simplification the structure of human body is modeled with 15-body model what are representing: toes, feet, calves, thighs, hip, breast, arms, forearm, neck with had. Model is shown in Fig. 12.

This model for movement analyses does not have palms. All bodies are joined with joins which are responsible for relative bodies movement—rotations and transfer forces between joined elements. This model was expanded with points

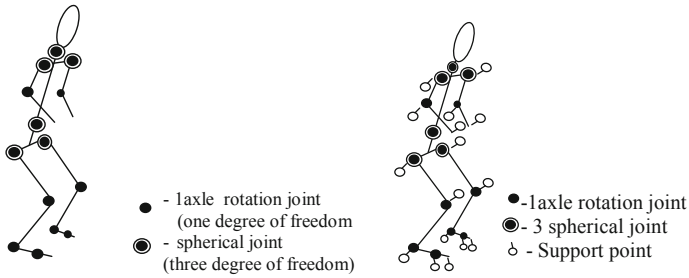

Fig. 12 Model of human body as the 15-bodies and joints system

where supporting forces effects on system. These forces represent ground reaction, or load weight force.

All bodies are modeled in the same way as a stiff stick with mass concentrated in mass center C which has defined location in space C[x,y,z], the flexible ends A and B in defined distance to C (model is presented in Fig. 13). The stick is oriented in space by angles set between stick and axle of reference system set (in figure only

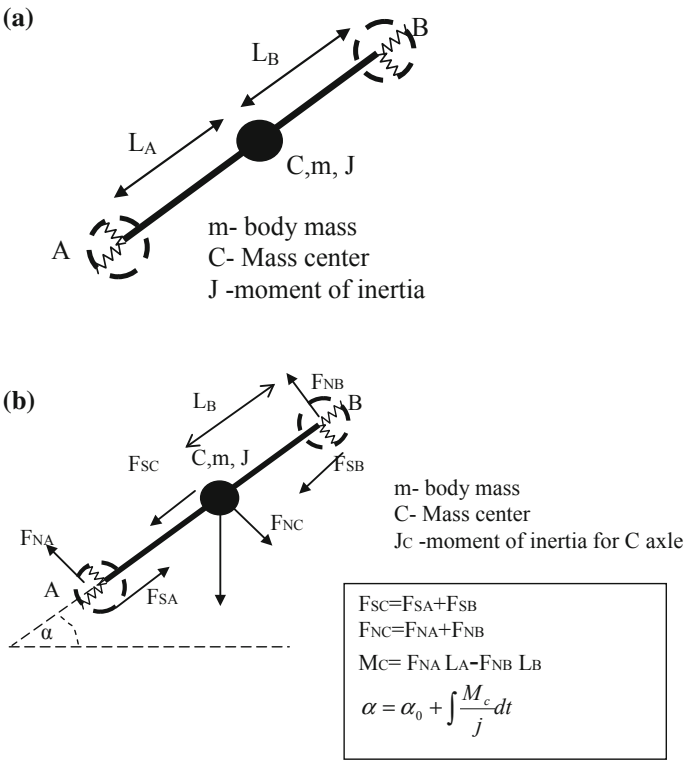

Fig. 13 Model of element in multi-body system

one "α" is presented). There are forces what effect on the mass center: the weight force and force coming from terminates a and B (ends): the tangential and axial/orthogonal/normal forces. These forces are summed in mass central causing its movement. The orthogonal forces produces torques what are summed and enforces retaliation of stich, changing the angle α and position of A and B.

In multi-body systems each element is joined at least to one other element (seen at figure) and affects on it. The exchange reaction force, appears as the spring force thanks to deformation difference between joined terminals positions. In this way so the changes of position of terminals of one body causes forces acting on others. Because of these forces bodies want to rotate around mass center but because the tangential forces the mass center is pushed and centrifugal force appears, so the body rotates around its end. In simplification we can say that in human body muscles produce torques what drive elements rotation. Model with torques is presented in Fig. 14b. If we have support only on one end, the second is free and moves according to forces on the second end and C. So if our chain is not supported on end it would like to move in this direction. If we support it the force will "reflect" and propels system in opposite direction.

The place of bodies affecting can be simplified by introducing joint model (presented in Fig. 15).

In these joins all reaction forces and torques appear and effects on the body by propelling the mass center enforce rotations. For simplification the joint can be used as the "gate" for (place of) acting of external forces and torques. Basing on this assumption computer model of human body was build. As in others model the start condition should be defined as the position of mass centuries and orientation of each element, their masses (weights). The structure of human body system made in Simulink is presented in figure. It consists of bodies and joints model and the calculator of start parameters. This calculator is prepared only for simplification of start bodies position estimation.

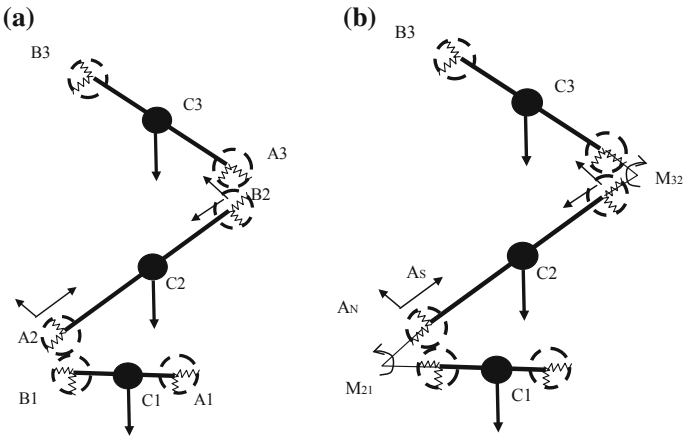

Fig. 14 Multi-bodies system model built of three effecting on each other's elements: **a** model of acting forces coming from gravity and bodies' reaction; **b** model of forces and torques produced e.g. by human muscles

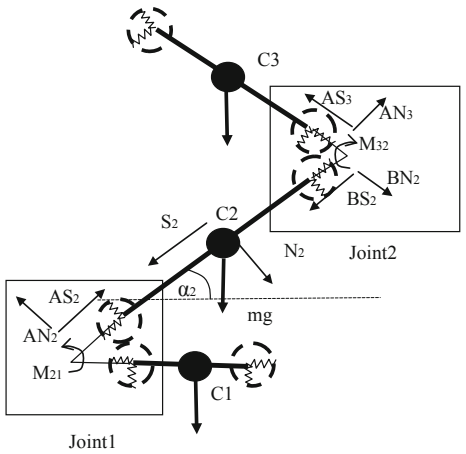

Fig. 15 Model of affecting bodies with marked reaction joint

4.2 Model Description

The model of human body was built according to rules mentioned above. The main problem what was solved is the multi-body model which would generate and transmit forces and torques as well as energy storage and conversion. The computer gives new possibilities of modeling not only by solving the system of differential equations, but can simulate bodies' behavior in time.

To present methods of modeling three bodies system was created with structure similar to lower limb. This model is presented in Fig. 16 In this example we have three bodies and two joints between and blocks for start point calculations. The lower body is resting on the ground which generates reaction force when the coordinate Y is lower than 0. The upper body is free. All of them have some mass, and start positions it means coordinates of their centers of gravity the angle of bending to horizon, moment of inertia, and two distances of stick ends to center of mass. The model of body is (presented in Fig. 17) quite universal. It consists of two terminals A and B and mass center. The body block has inputs for forces represented by components in horizontal and vertical reference systems) for two terminals a and B: FBXR (—terminal B component X Reaction force), FBYR (—terminal B component X Reaction force) and external forces: FBXE and FBYE, analogously FAXR, FAYR, FAXE, FAYE for terminal A. Mext—represents the external torque for body rotation. Additionally the start position of mass center X0 and Y0 with start angle ALFA) and distances of terminals from the mass center DLA and DLB are given. The outputs are: coordinated of real position terminal BX, CY, AX, AY and mass center CX and CY and real angle. Additionally two outputs of MA and MB representing torques generated in terminals are present for tests.

The structure of terminal model is presented in Fig. 18. This model consists of terminal position calculator market as DBXY (its structure presented in Fig. 19). The effect of calculation is given to outputs EY and EX. Forces from inputs Fx, FXr

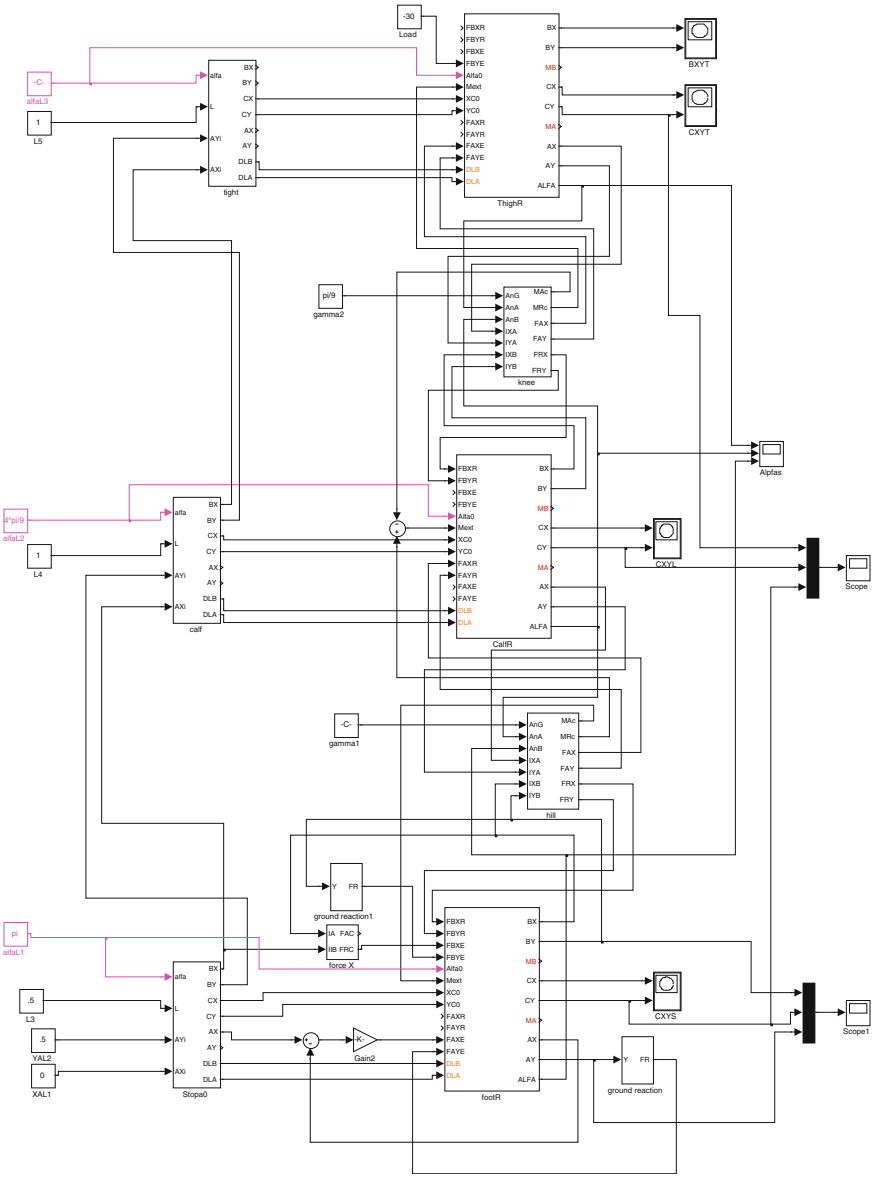

Fig. 16 The structure of three-bodies system

and Fy, FYr are summed and given together with real angle to XY2SN transformation block, where XY components are converted to SN component. The orthogonal force component is used for torque calculation. This Forces and torque are sent to mass center model.

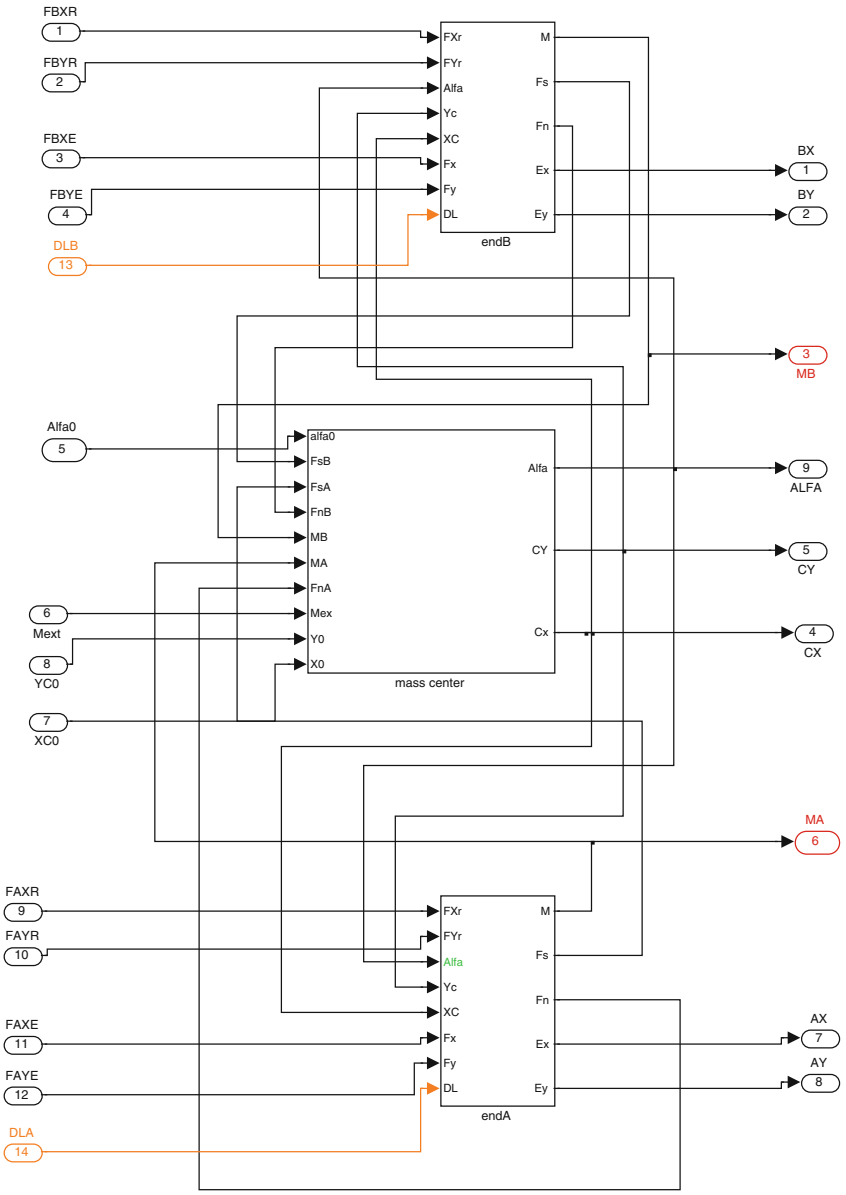

Fig. 17 The body model

Model of mass center is presented in Fig. 20. In this block the weight force appear and is transformed into SN components basing on actual rotation angle. This force is summed with forces coming from terminal and after dividing by mass value appears the acceleration in axles N and S. This acceleration is converted to XY

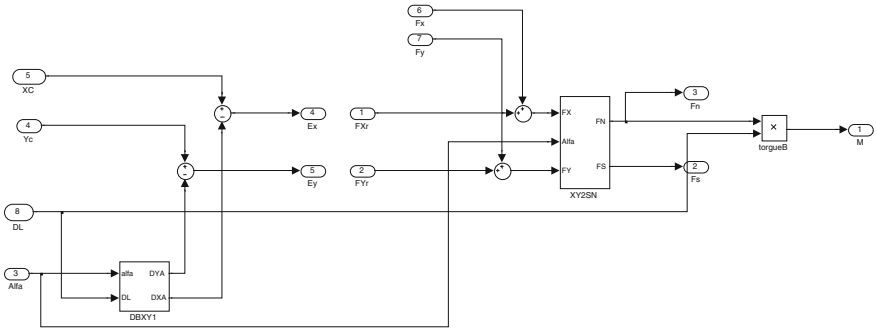

Fig. 18 The terminal model

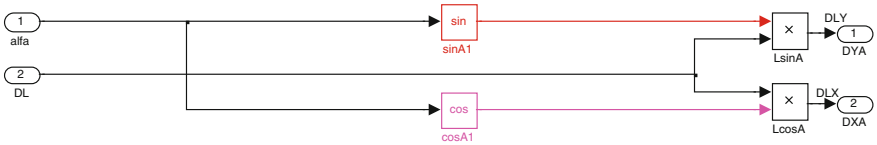

Fig. 19 Terminal position calculator

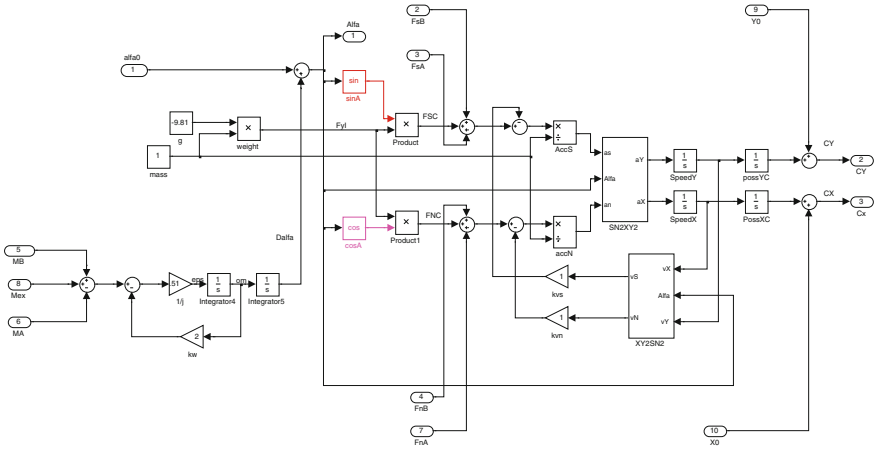

Fig. 20 The mass center block internal structure

coordinate and integrated for real speed and XY position. The real speed is reversely converted to SN coordinates for damping force calculations. The CX and Y position is estimated in reference to Y0, X0—start position.

In this block the toque is calculated as the sum torques coming from both terminals and from external. This torque accelerates the rotation proportionally to inversion of body inertia moment. After its double integration we get real angle of body bending.

The structure of joint is presented in Fig. 21. It consist of two blocks: Torques and reaction force generator. Their structures are shown in Figs. 22 and 23. The forces and torque are calculated in reference to displacement or bending flexible elements. So the forces are generated in place of displacement not as the free vector. In torque generator input Gamma the reference angle is added to move the zero torque point. Each force and torque are multiplied by "−1" to give the action and reaction force which are sent to both cooperating bodies.

One of important reaction block in general model is the ground reaction model. This reaction appear only when Y position component overcome the bound of ground. Structure of its model is presented in Fig. 24.

4.3 Model Verification

As the verification of model the experiment of falling body on the ground was chosen for presentation. It seems to be important because of kinetic energy and dynamically changed system structure. In this experiment free body was falling down from height of 0.5 m. In model the damping were set to imitate the human body landing.

In Fig. 25 the diagram of movement of free terminal and mass center highest body is shown. We can see that after landing this body is bending and rising. In

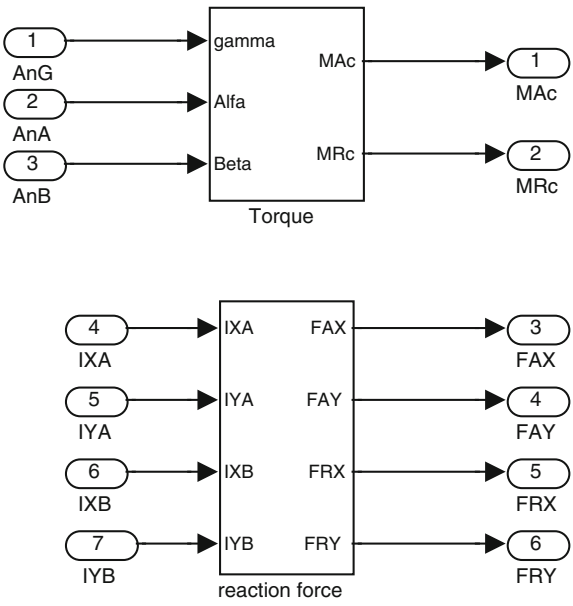

Fig. 21 Structure of joint model

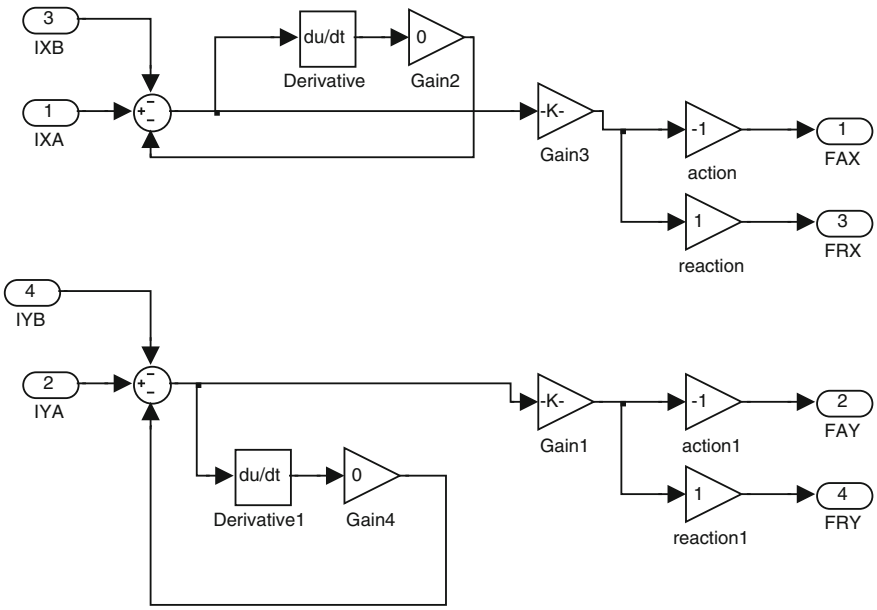

Fig. 22 Structure of reaction force generator

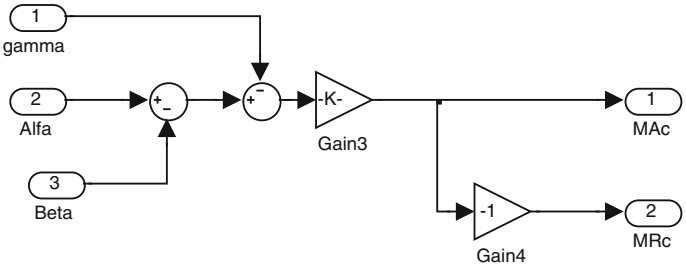

Fig. 23 Generator of reaction torque

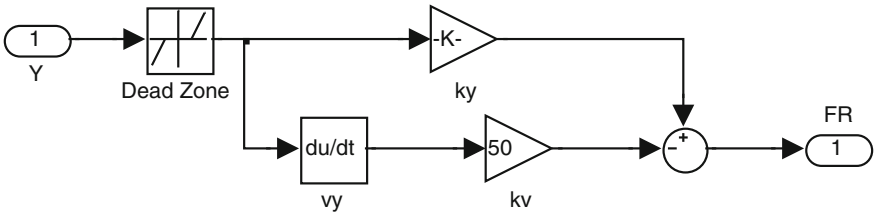

Fig. 24 Block of ground reaction

Fig. 26, we can see the way of mass centers of lower and middle part of system. They are moved almost on straight line.

In Fig. 27 we can see the position of bodies' mass centers. The highest body has biggest displacement and oscillations. In Fig. 28 we can see displacements of terminals and mass center of lowest bodies what imitated the food. It was set parallel to ground.

These results are in accordance with expectations. This experiment together with others confirmed quite good quality of this method.

Using this method the author build model of all body and simulate its behavior in responds to external forces and internal torques.

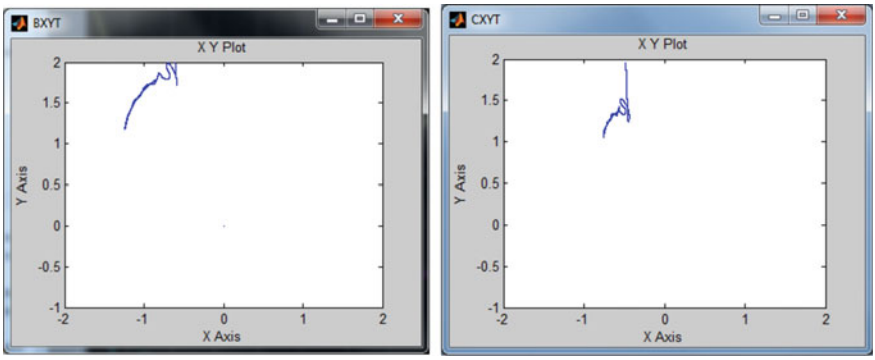

Fig. 25 Diagram of highest body movement

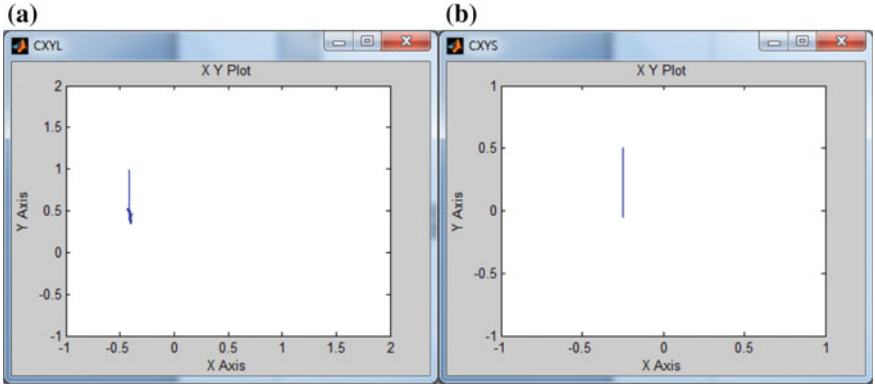

Fig. 26 Diagrams of mass centers movement for **a** middle and **b** lowest s

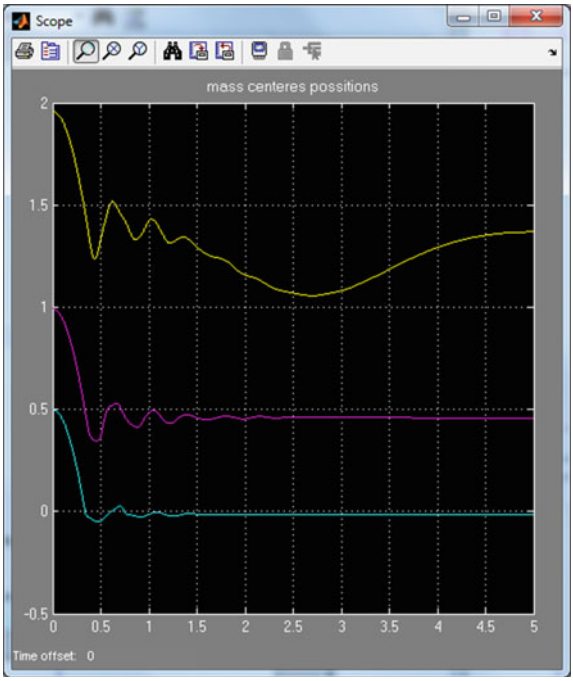

Fig. 27 Bodies' mass centers positions in time. *Yellow highest*, *magenta middle, blue-lowest* body

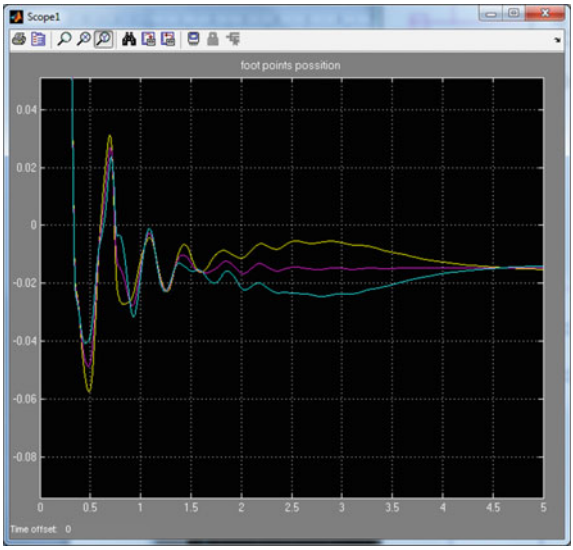

Fig. 28 Displacements of foot parts: *magenta*- mass center, *yellow* terminal B (hill) *blue* terminal A (toes)

5 Conclusion

The analyses of human body movement are still attractive and important for medicine, sport, and army.

There are many model of human movement, basing on measurement or theory of multi-body systems. But it is almost impossible to find universal model for human walking or running scenarios.

The author in this paper focused on model which will reflect the energy conversion during movement. Proposed model based on introduction of flexibility and force generation are the displacement effects.

Presented in paper method multi-body simulation seems to be quite simple and effective. The bodies displacement and deformation are the source of forces and torques gives advantages of positioning the forces actions and its flow from support to weight center. The differential equation system is built behind model ant the solution is done in time domain. Because of flexibility the system adjust itself its structure, positions and angles in accordance to its stiffness and always find solution.

Model respects the energy conversions, what is very important in analyses of human body movement mechanism.

Acknowledgments This method was work out and model was built in reference to Polish Exoskeleton NCBIR project No DOBR/0037/R/R/ID1/2012/03 …

References

1. A 3D Dual-SLIP Model of HumanWalking Over a Range of Speeds Yiping Liu*, Jim Schmiedeler**, Patrick Wensing***, and David Orin* * The Ohio State University, Columbus, OH, USA, liu.805@osu.edu, orin.1@osu.edu, ** University of Notre Dame, Notre Dame, IN, USA, schmiedeler.4@nd.edu *** Massachusetts Institute of Technology, Cambridge, MA, USA. http://biomechanics.osu.edu/dynamic-walking/abstractsfolder/liu_2015_dw.pdf
2. Hill, A.V.: First and Last Experiments on Muscle Machanics. Cambridge university press (1970)
3. Jose, L.: wearable robots: biomechatronic exoskeletons John Wiley and Sons Ltd. In: Dollar, A., Her, H. (eds.) Lower Extremity Exoskeletons and Active Orthoses: Challenges and State-of-the-Art. IEEE Transactions on Robotics, vol. 24, No. 1. Ponse CSIC, Madrit, Spain (2008)
4. Ghan, J., Kazerooni, H.: System identification for the Barkeley Lower Extremity Exoskeleton (BLEEX). In: Proceedings of the International Conference on Robotics and Automation. Orlando, Florida (2006)
5. Low, K., Yin, Y.: An integrated lower exoskeleton system towards design of a portable active orthotic device. Int. J. Robot. Autom. **22**(1) (2007)
6. Pillai, M., Kazerooni, H., Hurwich, A.: Design of a semi-active knee-ankle prosthesis. In: IEEE International Conference on Robotics and Automation. Shanghai, China (2011)

7. Valiente, A.: Design of a quasi-passive parallel leg exoskeleton to augment load carrying for walking. In: Master's thesis, Department of Mechanical Engineering. Massachusetts Institute of Technology, Cambridge (2005)
8. Zoss, A., Kazerooni, H.: Design of an electrically actuated lower extremity exoskeleton. Adv. Robot. **20**(9) (2006)
9. Zoss, A., Kazerooni, H., Chu, A.: On the mechanical design of the Berkeley Lower Extremity Exoskeleton. 2005 IEEE/RSJ International Conference on Intelligent Robots and Systems (2005)
10. Zoss, A., Kazerooni, H., Chu, A.: Biomechanical design of the Berkeley Lower Extremity Exoskeleton (BLEEX). In: IEEE/ASME Trans. Mechatron. **11**(2) (2006)

Fragility Estimation and Comparison Using IDA and Simplified Macro-Modeling of In-Plane Shear in Old Masonry Walls

Eduardo Charters Morais, László Gergely Vigh and János Krähling

Abstract The estimation of fragility functions associated with dynamic structural analysis provides the probability of a certain damage state given an intensity measure. The presented paper discusses this technique regarding its application to a method to estimate the magnitude of historical seismic events relying on the behavior and damage in real historical structures. A bin of 50 seismic records is selected matching the Komárom hazard spectrum and applied with Incremental Dynamic Analysis to generate the damage state points of a 2D one-story frame numerical model developed using Opensees code and calibrated to simulate the in-plane shear behavior of historical old clay and adobe masonry infilled walls. A scaling technique is applied and a damage type identification strategy adapted to the material model are developed to perform Incremental Dynamic Analysis and efficient fragility function fitting in MATLAB. Results highlight considerable uncertainties regarding the calibration of the numerical model, material and geometric nonlinearities and seismic record selection in this procedure. Despite efficiency, the methodology application and overview suggest that a full probabilistic approach fragility function fitting using the background of seismic hazard analysis and reliability theory, providing a concomitant sensitivity analysis, is important to proceed with variables weight evaluation and account for uncertainties.

E.C. Morais (✉) · L.G. Vigh
Department of Structural Engineering, BME, Megyetem rkp. 3.,
Budapest 1111, Hungary
e-mail: eduardo.charters@gmail.com

L.G. Vigh
e-mail: geri@vbt.bme.hu

J. Krähling
Department of History of Architecture and Monuments, BME, Megyetem rkp. 3.,
Budapest 1111, Hungary
e-mail: krahling@eptort.bme.hu

J. Awrejcewicz (ed.), *Dynamical Systems: Modelling*, Springer Proceedings
in Mathematics & Statistics 181, DOI 10.1007/978-3-319-42402-6_23

1 Introduction

Most of old masonry buildings have nowadays the status of cultural heritage, and despite being used as residences, offices, hotels, etc., their importance transcends mere usage. As symbols they connect us to culture, and to a sort of common history (political/economic history, architectural history, etc.) but as entities every single structure is as unique as its own singular history (construction materials, technology and philosophy, usage, loading history, damage history, etc.). Although these two perspectives are usually unseparated in historical study, the effort of studying structures as such or in the context of recalcitrant phenomena (i.e. shear or bending in structures, or structural elements, in the context of earthquakes historical earthquake effects) obliges us to a relative effort of abstraction and generalization in order to conveniently characterize both the structure, phenomena and the associated damage in a consistent and multifaceted transdisciplinary methodology.

A method of that kind is associated with the estimation of the magnitude of historical seismic events relying on the behavior and damage in real historical structures [1]. An early approach regarding this methodology [2] considered the identification of critical points in a late Romanesque church, in Zsámbék (Fig. 1a, b), which collapsed due to the historical earthquake of Komárom, in the June 28, 1763. In that paper a bilinear material model was used with shell elements representing the assumed homogeneous behavior of the medieval three-layered ashlar masonry walls and the general aspects of the design response spectrum were applied considering the hazard map of Hungary and local soil type [3]. Modal Response Spectrum and nonlinear Pushover Analysis suggested maximum stresses in key elements in the structure, maximum displacements in the towers and extensive plastification of the walls. Although, some difficulties for the application of [1] could be pointed: the complexity of both local and global scales mechanisms can be misleading, the difficult account for uncertainties and analysis time makes it prohibitive for the future development of the full methodology (see Fig. 2). Therefore, further developments should reduce the previous numerical model complexity by relying both on wall model simplification and failure modes selection. Although, the complexity of the local mechanism of the three-leaf medieval masonry wall will not be addressed here as the load transfer mechanisms and cyclic behavior need for considerations that fall from present scope.

1.1 Damage History Remarks

The Komárom 1763 historical earthquake left extensive damage near its epicenter [4, 5] despite some opposition regarding the reliability of the portraits [6] (Fig. 1c). In the city of Komárom, out of 1169 houses in total, 279 ended completely destroyed, 353 partially collapsed, 213 needed expensive repair and 219 cheap repair [4]. As most of the affected buildings (91 % of total) were typically composed of masonry

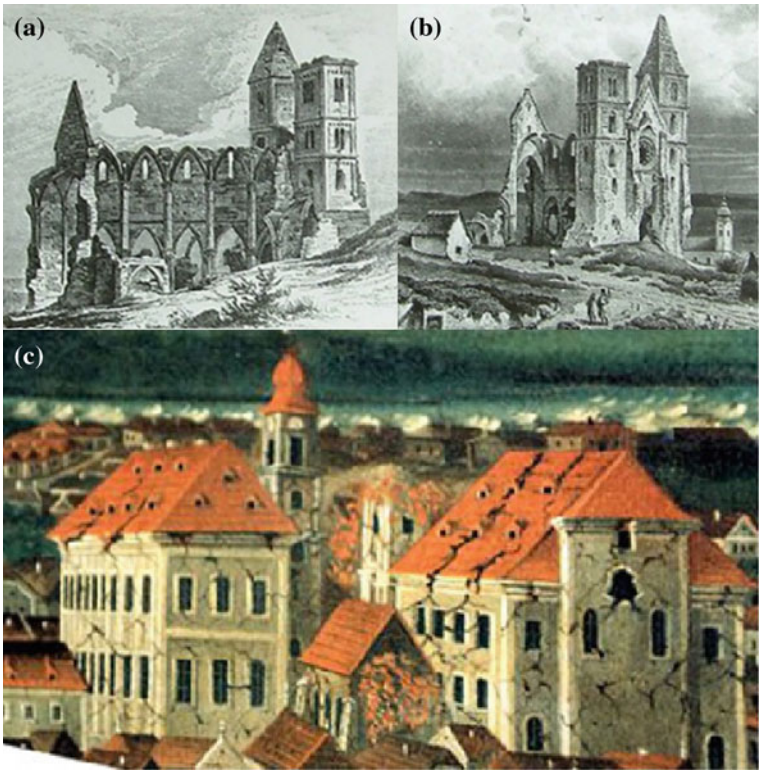

Fig. 1 Pictures **a** and **b** Zsámbék church ruin in 1857 and **c** Komárom after the 1763 earthquake

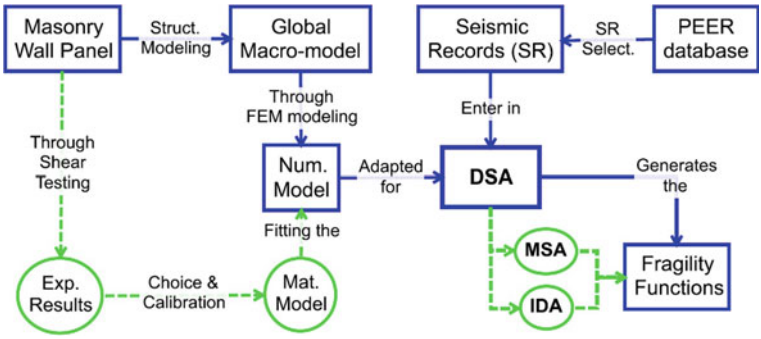

Fig. 2 Conceptual map with work steps systematization

walls (made of stone, clay or adobe with mortar infills) arches, vaults and/or wooden roofs, before assessing the earthquakes magnitude using the methodology in [1] it is important to develop structural and numerical models matching the structural types of the region, evaluate the specific damage, select the appropriate failure modes

(shear compression failure as arguably suggested in Fig. 1c) for verification and then address the generation and calibration of fragility functions. Here, only the in-plane shear with compression failure mechanism of unreinforced masonry walls subjected to the action of lateral loads will be discussed [7] and the shear tests experimental results of both clay [8, 9] and adobe [9–12] old masonry infill panels will be addressed here.

The majority of the houses of the town belonged to local peasants. These buildings were built of adobe and possibly with flexible willow-twigs; their constructions might be mud wall (sárfal) [13]. The foundation structure on which the walls were built was just the well-rammed level of soil. The typical peasant's houses were built with open chimney covering the kitchen in the middle therefore there were smoke-free living rooms as their stoves were heated from the kitchen. Their typical layout as seen from the street consists of room, entrance hall with doors to the rooms and connected to the kitchen, kitchen, room and pantry. The houses had beam ceiling, a gable roof or a hip roof, with thatch-roofing or covered with straw. Parallels to the rural houses can be seen at model plans of the region [14]. According to the records of the earthquake made by the eye-witness Johann Grossinger, the peasant's houses with their simple structures and one-story showed more resistance against the impacts of the earthquake then the brick-built public, ecclesiastical or civil houses of the town with possibly multiple stories, more embellishment and vaulted constructions [15].

2 Methodology

The methodology in [1] is rooted in the apparatus of Probabilistic Seismic Hazard Analysis (PSHA) and it presupposes the use of structural fragility functions in the form $P(dm_i|im,m,r)$ associated to one or more structure and/or damage types (dm_i), given an intensity measure (im), magnitude (m) and distance (r). Quantitative analysis of the structural damage record and the computation of attenuation relationship $f_{IM|M,R}$ (im|m,r), prior distribution of distance f_R (r) and prior distribution of magnitude f_M (m) are also required. In this early step the estimation of fragility functions associated with Dynamic Structural Analysis (DSA) is addressed. It provides the probability of occurrence of a certain damage state ($DM = dm_i$) given an intensity measure (IM) [16]. Thus, DSA tools as Incremental Dynamic Analysis (IDA) and Multiple Stripes Analysis (MSA) provide the statistical means to study structural damage due to seismic demand in structures. Fragility Functions are usually assumed to be represented by a lognormal cumulative distribution function:

$$P(DM|IM) = \boldsymbol{\Phi}\left(\frac{ln(x/\theta)}{\beta}\right) \tag{1}$$

The usual procedure consists of the estimation of function (1) parameters θ and β, respectively, the median of the fragility function and the standard deviation of ln(IM). DSA involves the time-history analysis of a global macro-model charac-

terizing the nonlinear behavior of a global macro-model calibrated to behave as a masonry infill wall, resorting to previously selected seismic/ground motion records [17] and using IDA and MSA for fragility function fitting. Considering present purposes, this work can be summarized in a conceptual map (Fig. 2). Issues related to the mainframe of the method [1] as the general method theoretical apparatus, account for uncertainties, ground motions (GM) selection, characterization of the seismic area, attenuation relationships, the nature and variability of damage descriptions will not be addressed here.

3 Experimental Sources

Old masonry subjected to in-plane shear with compression generally reveals highly nonlinear pinching behavior and considerable cyclic degradation [7, 8, 10]. Observations of the cyclic testing of an old clay masonry panel $590 \times 680 \times 290\ mm^3$ (with $290 \times 140 \times 65\ mm^3$ bricks) with a three ramp dynamic horizontal deflection loading [8] show initial elasticity followed by nonlinear hardening, and softening behavior after the 10 mm deflection (envelope, Fig. 3a, and cyclic behavior, Fig. 3b). Its cyclic behavior can be described as initially pinching with hysteretic behavior, strength degradation, unloading stiffness degradation but not clear, or perhaps inexistent, reloading stiffness degradation (Fig. 3).

Masonry shear behavior highly depends on confinement conditions and compressive normal forces largely affect the Young's modulus and therefore the shear modulus. To extend the model to larger wall panels cyclic parameters from empirical studies of [8] can be used. Despite the EC6 recommendation for shear modulus estimation, $G = 0.40 \times E$ [18], an empirical study suggests $G = 0.10 \times E$ to be a better match for experimental results [7], also appropriate to the experiments in [8] (see Fig. 4). As to the adobe masonry, its hysteretic curve layout (Fig. 4c) is not qualitatively very different from that of the old clay masonry, and so, a similar configuration with different material strength parameters can be applied.

4 Numerical Modeling

Usually masonry modeling resorts to Finite Elements (FEM) or Discrete Elements (DEM) methods associated with micro- and macro-modeling techniques, and model calibration regarding experimental results. These models can either be constituted by small discretized blocks or rectangles with or without mortar infills where interfaces are contact elements (micro-models), by a homogeneous shell or plate elements or by a reticular frame built and calibrated to simulate the behavior of the whole wall (macro-models). The composition of such simpler models constitutes the global model.

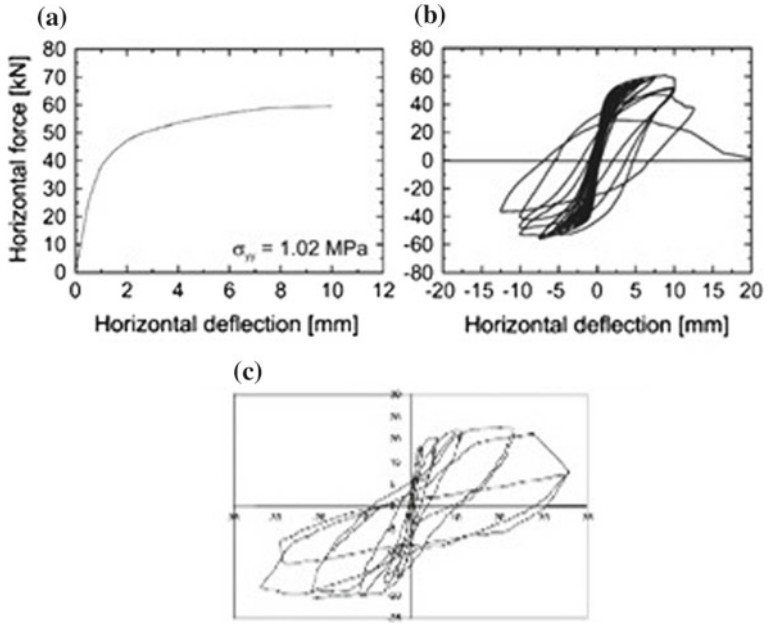

Fig. 3 Clay masonry wall **a** hysteretic behavior, **b** envelope curve [8] and **c** adobe masonry wall hysteretic curve [10]

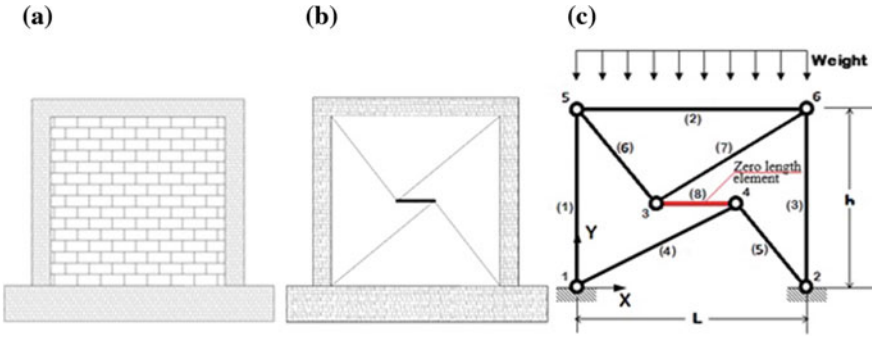

Fig. 4 **a** Simplified micro-model, **b** simplified macro-model [19], and **c** simplified macro-model

4.1 Structural Modeling

The structural model developed for calibration, a simplified macro-model (Fig. 4c), which represents the old masonry infill wall panel (L = 685 mm, h = 590 mm and d = 290 mm) in [16], tries to capture the idea of the common usage of masonry walls, generally pinched inside a concrete frame and wall intersections, or in older times between rigid ashlar columns and cornerstones.

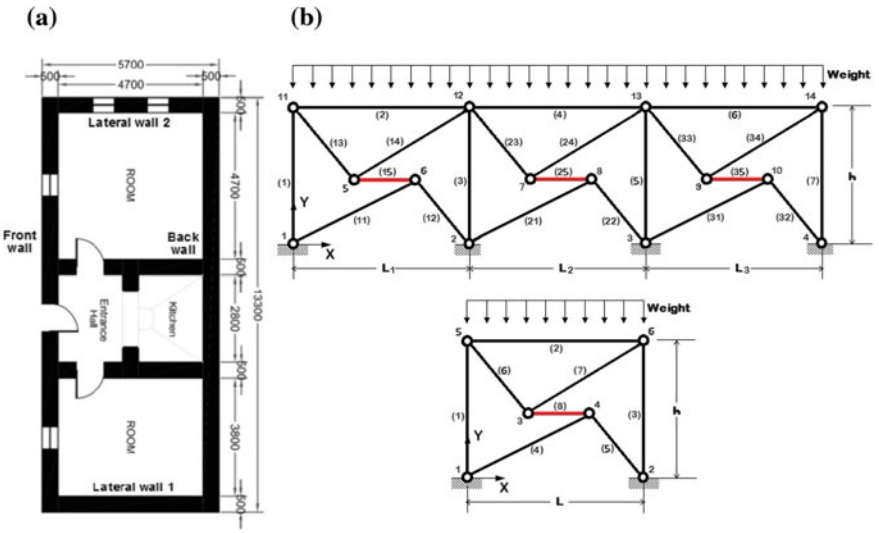

Fig. 5 Typical peasants house and structural models for the **a** *front*/*Back* wall (panels 3, 1 and 2, respectively) and **b** lateral walls (panel 3)

The present model (Fig. 4c) consists on an isostatic system composed by truss elements associated to uniaxial material models, where the trusses from (1) to (7) have a very high rigidity so that the zero length element [20] (8) be mostly responsible for the actual behavior of the frame as well as the rigidity of the system. The illustration of Fig. 5c schematically represents element 8 (as nodes 3 and 4 coincide in the coordinates (L/2, h/2)). The global mass is considered to correspond to half of the panel weight ($\gamma = 20\,\text{kN/m}^3$) and roofing portion (approx. $0.25\,\text{kN/m}^2$), as shear behavior is addressed, and it is distributed by the nodes 5 and 6. The GM ought to be inputted in horizontal direction as condition for both nodes 1 and 2.

Following the preliminary model results other structural models were developed with reference on a traditional peasant house typology (Fig. 5) of the sort affected by the 1763 Komárom earthquake and requiring minor repairs [21]. Effective length of each wall was calculated as $L_i = L_{span} + (t_i + t_f)/2$, with constant thickness t = 500 mm for all walls and resulting in $L_1 = 5200$ mm, $L_2 = 3300$ mm, $L_3 = 4300$ mm, $L_4 = 5200$ mm, and a constant height h = 2300 mm. Therefore two global-models are considered (Fig. 6) composed by panels 1, 2 and 3, respectively with $3300 \times 2300 \times 500\,\text{mm}^3$, $4300 \times 2300 \times 500\,\text{mm}^3$ and $5200 \times 2300 \times 500\,\text{mm}^3$. The dimensions and openings are used to determine the strength parameters of the walls. Despite great difference between these values in the literature [22] a Young's modulus of 1380.80 MPa, shear modulus of 138.08 and shear strength of 230 MPa are used for clay masonry [8]; and for adobe masonry ($\gamma = 15\,\text{kN/m}^3$), usually more flexible but with lower strength, a shear modulus of 39.80 MPa and shear strength of 0.026 MPa are adopted [12].

4.2 Material Modeling

The Pinching4 uniaxial material model can be found in OpenSees [20] catalogue. Along with a multilinear backbone it allows the simulation of cyclic degradation, mostly associated to the old masonry panel behavior in [8]. For the implementation, shown in Fig. 4 calibration of the model requires 16 parameters (8 as symmetric behavior is assumed) to define the response envelope (bold lines in Fig. 6), 6 parameters to define the two unload-reload paths (grey lines in Fig. 6), and 12 parameters to define the hysteretic damage rules. The present model is implemented by defining the four material states (both positive and negative loading, unloading and reloading), the rules, the control changes between states and the rules that govern evolution of the states [23].

The model application requires multilinear representation of the nonlinear backbone curve and the choice of its significant points (from Fig. 3a represented in Fig. 7) and the outline of the cyclic behavior (Fig. 3b) of the wall relating horizontal force and displacement. For the application of the material model and damage interpretation linear elastic range is considered between the points (ePd_1, ePf_1) and (eNd_1, eNf_1), no damage is attained. Plastification of the cross-section starts in the second linear steps (positive and negative sides) finishing in (ePd_2, ePf_2) and (eNd_2, eNf_2), meaning low damage (dm_1). The third step, finishing in (ePd_3, ePf_3) and (eNd_3, eNf_3), is interpreted as medium damage (dm_2), after which severe damage (dm_3) is considered. Total collapse (dm_4) occurs after (ePd_4, ePf_4) and (eNd_4, eNf_4).

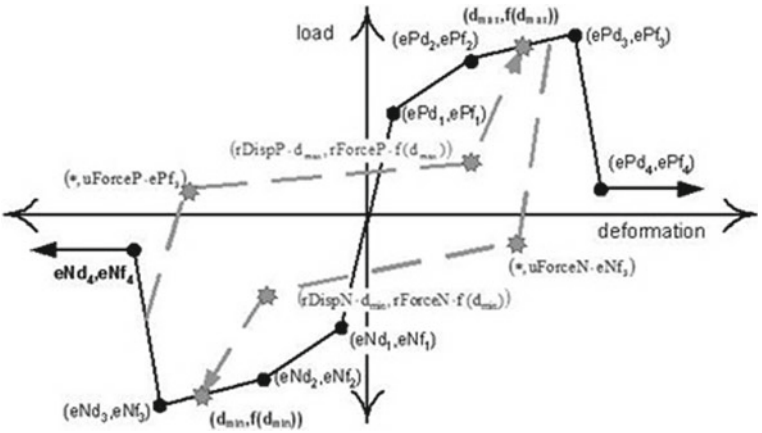

Fig. 6 OpenSees pinching4 uniaxial material model [20]

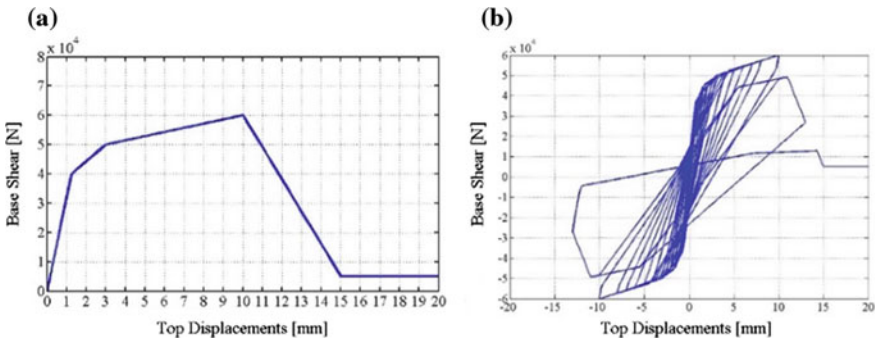

Fig. 7 **a** Backbone curve and **b** simulated cyclic response for material model pinching4

4.3 Calibration and Validation Procedures

The model calibration is taken in two main steps: adjustment of the backbone curve to the outline curve (Fig. 3a) and degradation parameters estimation to fit the hysteretic curve (Fig. 3b). Both steps rely on a trial-error procedure associated with static pushover analysis of the model (Fig. 1c). The backbone shaping was carried out using 0.25 mm increments until reaching 20 mm displacement. Some difficulty in calibrating the pinching and hysteretic behavior was observed, as the reloading stiffness degradation distorts the originally fitted backbone.

As the simulated response generally fits the experimental results (Fig. 3), the 2D pinching numerical model, a linear elastic SDOF and 2D versions were compared to check model consistency. With SDOF lateral rigidity equal to initial rigidity ($k_0 = 32000$ N) the structure was studied using a GM record and compared using varying mass (PGA = 0,617g) and PGA (mass of 233 kg) routines. The models behaved similarly until 1.25 mm deflection (linear range limit) where nonlinearities start to appear. For the present model (not representative of a real structure) to work in the range, where shear-based damage occurs it would require a mass between 13 and 16 tons or a PGA between 60 and 100 g.

The same calibration procedure was used to match the mechanical characteristics of the walls models (Fig. 5). To calculate their material model coordinates the basic equations of strength of materials were applied: shear strength $\tau = G \times \gamma$, $\tau = F/A_w$, shear strain $\gamma = \delta x/h$, and initial lateral rigidity $K_0 = G \times A_w/h$ (where G is the shear modulus, γ the shear strain, F the horizontal force, A_w the shear area, δx the horizontal displacement, and h the wall height). It was also assumed that the tendency of rigidity degradation during loading is material and wall dimensions independent (Table 1).

Table 1 Significant force coordinates ePf_i and eNf_i [kN], and displacement coordinates ePd_i and eNd_i [mm] for the calibration model, and both clay and adobe masonry walls

		ePf_i/eNf_i[kN]				ePd_i/eNd_i[mm]			
	i	1	2	3	4	1	2	3	4
Calibration model		40.00	50.00	60.00	5.00	1.25	2.50	10.00	15.00
Clay panels	1	385.74	482.17	578.61	48.22	3.89	7.79	28.28	41.95
	2	502.63	628.29	753.95	62.83	3.89	7.79	28.28	41.95
	3	619.52	774.40	929.28	77.44	3.89	7.79	28.28	41.95
Adobe panels	1	42.90	53.63	64.35	5.36	1.50	3.01	10.91	16.81
	2	55.90	69.88	83.85	6.99	1.50	3.01	10.91	16.81
	3	68.90	86.13	103.35	8.61	1.50	3.01	10.91	16.81
Adobe panels (with openings)	1	24.70	30.86	37.05	3.09	1.50	3.01	10.91	16.81
	2	37.70	47.13	56.55	4.71	1.50	3.01	10.91	16.81
	3	50.70	63.38	76.05	6.34	1.50	3.01	10.91	16.81

5 Dynamic Structural Analysis

To perform DSA a new algorithm for transient analysis with GM input was written. The calibration process and PGA parametric study were repeated and a bin of GM [24] matching the target spectrum for Komrom region (PGA = 0.15 g, EC8-1) was used for fragility function fitting. A PGA estimation for the Komrom earthquake is given by a GM model [24]: for m = 6.5, r = 10 km, strike-slip fault mechanism [4] soft/stiff soil on site, the PGA estimate for the seismic event is 0.223 g.

5.1 Incremental Dynamic Analysis

The structural model and the newly calibrated material model were adapted to a new code. In DSA, IDA is carried out scaling each GM until the structure collapses. Four damage states are assessed and used to calibrate the probability distribution parameters used to fit each of the lognormal CDF, or fragility functions. The lateral 1 and back clay and adobe masonry walls (without openings) will be analyzed first:

Clay masonry (Figs. 8a and 9a), as expected (Fig. 8), generally offers much more resistance than the adobe masonry (Figs. 8b and 9b). In result the specter of accelerations necessary to achieve damage states are very high and a null probability of damage given a seismic event with PGA = 0.233 g. Despite revealing lower related to damage PGAs the adobe walls still do not reach even a small probability. The models of Figs. 8 and 9 did not take into account the wall openings (which reduce the strength and rigidity of the wall), although the reduction of damage related PGA is expected. The two front and lateral walls have openings in all spans, for which the results were presented in Fig. 10. The median and standard deviation values for

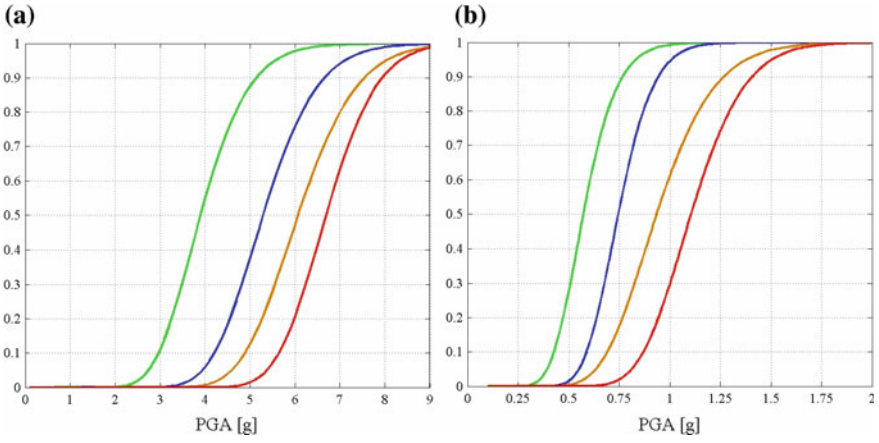

Fig. 8 Lateral wall 1 fragility function for each damage states, both for **a** clay and **b** adobe

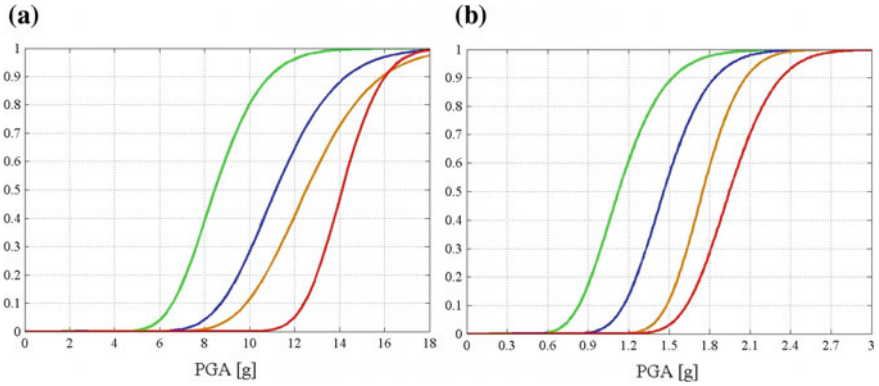

Fig. 9 Back wall fragility functions for each damage state, both for **a** clay and **b** adobe

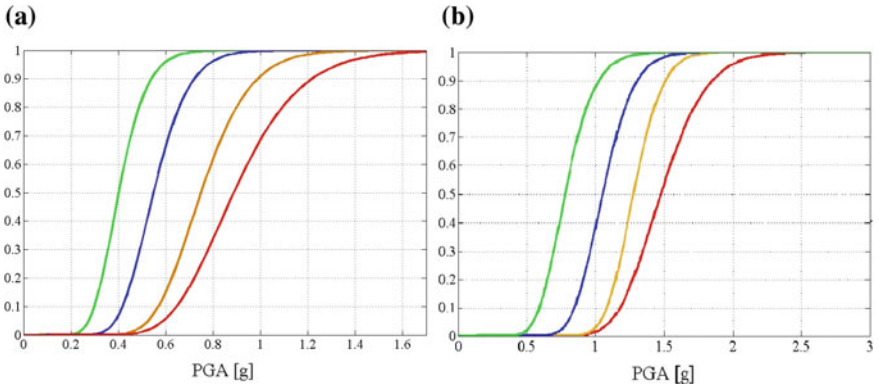

Fig. 10 Fragility functions for **a** the lateral 2 and **b** front adobe walls for each damage state (considering openings, see Fig. 5)

multiple damage states were calculated for the front, back and lateral clay and adobe masonry walls. The results are summarized in the following table (Table 2).

With the generation of the fragility functions it can be seen that within the range of wall structures tested for shear a probability of less than 10 % that a dm_1 damage type happens (Fig. 10a) given PGA of 0.223 g (m = 6.5; r = 10 km; Soft/Stiff soil and S-S fault type). The previous statement can be formalized as $P(dm_1|0{,}223g) = 6.98\,\%$. The significance of this result does not agree with the observations of Johann Grossinger regarding the light damage (here assumed to correspond to dm_i) in peasant houses. Despite the results support that it is most likely that those houses were not made out of clay masonry (because of high PGA_{dm_i} values), it is possible that they were made out of adobe, as the shear strength and shear modulus values used here are still relatively high, and it is definitely possible that they were made out of sárfal (for which no structural cyclic data was available).

Table 2 IDA analysis results in logarithmic scale ($PGA_{dm_i} = e^{\theta_i} \pm e^{\beta_i}$) for clay and adobe walls

	Lateral wall 1				Back wall				Lateral wall 2		Front wall	
DM	Clay		Adobe		Clay		Adobe		Adobe		Adobe	
	θ	β	θ	β	θ	β	θ	β	θ	β	θ	β
dm_1	1.362	0.215	−0.558	0.228	2.131	0.199	0.119	0.237	−0.910	0.230	0.248	0.214
dm_2	1.667	0.178	−0.294	0.184	2.427	0.146	0.380	0.179	−0.598	0.212	0.052	0.168
dm_3	1.804	0.169	−0.079	0.235	2.536	0.160	0.560	0.130	−0.287	0.215	0.246	0.130
dm_4	1.902	0.133	0.086	0.188	2.638	0.100	1.950	0.134	−0.119	0.247	0.391	0.176

6 Conclusions

Regarding the results it can be stated that peasant houses were probably not made of clay masonry when the 1763 Komárom historical earthquake, and possibly made of adobe or srfal. Masonry is a highly complex composite material and this complexity increases with the complexity of the composition creating global mechanisms that locally depend on the relative strength of bricks and mortar resistance, on their assembly and L/h aspect ratio: there is a great deal of uncertainty on the masonry behavior to account for. This difficulty can be overcome resorting to simplified micro modeling techniques together with DEM analysis, which can enable the establishment of simplified macro-models of these walls. Although, the appropriate cyclic parameters for the materials is still a begging question, a sensitivity analysis would help to enlighten it. Another pendent question is that given the lack of precise damage descriptions, if the light damage on peasant houses is associated to a mechanism in shear walls. Nonetheless, a better material model calibration can be achieved through optimization, using a genetic algorithm [25].

Regarding the method for magnitude estimation described in [1], its full methodology requires applying fragility functions of the type P(DM|IM,M,R) and the development of MSA with enhancement of results [16] is relevant. Also, accounting for uncertainties can provide considerable shift in the fragility function parameters. In the present case damage description, material model and strength parameters, structural model, weight, earthquake direction and duration, intensity measures, wall construction, structural elements to analyze, etc. are all uncertainties weighting on the reliability of results. So, and despite efficiency, the methodology application and overview suggests the development of a full probabilistic approach to fragility function fitting using the background of reliability theory [19], providing a concomitant sensitivity analysis and variables weight evaluation.

Acknowledgments To Ádám Zsárnoczay, József Simon, and Tamás Bálogh we extend our profound gratitude for making the research work pleasant. Proper acknowledgements to CAPES for allowing the present research (proc. no. 9178-13-9). This research was supported by the János Bolyai Research Scholarship of the Hungarian Academy of Sciences.

References

1. Ryu, H., et al.: A probabilistic method for the magnitude estimation of a historical damaging earthquake using structural fragility functions. Bull. Seism. Soc. Am. **99**(2), 520–537 (2009)
2. Morais, E.C., Vigh, L.G., Krähling, J.: Global response evaluation of a hungarian late romanesque church due to a historical seismic event. In: Proceedings of the 2nd International Conference for PhD Students in Civil Engineering and Architecture, pp. 27–34. Cluj-Napoca, Romania (2014)
3. CEN (2004), Eurocode 8: design of structures for earthquake resistance, part 1: general rules, seismic actions and rules for buildings, EN 1998-1:2004, Brussels
4. Varga, P., Szeidovitz, G., Gutdeutsch, R.: Isoseismical map and techtonical position of the komárom earthquake of 1763. Acta Geod. Geophys. Hung. **36**(1), 97–108 (2001)

5. Szeidovitz, G.: Earthquakes in the region of Komárom, Mór and Várpalota. Geophys. Trans. **32**(3), 255–274 (1986)
6. Eisinger, et al.: Historical earthquake research, an example of interdisciplinary cooperation between geophysicists and historians. Abh Geol B A **1**, 33–50 (1992)
7. Tomaževič, M.: Shear resistance of masonry walls and eurocode 6: shear versus tensile strength of masonry. Mat. Struct (2008). doi:10.1617/s11527-008-9430-6
8. Zimmermann, T., Strauss, A., Bergmeister, K.: Numerical investigation of historic masonry under normal and shear load. Constr. Build. Mater. **24**, 1385–1391 (2010)
9. Caporale, A., et al.: Comparative micromechanical assessment of adobe and clay brick masonry assemblages based on experimental data sets. Compos. Struct. **120**, 208–220 (2015)
10. NIKER D4.1 (2010) Specification for laboratory specimens and testing strategies on walls, Padova. http://www.niker.eu/downloads/
11. Vargas, J., et al.: Seismic strength of adobe masonry. Mater. Struct. (1986). doi:10.1007/BF02472107
12. Varum, H., et al.: Structural behaviour and retrofitting of adobe masonry buildings, In: Costa, A. et al. (eds.) Structural Rehabilitation of Old Buildings, Building Pathology and Rehabilitation, vol. 2, pp. 37–75 (2014)
13. Barabás, J., Gilyén, N.: Magyar népi építészet. Müszaki, Budapest (1987)
14. Balassa, I., Füzes, E., Kisbán, E. (eds.): Életmód, magyar néprajz, 4th edn. Akadémiai K, Budapest (1997)
15. Grossinger, J.: Dissertatio de terrae motibus regni Hungariae. Györ (1783)
16. Baker, J.W.: Efficient analytic fragility function fitting using dynamic structural analysis. Earthq. Spectra **31**(1), 579–599 (2015)
17. Simon, J., Vigh, L.G.: Seismic vulnerability assessment of existing hungarian highway bridges using hazard compatible ground motions. In: 12th Hungarian Confrence on Theoretical and Applied Mechanics, Miskolc
18. CEN (2005) Eurocode 6: design of masonry structures - part 1-1: common rules for reinforced and unreinforced masonry structures, EN 1996-1-1:2005, Brussels
19. Choi, S., Grandhi, R.V., Canfield, R.A.: Reliability-based structural design. Springer-Verlag, London (2007)
20. Mckenna, F., Fenves, G., Scott, M., Jeremic, B.: Open system for earthquake engineering simulation (OpenSees). Berkeley, CA (2006)
21. Varga, P.: Az 1763 évi komáromi földrengés, Természet Világa, **145**(2) (2014). http://www.termeszetvilaga.hu/, http://www.chemonet.hu/TermVil
22. Furtado, A., Rodrigues, H., Arêde, A.: Modelling of masonry infill walls participation in the seismic behavior of RC buildings using opensees. Int. J. Adv. Struct. Eng. **7**, 117–127 (2005)
23. Lowes, L., et al.: A beam-column joint model for simulating the earthquake response of reinforced concrete frames. In: PEER 2003/10, Univ of California, Berkeley (2003). http://citeseerx.ist.psu.edu/viewdoc/summary?doi=10.1.1.500.4734
24. Akkar, S., Bommer, J.: Empirical equations for the prediction of PGA. PGV and spectral accelerations in Europe, the mediterranean region and the middle east. Seismol. Res. Lett. **81**(2), 195–206 (2010)
25. Vigh, L.G., Liel, A.B., Deierlein, G.G., Miranda, E., Tipping, S.: Component model calibration for cyclic behavior of a corrugated shear wall. Thin-Wall. Struct. **75**, 53–62 (2014)

Analytical Model of Dynamic Behaviour of Fatigue Test Stand—Description and Experimental Validation

R. Owsiński and A. Niesłony

Abstract In this paper, an analytical model to describe the dynamic characteristics of the test system was presented. Test system, which was the object under considerations, is designed for fatigue life determination of structural materials using bending moment resulting from inertia forces. Therefore, the test system was modelled with regard to one and two degrees of freedom system. The general analytical equations were solved and simulated in Matlab-Simulink using general method and symbolic method based on Laplace transforms field. Moreover, it was also presented further experimental determination of the logarithmic damping decrement based on measurement of acceleration using uniaxial accelerometers. Finally, dynamic characteristics of the test system was determined based on the finite element method and confirmed experimentally the correctness of all assumptions according to the number of degree of freedom and damping behaviour.

1 Introduction

Mechanical systems in dynamics are being described using displacements and their derivatives related with deformations and causing them forces. In mechanical systems, following mass components can be distinguished: material points—deformable and non-deformable solids, elastic and damping solids—such as springs and dampers. Dynamics of machines refer to conjugate variables describing system's state changes over time as signals. Regarding the complexity of mechanical systems with various number of degrees of freedom determining the degree of complexity of the machine, following can be distinguished:

R. Owsiński (✉) · A. Niesłony
Faculty of Mechanical Engineering, Department of Mechanics and Machine Design, Opole University of Technology, Opole, Poland
e-mail: r.owsinski@po.opole.pl

A. Niesłony
e-mail: a.nieslony@po.opole.pl

J. Awrejcewicz (ed.), *Dynamical Systems: Modelling*, Springer Proceedings in Mathematics & Statistics 181, DOI 10.1007/978-3-319-42402-6_24

- single degree of freedom system;
- systems with finite number of degrees of freedom (discrete systems);
- systems with infinite number of degrees of freedom.

For modelling mechanical systems fundamental magnitudes are being used, such as: mass, stiffness and damping factors [1].

With regard to the Newton's second law of motion, the acceleration of the mass of a solid object being equal to $\ddot{x}$ is directly proportional to the resultant of all forces F acting on the body.

$$F = m\,\ddot{x} \tag{1}$$

If rotational motion is described in terms of angular displacement φ of an object and the angular acceleration magnitude is expressed in $\frac{rad}{s^2}$, then the proportionality constant is the moment of inertia I of the object rather than its mass.

$$M = I\,\ddot{\varphi} \tag{2}$$

In the system, stiffness means a spring with k coefficient expressing the ratio of F force gain and the spring deflection as Δx.

$$k = -\frac{\Delta F}{\Delta \mathrm{x}} \tag{3}$$

The minus sign indicates that the force F is in opposite direction to the displacement.

In real physical systems being subject to dynamic forces, the amplitude of system response has a damping character, which results from the fact that real materials—due to the inhomogeneity of the structure and material defects—dissipate part of the excitation energy. This phenomenon is known as damping. Damping of mechanical systems can be interpreted as drag of the damper for which the dependence between the force and velocity is as follows:

$$F_D = -c\dot{x} \tag{4}$$

This is the basic dependence used by estimating the oscillation decay rate or the resonant model response. The substitute damping of the test system can be designated experimentally by signal excitation of the system. Exemplary image of the response is presented in Fig. 1.

Formulation of equations in dynamics for a system of material points without any degrees of freedom is more complicated because of the necessity to consider additional conditions derived from equations of bonds. This entails the need for introducing the reaction forces into the equations of dynamics. They constitute additional unknowns that are often difficult to displace. These difficulties can be eliminated by shifting from Cartesian coordinates to generalized coordinates. The generalized coordinates constitute a minimum number of independent coordinates

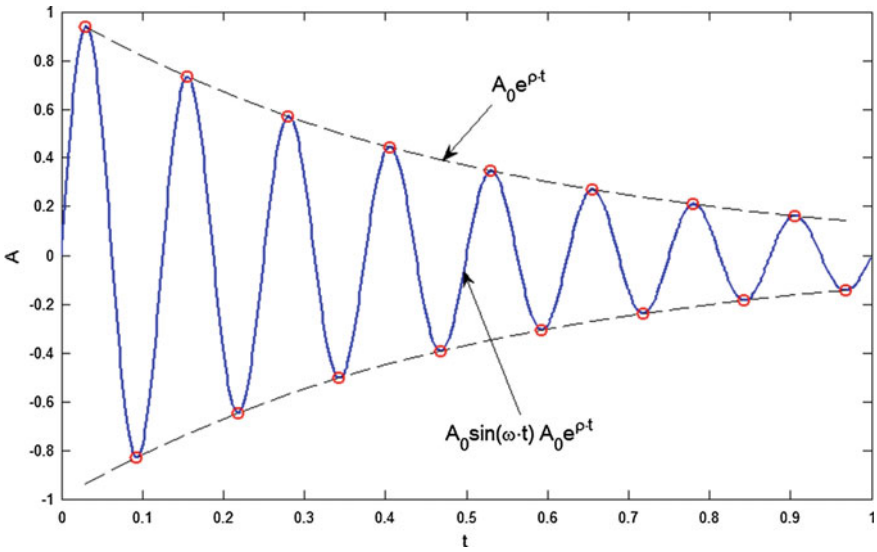

Fig. 1 Graphical chart of decreasing vibrations

clearly describing the in space position of the system. Most frequently, the generalized coordinates adopt the form of displacements. They can be either linear (translational) displacements or angular (rotational) displacements.

1.1 The Lagrangian Formalism

The formalism is based on the principle of least action. For the purpose of modelling, the Lagrange's equation of the second kind is being used, thus a description is derived as a system of differential equations. Depending on the type of interactions on the examined mechanical system, the Lagrange's equation of the second kind assumes the form of:

- Conservative and autonomous systems—without the impact of external forces;

$$\frac{\mathrm{d}}{\mathrm{d}t}\left(\frac{\delta L_k}{\delta \dot{q}_i}\right) - \frac{\delta L_k}{\delta q_i} = 0 \tag{5}$$

- Non-conservative and autonomous systems—energy dissipation occurs during movement of the system;

$$\frac{\mathrm{d}}{\mathrm{d}t}\left(\frac{\delta L_k}{\delta \dot{q}_i}\right) - \frac{\delta L_k}{\delta q_i} + \frac{\delta F_R}{\delta \dot{q}_i} = 0, \tag{6}$$

where F_R—the Rayleigh's dissipation function—power dissipation in a linear dissipative element expressed through the dependence:

$$F_R = \int_0^{\dot{q}} R_v d\dot{q} = \frac{1}{2} c\dot{q}^2, \tag{7}$$

where R_v—viscous drag force, c—viscous drag coefficient.

- Nonautonomous systems—being subject to external forces.

$$\frac{\mathrm{d}}{\mathrm{d}t}\left(\frac{\delta L_k}{\delta \dot{q}_i}\right) - \frac{\delta L_k}{\delta q_i} + \frac{\delta F_R}{\delta \dot{q}_i} = Q_i, \tag{8}$$

where Q_i—external generalized force corresponding to the generalized force, described as:

$$Q_i = \sum_{j=1}^{n} \left(P_{jx} \frac{\delta x_j}{\delta q_i} + P_{jy} \frac{\delta y_j}{\delta q_i} + P_{jz} \frac{\delta z_j}{\delta q_i} \right), \quad i = 1, \ldots, s, \tag{9}$$

where s—number of degrees of freedom in the analysed system.

1.2 Dynamic Characteristics of Mechanical Systems

At the stage of designing mechanical systems, there should be performed their comprehensive analysis taking into account dynamic interactions and their frequency characteristics. A critical aspect of any mechanical system is its resonant frequency by which interactions are being intensified in mechanical systems [1, 2].

At present, in order to determine the dynamic characteristics for industrial practices, electromagnetic inductors are used, which facilitate test performance, which provide accurate information about the frequency response of the test object to the extortion. By means of these devices it is possible to determine the range of occurrence of free vibrations. More and more frequently, they are components of test stands for testing durability on laboratory test pieces and on complex structural elements [3].

2 Test System

During the operation period elements of machinery and equipment are subject to complex loads being changed. These loads can result from ongoing work movements, or they also can be the result of external forces. Therefore, it is important to

Fig. 2 Overview of the test stand

be familiar with changes in the strength properties of the material in relation to the number of load changes [4]. There are many hypotheses on fatigue that enable the reduction of a complex state of stress into an equivalent uniaxial strain allowing for reproducing it at the test stands. None of the hypotheses take into account all factors determining formation of fatigue cracks.

In the specialized literature, there can be found a number of works in which the authors [5, 6, 7] review the criteria for multiaxial fatigue. There are a large number of criteria related to the accumulation of damage in a loaded element. It can be distinguished fatigue criteria based on stress [8], strain [9] and energy parameters [10]. In addition, there can be also distinguished a group of criteria based on the concept of critical plane [11–14]. Because the computations in the time domain are very time-consuming, more often, computations on the fatigue are performed in the frequency domain [15–17].

An interesting idea seems to be performing fatigue testing at higher frequency ranges of load changes. This results in significant reduction of time needed for performing a series of fatigue tests. The proposed test stand required deeper dynamics analysis, which would allow for proving the results obtained experimentally. The test stand is presented in Fig. 2.

3 Analytical Model of Single Degree of Freedom System

Adopted for the analysis test system consists of mounting bracket fixed to an actuator of the electromagnetic inductor with the test piece and additional load in the form of a square profile of specified dimensions. The system subjected to kinematic excitation is presented in Fig. 3. A deflection from the equilibrium position of the centre of gravity of a loader moved away at the distance of b from working cross section of the test piece was designated as w_c and illustrated in Fig. 4.The motion of the loader subjected to kinematic excitation with assumed

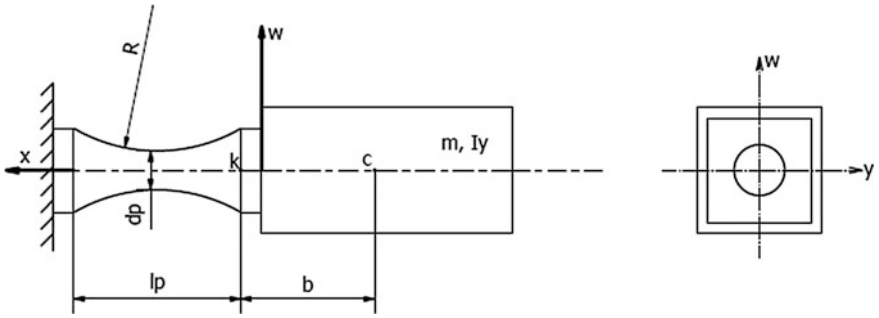

Fig. 3 Scheme of the test system

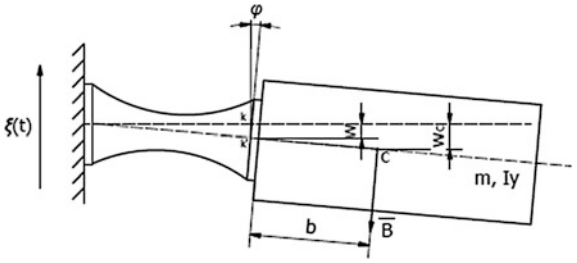

Fig. 4 Test system deflection from the equilibrium position

single degree of freedom system was described by differential equations. Differential equations of motion are written in the form of (10).

$$\begin{cases} E_K = \frac{1}{2} m \cdot \dot{w}_c^2 + \frac{1}{2} \cdot I_y \dot{\varphi}^2 \\ E_P = \frac{1}{2} k_g \cdot (w_c - \xi)^2 + \frac{1}{2} k_s \cdot \varphi^2 \\ R = \frac{1}{2} c_g (\dot{w}_c - \dot{\xi})^2 + \frac{1}{2} c_s \cdot \dot{\varphi}^2 \end{cases} \tag{10}$$

In the scheme presented in Fig. 4, there can be observed a close relationship between the vertical displacement of the centre of the loader mass w_c and the angle of rotation φ:

$$w_c = w + b\sin\varphi \tag{11}$$

The dependence (11) of small angles can be expressed as (12):

$$w_c = w + b\varphi, \tag{12}$$

where $\boldsymbol{w}$ is a vertical displacement of the final (free) cross section of the test piece due to its deflection, while φ is the angle of rotation of this cross section. It is therefore desired to perform diffraction analysis of the test piece with inertia load $\boldsymbol{B}$ and the moment of inertia $\boldsymbol{M}$ in cross section connecting the test piece with loader

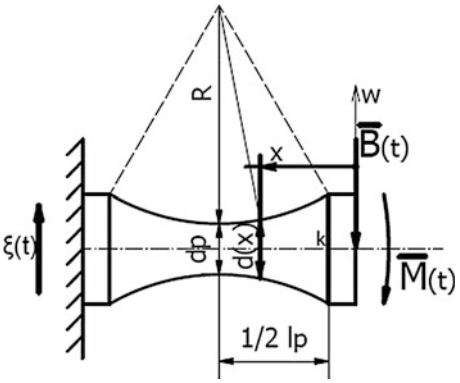

Fig. 5 Overview of the test piece with load scheme

—Fig. 5. Calculations were carried out for the static load, so instead of $\boldsymbol{B}$ force, $\boldsymbol{P} = \textbf{const}$ was introduced, and $\boldsymbol{M}_{(t)} \rightarrow \boldsymbol{M} = \textbf{const}$, where the $\boldsymbol{M}$ moment can be written as the product of $\boldsymbol{P} \cdot \boldsymbol{b}$.

By applying the differential equation of the deflection curve of the test piece for small deflections, the computations were performed:

$$w'' \cdot EI_{(x)} = P \cdot x + M \tag{13}$$

for the adopted dependence: $M = P \cdot b$, so the differential equation of the cross section deflection can be expressed as

$$EI_{(x)} \cdot w'' = P(x + b) \tag{14}$$

Value of the deflection angle of cross Sect. (15) is obtained by integrating the dependence (14), and the cross section dependence (16) is derived after two-dimensional integration of the dependence (14):

Deflection angle of cross section:

$$w'_{(x)} = \frac{P}{E} \cdot \left(\int \frac{x + b}{J_{(x)}} \mathrm{d}x + D_1 \right) \tag{15}$$

Cross-section deflection:

$$w_{(x)} = \frac{P}{E} \left\{ \int \left(\int \frac{x + b}{J_{(x)}} \mathrm{d}x \right) \mathrm{d}x + D_1 x + D_2 \right\} \tag{16}$$

If the designation $w'_{(x=0)} = \varphi$ is adopted, then for the analysed cross section of the test piece in the connection point with loader mass, it can be expressed as

$$\varphi = w_{(x=0)} \cdot \left. \frac{\int \frac{x+b}{J_{(x)}} \mathrm{d}x + D_1}{\int \left(\int \frac{x+b}{J_{(x)}} dx \right) \mathrm{d}x + D_1 x + D_2} \right|_{x=0} \tag{17}$$

by substituting

$$F_{(x=0)} = \left. \frac{\int \frac{x+b}{J_{(x)}} \mathrm{d}x + D_1}{\int \left(\int \frac{x+b}{J_{(x)}} dx \right) \mathrm{d}x + D_1 x + D_2} \right|_{x=0} \tag{18}$$

Finally, the following is obtained:

$$\varphi = w \cdot F \tag{19}$$

The designated dependence is being introduced into a system of Eq. (10), which is in the form of (20):

$$\begin{cases} E_K = \frac{1}{2} m \cdot \dot{w}^2 (1 + bF)^2 + \frac{1}{2} I_y \cdot \dot{w}^2 F^2 \\ E_P = \frac{1}{2} k_g (w(1 + bF) - \xi)^2 + \frac{1}{2} k_s \cdot w^2 F^2 \\ R = \frac{1}{2} c_g (\dot{w}(1 + bF) - \xi)^2 + \frac{1}{2} c_s \cdot \dot{w}^2 F^2 \end{cases} \tag{20}$$

By ordering the system of Eq. (20), finally the following was obtained:

$$\begin{cases} E_K = \left(\frac{1}{2} m \cdot (1 + bF)^2 + \frac{1}{2} I_y F^2 \right) \cdot \dot{w}^2 \\ E_P = \left(\frac{1}{2} k_g (w(1 + bF) - \xi)^2 \right) + \frac{1}{2} k_s \cdot F^2 w^2 \\ R = \left(\frac{1}{2} c_g (\dot{w}(1 + bF) - \xi)^2 \right) + \frac{1}{2} c_s \cdot F^2 \dot{w}^2 \end{cases} \tag{21}$$

The components of the Lagrange's equation are determined by the dependence (21):

$$\begin{aligned} \frac{\mathrm{d}}{\mathrm{d}t} \left(\frac{\partial E_K}{\partial \dot{w}} \right) &= \left(m(1 + bF)^2 + I_y F^2 \right) \ddot{w} \\ \left(\frac{\partial E_P}{\partial w} \right) &= k_g (w(1 + bF) - \xi) \cdot (1 + bF) + k_s F^2 \cdot w \\ \left(\frac{\partial R}{\partial \dot{w}} \right) &= c_g (\dot{w}(1 + bF) - \xi) \cdot (1 + b\dot{F}) + c_s F^2 \cdot \dot{w} \end{aligned} \tag{22}$$

Finally, a differential equation of oscillating motion was derived in the form of

$$\begin{aligned}&\left[m(1+bF)^2+J_yF^2\right]\cdot\ddot{\boldsymbol{w}}+k_g(\boldsymbol{w}(1+bF)-\xi)\cdot(1+bF)+k_sF^2\cdot\boldsymbol{w}\\&+c_g(\dot{\boldsymbol{w}}(1+bF)-\xi)\cdot\left(1+b\dot{F}\right)+c_sF^2\cdot\dot{\boldsymbol{w}}=0\end{aligned}\tag{23}$$

Oscillating system can be presented as (24)

$$\begin{aligned}&\ddot{\boldsymbol{w}}+\frac{k_g(1+bF)^2+k_sF^2}{m(1+bF)^2+I_yF^2}\cdot\boldsymbol{w}+\frac{c_g(1+bF)^2+c_sF^2}{m(1+bF)^2+I_yF^2}\cdot\dot{\boldsymbol{w}}=\\&=\frac{k_g(1+bF)}{m(1+bF)^2+I_yF^2}\cdot\xi_{(t)}+\frac{c_g(1+bF)}{m(1+bF)^2+I_yF^2}\cdot\dot{\xi}_{(t)}\end{aligned}\tag{24}$$

which, after arranging it according to the highest order derivative

$$\begin{aligned}&\ddot{\boldsymbol{w}}=-\frac{k_g(1+bF)^2+k_sF^2}{m(1+bF)^2+I_yF^2}\cdot\boldsymbol{w}-\frac{c_g(1+bF)^2+c_sF^2}{m(1+bF)^2+I_yF^2}\cdot\dot{\boldsymbol{w}}+\\&+\frac{k_g(1+bF)}{m(1+bF)^2+I_yF^2}\cdot\xi_{(t)}+\frac{c_g(1+bF)}{m(1+bF)^2+I_yF^2}\cdot\dot{\xi}_{(t)}\end{aligned}\tag{25}$$

the excitation $\xi_{(t)}$ adopts the form of harmonic, which can be expressed by the dependence of (26):

$$\xi_{(t)}=\xi_a\sin(\nu t)\tag{26}$$

3.1 The Level of Stresses in the Analysed Cross Section as a System with Single Degree of Freedom

For such described test system a relationship between arising stresses occurring in the given cross section of the test piece and its deflection can be formulated, as well. Knowledge on the level of stresses being generated in the test system is crucial from the perspective of experimental verification of the proposed system description.

As a function of (27)

$$B_{(t)}=m\cdot\ddot{w}_c\tag{27}$$

and after adopting (28), and consequently (29):

$$w_c=w+b\varphi=w(1+bF)\tag{28}$$

$$\ddot{w}_c = \ddot{w}(1 + bF) \tag{29}$$

The equation describing the bending moment at lower cross section is as follows:

$$M(t) = B(t) \cdot b = m \cdot b \cdot \ddot{w}(1 + bF) \tag{30}$$

If the bending moment arising in the cross section is known, the values of stresses in any cross section can be determined (based on data in Fig. 5):

$$\sigma_{(x)} = \frac{Mg(x)}{W_y(x)} = \frac{32}{\pi} m(1 + bF) \frac{b + x}{dp^3(x)} \ddot{w} \tag{31}$$

4 Analytical Model of the System Regarding Two Degrees of Freedom

The test system—subject of the research study—was analysed in the aspect regarding two degrees of freedom in it. The second degree of freedom is an additional deflection of the analysed cross section due to the forces of inertia acting on the system. The assumption is presented in Fig. 6.

Table 1 contains derivation of geometrical relationships for the purpose of further analytical considerations. By performing proper substitutions (32)–(34), the relationship for total deflection of the test system (35) during excitation is obtained.

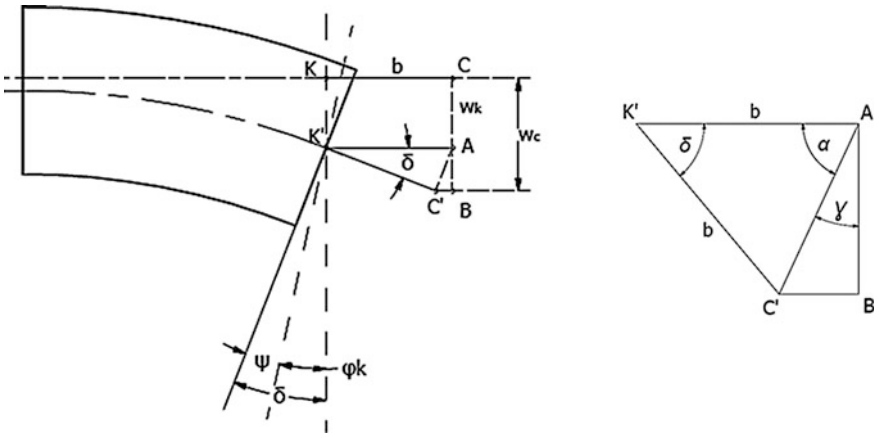

Fig. 6 Graphical illustration of values describing the adopted two degrees of freedom test system

Table 1 Geometric relationships of values from Fig. 6

$w_c = w_k + AB$	$\gamma = 90 - \alpha$
$AB = AC' \cos\gamma,$	$\alpha = 90 - \frac{1}{2}\delta$
$AB = AC' \cos\left(\frac{1}{2}\delta\right),$	$AC' = 2 \cdot b \cdot \sin\left(\frac{1}{2}\delta\right)$

$$AB = 2 \cdot b \cdot \sin\left(\frac{1}{2}\delta\right) \cos\left(\frac{1}{2}\delta\right) = b \cdot \sin\delta \tag{32}$$

$$w_c = w_k + b\sin\delta \approx w_k + b \cdot \delta \text{ for small } \delta(\delta < 0,1 \text{ rad}) \tag{33}$$

$$\delta = \varphi_k + \psi \tag{34}$$

And finally

$$w_c = w_k(1 + bF) + \psi \cdot b \tag{35}$$

By adopting generalized coordinates as $q_1 = w_k, q_2 = \psi$ of the differential equation describing the motion of the analysed system under kinematic excitation can be written as (36).

$$\begin{cases} E_K = \frac{1}{2}m \cdot \dot{w}_c^2 + \frac{1}{2} \cdot J_y\dot{\delta}^2 \\ E_P = \frac{1}{2}k_g \cdot (w_k - \xi)^2 + \frac{1}{2}k_s \cdot \delta^2 = \\ R = \frac{1}{2}c_g \cdot (\dot{w}_k - \xi)^2 + \frac{1}{2}c_s \cdot \dot{\delta}^2 \end{cases} = \begin{cases} \frac{1}{2}m(\dot{w}_k(1 + bF) + \dot{\psi}b)^2 + \frac{1}{2}J_{yc}(\dot{\psi} + \dot{w}_k F)^2 \\ \frac{1}{2}k_g(w_k - \xi)^2 + \frac{1}{2}k_s(w_k F + \psi)^2 \\ \frac{1}{2}c_g(\dot{w}_k - \dot{\xi})^2 + \frac{1}{2}c_s(\dot{w}_k F + \dot{\psi})^2 \end{cases} \tag{36}$$

Based on the system of Eq. (36), components of the Lagrange's equation for generalized coordinates of w_k and ψ adapt the form of (37) and (38), respectively.

$$\begin{aligned} \frac{\mathrm{d}}{\mathrm{d}t}\left(\frac{\partial E_K}{\partial \dot{w}}\right) &= m(\ddot{w}_k(1 + bF) + \ddot{\psi}\, b)(1 + bF) + J_{yc}(\ddot{\psi} + \ddot{w}_k F) \cdot F \\ \left(\frac{\partial E_P}{\partial w}\right) &= k_g(w_k - \xi) + k_s(w_k F + \psi) \cdot F \\ \left(\frac{\partial R}{\partial \dot{w}}\right) &= c_g(\dot{w}_k - \xi) + c_s(\dot{w}_k F + \dot{\psi}) \cdot F \end{aligned} \tag{37}$$

$$\begin{aligned}
&\frac{\mathrm{d}}{\mathrm{d}t}\left(\frac{\partial E_K}{\partial \dot{\psi}}\right) = m(\ddot{w}_k(1+bF) + \ddot{\psi}\, b)b + J_{yc}(\ddot{\psi} + \ddot{w}_k F)\\
&\left(\frac{\partial E_P}{\partial \psi}\right) = k_s(w_k F + \psi)\\
&\left(\frac{\partial R}{\partial \dot{\psi}}\right) = c_s(\dot{w}_k F + \dot{\psi})
\end{aligned} \tag{38}$$

And this—after ordering the variables—yields to the system of differential Eq. (39) describing the deflection from the equilibrium position during kinematic excitation.

$$\begin{cases}
\ddot{w}_k\left(m(1+bF)^2 + J_{yc}F^2\right) + \left(k_g + k_s F^2\right)\cdot w_k + \\
\left(c_g + c_s F^2\right)\dot{w}_k + \left(mb(1+bF) + J_{yc}F\right)\ddot{\psi} \\
+\ k_s F\psi + c_s F\dot{\psi} = k_g\xi + c_g\xi \\
\\
\ddot{w}_k\left(m(1+bF) + J_{yc}F\right) + \left(k_s F\right)\cdot w_k + \\
(c_s F)\dot{w}_k + \left(mb^2 + J_{yc}\right)\ddot{\psi} + k_s\psi + c_s\dot{\psi} = 0
\end{cases} \tag{39}$$

The excitation $\xi_{(t)}$ undertakes the form of harmonic, which can be presented as Eq. (40), which is the same as the adopted analysis of single degree of freedom (26).

$$\xi = \xi_a \sin(\nu t) \tag{40}$$

4.1 Stress Levels at the Analysed Cross Section by Assuming Two Degrees of Freedom System

Deviation from the equilibrium position of the system by kinematic excitation causes arise of bending moment in the analysed working cross section of the test piece (41).

$$Mg_{(x)} = B(b+x) + I_{yk}\delta \tag{41}$$

having regard to the relationships (42)–(44):

$$B = m\cdot \ddot{w}_c \tag{42}$$

$$\ddot{w}_c = \ddot{w}_k(1+bF) + \ddot{\psi}\, b \tag{43}$$

$$\delta = \ddot{w}_k F + \ddot{\psi} \tag{44}$$

the expression for bending moment at any cross section of the test piece adopts the form of (45):

$$Mg_{(x)} = m \cdot (\ddot{w}_k(1+bF) + \ddot{\psi}\, b)(b+x) + (I_{yc} + mb^2)(\ddot{w}_k F + \ddot{\psi}) \tag{45}$$

The value of bending moment arising in the cross section allows determining the value of stresses in any desired cross section (based on Fig. 5) according to the dependence (46):

$$\begin{aligned} \sigma_{(x)} &= \frac{Mg_{(x)}}{Wy_{(x)}} = \\ &= \frac{32(m \cdot (\ddot{w}_k(1+bF) + \ddot{\psi}\, b)(b+x) + (I_{yc} + mb^2)(\ddot{w}_k F + \ddot{\psi}))}{\pi \cdot dp^3_{(x)}} \end{aligned} \tag{46}$$

5 Simulation Model for Systems with Single and Two Degrees of Freedom

Based on the formulated differential equations of motion, being presented in sections **Błąd! Nie można odnaleźć źródła odwołania.** and **Błąd! Nie można odnaleźć źródła odwołania.** of this research paper, there was performed a simulation of the system run. Simulations were carried out in the Matlab/Simulink software environment. The equations written in order-based final forms for the case regarding single degree and two degrees of freedom system ((25) and (39), respectively) were modelled in the form of a block. For the purpose of additional verification of the results obtained, the simulation was based on two methods: general method and operator method with regard to the Laplace's transformation of integral to solve differential equation.

5.1 Dynamic Simulation of Single Degree of Freedom System

Single degree of freedom system model is based on Eq. (25), as follows, which in an unchanged form can be presented in the form of a block diagram.

$$\begin{aligned} \ddot{\boldsymbol{w}} = &- \frac{k_g(1+bF)^2 + k_s F^2}{m(1+bF)^2 + I_y F^2} \cdot \boldsymbol{w} - \frac{c_g(1+bF)^2 + c_s F^2}{m(1+bF)^2 + I_y F^2} \cdot \dot{\boldsymbol{w}} + \\ &+ \frac{k_g(1+bF)}{m(1+bF)^2 + I_y F^2} \cdot \xi_{(t)} + \frac{c_g(1+bF)}{m(1+bF)^2 + I_y F^2} \cdot \xi_{(t)} \end{aligned} \tag{47}$$

On the basis of the general method for modelling differential equations, the block diagram of the dynamic system is indicated in Fig. 7.

Amplification of signals contained in *gain*-type blocks correspond to the respective quotients in Eq. (47). At this stage, zero coefficient of system damping was adopted. Such undertaken action introduces a slight simplification of the system, however, differential equations of motion consider the impact of damping effects. After experimental verification, they can be substituted by numerical values.

Performance of the test system being modelled with single degree of freedom was presented in Fig. 8. The waveform is in stable working position, however, in turning points of the motion (extremes) additional harmonic component of the motion can be clearly observed.

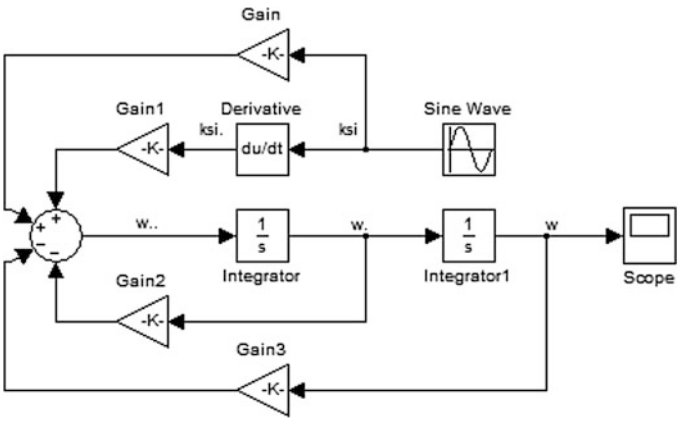

Fig. 7 Block diagram of single degree of freedom oscillator—general method

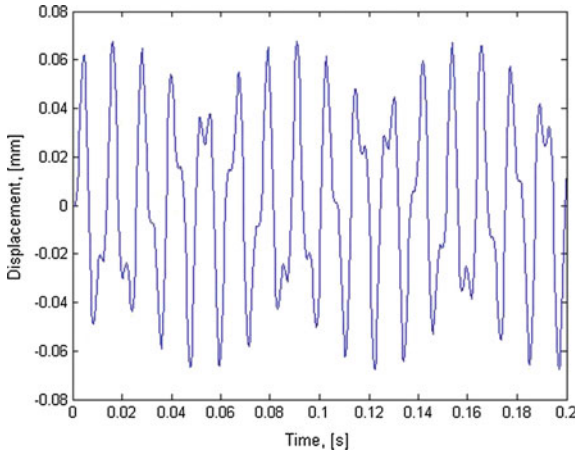

Fig. 8 Time waveform of the model test system operation (single degree of freedom)

5.2 Dynamic Simulation of Two Degrees of Freedom System

The system was also simulated using two degrees of freedom system model in accordance with (48)

$$\begin{cases} \ddot{w}_k\left(m(1+bF)^2+J_{yc}F^2\right)+\left(k_g+k_sF^2\right)\cdot w_k+ \\ \left(c_g+c_sF^2\right)\dot{w}_k++\left(mb(1+bF)+J_{yc}F\right)\ddot{\psi} \\ +\ k_sF\psi+c_sF\dot{\psi}=k_g\xi+c_g\xi \\ \\ \ddot{w}_k\left(m(1+bF)+J_{yc}F\right)+(k_sF)\cdot w_k+(c_sF)\dot{w}_k+ \\ \left(mb^2+J_{yc}\right)\ddot{\psi}\ +k_s\psi+c_s\dot{\psi}=0 \end{cases} \tag{48}$$

The above equation should be arranged according to the highest derivative (49), so it would be possible to form adequate block diagram for the simulation. The system of equations for the two degrees of freedom system is

$$\begin{cases} \ddot{w}_k=-\frac{\left(c_g+c_sF^2\right)}{\left(m(1+bF)^2+J_{yc}F^2\right)}\cdot\dot{w}_k-\frac{\left(k_g+k_sF^2\right)}{\left(m(1+bF)^2+J_{yc}F^2\right)}\cdot w_k- \\ -\frac{\left(mb(1+bF)+J_{yc}F\right)}{\left(m(1+bF)^2+J_{yc}F^2\right)}\cdot\ddot{\psi}- \\ \frac{c_sF}{\left(m(1+bF)^2+J_{yc}F^2\right)}\cdot\dot{\psi}-\frac{k_sF}{\left(m(1+bF)^2+J_{yc}F^2\right)}\cdot\psi \\ +\frac{c_g}{\left(m(1+bF)^2+J_{yc}F^2\right)}\cdot\xi+\frac{k_g}{\left(m(1+bF)^2+J_{yc}F^2\right)}\cdot\xi \\ \ddot{\psi}=-\frac{c_s}{\left(mb^2+J_{yc}\right)}\cdot\dot{\psi}-\frac{k_s}{\left(mb^2+J_{yc}\right)}\cdot\psi- \\ \frac{\left(m(1+bF)+J_{yc}F\right)}{\left(mb^2+J_{yc}\right)}\cdot\ddot{w}_k-\frac{(c_sF)}{\left(mb^2+J_{yc}\right)}\cdot\dot{w}_k \\ -\frac{(k_sF)}{\left(mb^2+J_{yc}\right)}\cdot w_k \end{cases} \tag{49}$$

Based on the general method for modelling differential equations, the block diagram is presented in Fig. 9.

Analogously as in the block system of single degree of freedom system, amplification of signals in *gain*-type blocks were introduced in their corresponding quotients described by Eq. (49). Two degrees of freedom system model also considers the issue of system damping, which at this stage of the study equals to the value of zero. After designation of damping values by experiment, the values will be updated.

Test system performance modelled by Eq. (48) and described in the block diagram (Fig. 9) is presented by changes in waveforms of w_k and ψ coordinates in Figs. 10 and 11.

In order to exclude the possibility of error occurrence in the general model of the modelling differential Eq. (48), the differential equations of motion were modelled by operator method based on the Laplace's transform of an integral (Fig. 12).

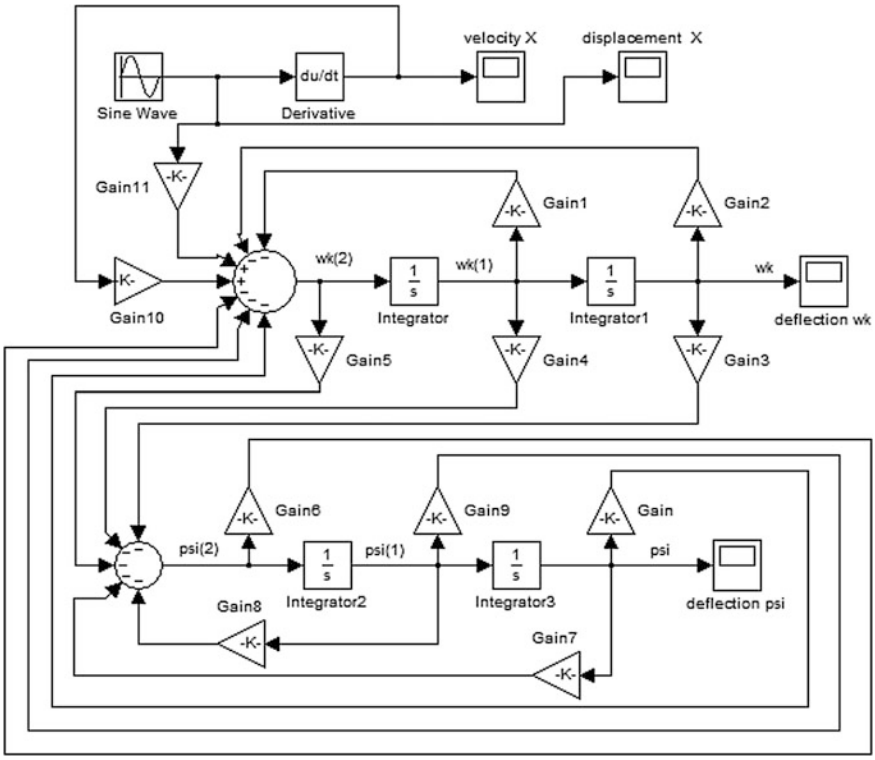

Fig. 9 Block diagram of a two degrees of freedom oscillator—general method

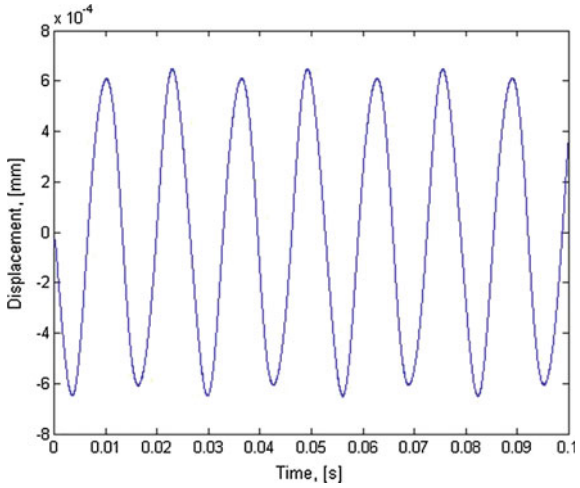

Fig. 10 Time waveform of the model test system operation—w_k coefficient

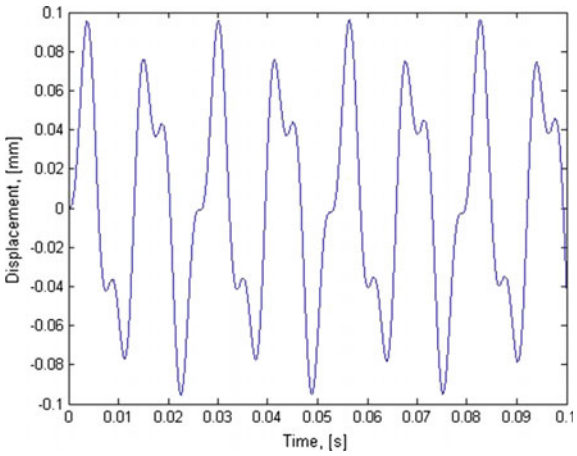

Fig. 11 Time waveform of the model test system operation—ψ coefficient

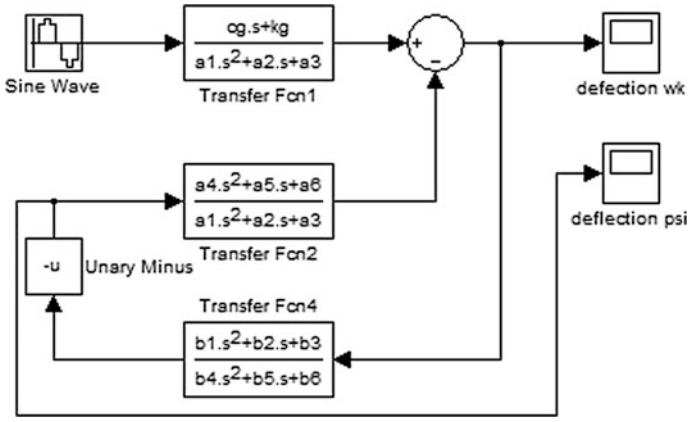

Fig. 12 Block diagram of two degrees of freedom vibration system—operational method

Into the block-based solution model, $a1 \ldots a6$ and $b1 \ldots b6$ variables were introduced that are numerators and denominators of quotients at derivatives of corresponding rows in the system of Eq. (49). Waveforms derived from the solution using this method are the same as results obtained using the general method (Figs. 10 and 11).

6 Modal Analysis of the Test System Using FEA

Test system should be analysed using finite element analysis (FEA) to test before experimental trials or analytical description is correct. With the help of appropriate computer software, modal analysis and simulation of dynamic simplified model of

the test system were carried out. For further analysis, kinematic extorsion in the form of displacement has been adopted.

Determination of the dynamic properties of the object, i.e. the form and frequency of vibrations, as well as a damping coefficient, is made by a modal analysis. FEA environments using CAD (Computer Aided Design) simulation are possible to identify the dynamic properties of the object. The test system (Fig. 2) subjected to modal analysis was simplified. In a simplified model, the bracket to force generator is omitted, because the withdrawal of degrees of freedom of the system can be accomplished using appropriate bindings. The model adopted in the simulation is shown in Fig. 13.

This model is tetrahedral finite elements (tetrahedral) of different magnitudes depending on the sensitivity in terms of the solution. It is natural that the finite element mesh is dense in the sample. The connector and loader with simple geometric shapes were adopted a grid with elements of the default size. Differentiation of finite elements is not critical in modal analysis, but its proper preparation for future dynamics simulation is important. Below are presented selected mode shapes and frequencies at which they occur (Fig. 14). The first and second modes occur at similar frequencies, due to the fact that the examined object is symmetrical about

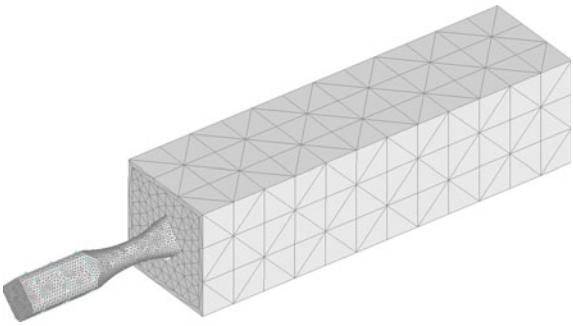

Fig. 13 Simplified model of the test system

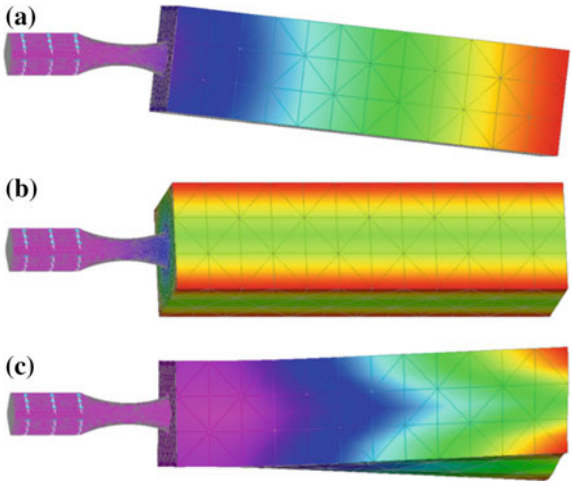

Fig. 14 Forms of natural vibrations at frequencies of: **a** 70.9 Hz, **b** 271.12 Hz and **c** 3336.67 Hz

two planes. Further, the third is in the form of rotation along the major axis of the system. For exemplary purposes additional mode was presented, the character of which is more complex and occurs at much higher frequency.

Determination of the resonance frequency, whose shape is compatible with the direction of the vector force kinematic, indicates that the operating range and the occurrence of dynamic located in the operating range of the electromagnetic inductor which is a force generator.

7 Attenuation in the Test System

The forces that depend on velocity are in oscillations referred to as drag forces. Their direction is opposite to the velocity. These forces cause the dissipation of energy which causes damping. The dependence of the resistance forces of the velocity is called damping characteristic. Determination of attenuation coefficients is crucial to achieve the correct analytical solutions and numerical, however, it is necessary to carry out the experiment and develop obtained results, respectively, because the sensitivity of analytical models, even small changes in these factors is significant for the solution.

The damped vibrations of a system can be registered during impulse output of the test system of the equilibrium position. Direct measurement of the amplitudes of displacement is not possible using acceleration sensors, built into the system under consideration. Double integrating the acceleration waveform provides information about the movement, however, it is decided to take advantage of changes in acceleration amplitudes that are directly recorded. This procedure is required to carry out mathematical proof, which would confirm the accuracy of the results. In addition, it is guaranteed that inaccuracies resulting from numerical integration do not affect the final outcome.

By assuming the characteristics of damping vibrations as (50)

$$x = Ae^{-\rho t}\sin(\omega t) \tag{50}$$

the first derivative, the characteristics of velocity can be described as (51),

$$\dot{x} = Ae^{-\rho t}(-\rho\sin(\omega t) + \omega\cos(\omega t)) \tag{51}$$

which after transformation can be written as (52)

$$\dot{x} = Ae^{-\rho t}\cdot\sqrt{\rho^2+\omega^2}\cdot\sin(\omega t + \psi) \tag{52}$$

because

$$\begin{aligned} -\rho &= B\cos\psi \\ \omega &= B\sin\psi \\ \frac{\omega}{-\rho} &= tg\psi \end{aligned} \tag{53}$$

and

$$\begin{aligned} B^2 &= \rho^2 + \omega^2 \\ B &= \sqrt{\rho^2 + \omega^2} \end{aligned} \tag{54}$$

Thus, the phase shift ψ can be expressed as (55)

$$\psi = \arctan\frac{\omega}{-\rho} \tag{55}$$

In this form of characteristics, the second derivative has the form (56):

$$\begin{aligned} \ddot{x} = {} & A\sqrt{\rho^2+\omega^2}e^{-\rho t}\cdot(-\rho)\sin(\omega t+\psi) \\ & + A\sqrt{\rho^2+\omega^2}e^{-\rho t}\cdot\omega\cos(\omega t+\psi) \end{aligned} \tag{56}$$

And after simplification (57)

$$\ddot{x} = A\sqrt{\rho^2+\omega^2}e^{-\rho t}((-\rho)\sin(\omega t+\psi)+\omega\cos(\omega t+\psi)) \tag{57}$$

By implementing analogous mathematical transformation, the form of the second derivative, the displacement amplitude as a function of time is (58):

$$\ddot{x} = A\cdot\left(\rho^2+\omega^2\right)e^{-\rho t}\sin(\omega t+\psi+\delta) \tag{58}$$

Thus, the amplitude of acceleration for subsequent maximum deviations takes the form of (59)

$$\begin{aligned} A_1(t_1) &= A\left(\rho^2+\omega^2\right)\cdot e^{-\rho t_1}\cdot 1 \\ A_2(t_1+T) &= A\left(\rho^2+\omega^2\right)\cdot e^{-\rho(t_1+T)}\cdot 1, \end{aligned} \tag{59}$$

where

$$\sin(\omega t_1+\psi+\delta) = 1 \tag{60}$$

Thus, the logarithmic decrement of attenuation takes the form of (62)

$$D = \ln \frac{A_1}{A_2} = \ln \frac{A(\rho^2 + \omega^2) \cdot e^{-\rho t_1}}{A(\rho^2 + \omega^2) \cdot e^{-\rho(t_1 + T)}} \tag{61}$$

$$D = \ln \frac{Ae^{-\rho t_1}}{Ae^{-\rho(t_1 + T)}} \tag{62}$$

The derived dependence (62) is similar to the relationship based on system displacement amplitude of damped-free vibrations. Thus, it is possible to use amplitudes of acceleration to describe the system damping.

8 Discussion of Results

Numerical and experimental data obtained by means of analytical solutions allow to understand the phenomena occurring in oscillating test system being applicable in laboratory practice. The system shown in Fig. 2 can be presented in block diagram, as shown in Fig. 15:

Test system uses electromagnetic exciters as a source of extortion and measuring and control system developed for the position of using LabVIEW. Information on the selected parameters load, such as the type of signal that forces the frequency and amplitude and the level of amplification are selected from the graphical user interface of the control system.

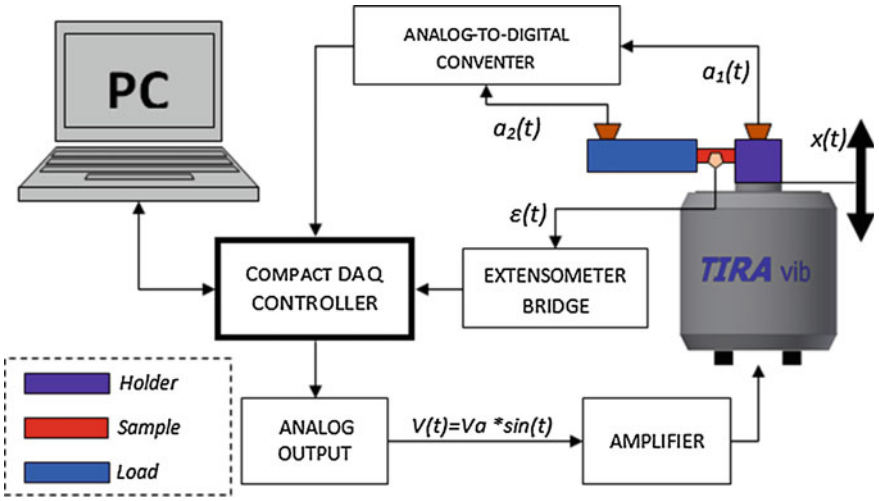

Fig. 15 Test stand diagram

Then, as defined signal is transmitted to the controller cDAQ in the form of a voltage, signal is sent to the driver amplifier TIRAvib TV 51 144 actuator that gives a signal. Recorded signals using accelerometers placed on the test system, and an optional strain gauge placed on the specimen after proper treatment are transferred by cDAQ driver to control and measurement software, where the acquisition of the waveform takes place.

Described test system was modelled using differential equations of motion, the finite element method and experimental as presented in this study. The results of the analyses must be discussed and verified. Impact of the attenuation coefficients on the operation of the system is illustrated in Fig. 16.

The waveform of changes in the amplitude of deflection from the equilibrium position described analytically is very sensitive to the damping parameter. A small change in this parameter significantly affects the character of the course trowel. Change in the parameter c_s significantly affects the course of changes in generalized coordinates. The amplitude of oscillation at non-zero attenuation starts to stabilize after the first few deflections. By changing the value c_g stabilization effect of the time course is being obtained. The system is far less sensitive to change in the value of the attenuation coefficient c_g than it was in the case of c_s coefficient. Determination of a substitute damping factor requires additional experimental verification, which will be the subject of further studies.

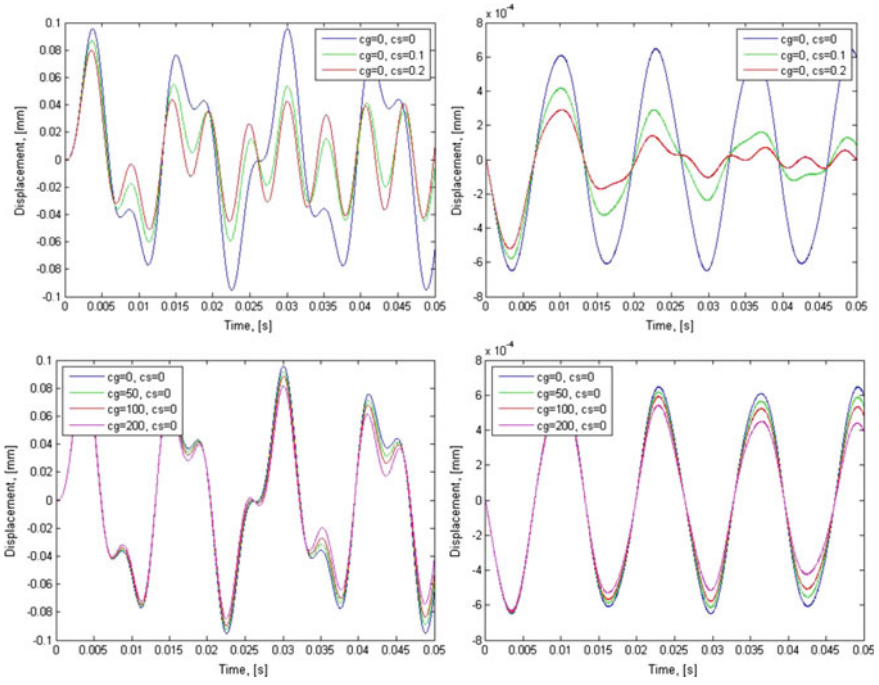

Fig. 16 The impact of changes in c_s and c_g attenuation coefficients on operating of the test system

Registered experimentally, acceleration signal in the axis of excitation indicates that the system stabilizes its operation immediately after the start-up. On the road the signal processing acceleration is recorded and velocity amplitude displacement of the test system is determined (Fig. 17). Knowing the amplitude of displacement, it is possible to carry out a dynamic analysis using the finite element method (FEM) to enable estimation of the stress generated in the operation section of the test piece. For the purposes of simulation, the waveform of acceleration was simplified to a sine wave with an amplitude of 0.3 mm, while the other signal parameters are unchangeable.

Dynamic analysis using FEA software was carried out without taking into account the damping factor, because it requires careful preparation and conducts an experiment by pulsed force a dynamic and appropriate registration and further signal processing system dynamic response. This problem is already being implemented.

By applying the FEM, the course of changes in the amplitude of free-end displacement was obtained in respect to the waveform forcing the test piece, as presented in Fig. 18.

The model used in modal analysis was adapted for the analysis of system time response under the influence of kinematic extortion. For this purpose, it was necessary to abandon all of the relevant degrees of freedom that exclude faults of the model in the restricted area. Extortion is defined as a function of the displacement, variable in time, synonymous with the function used in block models of differential equations.

$$x_{(t)} = A \cdot \sin \omega t \tag{63}$$

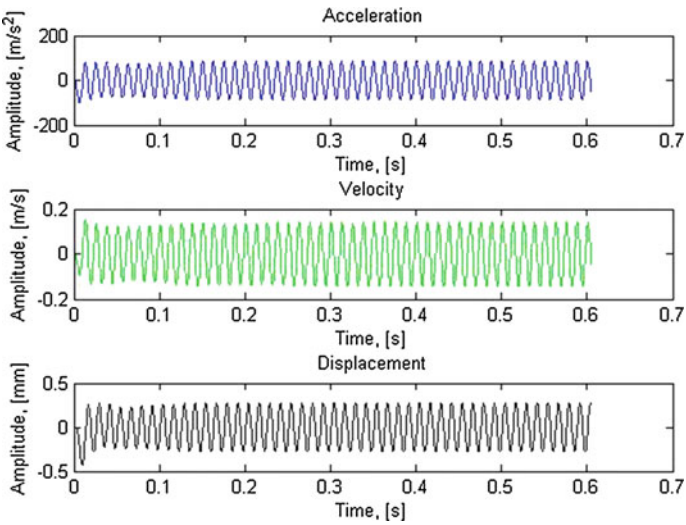

Fig. 17 Recorded changes in acceleration amplitudes and designated amplitudes of velocity and displacement

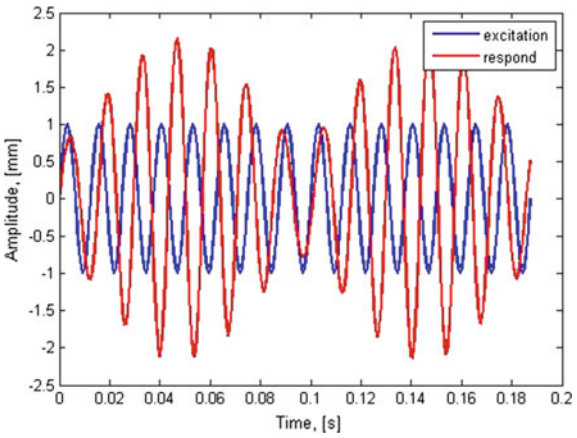

Fig. 18 Excitation and respond of numerical model of the test system

The correct interpretation of the results obtained is an important aspect of numerical analysis, which aims to show the authenticity of the mathematical model of solution in the context of values of the derived stresses in the test material.

9 Findings

By comparing the results obtained experimentally to the analytical one, the attention should be particularly paid to the mathematical description of the phenomena. The model test system which takes into account one degree of freedom can be used in a simplified model, however, the use of a model based on two generalized coordinates was adopted as an output. This is confirmed by the results simulation (Matlab/Simulink) as obtained amplitude deflections in the model by 1 degree of freedom are significantly lower than the registered experimentally. The two degrees of freedom model indicates a much better correlation with experimental results. The analytically derived amplitude of deflection for $c_g, c_s = 0$ gives a good approximation to the experimental values of $A_{exp} = 0.3$ mm, $A_{anl} = 0.49$ mm. Whereas, at non-zero values of attenuation coefficients, the correlation of results is even better.

The performed modal analysis (FEA) of the simplified system indicated the presence of the first system free mode in the form of deflation in line with the direction of excitation at the frequency of 70.9 Hz, the value of which is close to the value derived experimentally (78 Hz). Modal identification was carried out by swept-sine method based on excitation of the system with signal of increasing higher frequency (linear gain) and registration of deflection amplitudes.

Performance limitations of the electromagnetic exciter can cause decrease of the frequency at which there is the highest signal gain. This problem requires further experimental verification on a device with a higher power.

Particular attention should be given to proper and precisely accurate identification of the system's damping coefficient values to revise the mathematical model based on the registered corresponding acceleration signals.

The Project was financed from a Grant by National Science Centre (Decision No. DEC-2012/05/B/ST8/02520).

References

1. Lalanne, C.: Basic mechanics. In: Sinusoidal Vibration, ISTE, pp. 31–83 (2009)
2. Lalanne, C.: Swept sine. In: Sinusoidal Vibration, ISTE, pp. 273–298 (2009)
3. Owsiński, R., Niesłony, A.: Review of current state of knowledge on durability tests performed on electromagnetic shakers. Model. Eng. **53**(22), 117–123
4. Niesłony, A., Kurek, A., el Dsoki, C., Kaufmann, H.: A study of compatibility between two classical fatigue curve models based on some selected structural materials. Int. J. Fatigue **39**, 88–94 (2012)
5. Bannantine, J.A., Socie, D.F.: A variable amplitude multiaxial fatigue life prediction methods. In: ICBMFF3 (2013)
6. Karolczuk, A., Macha, E.: A review of critical plane orientations in multiaxial fatigue failure criteria of metallic materials. Int. J. Fract. **134**(3–4), 267–304 (2005)
7. Lieb, K., Horstman, R., Peters, K., Enright, C., Meltzer, R., Bruce Vieth, M., Garud, Y.: Multiaxial fatigue: a survey of the state of the art. J. Test. Eval. **9**(3), 165 (1981)
8. Papadopoulos, V., Davoli, P., Gorla, C., Filippini, M., Bernasconi, A.: A comparative study of multiaxial high-cycle fatigue criteria for metals. Int. J. Fatigue **19**(3), 219–235 (1997)
9. Macha, E. (ed.): Generalization of Strain Criteria of Multiaxial Cyclic Fatigue to Random Loading. VDI Verlag, Düsseldorf (1988)
10. Łagoda, T.: Energy models for fatigue life estimation under uniaxial random loading. Part I: the model elaboration. Int. J. Fatigue **23**(6), 467–480 (2001)
11. Karolczuk, A., Macha, E.: Selection of the critical plane orientation in two-parameter multiaxial fatigue failure criterion under combined bending and torsion. Eng. Fract. Mech. **75** (3–4), 389–403 (2008)
12. Łagoda, T., Macha, E., Będkowski, W.: A critical plane approach based on energy concepts: application to biaxial random tension-compression high-cycle fatigue regime. Int. J. Fatigue **21** (5), 431–443 (1999)
13. Macha, E., Niesłony, A.: Critical plane fatigue life models of materials and structures under multiaxial stationary random loading: the state-of-the-art in Opole Research Centre CESTI and directions of future activities. Int. J. Fatigue **39**, 95–102 (2012)
14. Walat, K., Kurek, M., Ogonowski, P., Łagoda, T.: The multiaxial random fatigue criteria based on strain and energy damage parameters on the critical plane for the low-cycle range. Int. J. Fatigue **37**, 100–111 (2012)
15. Nieslony, A., Macha, E.: Spectral Method in Multiaxial Random Fatigue. Springer (2007)
16. Niesłony, A., Růžička, M., Papuga, J., Hodr, A., Balda, M., Svoboda, J.: Fatigue life prediction for broad-band multiaxial loading with various PSD curve shapes. Int. J. Fatigue **44**, 74–88 (2012)
17. Halfpenny, A.: A frequency domain approach for fatigue life estimation from finite element analysis. Key Eng. Mater. **167–168**, 401–410 (1999)

Assessment of Modal Parameters of a Building Structure Model

Przemysław Palenica, Bartosz Powałka and Rafał Grzejda

Abstract This paper relates to the field of vibrations of contemporary building structures. The aim of this study is to develop methods to estimate the safety of use of buildings subjected to dynamic loads. Calculations are carried out based on selected computational models of the column-beam-plate system used at the design stage of monolithic building structures. For modeling, the finite element method (FEM) is used. The results of calculations are compared with laboratory tests of the special model mapping of a building structure.

1 Introduction

With respect to building structures, assessment of the modal parameters can be performed on the basis of experimental modal analysis [1, 3, 4, 7, 8] or numerical modeling using the finite element method [2, 10, 11]. In both cases, modal analysis is mainly applied for identification of modal shapes and natural frequencies.

One of the types of the structure currently used in the modern civil construction is the column-beam-plate system (Fig. 1). During creating a new one or remodeling an existing one of such structure [12], it is common to take into account a number of criteria optimization. One of them relates to the optimization due to the material consumption [6, 9]. Thanks to it, it is possible to gain a certain compromise between the safe structure and the structure generating manufacturing costs at an acceptable level.

P. Palenica · B. Powałka · R. Grzejda (✉)
Faculty of Mechanical Engineering and Mechatronics,
West Pomeranian University of Technology, Szczecin, Poland
e-mail: rafal.grzejda@zut.edu.pl

P. Palenica
e-mail: pepal@wp.pl

B. Powałka
e-mail: bartosz.powalka@zut.edu.pl

J. Awrejcewicz (ed.), *Dynamical Systems: Modelling*, Springer Proceedings
in Mathematics & Statistics 181, DOI 10.1007/978-3-319-42402-6_25

Fig. 1 Examples of the column-beam-plate system: **a** car park, **b** storage hall, **c** building

Designing an optimal structure at a given criterion of material consumption, loaded by static forces applied in specific, unchanging locations and having specific, constant directions, and values is a relatively simple task. However, in the case of the building structure loaded by forces changing in time and having variable locations, directions, and values, the optimization becomes a complex task, which may have more than one valid solution.

One of the common cases solved by structural engineers is to adjust the existing building structure for the new user needs. To make this happen, first thing to do is determining a set of loads imposed on the structure. Basing on Eurocode standards it is rather easy to increase its strength, size, etc. During this process, usually only static analyses are provided. However, there can appear circumstances where machines or cars are to be located on the structure. All of such devices causes dynamic effects which cannot be ignored. Therefore, it is recommended to predict the vibration response of the structure which is performed using computer simulations [13]. After such computations, the structure can be properly adjusted.

Activities described in this paper are a part of research on development of methods of safety assessment of building structures subjected to dynamic loads. The aim of the work is to perform both modal analysis of the sample column-beam-plate system using selected FEM-models with varying degrees of simplification and assessment of the similarity of modal shapes and corresponding natural frequencies. All analyses were carried out using the Midas NFX 2014 program. Results obtained numerically were compared with results of laboratory tests.

2 Object of Research and Its Numerical Models

The object of research is the column-beam-plate system model shown in Fig. 2.

The tested structure is build from the plate resting on the frame formed by the beams and supported by four column situated on the rigid foundation. For such a structure the following two numerical models are prepared:

Fig. 2 Physical model of the adopted column-beam-plate system

- model A—the simplified model, in which the elastic flexibility of structural nodes is not taken into account (Fig. 3a),
- model B—the advanced model, in which the elastic flexibility of structural nodes is taken into consideration (Fig. 3b).

In practice, modeling of column-beam-plate systems is frequently carried out using simplified models (similar to the model A), in which one introduces substitute spring properties of the nodes (Fig. 4b). Some novelty is modeling of such systems taking into account the structural joints (Fig. 4c). In the case of the model B, the following types of connections are considered:

- bolted joints between the columns and the frame formed by the beams, built with use of the rigid body bolt model [5], consisted of the flexible plain part of the bolt and the rigid head of the bolt,

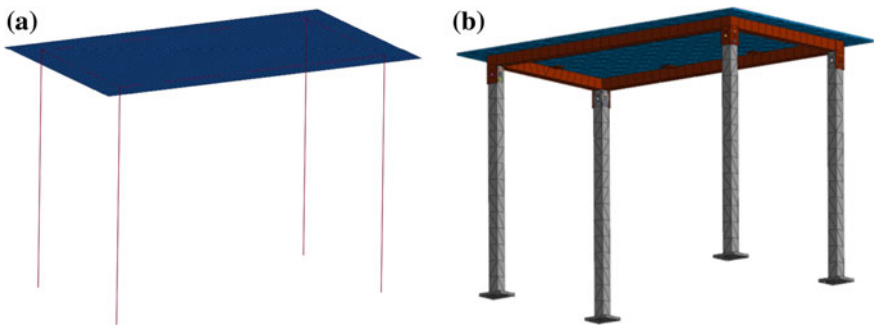

Fig. 3 FEM-models of the adopted column-beam-plate system: **a** model A, **b** model B

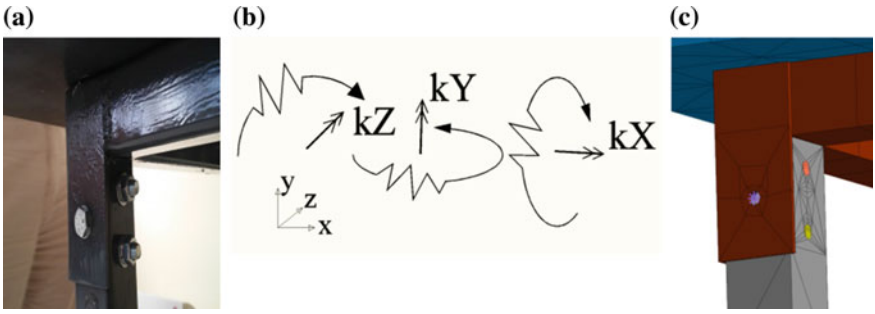

Fig. 4 Modeling of the column-beam-plate system: **a** real system, **b** modeling of substitute stiffness, **c** fragment of the type B of the FEM-model

- bolted joints between the frame formed by the beams and the plate, replaced by the welded type of the contact joint,
- contact connections between the columns and the frame formed by the beams, modeled using the bidirectional sliding type of the contact joint.

3 Analysis of Research Results

Modal shapes received, respectively, for the adopted FEM-models are shown in Figs. 5 and 6. The corresponding values of the natural frequency are specified in Table 1.

Comparing the values of the natural frequency achieved numerically, it can be concluded that in the case of the model A, they are lower than in the case of the model B by 17.3–21.4 %. This is related to more detailed representation of the

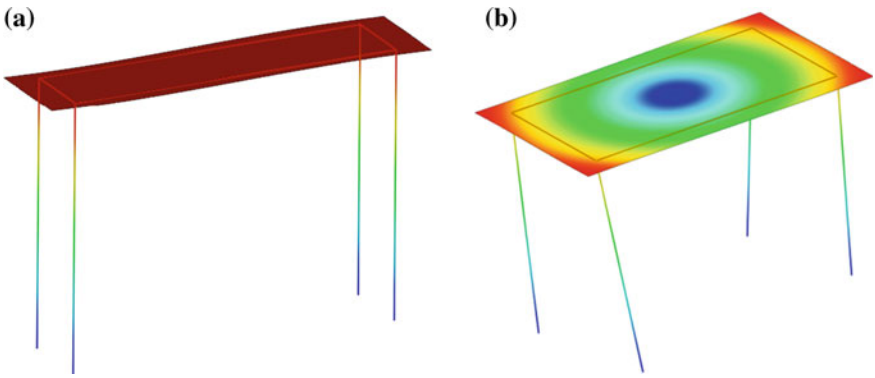

Fig. 5 Modal shapes obtained in the case of the model A of the column-beam-plate system: **a** for mode No. 1, **b** for mode No. 2

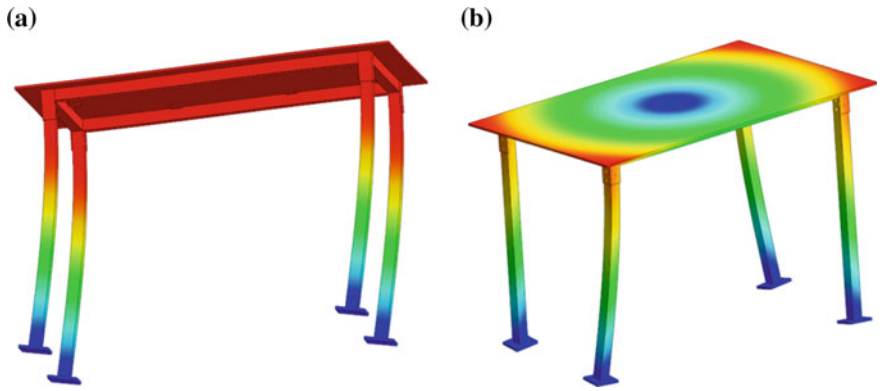

Fig. 6 Modal shapes obtained in the case of the model B of the column-beam-plate system: **a** for mode No. 1, **b** for mode No. 2

Table 1 Natural frequencies obtained for adopted models of the column-beam-plate system

Results source	Natural frequencies (Hz)	
	Mode No. 1	Mode No. 2
Model A	9.01	13.13
Model B	11.46	15.87
Experiment	10.96	15.79

model B, which reflects the real geometry of nodes occurred in the tested structure and introduces additional stiffness to the system. In contrast, the corresponding modal shapes for both models are similar.

Results of numerical investigations were compared with results of the laboratory tests on the stand, a fragment of which is shown in Fig. 7. On the basis of this summation, the following conclusions can be noted:

1. Applying traditional models of column-beam-plate systems can lead to underestimation of natural frequency values up to 18 % in relation to their real values.

Fig. 7 View of the test stand

2. Taking into account the elastic flexibility of structural nodes between elements of the system and occurrence of the bolted joints in the system can receive better accuracy of the results. Natural frequency values are then overstated by about 5 % in comparison to their real values.

4 Summary

In the paper, a new approach to modeling of column-beam-plate systems is proposed. It is based on the consideration in the process of modeling the real structure nodes occurring in this types of systems, which are the bolted joints and the contact joints. Due to this complement, it is possible to obtain numerical modal test results close to their experimental results. This particularly applies to designation of the natural frequency values.

In the case of analysis of modal shapes of column-beam-plate systems, the assessment can be conducted also with use of traditional (simplified) models. Their use ensures results that are comparable to results obtained with more advanced models.

In the next step of the research, it is planned to perform similar tests in order to assess the behaviour of the models in a wider range of frequencies. The aim of this research will be substantive evaluation of the suitability of the developed models to modal analysis of arbitrary column-beam-plate systems.

References

1. Alvin, K.F., Robertson, A.N., Reich, G.W., Park, K.C.: Structural system identification: from reality to models. Comput. Struct. **81**(12), 1149–1176 (2003)
2. Butt, F., Omenzetter, P.: Seismic response trends evaluation and finite element model calibration of an instrumented RC building considering soil-structure interaction and non-structural components. Eng. Struct. **65**, 111–123 (2014)
3. Davis, A.G.: The nondestructive impulse response test in North America: 1985–2001. NDT&E Int. **36**(4), 185–193 (2003)
4. Dziedziech, K., Staszewski, W.J., Basu, B., Uhl, T.: Wavelet-based detection of abrupt changes in natural frequencies of time-variant systems. Mech. Syst. Signal Process. **64–65**, 347–359 (2015)
5. Grzejda, R.: Modelling of bolts in multi-bolted connections using MIDAS NFX. Tech. Sci. **18** (1), 61–68 (2015)
6. Kripka, M., Medeiros, G.F., Lemonge, A.C.C.: Use of optimization for automatic grouping of beam cross-section dimensions in reinforced concrete building structures. Eng. Struct. **99**, 311–318 (2015)
7. Lang, Z.Q., Park, G., Farrar, C.R., Todd, M.D., Mao, Z., Zhao, L., Worden, K.: Transmissibility of non-linear output frequency response functions with application in detection and location of damage in MDOF structural systems. Int. J. Non-Linear Mech. **46**(6), 841–853 (2011)

8. Matta, E., De Stefano, A.: Seismic performance of pendulum and translational roof-garden TMDs. Mech. Syst. Signal Process. **23**(3), 908–921 (2009)
9. Miller, D., Doh, J.-H., Mulvey, M.: Concrete slab comparison and embodied energy optimization for alternate design and construction techniques. Constr. Build. Mater. **80**, 329–338 (2015)
10. Osmancikli, G., Bayraktar, A., Türker, T., Uçak, Ş., Mosallam, A.: Finite element model calibration of precast structures using ambient vibrations. Constr. Build. Mater. **93**, 10–21 (2015)
11. Türker, T., Bayraktar, A.: Finite element model calibration of steel frame buildings with and without brace. J. Constr. Steel Res. **90**, 164–173 (2013)
12. Varum, H., Pinto, A., Costa, A., Vila Real, P.: Simplified models for assessment and optimal redesign of irregular planar frames. Eng. Struct. **42**, 245–257 (2012)
13. Wang, S.-J., Chang, K-Ch., Hwang, J.-S., Hsiao, J.-Y., Lee, B.-H., Hung, Y-Ch.: Dynamic behavior of a building structure tested with base and mid-story isolation systems. Eng. Struct. **42**, 420–433 (2012)

Simplified Model of City Bus Dynamics as a Tool of an Energy Consumption Estimation

Tomasz Pałczyński

Abstract This paper presents a model of city bus dynamics as a tool of energy consumption estimation. This tool can provide preliminary parameters which enable estimation of transient states of the main elements of energy flow, especially the ones which are possible to be recovered (exhaust, cooling and brakes). The introduction describes the current state of affairs in simplified models of city bus dynamics. A concept of easy-to-use procedure of acquiring a real driving cycle as a velocity at time domain is presented. By combining this information with city bus dynamics model it is possible to build a model of this system in Matlab/Simulink environment. The influence of the main assumed parameters on accuracy of estimated parameters has been considered here. Measured average fuel consumption and producer data (maximum vehicle speed, time of acceleration) was used as the reference parameter. Then a procedure of tuning the simulation model according to the reference parameters is explained. In the following chapter there were presented simulation results based on real measurements of Lodz city traffic parameters and main groups of the city bus energy consumption possible to be recovered have been estimated.

1 Introduction

Energy consumption is a significant parameter of present-day means of transport, especially city buses. Considerable part of the energy supplied to IC engine is wasted as heat via coolant (30 %) and exhaust (40 %) systems [1–3]. Approximately 70 % of heat is irrevocably wasted. There is a similarity between the mentioned loses of engine energy and the energy generated by braking system during normal city driving cycle. City buses' producers had to take into consideration global energy flow balance during vehicle operation. The factor which

T. Pałczyński (✉)
Lodz University of Technology/Institute of Turbomachinery,
219/223 Wolczanska Street, 90-924 Lodz, Poland
e-mail: tomasz.palczynski@p.lodz.pl

J. Awrejcewicz (ed.), *Dynamical Systems: Modelling*, Springer Proceedings
in Mathematics & Statistics 181, DOI 10.1007/978-3-319-42402-6_26

mostly affects energy consumption is vehicle dynamics, which is determined by the driving cycle, especially in case of city buses, according to traffic and bus stops [4, 5]. Therefore knowing transient states of the analysed vehicle as accurately as possible is crucial for conscious operation of such a means of transport. GPS technology has created new possibilities for vehicle dynamic reconstruction because of their availability and accuracy [6–8]. Thanks to that, it is possible to acquire real city driving data which consist of actual vehicle position (speed and acceleration can be calculated) at the time domain. The measured data is used to set vehicle position, and energy consumption parameters are estimated for this purpose. On the other hand, it is easy to construct quite a simple model of vehicle dynamics at the Matlab/Simulink environment which can estimate the above-mentioned quantities of wasted heat. Finally, an application of system based on Organic Rankine Cycle for the recovery of indicated waste heat has been proposed. The research was carried out as a part of Maciej Idowski BSc degree engineering project and Łukasz Michalski MSc degree project, with the consent of MPK Łódź city transport company.

2 Conception of the Numeric Model

Numerical model of City Bus Dynamics (CBD) can be defined as a mechatronic system because it contains mechanically and thermodynamically coupled units with feedback control system. The model below presents the flow of information by means of signals linked to steering systems; the flow of mechanical power between the engine, gearbox and the identified vehicle, mainly by mass in forward motion. The main idea of the model was based on procedure of presented at [9, 10].

The main idea of the model presented in this article was described in the introduction, and can be summed up as follows:

- Downloading measurement data collected via GPS as a V_{set} as a simulation time function;
- Comparison with actual value of vehicle velocity, estimation of control error;
- Selection of Driving mode on the basis value of set acceleration calculated as a derivate of the set velocity. Driving mode is selected between acceleration and braking. Driving mode block also transports control error defined as a difference between actual and set vehicle velocity $e_V = V_{\text{set}} - V_{\text{actual}}$;
- Powertrain control block is a control loop feedback mechanism. It consists of three independent feedback loops dedicated to control degrees of engine load and braking. Powertrain control blocks also realize shift logic based on shifting lines whose switches required gear ratio i_b;
- Engine block estimates engine torque as the function of engine load and their angular velocity including engine inertia. There we can find two ways of energy transport: mechanical (arrow dashed), thermodynamic (clear arrow), and signal transmission (solid line);

- Gear Box and Vehicle block estimates influence of automatically chosen gear ratio and movement resistances (rolling, inertia of the masses at linear and angular movement, aerodynamics).

3 Recording City Bus Movement Parameters in Real Life Conditions

The objects of the research were city buses, (Lodz line 86), going between two Lodz districts, Polesie (more specifically, between its two parts, Retkinia and Stare Polesie) and Śródmieście downtown district. The registered cycles comprised almost the whole route, from Maratońska St to Plac Dąbrowskiego terminal, and the way back in opposite direction. The choice of a bus route was made based on the following criteria:

- at least a part of the route is within the heart of the city centre (which is typical of most bus routes in Lodz city region);
- the route cannot run along streets where major roadwork is being carried out, as frequent traffic jams affect traffic flow and the measurement results;
- the route cannot run along streets with bus lanes (so-called 'buspasy') as they only constitute a fraction of the city bus routes.

'Logger GPS' mobile phone application was used to record measurements. It is an easy-to-use program which enables to register chosen movement parameters, such as latitude and longitude, elevation above sea level, GPS time and speed, as a GPS trace which is saved in the mobile phone memory. One of the advantages of this kind of Logger device is its power independence, as opposed to other devices, for instance car navigation which has a very short built-in battery time and thus would require extra charging for the research purposes. The chosen application runs on mobile phone battery and makes it possible to carry out measurements for up to several hours without extra charging. Another reason why Logger system was selected is the possibility of choosing sampling rate 1 Hz. The selected Logger records a GPS trace in the well-known GPX format, which makes processing easier.

Additionally, it has been decided that given routes recordings will take place at various times of the day and days of the week, so that they reflect a range of traffic situations. Therefore research was carried out between Monday and Friday, except for rush hour peak (because of traffic jams), from Monday to Friday at rush hour peak, and at weekends (Saturday and Sunday, regardless of the time of the day).

4 Simulink Model of the CBD

According to the concept of the CBD presented above a Simulnik model shown in Fig. 1 was built in Matlab R2014a environment, license number: 290564, Fig. 2.

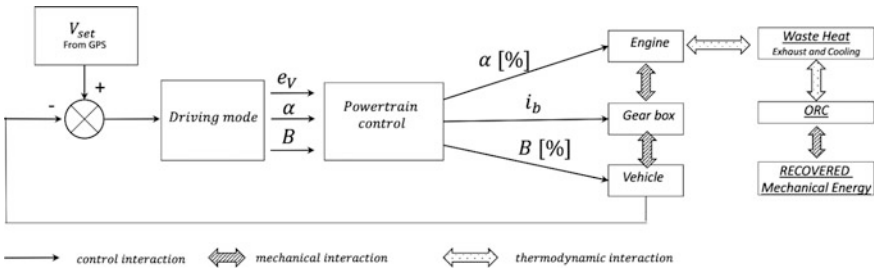

Fig. 1 Model of city bus dynamics

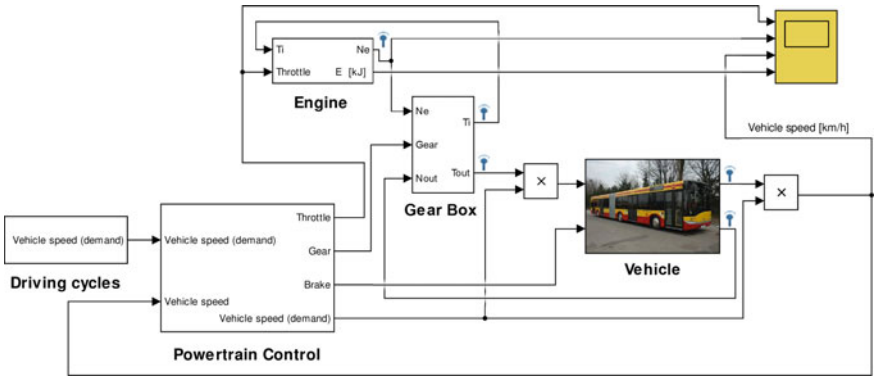

Fig. 2 Simulink model of the city bus powertrain

The proposed model was based on tutorial model, the so-called Modelling an Automatic Transmission Controller [11]. This model consists of six equations, which define: engine dynamics, vehicle dynamics and the other four describe how the powertrain's elements transmit power between one another.

Solaris Urbino 18 Bus is equipped with DAF PR228 engine with maximum power of 231 kW and maximum torque of 1300 Nm available at CAV 115–178 rad/s. Curb weight of the bus is 16000 kg and GVWR is 28000 kg (for further calculations, it has been assumed that the maximum mass of vehicle is 22 000 kg, which accounts for 79 % of maximum weight) [12].

Main gear ratio is 6.2 and gear ratios for subsequent gears of automatic gearbox are, respectively: 3.43; 2.01; 1.42; 1.00; 0.83. Universal engine torque characteristics T_e have been implemented to the model as a 3D map versus engine ω_e (rad/s) and engine load α (%). It is a quasi-statistic characteristics and therefore it has been extended with a dynamics model of the engine itself taking into account its inertia. Universal engine torque characteristics have been based on external characteristics of the engine assuming its linearity for fractional loads.

It has been assumed that the basic driving cycle of the research object is torque-determined motion, transferred from the engine to the driving wheel. In such

a case total indispensable energy expenditure, expressed with G_L (dm^3) product of supplied fuel and its caloric value W_d (kJ/dm^3) called total energy intensity, is defined by total energy consumption in motion and energy losses in engine and in powertrain.

$$G_L W_d = E + \Delta E_e + \Delta E_p, \tag{1}$$

where E (kJ)—energy consumption of motion, ΔE_e (kJ)—losses resulting from transforming energy in the engine, ΔE_p (kJ)—losses made during transmitting energy from engine to driving wheels.

$$G_L W_d = \frac{E}{\eta_p}, \tag{2}$$

where η_p—driving efficiency, which is a product of engine efficiency η_e and drivetrain efficiency η_t.

$$\eta_p = \eta_e \eta_t \tag{3}$$

The engine model was built based on '2D look at table', by downloading torque universal characteristic. Input values for his block are α and ω_e while output value is T_e.

$$I_e \dot{\omega}_e = T_e - T_1, \tag{4}$$

where I_e—engine moment of inertia ($kg \cdot m^2$), $\dot{\omega}_e$—angular engine acceleration (rad/s^2), T_e—engine torque (Nm), T_1—Torque at the pump of torque converter (Nm).

The torque converter was modelled based on two zero-dimensional characteristics: coefficient K and dynamic gear shift i_d (both via kinetic shift i_k). The following characteristics have been formulated based on criteria of selecting a torque converter as well as gear box producer data used in Voith Diwa D864.5 bus. The following equations show correlations between torque converter basic parameters:

$$T_1 = \frac{\omega_e^2}{K^2} \tag{5}$$

Dynamic gear ratio i_d is illustrated with the following equation:

$$i_d = \frac{T_2}{T_1}, \tag{6}$$

where T_1—is torque on input shaft torque converter (Nm), T_2—torque on output shaft torque converter (Nm). K factor and i_d are the function of an transmission ratio between input and output torque converter shafts.

Gear shifts are realized with gears which have the following effect on relations between input and output parameters:

$$T_{\text{out}} = i_{\text{gear box}} \cdot T_{\text{in}}, \tag{7}$$

where i_{gearbox}—gear box ratio, T_{in}—gear box input torque (Nm), T_{out}—gear box output ratio (Nm). Powertrain total gear, vehicle inertia as well as changes resistance affect vehicle dynamics as shown by the equation below:

$$I_v \dot{\omega}_{\text{wheel}} = i_{\text{total}}(T_e - T_{\text{load}}), \tag{8}$$

where I_v—is vehicle inertia with reduced mass ratio versus gear ($\text{kg} \cdot \text{m}^2$), $\dot{\omega}_{\text{wheel}}$—wheel angular acceleration (rad/s^2), i_{total}—drivetrain overall gear, T_{load}—vehicle load moment (Nm), which contains braking moment (which is a percentage of maximum braking force) and resistance: inertia which is reduced mass to forward motion, rolling resistance and aerodynamic resistance via vehicle speed squared as well as its aerodynamic parameters.

Fuel consumption G_L for distance L in movement forced by driving force F is:

$$G_L = \frac{1}{\eta_p W_d} \int_0^L F dx \tag{9}$$

while mileage fuel consumption Q (i.e. for a unit of the distance travelled) is illustrated with the following equation:

$$Q = \frac{E}{\eta_p W_d L} \tag{10}$$

5 Procedure of Tuning the Simplified Model of CBD

The proposed model has been tuned with the use of two independent tools to ensure its possibly high adequacy to real life conditions. The two tools are a method of setting in motion time and fuel consumption method. The author proposed to use a similar method in one of his papers [9, 10] as a part of the process of creating CVT drivetrain steering maps. Therefore it has been decided that the following parameters available in reference books or provided by the producer must be taken into account while working on the vehicle under analysis:

- Reduced masses ratio versus the subsequent gear shift changes cycle;
- Real vehicle inertia moment reduced to masses in forward motion;
- Simplified fuel consumption characteristic.

The gist of the two methods consists of the following procedure:

- Analysis, identification and selection of the model's key parameters in view of final results accuracy estimation. In this case, it has been decided that the parameter must be energy consumption in the analysed vehicle defined as in (2).
- Introducing a referential parameter (a real one) which will enable 'tuning the model to real life conditions'. In this case they are as follows:
  - Acceleration time from stopped start to velocities 16.6 and 22.2 m/s;
  - Average monthly mileage fuel consumption, which was, respectively: July 2013—54.77 $dm^3/100\,km$, August 2013—23.79 $dm^3/100\,km$;
  - Average mileage fuel consumption for a selected route from an on-board computer. For *C*2 route it was 54 $dm^3/100\,km$;
  - Registered movement trajectories in real-life conditions classified as *C*1–*C*6 routes.
- Multiparameter optimization with the use of Simulink Signal Constraint. Thanks to his device, a matrix of probable solutions can be searched obtaining specific values relevant to real life conditions.

Optimization process was performed in several stages.

Stage I.

Choice of drivetrain parameters

During the simulation procedure of setting the vehicle in motion to the speed of 16.6 and 22.2 m/s the parameters determining the object's dynamics were 'tuned'. During this test automatic regulation system α (%) and B (%) was disconnected. Constant $\alpha = 100$ %, was introduced, which was relevant to the maximum engine load while for the braking system 0 % constant was set, resulting in its deactivation in the simulation test. During the test the vehicle accelerated in 18 s to the speed of 60 km/h (as stated in the producer's data information), and then reached a maximum speed of 80 km/h and stayed at this speed as a constant. The outcome of the procedure provided carefully selected and adjusted simulation model parameters defining reduced masses ratio and reduced vehicle inertia. In this way the model was made more real as far as its dynamics are concerned.

Stage II.

Choice of Powertrain Control system parameters

In the proposed simulation model two PID regulators have been used (one for engine load degree regulation automatic system α (%) and braking power steering ratio B (%) in order to realize the downloaded driving cycle (*C*1–*C*6) as a parameter defined by a steering signal. In order to improve regulation quality it was necessary to perform value tuning of the six PID regulator parameters (three for each regulator). An indicator of regulation quality is maximum difference between set value and realized value, relevant to requirements for exhaust tests, i.e. below 5 % (1 m/s) maximum speed value was defined.

Stage III.

Choice of parameters related to fuel consumption

For this purpose a simplified characteristic was correlated with the following data: average monthly fuel consumption and mileage fuel consumption for *C*2 route.

6 Selected Results of Simulations

Based on the model presented above and a hybrid procedure of implementing research results in real life conditions, a number of tests related to further optimization of the created model have been carried out. Interest areas were: choice of a faster solver, more efficient time frame enabling fast and accurate calculations. As a result solver mode 45 and variable step have been selected, which enables making calculations for one route consisting of 3500 s real time test during a simulation lasting no longer than several minutes. Simulation tests have been carried out for all the six defined routes (*C*1–*C*6). Figure 3 presents example cycles of RMP changes, vehicle speed and estimated energy consumption (cycles and average ratio calculated from the start of the cycle) for first 200 s of cycle *C*2.

Figure 4 shows a 3D map of instantaneous energy consumption via engine speed and engine load. Dark spaces on the map are the individual simulation tests results for *C*3 route along its whole length. The map presents areas in which the engine runs most frequently during normal operation. It also makes it possible to use those

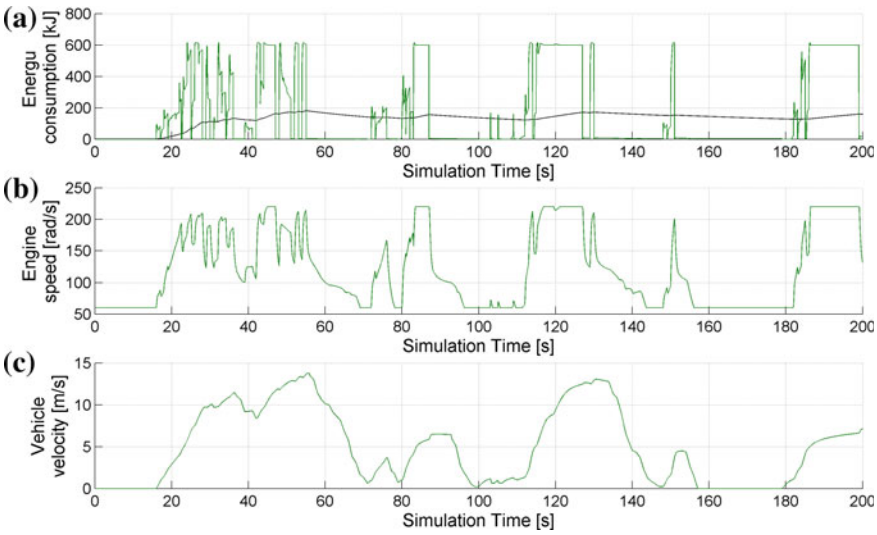

Fig. 3 **a** Energy consumption, **b** engine speed, **c** vehicle velocity

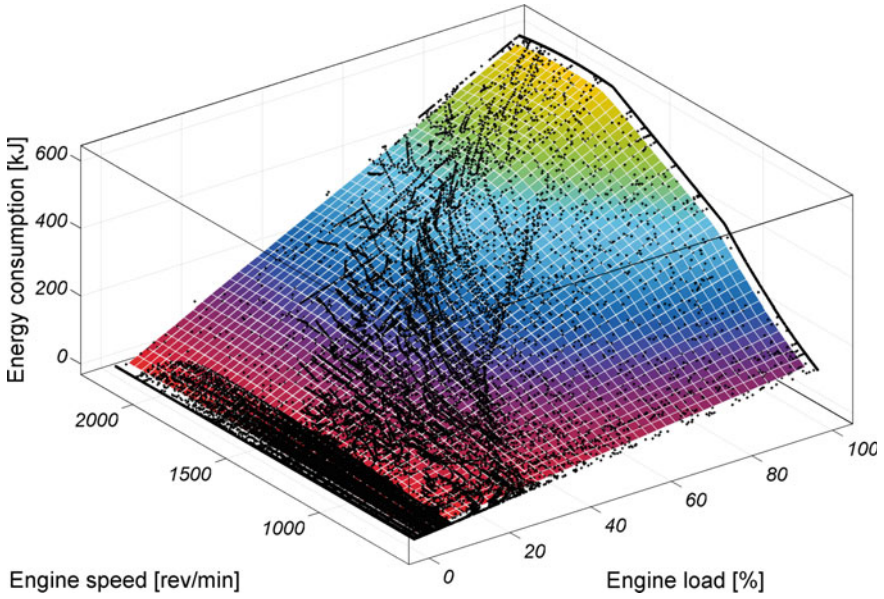

Fig. 4 Instantaneous city bus consumption via engine speed and engine load

results without the very time-consuming construction of a simulation model for estimating vehicle energy consumption.

6.1 An Energy Consumption Analysis of the City Bus Based on CBD Model

Simulation tests results have been divided into the following groups:

Group I

This group comprises bus cycles realized from Monday to Friday, with exception of the so-called rush hour. This group (cycles *C*2 and *C*6) reaches higher mileage energy consumption values due to higher traffic congestion levels, as compared to weekends. That, in turn, results in more frequent stops (apart from regular bus stops, which number is the same in each cycle) which result in extra fuel consumption due for setting the vehicle in motion again (initial acceleration phase).

Group II

This group comprises bus cycles realized from Monday to Friday, with exception of the so-called rush hour. This group (cycles *C*2 and *C*6) reaches higher mileage energy consumption values due to higher traffic congestion levels, as compared to weekends. That, in turn, results in more frequent stops (apart from regular bus stops, which number is the same in each cycle) which result in extra fuel consumption due for setting the vehicle in motion again (initial acceleration phase).

The final group (cycles *C*4 and *C*5) comprises only the rush hour cycles (mornings from 7 to 9 a.m. and afternoon from 3 to 5 p.m.) from Monday to Friday. Energy consumption for this group is the highest.

Table 1 illustrates estimated mileage energy provided at fuel consumption for individual cycles (for registered route). An analysis of all groups energy consumption proves that total energy consumption in cycles run from Monday to Friday with the exception of rush hour peak is approximately 25 % higher than in cycles run at weekends and approximately 16 % lower than in rush hour routes. Introducing dedicated bus lanes results in the fact that total energy consumption in rush hour cycles is up to approximately 55 % higher than at weekends, if they are not installed. It is also worth observing that the bus current fuel consumption can reach values up to over 600 kJ.

After the analysis of average energy consumption and fuel consumption in all above-mentioned groups, a route named Urban City Bus 86 Lodz operating Monday to Friday (except rush hour) was chosen as the most representative cycle for route 86 buses in Lodz city region. Two factors influenced the choice of the route. First, the chosen group, of the three accounts for the highest percentage of all cycles run during the whole week. Second, mileage energy consumption ratios and fuel consumption in this group are very close to averaged results between the two other groups (cycles registered at weekends and in rush hour compensate each other to a level marked as representative). Figure 5 shows the representative driving cycle Urban City Bus 86 Lodz.

Total energy intensity of a representative cycle is 84 kJ and falls into: motion energy intensity (27.7 kJ), cooling system losses (25.2 kJ), exhaust system losses (21 kJ) and other losses (10.1 kJ). The sum of cooling system losses and exhaust system losses is approximately 46 kJ while mileage fuel consumption is roughly 521/100 km.

6.2 *Example Calculation of ORC Waste Heat Recovery*

The Rankine cycle is a thermodynamic cycle which converts heat into work, where heat is supplied externally to a closed loop, which usually uses water as working

Table 1 Mileage energy provided at fuel consumption for individual cycles

Cycle nr	t (s)	L (km)	a_{aver} (m/s^2)	Average energy provided at fuel (kJ)/mileage energy provided at fuel (kJ/m)	Mileage fuel consumption (l/100 km)
*C*1	3274	16.5	0.57	70/21	48
*C*2	3066	16.9	0.60	92/30	54
*C*3	3172	17.5	0.55	62/20	49
*C*4	2919	18	0.64	105/36	60
*C*5	2941	17.3	0.62	99/34	58
*C*6	3019	16.8	0.59	84/28	52

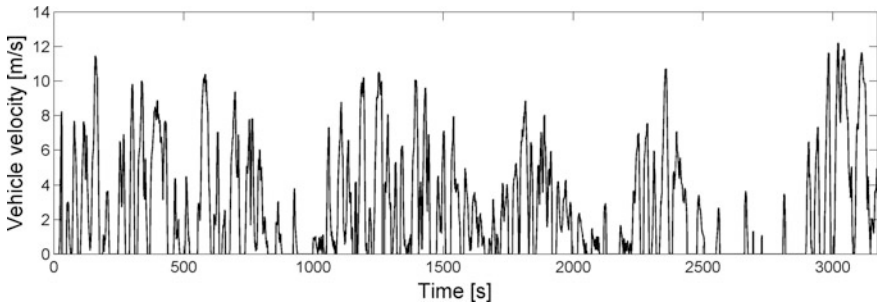

Fig. 5 Urban city bus 86 Lodz driving cycle

fluid. The organic Rankine cycle (ORC) is a Clausius–Rankine Cycle in which an organic working fluid is used instead of water, namely steam. In recent years it has become popular in energy production processes, due to the fact that it gives the possibility to use exhaust heat of low energy and temperature [1–3, 13]. Figure 6 illustrates a pattern of changes in electric power recovered on the turbine of the ORC system. They were obtained as a result of simulation tests carried out on a model built in a manner similar to the CBD model presented in this paper. Input values are [1–3, 13, 14]: turbine efficiency; pump efficiency; source properties (Temperature (K), mass flow (kg/s), pressure (kPa)); coolant properties (Temperature (K), mass flow (kg/s), pressure (kPa)); Cycle liquid properties: R245fa (from CoolProp software). Output values: thermal efficiency (%), heat input and output $(\mathrm{kg} \cdot \mathrm{m}^2/\mathrm{s}^2)$; Work generated by the turbine and the pump (J); cycle fluid flow (kg/s); temperature (K), entropy (kJ/kg), enthalpy (kJ/kg/K), pressure (kPa). The results are presented in coordinate systems typical of his kind of processes, namely T-s and p-h. The model was a subject to a tuning process similar to CBD. Experimental research test result carried out at MPK Lodz city transport terminal in Nowe Sady St. were used for that purpose. They included key data on temperature distribution along the length of the exhaust system (thermal imaging), exhaust gas flow versus engine load ratio (flowmeters), exhaust gas temperature changes in front of and behind catalytic convertor versus engine load and torque (diagnostic computer from DAF engine producer). As a result of simulation model hybridization with the use of the above-mentioned experimental data, a model of waste heat recovery from exhaust fumes was constructed. In this model vehicle dynamics is estimated in CBD model and implemented to ORC model. As can be seen in Fig. 6 illustrating changes in electric power generated on ORC system turbine (d), it is possible to estimate those parameters for individual driving cycles (a, b, c).

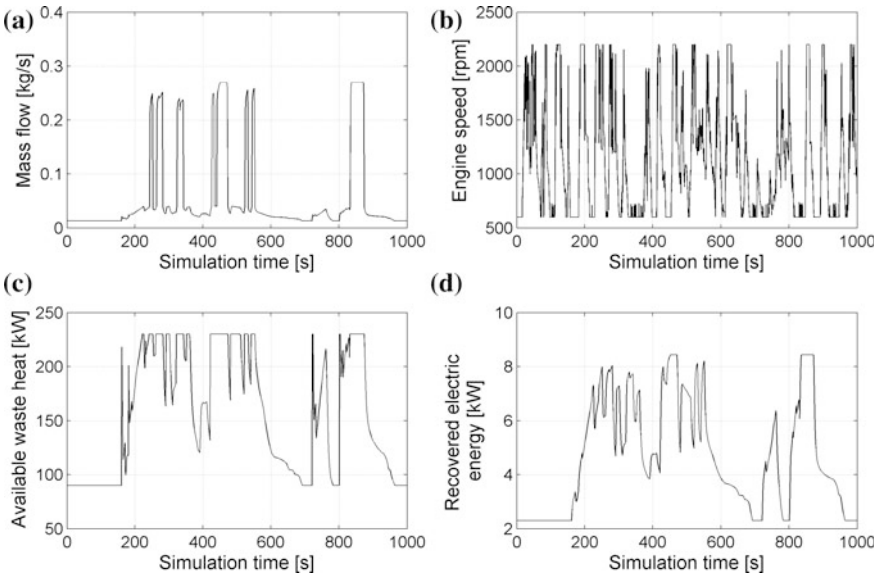

Fig. 6 **a** Mass flow, **b** engine speed, **c** available waste heat, **d** recovered electric energy

7 Conclusions

The presented tool enables easy analysis of a given vehicle's energy consumption, taking into account real life changes in movement variability registered with a simple, readily available GPS device. The proposed method makes it possible to adjust the model to real life conditions, thus creating a hybrid model, which combines the advantages of simulation with experimental research reflecting real life conditions in which the investigated phenomenon or process takes place.

The proposed CBD model enables creating resultant 3D maps, which in turn makes it possible to use those results without the need to organize time-consuming activities devoted to the construction of a simulation model for estimating an influence of vehicle energy intensity on the emission of waste heat which comes from the cooling system and the exhaust system in a compression ignition engine.

References

1. Hossain, S.N., Bari, S.: Waste heat recovery from the exhaust of a diesel generator using rankine cycle. Energy Conv. Manag. **75**, 141–151 (2013). ISSN 0196-8904
2. Katsanos, C.O., Hountalas, D.T., Pariotis, E.G.: Thermodynamic analysis of a rankine cycle applied on a diesel truck engine using steam and organic medium. Energy Conv. Manag. **60**, 68–76 (2012). ISSN 0196-8904

3. Wei, M.S., Fang, J.L., Ma, C.C., et al.: Waste heat recovery from heavy-duty diesel engine exhaust gases by medium temperature ORC system. Sci. China Tech. Sci. **54**, 2746–2753 (2011)
4. Zhang, Y.H., Jiao, X.H., Li, L., et al.: A hybrid dynamic programming-rule based algorithm for real-time energy optimization of plug-in hybrid electric bus. Sci. China Tech. Sci. **57**, 2542–2550 (2014). doi:10.1007/s11431-014-5690-2
5. Sun, D.Y., Lin, X.Y., Qin, D.T., et al.: Power-balancing instantaneous optimization energy management for a novel series-parallel hybrid electric bus. Chin. J. Mech. Eng. **25**, 1161–1170 (2012)
6. Palczynski, T., Pawelski, Z., Pfister, J.: A reference trajectory determination for road vehicles applications. Adv. Transp. Syst. Telematics **371** (2008)
7. Specht, C., Szot, T., Specht, M.: Accuracy of personal GPS receivers at dynamic measurements. TTS Technika Transportu Szynowego **10**, 2551–2555 (2013)
8. Jamrozik, A., Kociszewski, A.: The use of GPS satellite navigation system to determine the operating characteristics of the vehicle. Logistics (3), 2493–2500 (2014)
9. Pawleski, Z., Palczynski, T.: The properties of powertrain with diesel engine and CVT transmission steering. J. KONES **15**, 433–441 (2008)
10. Pawelski, Z., Palczynski, T.: Influence of steering course of CVT to diesel fuel consumption an exhaust emission at ECE cycle. J. KONES **14**, 335–342 (2007)
11. http://www.mathworks.com/help/stateflow/examples/modeling-an-automatic-transmission-controller.html. Accessed 10 Oct 2015
12. Koralewski, G., Wrona, R.: Local bus movement modeling for driving system optimization. Logistics (3), 3065–3074 (2014)
13. Kozanecki, Z., Łagodziński, J.: Magnetic thrust bearing for the ORC high-speed microturbine. Solid State Phenom. **198**, 348–353 (2013)
14. Quolin, S., Lemort, V.: Technological and economical survey of organic Rankine cycle systems. In: European conference on Economics and Management of Energy in Industry (2009)

Modeling of Buildings Behavior Under Blast Load

Jarosław Siwiński and Adam Stolarski

Abstract The work concerns the modeling of the behavior of buildings of reinforced concrete structures under blast load. On the basis of the properties of concrete and steel rebar, as well as the effective reinforcement ratio, we determined the parameters of homogenized substitute material model. Verification of the material model was performed for the beam and deep beam under dynamic loadings. All the structural elements and buildings were modeled using Abaqus system including the model of substitute material as the model of concrete with properly modified parameters. Subsequently two types of buildings were modeled. The first one was of the slabs—columns type of structure, and the second one—walls type of structure. Each of buildings was loaded by variable pressure in time caused by explosive charge located inside the room at the lowest level. The analysis of displacement, stress, and strain states was performed. The solutions adopted at the work are the basis for development of procedures for modeling of the failure mechanism of buildings under blast load and concerns the problems of safety assessment of buildings. Developed method of analysis enables determination of the failure area resulting from detonation of explosive charge, both for reinforced concrete simple structural elements as well as complex structures.

1 Introduction and Literature Survey

Modeling the failure mechanism of explosive loaded buildings has a significant influence on the design processes and the safety assessment of the structure.

In bibliography, there are two basic methods for analysis of explosive actions on structures: analytical and numerical, characterized by diversified levels of modeling

J. Siwiński (✉) · A. Stolarski (✉)
Faculty of Civil Engineering and Geodesy, Military University of Technology, Warsaw, Poland
e-mail: jaroslaw.siwinski@wat.edu.pl

A. Stolarski
e-mail: adam.stolarski@wat.edu.pl

J. Awrejcewicz (ed.), *Dynamical Systems: Modelling*, Springer Proceedings in Mathematics & Statistics 181, DOI 10.1007/978-3-319-42402-6_27

explosive loads and modeling of construction. With regard to modeling of complex and spatial structures, only Finite Elementary Method is practically applied with available software system, e.g., ABAQUS, AUTODYN, LS-DYNA, ANSYS, NASTRAN, MARC, and SAP2000.

Because of difficulty in modeling the properties of complex structural systems of buildings in the form of a heterogeneous reinforced concrete structure, an approach consisting in homogenization of reinforced concrete is applied. Approach based on homogenization of reinforced concrete structure was described among others in work [3]. Authors of the study applied the division of reinforced concrete element into the layers with different strength properties. However, it should be noted that with such approach, the model of substitute material is still heterogeneous. Other homogenization approach was applied in work of [8], who, in turn, referred on work of [12]. In these works, the substitute homogeneous material was applied with increased tensile strength and increased deformation modulus in comparison to the starting material (reinforced concrete). Procedure for determining the parameters of substitute material consisted in determination of deformation—strength characteristics of material in each case for examined object. In carrying out detailed calculations of the selected element recognized as the most critical element of the structure, the parameters of a substitute material were adapted so as to achieve the similar stress and strain distributions as in the reinforced concrete element.

In bibliography with regard to reinforced concrete structures under blast loading it is possible to distinguish slab—column systems, among others [7, 6], slab—column with external stiffening walls systems, [4], column—ribbed slab systems, [2], or slab—beam framed structures, [13]. However, solutions for slab—wall structures are rare. Analysis of destruction mechanism for buildings of this structure is reduced to numerical experiments of reinforced concrete deep beams (walls) and slabs (floors). It should also be noted that in none of these studies concerning on modeling of buildings of reinforced concrete structure, the modeling of progressive destruction mechanism was not presented.

In work of [12], an analysis of the progressive destruction mechanism until complete collapse of the structure is developed using a homogeneous substitute material model. Material model was used, taking into account the change of principal stress limit, without direct considering of the strain rate effect. However, in work of [8], the methodology of homogeneous substitute material was also applied, but with use of material model including strain rate effect by modification of yield limit. It should also be noted that depending on the capabilities of the applied software, the effect of strain rate under dynamic load is included directly in the material model, among others see work of [8], or—which is most frequently found—in a form of dynamic factor increasing material strength even twice. In case of reinforced concrete structures a value of dynamic strength factor is most often applicable in range of 1.0–1.5. For example in work of [2] it is 1.17 and 1.19, in work of [13] it is 1.2, in work of [4] it is 1.25, or in work [7] in which the dynamic strength factor values were separately applied for concrete 1.5 and for rebar 2.0. It is

also worthwhile to notice that some authors do not at all take into account or do not include any information on the influence of the strain rate effects on the dynamic behavior of the structure, e.g., in paper of [6].

2 Objective

Based on the performed literature review, we can formulate the following conclusions. In the all numerical experiments on the analysis of spatial structures software FEM were used, most often LS-DYNA, SAP2000 i ABAQUS. None of studies concerning the proceeding with use the homogeneous substitute material model represent a universal procedure for determining the deformation and strength parameters for this material. In case of explosive loads, the significant impact on final results has the application of strengthening the dynamic strength of material. The way for taking account of this effect is dependent on the material model used in a particular software system. The few software systems contain material models that enable directly taking into account the strain rate. A commonly used method is to increase the strength parameters through the use of constant coefficient of dynamic strength.

The aim of the work is to perform the effort analysis of large size, spatial, reinforced concrete building structures, subjected to action of explosive load, as the structures modeled with a use of hypothetical homogeneous substitute material model.

The following basic assumptions were adopted in the paper: (1) modeling of failure mechanism of buildings explosively loaded was applied to the buildings of reinforced concrete, (2) initial processes of forming of the failure mechanism of the building structure are subjected to analysis; (3) model of homogeneous substitute material that simulates the behavior of reinforced concrete, is characterized by the unlimited ductility, (4) areas of failure are treated as the areas in which the largest values of principal strains or principal stresses exceed the respective limit strains or dynamic strengths of concrete.

3 Homogenized Substitute Material Model

As substitute material model, the continuum plastic damage model for concrete was adopted, developed by [11], modified by [9], and included into the ABAQUS software, in which all of the deformation and strength parameters have been replaced by analogous substitute model parameters, determined in accordance with the assumptions of the homogenization theory, refer, e.g., [16].

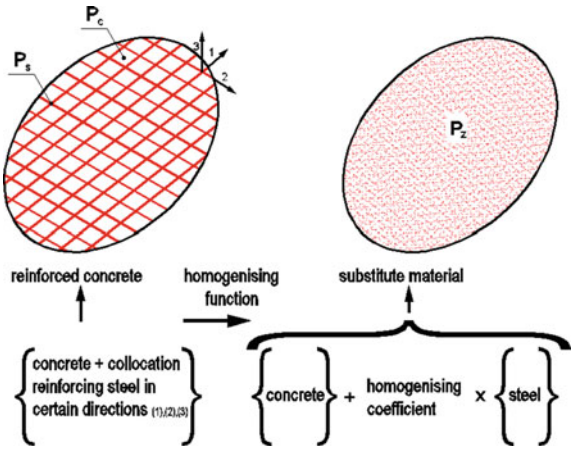

Fig. 1 Scheme of the homogenization of reinforced concrete

Figure 1 shows a scheme of the homogenization of reinforced concrete leading to determine the substitute material parameters.

The basis for determining the substitute material parameters, describing the reinforced concrete, is the following homogenization function:

$$P_z = P_c + F_H \cdot P_s, \tag{1}$$

where P_z—parameters of substitute material after homogenization, P_c—basic parameters of concrete, P_s—basic parameters of reinforced steel, F_H—homogenization coefficient.

The basic parameters P_c for concrete were adopted: initial compressive strength—f_{c0}, initial tensile strength—f_{ct0}, initial deformation modulus—E_{c0}, and volume weight—γ_c.

The following basic parameters for steel P_s were adopted: maximum yield stress $f_{y,\max} = \max\{f_{yi}\}$ as the greatest yield stress among the yield stresses $f_{y,i} = \max\{f_{y1}, f_{y2}, f_{y3}\}$ occurring in the reinforcing steel for the distinguished directions $i = 1, 2, 3$, deformation modulus—E_s, and volume weight—γ_s.

Homogenization coefficient was adopted in the form of effective reinforcement ratio:

$$F_H = \rho_{eff,y} \tag{2}$$

Effective reinforcement ratio was assumed as the resultant function of varied reinforcement ratios $\rho_i = \max\{\rho_1, \rho_2, \rho_3\}$ in distinguished reinforcement directions $i = 1, 2, 3$ and varied dimensionless coefficients of yield stresses in this reinforcement $\varphi_{yi} = f_{yi}/f_{y,\max}$:

$$\rho_{eff,y} = \sqrt{\left(\rho_1 \cdot \varphi_{y1}\right)^2 + \left(\rho_2 \cdot \varphi_{y2}\right)^2 + \left(\rho_3 \cdot \varphi_{y3}\right)^2} \tag{3}$$

After homogenization, we obtain the following parameters P_z of substitute material: initial compressive strength—f_{zco}, initial tensile strength—f_{zto}, initial deformation modulus—E_{zo}, and volume weight—γ_z.

In the substitute material model it is also possible the simplified taking into account the strain rate effect by introduction the generalized dynamic strength coefficient $k_d > 1$, which modify the compressive and tensile strengths of a substitute material

$$f_{zc}^d = k_d f_{zc0}, f_{zt}^d = k_d f_{zt0}, f_{zb}^d = k_d f_{zb0}. \tag{4}$$

Figure 2 shows a modified, "dynamic" limit function (red line) in the stress plane for the substitute material model, taking into account the generalized dynamic strength coefficient (4).

Considering the stress–strain idealizations for concrete it is possible the determination of the strength and deformation parameters describing the segmental idealizations of uniaxial compression and tension functions for substitute material model, Fig. 3.

In Fig. 3, accentuated areas denote the fracture energy of substitute material equal to the fracture energy of concrete. It can be seen that the area corresponding to the fracture energy under the stress–strain relations in case on the substitute material defines the different values of limit strains than in the case of concrete.

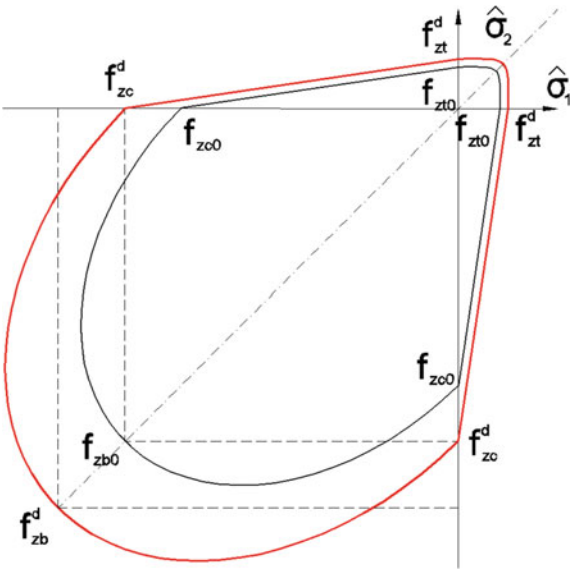

Fig. 2 "Dynamic" limit function in the stress plane for the substitute material model taking into account the dynamic strength coefficient k_d

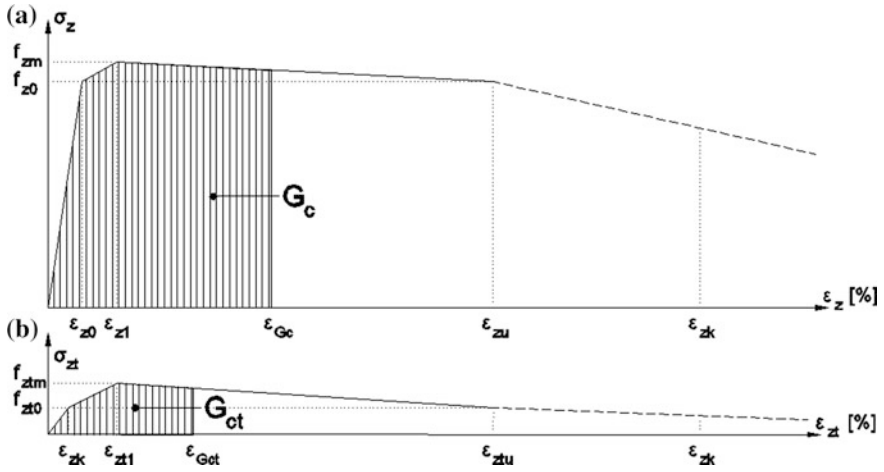

Fig. 3 Stress–strain idealizations for concrete. **a** Uniaxial compression, **b** uniaxial tension

4 Verification of a Material Model

The subject of numerical analysis in the range of dynamic actions is to compare the results obtained based on the numerical analyses for beam from substitute material with experimental results of reinforced concrete beam obtained by [5], marked in the experiment as a TEST 115, and with results of other theoretical analyses, [1]. Numerical model of the beam was developed using cubic finite elements type of C3D8R (eight node elements). In the model the division was used for finite element mesh for solid elements of HEX type and of 30 × 30 mm dimensions.

Based on numerical analysis, in Fig. 4 were presented the graph of displacement changes over time and a change of displacement velocity in the measuring point at the mid-span of the beam.

In the figure, the analysis results for the dynamic strength coefficient $k_d = 1.1$ were marked with the green line, and for $k_d = 1.15$—with a blue line, and for $k_d = 1.2$—with a red line.

As the result of comparative analysis a very good agreement of the obtained results using the beam model from homogeneous substitute material for dynamic strength coefficient $k_d = 1.15$ was stated with the experimental results for reinforced concrete beam of [5], and with results of numerical analysis of [15], as well as with the numerical results of experiment authors [5] obtained using ADINA program of finite element method, and with numerical results of [1] obtained using finite difference method.

Conducted analysis for dynamically loaded beam indicates a very good compatibility of results obtained using Abaqus program with parameters of homogeneous substitute material model modified by taking into account the dynamic

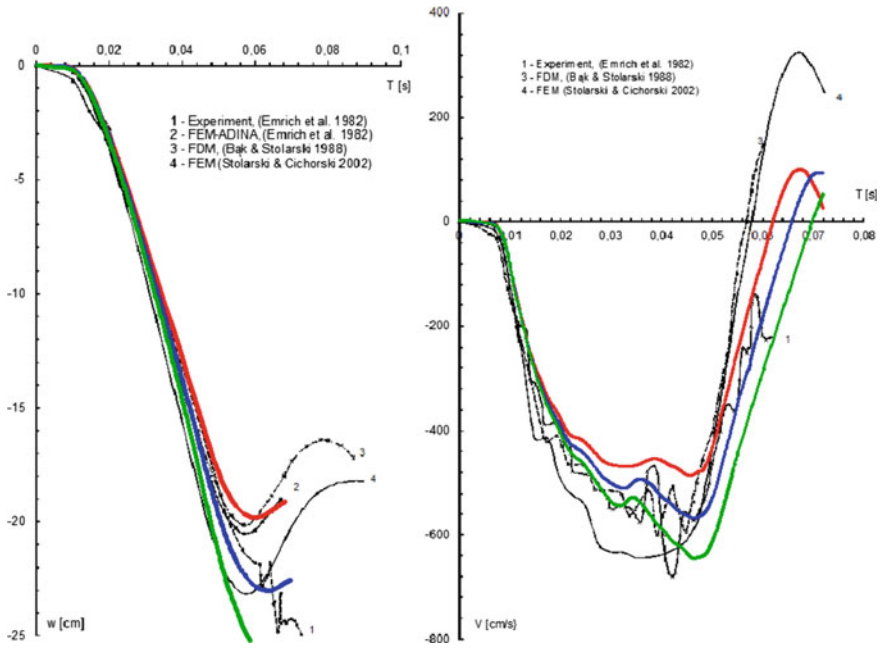

Fig. 4 Changes of displacement and displacement velocity over time at the mid-span of the beam

strength coefficient, in comparison with experimental results, as well as with results of other numerical solution taken from literature.

Dynamic analysis was also applied for reinforced concrete deep beam, which was the subject of static experiment carried out by [10], and described as WT3 experiment.

The aim of analysis was to compare the results obtained according to methodology of modeling of the deep beam from a homogeneous substitute material, with numerical results obtained by [15].

Dynamic analysis was carried out for different values of the intensity factor of the dynamic load in relation to the first load level of the deep beam $P_0 = 1031\,\text{kN}$, determined in work of [15] for solution indicated as L0:

$$\alpha = \frac{P}{P_0}, \tag{5}$$

where $P = p \cdot l$—total load of deep beam, p—and uniformly distributed on the upper edge of deep beam dynamic load constant over time, l—the length of the upper edge of deep beam.

Figure 5 shows the influence of strain rate effect by applying the dynamic strength coefficient for the substitute material $k_d = 1.05$ (green lines) and $k_d = 1.1$

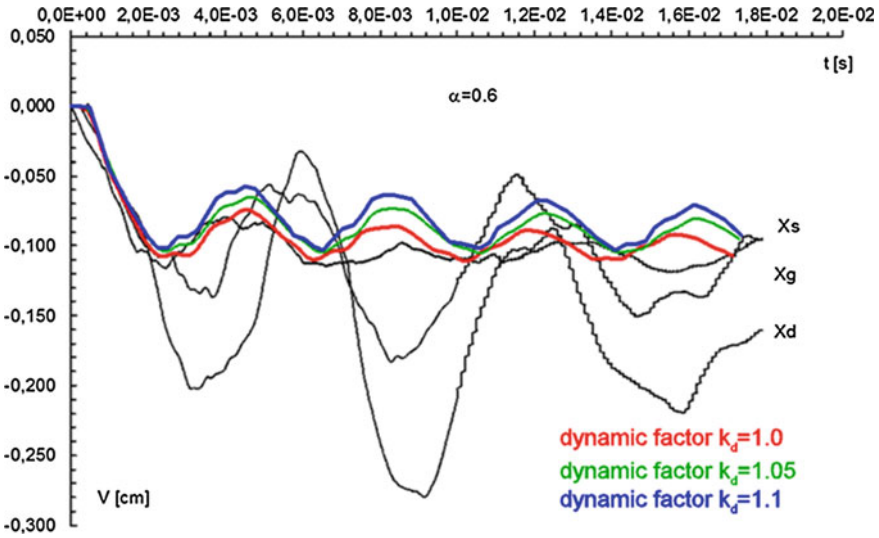

Fig. 5 The influence of strain rate effect by applying the dynamic strength coefficient for the substitute material in the deep beam

(blue lines) on the dynamic displacements of the x_d point located at the center of the bottom edge of the homogeneous deep beam, for the load level $\alpha = 0.6$, with reference to the numerical result of [15].

5 Numerical Modeling and Analysis of Results

The purpose of the numerical experiments is to analyze the behavior of reinforced concrete building structures type of slab—column (A) and slab—wall (B) under the accidental action resulting from detonation of explosive charge placed in a room on the ground floor.

Three-aisled structural system of the skeletal building (A) is characterized by outer dimensions in a horizontal projection of 20.0×39.5 m and total height of 51.7 m. The height of over ground storeys is 2.5 m. The load-bearing structure of the building is of monolithic reinforced concrete floors of 0.25 m thickness, supported on the columns with the cross-sectional dimensions of 0.5×0.5 m arranged in axial spacing in both directions equal 6.5 m. Building is built on the plate foundation with a thickness of 1.45 m. The structural system of three aisle, corridor's building (B), with outer dimensions identical as in the building (A), has the crosswise walls system with inner walls of 0.25 m thickness, outer walls of 0.375 m thickness, in axial spacing equal of 6.5 m, see Fig. 6.

The monolithic reinforced concrete structure is made of concrete strength class C30/37 of the compressive characteristic strength $f_c = 30$ MPa, tensile strength

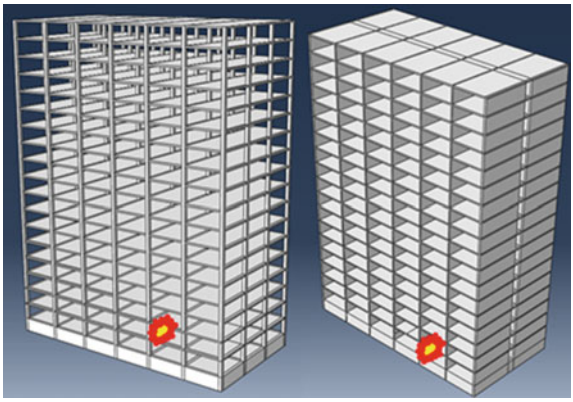

Fig. 6 Building structures of slab—column type (*A*) and slab—wall type (*B*) with placement of explosive charge

$f_{ct} = 3.8$ MPa, and a deformation modulus of $E_c = 32$ GPa, as well as of reinforcing steel RB500 W of the yield stress $f_y = 500$ MPa and deformation modulus of $E_s = 200$ GPa.

The parameters of homogeneous substitute material were determined on the basis of the developed homogenization method of reinforced concrete, assuming an average reinforcement ratio $\rho = 0.017$ in all elements of the entire structure and they were taken as follows: $f_{zc} = 38.5$ MPa, $f_{zct} = 12.3$ MPa, $E_{zc} = 35.4$ GPa. The dynamic strength coefficient $k_d = 1.15$ for compressive and tensile strength of a substitute material was used in the numerical analysis.

The numerical model of building was developed using cubic 8—nodes HEX type finite elements marked as C3D8R of 12.5×12.5 cm dimensions.

Building A was loaded with overpressure varying in time, caused by the detonation of TNT charge with a mass of $m = 10$ kg, placed inside the room on the ground floor, situated eccentrically in the outer room row (of front), at the distance of $r = 3.0$ m from the inner walls of the structure of this room. On the basis of considerations relating to the determination of the shock wave parameters on the structure surface from an internal explosion presented in the paper of [14], the function of pressure changes over time $p(t)$ according to Baker's approach, the value of maximum pressure $p_{QS} = 4.67$ MPa and time duration of overpressure phase $t_k = 20$ ms, were determined. Building B was loaded with overpressure varying in time, caused by the detonation of TNT charge with a mass of $m = 5$ kg, placed inside the room on the ground floor, situated eccentrically in the outer room row (of front), at the distance of $r = 3.25$ m from the inner walls of the structure of this room. Analogously to for building A, the following shock wave parameters were determined: the value of maximum pressure $p_{QS} = 2.4$ MPa, and time duration of overpressure phase $t_k = 27$ ms.

Figures 7 and 8 show distributions of the largest values of maximum and minimum principal strains in time instant $t = 0.07$ s with reduction of the tensile strain to the limit value $\varepsilon_{ct,G} = 0.00031$ and with reduction of the compressive strains to the limit value $\varepsilon_{c,G} = 0.0054$. The tensile deformation zones with the exceeded limit tensile strains were marked with gray color.

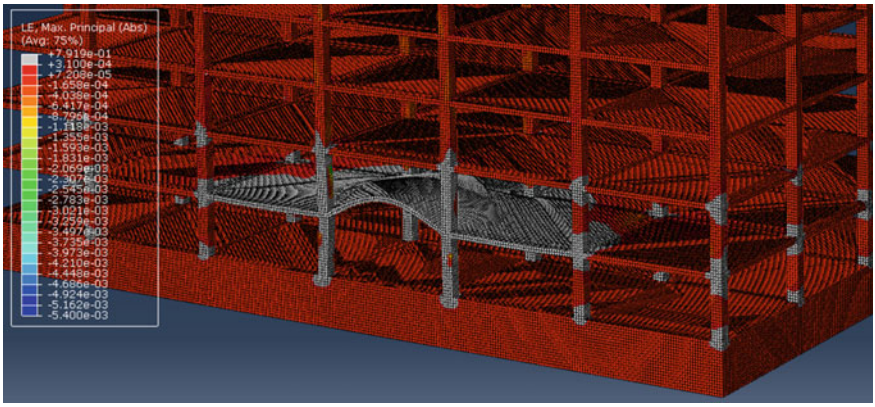

Fig. 7 Distributions the largest values of maximum and minimum principal strains in time instant t = 0.07 s with reduction of the tensile strains to the limit value $\varepsilon_{ct,G} = 0.00031$ and with reduction of the compressive strains to the limit value $\varepsilon_{c,G} = 0.0054$ for building of type *A*

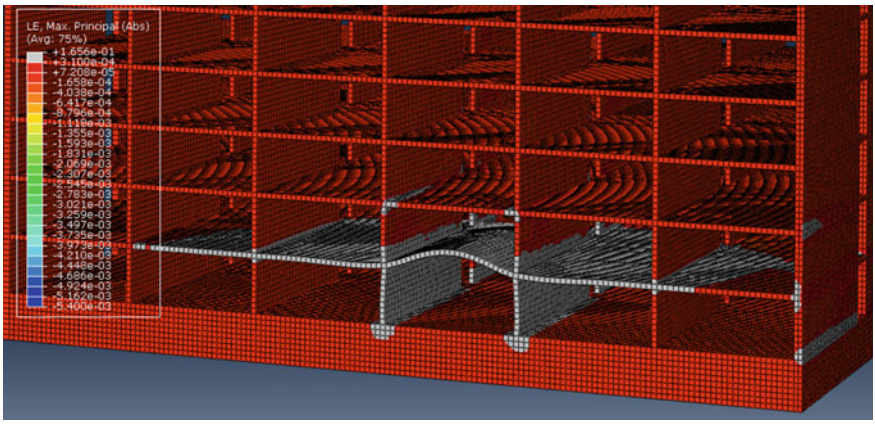

Fig. 8 Distributions of the largest values of maximum and minimum principal strains in time instant t = 0.07 s with reduction of the tensile strains to the limit value $\varepsilon_{ct,G} = 0.00031$ and with reduction of the compressive strains to the limit value $\varepsilon_{c,G} = 0.0054$ for building of type *B*

6 Conclusions

Analysis of beam under dynamic load was carried out based on Emrich, Herter, and Puffer experiment. Graphs of displacement changes over time were appointed using three values of dynamic strength coefficient k_d, as well as comparative analysis was conducted with experimental and numerical results taken from the literature. It was stated that the largest compliance of results in displacement and displacement velocity changes over time, obtained in solution for numerical model of beam from

substitute material, with experimental results and other numerical solutions taken from literature, was achieved for dynamic strength coefficient value $k_d = 1.15$. A very good compatibility of results, which were obtained in the dynamic analysis for deep beam of homogeneous substitute material, was stated in comparison with numerical results of reinforced concrete deep beam obtained by [15]. In the case of the analyzed deep beam the most accurate results were obtained using a dynamic strength coefficient value $k_d = 1.05$.

Inference about failure mechanisms was conducted on the basis of observations of the greatest values of maximum and minimum principal strains in compression and tension zones. The areas of strains with exceeded limit strain energy corresponding to the failure of concrete in tension, were regarded as the areas of potential failure (cracking areas).

The carried out considerations on the substitute material and numerical test results indicate the effectiveness of the numerical method enabling the analysis of the behavior mechanism of building structures under the explosive load.

The solutions applied in the paper are the basis for the further development of modeling procedures of failure mechanism of explosively loaded building structures and brings closer the issues of safety assessment of buildings.

The developed method of analysis enables to determine the range of the potential failure of the structure, resulting from the detonation of an explosive charge, as well as the assessment of the maximum resistance to blowing wave, both in terms of simple structural elements as well as more complex structures and buildings made of reinforced concrete.

References

1. Bąk, G., Stolarski, A.: Non-standard idealization of the dynamic behavior of concrete for uniaxial compression. Rozpr. Inż. Wars.**36**(2), 217–238 (1988). (in Polish)
2. Brun, M., Batti, A., Limam, A., Gravouil, A.: Explicit/implicite multi-time step co-computations for blast analyses on a reinforced concrete frame structure. Finite Elem. Anal. Des. **52**, 41–59 (2011)
3. Combescure, Ch., Dumontet, H., Voldoire, F.: Homogenised constitutive model coupling damage and debonding for reinforced concrete structures under cyclic solicitations. Int. J. Solids Struct. **50**, 3861–3874 (2013)
4. Draganić, H., Sigmund, V.: Blast Loading on Structures. Tech. vjesn., Croatia (2012)
5. Emrich, F., Herter, J., Puffer, G.: Nonlinear finite element analysis of reinforced concrete beams under impact load in comparison with experimental results. Comput. Struct. BAM, Berlin (West) **4**(2), 455–471 (1982)
6. Jayashree, S.M., Bharatwaj, R.R., Santhi, H.: Dynamic response of a space framed structure subjected to blast load. Int. J. Civ. Struct. Eng. **4**(1) (2013)
7. Jayasooriya, R., Thambiratnam, D.P., Perera, N.J., Kosse, V.: Blast and residua capacity analysis of reinforced concrete framed buildings. Eng. Struct. **33**, 3483–3495 (2011)
8. Kelliher, D., Sutton-Swaby, K.: Stochastic representation of blast load damage in a reinforced concrete building. Struct. Saf. **34**, 407–417 (2011)
9. Lee, J., Fenves, G.: Plastic-damage model for cyclic loading of concrete structures. J. Eng. Mech. 892–900 (1998)

10. Leonhardt, F., Walther, R.: Wandartige trager. Deutscher Ausschuss fur Stahlbeton, vol. 229, Berlin, Germany (1966)
11. Lubliner, J., Oliver, J., Oller, S., Onate, E.: A plastic-damage model for concrete. Int. J. Solids Struct. **25**(3), 299–326 (1989)
12. Luccioni, B.M., Ambrosini, R.D., Danesi, R.F.: Analysis of building collapse under blast loads. Eng. Struct. **26**, 63–71 (2004)
13. Parisi, F., Augenti, N.: Influence of seismic design criteria on blast resistance of RC framed buildings: a case study. Eng. Struct. **44**, 78–93 (2012)
14. Siwiński, J., Stolarski, A.: Analysis of the internal explosion action on the building barriers. Biuletyn WAT, vol. LXIV, Nr 2, 197–211, 2015, (in Polish)
15. Stolarski, A., Cichorski, W.: Static and dynamic modeling of inelastic behavior of reinforced concrete deep beams. Studia z zakresu Inżynierii (Stud. Field Eng.) Wars. **51** (2002). (in Polish)
16. Strzelecki, T., Auriault, J.L., Bauer, J., Kostecki St., P.W.: Mechanics of heterogeneous. In: Strzelecki, T. (ed.) Theory of Homogenisation. Dolnośląskie Wydawnictwo Edukacyjne (Lower Silesian Educational Publishers), Wrocław (1996). (in Polish)

Force Effect of Strike and the Possibility of Causing a Skull Fracture of a Human Head

Svoboda Martin, Soukup Josef, Jelen Karel and Kubový Petr

Abstract First, the article describes the force strike measurement of an athlete who performs competitively combat sports. Second, there are the results of scientific studies that deal with the human head injuries due to impacts of various kinds. These results were determined on the carcasses. During the actual measurement were determined time courses of forces impinging on the dynamometer plate, including size and the direction of the force. Dynamometer spanned forces up to 10000 N, frequency was set up at 1000 Hz, the accuracy of the estimate was 0.5 % of measured value. A composite plate was attached to a dynamometer which has a special steel construction. If we compare the results of force effect, we can find out that combat sports can cause fractures of the facial bones or other injuries of a human head or cervical vertebrae.

1 Introduction

The human head is the most studied problem of biomechanics. It is solved experimentally or by FEM methods. The works mostly deal with the causes of head injuries in the car accidents. Other works deal with the workplace injuries and how to reduce them by using protective equipments. There are also some works

S. Martin (✉) · S. Josef
Faculty of Production Technology and Management,
Jan Evangelista Purkyně University, Ústí Nad Labem, Czech Republic
e-mail: svoboda@fvtm.ujep.cz

S. Josef
e-mail: soukupj@fvtm.ujep.cz

J. Karel · K. Petr
Faculty of Physical Education and Sport, Charles University,
Prague, Czech Republic
e-mail: jelen@ftvs.cuni.cz

K. Petr
e-mail: kubovy@ftvs.cuni.cz

J. Awrejcewicz (ed.), *Dynamical Systems: Modelling*, Springer Proceedings
in Mathematics & Statistics 181, DOI 10.1007/978-3-319-42402-6_28

discussing the question of the direct strike to the head especially in combat sports. The aim is always to reduce the extent and number of injuries.

The impacts to the head are common element in contact sports. Look at the collision of opponent's heads in football or ice hockey matches, then falls to the ground or hitting the obstacles (cycling, horseback riding) and finally in combat sports where the opponents are trying to strike and kick the rival's head. Some adjustments of the rules or the necessity of using protective equipment are very often in these sports. The paradox is the AIBA's (International Boxing Association) regulations which came into effect on the world championship of boxing—November 2013. It was about removing the protective helmets even in amateur boxers especially in men's elite category. They wanted to increase the attendance of amateur gala evenings, tournaments, and boxing matches to make them attractive for the spectators. But this is in conflict with the reduction of number and the extent of injuries in athletes.

There is no objective measure that would evaluate brain degeneration due to the frequent impact of a different type. Other types of impacts also fall on a firm surface, hitting of the human head in car accidents, and so on. In this study we focus only on the force effects that can cause fractures of the skull bones of a human head. We will summarize here the results of major scientific works that dealt with this issue. Then we will describe the measuring of the force effects in combat sports—the direct punch.

2 Force Effect of Boxers

In this work [1] there was used the Hybrid III dummy for measuring of an impact dynamics. There were placed five accelerometers on the Hybrid II dummy. Sensors were used for the calculation of translational and rotational accelerations. Two accelerometers were placed on the palms of a boxer's hands and the overall dynamics of the hand was recorded. They were attached in right angle to each other. The lateral movement of the hand was neglected. Everything was fixed by boxing bandages to the hands.

To measure the loading of a neck and force impulses, there was used six axis sensor module, which was installed in the upper part of the neck. The switch identifying an initial contact between bowing gloves and the dummy's head was installed on the head of the dummy. That switch provides accurate ignition signal indicating the start of the countdown. The system IDDAS (somatic, Urbana, IL) was chosen as the primary data collection system. Data were collected on a sampling frequency 14.7 kHz.

The pressure sensor was installed between the surface of breakable dummy's head and the layer imitating the skin. The system registered the pressure and determined the contact area of the impact of the strike in each segment of a sensor. For the purpose of this study they used very thin (0.1 mm) Tescana sensor (model 9500). The scanning area was 71 × 71 mm and the sampling frequency of the

system was 1.4 kHz. This study monitored the strikes of 18 boxers. The impact force ranged from 1990 to 4741 N. The average impact force of those 18 boxers was 3427 N. The standard deviation out of average was 811 N.

3 Force Effects Leading to the Fractures of the Skull Bones

This chapter is a summary of the results of the scientific studies that dealt with the force effects causing skull fractures. Stated values were obtained by effecting of an impactor (area equals 6.45 cm^2) on the carcasses head [2]. Cadaver has been used only once. The impact always interfered at a specific location. The results confirmed that impact forces from around 1000 N to the face area are clinically relevant (more severe than hitting of the scalp). The average force for the fracture of the cheekbone is 1770 N.

The data of Nahum et al. [3] were obtained by the same wave. They examined the facial bones by the impactor size 6.5 cm^2. All experiments were carried out always on one sample, soft tissues included. The average force effects leading to the fracture of the upper jaw is 1150 and 2840 N for the lower jaw.

They also used five cadaver heads to find out their impact load by their fall on the horizontal surface. The impact velocity was in the range from 6.08 to 7.14 $m.s^{-1}$. The impact was headed to the chin from below. The result was a fracture of mandible condyle, in four of the experiments even on the both sites.

In the following chart there are impact forces causing the fractures of the facial bones.

4 Parameters Measurement of the Punch

Determination of the influence and the effects of the head load depend on the finding of the most accurate parameters of possible strikes. We have chosen the direct type of strike (headed mainly to the facial region) which is the most common in combat sports. The aim was to measure and determine the most important parameters to estimate the effects of the strike to the body of the opponent. We selected maximal operating power, speed of the limb during the impact, duration of the impact, and total energy passed by the strike.

The punch was scanned by dynamometric plate Kistler 9281 and by high speed camera Redlake HG 100, kinematics of the impact was measured by Qualisys system.

The results of experimental measurements should confirm the results of the major scientific papers dealing with the measurement of the force effects in combat sports or impacts of various kinds on the human head.

For the measurement they worked with a product usually used at the Taekwondo competitions. It is about two composite plates associated with the grooved lock, by this opening you can measure the impact energy. They asked only one Taekwondo athlete of the Czech national team to realize the measurement. So this is not a statistically significant sample. It is establishing of a good estimation of possible impact power. It was done in 10 punches (to do more strikes was not effected—indisposition of sportsmen). Only three of them were valid. These three punches did not open the lock of composite plates. The result of this was the accuracy of measured parameters because there was no force and speed reduction (Table 1 [2, 4–16]).

Composite plate was fixed by steel construction to the dynamometer. The stiffness of the dynamometer and construction is much higher than the stiffness of boards. This arrangement has a negligible effect on the measurement. From the time the record course of action of force was determined by its maximum value and duration of the impact and the work performed during the impact (Figs. 1, 2 and 3).

The results of the measurements are summarized in Table 2. The maximum force of punch is the maximum from the vector sum of the forces acting on the plate at the time of impact (formula 1). Impact velocity was calculated, numerical differentiation by time kinematic data is measured by the Qualisys system. The duration of impacts has been deducted from the graphs of force versus time measured with a dynamometer. Transmitted energy was calculated by numeric integration as the area under the curve of force versus time also from data measured with a dynamometer.

Table 1 The forces of facial bone fractures [2, 4–16]

Bone	Range (N)	Average (N)	Number of samples	Area of impact (cm^2)
Lower jaw	1980–4110	2840	6	6.5
Lower jaw	818–2600	1570	6	25.8
Lower jaw	4460–6740	5390	5	127
Upper jaw	623–1980	1150	11	6.5
Upper jaw	1100–1800	1350	6	ø20 mm
Upper jaw	788	788	1	ø25 mm
Facial	970–2850	1680	6	6.5
Facial	910–3470	1770	18	6.5
Facial	1120–1660	1360	4	6.5
Facial	1600–3360	2320	6	33.2
Facial	2010–3890	3065	4	ø25 mm
Facial	900–2400	1740	8	ø20 mm
Facial	1499–4604	2390	13	ø25 mm
Facial	1452–2290	1739	4	volant
Nasal	1875–3760	2630	5	ø25 mm
Face	–	>6300	5	181
Eye arch	4780–11040	8000	19	ø41 mm

Fig. 1 Example of very hard hitting of a boxer in the head

Fig. 2 Accelerometers in the palm of a boxer

$$F_{ABS} = \sqrt{F_x^2 + F_y^2 + F_z^2} \tag{1}$$

On Fig. 4 is the graph of force action on the board at the time t of the second valid strike. The three curves show the force components in the directions x, y, z. Absolute force component was obtained using the vectorial sum.

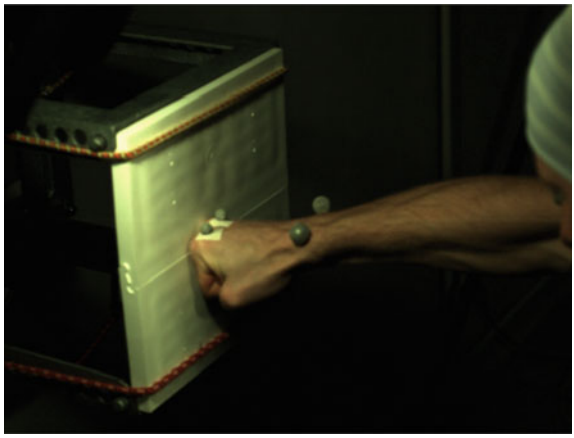

Fig. 3 Sample of high speed camera Redlake HG 100th

Table 2 Measured values of impact

Number of measurements	Max. impact force F_{max} (N)	Impact velocity v (m.s^{-1})	Duration of impact t (s)	Transmitted energy E (kJ)
1	1970	8.4	0.0109	13.1
2	2192	7.7	0.0129	14.7
3	2292	8.0	0.0119	15.7
Average	2151	8.0	0.0119	14.5

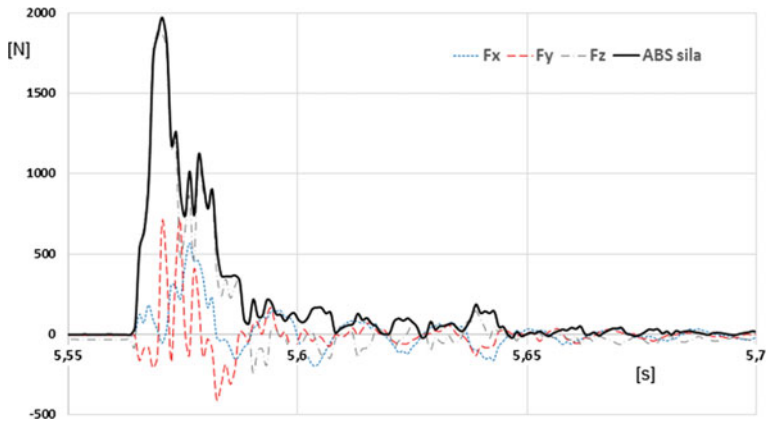

Fig. 4 Time course of force action on the board—first valid attempt

5 Conclusions

From these results, it is clear that the work of the boxing punches or blows and other combat sports (Karate, Taekwondo, etc.) can cause skull fractures.

It is not yet determined how much it changes size and circuitry of the brain after strokes collected during their boxing career, and what effect it has on brain degeneration. It is not known how these changes cause brain diseases such as Alzheimer disease or dementia (this measurement at present progress).

The intensity of the blow to the head of a live opponent may vary depending on different condition impacts (stiffness of tissues, inertia opponent's responses, volitional control, and motivation of the attacker, etc.). All these corrections tend to reduce our impact as measured by the possible intensity.

My personal opinion, after more than ten years of active boxing career, is that the main reasons are the approach, the coach and boxer in training, and the type of equipment that is used when a boxer in sparring. In training a great number of boxers did not use helmets. The coach should teach a technique that goes primarily to dodge blows against opponents. When blocking the force of the blow of course transmitted to the human head. Boxer should also be physically well prepared to match the entire period (training) and concentrated coordinately to manage defensive techniques.

Another important aspect is the weight of the boxer, affecting hardness and impact strength by the effect on the degeneration of brain tissue.

Thanks to modern technology the materials are better than before. For example helmets absorb more punches. The paradox is that all sports are trying to protect the health of athletes and boxing, the opposite happened. Profits are more important.

Acknowledgments This work was created with the support of SGS University of Jan Evangelista in Ústí nad Labem and thanks grant SD.

References

1. Walilko, T.J., Viano, D.C., Bir, C.A.: Biomechanika hlavy v reakci na údery do obličeje prováděné olympijskými boxery. Br. J. Sports Med. **39**, 710–719 (2005). doi:10.1136/bjsm.2004.014126
2. Nahum, A.M., Gatts, J.D., Gadd, C.W., and Danforth, J.P.: Impact tolerance of the skull and face. In: 2nd STAPP Car Crash Conference Proceedings, no. 680785. SAE, pp. 302–316 (1968)
3. Nahum, A.M., Ward, C.C., Raasch, F.O., Adams, S., Schneider, D.C.: Experimental studies of side impact to the human head. In: 24th STAPP Car Crash Conference Proceedings. SAE Society of Automotive Engineers (1980)
4. Arash, A.S., Eftychios, Ch., Benjamin, Z., Guy, M.G., Philip, V.B.: Deformation of the human brain induced by mild angular head acceleration. J. Biomech. **41**, 307–315(2008)

5. Parshuram, P., Ghodrat, K., Mariusz, Z.: Examination of brain injury under impact with the ground of various stiffness. Proc. Eng. **13**, 409–414 (2011)
6. Pintar, A.F., Philippens, M., Zhang, Y.J., Yoganandan, N.: Methodology to determine skull bone and brain responses from ballistic helmet-to-head contact loading using experiments and finite element analysis. Med. Eng. Phys. **35**, 1682–1687 (2003)
7. Allsop, D.L., Warner, C.Y., Wille, M.G., Schneider, D.C., Nahum, A.M.: Facial impact response comparison of the hybrid iii dummy and human cadaver. In: Proceedings of 32nd Stapp, no. 881719. SAE, October 1988, p. 139
8. Allsop, D.L.: Human facial fracture and compliance. Ph.D. dissertation, Department of Mechanical Engineering, Brigham Young University (1989)
9. Nahum, A.M., Ward, C.C., Schneider, D.C., Raasch, F.O., Adams, S.: A study of impacts to the lateral protected and unprotected head. In: 25th STAPP Car Crash Conference Proceedings. SAE Society of Automotive Engineers (1981)
10. Stalnaker, R.L., Roberts, V.L., McElhaney, J.H.: A study of impacts to the lateral protected and unprotected head. In: 17th STAPP Car Crash Conference Proceedings. SAE Society of Automotive Engineers (1973)
11. Got, C., Patel, A., Fayon, A., Tarriere, C., Walfisch, G.: Results of experimental head impacts on cadavers: the various data obtained and their relations to some measured physical parameters. In: 22th STAPP Car Crash Conference Proceedings. SAE Society of Automotive Engineers (1978)
12. Ommaya, A.K., Goldsmith, W., Thibault, L.: Biomechanics and neuropathology of adult and paediatric head injury. Review. Br. J. Neurosurg. **16**(3), 220–242 (2002)
13. Pellman, E.J., Viano, D.C., Tucker, A.M., et al.: Concussion in professional football: reconstruction of game impacts and injuries. Neurosurgery, pp. 799–812 (2003)
14. Pellman, E.J., Viano, D.C., Tucker, A.M., et al.: Concussion in professional football: location and direction of helmet impacts—part 2. Neurosurgery 1328–41 (2003)
15. Hagara, M., Schrötter, M., Lengvarský, P.: An investigation of the temperature influence on a shift of natural frequencies using digital image correlation. Appl. Mech. Mater. **611**, 506–510 (2004)
16. Dižo, J., Blatnický, M., Skočilasová, B.: Computational modelling of the rail vehicle multibody system including flexible bodies. In: Communications: Scientific Letters of the University of Zilina, vol. 17, issue 3, pp. 31–36 (2015). ISSN 1335-4205

Hydraulically Driven Unit Converting Rotational Motion into Linear One

Olga Szymanowska, Gabriel Szymkiewicz, Donat Lewandowski, Dariusz Grzelczyk and Jan Awrejcewicz

Abstract The contribution concerns a unit which can be implemented in driving hand prostheses, surgical manipulators and other equipment, the operation of which is based on linear motion. The state-of-the-art research presents several medical devices usually driven by means of electric or hydraulic, complex elements. The primary purpose of this work is to provide a solution that, due to simplicity of its design, will be an alternative to existing expensive devices. Simultaneously, the goal of the efforts is to ensure high precision and repeatability of linear movement. The proposed device comprises two hydraulic actuators driven by a stepper motor. Apart from presenting the design of the unit, the following work comprises description of modelling of the unit operation supplemented with presentation of the constructed prototype and results of initial experimental evaluation. Eventually, conclusions are drawn, pointing several amendments which are recommended for implementation in the future work.

1 Introduction

Extremity and limb amputations have been known to humans for centuries. Archaeological findings show that people have been trying to replace missing parts of their bodies with artificial substitutes already in the Ancient Egypt [1]. Despite many ages that have passed accompanied by development of technology, still, replacing the lost body part with an artificial one, being able to resemble natural functioning, is one of the most challenging aspects in the field of rehabilitation and prosthetic technology.

O. Szymanowska (✉) · G. Szymkiewicz · D. Lewandowski · D. Grzelczyk · J. Awrejcewicz
Department of Automation, Biomechanics and Mechatronics, Lodz University of Technology, 1/15 Stefanowski St., 90-924 Lodz, Poland
e-mail: szymanowska.olga@gmail.com

J. Awrejcewicz (ed.), *Dynamical Systems: Modelling*, Springer Proceedings in Mathematics & Statistics 181, DOI 10.1007/978-3-319-42402-6_29

Many attempts have been made throughout years to solve the abovementioned problem and mimic the movement of, for instance, a human hand, the prosthesis of which will be the concern of this work.

Prosthetic extremities are met in a variety of forms and applied technologies. The simplest designs are purely cosmetic and are used to mimic the shape of the missing hand. However, one of the biggest needs of amputees is to have the functioning of their extremities resembled to the possibly greatest extent. This is the reason that led to many efforts aimed at creating prostheses allowing to perform movements in a manner similar to the one of the natural hand. Most of hand prostheses are comprised of body-powered devices, including hooks or multi-fingered devices employing cables to manipulate their elements. The patient is supposed to wear a dedicated harness and manipulate the hand by means of moving the opposite shoulder. However, due to unsatisfactory and uncomfortable operation of such units, the improvement in the field of extremity prosthetics is one of the topics which is still under investigation.

The breakthrough in the design of such devices may be hard to achieve, since, as mentioned in [2], only few major enhancements have been observed since the early 1960s. Employment of external power was one of the hand prosthesis improvements which aimed at aiding the body-powered device. One of the examples of artificial hands is the Utah-MIT hand, being the robotic, four-fingered end effector powered pneumatically and using tendon-like cables [3]. Tendons have been also employed in the Salisbury hand [4], where they have been supplemented with electric drive motors as well as potentiometers and accelerometers to manipulate three fingers. Another example can be the BarrettHand [5]. All the aforementioned devices were capable of grasping and other manipulatory tasks, however, their operation was still far from the one of a human extremity. Among modern devices, the one referred to as the IOWA hand should be mentioned, the fingers of which are spring-like. The hand has been described in [2]. Special attention should be paid to the HANDLE project [6] conducted by researchers from the European Union. The project has resulted in a device being equipped with a number of sensors, including pressure sensors, and elements of artificial intelligence. The hand not only mimics movements of a human extremity, but also resembles its appearance. Modern prostheses comprise also hydraulic devices. Fluidhand [7] and i-limb [8] are hydraulically driven hand prostheses resembling both the appearance and functionality (manoeuvrability) of a human extremity to a large extent. i-limb has been successfully introduced onto the market by Touch Bionics Inc. Another interesting design of a hydraulic prosthesis, the Delft Cylinder Hand, has been proposed by Delft University of Technology [9]. The prosthesis is claimed to be about 50 % lighter than corresponding electrical instruments.

The aforementioned hydraulic devices are a competitive alternative for electric and, undisputedly, also for cosmetic prostheses. However, other solutions should be still taken into consideration in order to develop devices of simpler (less complex) and thus less expensive design. Development of the device fulfilling the aforementioned requirements is the goal of our efforts.

The solution presented in this work is intended to be introduced also into surgical manipulators, since the demand for such specialistic devices is constantly growing. Both the surgical manipulators and their drive units must be sufficiently tight and resistant to corrosion. They must be made of materials (e.g., surgical steel) that do not negatively influence living organisms. High precision is necessary while constructing devices which are intended to get into contact with an organism, since lack of tightness may lead to leakage of body fluids to the inside of a device, and vice versa.

To drive medical equipment, such as the abovementioned manipulators, the operation of which is based on linear motion, electric actuators are usually used. However, their main disadvantage is, as in the case of electrically driven hand prostheses, complex design accompanied by the fact that the drive unit cannot be placed in close vicinity of the piston executing the linear movement. Thus, the drive unit has to be located at a distance from the surgical site and be connected to the piston by means of special rods and tension members. As a result, the range of motion that can be achieved by the device is limited.

Apart from the above mentioned applications, the design presented in this work can be also implemented in other devices that require precise movement and stiffness accompanied by reproducibility of performed linear motion.

The presented paper comprises supplementary information basing on the former work [10].

2 The Idea

The proposed unit converting rotational motion into linear motion is chosen to be hydraulically driven, since the authors claim that such a solution is favourable over typical electric drives. In hydraulic actuators, the drive unit is used only to produce pressure and to force the fluid flow through the tube to other parts of the device. In such a way, it can be separated from the end actuator, what is desired in the case of both hand prostheses and surgical manipulators. Furthermore, elements of the unit are connected with each other by means of elastic tubes, what ensures greater range of motion than in the case of electrically driven devices and possibility of reaching hardly accessible locations. If small enough, tubes can be placed inside patient's body.

The idea implemented in the unit is to use a stepper motor connected to a driving actuator which, in turn, is linked with an executing actuator by means of an elastic tube. As a result of rotational motion of the stepper motor's rotor, hydraulic fluid is pushed through the driving actuator and further, through the tube, in a linear manner causing linear motion in the executing actuator.

Two propositions of the unit design have been provided. In the first concept (see Fig. 1a), the stepper motor is intended to be fixed to the foundation. An internally threaded piston is incorporated inside the driving actuator while the shaft connected to the stepper motor has an external thread. The shaft screws the piston into the

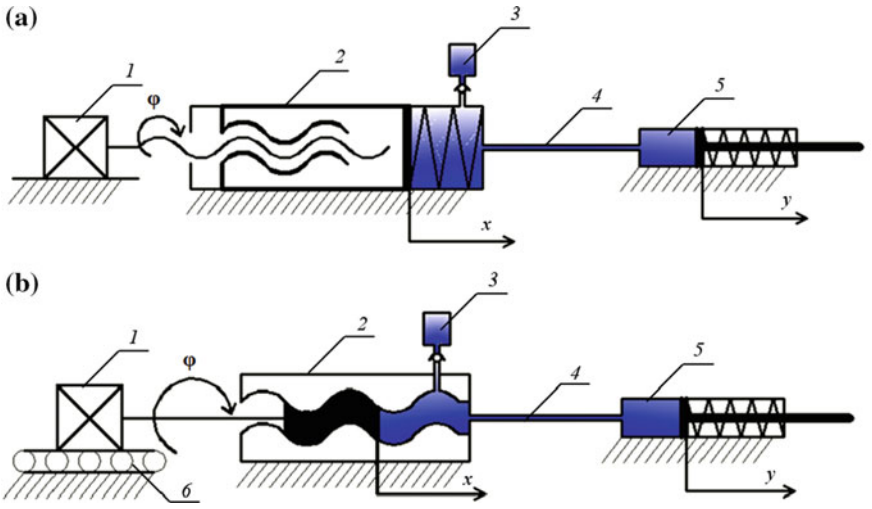

Fig. 1 Conceptual drawings of the unit: **a** variant with fixed stepper motor, **b** variant including a roller guideway. *1* stepper motor, *2* driving actuator, *3* compensation container, *4* hydraulic tube, *5* executing actuator, *6* roller guideway, φ rotation of the stepper motor shaft, x, y position of the actuators [10]

actuator and the pressure generated by the moving piston causes the fluid to flow out of the actuator, inducing in this manner motion in the executing actuator. Both actuators are single acting, i.e. they are comprised of springs, the role of which is to facilitate backwards motion of the pistons during their withdrawal from the actuators.

The second concept (see Fig. 1b) assumes having the stepper motor placed on a linear type roller guideway. Due to implementation of such solution, the drag of the stepper motor is reduced and its movement is possible. The design of the driving actuator is simplified in comparison to the first concept. The spring is removed, and so is the piston. The role of the latter is taken by the motor's shaft which, in this variant, is ended with an element the shape of which corresponds to the internal thread of the actuator. In this manner, the element connecting the motor and the actuator is a shaft and a piston at the same time. In addition, both concepts comprise the presence of a compensation container. Due to improved simplicity of design, the second concept has been chosen for further investigations.

Elements presented in Fig. 1 are supplemented with a power supply and a controller of the stepper motor. In addition, a metal bellow is located at the interface between the stepper motor and the driving actuator in order to create a proper connection between the shaft and the piston.

3 Modelling

As the concept of the unit has been chosen, its behaviour could have been also modelled. For this purpose, mathematical as well as simulation models have been developed and, on their basis, an analysis has been conducted.

First of all, a model comprising all necessary physical variables has been created as shown in Fig. 2.

In Fig. 2 x and y indicate linear motion of actuators; p_1 and p_2 stand for pressure of the hydraulic fluid inside the driving actuator and the executing actuator, respectively; V_{10} and V_{20} describe initial volumes of the actuators; E is the bulk modulus of the hydraulic fluid; S_1 describes the area of the piston of the driving actuator; S_2 and m_2 stand for area and mass of the piston of the executing actuator, respectively; c_2 and α represent viscous damping coefficient and Coulomb damping ratio between the piston and the cylinder of the executing actuator, respectively; k describes capacity of the hydraulic tube, k_2—stiffness of the spring inside the executing actuator, while F indicates external force.

In the next step of modelling, a mathematical model of the unit has been created, consisting of three differential Eq. (1), based on the information provided in Fig. 2. Two of these equations are related to the hydraulic balance in the system, i.e. the first equation of (1) describes the output of the driving actuator while the second represents the input to the executing actuator. The last equation of (1) gives information concerning the force balance in the second actuator.

$$\begin{aligned}\left(\frac{V_{10}}{E}-\frac{S_1}{E}x\right)\dot{p}_1 &= S_1\dot{x}+k(p_1-p_2),\\ \left(\frac{V_{20}}{E}+\frac{S_2}{E}y\right)\dot{p}_2 &= -S_2\dot{y}+k(p_1-p_2),\\ m_2\ddot{y}+c_2\dot{y}+k_2y &= S_2p_2-\alpha S_2p_2\mathrm{sgn}\dot{y}-F,\end{aligned} \tag{1}$$

where meaning of the symbols follows the description provided below Fig. 2.

Having the mathematical model, a simulation model could have been developed. For this purpose, Matlab Simulink environment has been employed.

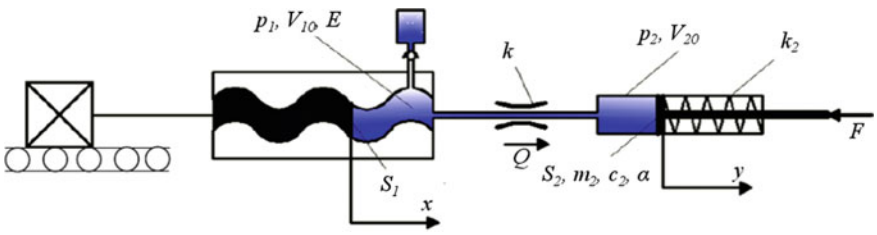

Fig. 2 Physical variables describing the considered unit [10]

The simulation has been performed for the first second of operation of the unit ($\tau = 1$ s). Velocity of the first actuator ($\dot{x}$) has been used as an exciting factor having the most significant influence on the mathematical model. It has been chosen as a sinusoidal signal $\dot{x} = 0.01 + 0.005 \sin(1000\, t)$ m/s. The areas of both pistons and initial volumes of the actuators have been chosen to be identical ($S_1 = S_2 = 201 \times 10^{-6}$ m^2, $V_{10} = V_{20} = 7.6 \times 10^{-12}$ m^3) in simulations in order to illustrate simultaneous operation of the actuators in a more convenient way. Capacity of the tube has been found with the employment of the Hagen–Poiseuille equation and equals to 7.9×10^{-12} m^4 s/kg. Other fixed parameters are: $m_2 = 0.03$ kg, $c_2 = 117.3$ N s/m, $k_2 = 195$ N/m, $E = 1.4 \times 10^9$ Pa, $\alpha = 0.1$. External force acting on the executing actuator $F = 10$ N. Simulation results are depicted in Figs. 3, 4, 5, 6 and 7.

What should be emphasized, an assumption regarding the driving actuator has been made while creating the mathematical model, i.e. resistance of the piston and the guideway against motion is assumed to be compensated by appropriate power of the stepper motor.

The difference between pistons position at the end of the simulation is at the level of c.a. 0.03 mm, as shown in Fig. 4. Such a value can be treated as almost negligible and stands for good correlation between actuators movement.

Figure 5 indicates that velocity of the piston of the executing actuator undergoes rapid changes in the initial part of the simulation (close-up of this part of the plot can be found in Fig. 6) and when external load F is applied. However, the curve reaches its final, stable trajectory within less than 0.005 s. Velocities are shifted in phase by 0.001 s.

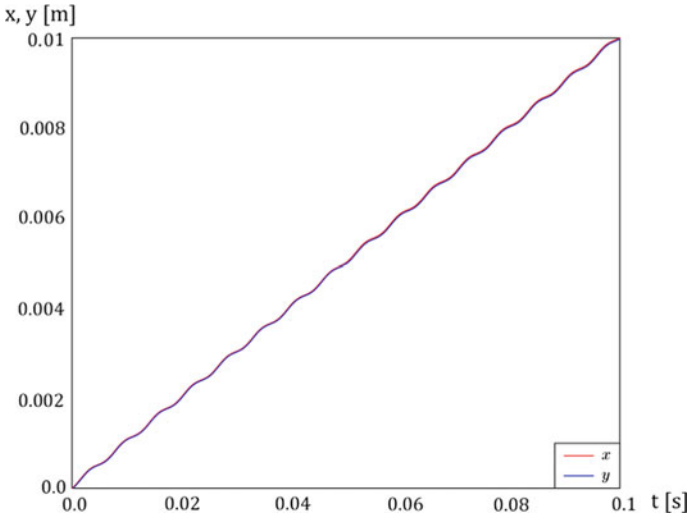

Fig. 3 Time versus position of the driving actuator piston (x) and the executing actuator piston (y)

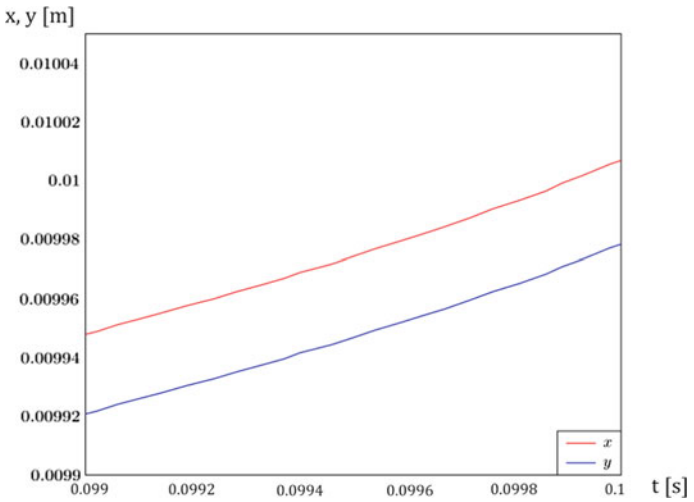

Fig. 4 Time versus position of the driving actuator piston (x) and the executing actuator piston (y) in the final part of the simulation

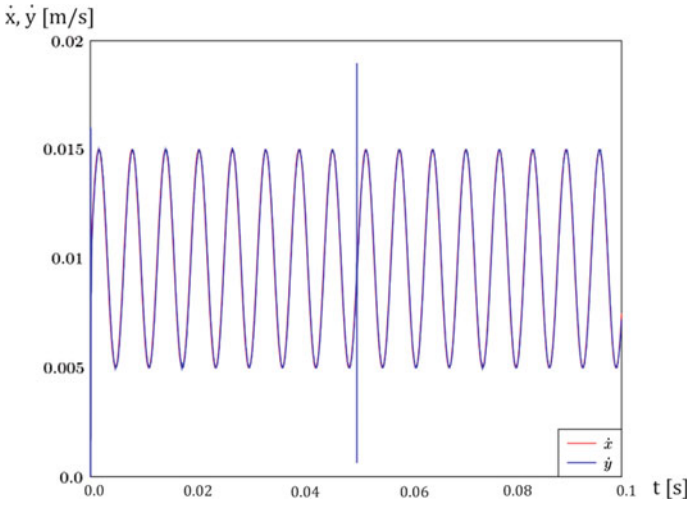

Fig. 5 Time versus velocity of the driving actuator piston ($\dot{x}$) and the executing actuator piston ($\dot{y}$)

As it can be noticed by looking at Fig. 7, pressure in the first actuator is higher than the one in the second actuator. Rapid increase in pressure is observed twice, i.e. when the driving actuator begins to operate and when the external load F is applied. In the latter case, pressure inside the unit raises by 0.3 MPa. Thus, velocity of the piston of the second actuator can be stabilised.

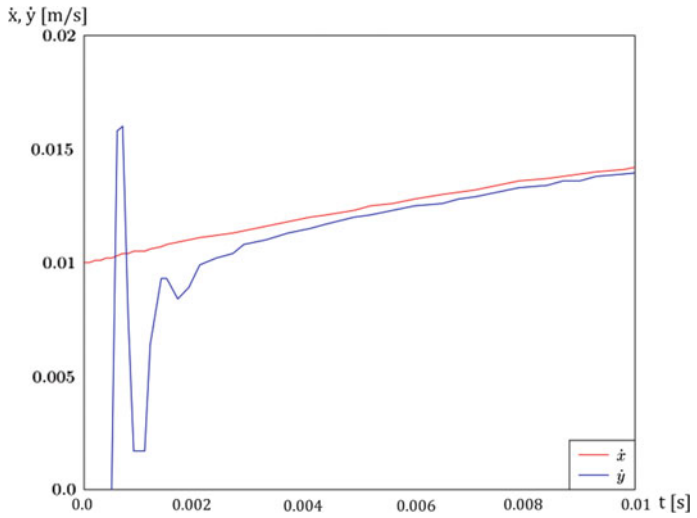

Fig. 6 Time versus velocity of the driving actuator piston ($\dot{x}$) and the executing actuator piston ($\dot{y}$) in the initial part of the simulation (0.01 s)

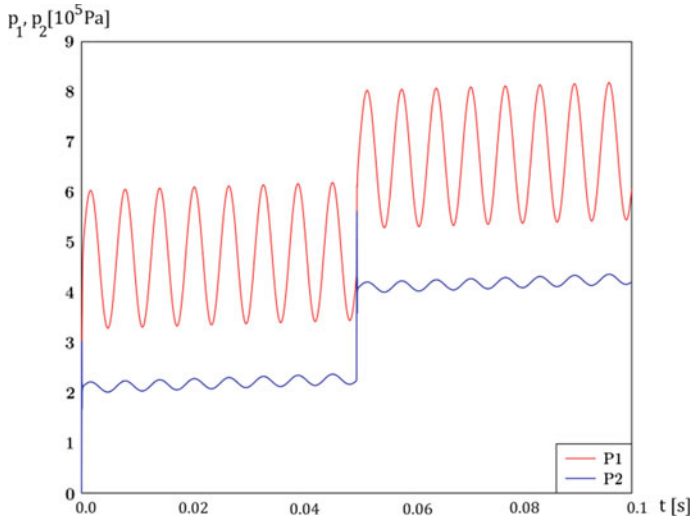

Fig. 7 Time versus pressure of the hydraulic fluid inside the driving actuator piston (p_1) and the executing actuator piston (p_2)

Furthermore, for the purpose of future analysis, transformation of Eq. (1) can be conducted in a manner as follows. Assuming dimensionless: time $\tau = t/\sqrt{\frac{m_2}{k_2}}$, positions $X = \frac{S_1}{V_{10}}x$, $Y = \frac{S_1}{V_{10}}y$, and pressures $P_1 = \frac{p_1}{E}$, $P_2 = \frac{p_2}{E}$ as well as dimensionless

parameters: $\beta = \frac{S_2 V_{10}}{S_1 V_{20}}$, $a_1 = \sqrt{\frac{m_2}{k_2}}\frac{kE}{V_{10}}$, $a_2 = \sqrt{\frac{m_2}{k_2}}\frac{kE}{V_{20}}$, $d = c_2\sqrt{\frac{1}{m_2 k_2}}$, $g = \frac{S_1 S_2 E}{k_2 V_{10}}$, α (as given before) and functions: $\operatorname{sgn}\left(\frac{V_{10}}{S_1}\sqrt{\frac{m_2}{k_2}}\dot{Y}\right) = \operatorname{Sgn}\dot{Y}$, $\frac{S_1}{k_2 V_{10}}F_2\left(\sqrt{\frac{m_2}{k_2}}\tau\right) = f(\tau)$, the counterpart dimensionless form of Eq. (1) is as follows:

$$\begin{aligned}(1-X)\dot{P}_1 &= \dot{X} + a_1(P_1 - P_2),\\ (1+\beta Y)\dot{P}_2 &= -\beta\dot{Y} + a_2(P_1 - P_2),\\ \ddot{Y} + d\dot{Y} + Y &= gP_2 - \alpha g P_2 \operatorname{Sgn}\dot{Y} - f_2(\tau).\end{aligned} \tag{2}$$

Eventually, the system depending on 10 parameters is reduced to the one depending on only 6 parameters. In both dimensional and dimensionless forms one function is also present, i.e. $F(t)$ and $f(\tau)$, respectively.

4 The Prototype

To study real behaviour of the developed unit converting rotational motion into linear one and compare the results with the outcome of modelling, a prototype has been created. For this purpose, a driving actuator has been manufactured according to the drawing depicted in Fig. 8 and connected to a ready-made hydraulic executive actuator.

The actuator can be tested in two variants, i.e. in the configuration shown in the above figure, corresponding to the concept being under consideration as well as in the configuration supplemented with additional elements used to provide better sealing of the actuator (see Fig. 9). In the first variant the sealing is assumed to result from tight fit of threads of both the piston and the cylinder.

As far as the configuration presented in Fig. 9 is considered, the principle of its operation is as follows. Motion of the threaded piston into the cylinder induces

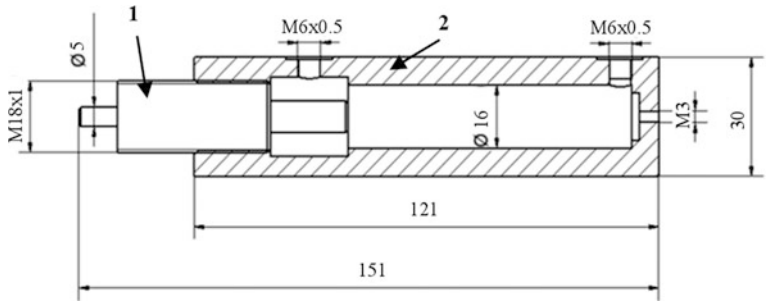

Fig. 8 Schematic diagram of the driving actuator. *1* Piston, *2* cylinder [10]

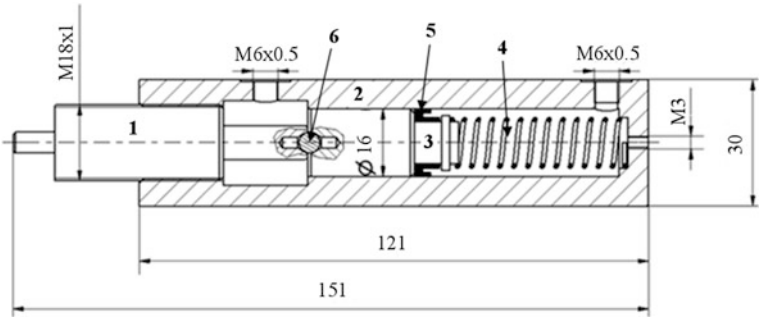

Fig. 9 Schematic diagram of the driving actuator in the second configuration. *1* Threaded piston, *2* cylinder, *3* intermediate piston, *4* spring, *5* seal, *6* metal ball [10]

motion of the intermediate piston which accompanied by a lip seal (or, in other words, radial shaft seal). The spring facilitates backwards motion of the intermediate piston during its withdrawal while the role of the metal ball is to reduce friction between pistons. The cylinder is manufactured of bronze due to low ratio of friction between the bronze cylinder and steel pistons. The prototype of the unit, including the abovementioned actuator, is shown in Fig. 10.

Experiments conducted with the use of both configurations of the driving actuator have shown that the first variant (Fig. 8) does not provide satisfactory fit of the internal thread of the cylinder and the external thread of the piston. As a result, hydraulic oil has leaked out of the actuator, what is the reason why further functional tests have been conducted for the configuration comprising additional internal elements (Fig. 9).

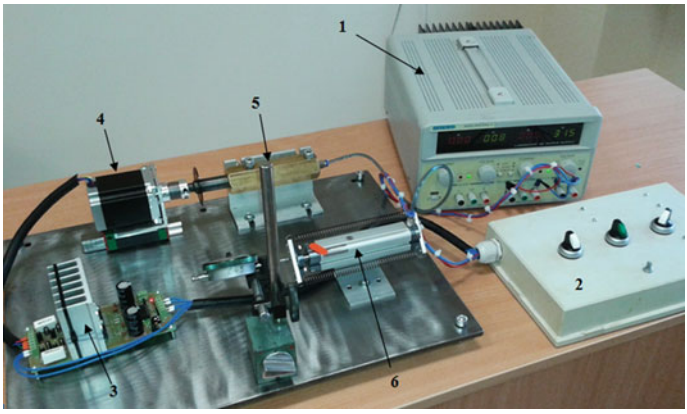

Fig. 10 The prototype of the hydraulic unit converting rotational motion into linear one. *1* Power supply, *2* stepper motor control panel, *3* driver of the stepper motor, *4* stepper motor on a roller guideway, *5* driving actuator, *6* executing actuator [10]

5 Testing

5.1 Unit Precision Test

To test the precision of conversion of rotational motion into linear one a scale wheel has been mounted to the shaft linking the stepper motor with the driving actuator (or, in other words, to the threaded piston of the driving actuator), see Fig. 11. In addition, a dial gauge has been installed on the surface of the piston of the executing actuator. Investigation of rotation of the scale wheel was facilitated by means of video capture and checking the recording frame by frame.

Conducted tests have shown that, for 1 mm thread pitch of the piston, one rotation of the stepper motor's rotor corresponds to the displacement of the executive actuator piston by 1 mm. The difference between positions of actuators has not exceeded 0.03 mm, what coincides with the results of numerical simulation.

5.2 Stiffness Test

Stiffness of the developed unit has been tested by means of applying external load to the piston of the executing actuator and measuring response of the unit with the use of a dynamometer. To measure displacement of the piston the dial gauge has been employed.

Response of the piston to the load of 10 N was equal to 0.01 m. Further increase in the acting force by 10 N has resulted in displacement of the piston by another 0.01 m. On the basis of these results the stiffness of the unit has been found which equals to $k = 1 \times 10^6 \left(\frac{\mathrm{N}}{\mathrm{m}}\right)$.

Apart from the conducted tests, further evaluation regarding response of the device to different load is supposed to be conducted.

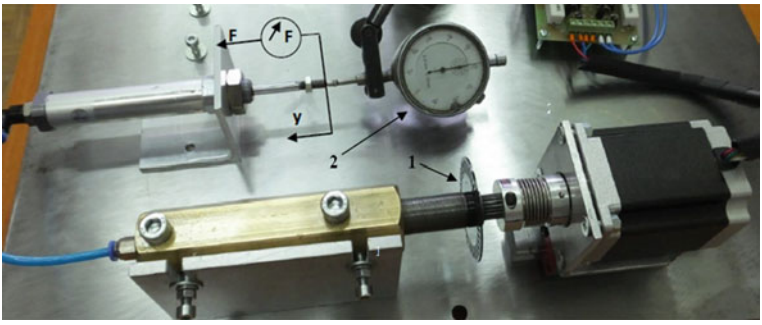

Fig. 11 Setup for precision test including a scale wheel (*1*) and a dial gauge (*2*)

6 Conclusions

Design of a hydraulically driven unit converting rotational motion into linear motion has been developed. Behaviour of the device has been modelled. A prototype has been constructed and experimentally evaluated. The first tests have given promising results regarding both precision and stiffness of the device. As far as the former is considered, the outcome also coincides with results of numerical simulation.

After implementation of further amendments, the device can be potentially used to drive hand prostheses, surgical manipulators or industrial manipulators. The design of the unit allows to place the driving actuator at a desired distance to the executing actuator, i.e. they can be separated in a way the driving actuator is placed outside the patient's body while the executing actuator—inside. The device can be also used in industrial manipulators, ensuring high stiffness and precision.

In future work, it is necessary to conduct tests evaluating the correctness of the positioning following a series of runs with different values of applied load. In addition, the variant of the prototype including driving actuator without any additional internal elements should be amended by means of tightening the thread at the interface between the piston and the cylinder. To reduce leakage to the minimum, the fissure between these threads should be less than 5 μm. Operation of the unit, in which the corrected actuator will be used, should be also tested.

Furthermore, to implement the unit in the medical equipment, material of which the actuators are manufactured should be changed to, e.g. surgical steel that can be used in direct contact with body fluids. Hydraulic oil should be replaced with some fluid that will not do harm to the patient in case of leakage—saline can be used for this purpose. However, it should be mentioned that, due to different bulk modulus, the stiffness of the unit will be changed, and thus tests of the device should be repeated. Last but not least, the unit must have its size changed (minimised) in order to use it for medical purposes—this conclusion applies in particular in the case of applying the unit to manipulate fingers of hand prostheses.

Acknowledgments The work has been supported by the National Science Centre of Poland under the grant OPUS 9 No. 2015/17/B/ST8/01700 for years 2016–2018.

References

1. Norton, K.M.: A brief history of prosthetics. InMotion **17**(7), 11–13 (2007)
2. Yang, J., Pitarch, E.P., Abdel-Malek, K., Patrick, A., Lindkvist, L.: A multi-fingered hand prosthesis. Mech. Mach. Theory **39**(6), 555–581 (2004)
3. Jacobsen, S., Iversen, E., Knutti, D., Johnson, R., Biggers, K.: Design of the Utah/M.I.T. dextrous hand. In: Proceedings of the IEEE International Conference on Robotics and Automation, San Francisco April 1986, vol. 3, pp. 1520–1532 (1986)
4. Salisbury, K.: Kinematic and force analysis of articulated hands. Dissertation, Stanford University (1982)

5. Townsend, W.: The BarrettHand grasper—programmably flexible part handling and assembly. Ind Robot **10**(3), 181–188 (2000)
6. Handle Project Website (2009). http://www.handle-project.eu. Accessed 20 Jan 2016
7. Gaiser, I.N., Pylatiuk, C., Schulz, S., Kargov, A., Oberle, R., Werner, T.: The Fluidhand III: a multifunctional prosthetic hand. J. Prosthet. Orthot. **21**(2), 1–6 (2009)
8. Touch Bionics Inc. Website (2016). http://www.touchbionics.com/products/how-i-limb-works. Accessed 16 Jan 2016
9. Smit, G., Plettenburg, D.H., van der Helm, F.C.T.: The lightweight Delft Cylinder Hand: first multi-articulating hand that meets the basic under requirements. IEEE Trans. Neural Syst. Rehabil. Eng. **23**(23), 431–440 (2014)
10. Szymkiewicz, G., Szymanowska, O., Lewandowski, D., Awrejcewicz, J.: Hydraulic unit of rotation into linear motion conversion—design, model, construction and testing. In: Awrejcewicz, J., Kazmierczak, M., Mrozowski, J., Olejnik, P. (eds.) Dynamical Systems—Mechatronics and Life Sciences, pp. 493–502. TUL Press, Lodz (2015)

The Recognition of Human by the Dynamic Determinants of the Gait with Use of ANN

Tomasz Walczak, Jakub Krzysztof Grabski, Magdalena Cieślak and Martyna Michałowska

Abstract In this paper human recognition method is based on dynamic parameters of the human gait. In the method the artificial neural network algorithm is employed. Some parameters of the gait are defined in order to describe and recognize characteristics of gait for each considered individual. In classical approach to human recognition, description of the gait pattern is based on sequence of images analysis and biometric parameters. In this paper we present method based on determining some dynamic characteristics of the gait, which together with other kinematic determinants should allow to describe the unique gait pattern for each individual. Necessary data were obtained from system of motion analysis BTS and force plates, commonly used in biomechanics. All considered gait parameters were calculated from data which were obtained for 15 persons with different characteristic of the gait. To implement the recognition process the back-propagation neural network algorithm was used. In the paper three configurations of the input data (only kinematic parameters from the BTS system, only dynamic parameters from the force plates and both types of parameters together) are investigated and compared.

T. Walczak (✉) · J.K. Grabski · M. Cieślak · M. Michałowska
Institute of Applied Mechanics, Poznan University of Technology,
ul. Jana Pawła 24, 60-965 Poznań, Poland
e-mail: tomasz.walczak@put.poznan.pl

J.K. Grabski
e-mail: jakub.grabski@put.poznan.pl

M. Cieślak
e-mail: grajmag@gmail.com

M. Michałowska
e-mail: martyna.michalowskaa@gmail.com

J. Awrejcewicz (ed.), *Dynamical Systems: Modelling*, Springer Proceedings in Mathematics & Statistics 181, DOI 10.1007/978-3-319-42402-6_30

1 Introduction

The gait is defined as the coordinated, cyclic combination of movements that result in human locomotion [6]. Healthy human gait is a periodic motion. The movements of each leg are repeated in each gait cycle in the same way. Thus the human gait has a pattern of movements which can be characteristic for each individual. In similar way, other kind of motions like running, jogging or climbing stairs can be described. Moreover, human motion analysis has many challenging issues, because of the difficulties occurring in description process of the structure of the human body. Human gait is also known to be one of the most universal and complex from all human activities. For that reason, the study of human gait has been increased extensive interests in various fields such as clinical analysis, biomechanics, robotics, and biometrics [2, 6, 13, 16, 21].

Mathematic description of human gait usually consists of kinetic or kinematic parameters, which are obtained from simple mechanical models. In those models the body's segments are assumed as pendulums and are characterized by simple harmonic motion. One should notice that those parameters could describe some gait patterns and it was observed that, each individual appears to have different and unique characteristics of gait. It implies a possibility to identify person on the base of its own gait [10, 11, 16]. It could be also useful in identifying of improper or pathological gaits.

In this paper presented approach for recognizing humans by their gait is based on using artificial neural network (ANN). The application of the ANN in biomechanics and gait analysis has received a quite extensive attention over the years in the literature. There are two comprehensive review articles on this topics [4, 14]. However the authors of the paper highlighted some new and important papers in this area. Barton and Lees applied the ANN for distinguishing patterns on the basis of hip-knee joint angle diagrams [3]. The main advantage of the ANN application in this case was that it combine quantitative and qualitative information from the diagrams. The presented ANN classified human gait into three categories: normal walking, simulation of leg length difference and simulation of leg weight asymmetry. Su and Wu used the genetic artificial neural network (GANN) for gait pattern recognition [17]. In this paper the GANN and the ANN were compared for classification problem of the gait patterns of patients with ankle arthrodesis and normal subjects. The authors used parameters of the reaction forces as inputs for the ANN and the GANN. In conclusions they suggested that the GANN is more suitable than the ANN to exploit the patient's gait pattern. The comparison of gait analysis using the ANN on the basis of time discrete or time continuous data sets was performed by Schöllhorn et al. [15]. They concluded that time continuous approach using the ANN is an effective tool for identifying subject and group specific locomotion characteristics. Hahn et al. [5] used the ANN for mapping gait measurements onto motion of whole body center of mass (COM) in the frontal plane. Alaqtash et al. [1] applied the ANN to distinguish between healthy, cerebral palsy, and sclerosis subjects. As the inputs for the ANN the authors used different

parameters obtained from three components of the GRF (mediolateral, anterio-posterior and vertical). In the paper the ANN classifier was compared with the nearest neighbor classifier (NNC). The results obtained by the authors show the same range of classification accuracy both for the NNC and the ANN. Application of the ANN for classification of knee osteoarthritis was presented by McBridge et al. [8]. The authors used kinetic and kinematic features for each leg (including ankle angle, ankle angular velocity, hip angle, hip angular velocity, and ground reaction force). The presented results show strong correlation between gait kinetics and joint deterioration and level of pain in osteoarthritis individuals. Michalski et al. [9] analyzed individual human gait symmetry based on vertical component of ground reaction force. The authors compared gait classification in female and male groups by means of the ANN and the authors' own quantitative index. The results of this study can be helpful for determination of ranges of physiological gait asymmetry. The comparison of two different classifiers, namely, the ANN and the support vector machine (SVM), for identification of patients with Parkinson disease was performed by Tahir and Manap [19]. The authors concluded that the SVM as classifier performed better as compared to the ANN. The human gait parameters are categorized in three groups: spatiotemporal, kinematic and kinetic. The results presented in the paper show that the basic spatiotemporal parameters as the inputs to classifier give better results both for the ANN and the SVM. Oh et al. [12] applied successfully the ANN to estimate ground reaction forces based on kinematics parameters. However the authors highlighted that the study of ground reaction forced estimation was performed only for normal gait. Thus it would be valuable to perform this study also for pathological gait.

Another problem is human recognition which in the literature is performed on the base of parameters obtained from human motion images. Application of the ANN for human gait recognition was presented for example by Yoo et al. [20] The input data come from 10 features extracted from images. The results obtained by the authors present high gait recognition performance. Tafazzoli and Safabakhsh [18] employed the NNC for this purpose. The parameters which were the inputs to the classifier were calculated from the human motion images. The authors computed the parameters based on the rotation variation of three articulated parts of the body: hip, knee, and arm. The presented results show promising performance in comparison to other similar methods of human gait recognition. Lee et al. [7] used the parallel genetic algorithm in combination with the selective neural network ensemble to improve gait recognition based on the features acquired from the images. The presented experimental results show that the performance of the proposed algorithm is much higher than for other gait recognition methods available in the literature. To the best knowledge of the authors there are not published works in which for human recognition problem the ANN with biomechanical data (ground reaction forces, kinematic, and kinetic parameters) is employed.

In this study the authors proposed three research approaches to compare which one would give the best results in human recognition based on gait parameters. The input data come from biomechanical measurements. These three approaches which are presented in the paper differ in the kind of data used to teach ANN. The first one

involves teaching ANN with use only of the parameters derived from GRF. In the second approach the authors used only these parameters that were derived from data form motion capture system. The last one approach involves a combination of earlier studies—ANN has been taught based on two earlier used kind of parameters. As a result the authors will present comparison of root mean square errors (RMSE) for each proposed way of learning.

2 Research Methods

Fifteen volunteers took part in this study, seven females, and eight males, in the Biomechanical Laboratory at Poznan University of Technology. Average ± SD values and ranges (min ÷ max) for selected characteristics of women amounted to:

- Age: 24 ± 3.9 (21 ÷ 33) years
- Height: 168.6 ± 3.8 (165 ÷ 176) cm
- Body mass: 60.1 ± 6.9 (54.6 ÷ 76) kg.

Male subjects information:

- Age: 25 ± 9.9 (18 ÷ 51) years
- Height: 181.6 ± 3.9 (176 ÷ 190) cm
- Body mass: 83.3 ± 14 (69 ÷ 113) kg.

The group comprised the subjects who did not suffer from any lower extremity pain or musculoskeletal disorders. Participants were asked to walk barefoot with self-chosen velocity and step frequency through 10-m-long walkway with two built in dynamometric platforms, monitored by six IR cameras. During this study subject was asked to step one foot on the one platform (always in the same configuration to differentiate left and right foot) to record ground reaction forces during one cycle of walk. Three-dimensional GRF were measured by AMTI BP400600 force plates (600 × 400 × 82.5 mm) with the 400 Hz sampling rate.

Prior to data collection eleven reflective spherical markers (five on the both side) were attached at eleven anatomical landmarks: sacrum, above greater trochanter, in the middle of knee (lateral side), heel, ankle, big toe (according to the previously prepared model). All markers, were placed in three-dimensional space with coordinates in the middle of walkway, between two force plates. The motion was repeated at least one hundred times and recordings that did not meet the requirements were rejected. The requirements applied to continuity of the data. If at least one recorded point was disappearing in the space for so long time, that there was no possibility to approximate the trajectory of this point in the right way, the recording was rejected. Kinematic data (position of the anatomical landmarks in 3D space) were collected by six IR cameras by the BTS Smart DX system at a sampling rate of 100 Hz (resolution 1400 × 1000px). Both signals, from dynamic and kinematic data, were recorded simultaneously, directly to the computer with SMART Capture

software. Afterwards, recorded 3D points were ascribed to the previously prepared model. Then all recorded trajectories of the markers were approximated, to avoid discontinuity of the data.

3 Indicators of the Human Gait

In this study authors proposed a set of the indicators, which were calculated for each person, based on data collected in way described previously. These parameters were divided into two groups according to the source data. First group contains parameters calculated from GRF (dynamic indicators), the second is based on position of the markers in 3D space recorded by motion capture system (kinematic indicators).

3.1 Dynamic Parameters

First considered group of indicators taken into consideration to describe gait patterns, contains the parameters obtained from forces characteristics measured by dynamometric platforms. One could observe that the force with which any individual is acting on the floor during the gait, has unique character. Generally, vertical component of this force has always two local maxima and one minimum, what is presented in the Fig. 1.

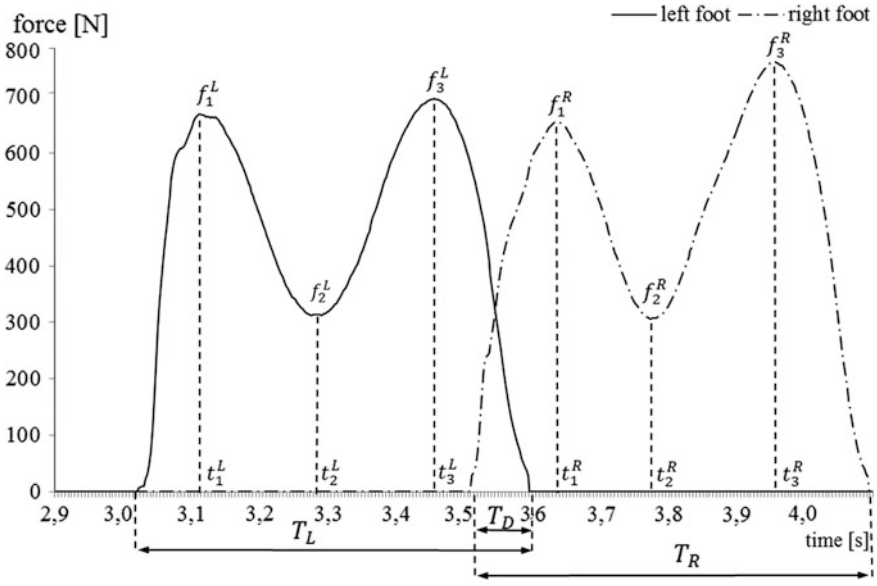

Fig. 1 Vertical components of ground reaction forces with parameters

To describe the characteristic shape of considered curves as accurate as it is possible, we have proposed a list of different parameters calculated for both legs in the time and force domain. One should also noticed, that all obtained data were firstly normalized by weight of each individual.

Vertical force parameters

- maxima of loading response phase for both feet f_1^L, f_1^R,
- minima of midstance phase for both feet f_2^L, f_2^R,
- maxima of terminal stance phase for both feet f_3^L, f_3^R,
- $f_1^L/f_2^L, f_1^L/f_3^L, f_3^L/f_2^L$ and $f_1^R/f_2^R, f_1^R/f_3^R, f_3^R/f_2^R$ ratios,
- the areas determined between curves and time axis for three gait phases: from start to maximum of loading response, between maxima and from maximum of terminal phase to the end of stance phase: $p_1^L, p_2^L, p_3^L, p_1^R, p_2^R, p_3^R$ respectively,
- the ratios of those areas $p_1/p_2, p_2/p_3$ calculated for both legs,
- coordinates of the geometrical curve center for both feet,
- number of inflection points (artifacts) occurring on the both curves, determined on the curve characteristic sections bounded by times t_1, t_2, t_3 with the curve smoothing factor $s = 10^{-6}$,
- height of artifact on the rising edge—AR_H. The maximum vertical distance analyzed curve and theoretical, smoothed curve with curve smoothing factor $s = 10^{-1}$.
- width of artifact on the rising edge—AR_W. The time interval in which there are inflection points on the curve, with curve smoothing factor $s = 10^{-1}$,
- artifact index on the rising edge—AR_T. Time of occurring the maximum height.
- artifact width and index on the falling edge—AF_W, AF_T,
- curve steepness (S) between maxima defined by the formulae:

$$S = \frac{\sum_{i=1}^{n} |y_i - y_{i+2}|}{n},$$

where n is number of samples. For time parameters we have chosen characteristic times when occurred the local maxima and minima and duration times of gait phases.

Time parameters

- times of contact with floor of both feet T_L, T_R,
- time of gait cycle T,
- occurrence times of characteristic vertical force parameters: $t_1^L, t_2^L, t_3^L, t_1^R, t_2^R, t_3^R$,
- duration times measured for both feet in stance phase: $t_2^L - t_1^L, t_3^L - t_1^L, t_2^R - t_1^R, t_3^R - t_1^R$,
- duration of double support phase: $T_D = T_R + T_L - T$.

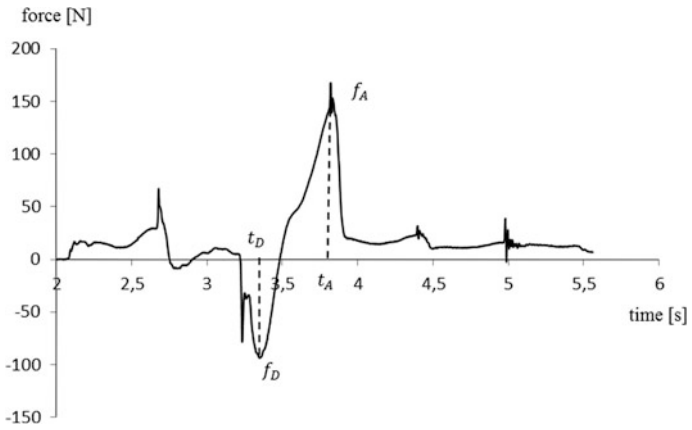

Fig. 2 Anterior-posterior component of ground reaction force with parameters

From the biomechanical point of view, the anterior-posterior component of considered force is also important and it is often taken into account by many researchers during the gait analysis. The example of curve representing this component is presented in the Fig. 2.

One should observe, that this curve is not as smooth as the vertical component. Only regularities that are characterized this kind of curves, could be described as occurring one visible minimum and one maximum (signed in the Fig. 2).

Anterior-posterior force parameters

- maximum of acceleration force f_A^L, f_A^R, and minimum of braking force f_D^L, f_D^R, measured for both feet (Fig. 3).

Time parameters

- time of occurrence of the maximum of acceleration force t_A^L, t_A^R, measured for both feet,
- time of occurrence of minimum of braking force t_D^L, t_D^R, measured for both feet.

The total number of considered dynamic parameters that have been used in recognition processes was 32 for each leg. Interesting fact observed during the registration of data process was, that the values of considered dynamic parameters could be completely different for different registration of the gait of the same individual. One can conclude that the reason of occurrence of such varied values is strongly dependence on gait speed. To improve accuracy of the recognition and to test more classical approach to the gait description we have also defined some kinematic indicators.

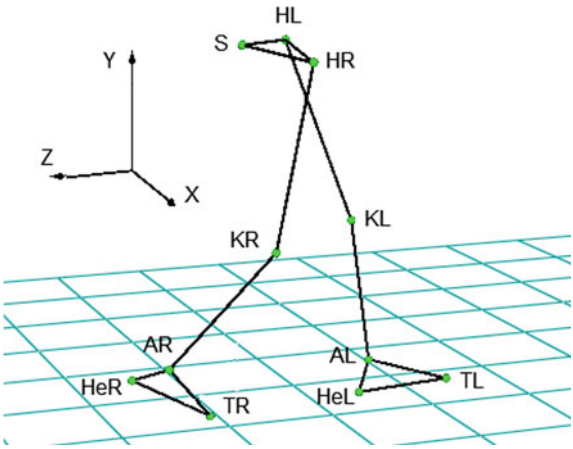

Fig. 3 Anatomical landmarks listed in considered human gait model

3.2 Kinematic Parameters

Human gait observation convinces us that every person characterizes peculiar way of moving. Sometimes it is feature connected with pelvis motility and sometimes it is the way of putting the foot on the floor. Authors of this study tried to describe these phenomenon as mathematical values named kinematic indicators. As a model in indicators inventing served common used in human biomechanics determinants of gait. All descriptions of proposed indicators listed below are based on designations in the Fig. 3.

The aforementioned kinematic parameters proposed by the authors are:

- velocity—time derivative of the Z coordinate of the S point [km/h] (medium value),
- ankles lift height—the maximum difference between Y coordinates, separately for the AR and AL point (right and left ankle),
- knees lift height—the maximum difference between Y coordinates, separately for the KR and KL point (right and left knee),
- sacrum (S) lift height—the maximum difference between Y coordinates of the point S,
- hips lift height—the maximum difference between Y coordinates, separately of the HR and HL points (right and left hip),
- an angle between feet—maximum, minimum and medium angle between line crossing TR, HeR points and line crossing TL, HeL points in XZ plane,
- an angle between knees—maximum, minimum and medium angle between line crossing KR, HR points and line crossing KL, HL points in XY plane.
- dorsiflexion of the foot - maximum, minimum and medium angle between line connecting toe (TL or TR) with heel (HeL or HeR) and line connecting knee (KL or KR) with ankle (AL or AR)—separately for the right and the left leg; in YZ plane,

- knee angle—maximum and minimum angle between HR, KR, AR points and separately for HL, KL and AL points; in YZ plane,
- maximum modulus of the angular velocity between feet and shank. The derivative of the eighth parameter (maximum modulus of time derivative of the angle KR, AR, TR and KL, AL, TL),
- maximum modulus of the angular velocity between shank and thigh. The derivative of the ninth parameter (maximum modulus of time derivative of the angle HR, KR, AR and HL, KL, AL),
- pelvic rotation—maximum angle between line crossing left and right hip (HR, HL) and the line crossing the S point, parallel to the X axis; XZ plane,
- lateral movement of the pelvis—maximum and minimum cute angle between line crossing left and right hip (HR, HL) and the line parallel to the Z axis,
- pelvic tilt—maximum angle between line crossing left and right hip (HR, HL) and the line parallel to the Y axis.

Total number of kinematic indicators used to describe gait patterns was 38. It should also be mentioned that one can choose much more kinematic parameters to describe gait. Some additional ones, could be based on positions of the head, the left and right shoulder or C7 (last cervical vertebrae), what should guaranteed recognition by, for example, unconventional head movement during the gait. In this paper we concentrate only on the characteristic kinematic parameters of lower limbs of human body.

4 Results and Conclusions

To examine the possibility of recognizing human by their gait, three neural networks were built in standard Matlab NN toolbox. First network was build only for dynamic parameters, where input vector has size of 33. One additional input was used to signed, for which leg the input vector contains data. It allow as to reduce the size of ANN. Two-layered perceptron was used, with 15 neurons included in hidden layer and 15 in output layer, where every output is connected with one considered individual. In similar way second network used for recognition just by kinematic parameters was built. Only difference was the size of the input vector—in that case was 38 with no additional input to mark a leg. The third considered ANN contained 102 inputs (both kinematic and dynamic indicators) with 18 neurons in hidden layer. It should be mentioned that in all cases the neural activation function was defined as '*tansig*' for hidden layer and '*purelin*' for output layer. The Levenberg–Marquardt algorithm was used in the learning process, where half of collected data were used. What is obviously, learning time was the longest in the case of third network, however all networks were learned with relatively small value of error.

Recognition tests were done for all recorded data unused in learning process. There were checked the networks responses for input data for all examined 15 persons, where proper answer for every output was either 0 or 1. Then, the root-mean-square errors (RMSE) of the recognition measured for three defined neural networks were calculated (presented in Table 1).

Analyzing data included in Table 1, one can conclude that in all three considered approaches it is possible to recognize person with relatively small recognition error. The values of calculated RMSE for each person should also guarantee satisfactory results and good accuracy of recognition for other individuals. If we take into consideration fact that maximum proper value of output in any case is 1, we can conclude that average recognition error is less than one percent in the case of ANN based on only dynamic parameters and in the ANN containing all of the parameters. One can observe that worst results were obtained in the case of recognition only by kinematic parameters. This was expected because the kinematic data need to be smoothed and they are strongly depend on measurement conditions. However the first tested approach, where only dynamic parameters were used to recognition of human gait was surprising. For almost all persons (excluding persons 5, 6, and 8), network based on dynamic indicators leads to the best results of the recognition. The RMSE of human recognition is very small and it leads to conclusion, that the level of human recognition based on the data obtained from dynamometric plates and the ANN with use of parameters proposed in this paper is very high. Proposed method of gaits description and its recognition could be also used and it should be helpful in clinical practices.

Table 1 Result of recognitions: RMSE calculated for each person in three considered approaches

Person	RMSE of recognition with use of dynamic parameters	RMSE of recognition with use of kinematic parameters	RMSE of recognition with use of both dynamic and kinematic parameters
1	0.0041	0.0628	0.0110
2	0.0036	0.1791	0.0056
3	0.0028	0.0599	0.0039
4	0.0028	0.0715	0.0094
5	0.0060	0.0363	0.0055
6	0.0069	0.0680	0.0046
7	0.0071	0.0452	0.0286
8	0.0044	0.0197	0.0002
9	0.0037	0.0535	0.0060
10	0.0071	0.1113	0.0171
11	0.0050	0.0452	0.0319
12	0.0042	0.0506	0.0063
13	0.0058	0.0800	0.0078
14	0.0039	0.0552	0.0169
15	0.0028	0.0557	0.0042

References

1. Alaqtash, M., Sarkodie-Gyan, T., Yu, H., Fuentes, O., Brower, R., Abdelgawad, A.: Automatic classification of pathological gait pattern using ground reaction forces and machine learning algorithms. In: Proceedings of the 33rd Annual International Conference of the IEEE EMBS, pp. 453–457 (2011)
2. Bartlett, R.: Artificial intelligence in sports biomechanics: new dawn or false hope? J. Sports Sci. Med. **5**(4), 474–479 (2006)
3. Barton, J.G., Lees, A.: An application of neural networks for distinguishing gait pattern on the basis of hip-knee joint angle diagrams. Gait Posture **5**(1), 28–33 (1997)
4. Chau, T.: A review of analytical techniques for gait data. Part 2: neural network and wavelet methods. Gait Posture **13**(2), 102–120 (2001)
5. Hahn, M.E., Farley, A.M., Lin, V., Chou, L.-S.: Neural network estimation of balance control during locomotion. J. Biomech. **38**(4), 717–724 (2005)
6. Inman, V.T., Ralston, H.J., Todd, F.: Human Walking. Williams & Wilkins (1981)
7. Lee, H., Lee, H., Kim, E.: A new gait recognition system based on hierarchical fair competition-based parallel genetic algorithm and selective neural network ensemble. Int. J. Control Autom. Syst. **12**(1), 202–207 (2014)
8. McBridge, J., Zhang, S., Wortley, M., Paquette, M., Klipple, G., Byrd, E., Baumgartner, L., Zhao, X.: Neural network analysis of gait biomechanical data for classification of knee osteoarthritis, Biomech. Sci. Eng. Conf. (BSEC) 1–4 (2011)
9. Michalski, R., Wit, A., Gajewski, J.: Use of artificial neural networks for assessing parameters of gait symmetry. Acta Bioeng. Biomech. **13**(4), 65–70
10. Narasimhulu, V.G., Jilani, S.A.K.: Back propagation neural network based gait recognition. Int. J. Comput. Sci. Inf. Technol. **3**(5), 5025–5030 (2012)
11. Nixon, M.S., Tan, T., Chellappa, R.: Human Identification based on Gait. Springer (2006)
12. Oh, S.E., Choi, A., Mun, J.H.: Prediction of ground reaction forces during gait based on kinematics and a neural network model. J. Biomech. **16**(14), 2372–2380 (2013)
13. Perl, J.: Artificial neural networks in motor control research. Clin. Biomech. **19**(9), 873–875 (2004)
14. Schöllhorn, W.I.: Application of artificial neural nets in clinical biomechanics. Clin. Biomech. **19**(9), 876–898 (2004)
15. Schöllhorn, W.I., Nigg, B.M., Stefanyshyn, D.J., Liu, W.: Identification of individual walking patterns using time descrete and time continuous data sets. Gait Posture **15**(2), 180–186 (2002)
16. Shukla, R., Shukla, R., Shukla, A., Sharma, S., Tiwari, N.: Gender identification in human gait using neural network. Int. J. Mod. Educ. Comput. Sci. **11**, 70–75 (2012)
17. Su, F-Ch., Wu, W.-L.: Design and testing of a genetic algorithm neural network in the assessment of gait patterns. Med. Eng. Phys. **22**(1), 67–74 (2000)
18. Tafazzoli, F., Safabakhsh, R.: Model-based human gait recognition using leg and arm movements. Eng. Appl. Artif. Intell. **23**(8), 1237–1246 (2010)
19. Tahir, N.M., Manap, H.H.: Parkinson disease gait classification based on machine learning approach. J. Appl. Sci. **12**(2), 180–185 (2012)
20. Xiao, Q.: A note on computational intelligence methods in biometrics. Int. J. Biometrics **4**(2), 180–188 (2012)
21. Yoo, J.-H., Hwang, D., Moon, K.-Y., Nixon, M.S.: Automated human recognition by gait using neural network. First Workshop on Image Processing Theory, Tools and Application, pp. 1–6 (2008)

Optimization of Micro-Jet Selective Cooling After Low Alloy Steel Welding

Tomasz Węgrzyn, Jan Piwnik, Aleksander Borek and Wojciech Tarasiuk

Abstract The paper focuses on low alloy steel after an innovative welding method with selective micro-jet cooling. Weld metal deposit (WMD) was carried out for MIG process with micro-jet cooling. This method is very promising mainly because of the high amount of acicular ferrite in low alloy steel WMD. That structure corresponds with high impact on the toughness of welds. Dynamical systems of micro-jet cooling just after welding can find application in automotive industry.

1 Introduction

Micro-jet technology gives the chance to obtain a weld that corresponds to a much better impact toughness of WMD compared with actual welding processes [1–5]. Generally speaking good mechanical properties of weld corresponds with low-nitrogen and low-oxygen processes. The amount of nitrogen and oxygen has a strong influence on the metallographic structure because of the influence on the acicular ferrite (AF) formation. The amount of AF must be treated as the most beneficial structure in low alloy steel WMD that directly corresponds with high

T. Węgrzyn gave a presentation of this paper during one of the conference sessions.

T. Węgrzyn (✉)
Transport Department, Technical University of Silesia, Gliwice, Poland
e-mail: tomasz.wegrzyn@polsl.pl

J. Piwnik · W. Tarasiuk
Mechanical Faculty, Bialystok University of Technology, Białystok, Poland
e-mail: j.piwnik@pb.edu.pl

W. Tarasiuk
e-mail: w.tarasiuk@pb.edu.pl

A. Borek
Plasma-System, Siemianowice Śląskie, Poland
e-mail: borek@systemsa.pl

J. Awrejcewicz (ed.), *Dynamical Systems: Modelling*, Springer Proceedings in Mathematics & Statistics 181, DOI 10.1007/978-3-319-42402-6_31

impact toughness of weld [6–8]. Acicular ferrite is formed with nonmetallic oxide inclusion contact inclusions of welds. In standard processes it is only possible to get maximum 50 % of AF in weld [9, 10]. Micro-jet cooling just after welding gives a new chance to increase the amount of AF in weld and consequently could affect the impact toughness of weld [11–15]. The micro-jet cooling was tested for low alloy steel with various micro-jet gases: argon, helium and nitrogen.

2 Aim and Plan of the Research

This paper aims to outline the micro-jet innovations in MIG welding process which represent steps ahead to achieve the following objective:

- a high amount of acicular ferrite in WMD,
- an increase in the impact toughness of WMD.

The weld metal deposit was prepared by welding by micro-jet cooling, with varied gases, and mixtures for MIG welding and dynamic micro-jet cooling process. To obtain various amounts of acicular ferrite in the weld, a welding process with a micro-jet injector was installed. The main parameters of micro-jet cooling were slightly varied:

- cooling steam diameter was varied twice (40 and 50 μm),
- number of cooling jets was varied twice (1 and 2),
- gas pressure was varied twice (0.4 MPa until 0.5 MPa),
- micro-jet gases were varied.

Figure 1 illustrates the assembly of the welding head with the micro-jet injector.

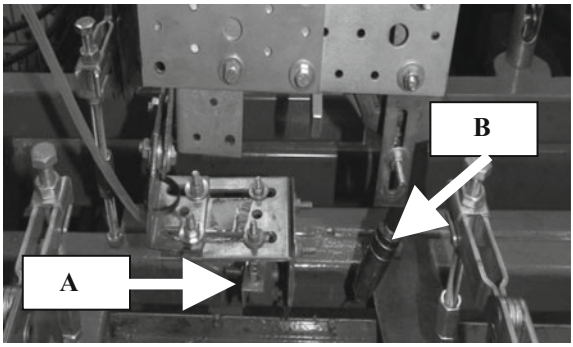

Fig. 1 Montage of welding head (*B*) and micro-jet injector (*A*) [4]

Table 1 Chemical composition of WMD without micro-jet cooling

Element	Amount
C	0.08 %
Mn	0.79 %
Si	0.39 %
P	0.017 %
S	0.018 %
O	380 ppm
N	50 ppm

3 Materials to Research

The basic material to research was S355J2G3 steel. Argon was chosen as the shielded gas for MIG welding. Micro-jet gases were varied (argon, nitrogen, helium, a gas mixture containing 79 % Ar and 21 % CO_2 and finally a gas mixture containing 90 % Ar and 10 % CO_2). A typical weld metal deposit has rather similar chemical composition in all tested cases, except for the amount of oxygen (Table 1).

4 Research and Discussion

Various welds of standard MIG welding process with and without micro-jet cooling were compared. Micro-jet gas has an influence on the intensive dynamic cooling conditions, but it does not have serious influence on chemical WMD composition. The oxygen amount in the WMD was counted only for the main micro-jet parameters:

- Diameter of micro-stream (40 μm),
- Number of jets (1),
- Gas pressure (0.4 and 0.5 MPa).

A typical weld metal deposit had rather similar chemical composition in all the tested cases, except for the amount of oxygen (Table 2).

For standard MIG welding, various amounts of oxygen in WMD were observed. It is easy to deduce that micro-jet cooling with gas mixtures after welding has a strong influence on the amount of oxygen in WMD. After chemical analyses, the metallographic structure analysis was carried out. The various amounts of acicular ferrite are shown in Table 3.

Tables 2 and 3 show that in all cases argon is the most beneficial micro-jet gas. Also, the experiment with a gas mixture of 90 % Ar and 10 % CO_2 can be understood to be a good choice. Helium must be taken as a very intensive cooling gas. Nitrogen as micro-jet gas could be considered as a wrong choice. In standard

Table 2 Oxygen and nitrogen in WMD after MIG welding with micro-jet cooling

Welding process	Diameter of micro-stream (μm)	Gas pressure (MPa)	Number of jets	Oxygen amount (ppm)
Without micro-jet cooling	–	–	0	380
He as micro-jet gas	40	0.4	1	375
Ar as micro-jet gas	40	0.4	1	375
N_2 as micro-jet gas	40	0.4	1	385
Gas mixture of (79 % Ar and 21 % CO_2)	40	0.4	1	530
Gas mixture of (90 % Ar and 10 % CO_2)	40	0.4	1	465
He as micro-jet gas	40	0.5	1	375
Ar as micro-jet gas	40	0.5	1	375
N_2 as micro-jet gas	40	0.5	1	385
Gas mixture of (79 % Ar and 21 % CO_2)	40	0.5	1	570
Gas mixture of (90 % Ar and 10 % CO_2)	40	0.5	1	485

Table 3 Acicular ferrite in WMD after welding with various micro-jet cooling

Micro-jet gas	Micro-jet gas pressure (MPa)	Micro-jet diameter (μm)	Ferrite AF (%)
–	–	–	55
He	0.4	40	60
He	0.5	40	61
Ar	0.4	40	71
Ar	0.5	40	73
N_2	0.4	40	53
N_2	0.5	40	50
79 % Ar and 21 % CO_2	0.4	40	64
79 % Ar and 21 % CO_2	0.5	40	68
90 % Ar and 10 % CO_2	0.4	40	68
90 % Ar and 10 % CO_2	0.5	40	71

MIG welding process, i.e., without micro-jet cooling there are higher amounts of grain boundary ferrite (GBF); there are also usually observed and site plate ferrite (SPF) fraction meanwhile after welding with micro-jet cooling both GBF and SPF structures were not so dominant. In all tested cases, MAC (self-tempered martensite, retained austenite, carbide) phases on the level of 3 % were also observed. Acicular ferrite with above 70 % could be obtained only in two cases: after MIG

welding with argon micro-jet cooling and after MIG welding with argon gas mixture (90 % Ar and 10 % CO2) micro-jet cooling (shown in Fig. 2 and in Table 3).

After the microstructure studies, the Charpy V impact toughness test of the deposited metal was carried out (5 specimens). The Charpy tests were only carried out at temperatures of −40 and +20 °C. The impact toughness of WMD was determined only for the same micro-jet parameters:

- Diameter: 40 μm,
- Number of jet: only one,
- Gas pressure: only 0.4 MPa (however structure was studied also for 0.5 MPa).

The impact toughness results are given in Table 4.

It is possible to deduce that impact toughness at ambient and negative temperature (−20 and −40 °C) of weld metal deposit is apparently affected by different

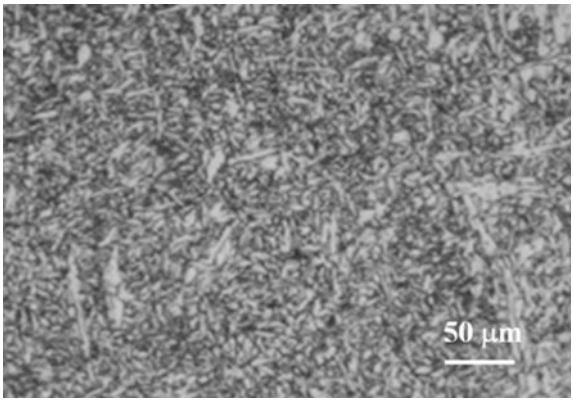

Fig. 2 High amount of acicular ferrite in weld (73 %) after an Ar micro-jet cooling

Table 4 The impact toughness of WMD after welding with various micro-jet cooling

Welding method	Micro-jet gases	Impact toughness KCV, J (at −40 °C)	Impact toughness KCV, J (at −20 °C)	Impact toughness KCV, J (at +20 °C)
MIG	–	43	65	181
MIG with micro-jet	Ar	59	81	195
MIG with micro-jet	He	51	64	182
MIG with micro-jet	N_2	below 40	46	155
MIG with micro-jet	79 % Ar and 21 % CO_2	53	76	191
MIG with micro-jet	90 % Ar and 10 % CO_2	56	79	193

types of micro-jet cooling. Micro-jet technology always has a strong effect on the impact toughness of WMD. Argon and gas mixture of 90 % Ar and 10 % CO_2 might be considered as proper micro-jet gases.

5 Conclusion

The results confirm that for low alloy steel welding there are two general types of tests performed: impact toughness and microstructure. Acicular ferrite and MAC phases (self-tempered martensite, upper and lower bainite, retained austenite, carbides) were fully analyzed and counted for each weld metal deposit. The innovative micro-jet technology was first recognized successfully for MIG welding. In this paper dynamic micro-jet cooling technology was also precisely described and tested for MIG welding process with various micro-jet gases: argon, helium, nitrogen, and various gas mixtures of argon and carbon dioxide. On the basis of investigation it is possible to deduce that micro-jet technology could be an important complement of both welding methods: MIG and MAG. An important part of this article was to analyze impact toughness of welds after dynamic micro-jet cooling. Final conclusions are as follows:

(a) micro-jet cooling could be treated as an important element of MIG welding processes,
(b) micro-jet cooling after welding can prove a significant amount of ferrite AF, the most beneficial phase in low alloy steel WMD,
(c) argon or gas mixture of argon and carbon dioxide could be considered as optional micro-jet gases for low alloy steel welding processes for MIG process,
(d) helium and nitrogen could not be considered as a a good choice for low alloy steel micro-jet welding; however, micro-jet helium cooling gives better results than simple MIG/MAG welding without micro-jet cooling.

References

1. Węgrzyn, T., Piwnik, J., Wieszała, J,. Hadryś, D.: Control over the steel welding structure parameters by micro-jet cooling. Arch. Metall. Mater. ISS 1 **57**(3), 679–685 (2012)
2. Piwnik, J., Hadryś, D., Skorulski, G.: Plastic properties of weld after micro-jet cooling. J. Ach. Mater. Manuf. Eng. **59**(1), 20–25 (2013)
3. Węgrzyn, T.: The classification of metal weld deposits in terms of the amount of oxygen. In: Proceedings of ISOPE 1999, Cupertino, California, USA, vol. IV, pp. 212–216 (1999)
4. Węgrzyn, T.: The classification of metal weld deposits in terms of the amount of nitrogen. In: Proceedings of ISOPE'2000, Seattle, USA, pp. 130–134 (2000)

5. Szczucka-Lasota, B., Formanek, B., Hernas, A., Szymański, K.: Oxidation models of the growth of corrosion products on the intermetallic coatings strengthened by a fine dispersive Al_2O_3. J. Mater. Process. Technol. **164–165**, 935–939 (2005)
6. Formanek, B., Jóźwiak, S., Szczucka-Lasota, B., Dolata-Grosz, A., Bojar, Z.: Intermetallic alloys with ceramic particles and technological concept for high loaded materials. J. Mater. Process. Technol. **164–165**, 850–855 (2005)
7. Formanek, B., Szymański, K., Szczucka-Lasota, B.: New generation of protective coatings intended for the power industry. J. Mater. Process. Technol. **164–165**, 850–855 (2005)
8. Słania, J.: Influence of phase transformations in the temperature ranges of 1250–1000 °C and 650–350 °C on the ferrite content in austenitic welds made with T 23 12 LRM3 tubular electrode. Metall. Mater. **50**(3), 757–767 (2005)
9. Burdzik, R., Folęga, P., Łazarz, B., Stanik, Z., Warczek, J.: Analysis of the impact of surface layer parameters on wear intensity of friction pairs. Arch. Metall. Mater. **57**(4), 987–993 (2012)
10. Burdzik, R.: Research on the influence of engine rotational speed to the vibration penetration into the driver via feet—multidimensional analysis. J. Vibroeng. **15** (4), 2114–2123 (2013)
11. Lukaszkowicz, K., Kriz, A., Sondor, J.: Structure and adhesion of thin coatings deposited by PVD technology on the X6CrNiMoTi17-12-2 and X40 CrMoV5-1 steel substrates. Mater. Sci. Eng. **51**, 40–47
12. Yoshifumi, A., Hozumi, G.: Friction and wear of carbon steel near T1-transition under dry sliding. Tribol. Int. **39**, 756–762 (2006)
13. Lisiecki, A.: Diode laser welding of high yield steel. In: Proceedings of SPIE 8703, Laser Technology 2012: Applications of Lasers, p. 87030S, 22 Jan 2013. doi:10.1117/12.2013429
14. Lisiecki, A.: Welding of titanium alloy by disk laser. In: Proceedings of SPIE 8703, Laser Technology 2012: Applications of Lasers, p. 87030T, 22 Jan 2013. doi:10.1117/12.2013431
15. Tarasiuk, W., Szczucka-Lasota, B., Piwnik, J., Majewski, W.: Tribological properties of super field weld with micro-jet process. Adv. Mater. Res. **1036**, 452–457 (2014). doi:10.4028/www.scientific.net/AMR.1036.452

Modelling of Thermoelectric Processes in FEM Environment Based on Experimental Studies

Michał Wikary, Stanisław Radkowski, Jacek Dybała and Kamil Lubikowski

Abstract Finite Element Method (FEM) is an effective and productive tool which is able to deal with sophisticated engineering requirements and successfully calculates expected output values often based on advanced boundary conditions and solution settings. The paper refers to modelling of thermoelectric generators in FEM environment (ANSYS software) which are based on popular Peltier modules that are frequently used in energy cogeneration branch of industry. The modelling process consists of geometry design, sensitivity study which focus on solver settings, discretization level and their impact into results (optimization of solution process total time). Last step engages parameter of Seebeck coefficient. Its modification allows adjusting the FE analysis to experimental data. The verified thermoelectric module will be able to reflect real capabilities of the commercially available thermoelectric devices. The main purpose of the process development is creation of Peltier modules (accessible in industry) FE models database. The devices from the database could easily be used in sophisticated FE analysis which consists of various physics systems (coupled) where simplified approach or indirect method will be limited or impossible to use.

M. Wikary (✉) · S. Radkowski · J. Dybała · K. Lubikowski
Warsaw University of Technology Institute of Vehicles,
Narbutta Street 84, 02-524 Warsaw, Poland
e-mail: m.wikary@mechatronika.net.pl

S. Radkowski
e-mail: ras@simr.pw.edu.pl

J. Dybała
e-mail: jdybala@simr.pw.edu.pl

K. Lubikowski
e-mail: k.lubikowski@mechatronika.net.pl

J. Awrejcewicz (ed.), *Dynamical Systems: Modelling*, Springer Proceedings in Mathematics & Statistics 181, DOI 10.1007/978-3-319-42402-6_32

1 Introduction

Poland as a member of European Union is obligated to meet requirements related to climate protection (40 % reduction of CO_2 emission, in comparison to year 1990) and development of Renewable Energy Sources systems (contribution up to 27 %,) and their efficiency (27 %) in the energy industry up to 2030 year. According to the mentioned data, the reduction of greenhouse gas emissions (40 % in comparison to year 1990) and the natural environment protection is very important aspect of modern technology progression in the near future. Industrial companies from various market sectors (automotive, military, electronic, etc.) direct their attention to distributed generation of energy sources [1–4]. Nowadays, so-called energy cogeneration becomes more and more popular not only in the industry market but also among private individuals. One of the common group of innovative technologies is Renewable Electricity Production. Examples of mentioned subject are systems which are based on solar energy, wave movements, piezoelectric devices, Peltier modules, etc. The last from specified subgroup is able to work as a thermoelectric generator (TEG). The main effect which allows electricity production in this case is Seebeck phenomenon (common usage of the modules refer to Peltier phenomenon) [5–7]. The thermoelectric generators are transforming heat energy from heat flow to pure electric energy. While heat flows in direction from hot to cold, free charge carriers, electrons or holes in the material are also driven to the cold end. The resulting value of voltage is proportional to the temperature difference multiplied by the Seebeck coefficient. Figure 1 presents structure of standard Peltier module [8–11]. Advantages such as low prize, availability, stability, predictability, reliability make the thermoelectric generator valuable in Renewable Electricity Production. There are many types of the product with wide range of

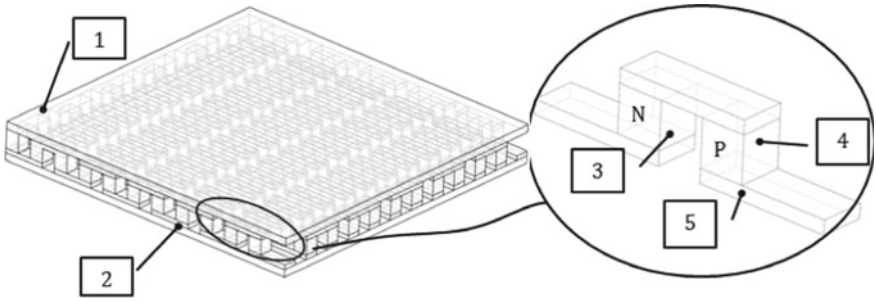

1. Ceramic plate (top)
2. Ceramic plate (bottom)
3. N type element
4. P type element
5. Strap (connector between n and p elements)

Fig. 1 Structure of standard Peltier module

capabilities in the market. Unfortunately most of the specifications added to the commercially available Peltier modules contain limited work characteristics range and information about Seebeck or Peltier coefficient. Considering the fact that the efficiency of thermoelectric generators is relatively low, all activities which could increase accuracy in determination of real efficiency should be considered. Especially that the Peltier module input values presented by companies are hard to be achieved in laboratory environment.

2 Laboratory Examination, Model Creation

The general approach of the algorithm was presented in Fig. 4. At the beginning of the procedure a commercial Peltier Module need to be examined in a laboratory. It enables to specify an output data (electromotive force) which will be a reference point for FE thermoelectric model. Next step refers to finite element model creation. Selection of finite elements allows determining a range of phenomena, which software shall include during solution process. In this case, SOLID90 and SOLID226 were selected. Figure 2 presents finite elements and their assignment to CAD model.

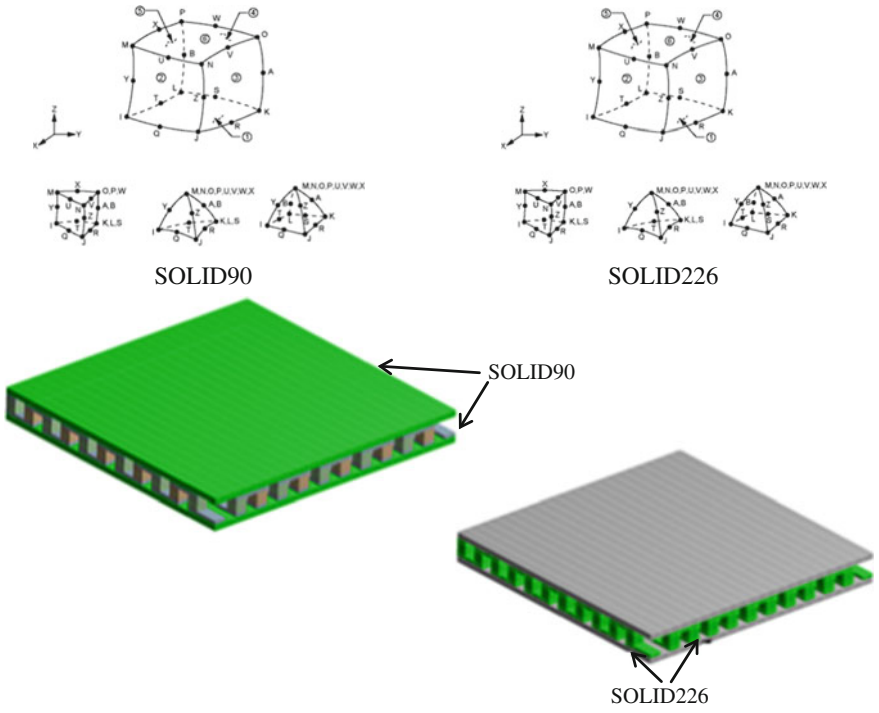

Fig. 2 Finite element and assignment to CAD model (ANSYS workbench) [13]

Both finite elements are higher order three-dimensional elements with additional midside nodes. Additional Gauss points are available which increase results in the accuracy without extra finite elements. It makes the calculation more time-effective [12]. Capital letters in the figure above indicate nodes distribution, the value in the circle number faces which creates a single finite element. SOLID90, as was mentioned, is a higher order element with 20 nodes and single degree of freedom (temperature) [13]. Solid226 consists of 20 nodes with maximum five degree of freedom (DOF). They may model such effects as elasticity, plasticity, viscoelasticity, viscoelasticity, creep, large strain, large deflection, stress stiffening effects, prestress effects, Seebeck, Peltier, Thomson effects, Joule heating, piezocaloric effect in dynamic analyses, and Coriolis effect. Its wide DOF capabilities cause the finite element valuable for coupled field analyses (coupled various physics) [13]. Next step determines discretization level. If the mesh quality will be too high the results accuracy may be changed beyond reasonable value (in comparison to measurement devices during laboratory examination) and impact in total time calculations. Figure 3 presents arrangement of three levels of model discretization which were used in the sensitivity study. The third option was considered as a proper balance between results and time of solution process. Apart from the investigation of total number of elements, additional check was carried out of one by one of Finite Element Quality based on Mesh Metric Options (Mesh Quality, Jacobian Ratio, and Maximum Corner Angle). The approach ensured the high quality of elements.

Last step of the model creation requires definition of boundary conditions. For thermoelectric coupled field analysis both temperature of hot and cold side of the thermoelectric generators were modelled and electrical potential. The analysis

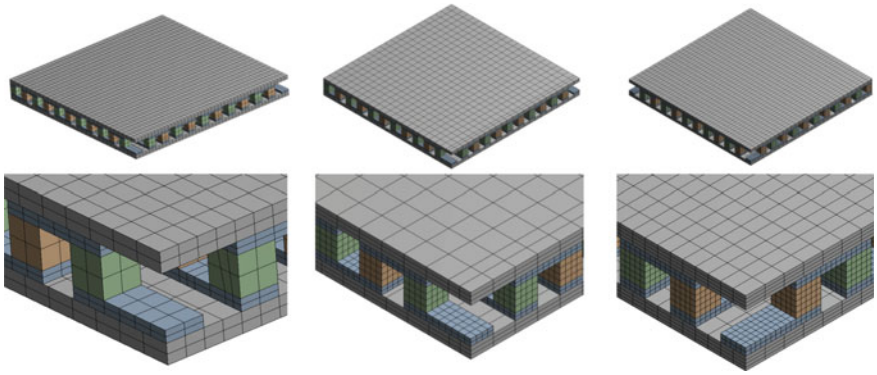

Discretization level 1	Discretization level 2	Discretization level 3
elements – 10298, nodes 67182, analysis did not converge	elements – 26181, nodes 154273, time 315 sec.	elements – 50240, nodes 276244, time 690 sec.

Fig. 3 Discretization level of thermoelectric generator (ANSYS workbench)

consisted of several loadsteps to allow suitable monitoring of solution process. Sparse Direct Solver was chosen for immediate solution of defined problem (adequate for time effective nonlinear solutions). It is based on the direct elimination of equation. Direct elimination requires the factorization of an initial very sparse linear system of equations into a lower triangular matrix followed by forward and backward substitution using triangular system [12]. The space required for the lower triangular matrix factors is typically much more than the initial assembled sparse matrix, hence the large disk or in-core memory requirements for direct methods [14, 12].

Considering the fact that sensitivity study was carried out before main calculation process, the Newton–Raphson residuals are not required in this approach [15]. The thermoelectric generator FE model was verified against discretization level and numerical instability (solution convergence) hence additional solution monitoring tools were excluded from primary analysis in order to optimise the total solution time. HEAT and AMPS convergence criterion was selected. Successful solution is indicated when the out-of-balance loads are less than the specified convergence criteria.

3 Parametrization, Model Adjustment

Completion of model creation stage allows moving on to next activity, parametrization. This step specifies what feature will be set as the parameter. Considering the fact that the fundamental effect in cogeneration (Renewable Electricity Production)

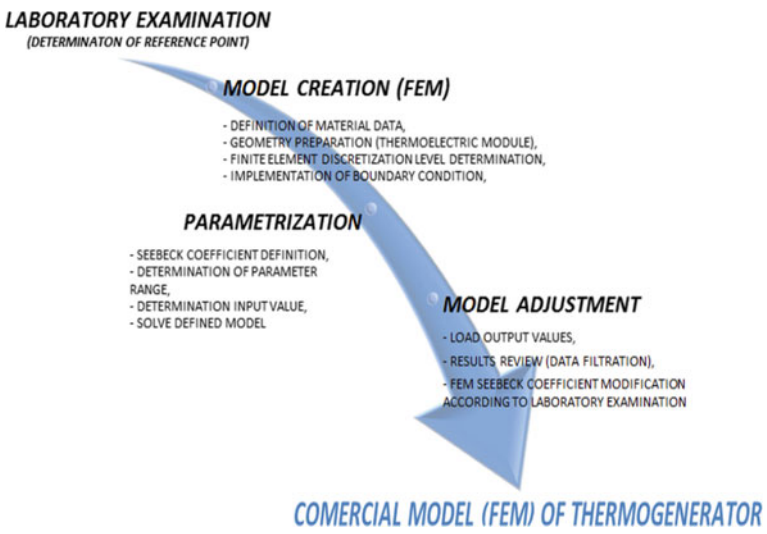

Fig. 4 General approach (Autors own work)

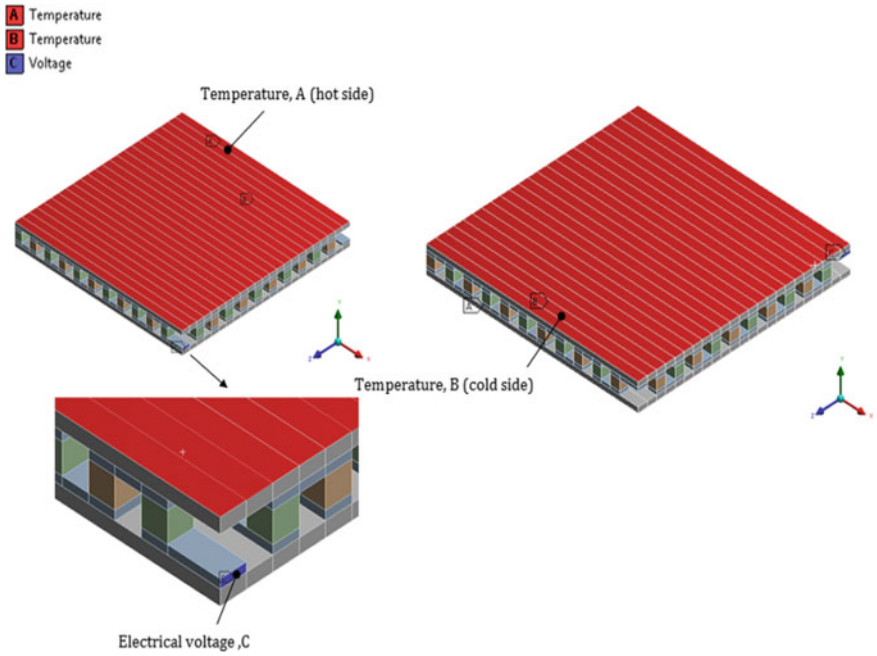

Fig. 5 Boundary condition of thermoelectric generator (ANSYS workbench Autors own work)

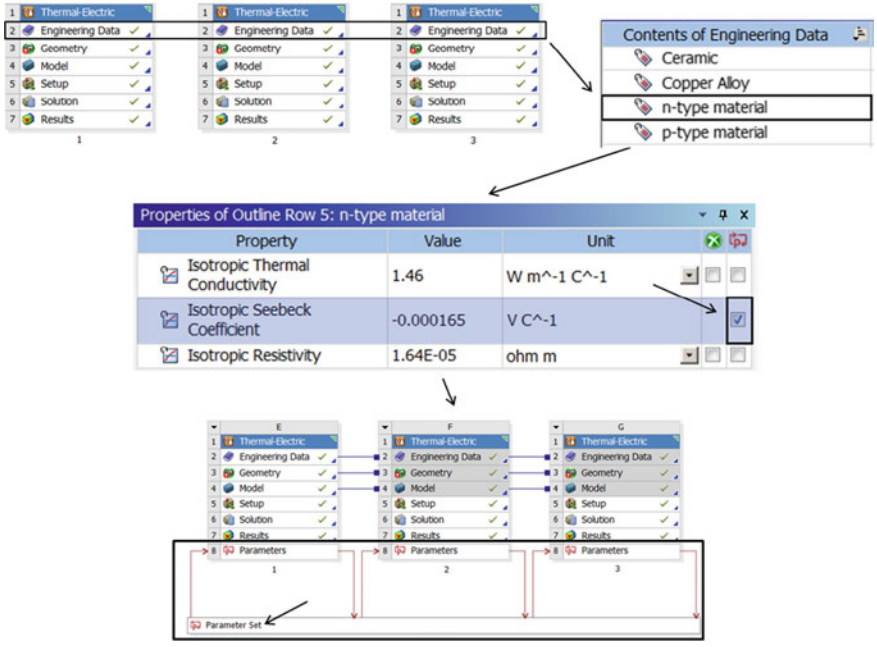

Fig. 6 Parameter definition process (ANSYS workbench)

performed by thermoelectric generator is Seebeck phenomenon, the Seebeck coefficient was selected as parameter in FE analysis. Additional information is required to absolutely define the variable, a parameter range. The span value directly affects total calculation time because solver takes into account all coefficient numbers and for them solution process is repeated in loop (Figs. 4 and 5).

If the procedure is carried out first time it is recommended to set parameter range based on maximum and minimum acknowledged material Seebeck coefficient (e.g. −0.000200–0.000250 V/(°C) with step −0.00010 V/(°C) [16–22]). Figure 6 presents parameter definition process in ANSYS Workbench.

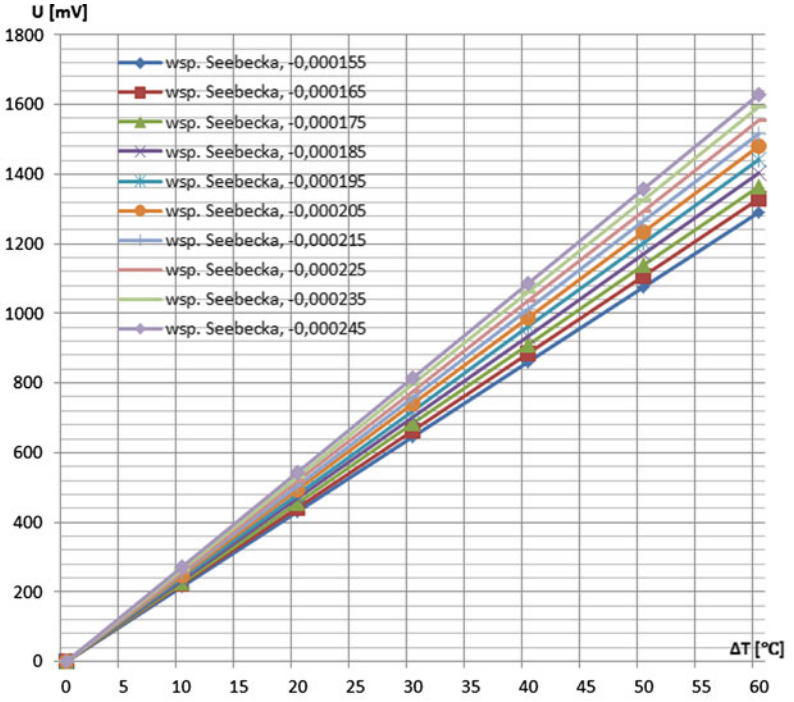

	0	10	20	30	40	50	60
wsp. Seebecka, -0,000155	0,00	215,09	430,18	645,27	860,36	1075,45	1290,54
wsp. Seebecka, -0,000165	0,00	221,38	442,76	664,14	885,52	1106,90	1328,28
wsp. Seebecka, -0,000175	0,00	227,67	455,34	683,01	910,67	1138,34	1366,01
wsp. Seebecka, -0,000185	0,00	233,96	467,92	701,87	935,83	1169,79	1403,75
wsp. Seebecka, -0,000195	0,00	240,25	480,49	720,74	960,99	1201,23	1441,48
wsp. Seebecka, -0,000205	0,00	246,54	493,07	739,61	986,14	1232,68	1479,22
wsp. Seebecka, -0,000215	0,00	252,83	505,65	758,48	1011,30	1264,13	1516,95
wsp. Seebecka, -0,000225	0,00	259,11	518,23	777,34	1036,46	1295,57	1554,69
wsp. Seebecka, -0,000235	0,00	265,40	530,81	796,21	1061,61	1327,02	1592,42
wsp. Seebecka, -0,000245	0,00	271,69	543,39	815,08	1086,77	1358,46	1630,16

Fig. 7 Results for selected parameter range (ANSYS workbench)

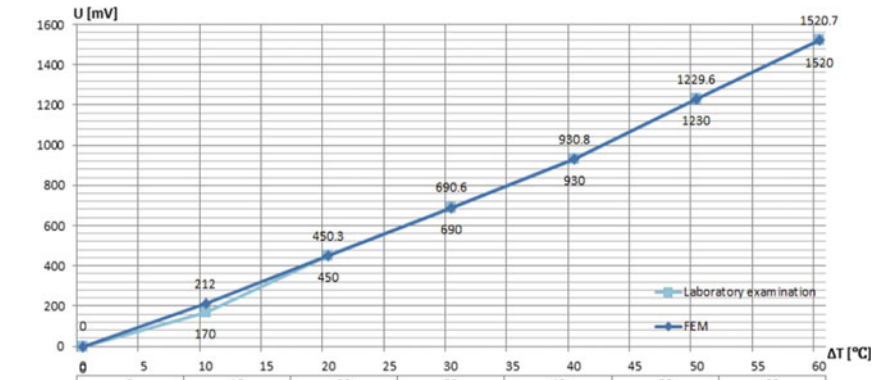

	0	10	20	30	40	50	60
Laboratory examination	0	170	450	690	930	1230	1520
FEM	0	212	450.3	690.6	930.8	1229.6	1520.7

Fig. 8 Model adjustment (ANSYS workbench)

The parametrization process is completed when the solver finish analysis in full range of parameter and output data are available (electromotive force). The model adjustment stage requires comparison between output values obtained for defined Seebeck coefficient range and reference measurements of laboratory examination.

Based on the experimental reference output points adequate value of calculated thermoelectric generator model should be selected. As has been mentioned in previous section, the analysis was divided into several load steps mainly in order to readout output values for gradually cumulated temperature difference between hot and cold side of analysed FE model Peltier module. Figure 7 presents results (electrical voltage) for selected range of the parameter (full range of loadsteps).

In Fig. 8 statement of laboratory results (reference point) and FEM output data for thermoelectric generator FE model was shown. The adjustment has been implemented and the commercial Peltier model is ready to use in more advance coupled field analyses for considered working range.

4 Conclusion

The examined and adjusted Peltier modules according to the presented methodology can be used in more sophisticated test stands designed in CAD software with accuracy which reflects laboratory results (without need to create physical test stand). It is dedicated for coupled field analyses in ANSYS Workbench. The advantages allow for fast examination of Peltier modules (commercial) and continuation of the researches in FE environment with corrected or extended work characteristics (in regard to original specification added to commercial Peltier module by manufacturer).

References

1. Wikary, M., Lubikowski, K., Radkowski, S., Szczurowski, K.: Energy scavenging in a vehicle`s exhaust system. J. KONES Powertrain Transp. **19**, 253–261 (2012)
2. Wikary, M., Lubikowski, K., Dybała, J., Rokicki, K., Szulim, P.: Thermal analyses of exhaust system on combustion engine. J. KONES Powertrain Transp. **19**, 173–178 (2012)
3. Sekretariat Generalny Rady: Konkluzje. Rada Europejska, Bruksela (2014)
4. Parlament europejski i rada unii europejskiej, Dyrektywa 2004/8/WE Parlamentu Europejskiego i Rady z dnia 11 lutego 2004 r. w sprawie wspierania kogeneracji w oparciu o zapotrzebowanie na ciepło użytkowe na rynku wewnętrznym energii oraz zmieniająca dyrektywę 92/42/EWG, parlament europejski i rada unii europejskiej, Bruksela, 2004
5. Rowe, D.M.: CRC Handbook of Thermoelectric. Florida, Boca Raton (1995)
6. Wikary, M., Lubikowski, K., Radkowski, S., Szczurowski, K.: Analysis of possibility of use Peltier modules in task of energy scavenging. Key Eng. Mater. **588**, 1–11 (2013)
7. Wikary, M., Lubikowski, K., Radkowski, S., Szczurowski, K.: Seebeck phenomenon, calculation method comparison. J. Power Technol. **95**, 63–67 (2015)
8. Sawieliew, I.W.: Wykłady z Fizyki. PWN, Warszawa (2000)
9. Salejda, W., Termodynamika z elementami termodynamiki statystycznej, Wrocław (2007)
10. Camargo, J., Costa de Oliveira, M.: Principles of Direct Thermoelectric Conversion. Heat Analysis and Thermodynamic Effects, pp. 93–105 (2011)
11. Snyder, G.J.: Small thermoelectric generators. Electrochem. Soc. Interface **17**(3), 54–56 (2008)
12. Zienkiewicz, O.C.: Metoda Elementów Skończonych. Arkady, Warszawa (1972)
13. ANSYS, Inc., Element Reference. ANSYS, Inc., Canonsburg, Pensylwania (2012)
14. ANSYS, Inc., Basic Analysis Guide. ANSYS, Inc., Canonsburg, Pensylwania (2012)
15. ANSYS, Inc., Mechanical User Guide. ANSYS, Inc., Canonsburg, Pensylwania (2012)
16. Beensh-Marchwicka, G., Procisów, E., Osadnik, S.: Materials for thin film thermal converters. In: Proceedings of 27th International Conference on IMAPS-Poland, pp. 43–49 (2003)
17. Sato, N., Takeda, M.: Fabrication and evaluation of a flexible thermoelectric device using metal thin films. In: Proceedings of 24th International Conference on Thermoelectrics, pp. 160–163 (2005)
18. Glatz, W., Muntwyler, S., Hierold, C.: Optimization and fabrication of thick flexible polymer based micro thermoelectric generator. Sens. Actuators A **132**, 337–345 (2006)
19. Ogura, H., Numanjiri, H., Narushima, H., Izuchi, M., Arai, M.: Emf changes of Pt/Pd thermocouples in the range from 420°C to 1080°C. In: Proceedings of SICE Annual Conference, pp. 1171–1174 (2003)
20. Wijngaards, D., De Graaf, G., Wolffenbuttel, R.: Single-chip micro-thermostat applying both active heating and active cooling. Sens. Actuators A **110**, 187–195 (2004)
21. Glatz, W., Durrer, L., Schwyter, E., Hierold, C.: Novel mixed method for the electrochemical deposition of thick layers of Bi2 + xTe3 − x with controlled stoichiometry. Electrochim. Acta **54**, 755–762 (2008)
22. Glatz, W., Durrer, L., Schwyter, E., Hierold, C.: Flexible Micro Thermoelectric Generator based on Electroplated Bi2 + xTe3-x. DTIP of MEMS & MOEMS, pp. 46–48

The Modeling of Nonlinear Rotational Vibration in Periodic Medium with Infinite Number of Degrees of Freedom

Artur Wirowski and Paweł Szczerba

Abstract The subject of the work is hypothetical 2D periodic medium with an infinite number of beams, each with a single degree of freedom, which allows on the rotation of the single plate around its center of gravity. Interaction by electrostatic forces of beams to each other, so that rotation of any of them induces rotation of the adjacent beams has been assumed. The motivation to undertake research in this field and adoption of such assumptions are potentially possible mechanism of optical phenomena in the atmosphere. Thus, in case the physical atmospheric phenomena, the hypothetical beams would be implemented by electrically charged plates of ice crystals. The aim of the work is to obtain the continuous nonlinear vibration model of such a medium. Large angle of rotation of plates was assumed, however each beam interacts with a 4-neighbors. The finite difference method and certain heuristic assumptions about the superposition of interactions have been used for modeling. As a result, the differential equation describing the behavior of such a medium in a continuous manner has been obtained. It is shown that under those conditions obtained final model equation is similar to the sine-Gordon equation. The next part of the work is possible examples of solutions coming from such a model for different sets of input data.

1 Introduction

The issues of nonlinear rotational vibrations are not completely new. Rotary discrete systems, such as: Josephson Junction Ladder (JJL) were modeled by several authors, for example: [1, 2]. It has been widely shown, such that systems can be

A. Wirowski (✉) · P. Szczerba
Department of Structural Mechanics, Technical University of Lodz, Lodz, Poland
e-mail: artur.wirowski@p.lodz.pl

P. Szczerba
e-mail: szczerba.paw@gmail.com

J. Awrejcewicz (ed.), *Dynamical Systems: Modelling*, Springer Proceedings in Mathematics & Statistics 181, DOI 10.1007/978-3-319-42402-6_33

described by the continuous equations of type sine-Gordon [3]. This leads to a number of mechanical phenomena, such as solitons and breathers [4], which may be present in these types of systems.

1.1 An Overview of Issues

In this paper, we model the medium mathematically similar to the JJL, but with completely different physical principles. Let us consider two-dimensional discrete system consisting of an infinite number of beams, with only one degree of freedom each. We assume that all the beams are equally charged electrically. Interactions between adjacent beams are induced by electrostatic forces. Therefore, the rotation of one beam causes a rotation of adjacent beams. As will be shown in this work, the model equation is similar to sine-Gordon equation. As in the case JJL, some solutions of obtained equations may have a form of solitons. However, despite the similarities with existing nonlinear mechanical equations, the resulting equation is completely new. Theoretical attempts to description this medium, appears in the papers on atmospheric optics [5–7]. However, in the works [5, 6] are more stringent assumptions, which consequently lead to a much simpler models. In paper [7] the author, have started from the same assumptions, however have made a few mistakes at the modeling stage, so resulting in a wrong equation model.

The theoretical system analyzed in this study may have important physical meaning. The most interesting application of this model is the atmospheric physics. In this case, we assume that our mathematical beams correspond to the electrically charged ice crystals. The resulted dynamic model of the cloud of such crystals can be used in the analysis of varying optical properties of such a medium [5]. Another example of application may be vibrations of crystal lattice. By assuming that our beams are the charged particles, proposed model describes the dynamics of such a medium on a macroscopic scale. Due to the relatively simple physical assumptions, the proposed model will be able to have many applications in other dynamic structures in future [8].

1.2 Aim of Contribution

The main aim of the contribution is to obtain continuous model describing the dynamic behavior of the analyzed medium. Next, for thus-formed equation we show and discuss exemplary solutions.

2 The Modeling

The nonlinear two-dimensional model has been presented in this paper. This chapter includes assumptions of this model, derivation the equation of rotational motion of individual crystal and outputting the continuous model of the vibrating periodic medium. In Sect. 2.5 authors have proved correctness of condition of synchronization of beams made during derivation the equation of rotational motion. At the end of this chapter authors have given exemplary solutions of derived equation, both analytical and numerical.

2.1 The Assumptions

Let us suppose, that it is given two-dimensional space R2. In this space, we consider a cloud of one-dimensional identically electrostatically charged beams in Ω area (Fig. 1). Let us introduce the following modeling assumptions:

- A homogeneous cloud of identical, electrically charged beams is given,
- beams are prismatic with a square cross-section,
- the beams are evenly distributed in the cloud both vertically and horizontally,
- we assume that the beams have only one degree of freedom that allows on the rotation of each of them around their center of gravity,

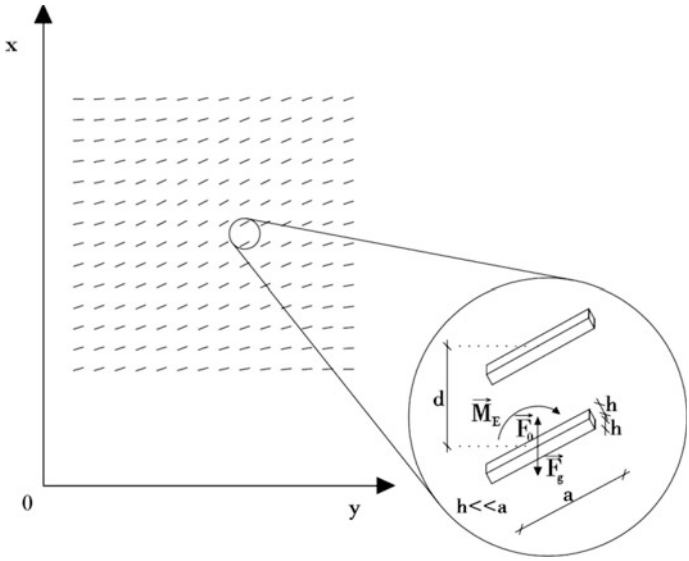

Fig. 1 The infinite cloud of charged beams. The *inset* shows a single beam with its neighbors

- the electric charge of the beams is uniformly distributed on its surface,
- we assume that the synchronization occurs between the beams, i.e., the difference between the rotation of adjacent beams is negligible.

2.2 The Equation of the Rotational Motion of an Individual Crystal

Our considerations aimed at obtaining differential equation, we start by writing the equations of motion for a single beam:

$$\vec{M} = I\vec{\varepsilon} \tag{1}$$

where:

$I = \frac{1}{12}h^2 a\rho(a^2 + h^2)$ the moment of inertia for the axis of beam's rotation, the beam has a square cross-section with side h, and the length of the beam a,

$\vec{M}$ the total resultant moment acting on the beam,

$\vec{\varepsilon}$ the angular acceleration in the rotational motion,

ρ density of beam's material

Due to the continuous charge distribution on the beams, in the following modeling we consider the moments derived from the interaction between the appropriate surfaces of adjacent beams. Then, we can expand the resultant moment as (Fig. 2):

$$I\vec{\varepsilon} = \sum_{\gamma} \int_{-\frac{a}{2}}^{\frac{a}{2}} \int_{-\frac{a}{2}}^{\frac{a}{2}} \vec{r}(\eta) \times \vec{F}\left(\eta, \xi_\gamma\right) d\xi_\gamma d\eta \quad \gamma = 1..4 \tag{2}$$

where:

$\vec{r}(\eta)$ conductive vector of an infinitely small segment of the surface of the analyzed beam,

$\vec{F}\left(\eta, \xi_\gamma\right)$ forces of the electrostatic interaction between the infinitely small segments of the surface of adjacent beams, respectively $d\eta$ and $d\xi_\gamma$,

η, ξ_γ local coordinates, running respectively on the surfaces of the center and adjacent beams and adopting the values from $-½a$ to $½a$ for the extreme edges of the beam and 0 in the midst of each surface (Fig. 2)

The resistance force, in accordance to the assumptions, is proportional to the linear velocity of segment $d\eta$, forces $\vec{F}\left(\eta, \xi_\gamma\right)$ are Coulomb forces and therefore:

$$\vec{F}\left(\eta, \xi_\gamma\right) = \frac{dq \cdot dq}{4\pi\varepsilon_r\varepsilon_0} \cdot \frac{\overrightarrow{P_\gamma O}}{\left|\overrightarrow{P_\gamma O}\right|^3} \tag{3}$$

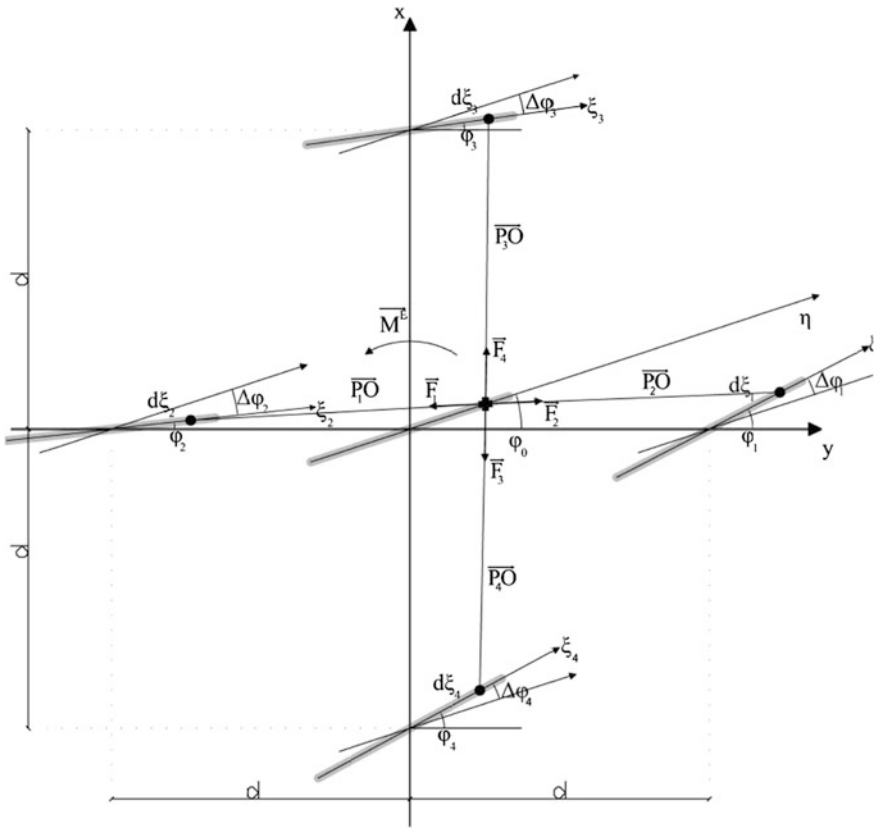

Fig. 2 The electrostatic forces between the infinitely small segments of the surfaces of the analyzed beams

where:

$\overline{P_\gamma O} = \begin{bmatrix} -d\left(\beta\sin(\varphi_0)+\alpha\cos(\varphi_0)-\xi_\gamma\cos\left(\Delta\varphi_\gamma\right)+\eta\right) \\ d\left(\alpha\sin(\varphi_0)-\beta\cos(\varphi_0)-\xi_\gamma\sin\left(\Delta\varphi_\gamma\right)\right) \end{bmatrix}$ vectors of beginnings and ends at the points Pg and O, respectively (Fig. 2), which are the points of the analyzed segments of beams' surfaces dη and $d\xi_\gamma$,

$\Delta\varphi_\gamma = \varphi_\gamma - \varphi_0$ differences between the angles of beams' rotations respectively for g-th and central beam,

dq charge of the analyzed segment of the beam's surface,

ε_r relative dielectric constant of air,

ε_0 dielectric constant of vacuum,

$$\gamma = 1 \rightarrow \alpha = 0 \wedge \beta = 1, \qquad \gamma = 2 \rightarrow \alpha = 0 \wedge \beta = -1,$$

$$\gamma = 3 \rightarrow \alpha = 1 \wedge \beta = 0, \qquad \gamma = 4 \rightarrow \alpha = -1 \wedge \beta = 0.$$

By substituting these relations into Eq. (2) and expanding the vector product we obtain:

$$I\vec{\varepsilon} = \frac{1}{4\pi\varepsilon_r\varepsilon_0}\sum_{\gamma}\int_{-\frac{a}{2}}^{\frac{a}{2}}\int_{-\frac{a}{2}}^{\frac{a}{2}}\frac{\eta\left(d(\alpha\sin\varphi_0-\beta\cos\varphi_0)-\xi_\gamma\sin\Delta\varphi_\gamma\right)(dq)^2d\xi_\gamma d\eta}{\left(\begin{array}{l}\left(-d(\beta\sin\varphi_0+\alpha\cos\varphi_0)-\xi_\gamma\cos\Delta\varphi_\gamma+\eta\right)^2\\+\left(d(\alpha\sin\varphi_0-\beta\cos\varphi_0)-\xi_\gamma\sin\Delta\varphi_\gamma\right)^2\end{array}\right)^{\frac{3}{2}}} \tag{4}$$

The Eq. (4) may be subject to certain simplifications. Let us note that due to the uniform charge distribution on the surface of each beam, we have:

$$Q = \int_{-\frac{a}{2}}^{\frac{a}{2}} dqd\xi_\gamma = \int_{-\frac{a}{2}}^{\frac{a}{2}} dqd\eta, \gamma = 1,2,3,4 \tag{5}$$

Due to the assumption of the synchronization of the beams, which means that the adjacent beams are rotated by almost the same angles, we have:

$$\Delta\varphi_\gamma << 1 \Rightarrow \sin\Delta\varphi_\gamma = \Delta\varphi_\gamma,\ \cos\Delta\varphi_\gamma = 1 \tag{6}$$

Due to these relations, the Eq. (4) can be simplified after some transformations to the form:

$$I\vec{\varepsilon} = \frac{Q^2}{4\pi\varepsilon_r\varepsilon_0}\sum_{\gamma}\int_{-\frac{a}{2}}^{\frac{a}{2}}\int_{-\frac{a}{2}}^{\frac{a}{2}}\frac{\eta\left(d(\alpha\sin\varphi_0-\beta\cos\varphi_0)-\xi_\gamma\Delta\varphi_\gamma\right)d\xi_\gamma d\eta}{\left(\begin{array}{l}d^2+\left(\xi_\gamma-\eta\right)^2+2d\left(\xi_\gamma-\eta\right)(\beta\sin\varphi_0+\alpha\cos\varphi_0)+\\-2\xi_\gamma d\Delta\varphi(\alpha\sin\varphi_0-\beta\cos\varphi_0)\end{array}\right)^{\frac{3}{2}}} \tag{7}$$

2.3 *The Derivation of the Discrete Equation of the Rotational Motion of the Crystal*

Although the solution of double integrals (7) exists in the general case, it is very complicated. In view of the fact that it is also a discrete equation of the rotation angle, which subsequently will be subject of conversion into a continuous form, the use of the exact solutions of the Eq. (7) for this purpose is impossible. To solve the

given problem we can find the approximate solution of double integrals (7) with a reasonable accuracy. We use the assumption of the synchronization of beams, i.e. the fact that the differences between the rotation angles of adjacent beams are relatively small. In this case, we try to share a moment described by integral Eq. (7) on the moment induced by the rotation of adjacent beams with identical angles—we call it $K0_\gamma$ and on the moment depended from small difference in angles between the adjacent beams—we call it KA_γ. The correctness of this assumption we will check a posteriori in Sects. 2.6. Let us denote the integrals from Eq. (7) as K_γ:

$$I\vec{\varepsilon} = \frac{Q^2}{4\pi\varepsilon_r\varepsilon_0}\sum_{\gamma=1}^{4}\vec{K}_\gamma \tag{8}$$

With the according to that we said above, we split the moment Kγ with the following formulas:

$$\sum_{\gamma=1}^{4} K_\gamma = \sum_{\gamma=1}^{4}\left(K_{0\gamma} + K_{A\gamma}\right) \tag{9}$$

$$K_{0\gamma} = K_\gamma\big|_{\varphi_0=\varphi_\gamma} \tag{10}$$

$$K_{A\gamma} = K_\gamma\big|_{\varphi_0,\,\varphi_\gamma=\varphi_0+\Delta\varphi_\gamma} - K_{0\gamma} \tag{11}$$

First we calculate the moments $K_{0\gamma}$. In this case we have $\varphi_\gamma = \varphi_0$ and $\Delta\varphi_\gamma = 0$ for $\gamma = 1 \ldots 4$:

$$K_{0\gamma} = \int_{-\frac{a}{2}}^{\frac{a}{2}}\int_{-\frac{a}{2}}^{\frac{a}{2}} \frac{(\eta d(\alpha\sin\varphi_0 - \beta\cos\varphi_0))d\xi_\gamma d\eta}{\left(d^2 + \left(\xi_\gamma - \eta\right)^2 + 2d\left(\xi_\gamma - \eta\right)(\beta\sin\varphi_0 + \alpha\cos\varphi_0)\right)^{\frac{3}{2}}} \tag{12}$$

After performing a integration (12) we simplified the exact solution to the form:

$$K_0 = \sum_{\kappa=1}^{2}(-1)^\kappa trig(-\kappa,\varphi)\left(2\hat{d} - p_\kappa^{\pm} - p_\kappa^{\mp}\right) + (-1)^\kappa trig(\kappa-1,\varphi)\ln\left(\frac{\hat{d}^2(trig(\kappa,\varphi)-1)^2}{l_\kappa^{\pm}l_\kappa^{\mp}}\right) \tag{13}$$

where:

$$trig(\kappa,\varphi) = \begin{cases} \sin(\varphi) & if \quad \kappa = 0 \vee 2 \\ \cos(\varphi) & if \quad \kappa = 1 \\ \tan(\varphi) & if \quad \kappa = -1 \\ \cot(\varphi) & if \quad \kappa = -2 \end{cases},$$

$$p_{\kappa}^{\pm} = \sqrt{\pm 2 trig(\kappa, \varphi)\hat{d} + \hat{d}^2 + 1},$$

$$l_{\kappa}^{\pm} = 1 + trig(\kappa, \varphi)\hat{d} + p_{\kappa}^{\pm}.$$

This solution we can approximate with great accuracy in case where $\hat{d}$ this is sufficiently large as follows:

$$K_0 = \sum_{\gamma=1}^{4} K_{0\gamma} = \frac{7}{24a\hat{d}^5}\sin(4\varphi_0) \tag{14}$$

It should be noted that formula (14) is the exact transformation of formula (13) for $\hat{d} \to \infty$ and that in practise for $\hat{d} = 4$ we obtain accurate approximations of 1.5 %, which is a sufficient condition from a practical point of view. The calculation of integrals $K_{A\gamma}$ is a more difficult task, because the moment $K_{A\gamma}$ depends on the difference of the angles $\Delta\varphi_{\gamma}$ and the angle φ_0 too. The direct integration of Eq. (7) is not possible in this general case, so we apply a numerical integration of formula (7) for different angles φ and we obtain moment $K_{\varphi\gamma}$. Next, from these formulas, we subtract the part derived from the rotation of beams with identical angles φ.

$$K_{A\gamma}\big|_{\varphi_0=\varphi} = K_{\varphi\gamma} - K_{0\gamma}\big|_{\varphi_0=\varphi} \tag{15}$$

When analyzing the obtained numerical relationship for $\hat{d} \geq 4$, we notice that, analogically to the case of K_0, we can find a very simple, elegant and a very accurate approximation according to the following formula:

$$K_A = \sum_{\gamma=1}^{4} K_{A\gamma} = \frac{1}{4a\hat{d}^3}\left[\begin{array}{l} \sin(\varphi_0)^2(\varphi_1 - \varphi_0) + \sin(\varphi_0)^2(\varphi_2 - \varphi_0) + \\ + \cos(\varphi_0)^2(\varphi_3 - \varphi_0) + \cos(\varphi_0)^2(\varphi_4 - \varphi_0) \end{array}\right] \tag{16}$$

Finally, the equation of the crystals' rotation takes the form:

$$I\frac{\partial^2\varphi_0}{\partial t^2} - \frac{Q^2a^2}{16\pi d^3\varepsilon_r\varepsilon_0}\left(\begin{array}{l} \frac{7a^2}{6d^2}\sin(4\varphi_0) + \sin(\varphi_0)^2(\varphi_1 + \varphi_2 - 2\varphi_0) + \\ + \cos(\varphi_0)^2(\varphi_3 + \varphi_4 - 2\varphi_0) \end{array}\right) = 0 \tag{17}$$

The Eq. (17) will provide us a basis for further deliberations aimed at obtaining continuous model equation for analyzed medium.

2.4 The Continuous Model of the Vibrating Periodic Medium

In order to achieve continuous model of infinite number of vibrating beams, we use finite difference method (FDM). Let us create a FDM grid, in analogous form to the beams distribution in the medium as shown in Fig. 3.

By denoting Eq. (17) for our grid we obtain:

$$I\frac{\partial^2\varphi_0}{\partial t^2} - \frac{Q^2a^2}{16\pi d^3\varepsilon_r\varepsilon_0}\left(\begin{array}{l}\frac{7a^2}{6d^2}\sin\left(4\varphi_{i,j}\right) + \sin\left(\varphi_{i,j}\right)^2\left(\varphi_{i-1,j}+\varphi_{i+1,j}-2\varphi_{i,j}\right) + \\ + \cos\left(\varphi_{i,j}\right)^2\left(\varphi_{i,j+1}+\varphi_{i,j-1}-2\varphi_{i,j}\right)\end{array}\right) = 0 \tag{18}$$

We use the classic FDM formulas for the second derivatives of the function [9].

$$\frac{\partial^2\varphi}{\partial x^2} = \frac{1}{d^2}\left(\varphi_{i+1,j} - 2\varphi_{i,j} + \varphi_{i-1,j}\right) \tag{19}$$

$$\frac{\partial^2\varphi}{\partial y^2} = \frac{1}{d^2}\left(\varphi_{i,j+1} - 2\varphi_{i,j} + \varphi_{i,j-1}\right) \tag{20}$$

$$\varphi = \varphi_{i,j} \tag{21}$$

Next we substitute formulas (19), (20), (21) into Eq. (18), and we assume, that the beams have a square cross section with a side h, and they are made of a material having a density ρ, and therefore theirs moment of inertia is given as:

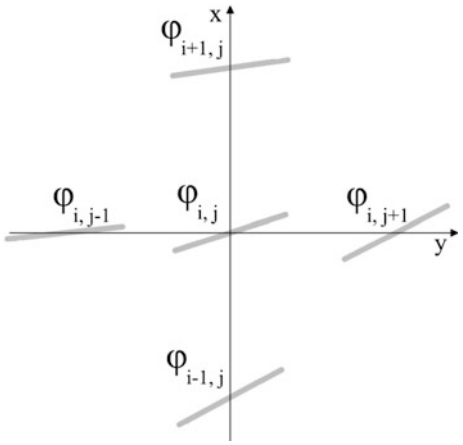

Fig. 3 The FDM grid

$$I = \frac{1}{12} h^2 a \rho \left(a^2 + h^2\right) \tag{22}$$

and finally after the mathematical transformation, we obtain the differential equation describing the analyzed medium as follows:

$$\begin{aligned} &\frac{8h^2\rho(a^2+h^2)\pi d^3 \varepsilon_r \varepsilon_0}{Q^2 a} \frac{\partial^2 \varphi}{\partial t^2} - \frac{7a^2}{d^2} \sin(4\varphi) + \\ &- 6d^2 \left(\sin^2(\varphi) \frac{\partial^2 \varphi}{\partial x^2} + \cos^2(\varphi) \frac{\partial^2 \varphi}{\partial y^2} \right) = 0 \end{aligned} \tag{23}$$

The Eq. (23) describes the nonlinear vibrations of the infinite cloud of the electrically charged beams in the continuous form in two dimensions. It takes into account their rotation by large angles. Denoting:

$$\alpha^2 = \frac{8h^2\rho(a^2+h^2)\pi d^3 \varepsilon_r \varepsilon_0}{Q^2 a} \tag{24}$$

We finally obtain:

$$\alpha^2 \frac{\partial^2 \varphi}{\partial t^2} - \frac{7}{d^2} \sin(4\varphi) - 6d^2 \left(\sin^2(\varphi) \frac{\partial^2 \varphi}{\partial x^2} + \cos^2(\varphi) \frac{\partial^2 \varphi}{\partial y^2} \right) = 0 \tag{25}$$

The resulting Eq. (25) is the highly nonlinear partial differential equation, similar to the sine-Gordon equation [10]. The exact analytical solution of this equation may not exist. In the next part of the paper, we will make attempts to finding analytical and numerical solutions of special cases of Eq. (25).

2.5 *Discussion on the Condition of Synchronization of Beams*

In the course of deriving the equation of the model (25) we have made assumption about the synchronization beams. This assumption means that every adjacent beams are rotated relative to each other with a relatively small angle. This makes possibility of computing integrals (7), and the use of FDM as formulas (19), (20), (21). Failure to meet this assumption would result in chaotic solutions and the inability to use Eq. (25). It is therefore important to check for what angles the assumption of synchronization of adjacent beams is met.

These conditions we will check with the following reasoning. Let us consider the static case in which torques acting on the beam is balanced. By using the formula (18) we obtain:

$$\frac{7a^2}{6d^2}\sin(4\varphi_0) + \sin(\varphi_0)^2(\varphi_1 + \varphi_2 - 2\varphi_0) + \cos(\varphi_0)^2(\varphi_3 + \varphi_4 - 2\varphi_0) = 0 \quad (26)$$

For simplicity further evaluation in this section we assume that:

$$\varphi_1 - \varphi_0 = \varphi_2 - \varphi_0 = \varphi_3 - \varphi_0 = \varphi_4 - \varphi_0 = \Delta\varphi \quad (27)$$

Then we can calculate the angle $\Delta\varphi$ which is needed to provide balance as:

$$\Delta\phi = -\frac{7}{12\hat{d}^2}\sin(4\phi_0) \quad (28)$$

In Sect. 2.3 we have assumed condition $\hat{d} \geq 4$. For this assumption we obtain:

$$\Delta\varphi \leq \left|\frac{7}{192}\right| << 1 \quad (29)$$

Therefore, the condition of synchronization is satisfied for any angle φ_0.

The above reasoning has been conducted for static issues. For dynamic issues, the problem is more complicated. However, if we accept the initial conditions, close to the equilibrium condition of the beams, and on this way we provide preliminary fulfillment of the synchronization condition, the resulting solution will be certainly correct.

2.6 *The Solutions of the Differential Equation Model*

The Eq. (25) is nonlinear partial differential equation of second order with respect to space and time. Unfortunately, in the general case, there are no analytical solutions. We can only solve it analytically in specific cases. However in the general case we can obtain a numerical solution.

The Analytical Solution of the Simplified Equation

The analytical solution can be found, among others in the following special case: we assume that all the beams are rotating at every moment for the same angle:

$$\varphi_0 = \varphi_1 = \varphi_2 = \varphi_3 = \varphi_4 = \varphi \quad (30)$$

In this case, the spatial derivatives in Eq. (25) disappears and the equation simplifies to the form:

$$\alpha^2 \frac{\partial^2 \varphi}{\partial t^2} - \frac{7}{\hat{d}^2} \sin(4\varphi) = 0 \tag{31}$$

In the general case, the solution of the above equation provides, inter alia, a function of the form:

$$\varphi(t) = \arctan\left(\frac{-JacobiSN\left(C_1(t+C_2), 2\sqrt{7}\sqrt{-\frac{1}{\alpha^2 \hat{d} C_1^2}} \right),}{\sqrt{1 - JacobiSN\left(C_1(t+C_2), 2\sqrt{7}\sqrt{-\frac{1}{\alpha^2 \hat{d} C_1^2}} \right)^2}} \right) \tag{32}$$

However, even in this case, problem of finding the constants C_1 and C_2 for any initial conditions is difficult, because of the form of a solution. In general, function (32) is in every case of periodical function. Sample form for a few selected combinations of fixed C_1 and C_2 shown in the Figs. 4 and 5.

In practice, these analytical solutions have not practical meaning, but it give us some insight on the solution of Eq. (25).

The Numerical Solution

The numerical solution of Eq. (25) has been found in program Mathematica 10.2. Runge−Kutta method had been used to solve this equation (Fig. 6).

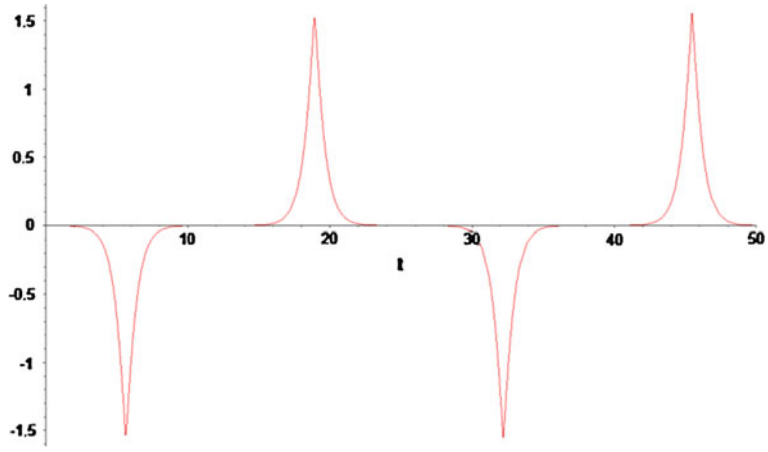

Fig. 4 The solution of the Eq. (32) for $C_1 = 0.0001$ and $C_2 = 1$

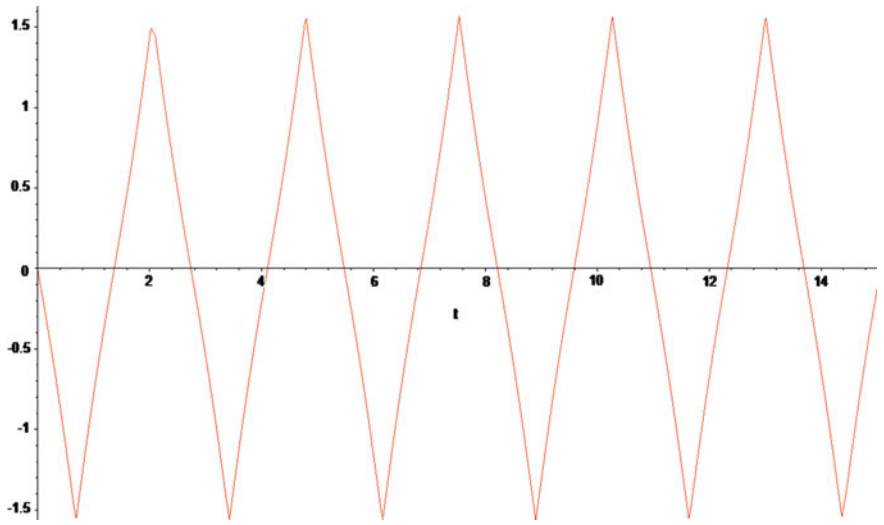

Fig. 5 The solution of the Eq. (32) for $C_1 = 2$ and $C_2 = 0$

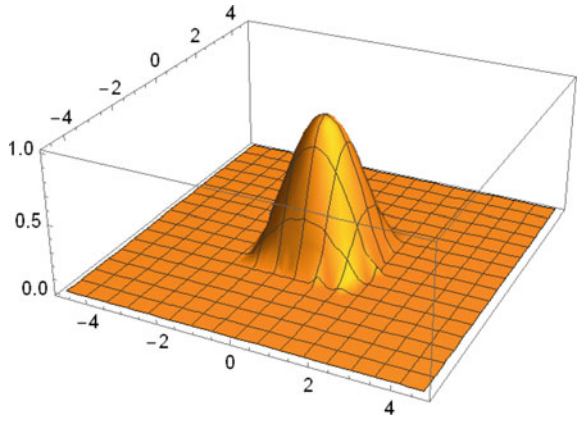

Fig. 6 Initial conditions of Eq. (25) presented in (33)

Model properties had been set to:

- $t \in (0, 15)$,
- $x \in (-5\pi, 5\pi)$,
- $y \in (-5\pi, 5\pi)$,
- approximate a numerical integral to at least 5 digits of accuracy,
- approximate an integral to at least 4 digits of precision
- Boundary and initial conditions had been specified as:

$$\text{for } |y| \le \frac{\pi}{2} \text{ and } |x| \le \frac{\pi}{2} \quad \varphi(0,x,y) = \cos(x)\cos(y) \tag{33}$$

$$\text{for } |y| > \frac{\pi}{2} \quad \text{and} \quad |x| > \frac{\pi}{2} \quad \varphi(0,x,y) = 0$$

$$\varphi(t,\pm 5\pi,y) = 0 \quad \text{and} \quad \varphi(t,x,\pm 5\pi) = 0 \tag{34}$$

$$\frac{\partial \varphi(0,x,y)}{\partial t} = 0 \tag{35}$$

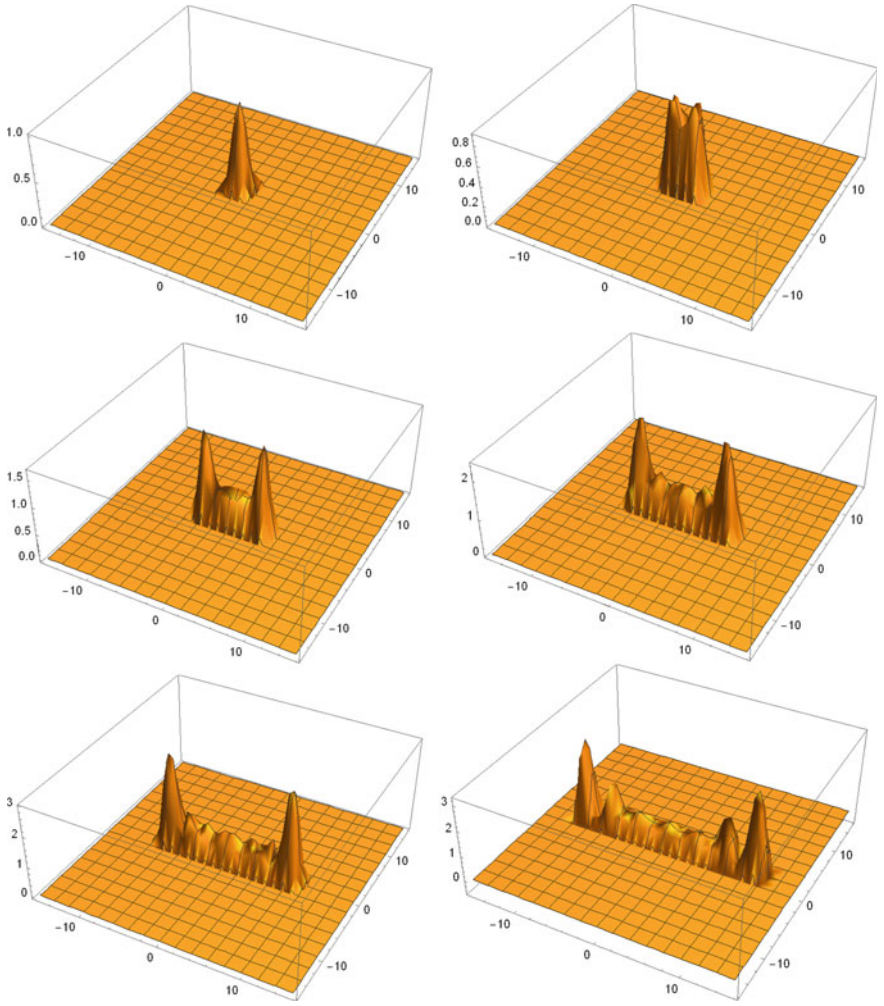

Fig. 7 Approximate solution of Eq. (25). **a** $t = 0$; **b** $t = 2$; **c** $t = 5$; **d** $t = 8$; **e** $t = 11$; **f** $t = 15$

At Fig. 7 presented function $\varphi(t, x, y)$ which is approximate solution of Eq. (25) to the conditions (33)–(35).

Approximate solution of Eq. (25) is a self-sustaining isolated wave caused by nonlinear effects occurring in the material, where this wave is spreading. Noting the fact that this is solution of nonlinear partial differential equation and it is of permanent form this solution can be named two-dimensional soliton. The difference between spreading the wave in two dimensions is caused by different effect on considered beam by horizontally adjacent beams and vertically adjacent beams (Fig. 2).

3 The Conclusions

It has been shown in this paper that medium consisting of an infinite number of electrically charged and interacting beams can be described with nonlinear partial differential equation of second order with respect to time and space. In general case, there are no analytical solutions of this equation, but we can solve it numerically, and we can find their soliton solutions. The resulting equation can be successfully used for the analysis of optical phenomena in the atmosphere, vibration analysis of some crystal lattice, and many other applications. During further research the authors will plan to expand discussed in this paper model from the two-dimensional to three-dimensional space.

References

1. Ryu, S., Yu, W., Stroud, D.: Dynamics of an underdamped josephson junction ladder. Phys. Rev. E **53**, 2190 (1996)
2. Dennison, C., Tang, C.: Phases of Josephson junction ladders. Phys. Rev. Lett. **75**, 3930 (1995)
3. Mazo, J.J., Ustinov, A.V.: The sine-Gordon equation in Josephson-Junction arrays. In: Nonlinear Systems and Complexity, vol. 10, pp. 155–175 (2014)
4. Trias, E., Mazo, J.J., Brinkman, A., Orlando, T.P.: Discrete breathers in Josephson ladders. Physica D **156**, 98–138 (2001)
5. Wirowski, A.: The non-linear modeling of the rotational vibrations of the electrically charged cloud of the ice crystals. Open J. Math. Model. **1**(2), 46–57 (2013). doi:10.12966/ojmmo.05.05.2013
6. Wirowski, A.: Modelling of the phenomenon known as "the miracle of the Sun" as the reflection of light from ice crystals oscillating synchronously. J. Modern Phys. **3**(3), 282–289 (2012). doi:10.4236/jmp.2012.33040
7. Wirowski, A.: The dynamic behavior of the electrically charged cloud of the ice crystals. Appl. Math. Phys. **2**(1), 19–26 (2014)
8. Vepa, R.: Dynamics of Smart Structures. Wiley (2010)
9. Thomas, J.W.: Numerical Partial Differental Equations—Finite Difference Methods, vol. 1. Springer (1995)
10. Whitham, G.B.: Linear and Nonlinear Waves. Wiley (1974)

Numerical Model of Femur Part

Wiktoria Wojnicz, Henryk Olszewski, Krzysztof Lipiński and Edmund Wittbrodt

Abstract The aim of the study is to create a new more accurate method of femur part modelling by using the finite element method. According to this new method, a femur part is treated as a complex structure composed of trabecular bone (internal part) and cortical bone (external part). The internal part is modelled as a scaffold, thus the external part is modelled as a coat (i.e. covering). Applying the programme ABAQUS, there were created four numerical models of trabecular femur part (regular shell bar-connected scaffold, regular solid bar-connected scaffold, irregular shell bar-connected scaffold, irregular solid bar-connected scaffold) and four numerical models of femur part composed of trabecular and cortical bone areas (regular shell bar-connected scaffold covered by shell coat, regular solid bar-connected scaffold covered by solid coat, irregular shell bar-connected scaffold covered by shell coat, irregular solid bar-connected scaffold covered by solid coat). Applying similar boundary conditions and similar load affected by muscles' forces and external moments, presented numerical models had been tested. Considering stress (strain) fields obtained from numerical researches of presented models, there were drawn conclusions about influence of material nonlinearity and geometry nonlinearity and application of proposed new method in clinical biomechanics.

W. Wojnicz (✉) · H. Olszewski · K. Lipiński · E. Wittbrodt
Mechanical Engineering Faculty, Gdansk University of Technology,
Str. G. Narutowicza 11/12, 80-233 Gdansk, Poland
e-mail: wiktoria.wojnicz@pg.gda.pl

H. Olszewski
e-mail: holszewsk@pg.gda.pl

K. Lipiński
e-mail: klipinsk@pg.gda.pl

E. Wittbrodt
e-mail: e.wittbrodt@pg.gda.pl

J. Awrejcewicz (ed.), *Dynamical Systems: Modelling*, Springer Proceedings
in Mathematics & Statistics 181, DOI 10.1007/978-3-319-42402-6_34

1 Introduction

A long bone of the human is composed of two types of bone tissue: cortical tissue (more dense structure) and trabecular tissue (less dense structure). The cortical tissue is composed of roughly cylindrical laminas that form a bone cortex. The trabecular tissue is composed of bone trabeculae formed a non-regular spatial scaffold (porous network) named spongy bone. This trabecular tissue is only located inside of a long bone epiphysis. From the mechanical point of view the cortical tissue and the trabecular tissue are nonlinear anisotropic materials. Moreover, each of these tissues is a nonlinear (irregular) geometric structure, which is formed through modelling and remodelling processes caused by an external load and adaptation of the human body skeletal system to this load.

To predict behaviour of the chosen skeletal fragment there are applied two approaches. The first approach treats a chosen bone fragment as a solid structure [7, 8]. The second approach models' behaviour of very small part of cortical tissue or trabecular tissue [2, 3]. Each of these approaches can be solved by applied principles of continuum mechanics and finite element method (FEM). Behaviour of the chosen skeletal fragment is estimated as a stress (strain) field that depends on: initial state of bone tissue, boundary conditions (BC), load, material properties, geometric structure and mesh model. It is worth noticing that meshing of chosen bone fragment is problematical due to its irregular structure since it causes obtainment a mesh with errors nodes (i.e. numerical nonlinearity).

The aim of the study is to create a new more accurate method of femur part modelling by using FEM approach. According to this new method, a femur part is treated as a complex structure composed of trabecular bone (internal part) and cortical bone (external part). The internal part is modelled as a scaffold, thus the external part is modelled as a coat (i.e. covering).

2 Modelling Principles

Numerical models of chosen skeletal parts were created by using the programme ABAQUS and the approach described in [6, 9]. It was assumed that a bone tissue is an isotropic material described by the Young modulus E equals 10 GPa and the Poisson's ratio ν equals 0.25) [1, 5].

Chosen skeletal parts were treated as shell structures (shell models) and solid structures (solid models). To model shell structures the quadratic triangular elements STRI65 were used. The STRI65 element is a 6-node triangular thin shell with thickness equals 0.2 mm (each node is described by five degrees of freedom). Also, this element imposes the Kirchhoff constraint numerically. To model solid structures the quadratic tetrahedral elements C3D10H were used. The C3D10H element is a 10-node quadratic hybrid tetrahedron with constant pressure (each node is described by three translation degrees of freedom).

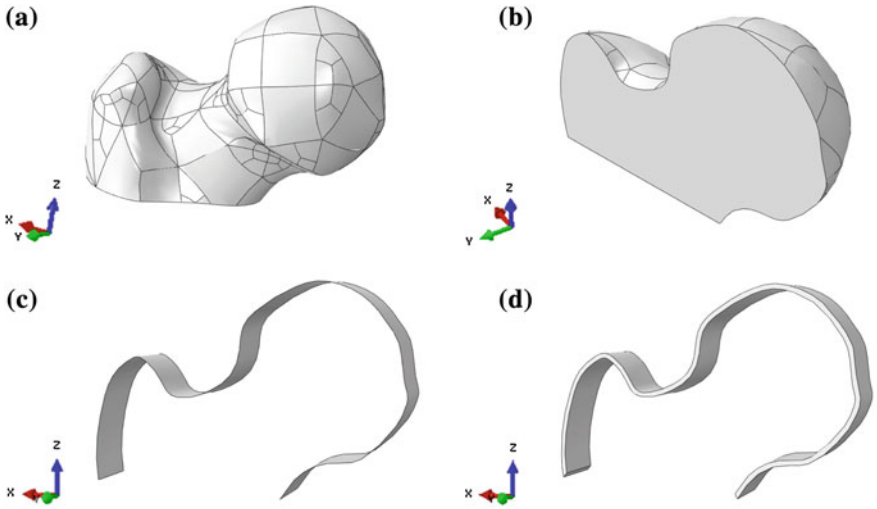

Fig. 1 **a** Solid model of femur upper part; **b** Solid model of half of femur upper part obtained from cutting in frontal plane; **c** Shell model of cortical bone (its thickness equals 0.2 mm); **d** Solid model of cortical bone (its thickness equals 0.5 mm)

To model a trabecular femur part there were created two types of scaffolds: regular scaffold structure and irregular scaffold structure. The first one was created according to approach described in [6]. The second one was created by taking into consideration a real trabecular structure, which is composed of bearing components (trabeculae) arranged along to the mechanical principal loading directions.
A femur part composed of trabecular and cortical bone areas was modelled as a connection of cortical bone model and trabecular scaffold model. To avoid problems caused by nonlinear geometry of modelled structure and limited computer capacity, a segment of this connection were taken into consideration. This segment is composed of cortical stripe (cortical bone model) and one part of trabecular scaffold (trabecular bone model). The cortical stripe was obtained by using outline of half of solid model of femur upper part (Fig. 1a, b). This cortical stripe was modelled as a shell model and solid model (Fig. 1c, d).

3 Numerical Models of Trabecular Femur Part

To model behaviour of trabecular bone of femur part there were created four numerical models: regular shell bar-connected scaffold (A1), regular solid bar-connected scaffold (B1), irregular shell bar-connected scaffold (A2) and irregular solid bar-connected scaffold (B2).

3.1 Regular Shell Bar-Connected Scaffold (A1)

The FEM model of regular shell bar-connected scaffold (A1) is composed of 49217 nodes and 26136 elements of STRI65 type (Fig. 2).

3.2 Regular Solid Bar-Connected Scaffold (B1)

The FEM model of regular solid bar-connected scaffold (B1) is composed of 94311 nodes and 58342 elements of C3D10H type (Fig. 3).

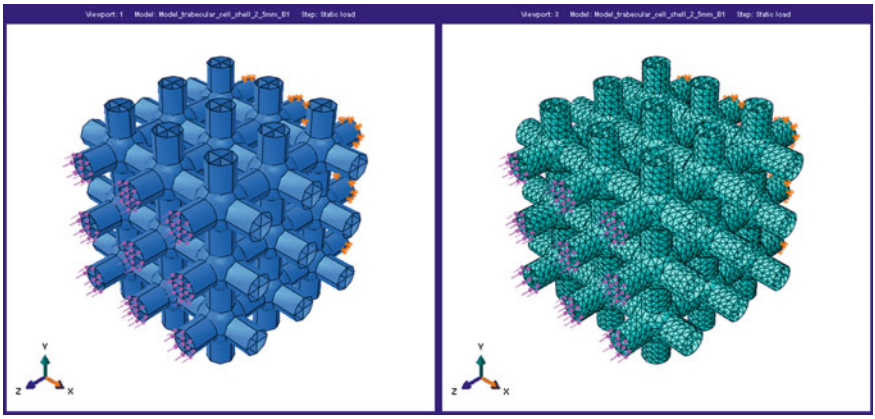

Fig. 2 Model of regular shell bar-connected scaffold (A1)

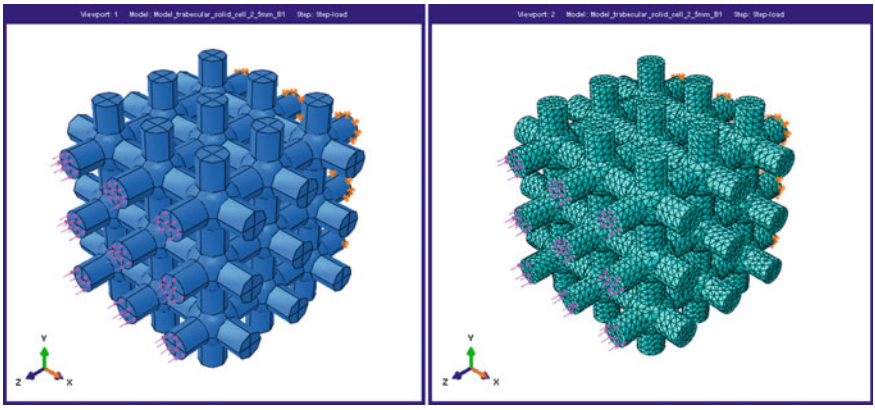

Fig. 3 Model of regular solid bar-connected scaffold (B1)

3.3 *Irregular Shell Bar-Connected Scaffold (A2)*

The FEM model of irregular shell bar-connected scaffold (A2) is composed of 48941 nodes and 23933 elements of STRI65 type (Fig. 4).

3.4 *Irregular Solid Bar-Connected Scaffold (B2)*

The FEM model of regular solid bar-connected scaffold (B2) is composed of 77085 nodes and 48119 elements of C3D10H type (Fig. 5).

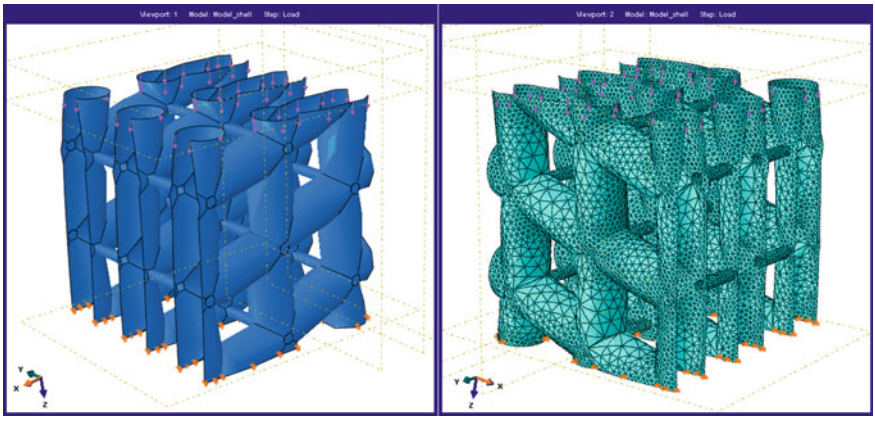

Fig. 4 Model of irregular shell bar-connected scaffold (A2)

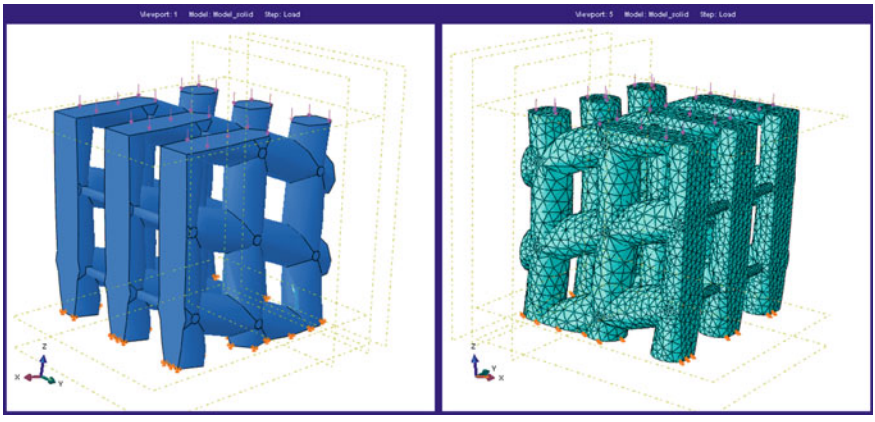

Fig. 5 Model of irregular solid bar-connected scaffold (B2)

4 Numerical Models of Femur Part Composed of Trabecular and Cortical Bone Areas

To model behaviour of femur part composed of trabecular and cortical bone areas there were created four numerical models: regular shell bar-connected scaffold covered by shell coat (C1A1) (type 1 and type 2), regular solid bar-connected scaffold covered by solid coat (C2B1) (type 1 and type 2), irregular shell bar-connected scaffold covered by shell coat (C3A2) and irregular solid bar-connected scaffold covered by solid coat (C3B2).

4.1 Regular Shell Bar-Connected Scaffold Covered by Shell Coat (C1A1)

The type 1 FEM model of regular shell bar-connected scaffold covered by shell coat (C1A1, type 1) is composed of 28681 nodes and 15902 elements of STRI65 type (Fig. 6). The type 2 FEM model of regular shell bar-connected scaffold covered by shell coat (C1A1, type 2) is composed of 44814 nodes and 24683 elements of STRI65 type (Fig. 7).

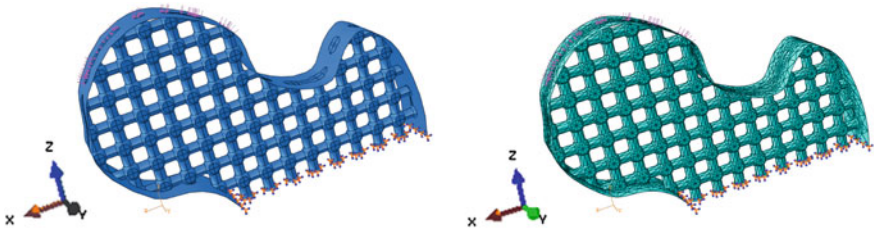

Fig. 6 The model of regular shell bar-connected scaffold covered by shell coat (C1A1, type 1)

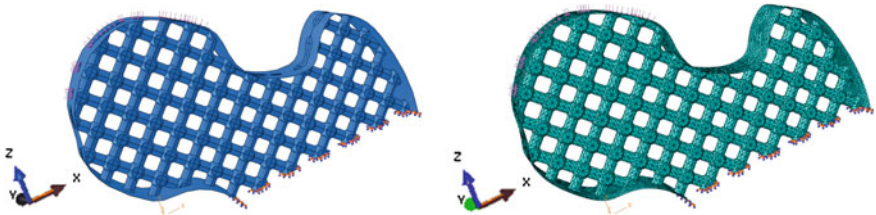

Fig. 7 The model of regular shell bar-connected scaffold covered by shell coat (C1A1, type 2)

4.2 Regular Solid Bar-Connected Scaffold Covered by Solid Coat (C2B1)

The type 1 FEM model of regular solid bar-connected scaffold covered by solid coat (C2B1, type 1) is composed of 40564 nodes and 19733 elements of C3D10H type (Fig. 8). The type 2 FEM model of regular solid bar-connected scaffold covered by solid coat (C2B1, type 2) is composed of 79869 nodes and 43428 elements of C3D10H type (Fig. 9).

4.3 Irregular Shell Bar-Connected Scaffold Covered by Shell Coat (C3A2)

The FEM model of irregular shell bar-connected scaffold covered by shell coat (C3A2) is composed of 28845 nodes and 14619 elements of STRI65 type (Fig. 10).

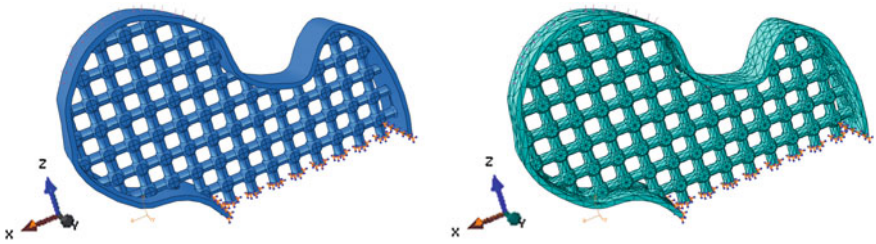

Fig. 8 The model of regular solid bar-connected scaffold covered by solid coat (C2B1, type 1)

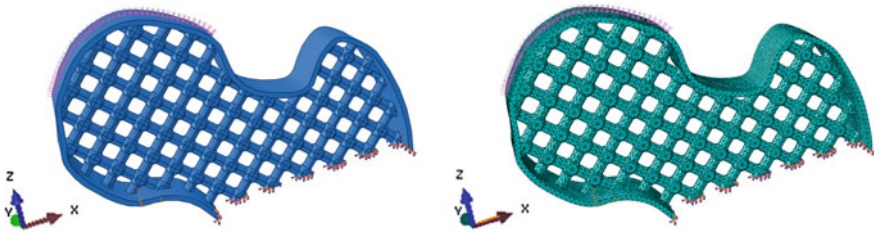

Fig. 9 The model of regular solid bar-connected scaffold covered by solid coat (C2B1, type 2)

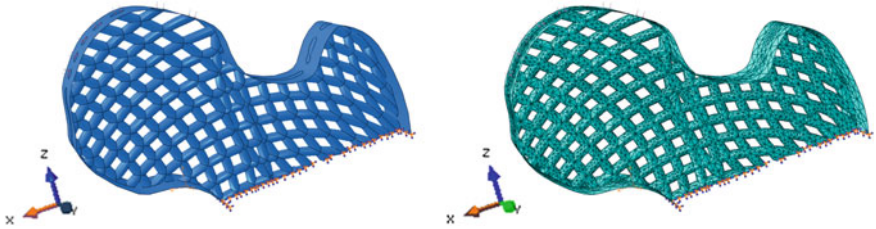

Fig. 10 The model of irregular shell bar-connected scaffold covered by shell coat (C3A2)

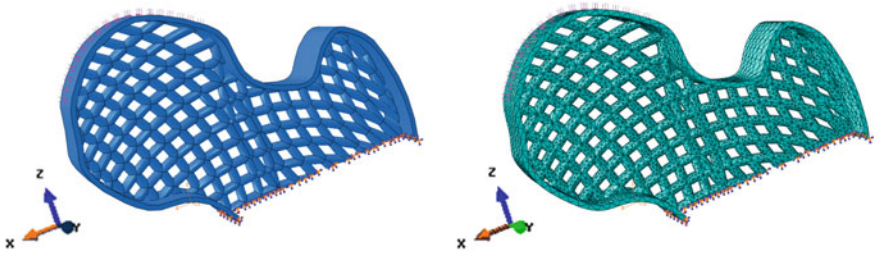

Fig. 11 The model of irregular solid bar-connected scaffold covered by solid coat (C3B2)

4.4 Irregular Solid Bar-Connected Scaffold Covered by Solid Coat (C3B2)

The FEM model of irregular solid bar-connected scaffold covered by solid coat (C3B2) is composed of 81996 nodes and 48076 elements of type C3D10 (Fig. 11).

5 Discussion

Applying the programme ABAQUS, proposed four numerical models of trabecular femur part (part 3) and four numerical models of femur part composed of trabecular and cortical bone areas (part 4) were examined. Using zero initial conditions, similar boundary conditions and similar external load these models had been tested. Numerical simulation results of trabecular femur part models are presented in the Table 1, thus numerical results of femur part models—Table 2.

Applying pinned boundary conditions, each model of trabecular femur part was loaded by compress force equals 1 N (this value was associated with the unit load). Obtained deformed structures are shown in the Figs. 12, 13, 14 and 15.

Table 1 Numerical simulation results of models of trabecular femur part

FEM model	Maximum mises stress, Pa	Maximum displacement, m	Load	BC
A1	1.660×10^{9}	5.123×10^{-4}	100888 Pa	Pinned u1 = u2 = u3 = 0
B1	2.033×10^{5}	8.633×10^{-8}	123335 Pa	
A2	1.771×10^{6}	2.402×10^{-7}	36 N/m	
B2	2.028×10^{6}	1.992×10^{-7}	123335 Pa	

Table 2 Numerical simulation results of models of femur part composed of trabecular and cortical bone areas

FEM model	Maximum mises stress, GPa	Maximum displacement, mm	Load, MPa	BC
C1A1 type 1	1.086	1.587	80	Encastre u1 = u2 = u3 = 0 ur1 = ur2 = ur3 = 0
C1A1 type 2	3.378	2.474		
C2B1 type 1	2.648	2.623		
C2B1 type 2	2.785	2.160		
C3A2	0.908	1.188		
C3B2	4.394	3.502		

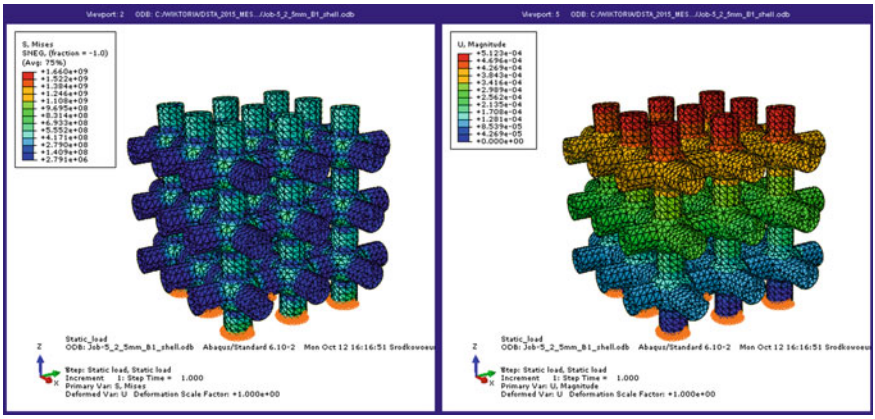

Fig. 12 Results of A1 model: stress field (*left*) and strain field (*right*)

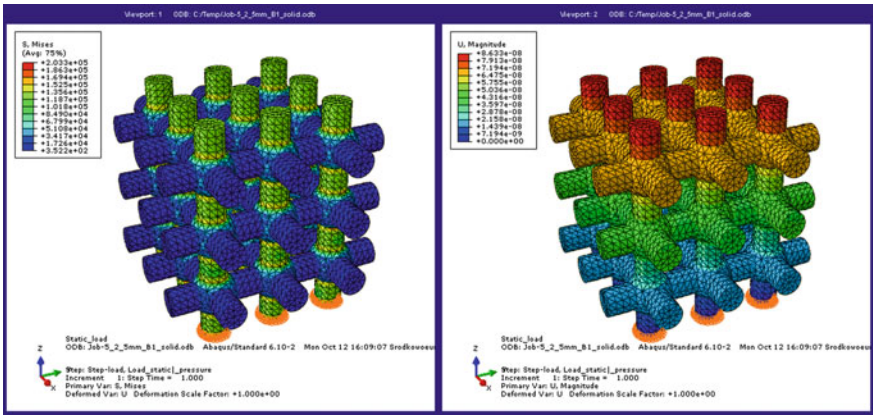

Fig. 13 Results of B1 model: stress field (*left*) and strain field (*right*)

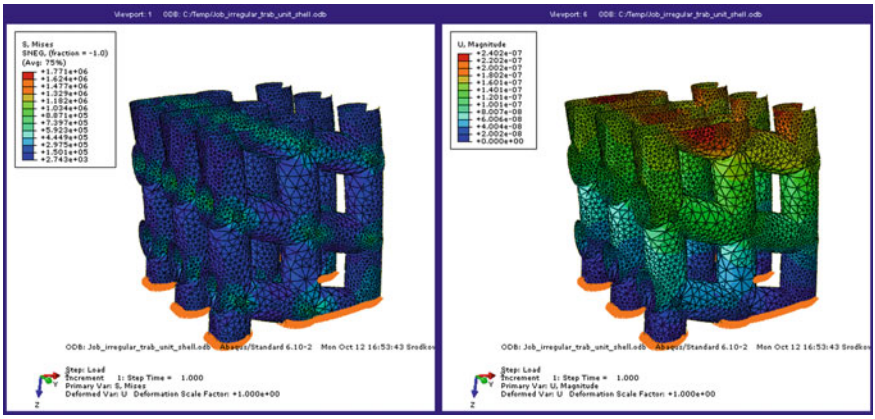

Fig. 14 Results of A2 model: stress field (*left*) and strain field (*right*)

Applying encastre (fixed) boundary conditions, each model of femur part (composed of trabecular and cortical bone areas) was loaded by compress pressure equals 80 MPa that results from one-legged load acting on the femur head [4]. Obtained deformed structures are shown in the Figs. 16, 17, 18, 19, 20 and 21.

Analysing results of models of trabecular femur part (Table 1), one can conclude that the less stiff structure is a regular shell bar-connected scaffold (A1) (because it is the most deformed structure). On the other hand, the most stiff structure is a regular solid bar-connected scaffold (B1) (because it is the less deformed structure).

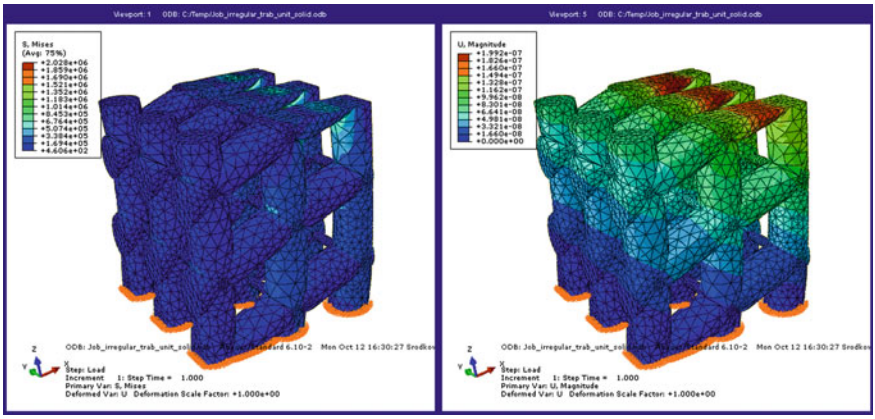

Fig. 15 Results of B2 model: stress field (*left*) and strain field (*right*)

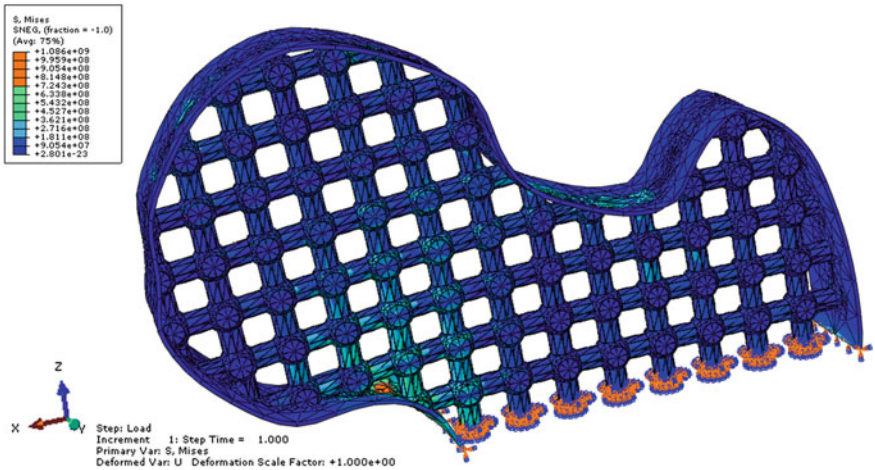

Fig. 16 Results of stress field of C1A1 model (type 1)

It is worth noticing that two irregular scaffolds (irregular shell bar-connected scaffold (A2) and irregular solid bar-connected scaffold (B2)) deform in the similar way.

Analysing results of models femur part (composed of trabecular and cortical bone areas) (Table 2), one can conclude that the less stiff structure (i.e. the most deformed structure) is an irregular solid bar-connected scaffold covered by solid

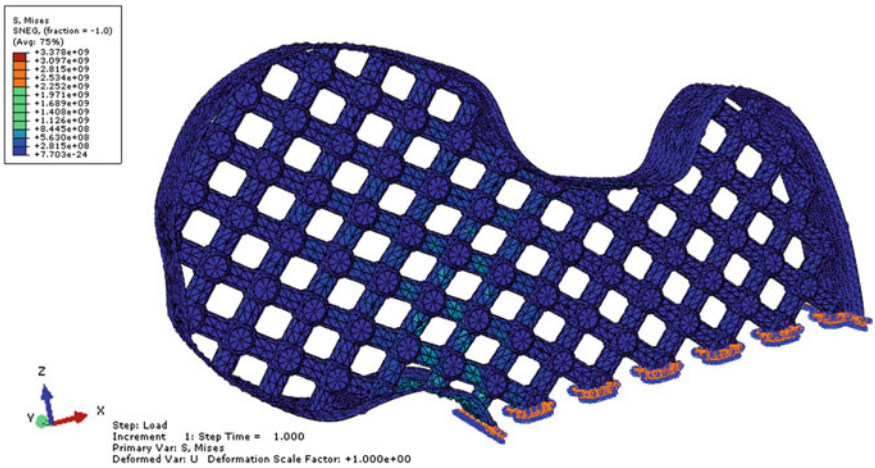

Fig. 17 Results of stress field of C1A1 model (type 2)

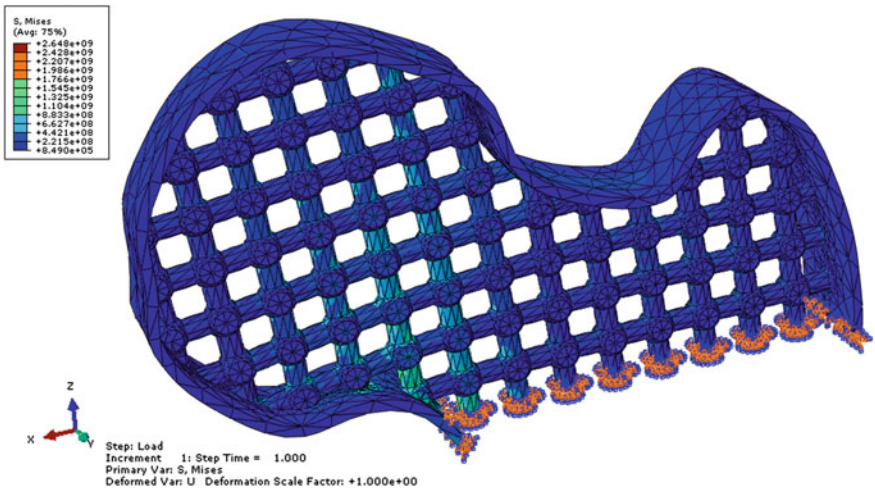

Fig. 18 Results of stress field of C2B1 model (type 1)

coat (C3B2), thus the most stiff structure (i.e. the less deformed structure) is an irregular shell bar-connected scaffold covered by shell coat (C3A2). On the other hand, deformations of the regular structures are similar. However, arrangement of trabecular part scaffold at the different angles (for the type 1 this angle equals 0°, thus for the type 2 this angle equals 45°) caused that:

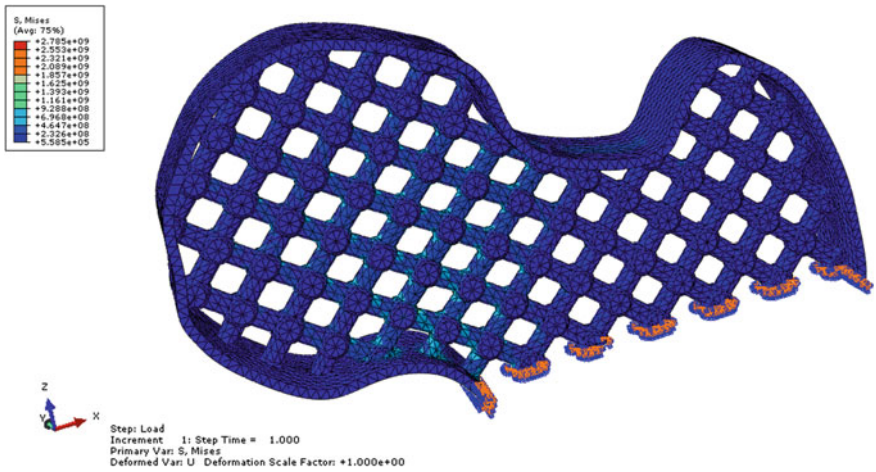

Fig. 19 Results of stress field of C2B1 model (type 2)

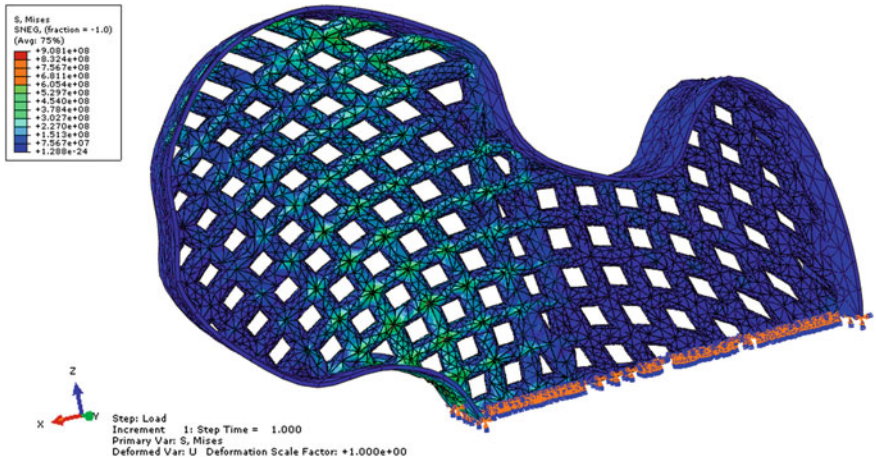

Fig. 20 Results of stress field of C3A2 model

1. the type 1 of regular shell bar-connected scaffold covered by shell coat (C1A1) is more stiff comparing with the type 2 of this C1A1 scaffold;
2. the type 1 of regular solid bar-connected scaffold covered by solid coat (C2B1) is less stiff comparing with the type 2 of this C2B1 scaffold.

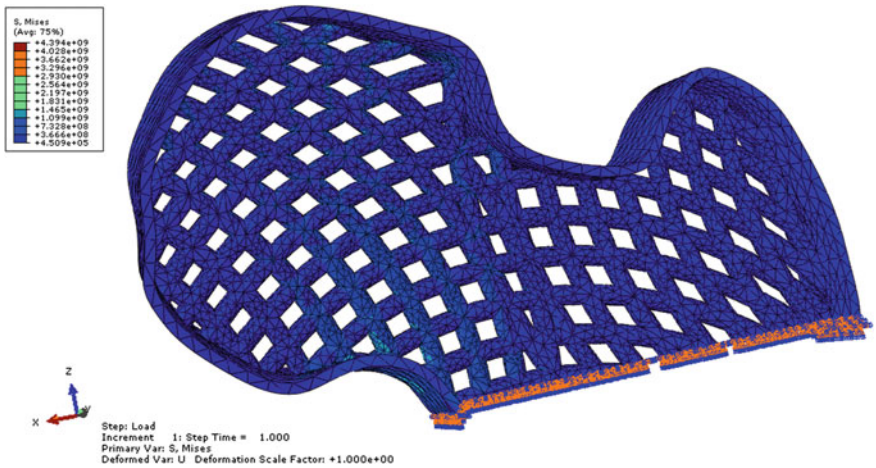

Fig. 21 Results of stress field of C3B2 model

6 Conclusions

The purpose of the paper is to present a new more accurate method of femur part modelling and present new FEM models of: (1) femur trabecular part; (2) femur part composed of trabecular and cortical bone areas. The femur trabecular part is modelled as a spatial scaffold. The femur part (composed of trabecular and cortical bone areas) is modelled as a connection of cortical stripe (cortical bone model) and one part of trabecular scaffold (trabecular bone model). This simplifying is mainly caused by a limited computer capacity since FEM models have many degrees of freedom.

Assuming that trabecular bone is an isotropic material, numerical models of femur trabecular part and models of femur part are implemented as

1. shell models and solid models;
2. regular structure models and irregular structure models.

It is worth noticing that an irregular structure of trabecular bone is created on the base of real trabecular network.

Considering stress (strain) fields obtained from numerical researches, we conclude that

1. irregular structure is more resistance to deliver external spatial load than the regular structure;
2. shell models are more suitable to describe a behaviour of bone tissue since this tissue is modelled as thin-walled and lightweight structures (like bone tissue);
3. modelling of irregular geometric structure causes an appearance of numerical nonlinearity (i.e. mesh model with errors);

4. modelling of chosen bone fragment and taking into consideration its material nonlinearity, geometric nonlinearity and numerical nonlinearity results to create a very complex numerical model, which solving cannot be achieved.

Numerical models proposed in this paper can be used to growing artificial bone fragments by using 3D printing. After that, by applying methods of bioengineering, one can grow an artificial bone tissue, which spatial structure will be function as a real bone tissue. Moreover, proposed numerical models can be applied to study implant-bone phenomena occurring during artificial joint wearing.

Acknowledgments The numerical simulations had been performed using computers of "Centrum Informatyczne Trójmiejskiej Akademickiej Sieci Komputerowej" in Gdansk, Poland.

References

1. Carnelli, D., Lucchini, R., Ponzonu, M., Contro, R., Vena, P.: Nanoindentation testing and finite element simulations of cortical bone allowing for anisotropic elastic and inelastic mechanical response. J. Biomech. **44**, 1852–1858 (2011)
2. Ilic, S., Hackl, K., Gilbert, R.: Application of the multiscale FEM to the modeling of cancellous bone. Biomech. Model. Mechanobiol. **9**, 87–102 (2010)
3. Kadir, M.R., Syahrom, A., Öchsner, A.: Finite element analysis of idealised unit cell cancellous structure based on morphological indices of cancellous bone. Med. Biol. Eng. Comput. **48**, 497–505 (2010)
4. Kwon, J.Y., Naito, H., Matsumoto, T., Tanaka, M.: Osteocyte apoptosis-induced bone resorption in nechanical remodeling dimulation—computational model for trabecular bone structure. In: Medicine—Apoptosis and Medicine, pp. 25–46 (2012)
5. Lievers, W.B., Waldman, S.D., Pilkey, A.K.: Minimizing specimen length in elastic testing of end-constrained cancellous bone. J. Mech. Behav. Biomed. Mater. **3**, 22–30 (2013)
6. Olszewski, H., Wojnicz, W., Wittbrodt, E.: Method of skeletal system modelling. The Archive of Mechanical Engineering, vol. LX (3), pp. 335–346 Polish Academy of Sciences (2013)
7. Sanz-Herrera, J.A., Garcia-Aznar, J.M., Doblare, M.: Micro-macro numerical model ling of bone regeneration in tissue engineering. Comput. Methods Appl. Mech. Eng. **197**, 3092–3107 (2008)
8. Tezuka, K., Wada, Y., Takahashi, A.: Computer-simulated bone architecture in a simple bone-remodelling model based on a reaction-diffusion system. J. Bone Miner. Metab. **23**, 1–7 (2005)
9. Wojnicz, W., Olszewski, H., Wittbrodt, E.: Chosen aspects of skeletal systems modeling—numerical solid and shell models of femur part. Shell Struct.—Theory Appl. **3**, 359–362 (2014)

FEA-Based Design of Experiment for the Damping Determination of Thermoplastic-Rubber Compounds

Mario Wuehrl, Matthias Klaerner and Lothar Kroll

Abstract In terms of recycling, polymer blends with rubber crumb filler material offer a high potential in adjusting both static and dynamic material properties. While the influence on stiffness and strength is considerably treated in literature, there are minor examinations on the damping of such compounds. Combining the properties of thermoplastics and elastomers, these materials tend to show a wide range of nonlinear influences such as frequency, temperature and amplitude dependency. Especially the amplitude dependency is critical due to the transferability of the results between different stress states, loads and part geometries as well as the applicability in FEA simulations. In detail, the average strain energy per volume has been chosen as a physical measure for the amplitude dependency. This study provides extensive results of the influence of recycled rubber crumb filler on the stiffness and damping of Polyamide 6. A FE-based experimental design was developed to assure the comparability of the strain energy related dynamic properties. For the different testing conditions the average strain energy is not directly measurable and thus needs to be determined numerically. Cyclic tension and bending in a dynamic mechanical analyses, free decay of cantilever beams as well as modal analysis of plates have been analysed experimentally and numerically for validation. In addition, the boundary conditions have been varied to generate different stress states in the specimens. The results show perspectives and limits of the transferability of the results.

M. Wuehrl (✉) · M. Klaerner · L. Kroll
Institut für Strukturleichtbau, Technische Universität Chemnitz,
Reichenhainer Str. 31-33, 09126 Chemnitz, Germany
e-mail: mario.wuehrl@mb.tu-chemnitz.de

M. Klaerner
e-mail: matthias.klaerner@mb.tu-chemnitz.de

L. Kroll
e-mail: lothar.kroll@mb.tu-chemnitz.de

J. Awrejcewicz (ed.), *Dynamical Systems: Modelling*, Springer Proceedings
in Mathematics & Statistics 181, DOI 10.1007/978-3-319-42402-6_35

1 Introduction

The insolubility and infusibility of elastomers make their recycling process difficult. According to The European Tyre and Rubber manufacturers' association ~4.67 million tonnes of tyres were 2013 produced in the EU, which makes it the biggest application for elastomers [3]. Due to the mentioned impossibility of direct material recycling of elastomers, the most common way today of material recycling for used tyres is granulation [3]. The result of this recycling is referred to as rubber crumb or specifically ground tyre rubber (GTR) in literature [4]. The most cost-effective method of reusing the grinded rubber is to blend it with polymers.

A large overview of the literature about rubber-crumb-polymer blends is given by Karger-Kocsis et al. [5]. While this overview mainly focuses on static characteristics such as stiffness and strength, the investigation on the effect of GTR on dynamic properties of polymers stays untreated. On the one hand, some prior studies investigate the effect of GTR on dynamic and acoustic properties of ethylene vinyl acetate [9], styrene–butadiene–styrene copolymer compound [10] and high-density polyethylene [6]. On the other hand, the influence of powdered rubber on Nylon 6 (Polyamid 6, PA6) was investigated considering the blend's crystallisation behaviour and its mechanical properties [2]. However, no studies of a blend consisting of PA6 and unmodified GTR considering its dynamic mechanical properties have been found in literature. Although, the mentioned articles show an increase on damping raising the polymers suitability for acoustic applications. Therefore, PA6 with different fractions of GTR were examined in this study.

2 Experimental Damping Determination

Rubber, in general as well as the used recycled rubber powder, has viscoelastic properties. Thus, the material remains in a constant shape after deformation while it absorbs mechanical energy [8]. This leads to the phase angle δ which represents the phase displacement of stress and strain in the material under sinusoidal load. When it comes to the determination of material damping represented by $\tan(\delta)$, which is equal to the loss factor η, [8] different methods are used.

2.1 Classification and Comparability of Damping Measuring Methods

These methods can be sorted by different criteria. The first criterion to distinguish different dynamic mechanical tests is the excitation. First, the specimen can be either analysed while it performs a free vibration with its natural frequency after an initial excitation or the vibration is under continuous excitation with a forced frequency.

Secondly, damping determination can be performed under different mechanical stress states (bending, torsion, tension, compression, shear) in the specimen.

The third distinguished criterion is the specimen geometry. The last criterion to mention by which test methods can be sorted is the load type. For dynamic tension tests a preload is common, to prevent buckling, which leads to a pulsating force. In contrary, the free vibration testing has to be performed in alternating form.

The damping of polymers is dependent on frequency and amplitude [7]. The displacement and respectively the applied force of different testing methods cannot be compared directly. For example, the same amplitude in free vibration bending as in longitudinal tension leads to different stresses and stress distributions in the material.

The above mentioned damping values $\tan(\delta)$ and η of a material can be written as [1]

$$\tan(\delta) = \eta = \pi \frac{\Delta U}{U}. \tag{1}$$

With U representing the maximum stored strain energy and ΔU the energy dissipation per cycle, material damping is an energy related quantity. Therefore, the strain energy was used in this study to achieve comparability between the different tests. The strain energy itself cannot be measured directly and was thus calculated in an FE simulation (see Sect. 3.1) of the following tests.

Experimental Designs in This Study

For this study mainly two different one dimensional testing methods were used. The first testing method was a dynamic mechanical analysis (DMA) under tension, which was performed on an Instron ElectroPuls E10000. The applied force was recorded by a 250 N force sensor.

The second test method is the free vibration of cantilever beams. The measuring setup is shown in Fig. 1 and consists of:

- A Laser-Doppler-vibrometer (out-of-plane) with a single-point sensor head Polytech OFV-503 (1)
- a specimen holder (2) with force sensor (3)
- a specimen (4) and
- an excitation coil (5).

As additional hardware a modular vibrometer controller Polytech OFV-5000 with the digital broadband velocity decoder VD-09 was used. This hardware is connected via a PXI 5922 A-D-converter from National Instruments to a PC, where data processing is realised within National Instruments LabVIEW Software.

The cantilever beam specimens have been excited harmonically in their first natural frequency until a steady state vibration occurred. Then, the signal was interrupted for measuring the decay curve. The excitation is realised inductively to avoid influences of a contact stiffness. As the polymer is non-magnetic, a thin piece of sheet metal with negligible mass was glued on the specimen.

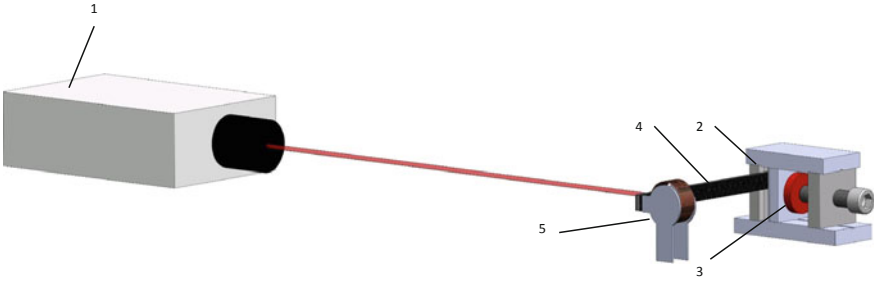

Fig. 1 Setup of experiment for free decay of cantilever beams

To avoid the influence of temperature on the damping, all tests were carried out at room temperature (22 °C). It is well known that PA6 is highly hygroscopic, which is the reason why all specimens were dehumidified prior to the experiments.

The frequency of the free vibration test can be calculated with:

$$\omega_i = \lambda_i^2 \sqrt{\frac{EH^2}{12\rho L^4}} = 2\pi f_i \tag{2}$$

the YOUNG modulus E, the vibration length L, density ρ and the height H of a rectangular cross section. Using the first solution $\lambda_1 \approx 1.8751$ of the frequency equation of cantilever beams

$$1 + \cos\lambda \cdot \cosh\lambda = 0 \tag{3}$$

the vibrating frequency can be calculated.

Due to the frequency dependency of the damping both test methods have been performed at equal material specific frequencies.

3 Strain Energy Based Experimental Designs

As already mentioned in Sect. 2.1 the strain energy was determined by a FE simulation of the free decay of cantilever beams as well as of the dynamic tension test. Below, the details of the used models are given.

3.1 FEA Models

The experiments were modelled using a beam with twenty-node brick elements with reduced integration (C3D20R). The model consisted of ~1600 elements with ~6200 nodes. The dimensions of the volume were chosen according to the specimens used

Table 1 Static properties of blends in this study

Blend fractions in m%	ρ in g/cm^3	YOUNG's modulus in MPa
100 PA6	1.130	1712
90PA6+10GTR	1.140	1703
70PA6+30GTR	1.146	1103
50PA6+50GTR	1.154	518

in the experimental damping determinations. The different load cases were modelled with force excitation. All calculations were done using Abaqus 6.14-1. The elastic material characteristics were evaluated using a static tension test according to the standard DIN EN ISO 527-1 and a density measurement according to standard DIN EN ISO 1183-1. The determined values can be found in Table 1.

3.2 Strain Energy Determination

The strain energy shall be used in this study to gain comparability between the different experimental setups. Thus, it has to be determined from the solved FE models of the experiments, which was achieved by a Python post processing script calculating the summation of the strain energy over all N elements by

$$U_{ij} = \sum_{n=1}^{N} \frac{1}{2} V_n \sigma_{n_{ij}} \epsilon_{n_{ij}} \; with \; i,j = 1,2,3. \tag{4}$$

For the used 3D elements the strain energy has six components which were summed up to U_{tot}

$$U_{tot} = U_{11} + U_{22} + U_{33} + U_{12} + U_{13} + U_{23}. \tag{5}$$

There, $11, 22, 33$ represent the strain energy in the three normal directions whereas $12, 13, 23$ represent the shear strain energy.

For both tests a FE model with equal volume was used. In this case, the calculated total strain energy is synonymous to the equal strain energy density.

In Sect. 2.1 the different testing methods were classified. One criterion used is the load type (pulsating vs. alternating). Therefore, an algorithm calculating a rectified value for each vibration cycle was developed. For the free vibration test the rectified value can be calculated with

$$U_{rec} = \frac{1}{2} \hat{U}_{tot}. \tag{6}$$

However, for the dynamic tension test with preload the curve of the strain energy is shown in Fig. 2. Clearly, the curve of the tension test is not symmetric at $\frac{\pi}{2}$. Thus,

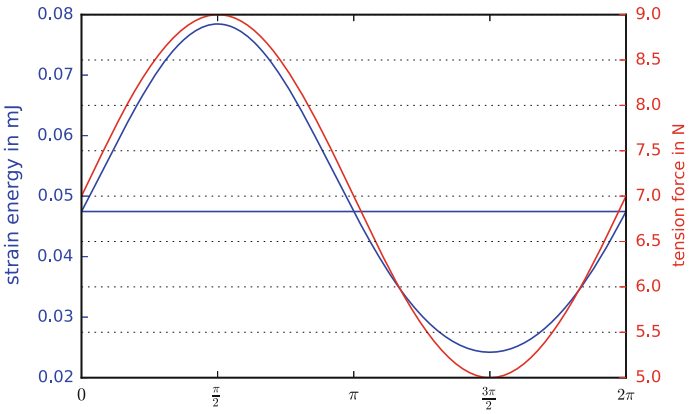

Fig. 2 Strain energy under tension of one vibration cycle

the rectified value cannot be simply calculated but was determined by a BROYDEN-FLETCHER-GOLDFARB-SHANNO optimisation algorithm, which searches for the minimum in

$$\left| \int_0^{\pi} U_{tot}(\varphi) d\varphi - U_{rec} \right| - \left| \int_{\pi}^{2\pi} U_{tot}(\varphi) d\varphi - U_{rec} \right| \rightarrow min(U_{rec}). \tag{7}$$

3.3 *Derived Experimental Designs*

As mentioned in Table 1, the investigated materials differ in their stiffness and density. Thus, different amplitudes for each test had to be used to achieve identical strain energies. In Fig. 3 the influence of the YOUNG's modulus on the determined strain energy under static load is plotted. While the strain energy shows a linear behaviour with displacement excitation, it is highly nonlinear with force excitation. This correlation can be observed for both tests and therefore for both stress distributions, which leads to the assumption that the calculated strain energy as a function of the YOUNG's modulus depends on the excitation form (force vs. displacement) but not on the stress distribution in the material.

Consequently, for neither of the two test methods the amplitude can be constant for all investigated materials. Since the measurement of the cantilever beam is displacement controlled, the displacement amplitude of the experiment increases with decreasing material stiffness. In contrast, the tension test is force controlled and thus the experimental force amplitude has to decrease with the decreasing stiffness of higher elastomer fractions.

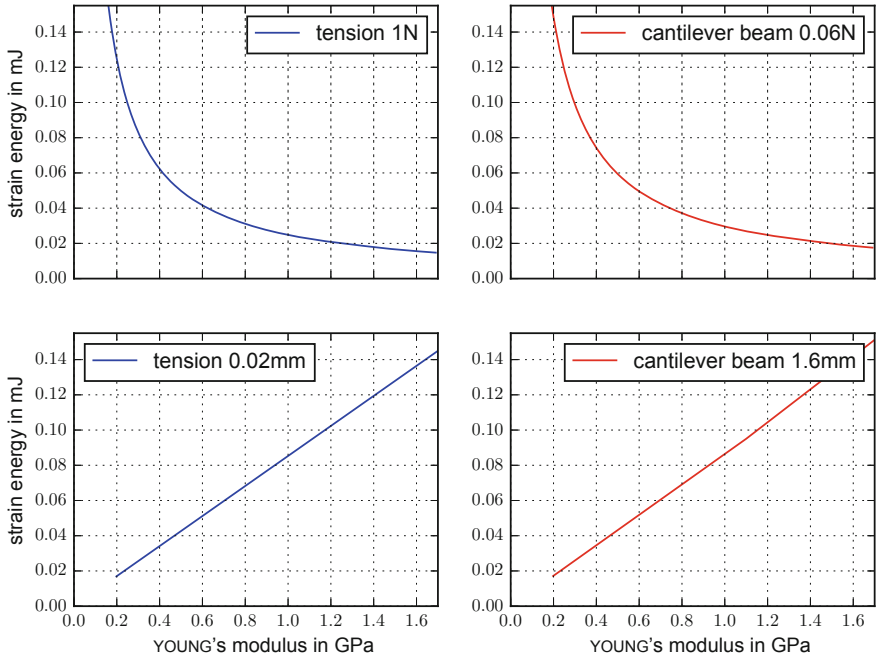

Fig. 3 Influence of the YOUNG's modulus on the strain energy

Table 2 Derived experimental amplitudes

Blend fractions in m%	Amplitudes	
	Cantilever beam in mm	Tension force in N
100 PA6	1.244	6 ± 5
90PA6+10GTR	1.245	6 ± 5
70PA6+30GTR	1.547	5 ± 4
50PA6+50GTR	2.255	3.5 ± 2.5

Considering the numeric strain energy estimates as well as restrictions due to the experimental setups, the maximum strain energy per cycle of all tests has been chosen at 0.045 mJ. This leads to the experimental designs listed in Table 2.

4 Experimental Results

All tests were performed with five specimens of each material. The results of the damping determinations with the above mentioned amplitudes are shown in Fig. 4.

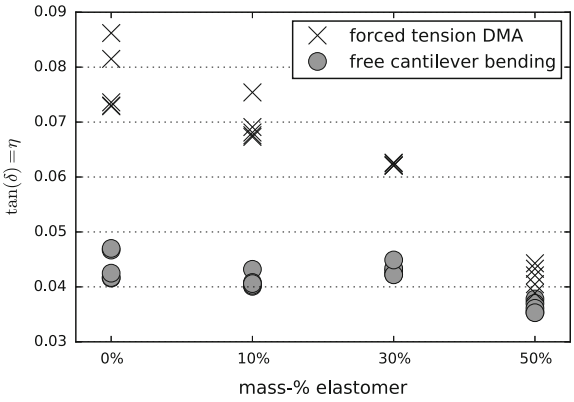

Fig. 4 Experimental results

The results show good correlation for 50 % GTR only, which is the material with the lowest stiffness. The mean difference between the determined damping increases up to 43 % for pure PA6.

The results of the dynamic tension test show a significant influence of the fraction of GTR on the viscoelastic behaviour. However, this cannot be stated for the cantilever beams. This leads to the assumption that either the stress distribution (constant vs. linear over cross section) or the form of excitation (alternating in the cantilever beams versus pulsating under tension) have high influence on the material's dynamic properties. Of course, also a combination of both factors could lead to the observed differences of the evaluated damping.

For both tests the YOUNG's modulus was ascertained. Using the vibration frequency of the cantilever beams the YOUNG's modulus was calculated according to Eq. 2 and compared to the magnitude of the complex modulus of the tension DMA tests.

According to Table 3 all dynamic results drop below the static tests. Within all tests, a small elastomer content of 10 m.% does not affect the stiffness. Higher elastomer fractions up to 50 m.% cause a compliance up to 70 m.% in static tests and up to 50 m.% in all dynamic results. In detail, cantilever beam results are a bit over the tension DMA representing quite similar effects of the elastomer fractions.

It should be stated that there was a time delay of static and dynamic testing past the specimen production. We reasonably assume the material having significant ageing effects after achieving these results.

In prior investigations, different factors of influence were observed. An amplitude dependency has not been proven for the cantilever beams in an investigated range of the initial elongation between 0.5 and 2.26 mm. In contrast, a strong frequency dependency has been observed by the tension DMA with a frequency sweep from 1 to 50 Hz. For all investigated materials the damping drops about 20 % within this frequency range.

Table 3 YOUNG's modulus in MPa measured of the dynamic tests versus static tension tests

Blend fractions in m%	Forced tension DMA	Free cantilever bending	Static tension test
100 PA6	1126	1264	1712
90PA6+10GTR	1131	1264	1703
70PA6+30GTR	899	941	1103
50PA6+50GTR	589	626	518

5 Conclusion and Outlook

Polyamid 6 with different fractions of ground tire rubber was examined in this study regarding the influence on the dynamic properties of the material using two different test methods.

Using a prior FEA simulation of the experiments the overall strain energy was calculated to achieve comparable amplitudes even though the specimens undergo different stress distributions and load cases. Although, the results show good correlation for the highest fraction of GTR, the evaluated damping and elasticity of the other materials still deviate.

Even though the hygroscopic properties of PA6 were taken into account, the materials still show ageing effects that should be covered in further investigations. As comparability for the different stress distributions was not achieved for all materials as well as dynamic properties strongly differ from static properties the material behaviour of GTR-PA6 compounds is under the influence of a large number of factors and has to examined in more detail.

However, the strain energy density should be taken into account as comparative criterion for different stress states and load cases in damping measurements, especially when expecting an amplitude dependency. As this is an energy based property, it enables the transfer of the amplitude dependent damping results to problems of complex geometries and combined load cases.

Acknowledgments The project is funded as a project of industrial research under grant no AiF 17895 BG of the Research Association EFB e.V. financed and supervised by the German Federation of Industrial Research Associations (AiF) within the framework of the program for the promotion of industrial research and development (IGF) by the Federal Ministry for Economical Affairs and Energy (BMWi).

References

1. Adams, R., Maheri, M.: Dynamic flexural properties of anisotropic fibrous composite beams. Compos. Sci. Technol. **50**(4), 497–514 (1994). doi:10.1016/0266-3538(94)90058-2

2. Ding, X., Xu, R., Yu, D., Chen, H., Fan, R.: Effect of ultrafine, fully vulcanized acrylate powdered rubber on the mechanical properties and crystallization behavior of nylon 6. J. Appl. Polymer Sci. **90**(13), 3503–3511 (2003). doi:10.1002/app.12961
3. ETRma: Statistics 2014 (2014). http://goo.gl/9wy6EO
4. Fuhrmann, I., Karger-Kocsis, J.: Use of surface grafted ground tyre rubber (gtr) in pa-6, pbt and pur. KGK-Kautschuk und Gummi Kunststoffe **56**(1-2 SPEC.), 42–48 (2003). Cited By 0
5. Karger-Kocsis, J., Meszaros, L., Barany, T.: Ground tyre rubber (GTR) in thermoplastics, thermosets, and rubbers. J. Mater. Sci. **48**(1), 1–38 (2013). doi:10.1007/s10853-012-6564-2. Cited By 29
6. Kim, J.I., Ryu, S.H., Chang, Y.W.: Mechanical and dynamic mechanical properties of waste rubber powder/HDPE composite. J. Appl. Polymer Sci. **77**(12), 2595–2602 (2000). doi:10.1002/1097-4628(20000919)77:12<2595::AID-APP60>3.0.CO;2-C
7. Nashif, A.D., Jones, D.I.G., Henderson, J.P.: Vibration Damping. Wiley-Interscience (1985)
8. Piersol, A., Paez, T.: Harris' Shock and Vibration Handbook (McGraw-Hill Handbooks), 6th edn. McGraw-Hill Education (2009)
9. Roche, N., Ichchou, M., Salvia, M., Chettah, A.: Dynamic damping properties of thermoplastic elastomers based on eva and recycled ground tire rubber. J. Elastomers Plast. **43**(4), 317–340 (2011). doi:10.1177/0095244311398631
10. Zhu, S.H., Penlidis, A., Tzoganakis, C., Ginzel, E.: Ultrasonic properties and morphology of devulcanized rubber blends. J. Appl. Polymer Sci. **124**(3), 2062–2070 (2012). doi:10.1002/app.35251